CONF-750569

VOLUME IV

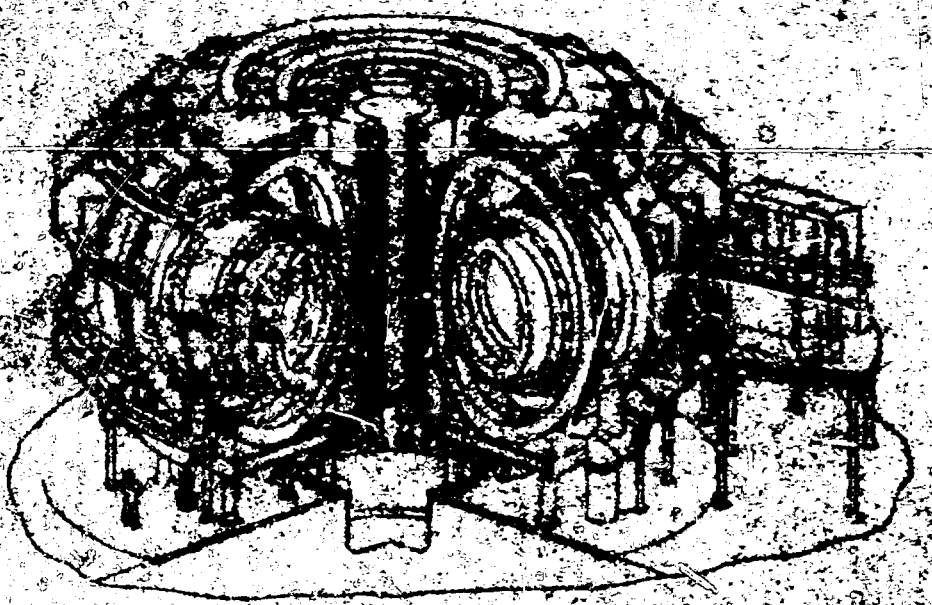

CONF-750989
VOLUME IV

PROCEEDINGS OF THE INTERNATIONAL CONFERENCE HELD AT GATLINBURG TENNESSEE, OCTOBER 1-3, 1975

Sponsored By

OAK RIDGE NATIONAL LABORATORY

UNITED STATES ENERGY RESEARCH AND DEVELOPMENT ADMINISTRATION

AMERICAN NUCLEAR SOCIETY

NUCLEAR METALLURGY COMMITTEE OF AIME

RADIATION EFFECTS *and* TRITIUM TECHNOLOGY *for* FUSION REACTORS

Editors

J. S. WATSON
F. W. WIFFEN

Compiling Editors

JULIA L. BISHOP
BRENDA K. BREEDEN
OAK RIDGE NATIONAL LABORATORY

MARCH, 1976

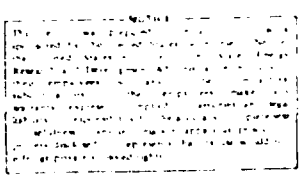

ORGANIZING COMMITTEE

D. Steiner, ORNL, General Chairman
C. J. McHargue, ORNL, Radiation Effects
W. R. Grimes, ORNL, Tritium Technology
J. L. Scott, ORNL, Arrangements

PROGRAM COMMITTEE

Radiation Effects

F. W. Wiffen, ORNL, U.S.A.
J. L. Brimhall, Battelle-Pacific Northwest Laboratory, U.S.A.
B. L. Eyre, AERE-Harwell, U.K.
G. L. Kulcinski, University of Wisconsin, U.S.A.
H. A. Ullmaier, KFA-Jülich, Germany
R. Watanabe, National Research Institute for Metals, Japan
K. M. Zwilsky, Division of Controlled Thermonuclear Research, ERDA, U.S.A.

Tritium Technology

J. S. Watson, ORNL, U.S.A.
F. Coffman, Division of Controlled Thermonuclear Research, ERDA, U.S.A.
E. Hennelly, Savannah River Laboratory, U.S.A.
R. Hickman, Lawrence Livermore Laboratory, U.S.A.
G. McCracken, Culham Laboratory, U.K.
V. Maroni, Argonne National Laboratory, U.S.A.
L. Wittenberg, Mound Laboratory, U.S.A.

PREFACE

Encouraging results during the past few years in magnetic and inertial confinement experiments have shown the need for larger-scale and more realistic experiments which "burn" deuterium and tritium and produce significant quantities of neutrons and a tritium breeding blanket. Some such experiments have been approved and are in advanced stages of design (the Tokamak Fusion Test Reactor, the Joint European Torus, and the [illegible]). Other more advanced experiments are in early stages of conceptual design (Tokamak Experimental Power Reactor and Fusion Demonstration Reactor). As fusion research moves into these large, complex experiments, increased attention is required to develop the technology to build and operate the reactor systems. If fusion power becomes a commercial reality and follows patterns set by other advanced technologies (e.g., nuclear fission), development of the supporting technologies may prove to be more difficult, time-consuming, and expensive than demonstration and evaluation of the fundamental concepts.

A growing interest in fusion technology has been evident in the greater number of national and international meetings that include sessions on fusion technology, the increased attendance at such sessions, and recently the organization of meetings devoted solely to the discussion of fusion technological problems.

As the logical outgrowth of these developments and as a means of fulfilling major current needs of the fusion program, the International Conference on Radiation Effects and Tritium Technology for Fusion Reactors was held in Gatlinburg, Tennessee, on October 1-3, 1975. This conference, which was sponsored by Oak Ridge National Laboratory, the Energy Research and Development Administration, the American Nuclear Society, and the Nuclear Metallurgy Committee of AIME, brought together scientists and engineers to discuss two elements of fusion technology: bulk radiation effects and tritium technology. In many ways, the presentation of papers on the two subjects in parallel sessions gave the effect of two separate conferences; however, several individuals attended sessions on both subjects. The conference was particularly timely because current conceptual design studies of Experimental Power Reactors have shown the immediate need for data on both subjects. In addition, it provided an excellent opportunity for workers from throughout the world to present their most recent results and to share insight into the remaining research needs. Judging from the quality of the papers, the number of attendees, and the interest and enthusiasm generated, the conference was eminently successful. We hope that publication of the proceedings will further enhance the benefits of the conference to all participants and also extend these benefits to others who were not able to attend.

The papers in these proceedings, which were published directly from copy supplied by the authors, are arranged in four volumes. The keynote address, delivered by E. E. Kintner of the Energy Research and Development Administration, is the first paper in Volume I. Papers concerned with radiation effects are included in Volumes I and II, while the tritium technology papers are collected in Volumes III and IV. The arrangement of the papers with regard to subject subdivision and order is the same as that used for presentation at the conference. Each of the four volumes contains a complete table of contents and author index for the entire proceedings.

The editors wish to express their gratitude to everyone who contributed to the success of the conference by assisting in the organization, chairing sessions, presenting papers, or participating in discussions throughout the conference. Special thanks are extended to J. I. Scott for conference arrangements and to D. Steiner, C. J. McHargue, and W. R. Grimes for their assistance with the organization.

J. S. Watson
F. W. Wiffen
Program Chairmen and Editors

CONTENTS

RADIATION EFFECTS

Plenary Session

Swelling and Microstructures (I)

Swelling and Microstructures (II)

Modeling and Damage Analysis

Mechanical Properties of Irradiated Metals

The Effects of Helium in Metals

Stress Effects, Magnets, and Insulators

System Design Studies

Experimental Studies, Part I

Experimental Studies, Part II

Special Topics

Permeation

RECENT EXPERIMENTAL RESULTS ON SOLUTIONS OF DEUTERIUM IN LITHIUM

H.R. Ihle and C.H. Wu

Institut für Chemie der Kernforschungsanlage Jülich GmbH

Institut 1: Nuklearchemie

D-5170 Jülich, FRG

ABSTRACT

The existence of a number of stable molecules containing lithium and hydrogen isotopes in the saturated vapor over dilute solutions of hydrogen isotopes in lithium causes an unexpectedly high density of hydrogen isotopes in the vapor at high temperature.

An evaluation of the partial pressures of the gas species Li, Li_2, LiD, Li_2D, LiD_2 and D_2 over solutions of deuterium in lithium measured in the temperature range 770-970 K, and extrapolation to higher temperatures, leads to the conclusion that the ratio of the atom fraction of deuterium in the gas to its atom fraction in the liquid exceeds unity above ≈1240 K; this ratio is independent of the deuterium atom fraction in the liquid at low concentrations.

Therefore the thermodynamic supposition that hydrogen isotopes can be separated from lithium by fractional distillation even at extremely low concentration exists. A direct verification of this phenomenon was made by Rayleigh distillation of Li-D solutions in the temperature range 970-1600 K. These measurements yield also the ratio of the deuterium atom fraction in the gas to that in the liquid and are in good agreement with the data obtained by extrapolation of partial pressures. The enrichment and depletion of deuterium in dependence on the number of theoretical plates of a distillation column at total reflux is calculated using our results.

INTRODUCTION

Experimental measurements of Sieverts constants for hydrogen isotopes in liquid lithium at low concentrations are required for calculations on CTR-concepts using liquid lithium as blanket material. The Sieverts constant, $K_{S_{D_2}}$, for solutions of deuterium in liquid lithium which contained between 1 and 100 ppm deuterium[1] was determined mass spectrometrically between about 770 and 970 K.

During these measurements we attempted to observe, besides D_2, also LiD, which has been investigated by optical spectroscopy[2], and triatomic molecules in the system Li-D, which were predicted to be stable by ab initio calculations[3,4]. Thermodynamically one is lead to expect that the saturated vapor over solutions of deuterium in lithium contains the molecules with one deuterium atom in high relative density, if the deuterium concentration in the liquid is low and the temperature is high[5].

EXPERIMENTAL

The techniques used to measure the partial pressures have been described in detail previously[1,6].

RESULTS

Fig. 1 shows as an example the resulting partial pressures measured by mass spectrometry as a function of temperature at a deuterium concentration of 10 ppm.

The existence of stable LiD^+ with a binding energy of 0.14 eV was proved by mass spectrometry[6]. It was found that p_{Li_2D} and p_{LiD} rise much more steeply with temperature than does p_{D_2}. The dependence of the partial pressures on the concentration of deuterium in the liquid phase at 773 K is

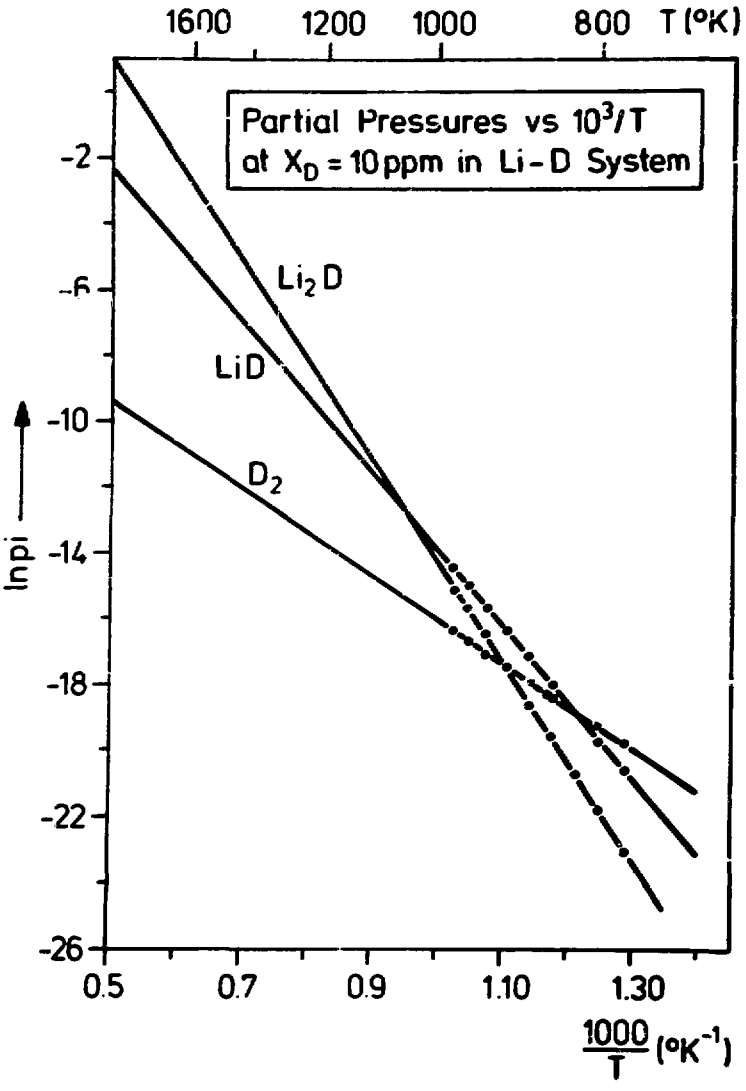

Fig. 1 Partial pressures of D_2, LiD and Li_2D as function of temperature at an atom fraction x_D = 10 ppm

shown in Fig. 2. It is seen that the deuterium pressure varies proportionally with the square of the concentration x_D, whereas p_{LiD} and p_{Li_2D} vary directly proportional with x_D. Combination of the results of these measurements leads to temperature functions of Sieverts constant, $K_{S_{D_2}} = p_{D_2}^{1/2}/x_D$, where x_D is the atom fraction of deuterium in the liquid; the solubility constants for the other deuterium containing molecules were defined correspondingly. The temperature dependence of these gas-liquid equilibria is best characterized by the respective heats of vaporization of the observed molecules. They are shown in Table 1.

Table 1. Enthalpy of Vaporization of Gas-species over Dilute Solutions of Deuterium in Lithium

Enthalpy of Vaporization $\Delta H^o_{v,873}$ kcal.	Molecule
37.2 ± 1.1	Li
48.0 ± 1.4	Li_2
72.0 ± 2.5	Li_3
44.5 ± 2	LiD
58.5 ± 2.5	Li_2D
39.0 ± 0.2	LiD_2
25.0 ± 0.2	D_2

Li_2D has the highest heat of vaporization of all the deuterium-containing molecules investigated. Li_3 has been observed as a new lithium polymer vapor species. LiD_2 was discovered very recently. The dissociation energies of molecules in the Li-D system, deduced from gas equilibria, are shown in Table 2. The experimental atomization energies are higher than those predicted[3,4]. Owing to the high vapor pressure

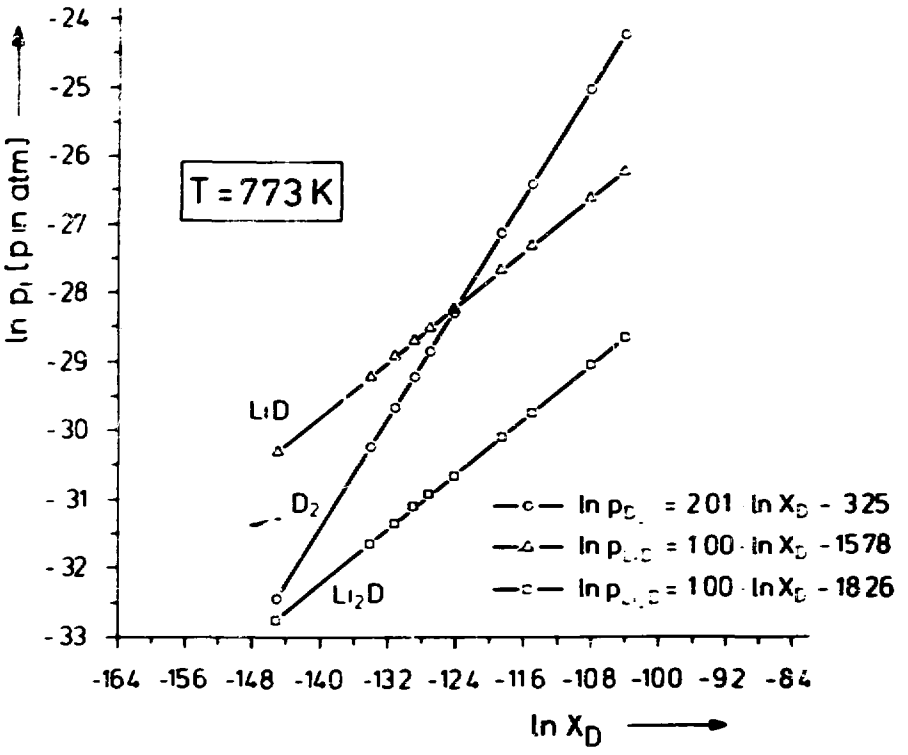

Fig. 2 Partial pressures of D_2, LiD and Li_2D in dependence on atom fraction x_D at 773 K

Table 2. Reaction Enthalpies and Atomization Energies of Gas-species in the System Lithium - Deuterium

Reaction	Enthalpy ΔH_o^o, Kcal	Atomization Energy D_o^o, Kcal	Molecule
$Li_2(g) \leftrightharpoons 2Li(g)$	25.5±0.2	25.5±0.2	Li_2
$2Li_2(g) \leftrightharpoons Li_3(g)+Li(g)$	10.7±0.2	40.2±0.3	Li_3
$3Li(l) \leftrightharpoons Li_3(g)$	73.0±0.4	42.5±0.3	
$Li(l) \leftrightharpoons Li(g)$	38.5±0.1		
$Li_2(g)+D_2(g) \leftrightharpoons 2LiD(g)$	15.5±0.7	57.3±0.9	LiD
$Li_2D(g)+Li(g) \leftrightharpoons LiD(g)+Li_2(g)$	11.5±0.5	94.0±1.0	Li_2D
$Li_2D(g)+Li_2(g) \leftrightharpoons LiD(g)+Li_3(g)$	21.5±0.5	94.8±1.0	
$LiD_2(g)+Li(g) \leftrightharpoons 2LiD(g)$	12.5	127	LiD_2

of lithium, these measurements were restricted to temperatures below 1000 K. The instrumental sensitivity made possible the detection of a partial pressure of 10^{-11} Torr within the Knudsen cell in the presence of a large excess of lithium vapor. The evaluation of the equilibrium constants for the gas-liquid equilibria involved lead to an expression for the ratio of the atom fraction of deuterium in the gas to that in the liquid, which is found to be greater than unity at temperatures above ≈1240 K by extrapolation of the results obtained experimentally.

To verify this finding, Rayleigh distillation experiments were carried out up to the boiling point of lithium (≈1600 K)[7]. The results proved that the expected high deuterium density in the saturated vapor exists. These experiments were conducted in the vacuum chamber of the mass spectrometer, which was also used for the partial pressure measurements (Fig. 3).

A known amount of dilute solutions of deuterium in lithium

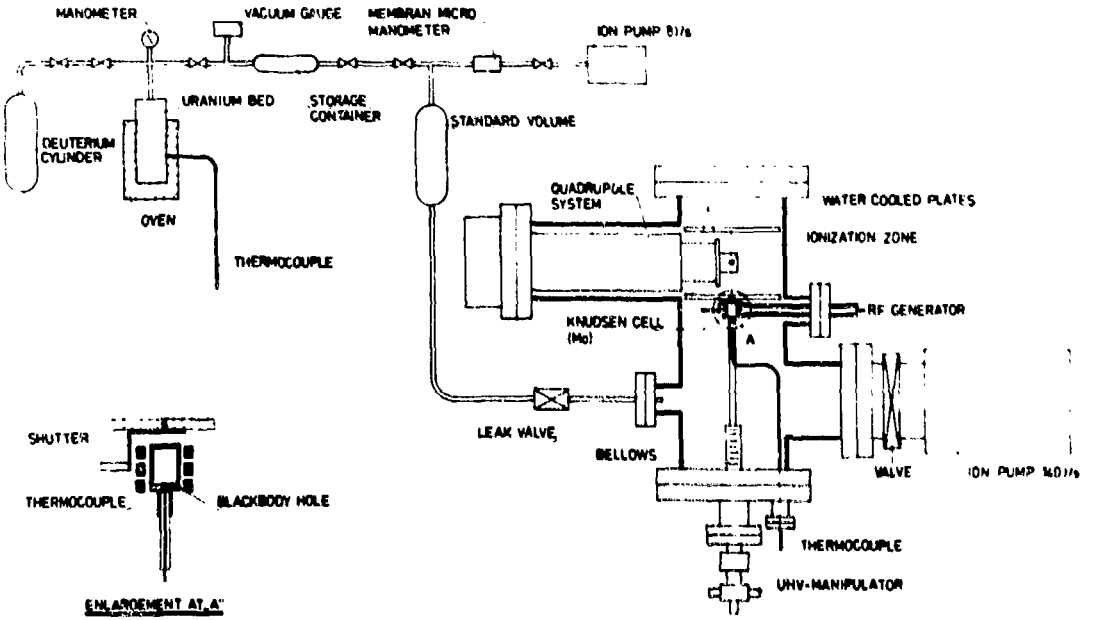

Fig. 3 Apparatus for partial pressure measurements and Rayleigh distillation experiments

was distilled off, while the shutter was kept closed. From the change in concentration before and after distillation, measured by the known relation between partial pressure and composition, one calculates the ratio of the atom fraction of deuterium in the gas to that in the liquid: $R = x_{D,gas}/x_{D,liquid}$. The Rayleigh distillation results, compared with calculations from extrapolated vapor pressures, are shown in Fig. 4. The evaluation of R from vapor pressures was carried out using the relation

$$R = x_{D,g}/x_{D,l} = \frac{K^{*}_{Li_2D} + K^{*}_{LiD} + 2K^{2}_{S_{D_2}} \cdot x_{D,l}}{p_{Li} + 2p_{Li_2}}, \qquad (1)$$

where:
$$K^{*}_{Li_2D} = p_{Li_2D}/x_{D,l}$$
$$K^{*}_{LiD} = p_{LiD}/x_{D,l}$$
$$K_{S_{D_2}} = p_{D_2}^{1/2}/x_{D,l}$$

The other symbols have their usual meaning. Note that for $x_{D,l} \ll 1$, R becomes independent of $x_{D,l}$. Hence at high temperatures R exceeds unity, regardless of how low the concentration of deuterium in the liquid might be.

Table 3 shows the variation of composition of the liquid $x_{D,l}$, and of the partial pressures p_i, with the number of theoretical plates N in a distillation column calculated from our results assuming "ideal" solutions. By operation at total reflux at ~1100 °C with a feed concentration $x_{D,l} = 10^{-6}$, a few theoretical plates would lead to an increase of $x_{D,l}$ and the partial pressures by several orders of magnitude. In this calculation the term $2K^{2}_{D_2} \cdot x_{D,l}$ in equation 1 has been neglected.

It is concluded that depletion of deuterium in the liquid phase by distillation is thermodynamically possible. The kinetics of the gas-liquid exchange will of course play an important role in a possible practical application for the

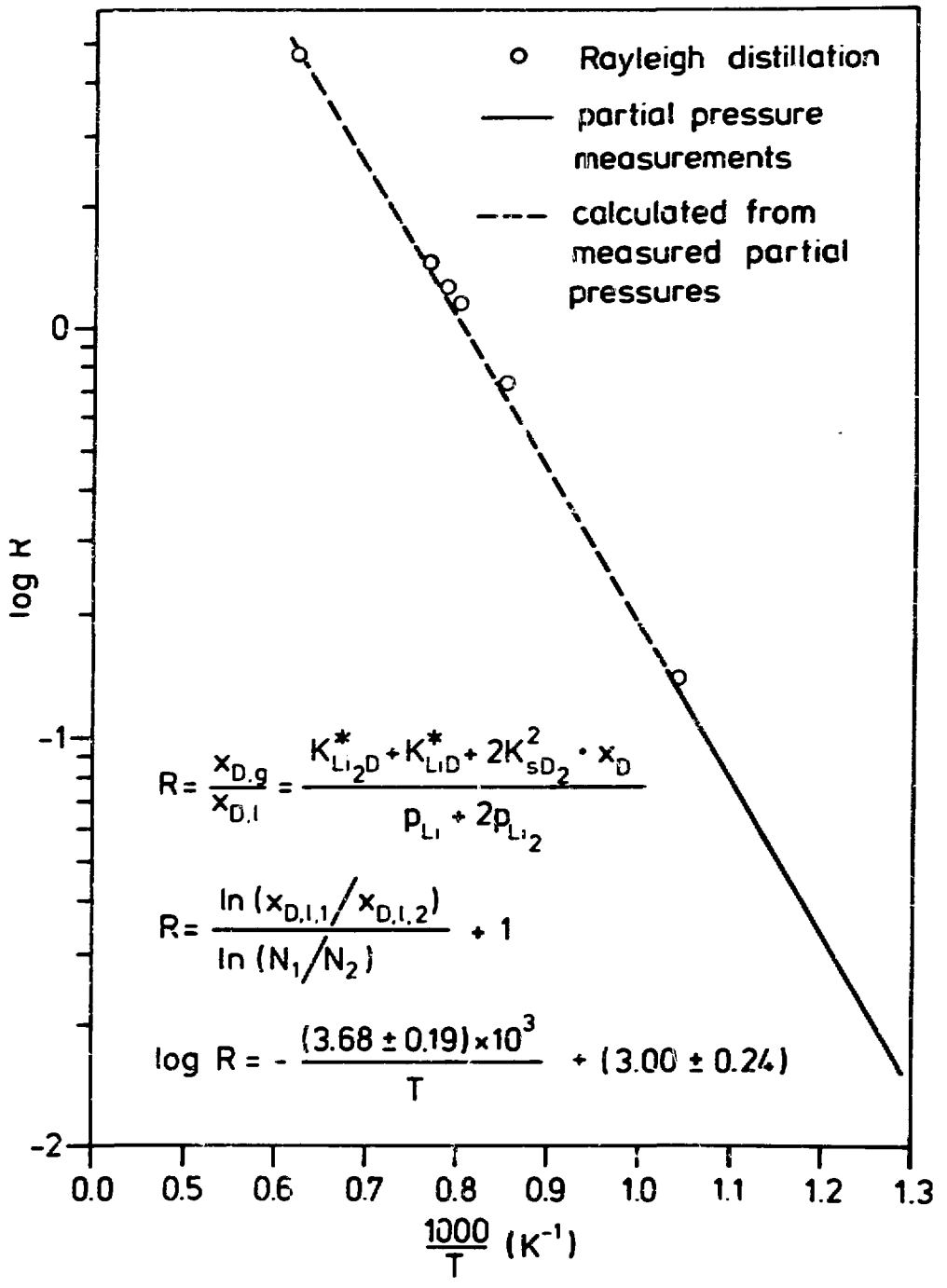

Fig. 4 Ratio of deuterium atom fractions $R = x_{D,g}/x_{D,l}$ as function of temperature

Table 3. Deuterium Atom Fraction $x_{D,1}$ and Partial Pressures in Dependence on the Number of Theoretical Plates N

$T = 1373\ K;\ x_{D,1}\ (Feed) = 1 \cdot 10^{-6}$

N	$x_{D,1}(N)$	$p_{Li_2D}(N)$	$p_{LiD}(N)$	$p_{D_2}(N)$
		ENRICHMENT		
0	$1.00 \cdot 10^{-6}$	$2.26 \cdot 10^{-7}$	$8.65 \cdot 10^{-8}$	$4.19 \cdot 10^{-11}$
1	$2.07 \cdot 10^{-6}$	$4.67 \cdot 10^{-7}$	$1.79 \cdot 10^{-7}$	$1.79 \cdot 10^{-10}$
2	$4.28 \cdot 10^{-6}$	$9.66 \cdot 10^{-7}$	$3.70 \cdot 10^{-7}$	$7.67 \cdot 10^{-10}$
3	$8.85 \cdot 10^{-6}$	$2.00 \cdot 10^{-6}$	$7.66 \cdot 10^{-7}$	$3.29 \cdot 10^{-9}$
4	$1.83 \cdot 10^{-5}$	$4.14 \cdot 10^{-6}$	$1.59 \cdot 10^{-6}$	$1.41 \cdot 10^{-8}$
5	$3.81 \cdot 10^{-5}$	$8.60 \cdot 10^{-6}$	$3.30 \cdot 10^{-6}$	$6.09 \cdot 10^{-8}$
6	$7.96 \cdot 10^{-5}$	$1.80 \cdot 10^{-5}$	$6.88 \cdot 10^{-6}$	$2.66 \cdot 10^{-7}$
7	$1.68 \cdot 10^{-4}$	$3.79 \cdot 10^{-5}$	$1.45 \cdot 10^{-5}$	$1.18 \cdot 10^{-6}$
8	$3.63 \cdot 10^{-4}$	$8.20 \cdot 10^{-5}$	$3.14 \cdot 10^{-5}$	$5.52 \cdot 10^{-6}$
9	$8.23 \cdot 10^{-4}$	$1.86 \cdot 10^{-4}$	$7.12 \cdot 10^{-5}$	$2.84 \cdot 10^{-5}$
10	$2.08 \cdot 10^{-3}$	$4.69 \cdot 10^{-4}$	$1.80 \cdot 10^{-4}$	$1.81 \cdot 10^{-4}$
		DEPLETION		
0	$1.00 \cdot 10^{-6}$	$2.26 \cdot 10^{-7}$	$8.65 \cdot 10^{-8}$	$4.19 \cdot 10^{-11}$
-1	$4.84 \cdot 10^{-7}$	$1.09 \cdot 10^{-7}$	$4.18 \cdot 10^{-8}$	$9.81 \cdot 10^{-12}$
-2	$2.34 \cdot 10^{-7}$	$5.28 \cdot 10^{-8}$	$2.02 \cdot 10^{-8}$	$2.29 \cdot 10^{-12}$
-3	$1.13 \cdot 10^{-7}$	$2.56 \cdot 10^{-8}$	$9.70 \cdot 10^{-9}$	$5.37 \cdot 10^{-13}$
-4	$5.47 \cdot 10^{-8}$	$1.24 \cdot 10^{-8}$	$4.74 \cdot 10^{-9}$	$1.26 \cdot 10^{-13}$
-5	$2.65 \cdot 10^{-8}$	$5.98 \cdot 10^{-9}$	$2.29 \cdot 10^{-9}$	$2.94 \cdot 10^{-14}$
-6	$1.28 \cdot 10^{-8}$	$2.89 \cdot 10^{-9}$	$1.11 \cdot 10^{-9}$	$6.88 \cdot 10^{-15}$

removal of tritium from lithium.

The experimental results reported are for the system lithium-deuterium. The corresponding tritium-pressures should be slightly higher.

REFERENCES

1. H. R. Ihle and C. H. Wu, "Experimental Determination of the Partial Pressures of D_2, LiD and Li_2D in Equilibrium with Dilute Solutions of Deuterium in Liquid Lithium", Proc. 8th Symposium on Fusion Technology, Noordwijkerhout, Netherlands, EUR 5182 e (1974), pp. 787-799.

2. W. C. Stwalley, P. Way and R. Velasco, J. Chem. Phys. 60, 3611 (1974).

3. A. L. Companion, J. Chem. Phys. 48, 1166 (1968).

4. A. L. Companion, D. J. Steible and J. Starshak, J. Chem. Phys. 19, 3637 (1968).

5. H. R. Ihle and C. H. Wu, "Mass Spectrometric Knudsen Effusion Measurements of Vapor Species in the System Lithium-Hydrogen", Proc. 7th Symposium of Fusion Technology, Grenoble, pp. 89-97 (1972).

6. H. R. Ihle and C. H. Wu, J. Chem. Phys. 63, 1605 (1975).

7. H. R. Ihle and C. H. Wu, "Rayleigh Distillation Experiments with Respect to the Separation of Deuterium from Dilute Solution in Lithium", J. phys. chem. in press.

ESTIMATED VALUES OF SOME CRYOGENIC PROPERTIES OF HYDROGEN ISOTOPES*

C. K. Briggs, R. G. Hickman, R. T. Tsugawa, and P. C. Somers

Lawrence Livermore Laboratory, University of California
Livermore, California 94550

ABSTRACT

The literature on cryogenic hydrogen isotopes from 4.2 to 25 K is reviewed for triple points, vapor pressures, liquid viscosities, surface tensions, and liquid and solid densities. Data are extrapolated to yield values for DT. Empirical equations are given for all isotopes for each property. At the estimated 19.71 K triple point of 1:1 D-T in D_2-DT-T_2 solution, the estimated properties are: vapor pressure, 19 420 Pa (145.7 Torr); viscosity 550 × 10^{-7} Pa•s; surface tension 4.23 × 10^{-3} N/m; liquid density, 0.0446 × 10^6 mol/m^3 (224 Kg/m^3); solid density, 0.051 × 10^6 mol/m^3 (256 Kg/m^3); and shrinkage upon freezing, -13 vol%. At 4.2 K, estimated values are: vapor pressure, 2.4 × 10^{-10} Pa (1.8×10^{-12} Torr) and solid density, 0.055 × 10^6 mol/m^3 (267 Kg/m^3).

INTRODUCTION

Controlled thermonuclear fusion as a source of energy has been a dream for the past generation. There is considerable activity in the magnetic confinement and laser-induced approaches to this goal. Both require heavy hydrogen DT, as fuel. To aid cryogenic engineers, we reviewed the literature of DT for triple point temperature, vapor pressure, density, viscosity, and surface tension for the liquid and solid phases along the saturation line, from 4.2 to 25 K. We extrapolated the known data to estimate values for DT and T_2 wherever gaps in knowledge appear. The data given are strictly for normal (n) H_2 and D_2 and for

*This work was performed under the auspices of the U.S. Energy Research and Development Administration, under Contract No. W-7405-Eng-48.

equilibrium, D_2, and T_2.* Changes in rotational energy, i.e., with ortho-para composition, do not greatly affect the accuracy of the listed values.

The constants listed for a given property do not always form a smooth sequence with molecular weight because of the inaccuracies of combining actual data for each isotopic species from several sources.

TRIPLE POINTS

Table 1 shows the triple point temperatures and pressures recommended by the National Bureau of Standards (NBS).[1] The molecular species DT has never been obtained in bulk quantities because the tritium beta

Table 1. Triple point temperatures and pressures of hydrogen isotopes. Estimates are underlined.[1]

Isotope	Triple point temp., K	Triple point vapor pressure Pa	(Torr)
HT	13.957	7205	(54.04)
HD	16.604	12400	(92.8)
HT_2	18.71	17130	(128.5)
DT	19.71	19420	(145.7)
T_2	20.62	21600	(162.0)

article causes a rapid equilibration to the three-component mixture D_2-DT-T_2.[2-4] The triple point of this solution has not been measured, and the estimated DT value of 19.71 K must be used for a 1:1 D-T mixture. The triple-point temperatures of the hydrogens do not form a smooth curve as a function of molecular weight; remeasurement of the non-T_2 values would be valuable.

*Normal hydrogen contains the rotational energy characteristic of room temperature. Equilibrium hydrogen contains the rotational energy characteristic of any other specified temperature. If quickly cooled, H_2 and D_2 remain metastably trapped in the normal form; HD and DT de-excite to the equilibrium form by transitions allowed in the mixed isotopes; DT and T_2 de-excite by radiation-induced reactions.

SATURATED VAPOR PRESSURES

Of great practical importance are the vapor pressures along the saturated (equilibrium) solid to vapor and liquid to vapor phase boundaries. We use the NBS recommended vapor pressures,[5] which include H_2, HD, D_2, and T_2.[6-12] We refined these data in a recent review[13] and replotted them using the Clausius-Clapeyron equation, altered for a perfect gas.[14] For the solid, we assume a latent heat of sublimation L that is linear with temperature:

$$L = R(A + BT) \tag{1}$$

where R is the gas constant (8.314 J/mol•K), A and B are constants, and T is the temperature. Insertion into the Clausius-Clapeyron equation yields a form attributed to both Kirchoff and Rankine:

$$\ln P = -\frac{A}{T} + B\ln T + C, \tag{2}$$

where P is the saturated vapor pressure and C is a new constant that determines the units of pressure. Equation (2) also closely describes the liquid, although it is more empirical because the heats of vaporization do not follow the form of Eq. (1). Using Eqs. (1) and (2), we calculate the latent heats from 0 K to the solid and liquid at the triple points. All constants are given in Table 2, and derived latent heats are given in Table 3. The error of our vapor pressure estimates must surely be large compared to solution irregularities. Hence, we use the NT vapor pressure

Table 2. Vapor pressures of hydrogen isotopes, Pa (Torr). (Estimates are underlined.)

Empirical formula: $\ln P = -\frac{A}{T} + B\ln T + C$

	Solid-vapor constants				Liquid-vapor constants			
Isotope	A	B	C, Pa	(Torr)	A	B	C, Pa	(Torr)
H_2	98.63	1.982	10.72	(5.832)	89.00	1.680	10.83	(5.937)
HD	109.2	2.840	8.023	(3.130)	112.4	1.412	12.23	(7.335)
D_2	137.1	2.378	10.11	(5.217)	137.1	1.067	13.95	(9.058)
DT	151.5	2.349	10.56	(5.667)	155.8	0.6712	15.77	(10.88)
T_2	156.4	2.333	10.50	(5.610)	166.0	0.6416	16.09	(11.20)

Table 3. Triple-point latent heats of hydrogen isotopes, J/mol. (Estimates are underlined.)

Isotope	Empirical formula: $L = R(A + BT)^a$ Sublimation	Fusion	Vaporization
nH_2	1050	115	935
HD	1300	170	1130
nD_2	1510	204	1306
DT	<u>1645</u>	<u>240</u>	<u>1405</u>
T_2	1700	210	1490

[a]For use with solid and triple point liquid. Gas constant R 8.314 J/mol·K.

to approximate the D_2-DT-T_2 mixture. At 4.2 K, the vapor pressure of DT is calculated to be only 2.4×10^{-10} Pa (1.8×10^{-12} Torr).

LIQUID VISCOSITY

The liquid viscosity estimates are based on H_2, HD, and D_2 data[15-17] which we recently reviewed.[18] Viscosities were plotted for temperature vs molecular weight. The isothermal curves were linear, and extrapolations were carried out for DT and T_2, with the liquid viscosity η expressed by the empirical equation

$$\eta = \frac{A_\eta}{T^{1.65}}, \qquad (3)$$

where T is the temperature and A_η is a constant given in Table 4 for the isotopes. As liquid hydrogen is cooled to the triple point, the viscosity rises more steeply in the last one or two degrees than expressed by Eq. (3). The actual values at the triple points (Table 4) are 3 to 5% higher than those calculated from Eq. (3).

Table 4. Viscosity, surface tension, and densities of hydrogen isotopes. (Estimates are underlined.)

Property				
Liquid viscosity				
Liquid vapor				
Liquid density				
Solid density				

Combining binary H-D solutions reduces the viscosity below that expected from a regular solution of the two constituents.[16]

The maximum decrease in regularity for a 1:1 mixture of liquid H_2-D_2 is -11.5%. This decrease falls with the difference in molecular weights: -7.0% for H_2-HD and -3.1% for HD-D_2. By extrapolation we estimate maximum viscosity decreases of -7.0, -3.8, and -3.1% for D_2-T_2, D_2-DT, and DT-T_2. However, the actual mixture is estimated to contain about 3:4:3 D_2-DT-T_2 respectively, for a chemically equilibrated solution of 1:1 D-T at the triple point of 19.71 K.[4,19] Although it is difficult to estimate the regularity decrease for a ternary solution of almost equal parts, we estimate decreases of -5 to -10% for D_2-DT-T_2. Using the -5% value, we calculate a liquid viscosity of 550 × 10^{-7} Pa•s at the 1:1 D-T triple point of about 19.71 K.

LIQUID-VAPOR SURFACE TENSION

Surface tension measurement have been taken on liquid H_2, HD, and D_2[20-22] and have been recently reviewed.[18] The isothermal surface tensions plotted vs molecular weight are again almost linear and allow ready extrapolation to the DT and T_2 estimates. We employ the empirical equation for surface tension γ;

$$\gamma = A_\gamma - B_\gamma T, \tag{4}$$

where the A_γ and B_γ are given for the isotopes in Table 4.

The surface tension of binary H-D solutions also shows a lower actual value than that expected for a regular solution.[21,23] For equimolar solutions, the maximum surface tension decreases from regularity are -3.8, -2.7, and -1.5% for H_2-D_2, H_2-HD, and HD-D_2. Considering the molecular weight differences, we estimate -2.3, -1.3, and -1.0% for D_2-T_2, D_2-DT, and DT-T_2. For the ternary D_2-DT-T_2 solution, this decrease could be -2 to -5% below regularity. Employing the -2% we estimate a triple-point surface tension of 4.23 × 10^{-3} N/m for liquid D_2-DT-T_2 at 19.71 K.

LIQUID DENSITY

National Bureau of Standards recommended values[24] include measurements of H_2, HD, D_2, and T_2[12,15,25,26] which we recently reviewed.[18] Estimates for DT are interpolated from isothermal molecular weight plots. The liquid density ρ_L to 25 K is estimated by the empirical formula:

$$\rho_L = A_L - B_L T^2, \tag{5}$$

where T is the temperature and the constants A_L and B_L are as listed in Table 4. Volume changes upon combining binary solutions of the hydrogens have been studied, but the results are contradictory,[27-30] and we do not attempt to estimate the deviation from regularity. The estimated liquid density of 19.71 K D_2-DT-T_2 is $0.0446 \cdot 10^6$ mol/m^3 (224 kg/m^3).

SOLID DENSITY

Some densities for H_2, HD, and D_2 have been measured by bulk methods.[6,31] More data are available on H_2, HD, D_2, and T_2 by x-ray, neutron, and electron diffraction.[32-35] We have summarized these data recently[36] with the empirical expression for solid density ρ_S:

$$\rho_S = A_S - B_S T^3, \tag{6}$$

where A_S and B_S are constants given in Table 4. The T^3 form is dictated by a few 10 to 11 K D_2 points, which could be high. The H_2 data can also be represented by the T^2 form of Eq. (5). Insufficient data exist for the other isotopes. Equation (5) is applicable to both the usual hexagonal-close-packed structure and to the face-centered-cubic structure that forms below 4 K. The errors inherent in the available density data are larger than the volume change of the crystallographic transition.[36] There are no solid solution density data, and no estimates of deviations from regularity are possible. For solid D_2-DT-T_2 of about 3:4:3 composition, the estimated 19.71 K density is 0.051×10^6 mol/m^3 (256 Kg/m^3). At 4.2 K it is not possible to estimate the chemical equilibrium so we employ the molecular DT estimate of 0.053×10^6 mol/m^3 (267 Kg/m^3).

Considerable shrinkage occurs upon freezing. For H_2, HD, and D_2, it is -11.0, -11.3, and -11.6 vol%.[36] For DT and T_2 we estimate -15 and -14%, respectively. These larger values for DT and T_2 result from a single T_2 density point measured at 4.2 K[37] and are therefore open to speculation. Nevertheless, considerable physical distortion is expected as liquid D_2-DT-T_2 freezes.

SIMPLE DROPLET EXAMPLES

To illustrate the uses of the preceding data, we estimate some values for a few properties of a D_2-DT-T_2 droplet. We first directly compare the forces of surface tension and gravity for a droplet falling in free space. We solve for the droplet radius a:

$$a = \sqrt{\frac{3}{2}\frac{\gamma F}{\rho_L g}} \quad , \tag{7}$$

where γ is the surface tension, ρ_L is the liquid density, g is the acceleration due to gravity; and F is the ratio of gravitational to surface tension forces. If F is 0.01, the radius is 170 μm; for F = 1 with considerable expected distortion, the radius is 1700 μm. The stability of the drops may be surprising, even with a small surface tension, but the liquid density is also low. Thus, the expected droplet radius for liquid DT is about half that calculated for water, which has a surface tension 12 times as great.

The oscillations of the DT droplet may also be calculated. The frequency of the second-order dumbbell oscillation f_2 is[38]

$$f_2 = \frac{1}{2\pi}\sqrt{\frac{8\gamma}{\rho_L a^3}} \tag{8}$$

and the time constant for damping the oscillation is[38]

$$t_2 = \frac{\rho a^2}{5\eta} \quad . \tag{9}$$

For triple-point liquid DT with a 170-μm-radius droplet, the oscillation frequency is 880 Hz with a damping time of only 24 ms.

REFERENCES

1. H. M. Roder, G. E. Childs, R. D. McCarty, and P. E. Angerhofer, Nat. Bur. of Stand. Tech. Note. 641 (U.S. Government Printing Office, Washington, D.C., 1973) Section II.
2. E. W. Albers, P. Hartech, and R. R. Reeves, J. Amer. Chem. Soc., 86 204 (1964).
3. R. Frauenfelder, F. Heinrich, and J. B. Olin, Helv. Phys. Acta, 38, 279 (1965).
4. P. C. Souers, R. G. Hickman, W. E. Wade, and R. T. Tsugawa, Lawrence Livermore Laboratory Rept. UCRL-51681 (1974).
5. Reference 1, Table 10-1.
6. H. W. Woolley, R. B. Scott, and F. G. Brickwedde, J. Res. Nat. Bur. Stand. Sect. A, 41, 379-475 (1948).
7. E. R. Grilly, J. Amer. Chem. Soc. 73, 843 (1951).
8. H. J. Hoge and R. D. Arnold, J. Res. Nat. Bur. Stand., 47, 63 (1951).
9. E. S. Borovik, S. F. Grishin, and E. Y. Grishina, Soviet Phys-Tech Phys., 5, 506 (1960).
10. H. Harrison, W. L. Fite, and G. Guthrie, General Dynamics Corp., General Atomic Div., San Diego, CA., Final Report No. AFOSR-2357 (Feb. 1962) Contr. No. AF 49(638)-301, GA-2972, Proj. No. 38, Part 2.
11. A. Van Itterbeck, O. Verbeke, F. Theewes, K. Staes, and J. Deboelpaep, Physica Utrecht, 30, 1238 (1964).
12. R. Prydz, Nat. Bur. Stand. Rept. No. 9276, April, 1967.
13. P. C. Souers, Lawrence Livermore Laboratory Rept., to be published.
14. W. J. Moore, Physical Chemistry, (Prentice Hall, Englewood Cliffs, N.J., 3rd edition, 1962), pp. 103-5.
15. D. E. Diller, J. Chem. Phys., 42, 2089 (1965).
16. N. S. Rudenko and V. G. Konareva, Sov. Phys. JETP, 22, 313 (1965).
17. V. G. Konareva and N. S. Rudenko, Russ. J. Phys. Chem. 41, 1289 (1967).
18. C. K. Briggs, R. G. Hickman, R. T. Tsugawa, and P. C. Souers, Lawrence Livermore Laboratory Rept. UCRL-51827 (1975).
19. W. M. Jones, J. Chem. Phys., 17, 1062 (1949).
20. V. N. Grigor'ev, Sov. Phys. JETP, 18, 72 (1964).
21. V. N. Grigor'ev and N. S. Rudenko, Sov. Phys. JETP, 20, 62 (1965)

22. Y. P. Blagoi and V. V. Pashkov, Sov. Phys. JETP, 22, 999 (1966).
23. V. N. Grigor'ev, Sov. Phys. Tech. Phys., 10, 266 (1965).
24. Reference 1, Section 2.2.
25. L. R. Grilley, J. Amer. Chem. Soc., 73, 5307 (1951).
26. N. S. Rudenko and V. P. Slyusar, Russ. J. Phys. Chem., 43, 434 (1969).
27. E. C. Kerr, J. Amer. Chem. Soc., 74, 874 (1952).
28. M. Lambert, Phys. Rev. Lett, 4, 555 (1960).
29. H. F. P. Knapp, M. Knoester, and J. J. M. Beenakker, Physica (Utrecht), 27, 309 (1961).
30. V. N. Grigor'ev and N. S. Rudenko, Sov. Phys. JETP, 13, 530 (1961).
31. H. D. Megaw, Phil. Mag., 28, 129 (1939).
32. R. L. Mills and A. F. Schuck, Phys. Rev. Lett., 15, 722 (1965).
33. K. F. Mucker, S. Talhouk, P. M. Harris, D. White, and R. A. Erickson, Phys. Rev. Lett., 15, 586 (1965).
34. A. F. Schuch and R. L. Mills, Phys. Rev. Lett., 16, 616 (1966).
35. K. F. Mucker, P. M. Harris, and D. White, J. Chem. Phys., 49, 1922 (1968).
36. C. K. Briggs, R. T. Tsugawa, and P. C. Souers, Lawrence Livermore Laboratory Rept.,to be published
37. V. S. Kogan, A. S. Bulatov, and L. F. Yakeminko, Sov. Phys. JETP, 19, 107 (1964).
38. Sir Horace Lamb, Hydrodynamics, (Dover, New York, 6th ed., 1932), pp. 473-75.

ESTIMATED D_2-DT-T_2 PHASE DIAGRAM IN THE THREE-PHASE REGION

P. C. Souers, R. C. Hickman, and R. T. Tsugawa

Lawrence Livermore Laboratory

ABSTRACT

A composite of experimental eH_2-D_2 phase-diagram data at the three-phase line is assembled from the literature. The phase diagram is a smooth cigar shape without a eutectic point, indicating complete miscibility of liquid and solid phases. Additional data is used to estimate the D_2-T_2, D_2-DT, and DT-T_2 binary phase diagrams. These are assembled into the ternary D_2-DT-T_2 phase diagram. A surface representing the chemical equilibrium of the three species is added to the phase diagram. At chemical equilibrium, we estimate that 50-50 liquid D-T at 19.7 K is in equilibrium with 42 mole % T vapor and 54% T solid. Infrared spectroscopy is suggested as a means of component analysis of liquid and solid mixtures.

*Work performed under the auspices of the U.S. Energy Research and Development Administration, under Contract No. W-7405-Eng-48.

INTRODUCTION

There is great current interest in controlled hydrogen fusion by magnetic confinement, electron beams, or laser implosion. The fuel that ignites at the lowest temperature is D-T. This is actually a mixture of the three compounds, D_2-DT-T_2, brought to chemical equilibrium with one another by beta particle catalysis. Since hydrogen fusion may be carried out with liquid or solid fuel pellets, it is of interest to consider the D_2-DT-T_2 phase diagram. No part of it has been measured, except for certain measurements on pure D_2 and T_2. Most work has been done on the binary combinations of H_2, HD, and D_2, and this will form the nucleus for our estimates.

the hydrogens solidify to a hexagonal-close-packed form upon freezing. The triple-point temperatures of interest to us here are: eH_2, 13.80 K; HD, 16.60 K; nD_2, 18.71 K; DT, estimated as 19.71 K; and eT_2, 20.62 K.*[1,2] A list of other pertinent physical properties is given in a companion paper to this one.[3]

The vapor pressures used in calculations for this paper are derived from the equations in the companion report.[3] We have considered the phase-diagram behavior in preliminary form[3] as well as possible infrared methods of analysis.[4]

BINARY HYDROGEN PHASE DIAGRAMS

Work on eH_2-D_2 solutions has shown total miscibility with the molar volumes being within 1% of the linearly added pure-component values, i.e. the solutions are regular.[5-7] Early Soviet work claimed to observe phase separation in the solid phase.[8,9] Later Soviet and American research found total miscibility in the solid state but left open the question of possible phase separation.[10-13] Theoretical studies also predict complete solid miscibility, at least to liquid-helium temperatures.[14-16]

The eH_2-D_2 phase diagram has been studied by thermal methods in four sources. Three provide data on the liquid-solid lines but fail to analyze the vapor above.[11-13] The fourth study centers on the three-phase region, where H_2-D_2 solutions exist simultaneously in solid, liquid, and vapor forms.[17] This work confirms the existence of the three-phase line as well as providing vapor pressures and vapor compositions. However, none of these sources provides data on the compositions

---

*Normal hydrogen (nH_2) contains the molecular rotational energy characteristic of room temperature equilibrium. For H_2 and D_2, this is metastable trapped on quenching to low temperatures. Equilibrium hydrogen (eH_2) possesses the equilibrium rotational energy at any temperature, to be specified, other than room temperature. Upon cooling, catalysts are required to quickly equilibrate H_2 and D_2. HD and DT equilibrate quickly due to transitions allowed by molecular asymmetry. DT and T_2 also equilibrate quickly due to beta particle catalysis.[2]

of the corresponding liquid and solid phases. Hence, we must assume the data of the first three sources to be three-phase data in order to construct the composite eH_2-D_2 phase diagram shown in Fig. 1. The phase-diagram surface is a smooth cigar shape, without eutectic points, of vapor, liquid, and solid lines. The liquid line is slightly above the straight reference line connecting the triple points of the two pure components. The ends of the "cigars" are closed at these triple points.

The validity of the composite data of Fig. 1 may be checked by calculating vapor compositions through the vapor pressures. The Soviet researchers find a maximum deviation from solution regularity at 17.90 K (about 53 mole % D_2) where the measured 18.9-kPa (141.8-Torr) vapor pressure is 5% higher than the calculated value.[17,18] We shall extend this calculation by use of our solid-and-liquid vapor-pressure formula for H_2 and D_2.*[3] The calculated mole fraction of D_2 in the vapor phase, N_2^V, is

$$N_2^V = \frac{N_2^L P_2^L}{N_1^L P_1^L + N_2^L P_2^L} \tag{1a}$$

based on the liquid phase, or

$$N_2^V = \frac{N_2^S P_2^S}{N_1^S P_1^S + N_2^S P_2^S} \tag{1b}$$

based on the solid phase, where N is the mole fraction and P the vapor pressure of the pure component. The superscripts, V, L, and S refer to vapor, liquid, and solid phases; the subscripts 1 and 2 refer to the lighter and heavier isotopic species. For D_2, P_2^L is an extrapolation of the liquid vapor pressure equation below the triple point. For H_2, P_1^S is an extrapolation of the solid vapor pressure equation above the triple point. Using our vapor pressures[3] and the liquid and solid

*The vapor pressure formula is strictly derived for nH_2 but should be indistinguishable within error for eH_2.

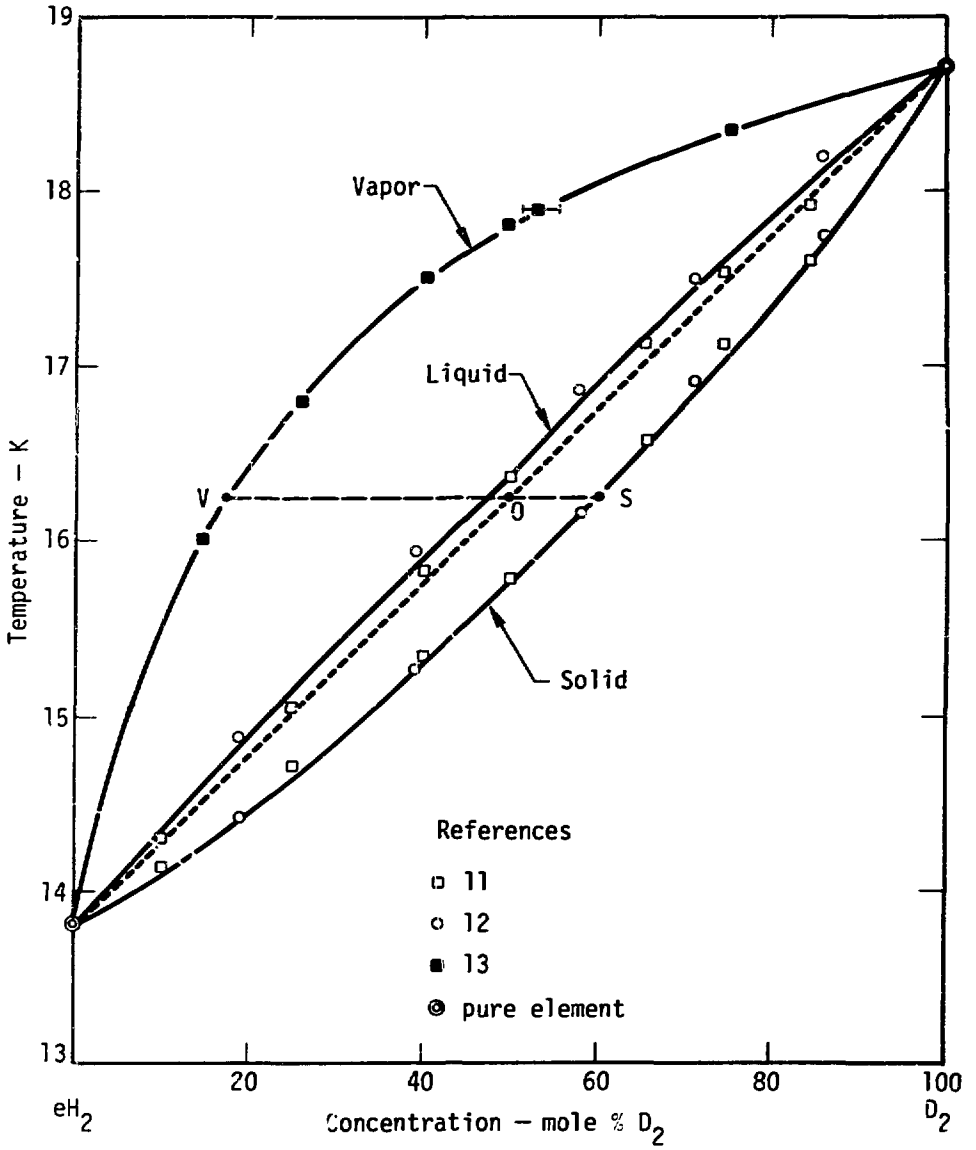

Fig. 1. Experimental data for the three-phase eH_2-D_2 system.

compositions of Fig. 1, we use Eq. (1) to calculate vapor compositions. These compositions, shown in Table 1, compare favorably with the actual experimental data. We may feel secure that the data of Fig. 1 represents the three-phase line of eH_2-D_2 to a few percent.

The binary liquid-solid phase diagrams for H_2-HD and HD-D_2 have also been measured.[11] These form "cigars" that are much more slender than the one for eH_2-D_2. The liquid line is indistinguishable from the straight reference line joining the triple points. We may, therefore, derive isothermal liquid compositions from this line, and then use the liquid portion of Eq. (1) to calculate the approximate vapor lines. This procedure may also be used for the binary systems D_2-T_2, D_2-DT, and DT-T_2, even though no experimental data is available.

The results of these calculations are summarized in Table 2. The origin is the 50-50 mixture point lying on the straight reference lines between triple points. (This is shown as point O in Fig. 1). An isothermal line is drawn through this origin, which intersects the vapor and solid lines at points V and S in Fig. 1. The derived points, V and S, in mole percents for the various binary components, are listed for the vapor and solid lines in Table 2. These lines may, therefore, be reconstructed by placing a curve from triple point to triple point through this single calculated reference point. The error in the use of a single reference point for very thin phase-diagram "cigars" cannot be large, compared to the uncertainties of the estimates themselves.

Table 1. Comparison of three-phase compositions of eH_2-D_2 vapor.

	D_2 in vapor - mole %		
		Calculated	
Temperature (K)	Experimental (Fig. 1)	Eq. (1a) (Liquid)	Eq. (1b) (Solid)
16	15	13	15
17	30	28	33
18	58	56	64

Table 2. Width of the binary hydrogen-phase-diagram "cigars" for three-phase equilibrium [estimates in parentheses].

	Median triple point temperature, K		Mole % heavier species	
		[Eq. (2)]	Vapor	Solid
H_2-D_2	16.26	0.302	18(13[a])	69
H_2-HD	15.20	0.184	(30[b])	55
HD-D_2	17.66	0.120	(34[b])	54
D_2-T_2	19.67	0.097	(36[b])	(57[c])
D_2-DT	19.21	0.052	(42[b])	(59[c])
DT-T_2	20.17	0.045	(43[b])	(59[c])

[a]Vapor pressure calculation [Eq. (1)] from experimental liquid data [Fig. 1].

[b]Vapor pressure calculation using straight lines between triple points.

[c]Extrapolations of experimental data using τ.

We must finally estimate the reference points for the solid lines for D_2-T_2, D_2-DT, and DT-T_2. We note that the "cigars" thin considerably as the relative molecular-weight differences or relative triple-point differences of the pure components decrease. The reference points so far calculated seem to best fit the function, τ,

$$\tau = \left(\frac{T_2 - T_1}{\frac{T_1 + T_2}{2}} \right) \qquad (2)$$

where T_1 is the triple point of the pure lighter component and T_2 the triple point of the heavier. We then extrapolate the solid line reference points to the various binary species as a function of T. This data is also listed in Table 2.

THE TERNARY PHASE DIAGRAM

The binary data may now be assembled to yield an estimate of the D_2-DT-T_2 phase diagram in the three-phase region. This is shown in Fig. 2. The diagram is a triangular prism, with a pure component at each edge. The mole percent is plotted along each side of the prism; temperature is plotted vertically. A binary phase diagram lies on each side of the prism, closed at the triple point temperatures at each edge of the prism. The straight lines connecting the triple points in the binary phase diagrams may now be extended to form a reference plane in the three-component phase diagram. The reference plane is tilted, because it is connected to the three different triple points. The vapor, liquid, and solid lines of the binary diagrams now become curved surfaces in the ternary diagram. The liquid surface will lie slightly above the reference plane and be bowed upward. Within error, however, we may take the reference plane to represent the liquid surface. The vapor surface lies above the reference plane and the solid surface below. Both planes may have considerable curvature, upward and downward, respectively. This curvature cannot be accurately estimated in our simple model and will require experimental measurement.

Let us simplify the problem by considering D-T liquid of 50-50 composition. This is the liquid line shown in Fig. 3. It runs from the DT triple point of 19.71 K to the 50-50 D_2-T_2 triple point estimated at about the same temperature (19.67 K in Table 2). Although this line is bowed upward above the reference plane, we may study its essential behavior by considering the line to be located in a 19.7-K isothermal cut across the phase diagram. Such a cut is shown in Fig. 3.

Within the 19.7-K-isothermal cut, we may apply the estimation procedures previously used to obtain vapor lines. The key is the D_2-T_2 binary phase diagram, where the 19.7-K vapor line intersects at 36 mole %

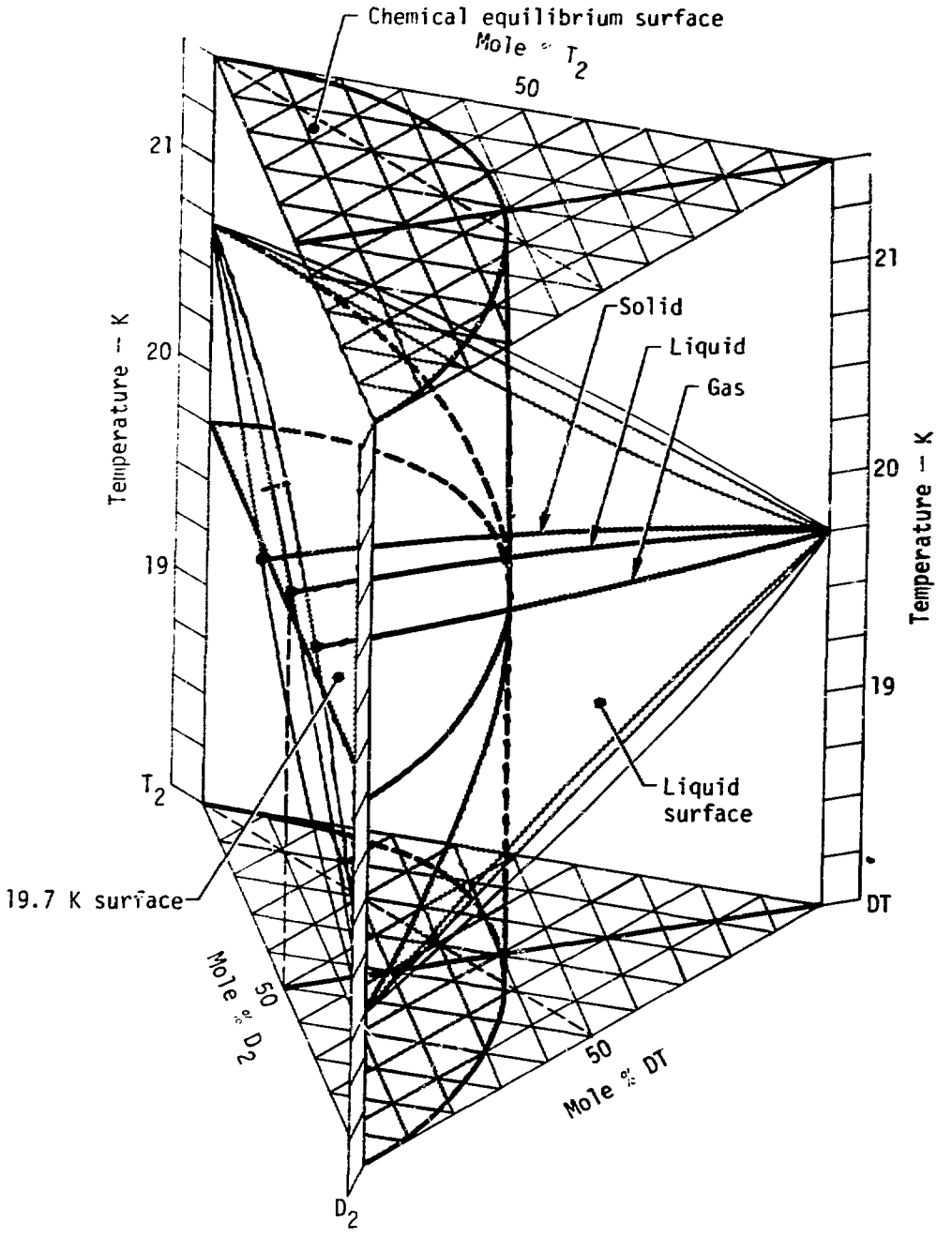

Fig. 2. Calculated triple-surface phase diagram of D_2-DT-T_2.

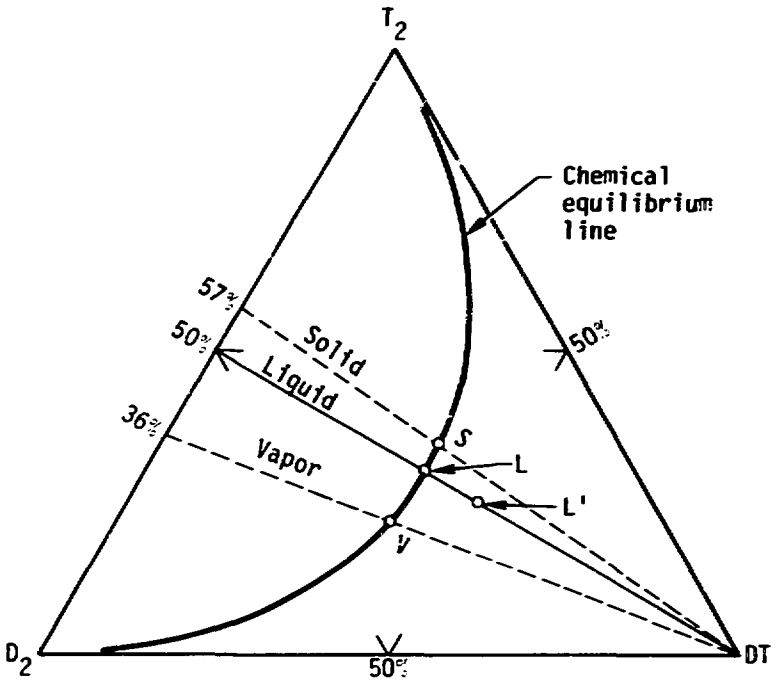

Fig. 3 The 19.7-K-isothermal cut of the D_2-DT-T_2 phase diagram.

T_2 and the solid line at 57% T_2. This means that the "cigars" for the three-phase D_2-DT-T_2 mixture will be closed at the pure DT end but will be open at the D_2-T_2 end. We now calculate the mole percent vapor compositions using the liquid term of Eq. (1) expanded to three components. The result, plotted in Fig. 3, amounts to virtually a straight line across the 19.7 K isothermal cut. We cannot define Eq. (2) for three components and therefore indicate the solid line by a straight line.

We need still another means of locating ourselves in the ternary phase diagram. We, therefore, consider the chemical equilibration of the reaction

$$D_2 + T_2 \rightleftharpoons 2DT \qquad (3)$$

to take place in a time rapid compared to our experiments. The kinetics of this reaction have never been measured but tritium workers feel that minutes or tens of minutes is the order of magnitude for equilibration time. In Eq. (3), we assume a moles of D_2 and b moles of T_2 being initially mixed, with 2x moles DT existing at equilibrium. The equilibrium constant is K, which is 4.00 at high, i.e., room, temperatures and is estimated to be 1.80 at 19.7 K.[3,19] The actual value of pressure for the vapor phase calculation of Eq. (3) does not matter, since the same number of moles appear on either side. We have the form[20]

$$K = \frac{4x^2}{(a - x)\ (b - x)} \tag{4}$$

The mole fractions at chemical equilibrium are:

$$D_2: \left(\frac{a - x}{a + b}\right) \tag{5}$$

$$DT: \left(\frac{2x}{a + b}\right) \tag{6}$$

$$T_2: \left(\frac{b - x}{a + b}\right) \tag{7}$$

where

$$x = \frac{(a + b)\ K - \sqrt{(a + b)^2 K^2 + 16\ abK}}{2(K - 4)} \tag{8}$$

Using Eqs. (5) through (8), we calculate the 19.7 K chemical equilibrium which is shown as a line in Fig. 3 and a surface in Fig. 2. This line intersects the vapor, 50-50 liquid, and solid lines at points V, L, and S, respectively. The arc VLS is the tie-line across the phase diagram. The compositions at these three points are listed in Table 3. These are approximate, since the actual vapor and solid lines curve in the three-dimensional phase diagram. Also, deviations of the vapor pressure from true additivity will modify the calculations based on Eq. (1).

Table 3. Predicted equilibrium compositions at triple-phase point, starting with 50-50 liquid D-T.

Species	Mole %		
	Vapor	Liquid	Solid
D_2	39	30	27
DT	39	40	39
T_2	$\frac{22}{100}$	$\frac{30}{100}$	$\frac{34}{100}$
D	58	50	46
T	42	50	54

Point L' in Fig. 3 represents the room temperature chemical equilibrium constant. Should chemical equilibration take longer than expected, a series of nonequilibrium tie-lines could exist in the region LL' of Fig. 3.

It is evident that considerable room for experimental work on the D_2-DT-T_2 phase diagram exists. The vapor pressures of the mixture at known compositions and temperatures should be measured, probably by mass spectroscopy. The compositions of the liquid and solid in equilibrium with the vapor should be measured. We suggest the use of infrared spectroscopy for this purpose. Although of low intensity, an induced molecular moment exists, and fundamental vibration-rotation resonances at 3.0-4.5 μm are expected for a 0.1-0.5 mm thickness of liquid or solid D_2-DT-T_2. Since hydrogen remains diatomic to the lowest temperatures, and vibrational frequencies are modified by the molecular weights, the three components are expected to show infrared absorptions at slightly different frequencies. This has never been measured for tritiated hydrogen. We have, therefore, calculated the infrared spectrum of eD_2-DT-eT_2 at 19.7 K.[4] This spectrum is shown in Fig. 4. A three-peak spectrum exists for each component (with the peaks indicating amounts of

rotational energy; i.e., ortho-para species). In practice, comparison of the peak areas with suitable standards would allow quantitative analysis of the components of the liquid and solid states.

Also of extreme interest are the chemical-equilibrium constants and reaction rates for Eq. (3) in all phases about the three-phase region. Again, infrared spectroscopy appears most suitable for the task of liquid and solid analysis.

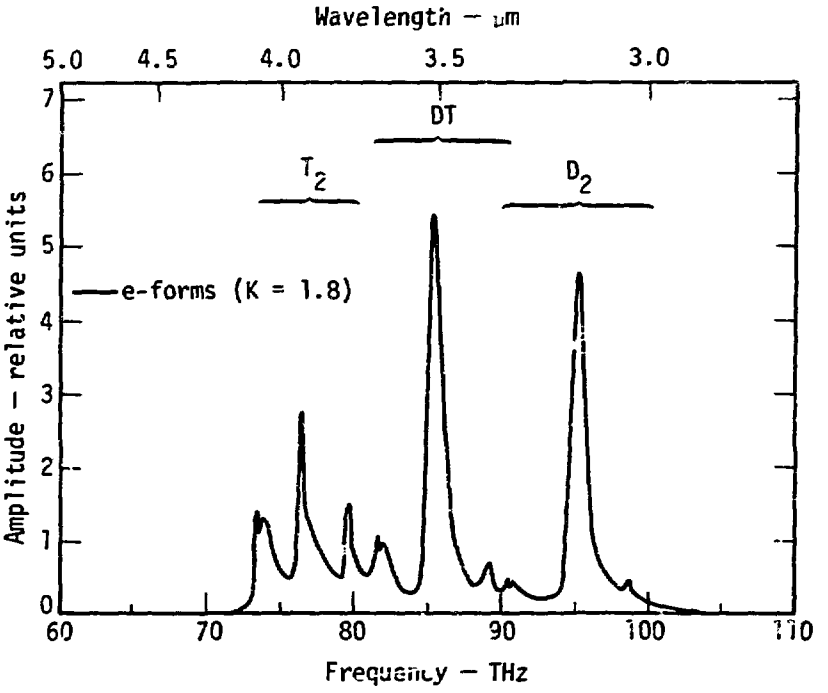

Fig. 4 Calculated fundamental infrared vibration-rotation spectrum for eD_2-DT-eT_2 at 19.7 K.

REFERENCES

1. H. M. Roder, G. E. Childs, R. D. McCarty, and P. E. Angerhofer, Survey of the Properties of the Hydrogen Isotopes Below their Critical Temperatures, National Bureau of Standards Technical Note 641, U.S. Department of Commerce, Washington, D.C., 1973, Section 7.

2. P. C. Souers, R. G. Hickman, W. Z. Wade, and R. T. Tsugawa, A Simple Model of D_2-DT-T_2 Equilibrium at Cryogenic Temperatures, Lawrence Livermore Laboratory, Rept. UCRL 51681 (1974).

3. C. K. Briggs, R. G. Hickman, R. T. Tsugawa, and P. C. Souers, Estimates of some Cryogenic DT Properties, Lawrence Livermore Laboratory, Rept. UCRL 76708, presented at the International Tritium Conference, Gatlinburg, TN, October 1-3, 1975.

4. P. C. Souers, R. G. Hickman, W. Z. Wade, and R. T. Tsugawa, Estimated Infrared Spectra of Cryogenic D_2-DT-T_2, Lawrence Livermore Laboratory, Rept. UCRL 51674 (1975).

5. M. Lambert, Phys. Rev. Lett. 4, 555 (1960).

6. H. F. P. Knaap, M. Knoester, and J. J. M. Beenakker, Physica 27, 309 (1961).

7. H. F. P. Knaap, R. J. J. Van Heijningen, J. Korving, and J. J. M. Beenakker, Physica 28, 343 (1962).

8. V. S. Kogan, B. G. Lazarev, and R. S. Bulatova, Sov. Phys. - JETP 7, 165 (1948).

9. R. F. Bulatova and V. S. Kogan, Sov. Phys. - JETP 21, 89 (1965).

10. J. R. Caines, E. M. de Castro, and J. G. Gaunt, Phys. Lett. 8, 167 (1964).

11. N. G. Bereznyak, I. V. Bogoyavlenskii, L. V. Karnatsevich, and V. S. Kogan, Sov. Phys. JETP 30, 1048 (1970).

12. D. White and J. R. Gaines, J. Chem. Phys. 42, 4152 (1965).

13. N. G. Bereznyak, I. V. Bogoyavlenskii, L. V. Karnatsevich, and A. A. Sheinina, Ukr. Fiz. Zh. 19, 472 (1974).

14. M. Simon, Phys. Lett. 9, 122 (1964).

15. C. E. Hecht and A. M. Sapse, Physica 41, 255 (1969).

16. W. J. Mullin and H. K. Sarin, Phys. Lett. 29A, 49 (1969).

17. N. G. Bereznyak, I. V. Bogoyavlenskii, L. V. Karnatsevich, and A. A. Sheinina, Sov. Phys. JETP 32, 838 (1971).

18. N. G. Bereznyak, I. V. Bogoyavlenskii, and L. V. Karnatsevich, Sov. Phys. JETP 36, 304 (1973).

19. W. M. Jones, J. Chem Phys. 17, 1062 (1949).

20. F. Daniels and R. A. Alberty, Physical Chemistry (John Wiley, New York, 1956) pp. 245-7.

THE URANIUM-TRITIUM SYSTEM - THE STORAGE OF TRITIUM

R. S. Carlson

Monsanto Research Corporation, Mound Laboratory

ABSTRACT

The thermodynamics of the uranium-tritium system were determined over the pressure range of 2×10^{-4} to 20 atm from experimental composition-pressure-temperature data. Both enthalpy and entropy were shown to vary slightly with composition by analysis of van't Hoff plots for the U-D system and the U-T system. The evolution of helium-3 borne in the lattice of a fully tritiated sample of uranium was studied over a period of several months, and the relative proportion of helium-3 and tritium in the evolved gas from an aged UT_3 sample was determined at several temperatures. The desorption and absorption characteristics of a typical uranium-tritium storage bed have been studied and observed for several years.

Mound Laboratory has had an intimate involvement with the science and technology of preparing, handling, and determining the fundamental properties of metal hydrides, deuterides, and tritides for a number of years. Of the tritides we have determined the thermodynamic properties of Pd-T, Pd-Ag-T, V-T, and U-T. One of the more useful of these materials is uranium, because of its ability to rapidly retrieve, store, and dispense tritium gas. Uranium as uranium tritide is commonly used at Mound Laboratory in tritium-handling gas racks where it performs the functions mentioned - those of storage and purification of a tritium-containing gas stream. Figure 1 is a diagram of a tritium-handling gas rack intended for studies of metal hydrides over a pressure range of about 10^9 atm, from 10^{-6} to 10^3 atm. A U-bed, a vessel containing uranium tritide, is an essential part of such a

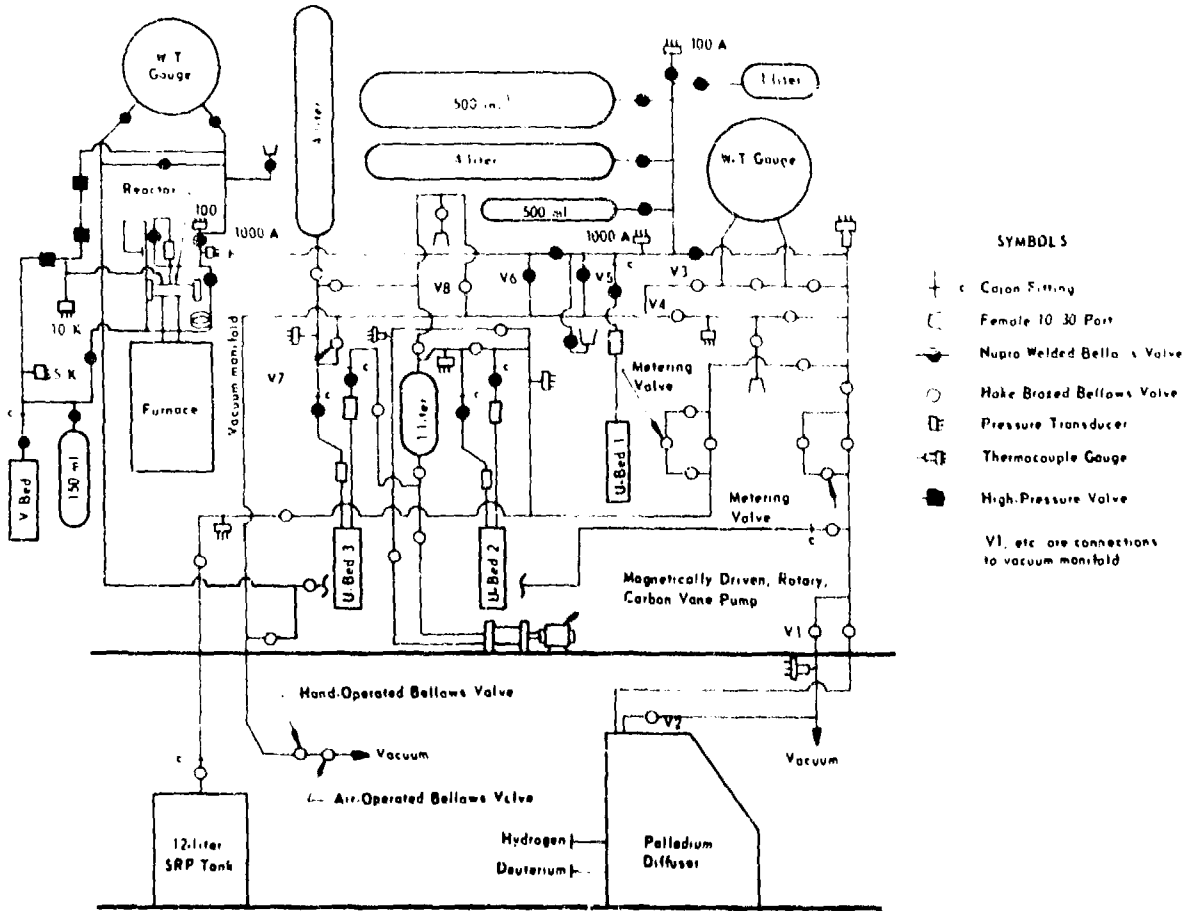

Fig. 1. Gas Rack Schematic.

gas rack. In this particular system, a palladium diffuser is used for purification of hydrogen and deuterium, and tritium is purified by circulation through a loop containing the U-bed.

Figure 2 is a photograph of this rack. It is located in a stainless steel fume hood 6 ft wide which has an air flow in excess of 200 linear ft/min with one door open. Type 347 stainless steel is the material of construction in the U-bed and in the doubly contained high pressure vessel in the vertical tube furnace. This material has performed satisfactorily at temperatures up to 700°C and at lower temperatures up to 1000 atm of tritium. Nupro stainless steel welded bellows valves and Hoke silver-soldered bronze bellow valves are used throughout and have given no trouble. HIP packed valves are used in the high pressure portion of the rack and do not leak if the valve stem is not moved while under high pressure. The opposite is also true. A HIP microcontrol valve permits withdrawing gas from the system at 13,000 psi and raising the pressure on the other side of the valve to 100 µm (as an example) following which the valve can be closed leak tight at the seat. This operation is repeatable many times but gas release is not reliable at low pressures; that is, at perhaps 200 psi and under. A new rack built today would of course be doubly enclosed. Heating the exposed U-bed shown, which has a capacity of about 60 liters, to cycle the contained tritium of about 1 mole would release about 50 Ci.

This figure is cited to indicate the losses that would occur without double containment by simple diffusion alone. Even at ambient temperature, diffusion proceeds rapidly enough so that a storage tank once used to contain tritium will forever continue to contaminate cold gases contained within, even after numerous purges. Such a tank can easily exhibit one tritium to contained hydrogen or ~2.5 µCi/ml of

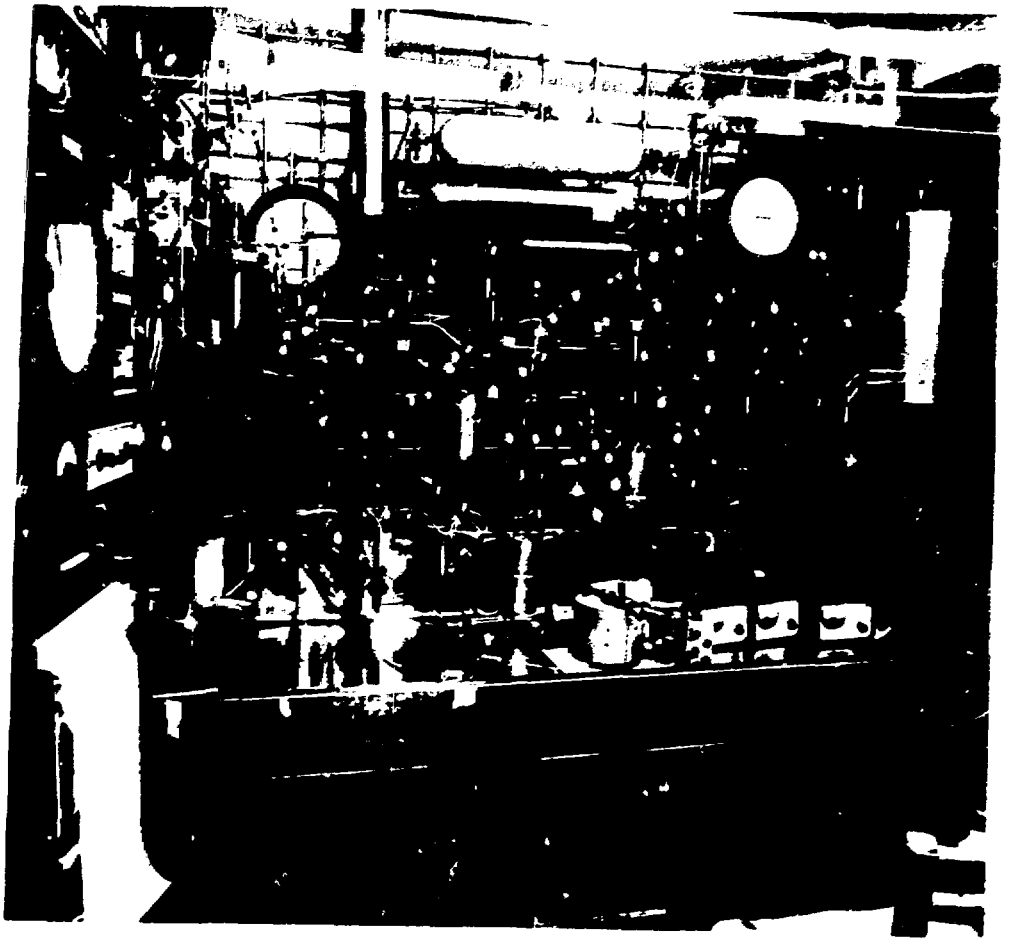

Fig. 2. Tritium Gas Handling Rack and Instrumentation.

hydrogen at STP. It should be remembered that 40 hr/wk of exposure to 1800 $\mu Ci/m^3$ of tritium (gas) or 5 $\mu Ci/m^3$ of HTO is equivalent to an adsorbed dose of 5 rem/yr.

The problem is the presence of helium-3 decay product in the tritium. A static system for separation of helium-3 from tritium will fail or, in other words, be of low efficiency in its ability to separate the isotopes because of "blanketing" of the gas-solid boundary by helium-3. Whether the boundary is palladium or uranium is relatively insignificant when the relative thermodynamic properties of the two materials are taken into consideration. The rate of generation of helium-3 in tritium is such that, after 10 days, 0.3% of the gas mixture is helium-3, yet this seemingly insignificant amount results in almost unsurmountable problems in static purification systems. Therefore, a dynamic purification system is imperative. Such a system should include, in addition to the palladium or uranium membrane, a storage vessel to permit a substantial volume of material to be handled and a rotary vane blower. A valveless pump such as a blower has the ability to operate at pressures down to any level of vacuum desired, whereas a valved pump will cease pumping when the system pressure drops below that required to open the valves. In the operation of the U-bed, introduction of impure tritium is periodically halted to allow the U-bed to absorb all the tritium in the loop; then the helium-3 is pumped off to the stack after passing through one or more scavenger U-beds to absorb any residual tritium. The cycle is then repeated.

Helium-3 buildup in the lattice of uranium tritide also contributes to the problem. Pure tritium is obtained from a U-bed by repeatedly cycling the system in such a manner as to desorb a substantial fraction of the tritium and helium-3 into a large volume, allowing the U-bed to cool, then reabsorbing the tritium, leaving the helium in the gas phase

to be pumped off. It is helpful in such a procedure to discard the first small aliquot of helium-rich gas.* Helium is desorbed from a U-bed at lower temperatures than tritium since it tends to accumulate in bubbles in the lattice, in contrast to tritium which occupies definite lattice sites. A second method by which essentially pure tritium can be obtained is to record the maximum temperature to which the U-bed is raised during the purification cycles; and then during the final desorption cycle of pure gas, the U-bed is heated to a temperature several degrees below the previous maximum. While I realize that tritium fuel for CTR machines can tolerate some helium contaminant, the foregoing is to be taken as advice.

Investigation of the properties of uranium tritide at Mound Laboratory has revealed some of the characteristics of helium release from a uranium tritide lattice. As mentioned, helium exists primarily as bubbles in the lattice, a topic to be fully described in the following talk by R. C. Bowman and A. Attalla of Mound Laboratory. Heating a uranium tritide lattice does not remove all the trapped helium-3. Furthermore, undisturbed uranium tritide slowly evolves helium-3 at a rate far less than the generation rate. Figure 3 is a plot of the helium release from uranium tritide with time. These data were obtained at Mound Laboratory by R. C. Bowman and C. J. Wiedenheft. This material was new uranium tritide which did not have a previous history of exposure to tritium and/or high temperature for any substantial length of time. It has a surface area of approximately 0.4 m^2/g. A similar experiment was conducted on uranium used in connection with studies of the thermodynamics

*As an example, during the 5th cycle (purification) helium-3 = 5.8% in initial 0.019 liter; 0.05% in following 0.75 liter (out of 20 liters total desorbed gas).

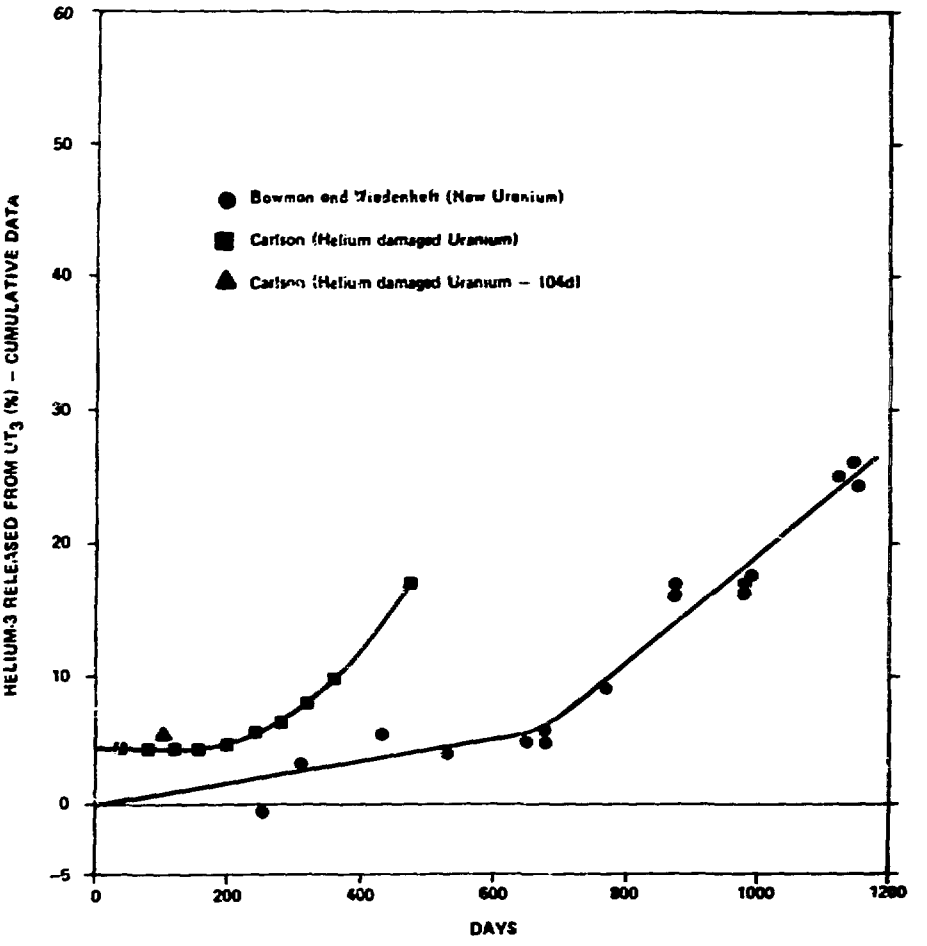

Fig. 3. Helium-3 Release Data for New and Old Samples of UT_3; Material Stored at Ambient Temperatures.

of the uranium tritide system (estimated to have a surface area of 1.5-2.5 m^2/g). At the beginning of this experiment, the high purity sample of uranium* I used had experienced a total of approximately 52 hr of exposure to tritium at temperatures of 450-600°C, the first half of the exposure being at a T/U ratio of 2.1 or less; the second half of the exposure to tritium being at a T/U ratio of 2.85 or greater. It can be postulated that deposition of helium-3 into a uranium lattice at high temperature would have created more damage than such deposition at room temperature. Of course, it can also be postulated that relaxation or healing processes also proceed faster at elevated temperature. It will be observe that release proceeds more rapidly for the first 1.3 yr with pre-aged uranium tritide than with new uranium tritide. Of course, the pre-aged uranium was not only damaged but still retained some fraction of the helium-3 previously trapped in the lattice before the experiment commenced, even though the sample had been heated to 700°C and stripped of all tritium, followed by thorough purging with deuterium and a second heating to 700°C to remove the deuterium, and followed finally by loading of tritium to a composition of $UT_{3.0}$. This material was allowed to stand for 104 days at room temperature; the evolved helium-3 overpressure was then measured and the gas sample analyzed by mass spectrometry. It was pure helium-3 and represented 5.4% of all the helium-3 born in the lattice. This helium-3 overgas was pumped off and the data in Figure 3 were subsequently obtained which agrees well with the 5.4% data point. It can be concluded that a damaged uranium lattice cannot be completely annealed at temperatures below 700°C and that the pre-induced lattice defects substantially increase the rate of helium release from uranium tritide.

*Analysis (ppm) Fe, 20; Si, 25; Mn, 5; Mg, 10; Ni, <10; Al, 25; Cu, <6; Cr, <8.

One other observation which may be of interest is that absorption of tritium dynamically on a U-bed proceeds smoothly and initially with great velocity generating substantial heat. Obviously the absorption of tritium eventually becomes self-limiting because of the exothermic nature of the reaction. Absorption ceases when an equilibrium temperature is reached, that is, equilibrium with reference to the composition-pressure-temperature plot of the uranium-tritium system. This temperature is about 400°C under normal conditions of about 1 atm tritium pressure. Emergency cooling is not really necessary because of this, as a runaway reaction is not possible; however, evolved heat must be removed to promote continued absorption. The observation I am referring to here is that after the composition of the U-bed has reached about T/U = 1.5, the absorption rate seemingly slows down. In other words, it is more difficult to absorb tritium on a half-filled U-bed than on an empty U-bed. This is contrary to the C-P-T plot which indicates a plateau or two-phase region of great width, from about $UT_{0.01}$ to $UT_{2.99}$, which implies no change in equilibrium pressure over that range. I believe this problem is related to the diffusion coefficient of tritium in the grain of uranium-uranium tritide in that after the grain of uranium is partly saturated, diffusion into the depth of the grain becomes the controlling factor in preventing rapid absorption of tritium into the uranium lattice.

Thus, a doubly contained U-bed, which has provisions for both circulation of gas through the bed and sufficient cooling capability to remove the heat of reaction and which is operated with some consideration of the relative properties of helium-3 and tritium in the lattice, has been found at Mound Laboratory to be one of the more useful devices for handling and storing tritium.

The thermodynamic properties of the uranium-tritium system were investigated over a pressure range of 10^5 atm from 119-572°C. The apparatus and material used were identical to those which were later used for the helium-3 release experiments, and exposure of the uranium metal to helium-3 damage at high temperature recurred during this experiment. Initially slices of high-purity uranium metal were deuterided and degassed until the massive metal was reduced to a fine powder. After all the deuterium had been removed by evacuating the system at 700°C at pressures in the micrometer region, the system was purged once with a small amount of tritium which was removed by the same method used to remove the deuterium.

A predetermined amount of tritium was now added to the uranium powder doubly contained in the high pressure reactor, and composition-pressure-temperature (CPT) points were obtained (Figure 4) by cycling the temperature up and then down stepwise, then recording the pressure and the temperature after they remained at equilibrium for 20-30 min. Equilibrium as here defined implies temperature and pressure changes no greater than ±0.5°C and ±0.2% of observed pressure for the period mentioned. All values for pressure are for desorption. Van't Hoff plots of 1000/T°K as a function of log pressure were then constructed at compositions of $UT_{2.90}$, $UT_{0.04}$, and by extrapolation $UT_{0.00}$. It will be noticed that the isotherms are not flat but are at lower pressures and are closer together at the high composition end of the plot. When van't Hoff plots of 1000/T°K as a function of log P are constructed (Figure 5), it will be noticed that the lines representing the three different compositions while straight are not quite parallel. No amount of redrawing sufficed to render the lines parallel. The conclusion is that ΔH and ΔS vary with composition for the uranium-tritium system.

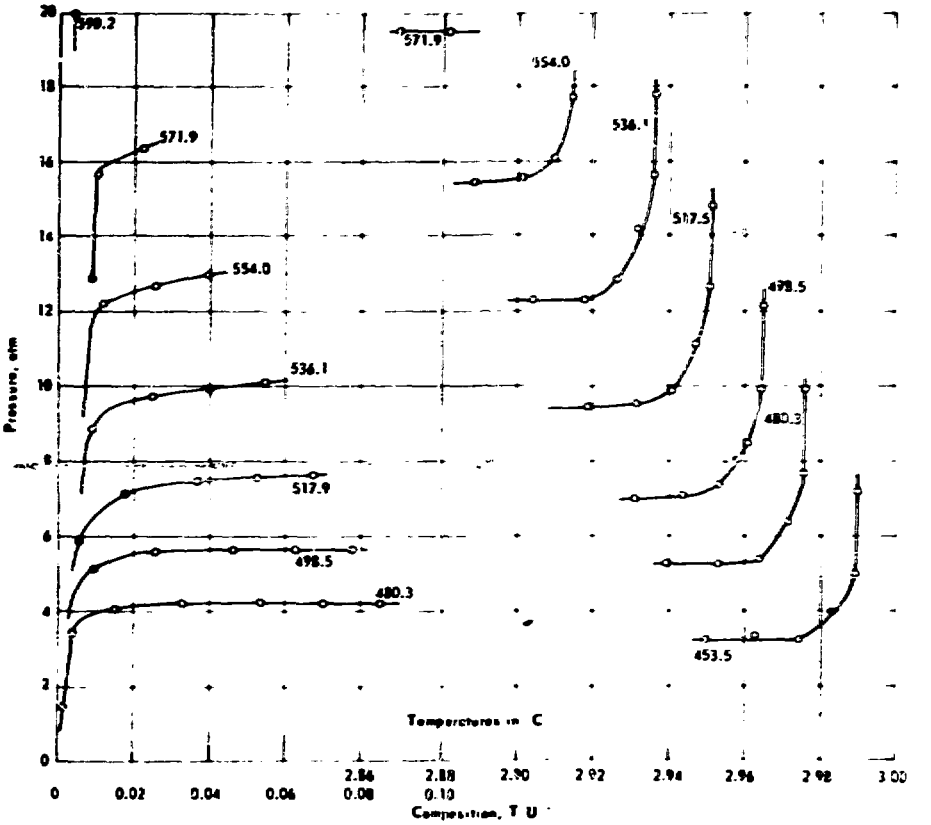

Fig. 4. Composition-Pressure-Temperature Plot of the Uranium-Uranium Tritide System.

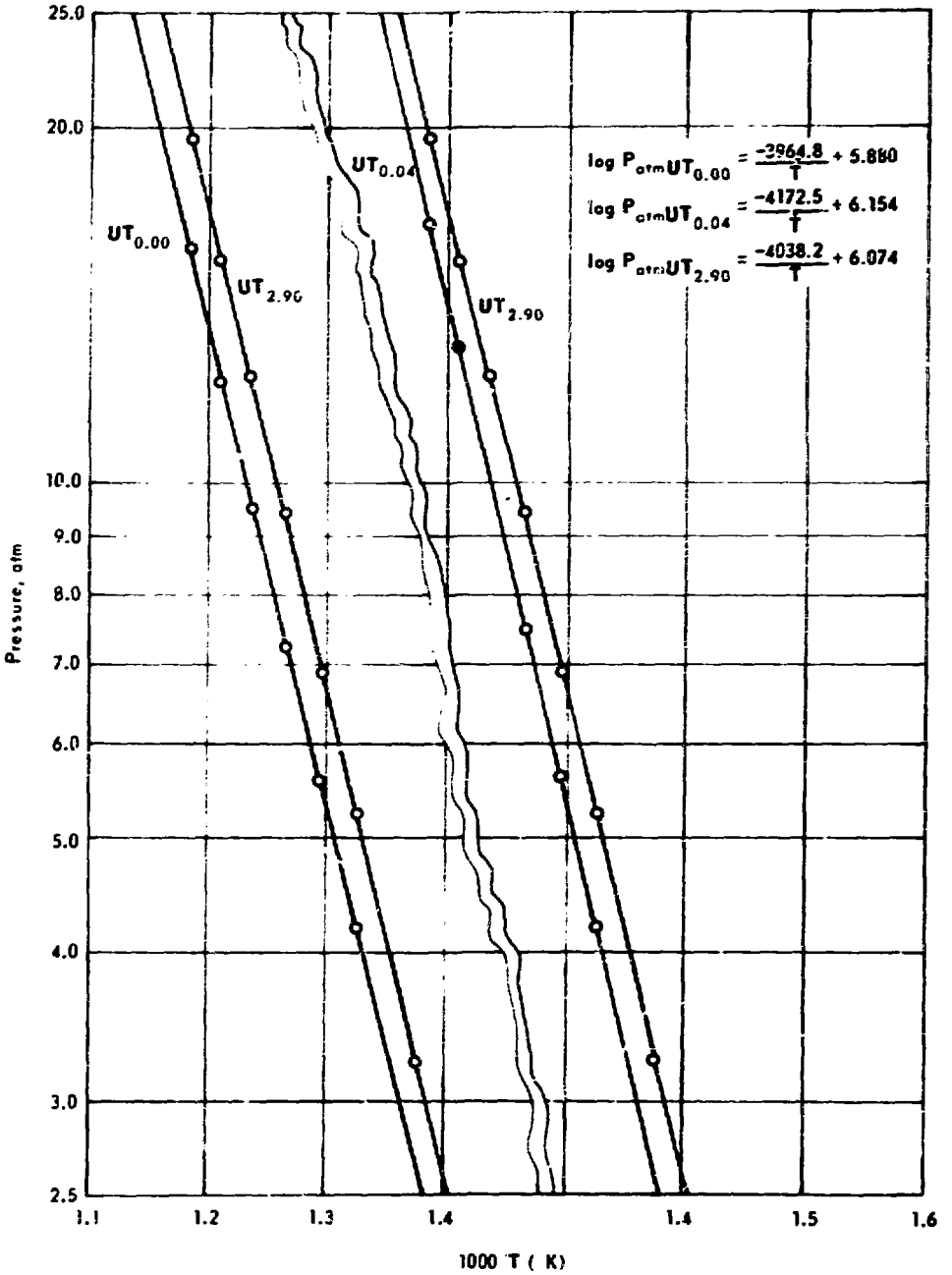

Fig. 5. Comparison of van't Hoff plots for Uranium-Uranium Tritide System.

To test this conclusion, an experiment was performed on the uranium after all the tritium was removed, whereby the system was deuterated to form UD_3 (Figure 6), and van't Hoff data were gained directly by lowering the composition stepwise to one of several values, which were then calculated. Next all valves were closed and the system was cycled up and down twice obtaining seven temperature-pressure equilibrium points during each cycle. When these data had been obtained, the composition was lowered to the next value and the cycles were repeated. All data were corrected for hot and cold volume and for small changes in composition caused by transfer of gas from solid to gaseous phase. In addition, the outer chamber of the doubly enclosed reactor was filled with argon, and this gas was periodically analyzed by mass spectrometry. Any deuterium buildup was noted and appropriate corrections were made. Van't Hoff plots constructed directly from these data were fitted to the equation log P atm = (-A/T°K) + B, and ΔH and ΔS values were calculated from these constants and plotted as shown. In most cases the second set of data from each temperature cycle at any composition was slightly lower in value than the first set of data and these values were chosen to avoid any problems that might have been related to the uranium deuteride "remembering' a previous composition by not having relaxed completely to the new D/U ratio. It will be observed that ΔH and ΔS are at their highest when the D/U ratio is relatively low and when there is a high degree of disorder in the uranium lattice coupled with a plethora of sites capable of accepting a deuterium atom. Conversely, values of ΔH and ΔS are lowest when the lattice is almost completely converted to β-phase uranium deuteride at which point the amount of disorder created by the introduction of a new deuterium atom would be lowest, and the competition for bonding sites (the ΔH value) would be at the highest level. It will be observed therefore that ΔH and ΔS in both uranium tritide and uranium deuteride are

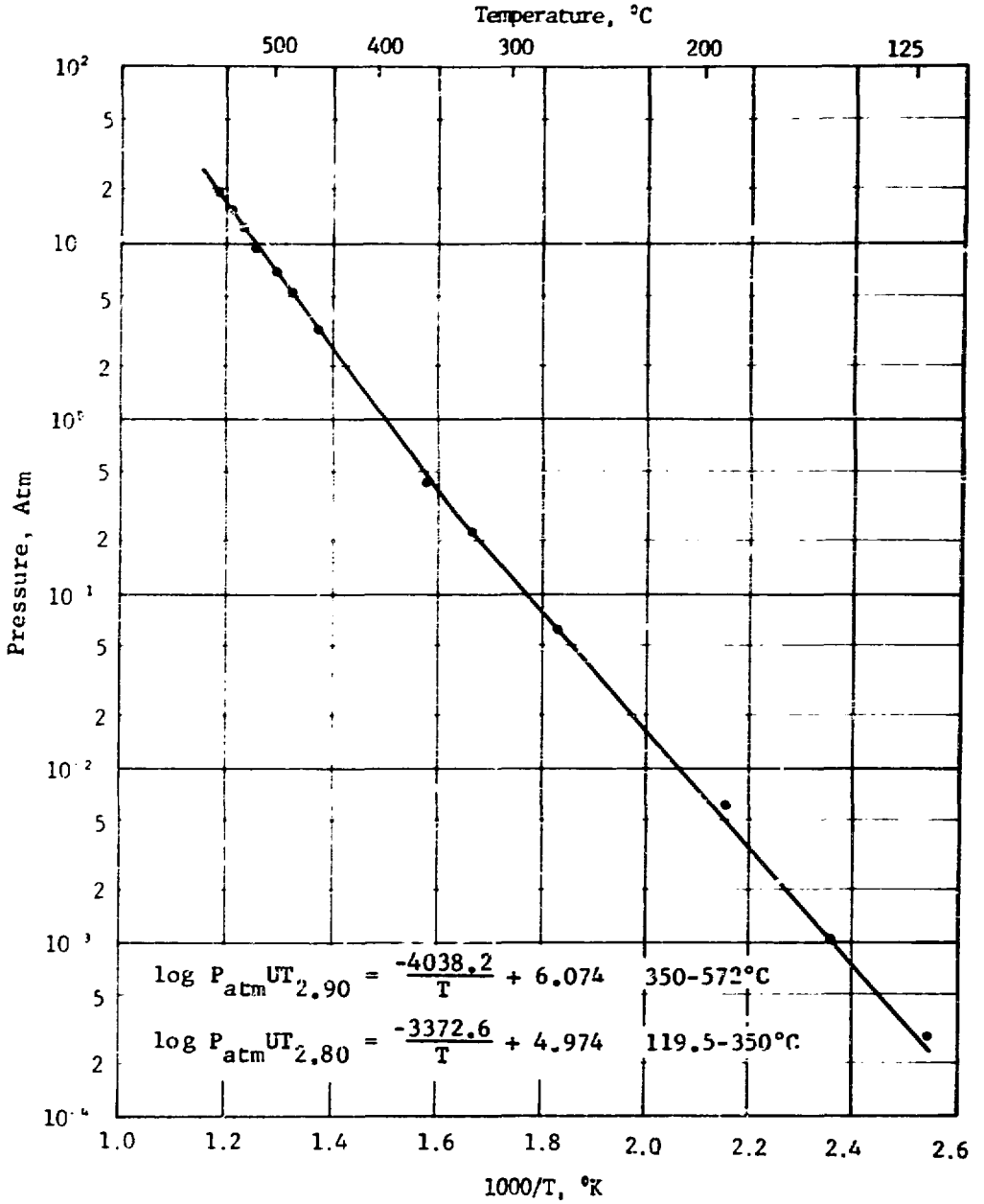

Fig. 6. Thermodynamic Properties as a Function of Composition for the Uranium-Deuterium System.

composition dependent and a weak pressure shift. It is clear that it is premature to speak of the "two-phase plateau region" having horizontal parallel isotherms in this and other metal hydride systems. It appears that minor factors not ordinarily considered in the phase rule may play a significant role in such systems and that the true form of the metal hydride isotherm is not invariably known even when thermodynamic data are precise.

Finally, this system was studied with tritium to form UTi$_{1.8}$ and pressure-temperature data were obtained at low values of both pressure and temperature to extend the van't Hoff plot (Figure 3) of the uranium-tritium system to lower temperatures than heretofore. Equilibrium data were obtained at several points and plotted. The 1 wt pressure for UT$_{1.8}$, 7.215 mm (1.43 x 10^{-5} atm), was a difficult one to make because the rate of pressure increase due to helium evolution at this temperature was very slow, and the time required for the system to reach equilibrium was on the order of 1.5-1.8 hr. It is gratifying that the last point fell near the line drawn through the other points. The slight difference in slope between the two sets of data is not understood at this time. A comparison of the thermodynamic data obtained from the study of the two systems UH$_{1.8}$ and UT$_{1.8}$ with that of other workers is shown in Table 4. The present values seem to agree fairly well.

REFERENCES

1. W. E. Winsche and R. M. Abraham, Dissociation Pressures of Uranium Hydride and Uranium Tritide, ANL-5104, Argonne National Laboratory, Lemont, Ill. (1956), 9 pp. NSA 9:2770.

2. F. H. Spedding, A. H. Daane, K. W. Herrmann, J. A. Wolf, L. Johnson, R. W. Mattern, L. B. Muhleman, and A. H. Krahn, Nucleonics, 4, 4-15 (1949). CA 43:5761d.

3. E. Wicke and F. Otto, Z. Elektrochem., Ber. Bunsenges. Physik. Chem., (Frankfurt), 58, 162-249 (1954). (in German). CA 49:9901i.

4. [illegible], Trans. Faraday Soc., 54, 71 (1958).

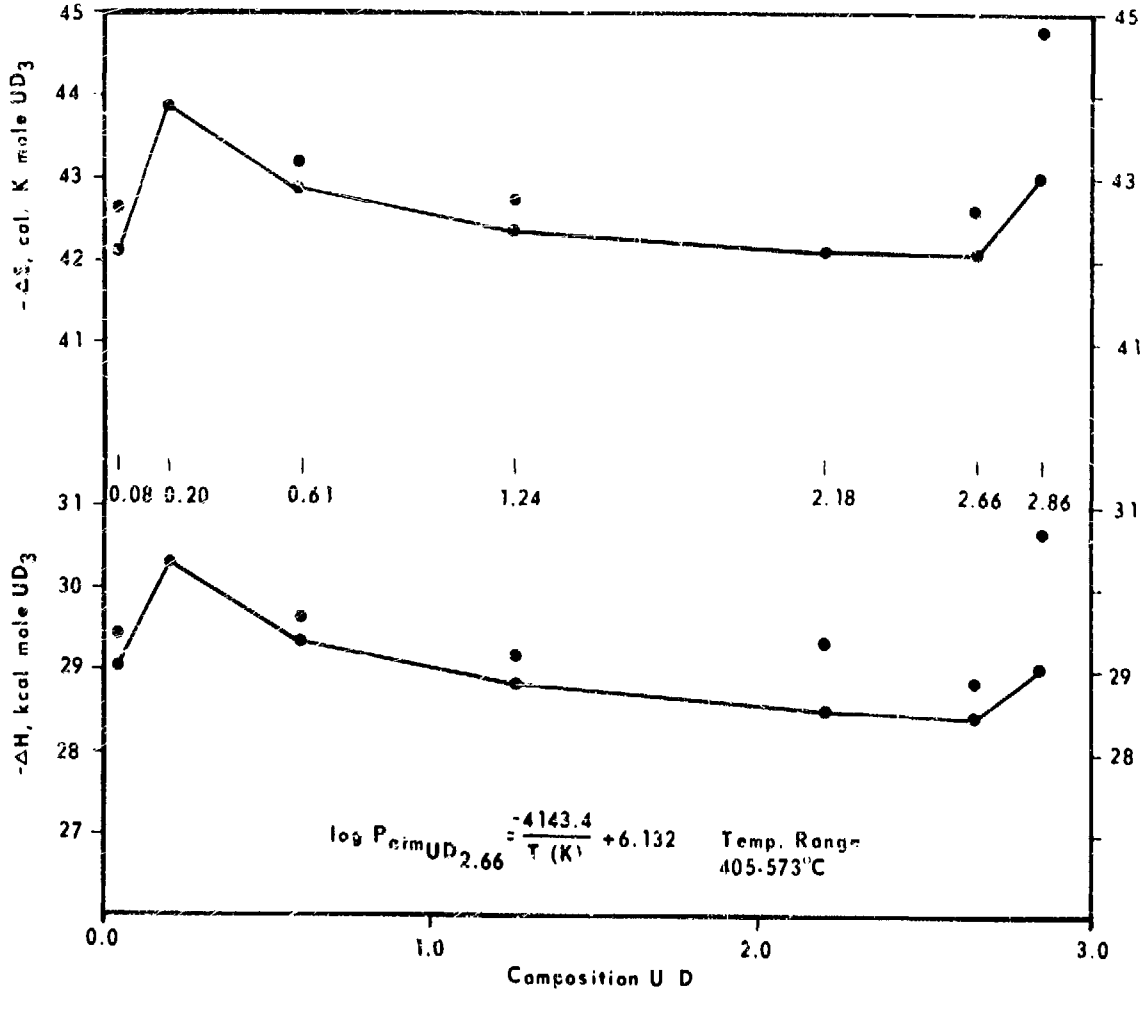

Fig. 7. van't Hoff Plot for the Uranium-Uranium Tritide System.

Table 1. Thermodynamic Properties of Uranium Hydrides

	ΔH_S (kcal/mole)	ΔS_S (cal/°K/mole)
$UH_{3.0}$[a,b,c]	-30.5[f]	-43.4
UH_3[d]	-28.96	-41.43
UD_3[b,c]	-30.8[g]	-44.8
$UD_{2.66}$[c]	-28.4	-42.09
UT_3[a]	-30.75	
$UT_{0.00}$[c]	-27.2	-40.4
$UT_{0.04}$[c]	-28.6	-42.2
$UT_{2.90}$[c]	-27.7	-41.7

[a] Reference 1

[b] Reference 2

[c] Reference 3

[d] Reference 4

[e] Present work by R. S. Carlson

[f] Average of data in References 1, 2, 3

[g] Average of data in References 2 and 3

HELIUM RELEASE FROM URANIUM TRITIDE

M. L. Malinowski P. R. Coronado

Sandia Laboratories, Livermore, CA

ABSTRACT

The release of ^3He from coarse (0.6 m^2/g) stoichiometric uranium tritide has been measured as a function of time up to a tritide age of 1200 days. Less than 2% release occurs until approximately 280 days, after which the release increases dramatically, with the ^3He release rate approaching generation rate after 1000 days. This release is particle-size dependent and can be fitted with good results with a semi-empirical model which assumes diffusive movement out of the solid after the initial hold-up period.

INTRODUCTION

Thermal decomposition of uranium tritide is commonly used as a safe, convenient means of supplying high-purity tritium for laboratory applications. One of the many factors which could influence the purity of the delivered gas is the release of ^3He from the tritide lattice during either thermal decomposition of the uranium bed or during long term storage of the tritide at room temperatures. It seems appropriate, therefore, to accurately measure the helium release from UT_3 as a function of time. In addition to providing useful information directly applicable to the operational performance of uranium beds stored under tritium overpressures, these release experiments would also result in data which would aid in an atomistic understanding of ^3He release from metal tritides, an area in which experimental and theoretical work is now actively being pursued.[1,2,3]

The experiments described in this paper were performed on fully stoichiometric UT_3. The tritium lost through decay has been continually replenished with gaseous tritium to maintain a constant tritium/metal atom ratio in the solid. The release behavior of sub-stoichiometric uranium tritide should be considerably different from that of fully stoichiometric UT_3.

EXPERIMENTAL PROCEDURES

Tritide Preparation

Each uranium tritide sample is formed in-situ in a special container by the direct reaction of high purity uranium metal with 99+ % pure tritium gas. As shown in Figure 1, the tritide is located in a gold-plated container with a volume of approximately 55 cc. Attached to this volume is a small "back-to-back" valve arrangement, which is used to sample the tritium overpressure gas, a procedure described below.

The primary container volume, sampling volume, uranium tritide sample mass, and amount of overpressure gas are sized such that there will be sufficient tritium in the overpressure gas to maintain stoichiometry in the tritide for ~ 5 years.

Prior to tritiding of the metal, the gold-plated "primary" container is outgassed at ~ 600°C for 24 hours $< 10^{-7}$ torr on an ion-pumped system. Then electropolished uranium chunks are placed into the primary container, the container is sealed to the two valve manifold, and the entire assembly is evacuated and leak-checked. The container and uranium chunks are outgassed together at ~ 400°C until a pressure of $\lesssim 10^{-7}$ torr is achieved on the ion-pumped outgassing manifold. The sample is valved off, cooled down, and moved to a different manifold for tritiding.

Tritiding of the sample is performed by a conventional Sieverts' technique. High purity (~ 99%) T_2 is supplied to the gas rack from a thoroughly scrubbed uranium bed. Normally the uranium is heated to approximately 200°C to initially accelerate the tritiding process. As soon as the tritium is absorbed, the sample heating is discontinued and the reaction is allowed to go to completion. This method of tritiding uranium typically produces UT_3 with a surface area/mass ratio of ~ 0.6 m^2/g, as determined by B.E.T. surface area determinations. Tritium-to-metal atom ratios of 2.95 → 3.05 are typically achieved, and the total gas uptake of the sample is known to an accuracy of ~ ± 2%. X-ray measurements on deuterides prepared this way indicated β-UT_3 is

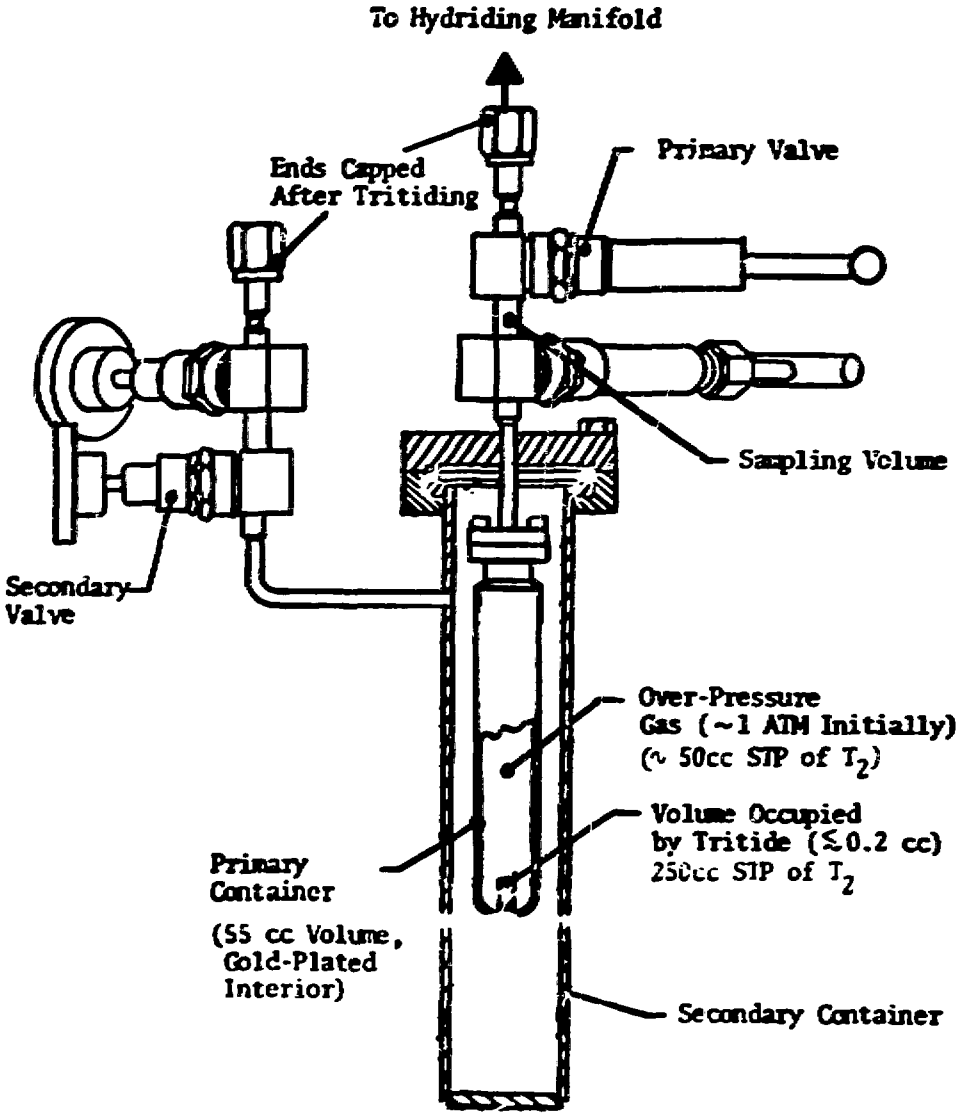

Figure 1. Typical Uranium Tritide Sample Container.

formed with no α-UT_3 being produced.[4]

After the tritiding of a sample is completed, an overpressure of $\sim$ 800 torr of T_2 is left over the sample. Since the equilibrium overpressure of UT_3 at room temperature is $\sim 4 \times 10^{-6}$ torr,[5] this gas phase tritium will presumably replace any tritium lost in the lattice due to decay and, hence, maintain the stoichiometry of the tritide. Then, the sample is valved off, the sampling volume (see Fig. 1) is evacuated, all valves are closed and capped, and for safety reasons, a secondary container is mounted around the primary container and the entire assembly is stored at ambient temperatures.

Gas Samplings

The composition and total pressure of the overpressure gas in the primary container are periodically measured by withdrawing samples of gas. This is done by the "back-to-back" valving on the primary container. An accurate determination of this sampling volume is necessary to compute the total gas withdrawn during each sampling; therefore, this volume, typically $\sim$ 1 cc, is measured on each sample container to accuracies of $\sim \pm$ 0.005 cc on a separate system prior to assembly of the manifold to the primary container.

The data from these gas samplings are used together with the data obtained at the time of tritide fabrications (viz. sample mass, mass of tritium in the solid and overpressure) in mass balance calculations. The ^3He release and tritium-to-metal atom ratio of a tritide result from these computations.

EXPERIMENTAL RESULTS

The helium release from six separate uranium tritide samples is shown in Figure 2. In Figure 3 are plotted the tritium-to-metal atom ratios for the same samples. Note that the different symbols refer to the different sample numbers.

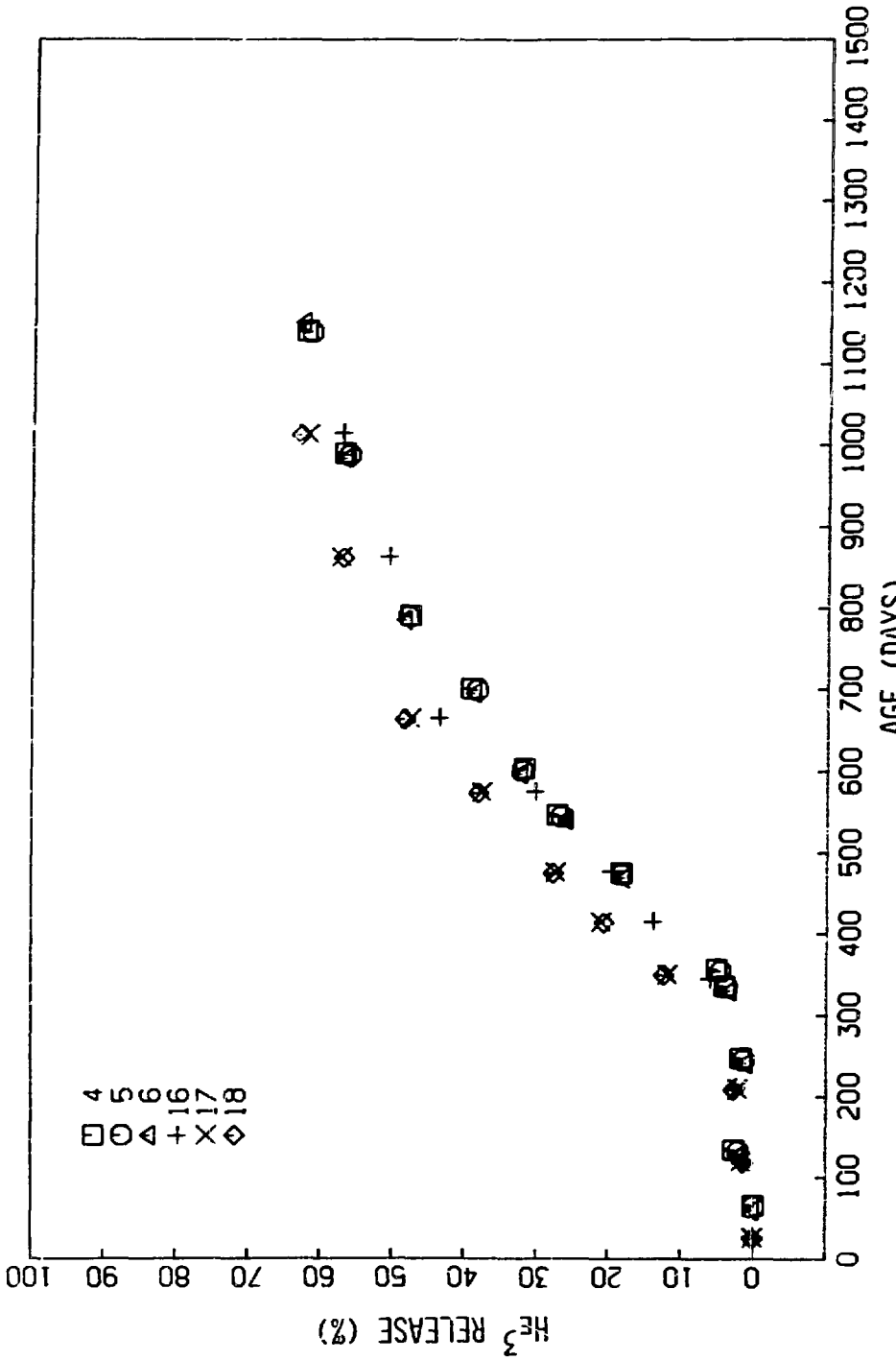

Figure 2. Helium Releases in HT_3 Samples.

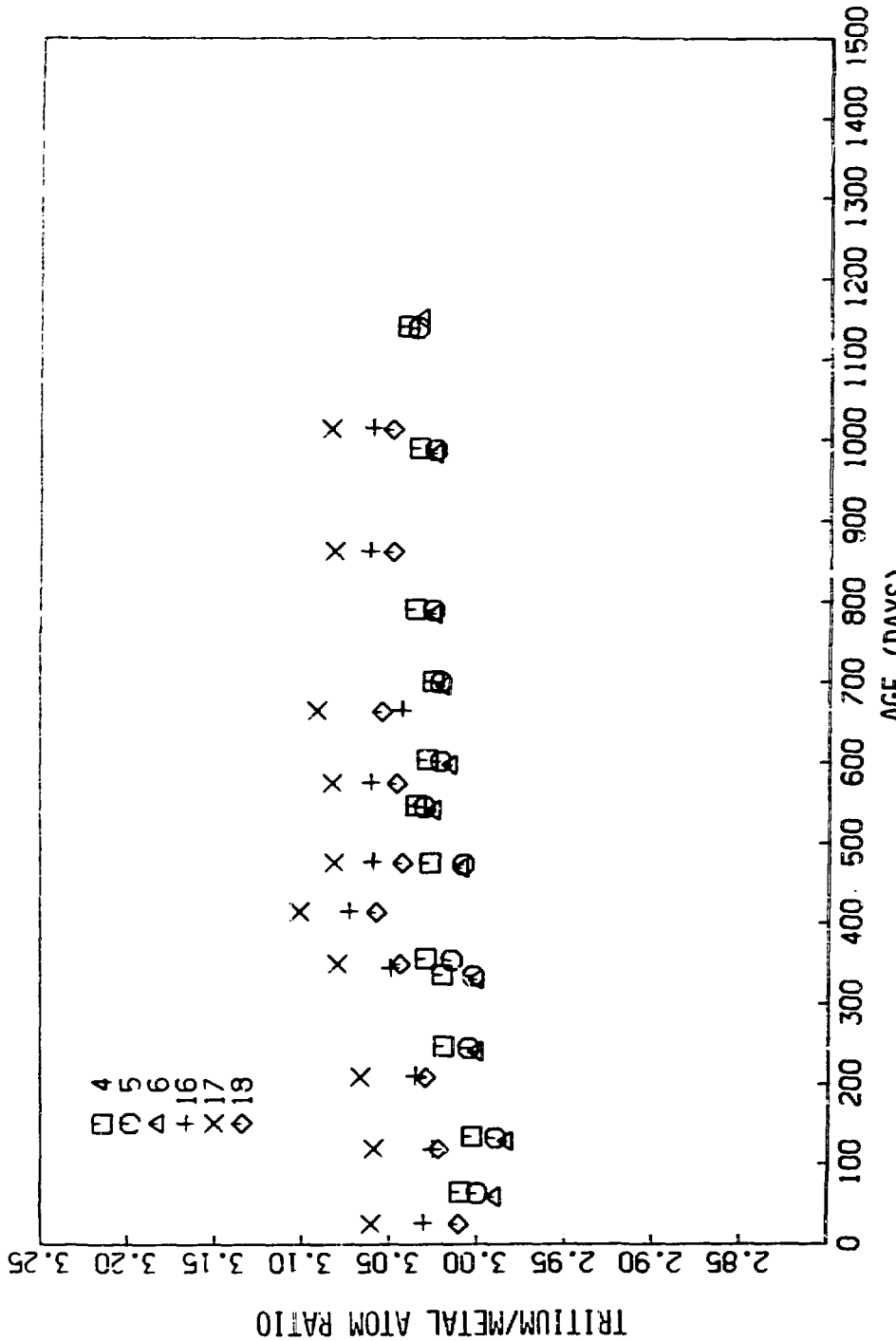

Figure 3. Stoichiometry Maintainance in UT_3 Samples.

Several interesting observations regarding the helium release (shown in Fig. 2) can be made: (1) less than 2% helium release occurs until sample ages of between 250 to 300 days; (2) after the initial delay in helium release, the release abruptly increases; and (3) the onset of accelerated release in samples 4, 5, 6, 16 occurs at a slightly later age ~290 days vs. 250 days - than in samples 17 and 18. As indicated in Figure 3, to within experimental accuracies, the stoichiometries of the samples are being maintained.

DISCUSSION

The first of the observations above to be addressed is (3), the fact that the helium release data from all the samples seem to cluster into two distinct groups, namely samples 4, 5, 6, and 16, and samples 17 and 18. The probably cause for the difference in release behavior between these groups is the method of preparation. All samples in the first group (nos. 4, 5, 6, 16) were prepared as described above, that is, were tritided at ~ 200°C. The samples in the second group (nos. 17 and 18), however, were tritided at lower initial temperatures of ~100°C. The lower the tritiding temperature, the more brittle the uranium/uranium tritide is, resulting in a finer (smaller particle size) UT_3 powder. Therefore, it is likely that samples 17 and 18 have a finer particle size than the UT_3 of the other samples. The likelihood of this possibility is supported by the data shown in Figure 4. The helium release data from UT_3 produced by repeated deuteriding and outgassing prior to tritiding is shown compared to the smoothed data from Figure 3. This deuteriding/outgassing procedure is known to produce UT_3 with particle sizes smaller than is obtainable by a "single-shot" tritiding of uranium chunks. It seems likely, therefore, that the UT_3 particle size does have a profound effect on ^3He release, with finely powdered uranium releasing earlier than coarser uranium. These results are corroborated by similar experiments underway at Mound Laboratory[5] and at Los Alamos Scientific Laboratory.[6]

An estimate of the ranges of approximate particle sizes of the UT_3 for which the data shown in Figures 2 and 4 were taken can be made

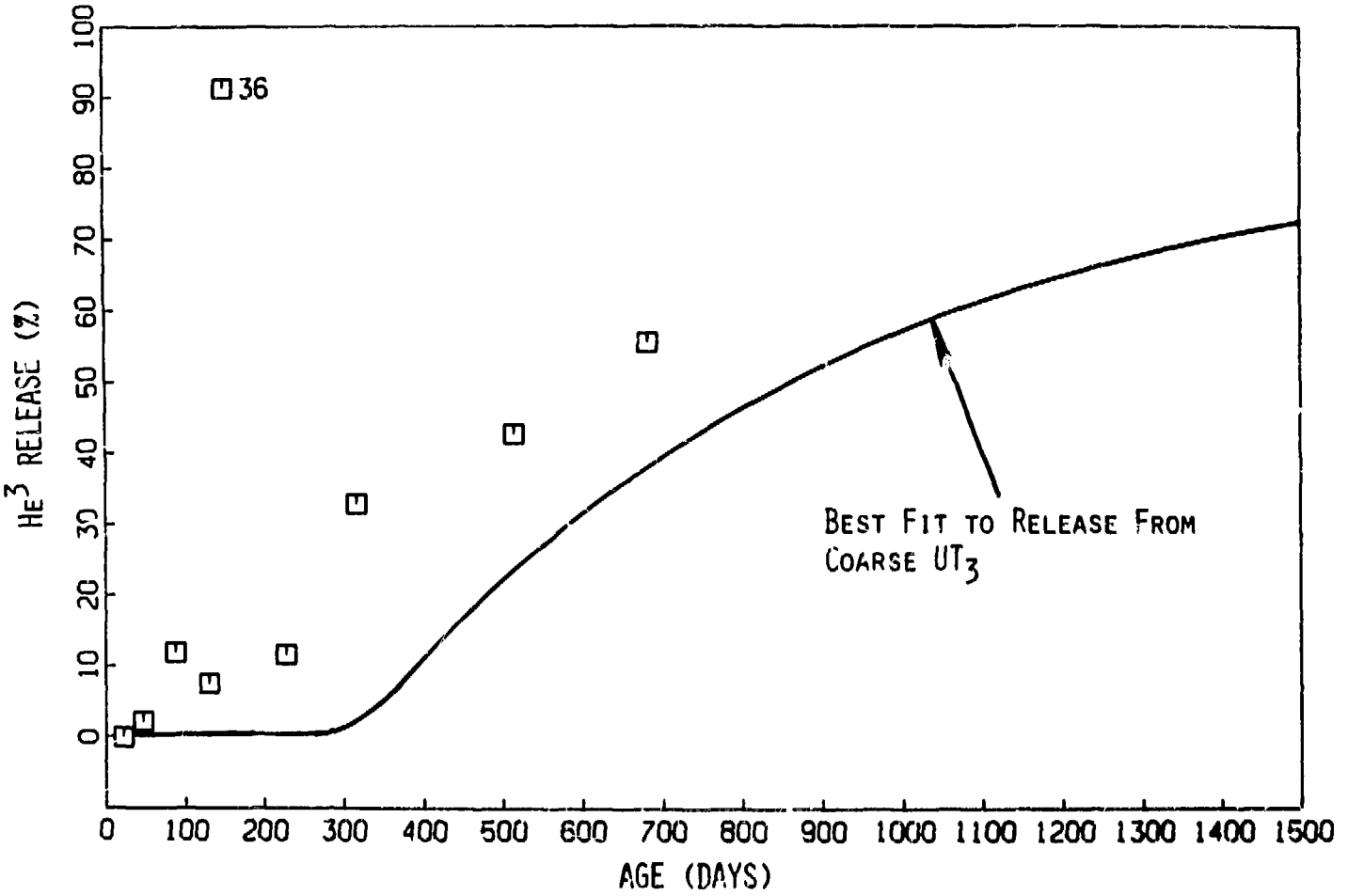

Figure 4. Helium Release From a Finer UT_3.

from B.E.T. surface area data taken on UT_3 fabricated using differing pre-treatments.[6] Single-pass material, formed by directly tritiding uranium chunks, has a specific surface area of $\sim 0.6\ m^2/g$, while UT_3 formed after two to three deuteriding/outgassing pretreatments has a specific area of typically $\sim 3.2\ m^2/g$. Assuming that the uranium tritide is in the form of equi-sized spheres, these specific areas correspond to particle sizes of $\sim 1\ \mu m$ and $\sim 0.2\ \mu m$, respectively.

The other characteristic of the helium release, namely the hold-up period followed by accelerated release is, at this time, not well understood. The presently proposed explanations for this behavior involve either percolation theory or the nucleation and growth of bubbles.[1,2,3,9] The strong particle size dependence of helium release mentioned above, together with recent NMR results by Bowman[2] indicating the motion of ^3He prior to accelerated release would seem to favor the bubble explanation over percolative arguments.

Inert gas bubble formation, growth, rupturing and subsequent gas release have been both extensively studied with implantation methods and modeled theoretically.[10] Unfortunately, at present, no UT_3 samples have been examined by scanning electron microscopy to determine if this growth and rupturing mechanism dominates the ^3He release process.

The release of helium from bubbles would occur after the bubbles reach a grain or particle boundary.[11] Once this boundary is reached, rapid release of gas from the bubble by, for example, grain boundary diffusion, might be possible. In fact, an empirical fit to the data of Figure 2 after accelerated release can be made using a simple diffusion-controlled model.[12]

This "diffusion" model assumes that the tritide particles can be approximated by infinite slabs* all of thicknesses 2ℓ, with constant generation rates of ^3He/volume. The helium concentration on the slab's

*The results for diffusion from spheres is identical within a geometrical factor of order unity.

surface is assumed to be zero. For this geometry and boundary conditions, the diffusion equation can be solved for the total helium in the slab.[13] The result

$$M_1(t) = \frac{M_o \alpha}{12\beta}\left\{1 - \frac{96}{\pi^4}\sum_{m=1}^{\infty}\frac{1}{(m+1)^4}\exp\left(-\pi^2(m+1)^2\beta t\right)\right\} \qquad (1)$$

where

t = tritide age measured from the time of accelerated release, t_{acc},

M_o = original T_2 mass,

α = T_2 decay constant,

β = $D/4\ell^2$, with

D = the diffusion constant of ^3He, and

2ℓ = the slab thickness.

The total mass of tritium (M(t)) retained by the tritide as a function of time is therefore

$$M(t) = M_1(t) + M_o\alpha\ t_{acc}, \text{ for } t > t_{acc} \qquad (2)$$

The ^3He release, F(t), is defined as

$$F(t) = \frac{\text{Total } ^3\text{He mass generated - Total } ^3\text{He mass retained}}{\text{Total } ^3\text{He mass generated}}$$

$$F(t) = 1 - \frac{M(t)}{M_o\alpha\ t} \qquad (3)$$

Equation (3) has been fitted to the data by a least mean squares method. The result for the first sample group (nos. 4, 5, 6, and 16) is shown in Figure 5. The fit to the samples in the second group is similar. The fitting parameters used for both groups are listed in Table 1. One could take the derived value of β, $\sim 8\times10^{-9}$ sec^{-1} and, assuming a value of $2\ell \approx 1$ μm, calculate the effective "diffusion constant" to be $\sim 8\times10^{-17}$ cm^2/s. However, this diffusion constant may not bear any direct correspondence to the actual diffusion constant of ^3He in UT_3 for two reasons. First, the fits described above have no atomistic foundations and, second, the effective diffusion length (2)

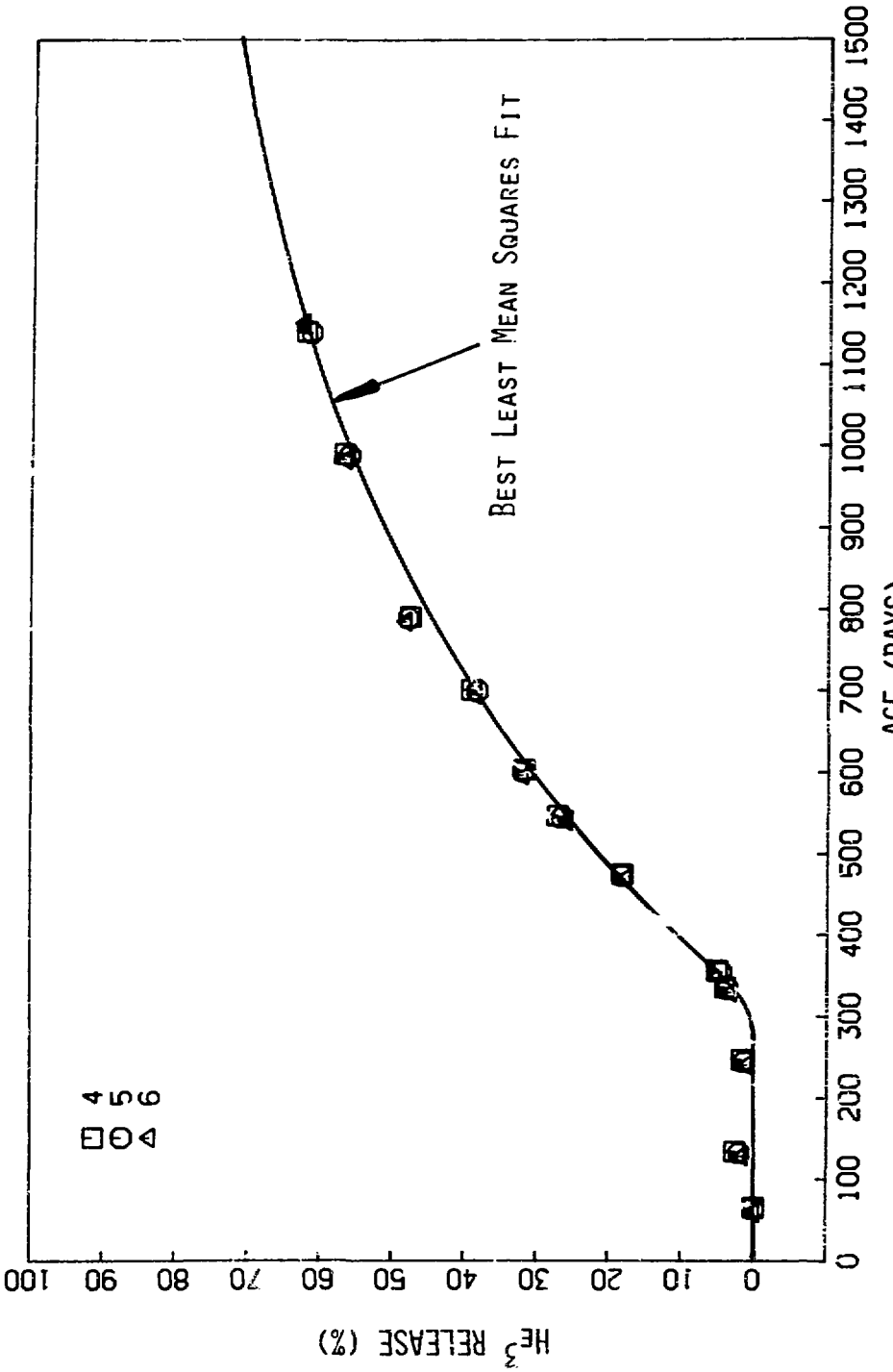

Figure 5. Semi-empirical Fit to The Helium Release Data.

may be related to quantities other than particle size, such as grain size. These semi-empirical fits seem to be useful, however, for predicting the amounts of ^{3}He released by the tritide for times after accelerated release. Fits made with ^{3}He data up to ~ 800 days have successfully predicted the release at 1200 days.

Table 1. Parameters for the Semi-Empirical Fit to ^{3}He Release Data

Sample Nos.	Fitting Parameters	
	t_{acc} (days)	$\tau = D/4r^2$ (sec^{-1})
4, 5, 6, 16	291	7.21×10^{-9}
17, 18	251	8.95×10^{-9}

If one uses the curve fit to the data to calculate the normalized release rate of ^{3}He from UT_3 (release rate of ^{3}He divided by the generation rate), one obtains the curve shown in Figure 6. It is evident that after ~ 1000 days, ^{3}He is being released from the solid at generation rate. However, up until this age, helium has accumulated in the lattice. Figure 7 shows the ratio of helium atoms to tritium atoms* in the lattice, and the limiting amounts of helium in the tritide are evident.

As described above, this semi-empirical model does not have a firm atomistic foundation. For a microscopic description of ^{3}He release to be complete, the effects of temperature, grain and particle size, lattice strains, bubble growth and surface oxides must be included.

SUMMARY

The measurement of helium release from coarse UT_3 reveals a hold-up time followed by a period of accelerated release. The release is particle-size dependent, and can be fit to a semi-empirical theory

*A constant amount, since stoichiometry is maintained in these samples.

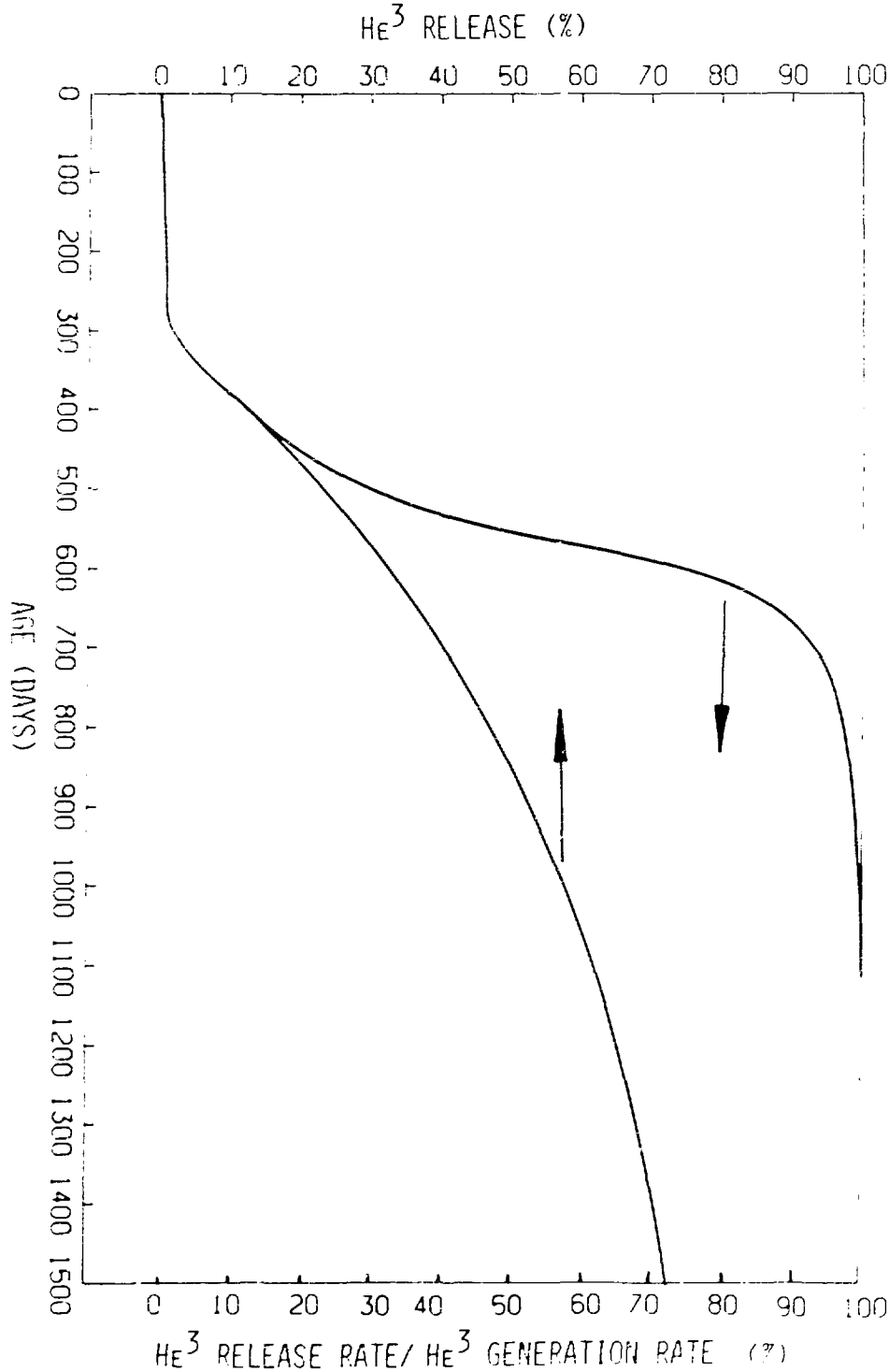

Figure 6a. Helium Release Rate of the Lunar UH_3 Samples.

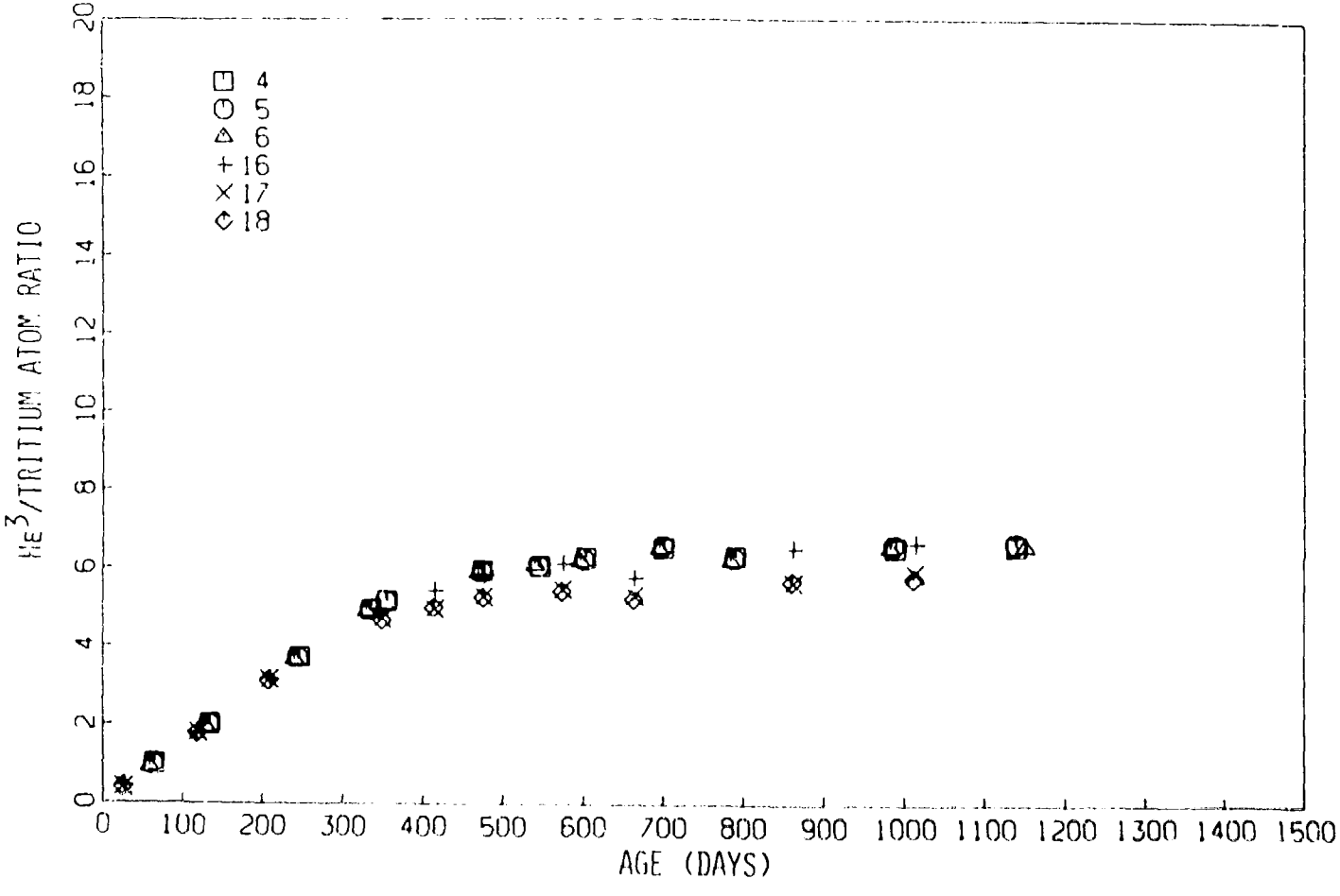

Figure 7. Helium Concentration in the HT_3 Samples.

with good results. Additional experimental and theoretical work is necessary before an atomistic understanding of the release process will be achieved.

ACKNOWLEDGEMENTS

Thanks go to R. Stump of Lawrence Livermore Laboratory for performing valuable mass spectrometer work, to M. C. Nichols of Sandia Laboratories Livermore for X-ray measurements, to Mound Laboratory for B.E.T. measurements, and to K. L. Wilson for valuable conversations.

REFERENCES

1. R. J. Carp and H. T. Weaver, to be published in Phys. Rev. B.

2. R. C. Bowman, Jr., and A. A. Attala unpublished results and the Proceedings of this Conference.

3. W. D. Wilson and M. I. Baskes, unpublished results.

4. R. N. R. Mulford, F. H. Ellinger, W. H. Zachariasen, J. Amer. Chem. Soc. 76, 297 (1954).

5. C. J. Northrup, Jr., J. Phys. Chem. 79, 726 (1975).

6. This pretreatment was first used by D. Larsen, LASL, and Conden, et al, at ORNL.

7. R. C. Bowman, Jr., and K. Foster, unpublished results.

8. R. Alire, unpublished results.

9. K. L. Wilson, Sandia Laboratories Livermore, private communication.

10. See, for example, Walter Bauer and W. D. Wilson, "Helium Migration in Metals," in the Proceedings of the 1971 International Conference on Radiation-Induced Voids in Metals.

11. W. D. Wilson and C. L. Bisson, private communication.

12. M. J. Malinowski and W. D. Wilson, unpublished results.

13. H. S. Carslaw and J. C. Jaeger, "Conduction of Heat in Solids," p. 150ff, Oxford University Press (New York, 1959).

STUDIES OF HELIUM DISTRIBUTION IN METAL TRITIDES

R. C. Bowman, Jr.
A. Attalla

Monsanto Research Corporation, Mound Laboratory

ABSTRACT

The distribution of helium (^{3}He) in LiT, TiT_2, and UT_3, which are regarded as representative metal tritides, was investigated using pulse nuclear magnetic resonance (NMR) techniques. Analyses of the NMR lineshapes and nuclear relaxation times indicate the ^{3}He atoms are trapped in microscopic gas bubbles for each tritide. The effects of concentration and temperature on the ^{3}He distributions were investigated as well.

INTRODUCTION

Since the first generation of Controlled Thermonuclear Reactors (CTR) is based upon deuterium-tritium (DT) fusion, metal tritides are certain to be involved. Whether metal tritides are used intentionally as fuel material, tritium storage agents, and tritium getters or are accidentally formed by chemical reactions between tritium gas and various structural materials, their physical characteristics will be important criteria in CTR designs. Although many properties of the metal tritides can be predicted from the available data on corresponding hydrides or deuterides, the effects of the transmutation of tritium into helium (^{3}He) cannot be readily established from the behavior of hydrides or deuterides. Besides the possibility of extensive radiation damage to the metal tritide lattice from tritium decay, the presence of large quantities of ^{3}He in the DT fuel would be detrimental to obtaining and sustaining the fusion reaction. Hence, the

helium distributions and release characteristics of the metal tritides expected to be found in CTR systems need to be carefully evaluated.

Several previous studies[1-7] indicated that various metal tritides can retain significant quantities of ^3He before releasing ^3He to the gas phase. The helium atoms could be either individually dispersed in the metal tritide lattice (i.e., located in interstitial sites, vacancies, impurity-vacancy pairs, etc.) or trapped in gas bubbles created in the host lattice. While some studies[6,7] indicate that helium can exist in gas bubbles, most of these studies are not adequate to permit a detailed understanding of the helium distribution in metal tritides and the influences of temperature and age.

A broad-based investigation of the properties of various metal tritides has been in progress for several years at Mound Laboratory. Included in this program is the systematic evaluation of radiation damage behavior and studies of the distribution and release of helium. Pulse nuclear magnetic resonance (NMR) spectroscopy is a valuable technique in this program since the nuclear relaxation times can be related, in principle, to the helium distribution. Recent NMR studies of ^3He in lithium tritide (LiT), titanium tritide (TiT_x), and uranium tritide (UT) are presented in this paper and interpreted in terms of the helium atoms being trapped in microscopic gas bubbles for each tritide host.

PULSE NMR - THEORY AND TECHNIQUES

The phenomenon of nuclear magnetic resonance can occur when nuclei possessing nonzero spin moments are placed in external magnetic fields. The nuclear spin energy levels which were degenerate in zero magnetic field are now split and transitions between adjacent levels become possible if

[illegible] magnetic radiation [illegible] applied [illegible] type-
[illegible] energy obeys

[illegible] (1)

where [illegible] the radio-frequency field radiation [illegible] Hertz, H_1 is the magnetic field strength, and γ is the nuclear magnetogyric constant which is a unique [illegible] nuclear species. In pulse NMR the rf radiation is applied in short bursts [illegible], 1-10 msec) at a discrete frequency. The types of information obtainable from pulse NMR measurements are summarized in Table 1. The present work was concerned with determining the ^{1}H concentrations by spin counting and the spin-lattice nuclear relaxation times. The number of protons is directly proportional to either the initial height of the free induction decay (FID) if all were in a solid (i.e., the y-intercept of the maximum NMR signal) or the maximum amplitude of the spin echo (extrapolated to zero time between the pulses). In both cases, the resulting signal is proportional to the NMR signal amplitude of a known standard with similar amplitude characteristics. The nuclear relaxation time of the spin-lattice relaxation, also called the [illegible] time, T_1, is the characteristic time [illegible] for the [illegible] to return to [illegible] its equilibrium value, M_0. The T_1 value is [illegible] by the application of a 180° pulse followed by a 90° pulse. The [illegible] is measured by varying the [illegible] between the pulses. The pulse relaxation time, T_2, [illegible] is the characteristic time [illegible] for the [illegible] to return to [illegible] its equilibrium value, M_0. The T_2 value is [illegible] by the application of a 90° pulse followed by a 180° pulse. The [illegible] is measured by varying the [illegible] between the pulses. Because [illegible] nuclear relaxation times are usually [illegible] by molecular motion, the nuclear relaxation times are often [illegible] as the time it takes the NMR signal to [illegible] 1/e of the original value.

[illegible] applies the nuclear relaxation times [illegible] primarily related to the physical state of the sample [illegible]. There are two limitations [illegible] of which NMR [illegible] establish

Table 1. Summary of Information Obtained Using Pulse NMR

NMR-Parameter	Symbol	Type of Information
Initial FID Amplitude	--	Spin Concentration
Extrapolated Echo Amplitude	--	Spin Concentration
Frequency Shifts	$\delta\nu$	Knight, Chemical, etc.
Linewidth	T_2^*	Local and External Fields
Spin-spin Relaxation Time	T_{2m}	Homogeneous Spin Interactions
Spin-lattice Relaxation Time	T_1	Spin Dynamics

the local environment. When the nuclei are situated in rigid lattice positions, the relaxation times obey

$$T_{2d} \sim T_2^* \approx T_{2m} \ll T_1 \qquad (2)$$

where T_{2d} is the dipolar spin-spin relaxation time which can be calculated using the Van Vleck[9] formalism if the lattice positions are known. On the other hand, the molecular motion in macroscopic quantities of gas averages the dipolar interactions to zero and yields

$$T_{2d} \ll T_2^* < T_{2m} \sim T_1. \qquad (3)$$

The differences in the nuclear relaxation times are dramatic with T_2^* and T_{2m} increasing by 2 to 4 orders of magnitude. However, there are also two possibilities for relaxation times to have the intermediate behavior

$$T_{2d} < T_2^* < T_{2m} < T_1. \qquad (4)$$

If the diffusion rate in a solid is sufficient, the relaxation times obey either Eq. (3) or Eq. (4) depending[10] on the mobilities of the diffusing species and the strength of the dipolar interactions. If the dimensions of gas bubbles are sufficiently small (i.e., $\lesssim$1000Å), collisions with wall surfaces will dominate[11] the relaxation rates and tend to reduce T_2^* and T_{2m} relative to T_1. Careful analyses of the NMR data can distinguish between wall relaxations in microscopic

gas bubbles and bulk diffusion in solid particles. For ^3He the same general considerations are valid with the possible addition of spin exchange effects occurring at low temperatures and high densities. Unfortunately, complications can occur in metallic materials which make the analyses somewhat less than straightforward. Examples of some of these complications for ^3He in the metal tritides will be discussed later.

EXPERIMENTAL DETAILS

The metal tritides were prepared by direct reactions between high purity metals and tritium gas. Samples suitable for NMR measurements were loaded into 9 mm o.d. pyrex tubes which were evacuated and sealed. A Bruker variable frequency B-KR 323S spectrometer was used for both the spin counts and relaxation time measurements. Because the ^3He resonance signals were generally weak and often required large receiver bandwidths due to short decay times, extensive signal averaging was usually necessary. The signals were digitized by a Biomation 8100 transient recorder and stored in the memory of a Nicolet 1074 signal averager for signal-to-noise enhancement and baseline subtraction. The spin standards were protons in H_2O/D_2O solutions containing small quantities of $MnCl_2$ to shorten T_1. Relative sensitivity corrections were made between the ^3He and proton counts. The accuracy of the spin counts is ~10-20% depending upon concentrations and relaxation times. All NMR measurements were performed at room temperature which usually varied between 19-22°C.

RESULTS AND DISCUSSION

Representative pulse NMR spectra for ^3He in LiT, $TiT_{1.7}$, and UT_3 are presented in Figure 1. The LiT FID with its long exponential decay is exactly as predicted for atoms in gas bubbles. Although T_2^* for $TiT_{1.7}$ is an order of magnitude

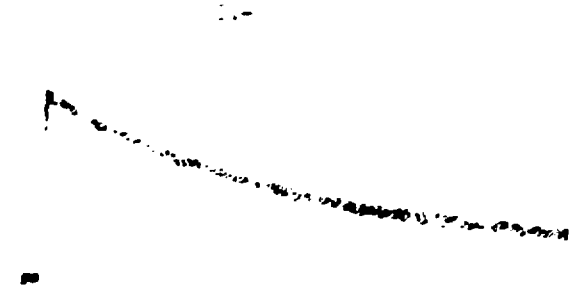

A. LiT : T_2^* = 1330 μs

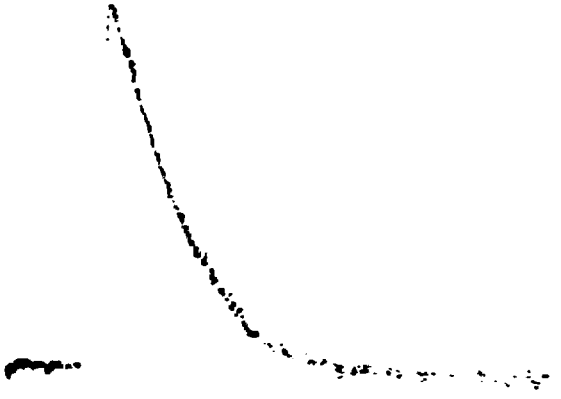

B $TiT_{1.7}$: T_2^* = 78.0 μs

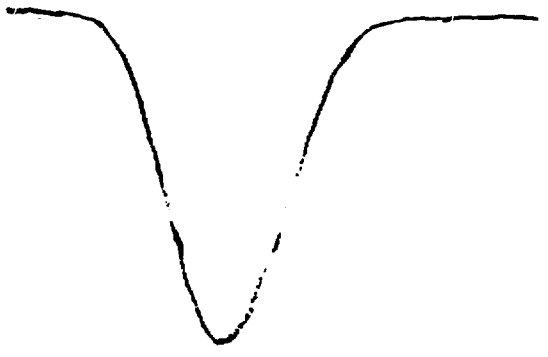

C UT_3 – Spin Echo : T_2^* = 15.4 μs

Fig. 1. Representative NMR Spectra for ^3He in LiT, TiT and UT_3. Resonance Frequency is 45.7 MHz.

shorter, it is still consistent with ^{3}He atoms in gas bubbles since the calculated T_{2d} for ^{3}He atoms in octahedral interstitials is ~15 μs. The ^{3}He lineshape for UT_3 is Gaussian and T_2^* nearly equals the predicted T_{2d} value of ~10 μs. Recent analysis[12] of the magnetic field dependence of the UT_3 lineshape as well as very long T_{2m} values (see Table 2) indicates the short T_2^* is caused by magnetic field gradients arising[13] from the paramagnetic UT_3 powder and the ^{3}He atoms are trapped in gas bubbles in this material as well. The nuclear relaxation times for samples maintained at room temperature for approximately 2-3 years are given in Table 2. In each case, the ^{3}He relaxation times are seen to obey the general relations of Eq. (4). This behavior also indicates that ^{3}He atoms are being trapped in microscopic bubbles in each metal tritide. Analysis of the relaxation times for ^{3}He diffusion in the solid leads to large effective diffusion constants which would be inconsistent with the high ^{3}He content found. In other words, if the helium mobility in the metal tritide lattice was sufficient to yield the relaxation times in Table 2, the helium atoms should be reaching particle surfaces in short times. Since the helium is expected to escape the lattice at these surfaces, the net ^{3}He content in the lattice would be very small. However, at least 80-90% of the helium generated in these tritides has been observed. Hence, the relaxation times in Table 2 indicate the ^{3}He atoms are trapped in gas bubbles sufficiently small that surface relaxation at the bubble walls reduces T_{2m} relative to T_1. Since the relaxation mechanisms for ^{3}He spins in pure gas are very ineffective, the predicted T_1 is $\geq 10^4$ sec for macroscopic quantities of gas. However, interactions with conduction electrons or paramagnetic impurities at the bubble wall can greatly reduce T_1 to the values in Table 2. As expected, the magnitudes of T_1 are very dependent on the host metal tritide and follow the trend of decreasing as the predicted susceptibility increases from LiT to UT_3.

Table [illegible] Relaxation Times for the [illegible] Aged [illegible] Days at [illegible] Mole.

	T_1^a	T_{1m}^a	T_1
[illegible]	150	14	11
[illegible]	7	[illegible]	4.6
[illegible]	15.4	[illegible]	[illegible]

[a] Obtained from NMR pulse separation with pulse spacing [illegible].

The effects of age and temperature on the helium content in LiT are illustrated in Figure 2 where NMR spin count data for helium at room temperature (~ 23°C) and 75°C are compared with the amount of helium generated from tritium decay. Two observations can be made from these results: 1) increasing the temperature significantly reduces the helium trapped in the bubbles, and 2) after retaining most of the helium for [illegible] days at room temperature the ^3He content apparently saturates at 1.4×10^{19} atoms/mol tritium. It is believed the ^3He not detected by NMR has been released from the LiT while only no evidence for helium atoms in the lattice [i.e., obeying Eq. (2)] have been observed. As indicated in Table 4, differences in the relaxation times T_{1m} and T_1 occur with both age and temperature. Raising the temperature significantly increases the relaxation times and they also increase with age. Taken together, the spin counts and relaxation times indicate the helium bubble dimensions increase with both age and temperature. Since the ^3He relaxation times are mainly controlled by interactions with the bubble walls, the increases in the average gas bubble dimensions during the trapping of additional helium atoms will give longer relaxation times. This process will continue

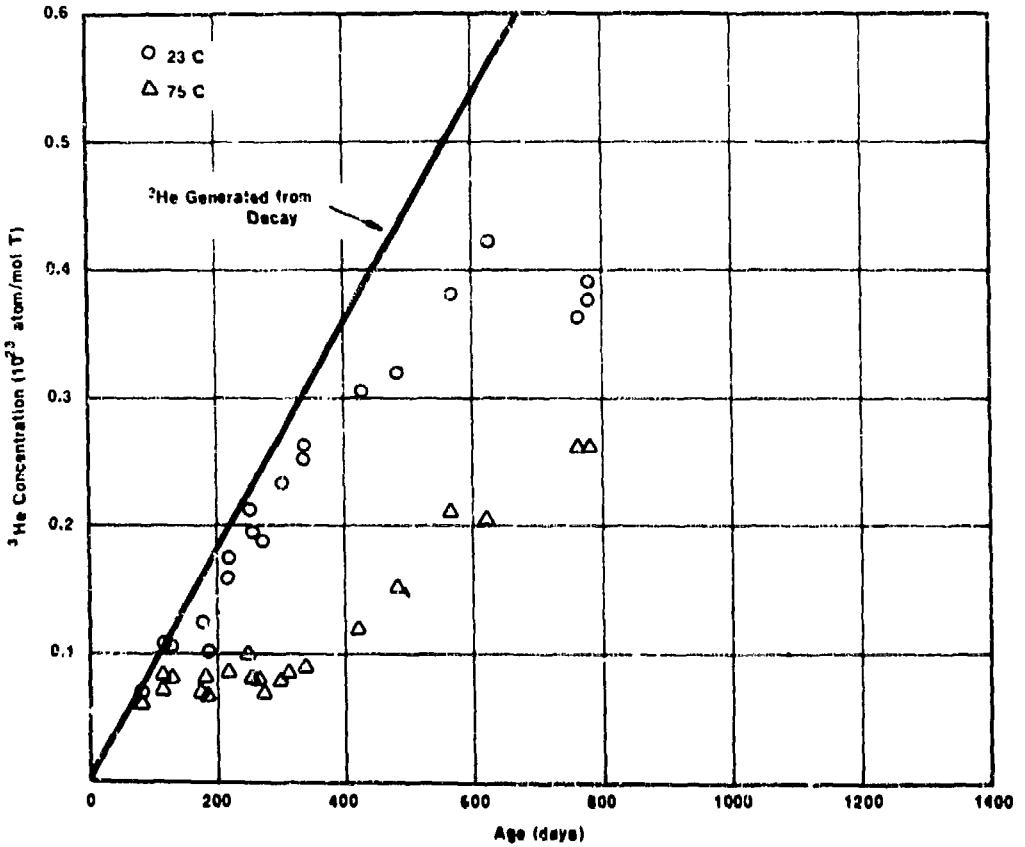

Fig. 2. ^{3}He Concentrations in LiT Samples Maintained at Room Temperature and 75°C as Determined from NMR Spin Counts.

Table 3. The Effects of Age and Storage Temperature on the ^{3}He Relaxation Times in LiT. Resonance Frequency is 45.7 MHz.

Age (days)	Storage Temperature (°C)	T_{2m} (ms)	T_1 (s)
184	23	15	6.5
346	23	33	7.8
573	23	60	10.0
798	23	160	10.7
346	75	100	9.7
573	75	140	12.2
346	100	380	22.4
541	100	~500	24.3

until the stresses on the LiT lattice induced by the expanding bubbles causes a mechanical failure and the bubble ruptures. The elastic properties of the LiT lattice are temperature dependent and should greatly affect the distributions of the helium bubble dimensions for different temperatures. Unfortunately, this situation for LiT is complicated by the presence[7,14] of large (i.e., ~5-15 atom percent) quantities of molecular tritium (also trapped in the gas bubbles), which was produced by the radiolysis effects of the beta-electrons. However, the general distribution of helium in LiT is well represented by the present qualitative model. Crude estimates of the helium bubble sizes can be obtained by comparing the ^{3}He and molecular tritium relaxation times for LiT with the results of Souers et al.[15] for molecular protium in gamma irradiated LiH. Souers et al. found a distinct correlation between the proton relaxation times and the average gas bubble dimensions. If the gas bubbles in LiT consist of a mixture of molecular tritium and helium atoms and if the tritium data for LiT correspond to

the protium data in LiH (which is expected since both nuclei have spin quantum number 1/2 and their magnetic moments differ by only ~7%), the average bubble size after ~1 year are estimated to be ~50 Å for room temperature and ~500 Å for 100°C. Naturally, a distribution of bubble size is expected and a better estimate is not possible from the present data.

The retention of helium in UT_3 at room temperature is shown in Figure 3. Here, the closed symbols represent the helium contents obtained by pressure-volume-temperature mass-spectrometry analysis of the gases released during thermal decomposition to ~1000°C. The results of the ^3He spin counts correspond to the open symbols. The spin counts yield helium contents which are ~10% lower than the thermal analyses. It seems very unlikely this discrepancy is due to the presence of ^3He atoms being individually dispersed in the UT_3 lattice since no contributions to the NMR relaxations that obey Eq. (2) have yet been found. Two other explanations are: 1) the $\pi/2$ and π pulse widths are not much shorter than T_2^* - which permits a partial reduction in the measured magnetization (i.e., signal amplitudes) - and 2) systematic errors may be occurring from the use of the proton standards although no apparent difficulties were found during previous studies[16] on LiT. Nevertheless, both techniques indicate that nearly all the helium generated from tritium decay is retained by the UT_3 lattice for ~700 days. After this time significant amounts of the helium are being released as free gas until, after 1200 days, only 75% of the helium formed in the UT_3 is still retained. During recent measurements[12] of the ^3He relaxation times in UT_3 samples kept at room temperature, T_{2m} and T_1 were found to increase by a factor of 10 and 3, respectively, for sample ages between 100 and 1000 days. These results can be used to interpret the release of helium from UT_3 as follows: The helium atoms form small gas bubbles which can expand by trapping additional atoms. This process continues

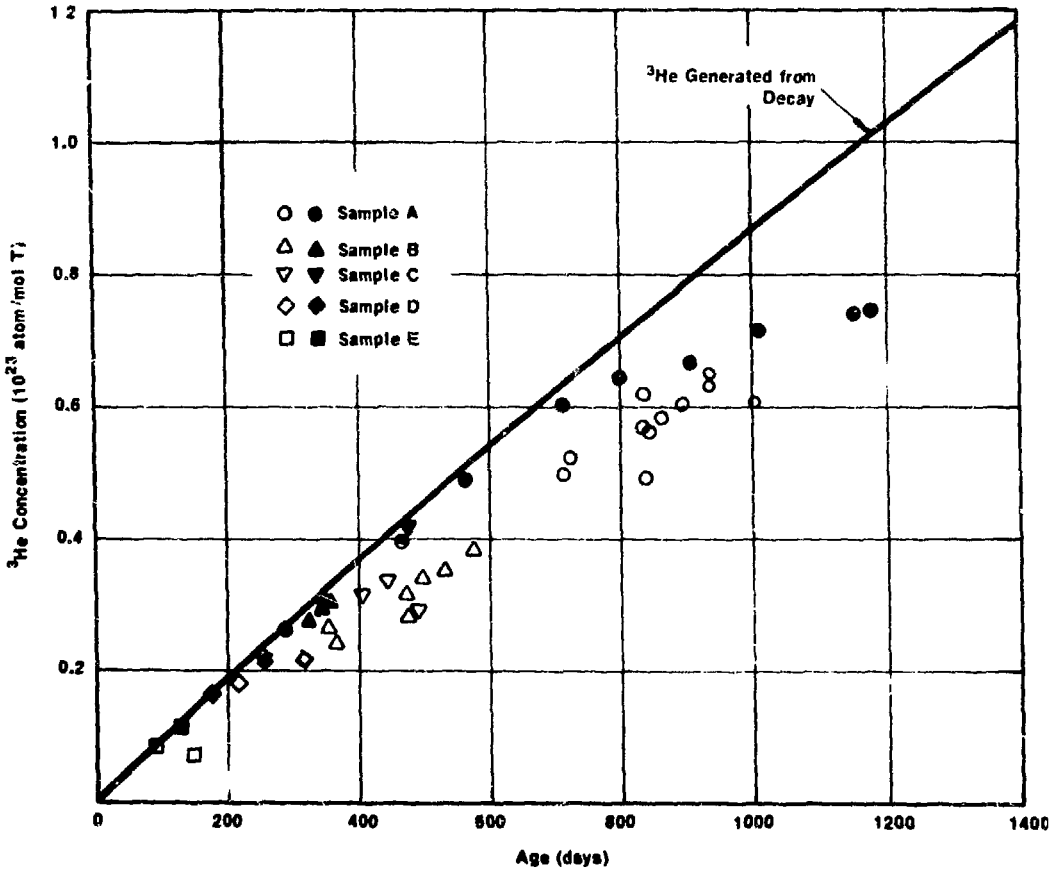

Fig. 3. Concentrations of ^{3}He in UT_3 Maintained at Room Temperature. Closed symbols represent results from thermal decomposition of aged powder while open symbols correspond to NMR spin counts.

in a random fashion yielding a distribution of bubble sizes where the average bubble size increases. Ultimately, a gas bubble reaches a critical dimension or pressure and will rupture releasing the helium contents of that bubble. As the UT_3 ages, more bubbles approach the critical conditions. The criteria for bubble bursting is unknown but probably depends upon the strength of the UT_3 lattice and the particle or grain sizes (i.e., gas bubbles formed near a surface should burst at lower pressures than bubbles in the interior of the particle). Preliminary NMR data for UT_3 samples kept at elevated temperatures suggest the helium bubble sizes are not very temperature dependent, which is very different from LiT. However, trapped molecular tritium has not been observed in UT_3, and its absence may influence bubble growth processes since the helium atoms must form their own trapping sites in UT_3.

In very recent work, Weaver and Camp[17] studied the distribution of helium in samples of $TiT_{1.4}$ and $TiT_{1.7}$ using NMR techniques. They concluded that helium is trapped in gas bubbles in old TiT_x (i.e., ages >1 year), but helium atoms occupy octahedral interstitials in young TiT_x crystals. Weaver and Camp propose a percolative mechanism for the formation of gas bubbles from the interstitials. The results in Table 2 for a 3-year old sample of $TiT_{1.7}$ are certainly consistent with helium atoms in gas bubbles. In order to determine whether the percolation model of Weaver and Camp or a bubble growing model analogous to the UT_3 example described above is a better physical description of ^3He retention in TiT_x, additional $TiT_{1.9}$ samples were prepared approximately seven months ago. These samples are being kept at room temperature, 75°C, and 100°C. Unfortunately, not enough data are currently available to firmly establish either model. Studies in this area are being continued.

CONCLUSIONS

The present studies indicate that pulse NMR is a valuable method for evaluating the distributions of helium atoms in metal tritides. The nuclear relaxation times for three representative metal tritides, LiT, $TiT_{1.7}$, and UT_3, indicate that helium atoms are trapped in microscopic bubbles - at least, in samples ~2-3 years old. Although the present studies indicate the helium bubble sizes depend upon both temperature and age, additional work is required before quantitative descriptions are possible. Nevertheless, NMR can be used to characterize the helium distribution in metal tritides with CTR applications. The main limitations of NMR are lack of sensitivity (i.e., $\sim 5 \times 10^{20}$ spins are required for quantitative measurements) and complications for bulk powder magnetization effects.

ACKNOWLEDGMENTS

The authors wish to thank J. E. Glaub and G. Mullins for preparing the NMR samples and R. E. Sprague for performing the gas analyses. Finally, the authors express their appreciation to Dr. H. T. Weaver for providing a preprint of his unpublished work and helpful discussions.

REFERENCES

1. A. M. Rodin and V. V. Surenyants, Fiz. Metal. Metalloved, 10, 216 (1960).

2. P. M. S. Jones, The Physical Stability of Metal Tritides: Lithium Tritide and Deuterotritides, AWRE (UKAEA) Report 0-27167 (1967).

3. P. M. S. Jones, W. Edmondson, and W. J. McKenna, J. Nucl. Material, 23, 309 (1967).

4. V. P. Vertebnyi, M. F. Vlasor, A. L. Kirilyuk, R. A. Zatserkovskii, M. V. Pasechnik, and V. A. Stepanenko, At. Energ (USSR) 22, 235 (1967).

5. A. M. Rodin and V. V. Surenyants, Russ. J. Phys. Chem. 45, 612 (1971).

6. L. C. Beavis and C. J. Miglionico, J. Less-Common Metals 27, 201 (1972).

7. P. C. Souers, T. A. Jolly, and C. F. Cline, J. Phys. Chem. Solids 23, 1717 (1967).

8. T. C. Farrar and E. D. Becker, Pulse and Fourier Transform NMR (Academic Press, New York, 1971).

9. J. H. Van Vleck, Phys. Rev. 74, 1168 (1948).

10. R. M. Cotts, Ber. Bunsen-Gesellschaft 76, 760 (1972).

11. R. C. Wayne and R. M. Cotts, Phys. Rev. 151, 264 (1966); R. Robertson, Phys. Rev. 151, 273 (1966).

12. R. C. Bowman, Jr. and A. Attala, Bull. Am. Phys. Soc. 2, 499 (1975); full paper to be published.

13. L. E. Drain, Proc. Phys. Soc. (London) 80, 1380 (1962).

14. R. C. Bowman, R. S. Carlson, A. Attalla, C. J. Wienkheft, and R. J. DeSando, Proceedings of the Symposium on Tritium Technology Related to Fusion Reactor Systems, October 1 and 2, 1974, ERDA-50, pp. 89-104.

15. P. C. Souers, T. Imai, T. S. Blake, R. M. Penpraze, and H. R. Leider, J. Phys. Chem. Solids 31, 1461 (1970).

16. A. Attalla and R. C. Bowman, Jr., Anal. Chem. 47, 728 (1975).

17. H. T. Weaver and W. J. Camp, Phys. Rev. B (to be published).

^{3}He RELEASE CHARACTERISTICS OF METAL TRITIDES AND SCANDIUM-TRITIUM SOLID SOLUTIONS*

W. G. Perkins, W. J. Kass and L. C. Beavis

Sandia Laboratories, Albuquerque, New Mexico 87115

ABSTRACT

Tritides of such metals as scandium, titanium, and erbium are useful materials for determining the effects of helium accumulation in metallic solids, for example, CTR first wall materials. Such effects include lattice strain and gross deformation, as reported elsewhere, which are related to ^{3}He retention and ultimate release. Long term gas release studies have indicated that, during the early life of a metal ditritide, a large fraction of the ^{3}He is retained in the solid. At more advanced ages (2-4 years, depending on the parent metal), the ^{3}He release rate becomes comparable to the generation rate. Statistical analysis of the data indicates that the acceleration in ^{3}He release rate depends on accumulated ^{3}He concentration rather than strictly on age. ^{3}He outgassing results are presented for thin films of ScT_2, TiT_2, and ErT_2, and the critical ^{3}He concentrations are discussed in terms of a percolation model. Phase transformations which occur on tritide formation cast some doubt on the validity of extrapolating results obtained for metal tritides to predictions regarding the accumulation of helium in metals. Scandium is unique among the early transition and rare-earth metals in that the metal exhibits a very high room temperature tritium solubility ($T/Sc=0.4$) with no phase transformation. Indeed, even the lattice parameters of the hcp scandium lattice are only minimally changed by tritium solution, and we have succeeded in obtaining single crystal $ScT_{0.3}$ samples in two crystallographic orientations. Using a very sensitive technique, we have measured ^{3}He emission from both these samples, as well as from fine-grained thin film scandium-tritium solid solution samples ($ScT_{0.3-0.4}$). The fine-grained film samples release ^{3}He at 2-3% of the generation rate, while the emission rate from the single-crystal samples is $\sim$ 0.05% of the generation rate, indicating a strong grain size effect.

*This work was supported by the U. S. Energy Research and Development Administration.

INTRODUCTION

The early transition metals and rare-earth metals form dihydrides which are quite stable at room temperature and even at mildly elevated temperatures.[1] Indeed, for ErH_x ($0.5 \leq x \leq 1.8$), even at 700 K (427°C), the decomposition pressure is only 0.13 mPa (1×10^{-6} Torr).[2] Because of this stability and the fact that the hydrides behave electronically like metals,[2] the ditritides are attractive vehicles for the study of helium accumulation effects in metallic systems. Indeed, Hickman[3] has recently suggested the use of tritium decay to accumulate ^3He in niobium as an alternative to helium-ion implantation. Significant concentrations of ^3He may be retained in metal tritide samples, as is indicated by the work of Rodin and Surenyants[4] on titanium tritides.

One purpose of the present paper is to present our results on the ^3He release and retention characteristics of ditritides of scandium, titanium, and erbium. However, we also will present some initial data on the ^3He release and retention characteristics of scandium-tritium solid solutions. It should be noted that formation of the metal ditritide involves a phase transformation from the hcp metal lattice to the CaF_2-type hydride lattice, and that the phase transformation may cast some doubt on the application of hydride results to predictions of the behavior of high concentrations of helium in the parent metals. On the other hand, hcp scandium can accommodate solid solutions of tritium up to concentrations of T/Sc = 0.4, with no change in crystal symmetry and little change in lattice parameter.[5] Thus, ^3He release and retention experiments performed on scandium-tritium solid solutions may be more representative of the behavior of the helium-implanted metal.

EXPERIMENTAL

We have measured the ^3He release from metal tritides by two techniques. In the older, "static" technique, a film ($\sim$ 2 μm thickness) of the desired tritide was deposited on a substrate (generally molybdenum) and then sealed in an evacuated, baked (725 K) glass bulb which was equipped with an extended range Pirani gauge. Selected bulb-gauge combinations were calibrated at a series of known ^3He pressures ranging

from 1.3 mPa to 13 Pa (1×10^{-5} - 1×10^{-1} Torr).[6] Recalibrations and bulb gas analysis have indicated that all the gauges used over a seven-year period have given reproducible ^{3}He pressure readings, within ± 10%, for the pressure range indicated. Compositions of the tritide films were inferred from gas and metal analysis of companion film samples which were prepared simultaneously with the actual samples. The quantity of ^{3}He released from each film was inferred from periodic pressure measurements (at ∿ 30-day intervals). The glass bulbs were also equipped with breakseals which allowed mass spectral analysis of the bulb contents. Except in rare cases, the gas was found to be > 99% ^{3}He.

More recently, we have performed "dynamic" gas release measurements in an all-metal ultrahigh vacuum system. In this system, various tritium-containing samples are contained in small chambers (∿ 15 cm^3) which are separated from the main vacuum system by solenoid-actuated valves. The rate of ^{3}He release may be determined either by measuring gas accumulation during a fixed hold period or by measuring the steady ^{3}He flow rate into the dynamically pumped system. Flow rate and quantity measurements are made using a UTI 100B residual gas analyzer which is calibrated for ^{3}He by measurement of flow through a standard leak. Full details of the technique will be published elsewhere.

RESULTS

Static Technique

There are a variety of ways to present the results of the measurements, either in terms of ^{3}He release or retention. In the static case, we infer the quantity of ^{3}He retained in the tritide by calculating the quantity generated and measuring the quantity released. In the case

of the dynamic measurements, we determine the ^3He release rate. Figure 1 shows the ^3He retention of titanium ditritide samples as a function of sample age. Actually, the data are normalized for tritium quantity by plotting the retained ^3He-to-Ti atomic ratio. For these data, we note that the titanium tritide retains nearly all the ^3He generated out to $\sim$ 1100 days age, at which time the release rate changes rapidly from a very small value to values oscillating about the generation rate. It is as though the ^3He retention saturates at some critical concentration, which is of the order

$$^3He(\text{retained})/Ti = 0.32.$$

It is interesting that Rodin and Surenyants[4] found similar behavior for $TiT_{1.5}$ samples, but that they found the ^3He release rate to increase sharply only for ages $\geq$ 1500 days. This apparent discrepancy can be explained by postulating that the acceleration in ^3He release rate is concentration dependent rather than time dependent. The ^3He concentration calculated at 1500 days for $TiT_{1.5}$ is

$$^3He(\text{generated})/Ti = 0.31,$$

in good agreement with our data. Rodin and Surenyants obtained their data in a slightly different manner than ours. In their technique, a tritide sample of given age and known initial composition was sealed in an evacuated bulb for a fixed period of time (6 to 45 days), after which the gaseous ^3He was determined by mass spectrometry. Division of the ^3He quantity released by the quantity generated during the storage period then yields a good approximation of the normalized release rate (which would be defined exactly as the ratio of the release rate to the generation rate). Our data can be compared very well with those of Rodin and Surenyants, provided we plot normalized ^3He release rate as a function of ^3He concentration generated in the tritide, as shown in Fig. 2.

From Fig. 3, we note that erbium tritide exhibits the same general behavior as does titanium tritide, with the exception that the saturation ^3He concentration is somewhat lower. A plot of normalized ^3He release

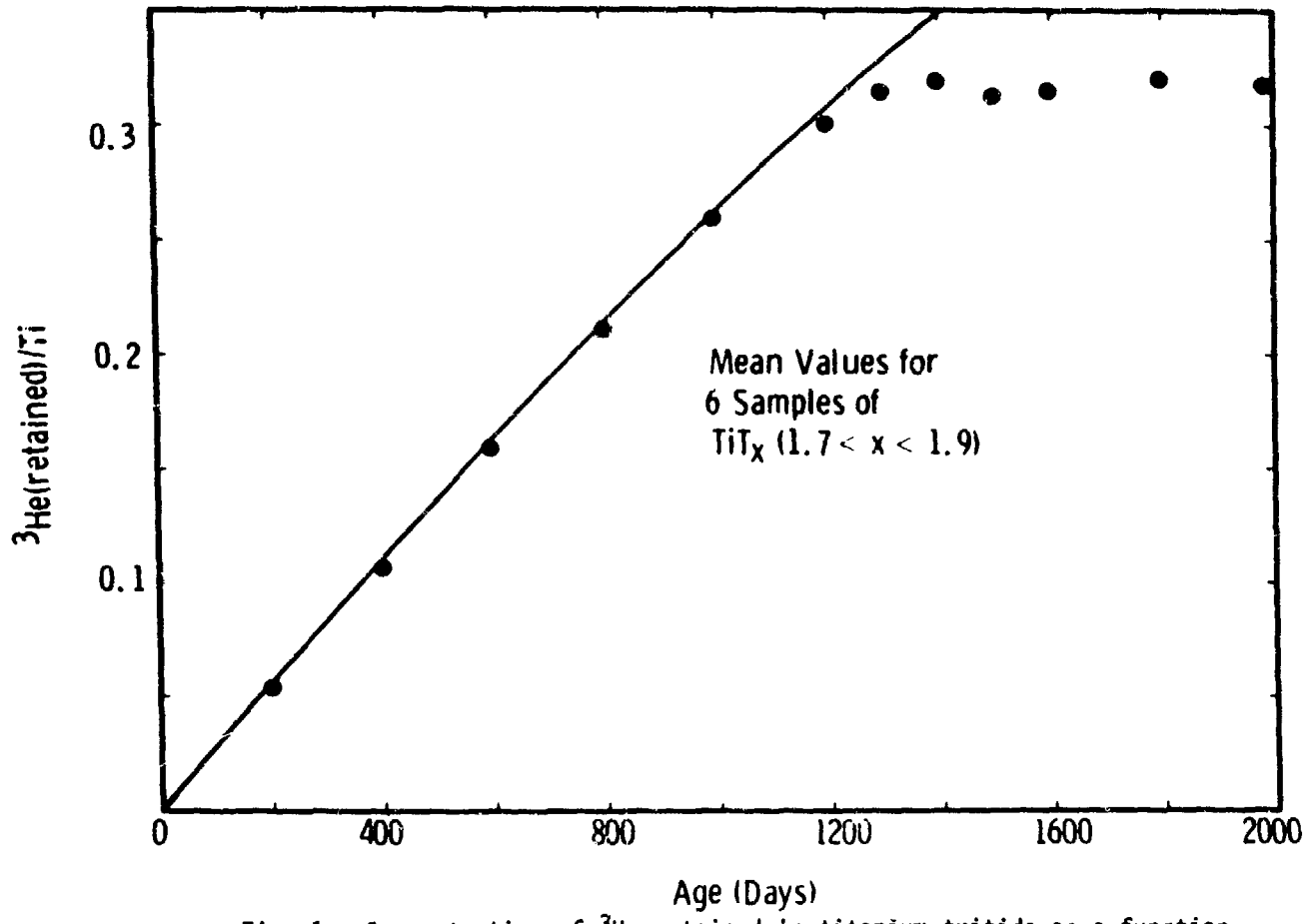

Fig. 1. Concentration of ^{3}He retained in titanium tritide as a function of age. Points indicate ^{3}He retention inferred from gas release data. Solid curve indicates ^{3}He concentration expected if the ^{3}He were completely retained in the aging tritide.

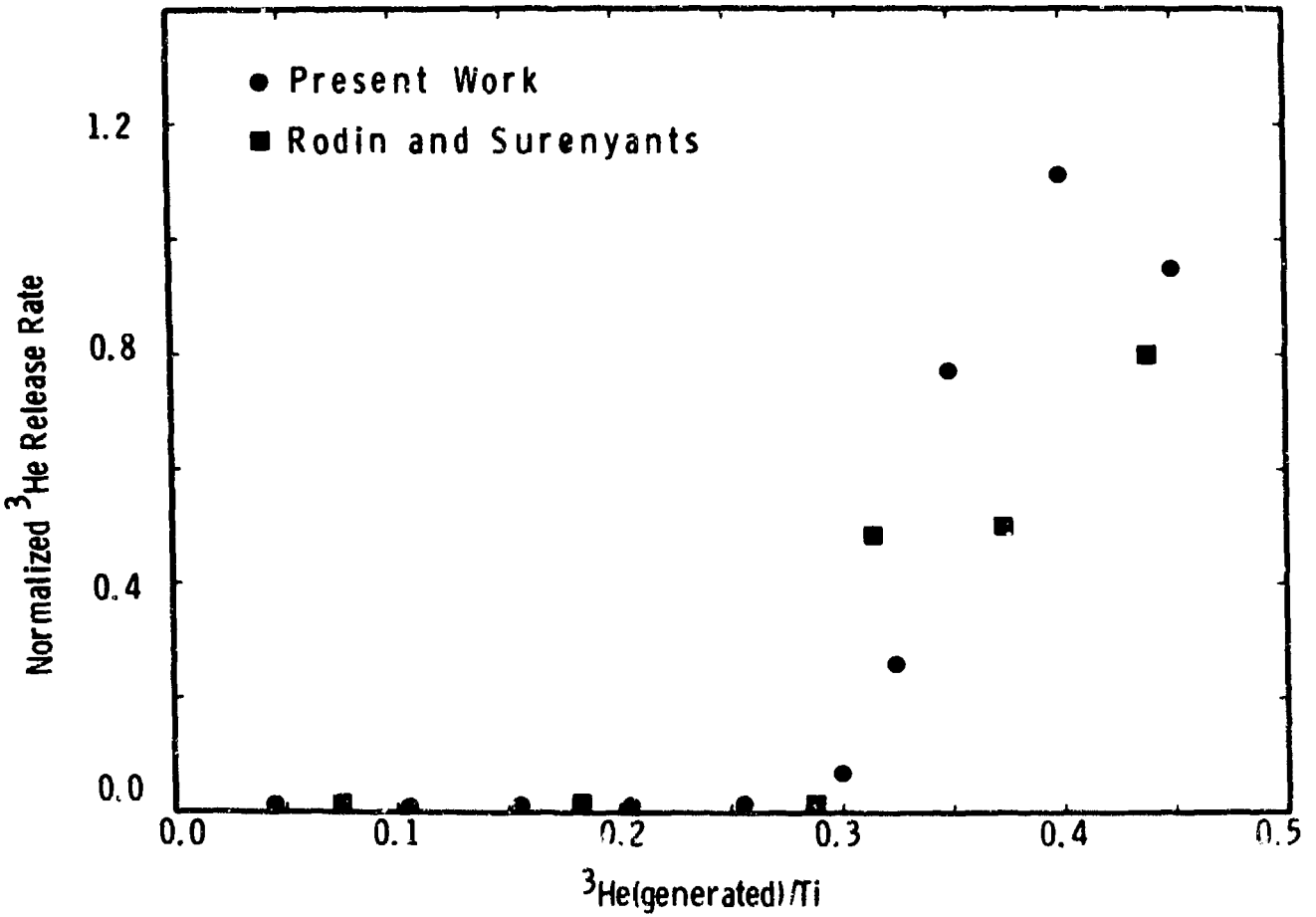

Fig. 2. Normalized ^{3}He release rate from titanium tritide samples as a function of the generated ^{3}He concentration. Data are compared from the present study (●) and the work of Rodin and Surenyants[4] (■).

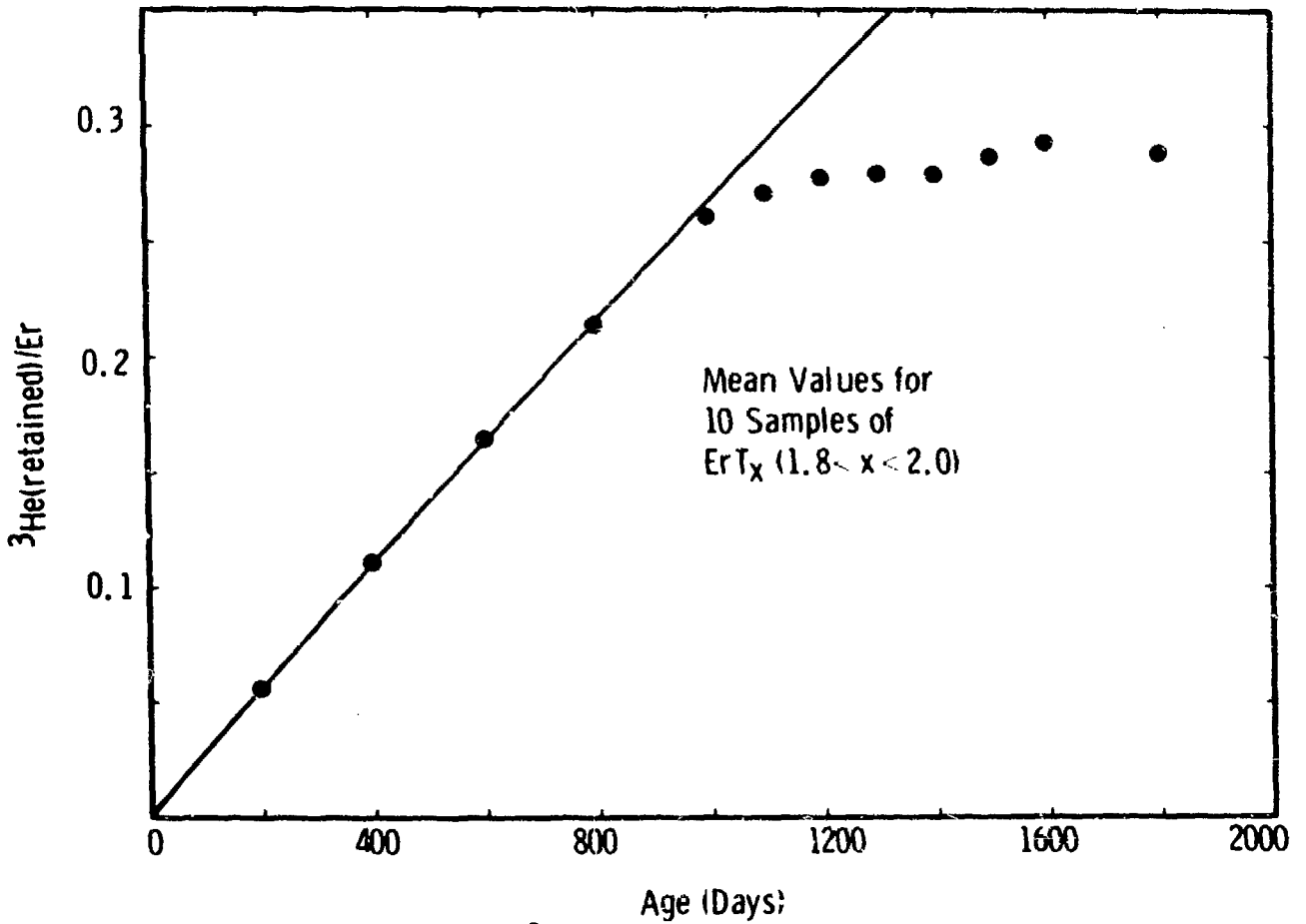

Fig. 3. Concentration of ^{3}He retained in erbium tritide as a function of age. Points indicate ^{3}He retention inferred from gas release data. Solid curve indicates ^{3}He concentration expected if the ^{3}He were completely retained in the aging tritide.

rate vs. ^3He concentration (Fig. 4) indicates that the critical concentration for accelerated ^3He release is

$$^3He(generated)/Er \approx 0.25.$$

Finally, similar plots for scandium tritides (Figs. 5 and 6) indicate that this material exhibits the same general retention and release pattern, except that the sharp increase in release rate occurs somewhat earlier yet, at

$$^3He(generated)/Sc \approx 0.20.$$

It should be noted from Figs. 2, 4, and 6 that, after critical ^3He concentration is achieved, the normalized release rate appears to vary widely from month to month, with the release rate ranging from 0.5 to 5 times the generation rate. The long-term average ($\sim$ one year) release rate, however, is nearly equal to the generation rate.

Dynamic Technique

We have used the dynamic technique to measure ^3He release from scandium ditritide and from scandium-tritium solid solution samples. The ditritide sample exhibits behavior similar to that observed for the static samples, and it will not be discussed further here. The scandium-tritium solid solution samples are rather interesting, however, because they represent the possibility of injecting significant quantities of ^3He into the metal lattice without phase transformation. Indeed, using single crystals of scandium as starting material, it has been possible to obtain $ScT_{0.3}$ samples which still exhibit x-ray diffraction patterns characteristic of the hcp Sc single crystal.

Normalized ^3He release rates for the $ScT_{0.3}$ single crystals and for a polycrystalline $ScT_{0.2}$ thin film are shown in Fig. 7. The large difference between the release rate for the film and that for the single crystals may result in part from relative grain size effects.

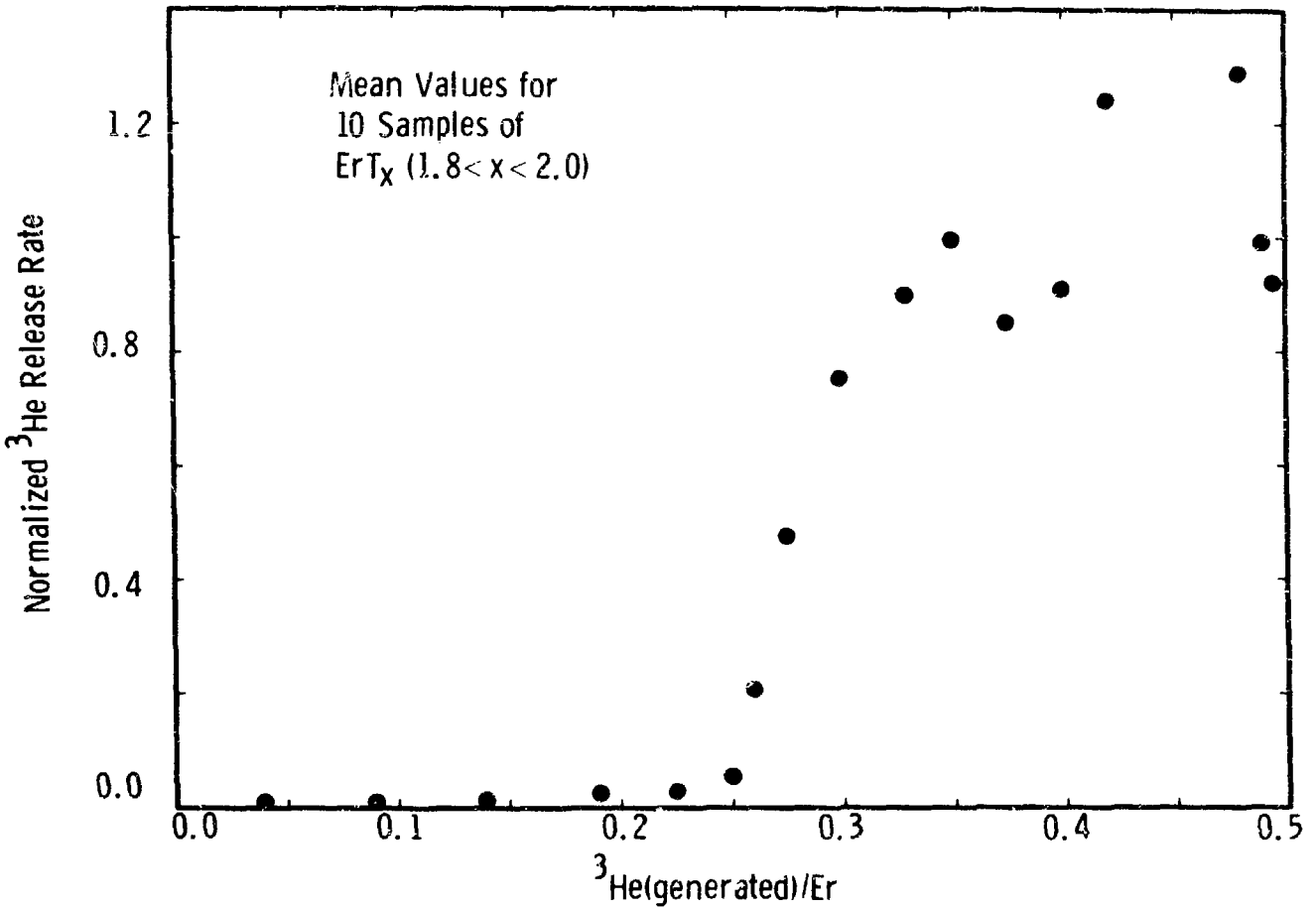

Fig. 4. Normalized ^{3}He release rate from erbium tritide samples as a function of the generated ^{3}He concentration.

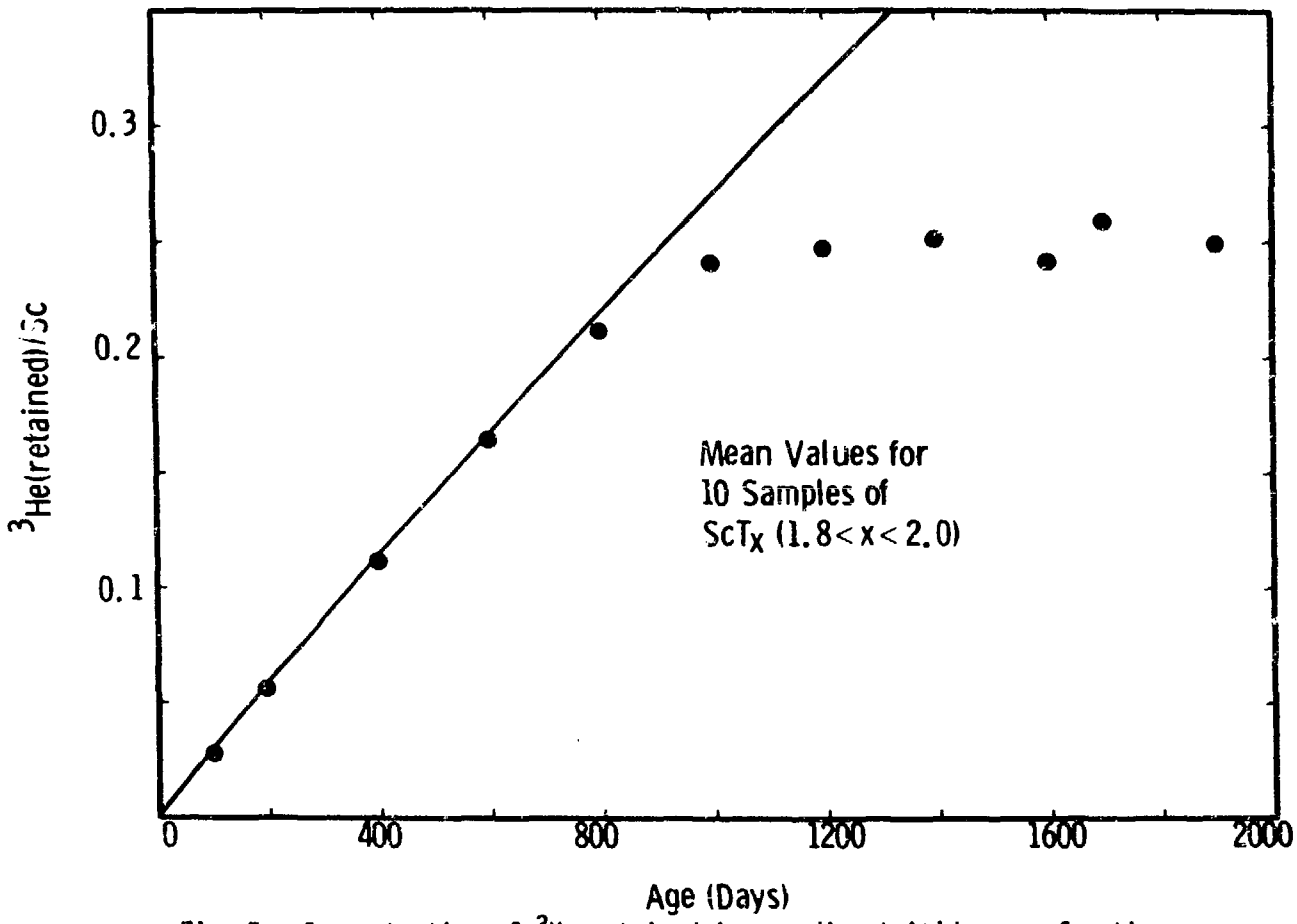

Fig. 5. Concentration of ^{3}He retained in scandium tritide as a function of age. Points indicate ^{3}He retention inferred from gas release data. Solid curve indicates ^{3}He concentration expected if the ^{3}He were completely retained in the aging tritide.

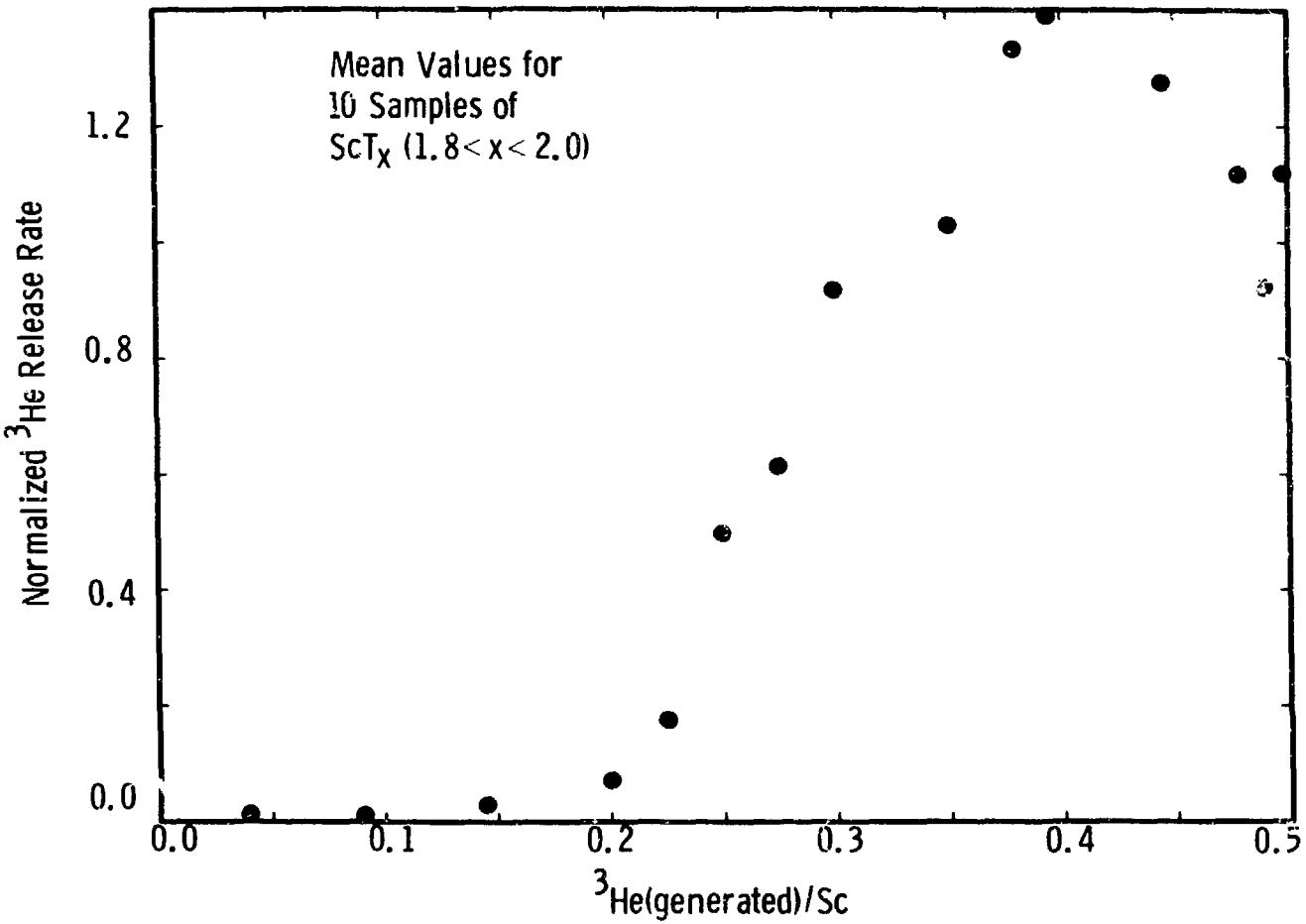

Fig. 6. Normalized ^{3}He release rate from scandium tritide samples as a function of the generated ^{3}He concentration.

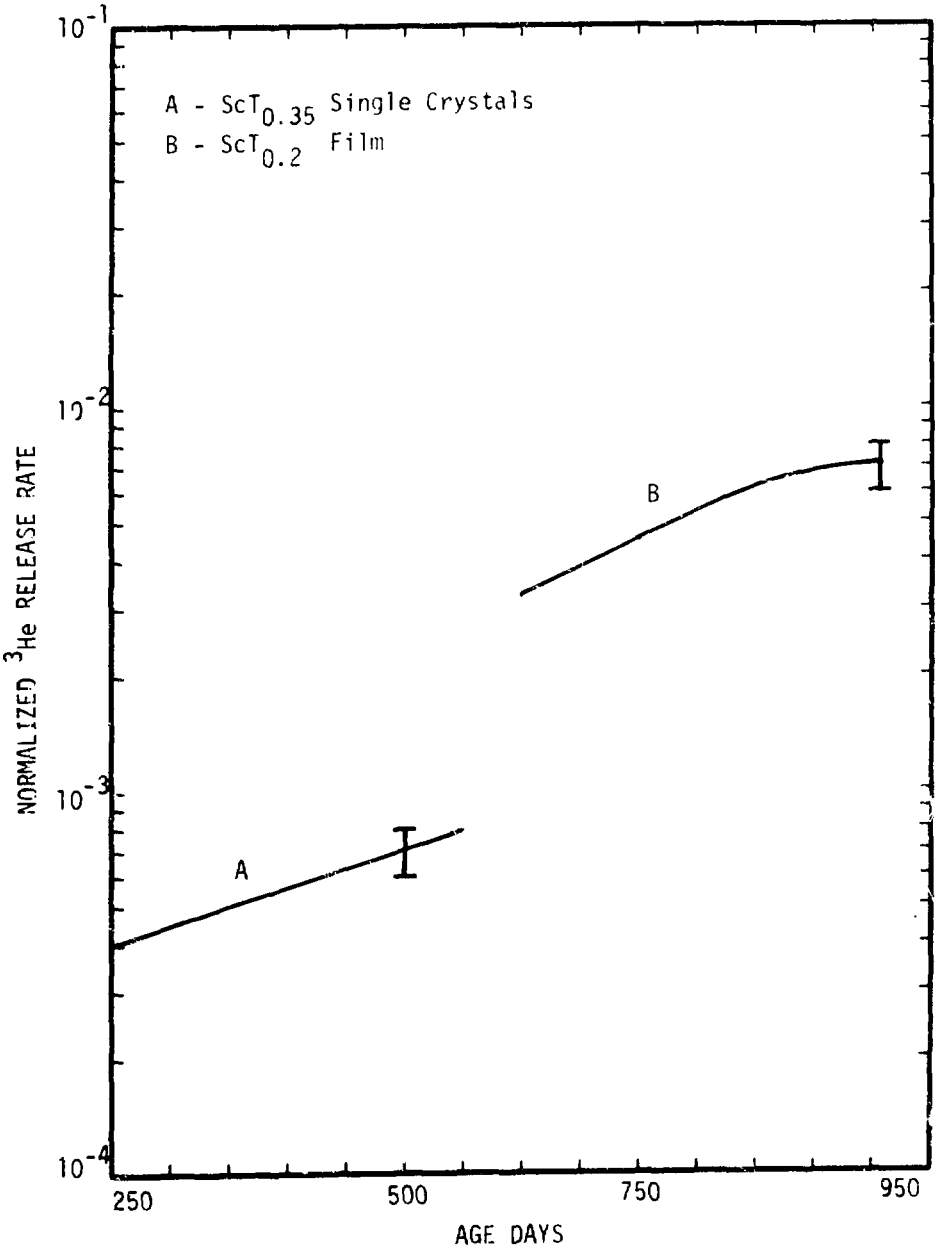

Fig. 7. Normalized ^3He release rate vs. time for scandium-tritium solid solution samples.

Mechanical Behavior

All the thin film samples used in this study eventually exhibited some mechanical damage, which usually became apparent well after rapid ^3He release had begun. The damage observed ranged from the appearance of small flaked areas up to nearly complete flaking of the film from its substrate. The behavior was very similar to that reported earlier by Beavis and Miglionico,[8] which they concluded must result from the agglomeration of ^3He into bubbles from which it is subsequently released due to mechanical failure of the material.

DISCUSSION

It appears that, during the early life of a metal ditritide, the ^3He generated via tritium decay is effectively immobile. Farnum[9] used x-ray diffraction data to conclude that the ^3He was immobilized in the octahedral interstitial site of the CaF_2-type ditritide lattice. More recently, Weaver and Camp[10] have used NMR spectra to study ^3He in young ($\sim$ 1 year old) and aged ($\sim$ 8 years old) titanium tritide samples. For the young tritide, their results suggest that the ^3He occupies an octahedral site whose immediate environment is highly strained. For the old tritide, however, they find the majority of the retained ^3He in gas bubbles. Thus, at some point in the life of the aging tritide, a dramatic transformation occurs.

It has been pointed out by Wilson, Bisson, and Amos,[11] and by Weaver and Camp[10] that phenomena which occur sharply at a given critical concentration can often be described in terms of a percolation model.[12] That is, as the concentration of randomly-distributed, immobilized ^3He atoms grows, the probability of the occurrence of near neighbor ^3He interaction also increases. A connected cluster of nearest neighbors ^3He atoms first appears with nonzero probability at a concentration of $^3He/Metal \approx 0.2$. By the time $^3He/Metal$ reaches 0.32, percolation theory indicates that nearly every ^3He atom in the solid will be contained in a connected cluster.[12] It is interesting to note that our range of critical concentrations (for the onset of rapid ^3He release) almost exactly spans the mathematical concentration range inferred from percolation

theory. Using the percolation theory as a mathematical guide, we may summarize the ^3He release characteristics of a metal tritide as follows.

1. During the early life of the sample, the vast majority (> 99%) of the ^3He generated is retained. Only those ^3He atoms generated near a grain surface are released.

2. As the critical concentration is reached the internal ^3He atoms become more mobile as a result, perhaps of cooperative strain effects,[10] or of a concentration-dependent diffusion coefficient.[11] Some of the ^3He is released directly from the solid, while some remains in the lattice and some accumulates in bubbles. It is probably the random rupture of such bubbles that accounts for the large month-to-month variation in the normalized ^3He release rate for aged tritide samples.

Many factors which may have bearing on the retention and release of ^3He from metal tritides remain unknown. Before one can unequivocally identify the mechanisms involved in the aging of these materials, it will be necessary to quantify the effects of temperature, grain size, and surface chemistry.

REFERENCES

1. L. C. Beavis, J. Less-Common Metals 19, 315 (1969).

2. W. M. Mueller, J. P. Blackledge, and G. G. Libowitz (eds.), Metal Hydrides, p. 434, Academic Press, New York, 1968.

3. R. G. Hickman, "Helium Doping of Niobium with Tritium," Report No. UCRL-75252, University of California, Lawrence Livermore Laboratory, Livermore, California, 1975.

4. A. M. Rodin and V. V. Surenyants, Zhur, Fiz. Khim. 45, 1094 (1971); Russ. J. Phys. Chem. 45, 612 (1971).

5. C. E. Lundin, "Structural Study of the Erbium-Erbium Dihydride and Scandium-Scandium Dihydride Systems," Contract Report DRI #2489, Denver Research Institute, Denver, Colorado, 1969.

6. J. L. Provo and C. J. Biver, private communication.

7. J. L. Provo and W. Welbon, private communication.

8. L. C. Beavis and C. J. Miglionico, J. Less-Common Metals 27, 201 (1972).

9. E. H. Farnum, "Calculation of Helium Induced Strain in ErT_2 and ScT_2," Report No. SC-RR-70-753, Sandia Laboratories, Albuquerque, New Mexico, 1970.

10. H. T. Weaver and W. J. Camp, Phys. Rev. B 12, 3054 (1975).

11. W. D. Wilson, C. L. Bisson, and D. E. Amos, J. Nucl. Mater. 53, 154 (1974).

12. V. K. Shante and S. Kirkpatrick, Adv. Phys. 20, 325 (1971).

TRITIUM EFFECTS IN AUSTENITIC STEELS*

M. R. Louthan, Jr., G. R. Caskey, Jr.,
D. E. Rawl, Jr., and C. W. Krapp

Savannah River Laboratory
E. I. du Pont de Nemours and Company
Aiken, South Carolina 29801

ABSTRACT

Conditions of tritium absorption and helium build-in simulating those expected in long service in a fusion reactor had little effect on the ductility of Types 304L and 309S austenitic stainless steels. Long (25 to 50 years) exposures of prospective component and structural materials to reactor conditions were simulated in short-duration tests by matching tritium concentration gradients in test samples at time of testing with those expected in reactor service, without regard to time required to obtain desired tritium concentrations. Tritium effects on ductility of 304L samples were not significantly different from those caused by protium or deuterium. Surface finish and metallurgical condition can influence the tritium concentration gradient by increasing diffusivity and solubility and by trapping tritium at extraordinary sites. Build-in of ^{3}He in concentrations as great as 0.14 cc/cc of metal caused no significant ductility losses except when tensile tests or postexposure anneals were conducted at temperatures high enough to cause helium agglomeration. The lack of significant He-induced effects at near ambient temperatures agrees with results of ion bombardment studies made by other investigators.

INTRODUCTION

During design of tritium handling facilities for fusion reactors the potential for tritium permeation from containment systems, tritium embrittlement of structural components, and effects of tritium-decay helium must be understood. Absorption is a necessary step in the embrittlement process. Absorption, in turn, depends on both temperature and duration of exposure. Under ideal conditions the quantity

* This paper was prepared in connection with work under Contract No. AT(07-2)-1 with the U. S. Energy Research and Development Administration.

of tritium absorbed by a material is determined by the solubility and diffusivity of tritium in the material. These quantities are, in theory, relatively simple functions of exposure conditions. Thus, with proper control, the effects of long-term exposures may be simulated by tests of short duration. Such simulations are necessary to predict long-time compatibility of potential structural materials with the tritium environments expected for fusion reactor applications. Hydrogen transport in most structural materials is, however, complicated by surface effects, reversible trapping, and chemical reactions; these phenomena have significant effects on the validity of exposure simulations. This report describes an approach to exposure simulation and, by using austenitic stainless steels as an example, illustrates several difficulties in establishing the requirements for reasonable simulation.

SIMULATION TECHNIQUES

One approach to exposure simulation is to match tritium concentration gradients in experimental and service systems. For example, a service exposure (assuming a permeation experiment) of t_s seconds to tritium pressure p_s at a temperature T_s gives a concentration gradient defined by

$$C_X = \frac{CX}{\ell} + \frac{2C}{\pi} \sum_{n=1}^{\infty} \left(\frac{\cos n\pi}{n}\right) \left(\sin \frac{n\pi X}{\ell}\right) \left(\exp - D_s t_s n^2 \pi/\ell\right) \qquad (1)$$

where C_X is the concentration at a distance X from the exposed surface, ℓ is the thickness of the foil, C is the tritium solubility under exposure conditions, and D_s is the tritium diffusivity in the service system. Solubility of hydrogen at pressure, p, is independent of time and is expressed by

$$C = C_o \, p^{\frac{1}{2}} \exp(-\Delta H_c/RT) \qquad (2)$$

where ΔH_c is the activation energy of solution of the gas, and C_o is a constant for the system. Thus, one requirement for matching concentration gradients is that

$$1/2 \ln\left(\frac{p_s}{p_L}\right) = \frac{\Delta H_c}{R} \left(\frac{T_L - T_s}{T_L T_s}\right) \qquad (3)$$

where p_L and T_L are the tritium pressure and exposure temperature for the laboratory tests. A second requirement for matching concentration gradients is that

$$D_s t_s = D_L t_L \tag{4}$$

where D_L is diffusivity in the laboratory simulation. Since

$$D = D_o \exp(-\Delta H_D/RT) \tag{5}$$

where D_o is a constant, this requirement becomes

$$\ln\left(\frac{t_s}{t_L}\right) = \frac{\Delta H_D}{R}\left(\frac{T_L - T_s}{T_L T_s}\right) \tag{6}$$

Comparison of Eqs. (3) and (6) shows that assignment of one exposure parameter for the laboratory simulation fixes the other two parameters. For example, with activation energies (in cal mol^{-1}) for tritium diffusion (ΔH_D) and solution (ΔH_c) of 12,400 and 1,400, respectively, in Type 304L stainless steel,[2] a ten-year service exposure at 300°K to 0.1-MPa tritium can be simulated by a three-month laboratory test made at 361.6°K in 0.045-MPa gas. This type of exposure assumes that the effects to be simulated depend on the tritium concentration at the time of testing but are not affected by the time required to obtain the desired concentration. Clearly this is not the case if tritium-decay helium is of concern. The quantity of helium developed within a material by decay of absorbed tritium during time t can be represented by

$$[He] = \int_o^t f(C,D,t)(1-e^{-\lambda t})dt \tag{7}$$

where C and D are the solubility and diffusivity under the exposure conditions and $\lambda = 1.82 \times 10^{-9} s^{-1}$, the radioactive decay constant for tritium. Analysis of Eq. (7) for several sample configurations and exposure conditions indicates that matching of helium concentrations throughout a material is not generally feasible unless exposure conditions are such that tritium concentration remains constant with time and that the time at steady state is very much greater than the time

to attain steady state. Under these conditions helium concentrations in the laboratory and service systems, C_s and C_L, can be matched by exposures which give

$$C_s \left(1-e^{-\lambda t_s}\right) = C_L \left(1-e^{-\lambda t_L}\right) \quad (8)$$

for a laboratory exposure of t_L. It should be emphasized that helium concentrations cannot be simulated for transient exposure conditions where tritium concentration gradients vary with time.

The simulation techniques described above have been used to study the effects of tritium exposure and helium build-in on the mechanical properties of austenitic steels. The remainder of the paper emphasizes those studies.

EFFECTS OF TRITIUM

The effects of hydrogen on the mechanical properties of austenitic stainless steels have been widely studied,[3-15] and results generally show that "austenitic steels as a class perform fairly well."[5] However, hydrogen-induced losses in strength and ductility are often observed. These losses have been attributed to localized accumulations of high hydrogen concentrations. Although various mechanisms have been proposed to explain how these localized accumulations lead to embrittlement (see References 6, 8, 9, and 13 for example), there is little reason to expect that the effects of tritium per se should differ significantly from those of deuterium or protium. This was confirmed by testing several tubular Type 304L specimens (see Reference 16 for description of this type of specimen) to failure in 69-MPa helium, protium, and tritium after exposure to the test gas at elevated temperatures. Exposure to the hydrogen isotopes reduced the ductility (Table 1) and caused surface cracks to form during plastic deformation. These effects have been extensively studied for samples exposed to protium and the present results indicate that tritium effects are not significantly different.

Table 1. Effect of Test Environment on Tensile Properties of Type 304L Stainless Steel[a]

Exposure Conditions			Tensile Properties		
Gas	Temperature, K	Time, days	σ_y, MN/m^2	σ_{ult}, MN/m^2	% Elong.
He	425	32	270	560	59
H_2	425	32	320	480	19
T_2	425	32	300	490	22
H_2	425	8	260	490	26
T_2	425	8	250	490	22

[a]All tensile tubes tested at room temperature with 69-MPa gas; data reported are averages of at least two samples.

The agreement between the effects of exposure to different hydrogen isotopes was further confirmed with charged samples tested in air at room temperature. Foil specimens (0.025 cm thick) were charged to saturation at 343°K in 69-MPa deuterium and tritium. This exposure reduced the elongation-to-fracture by approximately 50% in both cases. Other studies with tritium-charged tensile bars tested in air also showed losses in strength and ductility equivalent to those for comparably charged samples exposed in hydrogen (Table 2). This equivalency indicates the validity of using hydrogen test results to predict tritium effects (excluding those of build-in of decay helium) on mechanical properties.

EFFECTS OF SPECIMEN CONDITION ON TRITIUM ABSORPTION

Tests of samples with various surface finishes and metallurgical conditions indicate potential difficulties in using short-term exposures to simulate long-term service behavior of any of the three hydrogen isotopes with austenitic steels. Tritium absorption studies[2] have shown that surface finish and cold work influence the tritium concentration gradient which develops during exposure of Type 304L stainless steel. Cold work increases the apparent diffusivity; both cold work and surface finish affect apparent solubility (Fig. 1). The tritium concentration gradients shown in Fig. 1(a) indicate variations in diffusivity from 2.9×10^{-13} cm^2sec^{-1} (Curve C_1) to 4.1×10^{-11} cm^2sec^{-1} (Curve C_6) and in apparent solubility from 0.9 (Curve C_4) to 0.21 cc(gas)/cc(metal). Corresponding values of diffusivity (D) and solubility (C) for the actual exposure conditions are

$$D = \frac{4.7 \times 10^{-3}}{\sqrt{3}} \exp(-12{,}900/RT) = 1 \times 10^{-12} \text{ cm}^2/\text{sec} \qquad (9)$$

and

$$C = 1.28\, p^{\frac{1}{2}} \exp(-1400/RT) = 1.6 \text{ cc(gas)/cc(metal)} \qquad (10)$$

These variations between measured and calculated values are caused by surface control of tritium absorption, short-circuit diffusion, and tritium trapping at extraordinary sites,[2] and although the causes of the variations are known, the effects of these phenomena are difficult

Table 2. Effect of Hydrogen (Tritium) Exposure on Tensile Properties of Type 304L Stainless Steel[a]

Exposure	Strength, MN/m^2		Ductility	
	Yield	Ultimate	% Red. in Area	% Elong.
None	215	610	77	73
Hydrogen	220	530	32	33
Tritium	217	530	31	34

[a]Data averages for at least three specimens.

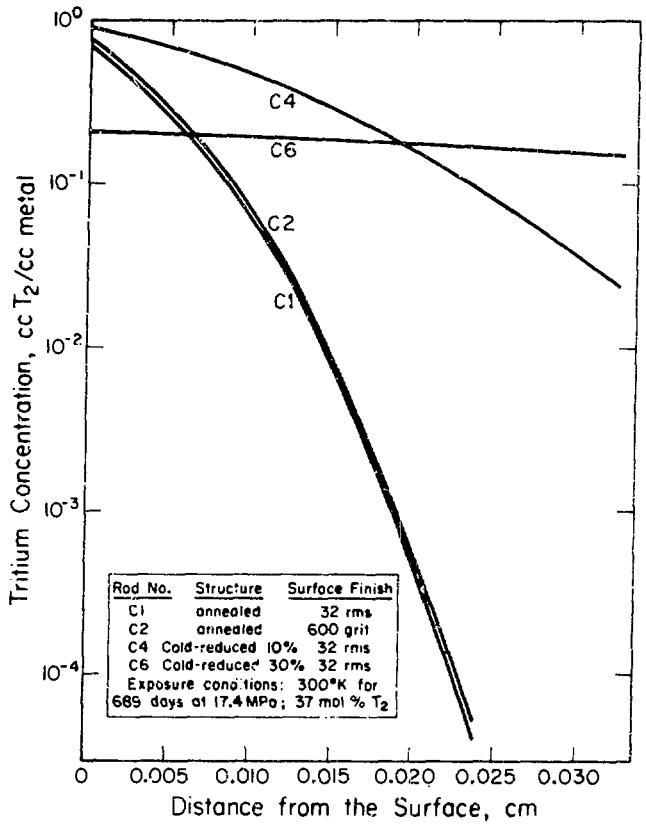

Fig. 1(a). Tritium Concentration Gradients in Type 304L Stainless Steel

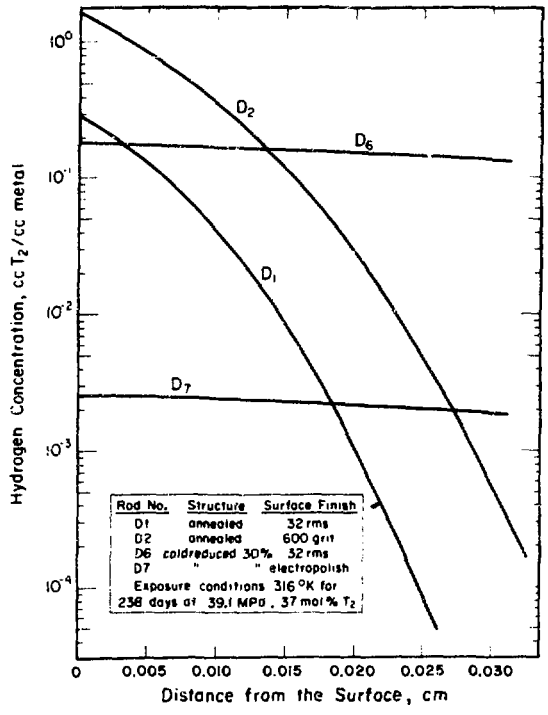

Fig. 1(b). Hydrogen Concentration Gradients in Type 304L Stainless Steel

to include in exposure simulation techniques. Therefore, any attempt to simulate long-term exposure by short-term tests should include both careful control of exposure and specimen conditions to minimize the effects of surfaces, and analysis to account for potential effects of trapping and short-circuit diffusion. A simple technique to minimize surface effects in austenitic steels is described in Reference 17, and Reference 18 presents a computer technique to analyze simultaneous diffusion and trapping.

EFFECTS OF HELIUM BUILD-IN

Tests of Types 309S and 304L stainless steels indicate that ^{3}He formed in the metal by tritium decay does not seriously reduce the ductility of these steels at ambient temperature. Foil specimens (0.025 cm thick) were exposed to 47.5-MPa tritium at 343°K for 17 months; helium build-in was estimated at 0.14 cc (^{3}He)/cc(metal). Subsequent tests at room temperature (Table 3) indicated that the exposure increased the yield strength, but had little effect on the ductility of the 309S specimens, although the ductility of Type 304L was lowered. Microvoid coalescence (Fig. 2) was the primary fracture mode, and there was no evidence of helium bubbles even after a 21-day anneal at 425°K (Fig. 3). Reference to Eqs. (8) and (10) indicates that if surface effects on tritium absorption are eliminated, the 17-month exposure at 343°K is equivalent to the exposures shown in Fig. 4. Equivalency is based on the assumption that effects of tritium decay depend on the quantity of ^{3}He developed in the lattice.

Tests of samples charged with tritium-helium showed that the above assumption is not valid at elevated temperatures. Gas bubbles formed on dislocation networks [Fig.5(a)], and grain boundaries formed [Fig.5(b)] during 0.5-hour anneals at 1273°K. Further, a tensile test at 973°K showed that the helium, which had built in during the charging, agglomerated during the test, causing the fracture mode to change from ductile rupture to intergranular separation (Fig. 6) and reducing the strength and ductility of both 309S and 304L stainless steels. These observations agree with the results

Table 3. Tensile Properties of Types 309S and 304L Stainless Steels Containing Hydrogen and Helium

Alloy	Test Temperature, °K	Exposure Before Test	Strength, MN/m² Yield	Strength, MN/m² Ultimate	Elongation, %
309S[a]	300	None	241	614	57
	300	None	255	614	59
	300	None	234	607	53
	300[b]	[c]	296	614	57
	300[b]	[c]	303	614	48
	300[b]	[c]	305	627	55
	300[b]	[d]	379	655	45
	300[b]	[d]	386	662	53
	973	None	131	303	25
	973	None	131	289	29
	973[e]	[d]	227	234	1
	973[e]	[d]	-	158	<0.1
304L[a]	300	None	324	731	56
	300	None	331	737	49
	300[b]	[c]	400	737	32
	300[b]	[c]	400	724	28
	300[b]	[c]	400	737	30
	300[b]	[d]	434	744	29
	300[b]	[d]	434	744	26
	973	None	152	220	33
	973	None	152	255	29
	973[e]	[d]	193	200	1
	973[e]	[d]	165	179	2

a. Foil specimens (0.0254 cm x 0.381 cm x 2.54 cm gauge) tested in air at 0.01 cm/cm per minute.

b. Specimens contained tritium and helium-3.

c. Specimens contained 2.2 cc hydrogen isotopes and 0.040 cc helium isotopes per cc metal.

d. Specimens contained 0.14 cc hydrogen isotopes and 0.14 cc helium isotopes per cc metal.

e. Specimens of type held 1/2 hour at 973°K to permit helium to agglomerate and to drive off hydrogen before testing.

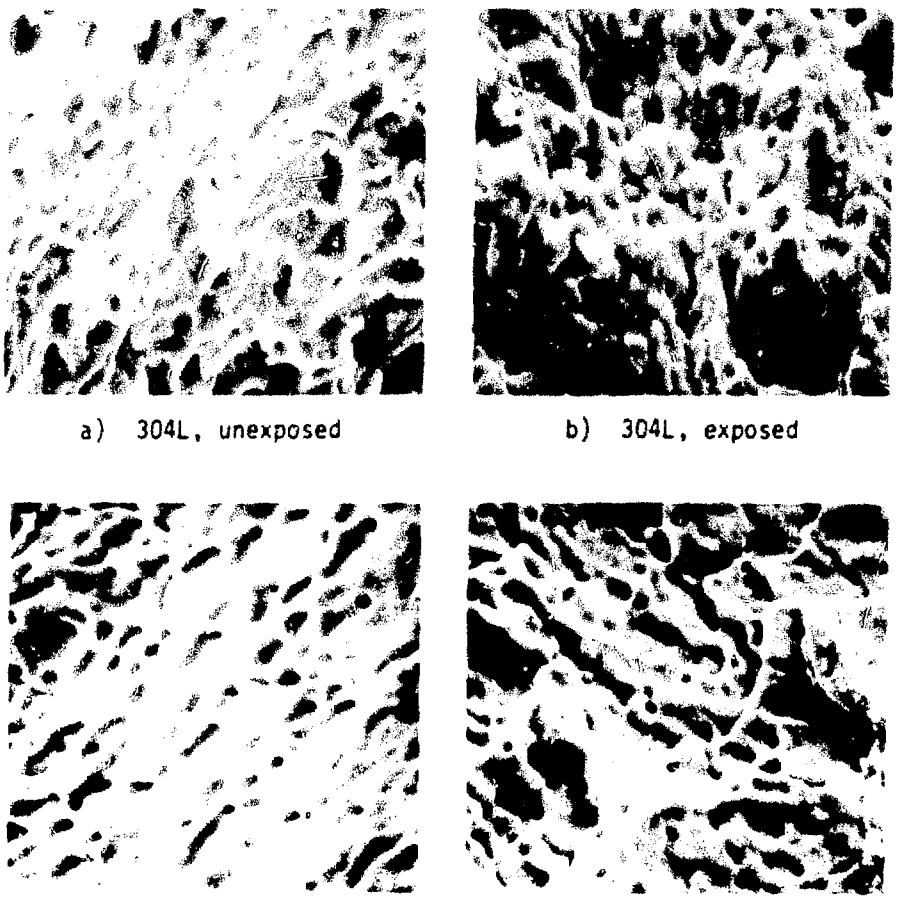

a) 304L, unexposed

b) 304L, exposed

c) 309S, unexposed

d) 309S, exposed

Fig. 2. Effect of Tritium Exposure on Fracture Topography of Austenite Steels. Samples exposed in tritium for 17 months, then tested to fracture at room temperature.

Figure 3. Typical Dislocation Substructure on Tritium-Charged Sample after 21-Day Anneal at 425°K

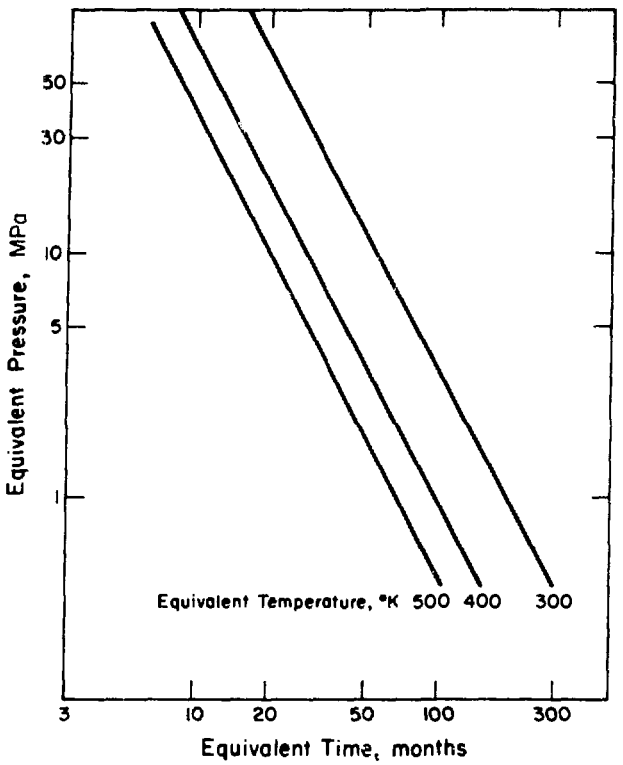

Fig. 4. Exposure Conditions Calculated to be Equivalent to 17 Months Exposure to 47.5-MPa Tritium at 343°K. Calculations are designed to give same amount of ^{3}He after test.

a) Bubbles at dislocation nodes

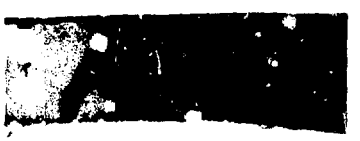

b) Bubbles at grain boundaries and dislocations

Figure 5. Helium Bubble Formation at Dislocations of Grain Boundaries on Sample Annealed at 1273°K

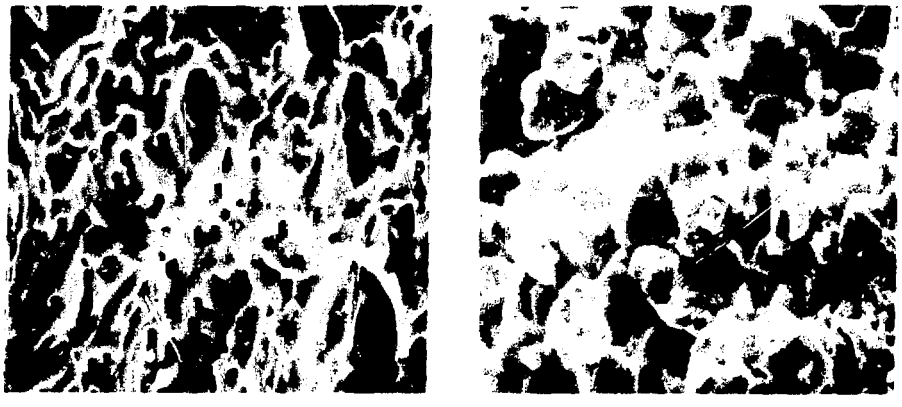

a) 304L unexposed

b) 304L, ∿0.14 cc ^{3}He

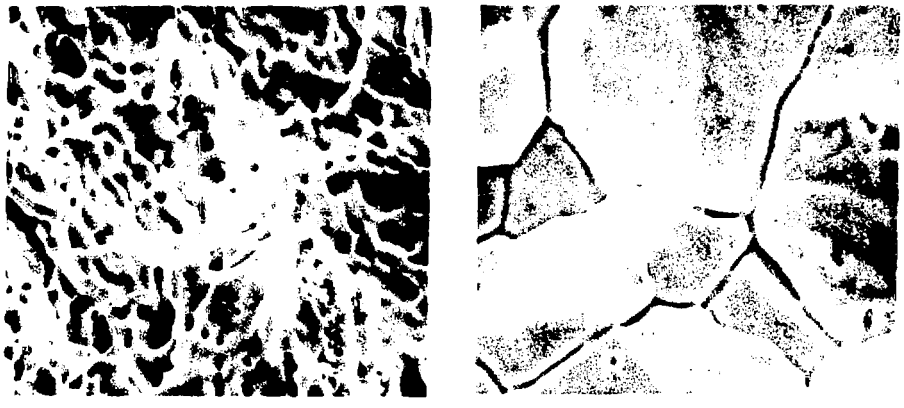

c) 309S, unexposed

b) 309S, ∿0.14 cc ^{3}He

Fig. 6. Effect of ^{3}He Buildin on Fracture Topography of Austenitic Steels Tested at 973°K

of studies of helium embrittlement of ion-bombarded Type 304 stainless steel.[19] The lack of significant effects at near-ambient temperatures also agrees with the ion-bombardment studies which showed no effects of irradiation at temperatures below 923°K. These results indicate that the wealth of data on helium effects available from various irradiation studies is, to a first approximation, applicable to helium effects resulting from buildin of ^{3}He from tritium decay. This conclusion, coupled with the equivalency curves shown in Fig. 4, indicates that helium build-in should have little or no effect on the mechanical properties of austenitic stainless steel components exposed to >0.1-MPa tritium at ~300°K within a 25 to 50-year design lifetime.

CONCLUSIONS

The effects of tritium absorption and subsequent helium build-in on the tensile properties of Types 304L and 309S austenitic stainless steel show that long exposures to tritium such as those expected in a fusion reactor should have no serious effects on structural integrity of these materials. The effects of hydrogen are similar to those of tritium and effects of tritium-daughter helium are similar to the results predicted from α-ion bombardment studies. These similarities indicate that the large volume of hydrogen and helium data available from other studies may be applicable to fusion reactor problems. However, difficulties in applying short-time test results to predictions of long-time compatibility arise primarily because gas trapping, metal surface effects, and short-circuit gas diffusion influence exposure simulation parameters.

REFERENCES

1. M. R. Louthan, Jr., G. R. Caskey, Jr., J. A. Donovan, and D. E. Rawl, Jr., Mater. Sci. Eng. 10, 357 (1972).

2. M. R. Louthan, Jr., J. A. Donovan, and G. R. Caskey, Jr., Nucl. Technol. 26, 192 (1975).

3. W. T. Chandler and R. J. Walter, "Hydrogen-Environment Embrittlement of Metals and Its Control" in Proceedings of the Hydrogen Economy Miami Energy (THEME) Conference, sponsored by The School of Engineering and Environmental Design, University of Miami, Coral Gables, Florida, March 1974, S6-S15.

4. J. P. Fidelle, R. Bernardi, R. Broudeur, C. Roux, and M. Rapin, "Disk Pressure Testing of Hydrogen Environment Embrittlement." ASTM STP 543, p. 221, American Society for Testing and Materials, Philadelphia (1974).

5. A. W. Thompson, "High Pressure Hydrogen" to be published in Handbook of Stainless Steels. McGraw Hill Handbook Series, edited by D. Peckner and I. M. Bernstein.

6. M. R. Louthan, Jr., J. A. Donovan, and D. E. Rawl, Jr., Corrosion 29, 108 (1973).

7. B. C. Odegard and A. J. West, "On the Thermo-Mechanical Behavior and Hydrogen Compatibility of 22-13-5 Stainless Steel." To be published in Mater. Sci. Eng.

8. A. W. Thompson, Hydrogen in Metals, p. 91, ASM, Metals Park, Ohio (1974).

9. M. R. Louthan, Jr., Hydrogen in Metals, p. 53, ASM, Metals Park, Ohio (1974).

10. R. M. Vennett and G. S. Ansell, Trans Amer. Soc. Metals 60, 242 (1967).

11. R. M. Vennett and G. S. Ansell, Trans. Amer. Soc. Metals 62, 1007 (1969).

12. R. B. Benson, Hydrogen in Metals, p. 183, ASM, Metal Park, Ohio (1974).

13. R. B. Benson, Jr., R. K. Dann, and L.W. Roberts, Jr., Trans. AIME 242, 2199 (1968).

14. R. R. Vandervoort, Metals Eng. Quart. 12, 10 (1972).

15. M. R. Louthan, Jr., D. E. Rawl, Jr., J. A. Donovan, and W. G. Holmes, Trans. ANS 21, 158 (1975).

16. J. A. Donovan, "Sorption of Tritium by Nickel During Plastic Deformation." To be published in Metallurgical Transactions.

17. M. R. Louthan, Jr. and R. G. Derrick, to be published in Corros. Sci.

18. G. R. Caskey, Jr. and W. L. Pillinger, Met. Trans. 6A, 467 (1975).

19. D. Kramer, H. R. Brayen, C. G. Rhodes, and A. G. Part, J. Nucl. Mater. 25, 121 (1968)

HYDROGEN EFFECTS IN ALUMINUM ALLOYS*

M. R. Louthan, Jr.
G. R. Caskey, Jr.
A. H. Dexter

E. I. du Pont de Nemours & Co.
Savannah River Laboratory
Aiken, South Carolina 29801

ABSTRACT

The permeability of six commercial aluminum alloys to deuterium and tritium was determined by several techniques. Surface films inhibited permeation under most conditions; however, contact with lithium deuteride during the tests minimized the surface effects. Under these conditions

$$\phi_{D_2} = 1.9 \times 10^{-2} \exp(-22{,}400/RT) \text{ cc(NTP)atm}^{-\frac{1}{2}}\text{sec}^{-1}\text{cm}^{-1}$$

The six alloys were also tested before, during, and after exposure to high pressure hydrogen, and no hydrogen-induced effects on the tensile properties were observed.

---

* The information contained in this article was developed during the course of work under Contract No. AT(07-2)-1 with the U. S. Energy Research and Development Administration.

INTRODUCTION

Aluminum and its alloys are generally considered immune to embrittlement by exposure to gaseous hydrogen. The tensile properties of many aluminum alloys are not noticeably affected by testing in 69-MPa hydrogen;[1,2] quantitative fracture mechanics data on 2219 aluminum show that the stress intensities at crack arrest are the same in 34.5-MPa hydrogen and helium;[3] measurements of fatigue crack growth rate in dry hydrogen and argon show no hydrogen-induced enhancement of crack growth rates;[4] disk rupture tests of 7075 aluminum indicate little or no sensitivity to hydrogen embrittlement.[5] However, corrosion studies,[6] investigations of blistering,[7] and studies with cathodically charged alloys[8] have provided evidence indicating that when sufficient hydrogen is absorbed, hydrogen embrittlement will result.

Hydrogen absorption by aluminum alloys exposed to gaseous hydrogen environments is probably severely restricted by a surface oxide film. Early measurements showed that the permeability constant for hydrogen in aluminum varied by four hundred fold, depending on surface treatment.[9] Differences in surfaces also must contribute to the wide spread in reported values for the permeation activation energy ($\sim$26 to $\sim$10 kcal $mole^{-1}$)[10] and activation energy for diffusion ($\sim$9.2 to $\sim$33.5 kcal $mole^{-1}$).[11,12] Because the potential for embrittlement of aluminum alloys is apparently related to hydrogen absorption, the nature of the surface may also be important in embrittlement considerations.

Aluminum is a candidate structural material in a minimum-activity concept for fusion reactor blankets.[13] This concept requires that the alloy selected have reasonable strength at elevated temperatures and be compatible with low-pressure tritium from both a strength and permeation standpoint. Savannah River Laboratory has investigated the ^{3}H-Al system from both of these standpoints for several years. This paper summarizes the results of those studies.

DISCUSSION

Permeation

The permeability of aluminum alloys to deuterium and tritium was determined with several types of specimens. The majority of the deuterium data was obtained with foil specimens using techniques previously described for austenitic stainless steels.[14] Measurements with type 3003 aluminum showed that the apparent permeability of aluminum to deuterium was increased when lithium deuteride was in contact with the deuterium side of the permeation specimen (Fig. 1). Least squares analysis of the permeation data indicated that contact with LiD increased the permeability coefficient and decreased the activation energy. This effect has been reported for austenitic steels and is attributed to removal of surface oxide films through reaction of the film with the lithium deuteride powder.[14] In the present case, however, the reaction

$$Al_2O_3(s) + 6LiH(s) \rightarrow 3Li_2O(s) + 2Al(s) + 3H_2(g)$$

is not likely to occur since $\Delta G \sim +73{,}000$ cal mole^{-1} for hydrogen at 0.1 MPa. However, most air-formed oxide films on aluminum alloys are hydrated, and ΔG° is negative for a reaction of the type

$$\alpha Al_2O_3 \cdot H_2O + LiH \rightarrow \alpha Al_2O_3 + LiOH + H_2$$

Thus, contact with lithium deuteride could affect the characteristics of surface films and thus the permeability to deuterium as was found by Cockran.[9]

The permeability of aluminum alloys 5086, 5083, and 7039 (compositions in Table 1) to deuterium was in agreement with the 3003 data (Fig. 2) and is represented by

$$\phi_{D_2} = 1.9 \times 10^{-2} \exp(-22{,}400/RT) \text{ cc(NTP) atm}^{-\frac{1}{2}} \text{sec}^{-1} \text{cm}^{-1} \qquad (1)$$

Thus, small differences in alloy composition did not significantly affect permeability at temperatures as low as $\sim$500°K, when lithium deuteride was in the permeation cell. This observation is in agreement with Cockran's results for 1100, 5050, and 8001 alloys.

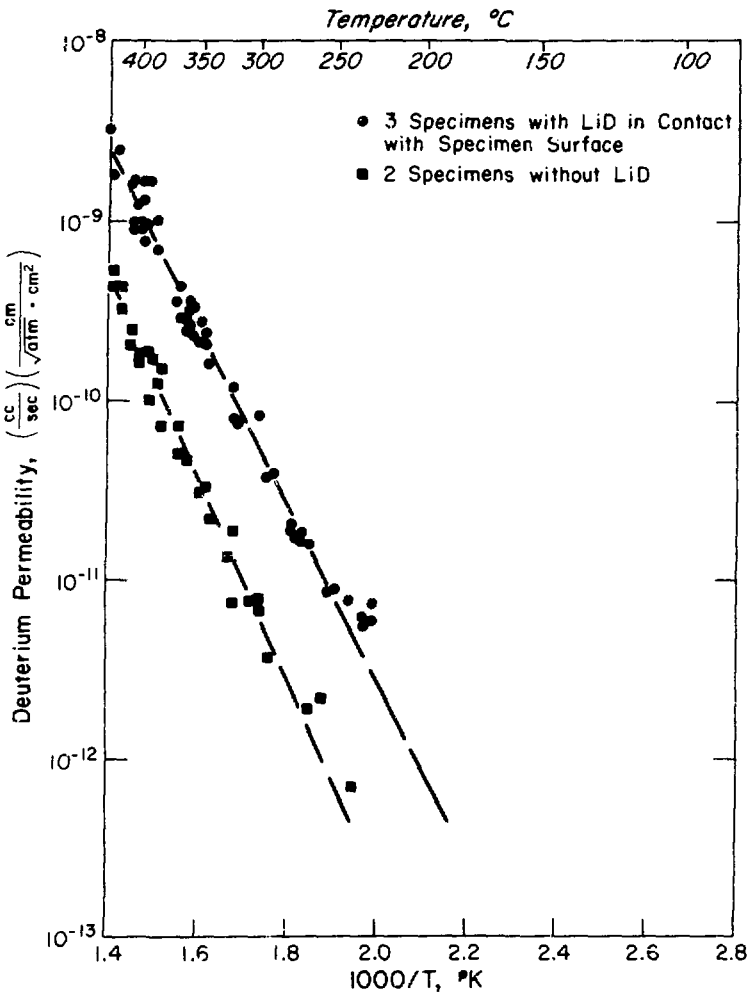

Fig. 1. Effect of LiD on the Permeability of Deuterium through 3003 Aluminum

Table 1. Aluminum Alloy Compositions

Alloy	Nominal Composition, wt %
3003	0.6Si-0.7Fe-0.12Cu-1.2Mn-0.1Zn, balance Al
5083	0.40Si-0.40Fe-0.10Cu-0.65Mn-0.2Zn, balance Al
5086	0.40Si-0.50Fe-0.10Cu-0.45Mn-0.2Zn, balance Al
7039	0.30Si-0.40Fe-0.10Cu-0.25Mn-4.0Zn, balance Al
2011	0.40Si-0.7Fe-5.5Cu-0.4Bi-0.4Pb, balance Al
2024	0.50Si-0.5Fe-4.4Cu-0.6Mn-1.5Mg, balance Al
6061	0.60Si-0.7Fe-0.27Cu-1.0Mg-0.2Cr, balance Al
6063	0.40Si-0.35Fe-0.10Cu-0.10Mn-0.7Mg, balance Al

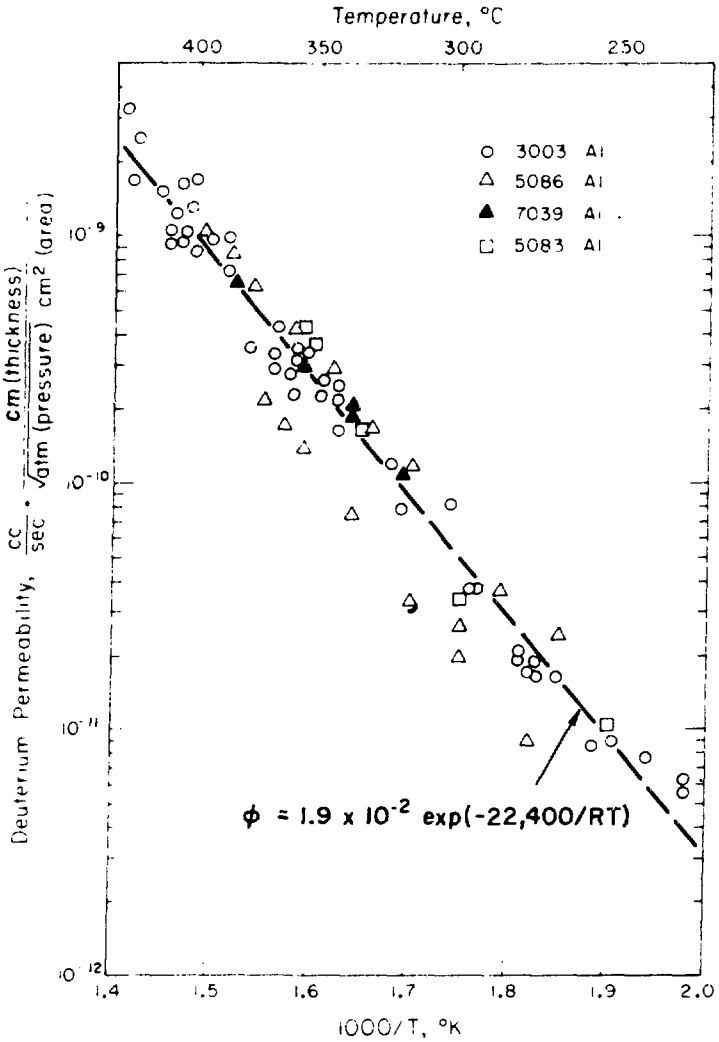

Fig. 2. Deuterium Permeability of Aluminum Alloys in Contact with Lithium Deuteride. Several specimens of 3003 and two specimens of 5087 aluminum were used.

The data shown in Fig. 2 also indicate that cold work does not affect the permeability to deuterium. Several of the 3003 and the 5083 Al specimens used to obtain the data were initially in a cold-worked condition. These specimens recrystallized during the high-temperature permeation experiments. However, recrystallization had no effect on permeation. Duplicate measurements before and after recrystallization were nearly identical, and no changes in slope or discontinuities in the Richardson-Arrhenius plot are noted at either the recovery or recrystallization temperatures. This indicates that dislocation networks, grain boundaries, and other such defects do not provide high permeability paths. The lack of grain boundary effects is apparently in contrast to the autoradiographic results of Haynie and Boyd.[15] Their studies indicate that hydrogen is present in higher concentrations at grain boundaries than within the grains of stressed Al-Zn-Mg alloy. However, the permeation specimens used in the present study were not stressed significantly during test; thus the result may be interpreted as indicating the importance of stress in promoting grain boundary segregation of hydrogen (and perhaps stress-corrosion cracking) in aluminum alloys.

Another series of permeation measurements for 7039 aluminum with both tritium and deuterium at lower temperature (to 400°K) was made with tubular samples as shown in Fig. 3. These samples did not contain lithium deuteride because of the potential for deuterium-tritium exchange during measurements with tritium. The deuterium permeability for the same samples was in agreement with the tritium data when corrected for isotope effects using the inverse square root of mass correction, Fig. 4. As shown on the figure, these data are in reasonable agreement with the measurements on 3003 aluminum foils without LiD given in Fig. 1. The permeability data for both alloys are described reasonably well by the expression

$$\phi = \frac{10^3}{\sqrt{m}} \exp(-35{,}700/RT) \text{ cc(NTP)atm}^{-} \text{ cm}^{-1}\text{sec}^{-1} \qquad (2)$$

This equation predicts room-temperature permeabilities 10^{-3} to 10^{-4} of those from Eq. (1) for specimens in contact with lithium deute-

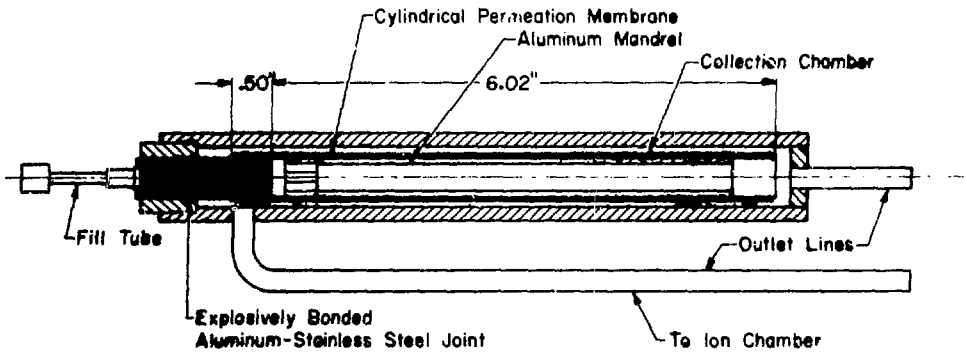

Fig. 3. Test Apparatus for Measurement of Tritium Permeation through Aluminum Alloys

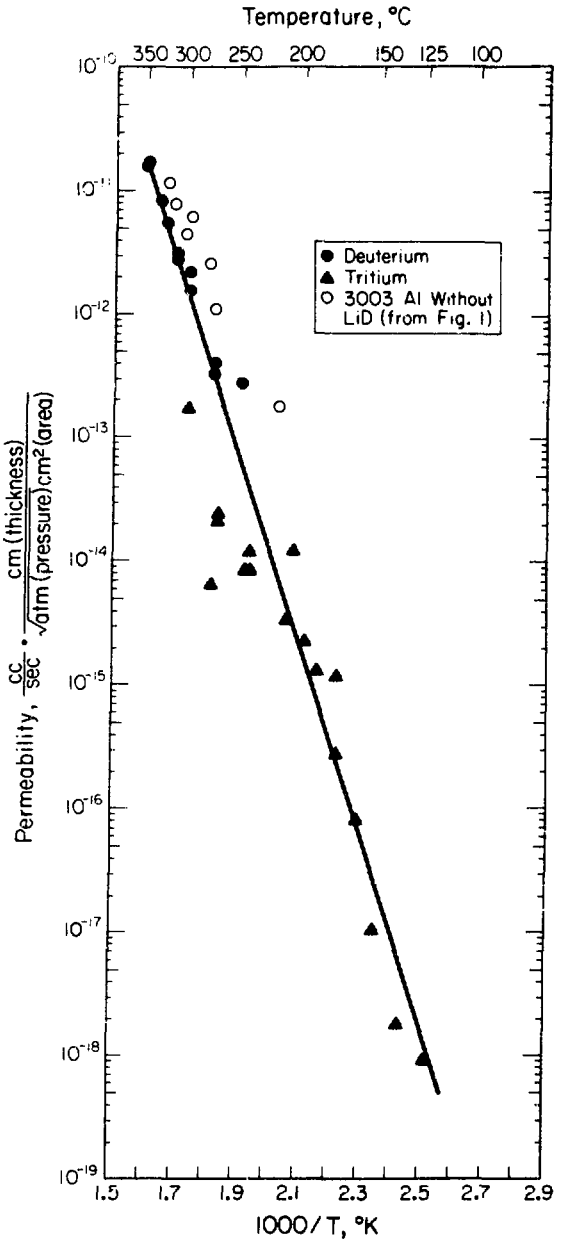

Fig. 4. Permeability of Deuterium and Tritium through 7039 Aluminum

ride. As previously described, it is assumed that a surface oxide was present on all the samples tested, regardless of the presence of lithium deuteride. It is tempting to conclude that values for ϕ_o and ΔH_ϕ for aluminum are irrelevant[16] and that permeability equations primarily describe only the effects of the surface films. Published solubility and diffusivity measurements tend to confirm this conclusion; diffusion activation energies between 9.7 and 33.5 kcal mole^{-1} have been reported[11,12,17,19] and activation energies for hydrogen solution vary between 9.5 and 16.3 kcal mole^{-1}.[18,19,20] Combination of these values yields permeation activation energies between 18.5 and 49.8 kcal mole^{-1}.

Evaluation of the available data, however, indicates that apparent differences in activation energy (and diffusivity and solubility constants) are emphasized because studies have often been confined to a narrow temperature range. Most of the solubility data are in reasonable agreement and fall within a factor of two of the solubility equation proposed by Eichenauer[19] in 1968 for 99.999% aluminum:

$$C = 3.43\ p^{\frac{1}{2}} \exp(15{,}100/RT)\,cc(NTP)cm^{-3} \qquad (3)$$

where C is the solubility of hydrogen at pressure p and temperature T. The highest reported values for hydrogen diffusion were those of Eichenauer, Hattenback, and Pebler.[11] Least squares fit of their data gave a diffusivity D,

$$D = 0.011\ \exp(-9{,}200/RT)\,cm^2 sec^{-1} \qquad (4)$$

The highest reported values of D were selected because surface effects decrease the apparent diffusivity, so the highest value should represent minimum surface effects. Combination of Eqs. (3) and (4) yields

$$\phi_{H_2} = 3.7 \times 10^{-2}\ \exp(-24{,}300/RT) \qquad (5)$$

for permeability ϕ_{H_2}, which is in reasonable agreement with Eq. (1). These results indicate that diffusion-controlled permeability is represented by Eq. (1) and that Eqs. (3) and (4) provide reasonable estimates of the solubility and diffusivity of hydrogen in aluminum.

The apparent lack of significant surface effects on hydrogen permeability through the alloys in contact with lithium deuteride indicates

that the surface oxide is highly defected and that the defects are high permeability paths. Measured tritium diffusion coefficients in single crystal and polycrystalline Al_2O_3[21] show that the activation energy for hydrogen diffusion is significantly less for polycrystalline samples and that the diffusivity increases with decreasing grain size. These data support the contention that an air-grown oxide film on a commercial aluminum alloy forms a permeation barrier. Exposure at that barrier to LiD dehydrates the oxide and could create a significant number of high-permeability paths. Such paths would be expected if removal of the water of hydration either lowered the density or caused cracking and/or spalling of the typical air-grown film. Thus, hydrogen permeation experiments in the absence of techniques to dehydrate the $Al_2O_3 \cdot H_2O$ would be under surface control and low permeabilities would be observed [Eq. (2)]. Contact with lithium deuteride would dehydrate the film, create high-permeability paths, and permit diffusion-controlled permeation to be measured.

Mechanical Properties

The mechanical properties of a wide group of aluminum alloys were not affected either by exposure to or testing in gaseous hydrogen. Foil-type specimens (0.025 cm thick) of annealed 3003 aluminum were tested in room air at 223 to 383°K after exposure to 69-MPa deuterium gas at 343°K for 28 hours (sufficient time to saturate the alloy). Half of the specimens were simply exposed to the deuterium gas; half were in contact with lithium deuteride during the exposure. Neither exposure significantly affected the mechanical properties (Table 2). Good compatibility with hydrogen was confirmed for six other aluminum alloys (2011, 2024, 5086, 6061, 6063, and 7039) which were tested at 300°K in room air, 69-MPa hydrogen, and 69-MPa helium (Table 3). These results, coupled with the favorable results of long-time exposure tests with 7039 aluminum (Table 4) provide an excellent justification for use of aluminum-base alloys in hydrogen service. Other studies with annealed 1100 aluminum showed that long-time exposure to tritium and the resulting build in of tritium-decay helium had no adverse effects on the mechanical properties (Table 5).

Table 2. Effects of Dueterium Exposure on Annealed 3003 Aluminum

Exposure	Test Temperature, °K	Strength, MPa Yield	Strength, MPa Ultimate	Elongation, %
None	383	30.3	81.4	35
	343	29.6	91.7	32
	303	42.7	111.7	20
	263	39.3	110.3	32
	223	42.7	111.7	35
D_2 Gas[a]	383	34.5	77.2	33
	343	39.3	86.2	31
	303	42.7	97.9	23
	263	32.4	100.7	31
	223	48.9	106.2	27
LiD + D_2 gas[a]	383	42.1	83.4	32
	343	38.6	92.4	31
	303	40.0	95.1	24
	263	38.6	99.3	26
	223	47.6	107.6	27

a. 69 MPa pressure deuterium gas for 28 hours.

Table 3. Hydrogen Effects on Aluminum Alloys

Alloy	Test Environment	Strength, MPa Yield	Strength, MPa Ultimate	Ductility, Red. in Area, %	Ductility, Elong., %
2011	0.1-MPa	269	338	48	17
	69-MPa He	227	296	57	18
	69-MPa H_2	220	296	58	17
2024	0.1-MPa Air	358	489	33	15
	69-MPa He	324	441	36	19
	69-MPa H_2	310	427	35	18
5086	0.1-mPa Air	193	303	49	18
	69-MPa He	151	248	55	20
	69-MPa H_2	138	248	57	21
6061	0.1-MPa Air	179	234	75	14
	69-MPa He	131	179	82	15
	69-MPa H_2	138	186	82	14
6063	0.1-MPa Air	214	241	62	13
	69-MPa He	158	193	83	15
	69-MPa H_2	158	200	84	15
7039	0.1-MPa Air	152	179	80	14
	69-MPa He	124	138	85	14
	69-MPa H_2	117	138	86	14

Table 4. Effect of Prolonged Hydrogen Exposure on the Tensile Properties of 7039 Aluminum

Condition	σ_y, MPa	σ_{ult}, MPa	Ductility, Red. in Area, %	Elong., %
Unexposed	303	379	44	13
Exposed[a]	310	372	45	14

a. Exposed 524 days to 69-MPa H_2 at 343°K; data averages of at least three samples.

Table 5. Effects of Tritium Exposure on the Mechanical Properties of 1100 Aluminum at 300°K

Exposure	σ_y, MPa	σ_{ult}, MPa	% Elongation in 2.54 cm
None	34	90	32
None	49	90	33
69 MPa for	34	96	36
38 days	41	96	39
at 343°K	34	96	34
69 MPa	41	90	29
for 510 days	41	90	33
at 343°K	41	90	30

CONCLUSION

The combined results of the mechanical property and hydrogen-transport data show that aluminum alloys should be considered when potential applications require both mechanical compatibility with hydrogen isotopes and low hydrogen permeation rates. Eqs. (1) and (2), respectively, provide estimates of the permeability of aluminum alloys to hydrogen isotopes under conditions of diffusion and surface control.

REFERENCES

1. W. T. Chandler and R. J. Walter, ASTM STP 543, p. 170 (1974).

2. M. R. Louthan, Jr., G. R. Caskey, Jr., J. A. Donovan, and D. E. Rawl, Jr., Mater. Sci. and Eng. 10, 357 (1972).

3. R. J. Walter and W. T. Chandler, NASA CR-124410, Rocketdyne, Canoga Park, California (1973).

4. M. O. Speidel, Hydrogen in Metals, p. 249, ASM, Metals Park, Ohio, 1974.

5. J. P. Fidelle, R. Bernardi, R. Broudeun, C. Roux, and M. Rapin, ASTM STP 543, p. 221 (1974).

6. L. Montgain and P. R. Swann, Hydrogen in Metals, p. 575, ASM, Metals Park, Ohio, 1974.

7. P. D. Hess and G. K. Turnbull, Hydrogen in Metals, p. 277, ASM, Metals Park, Ohio, 1974.

8. R. J. Guest and A. R. Troiano, L'Hydrogen dans'es Metaux, p. 427 Editions Science at Industrie, Paris, 1972.

9. C. N. Cockran, J. Electrochem. Soc. 108, 317 (1961).

10. P. S. Flint, The Diffusion of Hydrogen Through Materials of Construction, KAPL-659 (December 14, 1951).

11. W. E. Eichenauer, K. Hattenback, and A. Pebler, Z. Metallkunde 52, 682, (1961).

12. C. E. Ransley and D. E. Talbot, Z. Metallkunde 46, 328 (1955).

13. J. Powell, A. Aronson, P. Bezler, F. Miles, and W. Winsche, The Proceedings of the First Topical Meeting on the Technology of Controlled Nuclear Fusion, p. 533, ANS (Conf-740402-p1) San Diego, California, 1974.

14. M. R. Louthan, Jr. and R. G. Derrick, to be published in Corros. Sci. (1975).

15. F. H. Haynie and W. K. Boyd, Proceedings of Conference on Fundamental Aspects of Stress Corrosion Cracking, NACE, Houston, p. 580 (1969).

16. P. Boeschoten, W. V. Egmond, and H. M. J. Kinderdijk, Appl. Sci. Res. 8 B, 378, (1960).

17. S. Matsuo and T. Hirata, Nippon Kinzouku Gakkaishi 31, 590 (1967).

18. W. Eichenauer and A. Pebler, Z. Metallkunde 48, 373 (1957).

19. W. Eichenauer, Z. Metallkunde 59, 813 (1958).

20. C. E. Ransley and H. Neufeld, J. Inst. Metals 74, 599 (1948).

21. T. E. Elleman, Tritium Diffusion in Nonmetallic Solids of Interest for Fusion Reactors, progress report 12/1/74 through 3/1/75. North Carolina State University.

[illegible] MATERIALS

[illegible] Laboratory

A scanning electron microscope (SEM) facility for the examination of [illegible] materials is operational at Mound Laboratory. The SEM is installed with [illegible] incorporated as an integral part of the [illegible] facility to enable easy handling of reactive and pyrophoric materials. A [illegible] Model S-1) was modified to meet [illegible] and safety-related requirements. A glovebox was designed and fabricated with a [illegible] access with the glovebox to allow [illegible] SEM sample chamber to facilitate [illegible] and [illegible] replacement and repairs. [illegible] combining the electron optics [illegible] was interfaced to the [illegible], such that [illegible] follows so that [illegible] is initiated with the blower [illegible] micrographs of [illegible] the usefulness of this [illegible] modifications involved in the [illegible] materials are also discussed.

A new [illegible] of reactive pyrophoric [illegible] scanning electron microscopy (SEM) technique [illegible]. This SEM installation [illegible] chamber was incorporated [illegible] glovebox to enable easy handling [illegible] modifications required [illegible] involved considerable [illegible] instruments.

The enclosed specimen chamber concept required that the design of the SEM be such that it could be interfaced with a glovebox by vibration damping techniques and that it not be easily contaminated. In addition, all parts of the chamber needed to be accessible for cleaning or sealing off for removal of detectors for maintenance and repair.

The SEM's of only two manufacturers, AMR and ETEC, were considered as they were the only ones equipped with column liner tubes. The ETEC instrument was chosen because its column liner tube was continuous and the chamber was more accessible for cleaning and decontamination.

A rubber boot interface concept was designed for coupling the front side of the specimen chamber to the back side of a glovebox, and a specially shortened glovebox was purchased to enable a person of average size to reach to the back of the microscope chamber through the glove ports. The box was 12 in. deep and the chamber was 9 in. deep. ETEC changed its standard instrument to meet our mating needs and designed special isolation valves for the column and gun. Port covers also were designed by ETEC. These adaptations now allow every entrance to the chamber to be blocked from the glovebox atmosphere for repair and maintenance without opening the glovebox atmosphere to the room.

The appearance of the boxline installation is shown in Figure 1. A fumehood for introducing samples into a vacuum passbox is shown in the back of the room. The passbox opens into the glovebox which contains a circulating dry argon atmosphere purified by an individual Dri-train system. In addition, the atmosphere is circulated through a separate catalytic deoxo unit which is used to remove tritium gas and keep the contamination level to a minimum. A Pedatrol pressure control system can also be seen. This system maintains the desired glovebox pressure by admitting pure argon or exhausting to the

Fig. 1. Appearance of the SEM Glovebox Installation from the Front.

Effluent Recovery System as required. The overhead pipes lead to the Dri-train system in the adjacent room and to the house argon, chill water, and Effluent Recovery System lines. A Kanné monitor is located above the hood opening.

Figure 2 shows the back of the glovebox with the electron optical column and the rubber boot interface. The system is monitored by a Panametrics moisture analyzer and a Delphi oxygen analyzer. An ORTEC energy dispersive x-ray analyzer is shown in the foreground. The microscope chamber is mounted on a table top supported by hydraulic vibration dampers. The operating consoles for the SEM and the ORTEC are shown in Figure 3.

The specimen chamber door is shown in Figure 4 through the glovebox window. The stage controls shown can all be operated remotely at the main console. These five different motions are X, Y, Z, tilt, and rotate. The specimen stage is

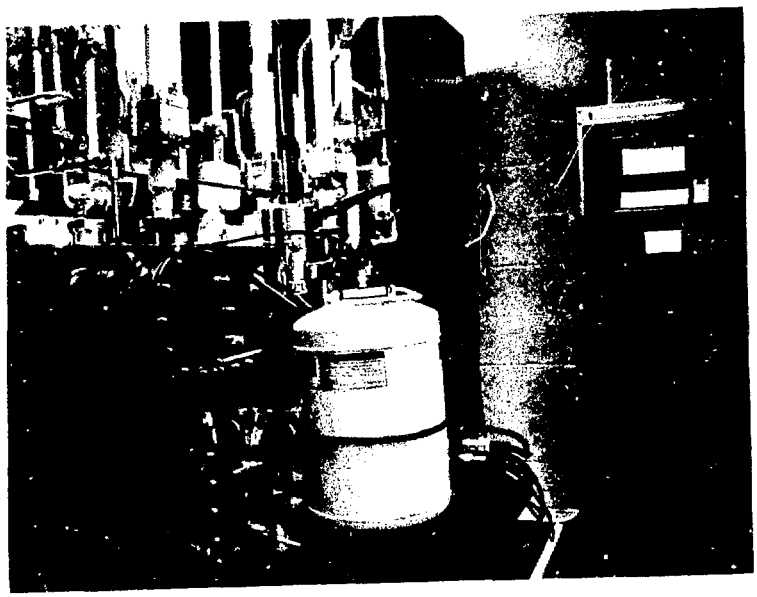

Fig. 2. View from Behind the Glovebox Showing the Electron Optical Column, Chamber to Glovebox Interface and Energy Dispersive X-ray Analyzer.

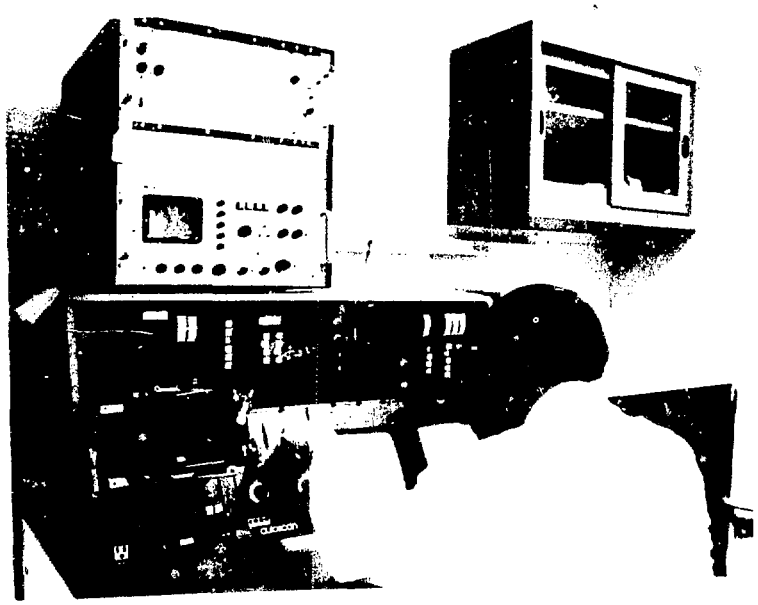

Fig. 3. The Operating Console for the SEM and the ORTEC Energy Dispersive X-ray Analyzer.

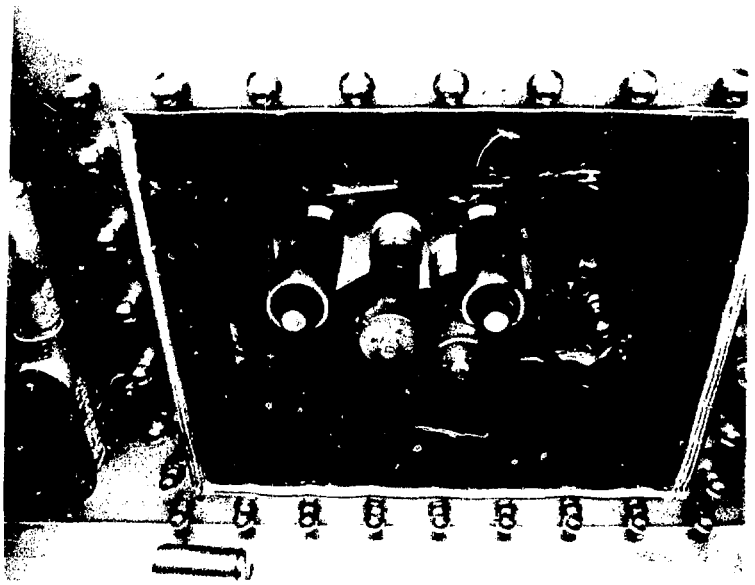

Fig. 4. View of the Specimen Chamber Door; the Stage Controls Shown Have All Been Remotized.

affixed to the door as shown in Figure 5. With the door open the chamber is empty except for analyzers and can be readily cleaned or decontaminated. The stage door is removable for changing types of stages or to bag out if decontamination or repair is necessary.

In a nearby laboratory a vacuum coating unit is also enclosed in a glovebox. A rapid access passbox is available at the rear of the glovebox for small samples only. Entry for larger samples or supplies is three boxes removed.

Samples from the evaporator or sample preparation box are transferred using the container shown in Figure 6. This is a common calorimeter can to which a flat Lucite plate is attached with epoxy so that it sits upright. Pin-type SEM sample stubs are placed in the holes of a half-cylinder cut from aluminum rod. This assembly fits inside the can which

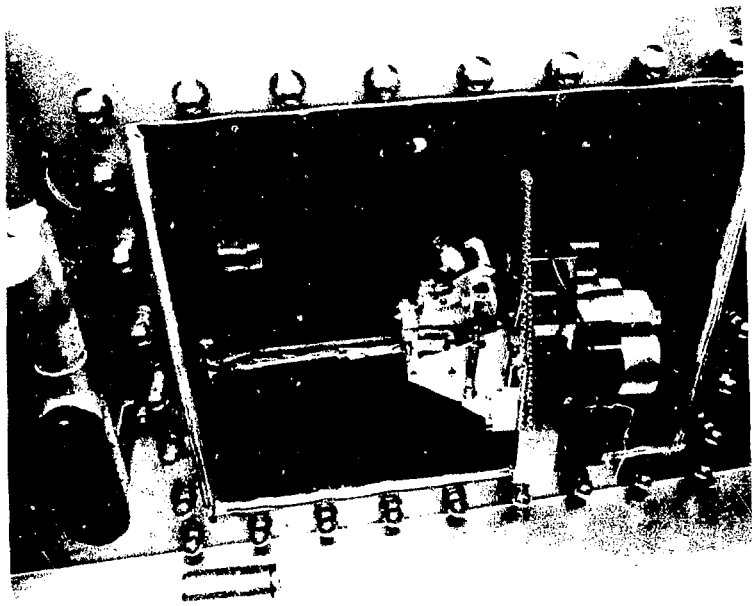

Fig. 5. View of the Specimen Stage and Chamber.

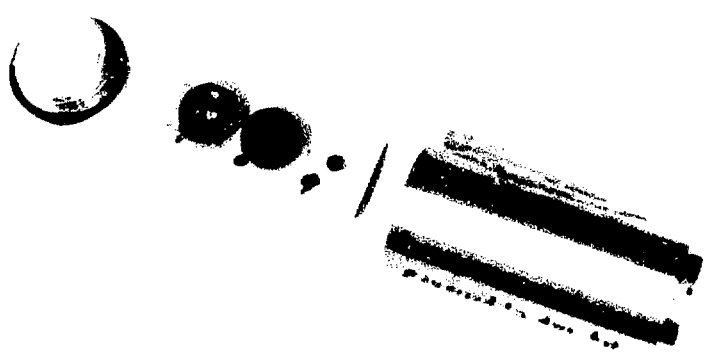

Fig. 6. A Sample Container for Moving Samples from the Sample Preparation Box to the SEM Glovebox.

is closed with an O-ring sealed cap. The sample container is double-bagged out for transfer to the SEM passbox.

The operational procedures and glovebox atmospheres were first checked on pyrophoric nonradioactive samples, finely divided LiH. The powder was mounted using a technique obtained from T. Gregory (formerly at LASL) on similar material. The powder was sprinkled on a sample stub which previously had been covered with double-faced tape and heavily coated by vapor deposition of gold. The appearance of the particle distribution is shown in Figure 7A. The appearance at higher magnification (5000X) is shown in Figure 7B. This material was investigated at magnifications up to 20,000X, uncoated, with no apparent charging in a 20 kV beam and no apparent reaction with the atmosphere.

Initial investigations of small quantities of radioactive material were then initiated by examining lithium hydride containing approximately 1 mol % tritium. This was examined with only a carbon coating, and no differences were observed between this and the cold material. Typical photomicrographs are shown in Figures 8A and 8B. Samples of lithium and uranium hydrides containing approximately 30-50 mol % tritium were then examined. These materials were then removed from the SEM glovebox, and the equipment was surveyed for radioactivity. Wipes of 100 counts/min were obtained from the gun anode; however, no counts were obtained on the grid cap or the column liner tube. A single wipe covering 1/3 to 1/2 of the surface area of the glovebox interior counted 10,000 counts/min, and a cold sample, left open during the examination of the hot material, wiped 2000 counts/min. A cold sample examined after removal of all hot material was found to wipe less than 50 counts/min after examination.

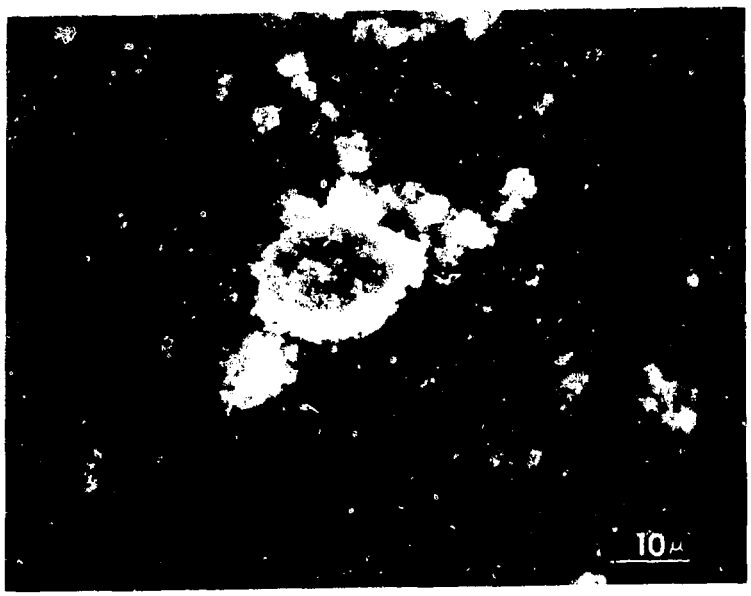

(A)

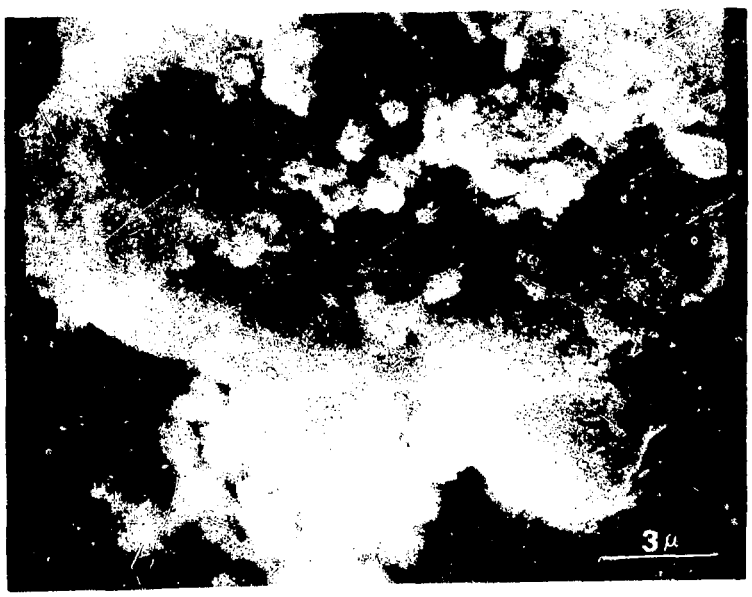

(B)

Fig. 7. Ultrafine LiH Powder Showing Sample Distribution (A) and an Agglomerate at Higher Magnification (B).

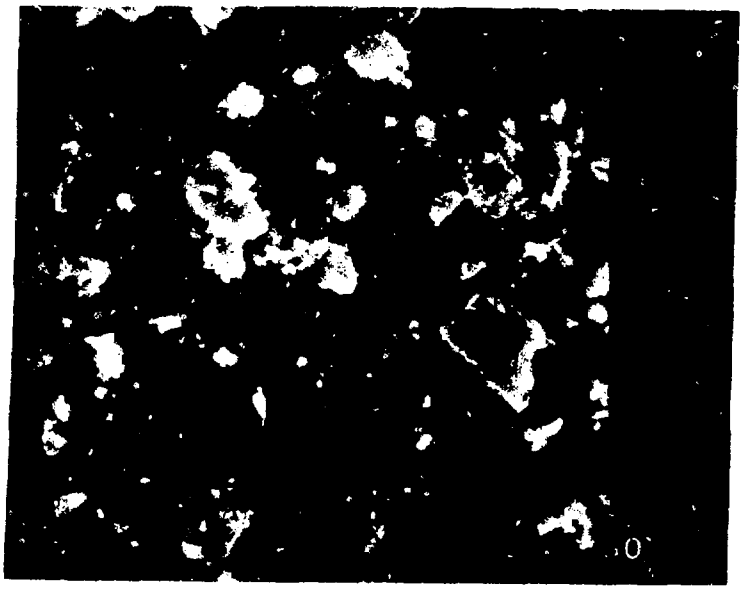

(A)

(B)

Fig. 8. LiH Containing Approximately 1 mol % Tritium, 60 Mesh Material at Low Magnification (A) and High Magnification (B).

Samples of uranium tritide were then prepared and a photomicrograph of the reaction product is shown in Figure 9. This material appears to have formed in layers due to columnar growth of the tritide grains from the metal with subsequent spalling and cracking of the layers due to stresses arising from volume change. After spalling the reaction proceeds with the freshly exposed metal.

In summary, an SEM facility for investigating radioactive, pyrophoric materials is currently in operation at Mound Laboratory. This facility has many applications in the study of tritium-contaminated materials. There is a limitation in the amount of tritiated material that can be examined because of the high background of secondary electrons from the β-radiation of the sample itself. This limit has not yet been determined quantitatively; however in practice, when this phenomenon is understood, compensations in techniques can be made. An ion

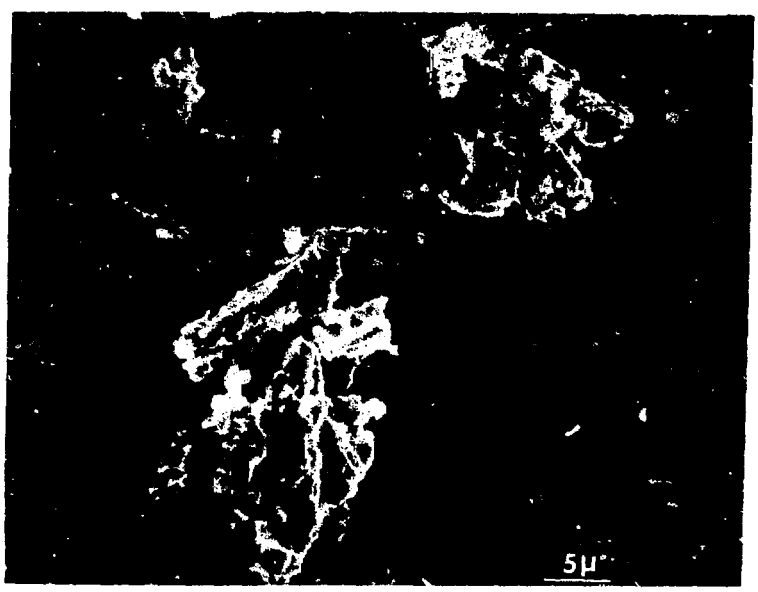

Fig. 9. Uranium Tritide.

mass analyzer attachment for this instrument has been purchased and is scheduled for installation in the near future. This will make possible analysis for masses from 1 to 300 amu.

REACTION RATES AND ELECTRICAL RESISTIVITIES OF THE HYDROGEN ISOTOPES WITH, AND THEIR SOLUBILITIES IN, LIQUID LITHIUM.

R. J. Pulham P. F. Adams P. Hubberstey

G. Parry Anne E. Thunder

Chemistry Department, University of Nottingham, England.

ABSTRACT

The rate of reaction, k, of hydrogen and of deuterium with liquid lithium have been determined up to pressures of 20kNm^{-2} and at temperatures between 230 and 270°C. The reaction is first order with an apparent activation energy of 52.8 and 55.2 kJmol^{-1} for hydrogen and deuterium, respectively. The deuterium isotope effect, k_H/k_D, decreases from 2.95 at 230 to 2.83 at 270°C. Tritium is predicted to react even more slowly than deuterium. The freezing point of lithium is depressed by 0.082 and 0.075°C, respectively, by dissolved hydride and deuteride giving eutectics at 0.016 mol%H and 0.012 mol%D in the metal-salt phase diagrams. The depression and eutectic concentration are expected to be less for tritium. The increase in the resistivity of liquid lithium caused by dissolved hydrogen isotopes is linear and relatively large, 5×10^{-8} Ωm (mol% H or D)$^{-1}$. The solubility of lithium hydride and deuteride were determined from the marked change in resistivity on saturation. The liquidus of the metal-salt phase diagram rises steeply from the eutectic point to meet the two-immiscible liquid region. At the lithium-rich end, hydride is more soluble than deuteride; the solubilities are given by

$\log$ (mol%H) = 3.523 - 2308/T $523 \leq T \leq 775$K

$\log$ (mol%D) = 4.321 - 2873/T $549 \leq T \leq 724$K

Tritium is expected to be less soluble than deuterium. The partial molar enthalpies of solution are 44.2 and 55.0 kJmol^{-1} for hydrogen and deuterium, respectively. These values are used to calculate the solvation enthalpies of the isotope anions in the metal.

INTRODUCTION

The chemical and physical properties of liquid lithium are of current interest due to the possible use of the metal as a combined tritium breeder and heat transfer medium. Although the lithium-tritium system remains largely unexplored, the reactions of the more easily handled isotopes, hydrogen and deuterium, can be used to delineate the probable relationships of tritium with the metal. Thus kinetics, and resistivities, together with phase and thermochemical properties for the lighter isotopes are not only of intrinsic interest but also indicate the probable behaviour of tritium in these areas.

EXPERIMENTAL

The multipurpose apparatus is shown in Fig. 1. For kinetic work the apparatus (stainless steel, AISI 321) comprised the cylindrical reservoir A (100 mm long, 70 mm diam.), dc. electromagnetic pump P_1 and thermocouple well T_1. It was charged with solid lithium (10g, 99.98%) under argon and mounted in an air oven so that the neck B protruded through an aperature for attachment to a vacuum frame. The transition from steel to glass was made through the seal M. The argon was replaced by hydrogen (99.98%) which reacted with the jet of liquid metal issuing from the pump. The reactions were sufficiently slow up to 300°C that the decrease in isotope pressure could be followed manometrically. Starting pressures were near 20 kNm^{-2}. Experiments were performed alternately with hydrogen and deuterium (99.50%) using the same metal at 229, 252 and 268°C; these were augmented by separate experiments with deuterium at 280 and 297°C.

For thermal analysis, the reservoir was narrower (254 mm long,

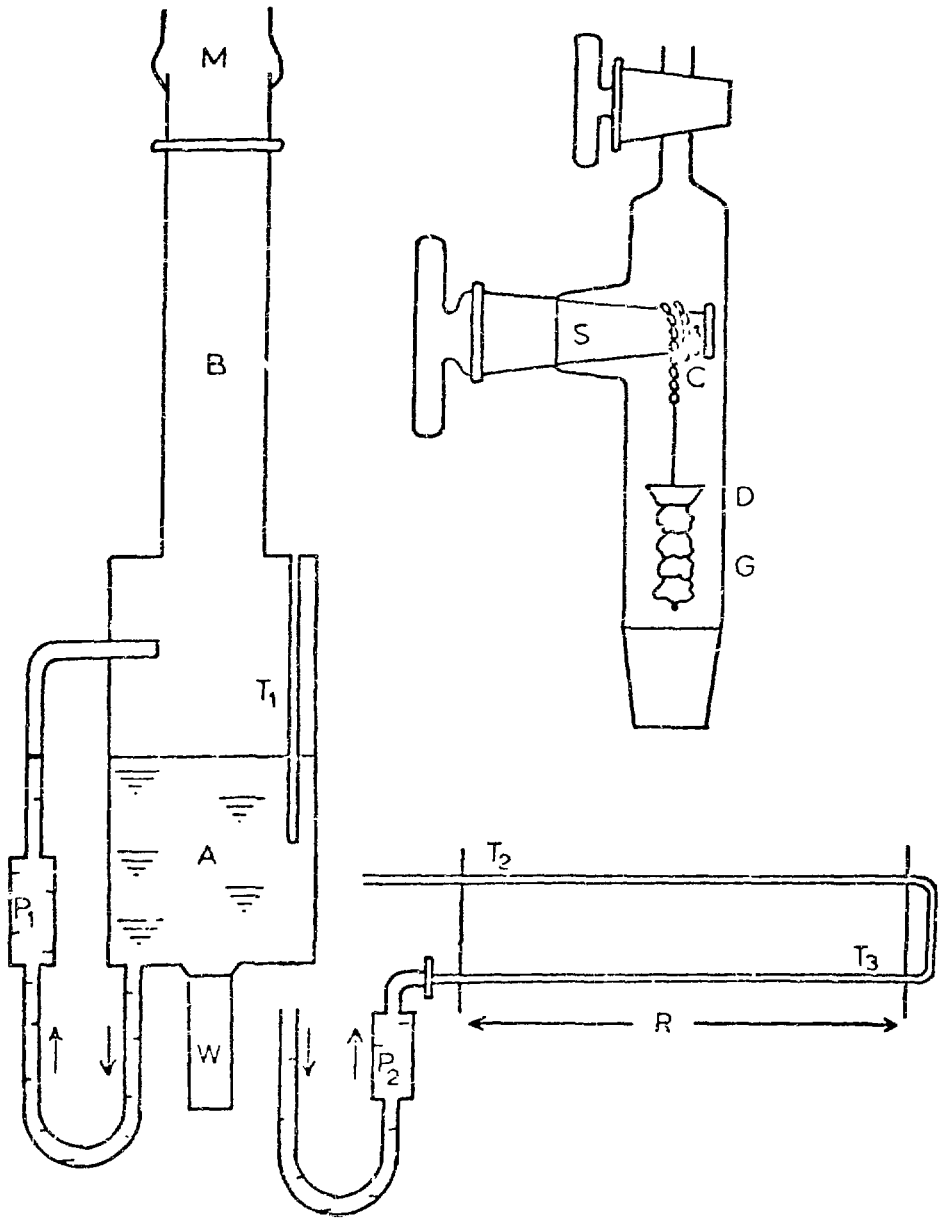

Fig. 1. Apparatus for the determination of kinetics, freezing point depression, resistivity and solubility.

38 mm diam.) and, prior to use, the liquid metal was gettered with yttrium sponge (5g, 99.9%) which was suspended by a chain C from a winding device S. This assembly was mounted above the seal M. After purification at 400°C, the getter was isolated in the well W which was sealed by a chamfered lid D, or completely removed. Successive volumes (ca $10^3 mm^3$ at STP) of hydrogen were admitted which reacted rapidly at 400°C. The pump P_1 was used to ensure homogeneity of the solution which was cooled at 10° h^{-1}. This slow rate gave reproducible freezing arrests which were measured using a chromel-alumel thermocouple in T_1 and a vernier potentiometer.

For resistivity measurements, the reservoir A (100 mm long, 50 mm diam.) was equipped with a steel capillary loop (1.5 mm id., 350 mm long). This was bridged by two circular discs near thermocouples T_2 and T_3 between which the resistance R was measured. The liquid was initially gettered as before and hydrogen or deuterium was added to the metal in small volumes (ca $10^4 mm^3$ at STP) at constant selected temperatures. Reaction occurred to form the salts LiH and LiD which dissolved in the metal. Resistivities were calculated from the resistance and the dimensions of the capillary using the formula for conductors in parallel.[1]

KINETICS

In the reactions (eq. (1)) of liquid lithium with the isotopes

$$Li(l) + \tfrac{1}{2}X_2(g) = LiX(s) \qquad (1)$$

X_2(X = H or D), pressures of gas fell smoothly with time as shown in Fig. 2 where log P is plotted against t. Linear relationships were obtained for both isotopes as expected for first order kinetics

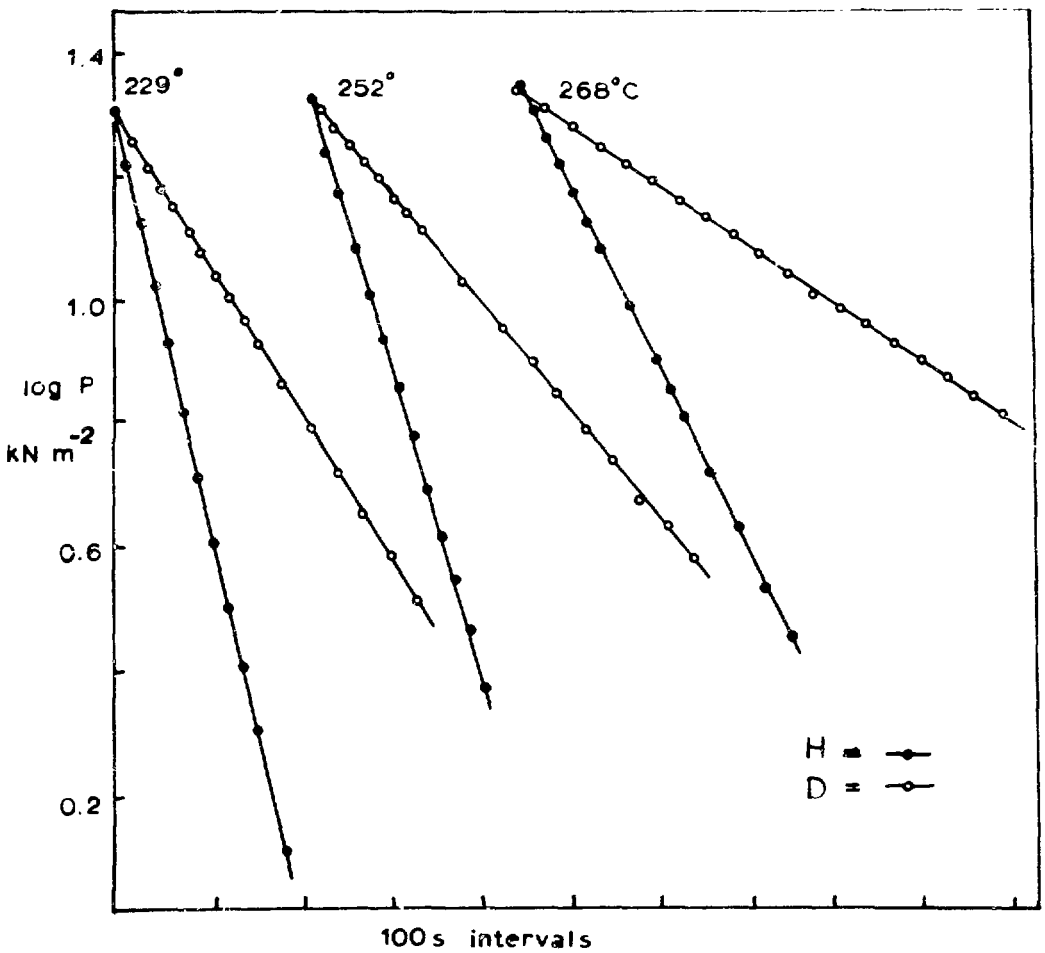

Fig. 2. Pressure changes in the reactions of liquid lithium with hydrogen and deuterium.

according to eq. (2).

$$-dP/dt = k_p P \text{ or } \ln P = -k_p t + \ln P_o \qquad (2)$$

The rate constant, k_p, was derived from the slopes and increased with increasing temperature according to eq. 3 as shown in Fig. 3.

$$k_p = Ae^{-E^{\ddagger}/RT} \text{ or } \ln k_p = \ln A - E^{\ddagger}/RT \qquad (3)$$

The present experiments were inadequate (three) to assess the slope for hydrogen. This was established, therefore, in Fig. 3 from previous data.[2] The apparent activation energy, $E^{\ddagger}$, for the reactions of hydrogen and deuterium as given by the gradients were 52.8 and 55.2 $kJmol^{-1}$, respectively. Hydrogen reacted nearly three times faster than deuterium under identical conditions; the deuterium isotope effect, k_H/k_D, was 2.95, 2.92, 2.88, 2.85 and 2.83 at 250, 240, 250, 260 and 270°C, respectively. More than half of the isotope effect can be accounted for by the difference in $E^{\ddagger}$. The ratio, however, is only half that predicted were the difference in zero point energies of the isotopes solely responsible. Thus eq. (4) gives $k_H/k_D = 5.93$.

$$k_H/k_D = e^{\frac{E_{oD} - E_{oH}}{RT}} \qquad (4)$$

where T = 503K, E_{oH} = 25.9, and E_{oD} = 18.4 kJ.[3] Cases where the isotope effect is less than expected are often attributed to a process in which a new bond is formed simultaneously as the old bond is broken leading to a difference in zero point energy of the activated complex which cancels in part the difference in zero point energy of the reactants.[4] This is shown in Fig. 4. The tritium isotope effect, k_H/k_T, predicted from eq. (4) at 230°C is 13.0. Assuming that this is reduced by half as found for deuterium, k_p values would

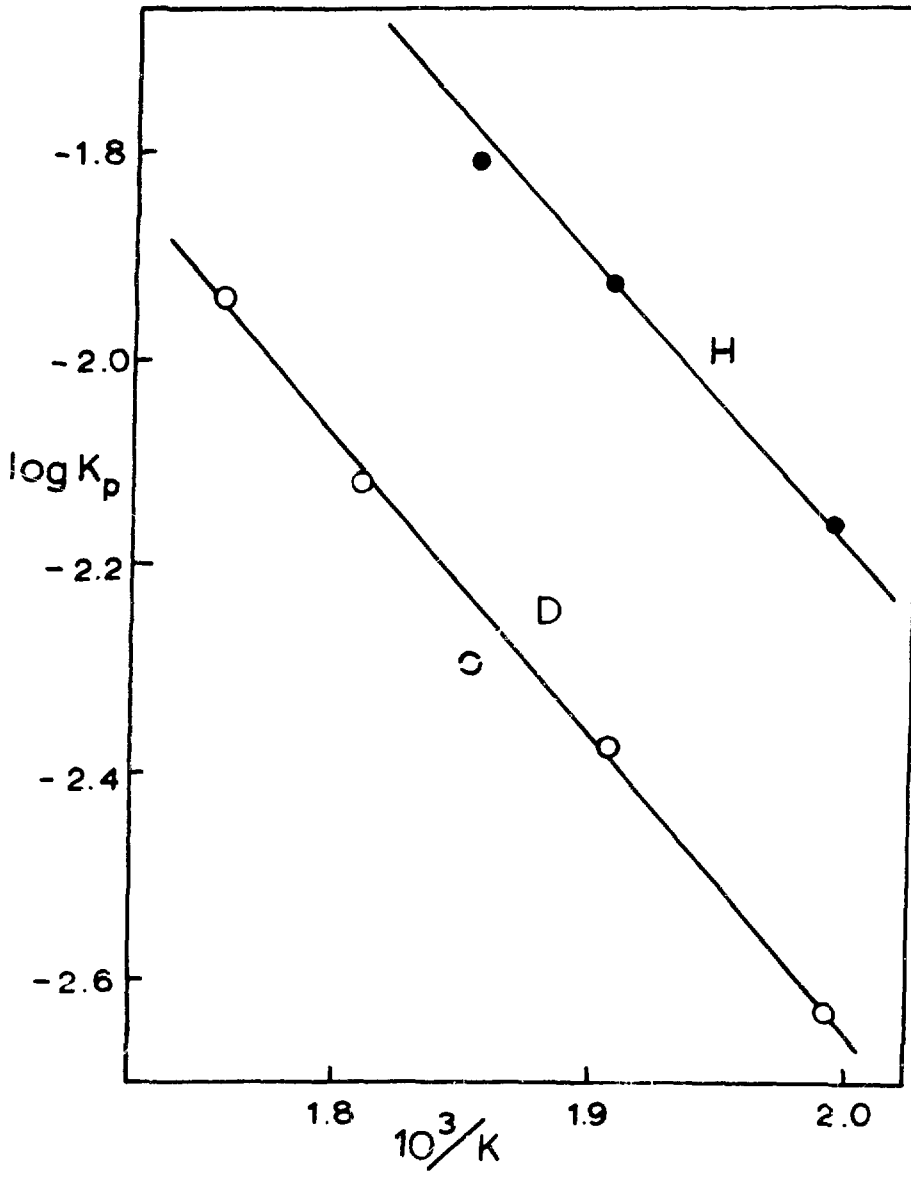

Fig. 3. Effect of temperature on the rates of reaction of hydrogen and deuterium with liquid lithium.

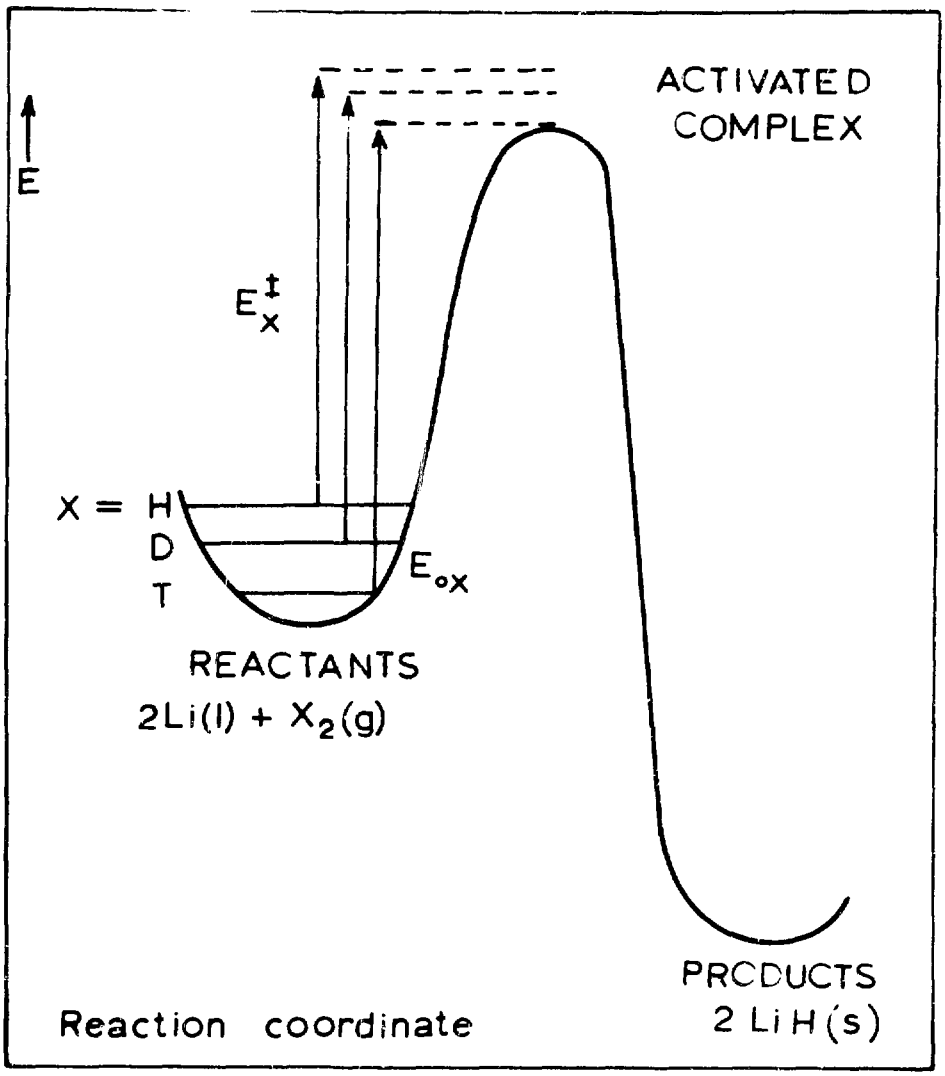

Fig. 4. Potential energy profile for the reaction of the hydrogen isotopes with lithium.

in the ratio 6.5:2.9:1 for the reaction of hydrogen, deuterium and tritium, respectively, with lithium.

DEPRESSION OF FREEZING POINT

The pure metal melted at 180.50°C but this was depressed by 0.08(2) and 0.07(5) by dissolved hydride and deuteride, respectively, as shown in Fig. 5. The hypoeutectic liquidus and eutectic horizontal were derived from three separate experiments with hydrogen and one with deuterium. The eutectic points occurred at 0.016 mol%H and 0.012 mol%D, and the steep hypereutectic liquidus shown is an interpolation between this point and the solubilities determined by resistivity (see later). The hypereutectic liquidus and also the hypoeutectic horizontal could not be detected by thermal analysis. The solid solubility of LiX(X = H or D) in Li was estimated from the ideal solution equation.[5] Following the direction set by these isotopes, we expect tritium to depress the freezing point by ca. 0.07°C, and the solid and liquid solubility of the tritide to be slightly less than for deuterium. The eutectic point is of practical value in connection with purification of the metal by filtration and shows that isotope concentration can not be reduced below that at the respective eutectic by this method. Similarly it follows that isotope enrichment by cooling the hypoeutectic solution should give concentrations no richer than that at the respective eutectic.

RESISTIVITY AND SOLUBILITY

The electrical resistivity of liquid lithium increased linearly with increasing concentration of hydride as shown in the upper part of

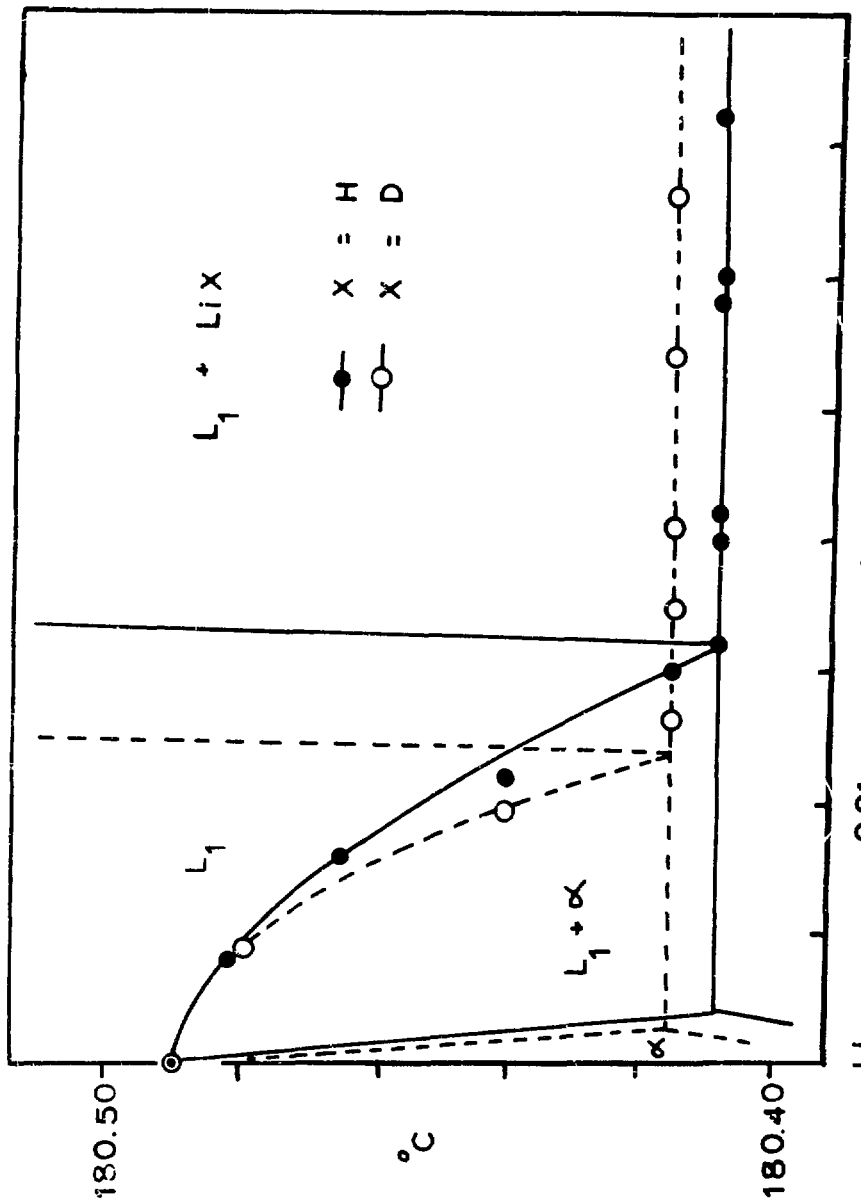

Fig. 5. Partial phase diagram of Li-LiX systems.

Fig. 6 at 411, 499 and 525°C. In each case the resistivity levelled when the solution became saturated. Further hydrogen merely produced increasing amounts of solid hydride. The unit increase in resistivity $\Delta\rho/x$ (x = mol%H) was relatively large, ca. $5X10^{-8}\Omega m\ (mol\%H)^{-1}$, though smaller than for nitrogen, $7X10^{-8}\Omega m(mol\%)^{-1}$.[6] A slight temperature dependence was observed i.e. at 240 and 540°C the values were $4.25X10^{-8}$ and $5.35X10^{-8}\Omega m(mol\%H)^{-1}$, respectively. The technological aspect of these results is that the electrical conductance and hence the thermal conductance of lithium diminishes considerably with increasing hydride concentration; the resistivity, however, constitutes a sensitive method, albeit nonselective, of monitoring the hydride concentration.

Although $\Delta\rho/x$ was virtually the same for hydrogen and deuterium (and presumably for tritium also), the solubility of the isotopes differed. This is shown in the lower part of Fig. 6 where the liquidus (derived from the resistivity changes above) is shown for the Li-LiH and Li-LiD systems. The liquidus rose smoothly from the eutectic point in each case but hydrogen was more soluble than deuterium. In the case of hydrogen, the liquidus extrapolates from 555°C to meet the values of Messer[7] which commence at 624°C. Subsequently a two-liquid region occurs which, at the monotectic temperature 685°C, extends from 19.0 to 49.5 mol%H.[6] The present solubilities are summarised by eq. (5) and eq. (6).

$$\log (mol\%H) = 3.523 - 2308/_T \quad 523 \leq T \leq 775K \qquad (5)$$

$$\log (mol\%D) = 4.321 - 2873/_T \quad 549 \leq T \leq 724K \qquad (6)$$

The solubility of tritium is expected to be slightly less than for deuterium.

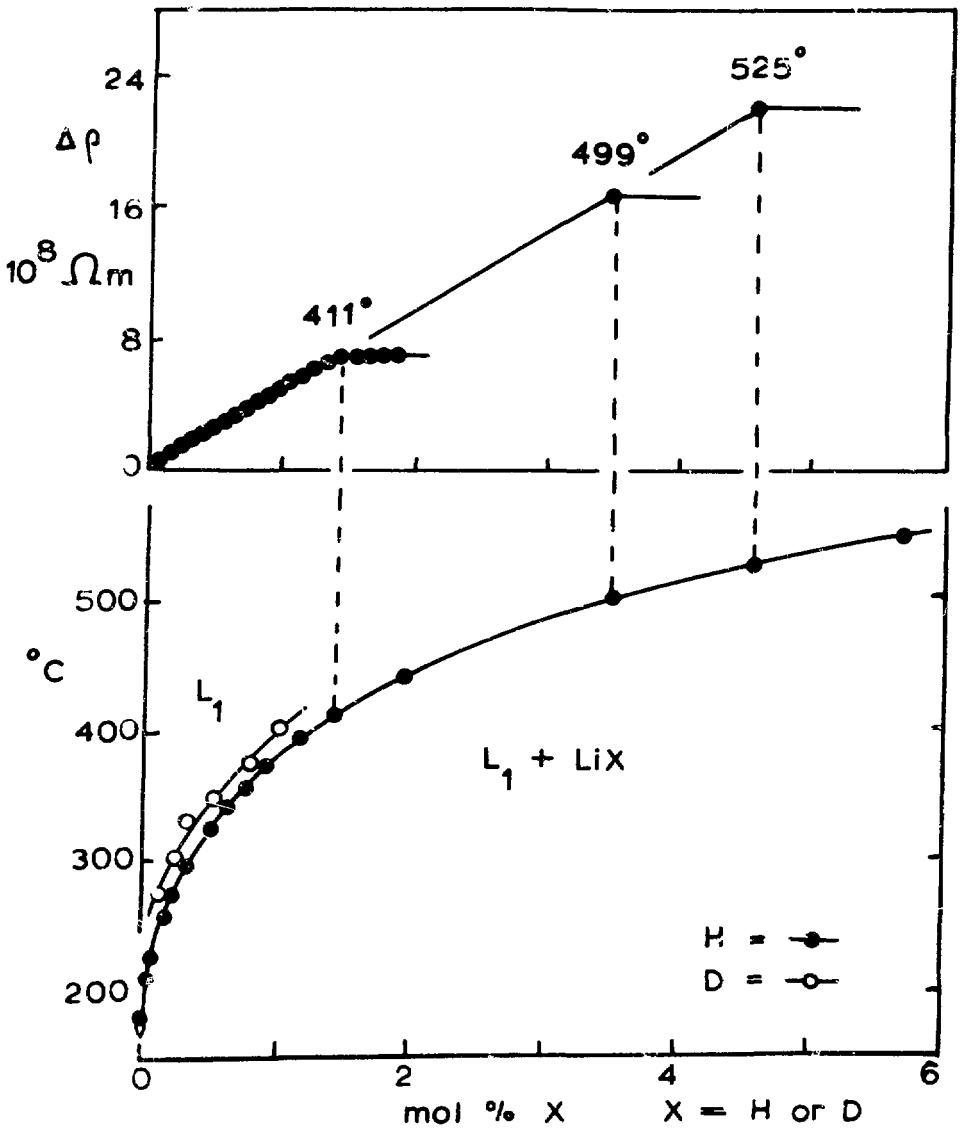

Fig. 6. Resistivity and solubility of LiX in lithium.

SOLVATION ENTHALPY

The solubility provides a value of the partial molar enthalpy of solution, H(soln), of the isotope with respect to the precipitating phase.[6] The solution may be considered to consist of anions, X^-, solvated by cations, in a matrix of cations and free electrons. The relation ship of H(soln) with the other terms in the solution process is then shown by the cycle.

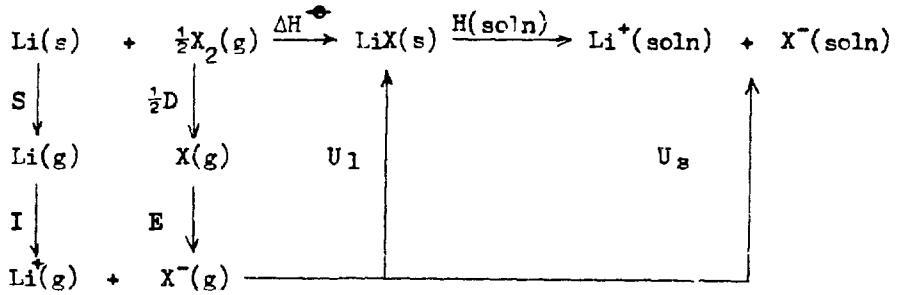

Using this ionic concept, the solvation enthalpy, U_s, for the components of LiX is analogous to the lattice enthalpy, U_l, and H(soln) is generally a small positive difference between these two large negative terms. The overall solution enthalpy change ($\Delta H^{\ominus}$ + H(soln)) is negative and therefore both isotopes dissolve. Similarly for other salts. Values of U_s calculated from the cycle for LiH, LiD, Li_2O and Li_2N are given in the Table.

Table. Solvation enthalpies (kJ mol^{-1}) for solutes in liquid lithium

Solute	H(soln)	U_s	U_x
Deuterium	55.0	-860	-413
Hydrogen	44.2	-874	-427
Oxygen	52.5	-2856	-1991
Nitrogen	39.2	-4817	-3460

The individual solvation enthalpy of the anion, U_X, can be extricated from U_s by the approximation $U_X = U_s + I + S - \phi$ where ϕ is the work function of lithium.[8] Values of U_X so derived are included in the Table. As might be expected, U_X becomes more negative with increasing charge on the anion. The isotope effect suggests that deuterium is less strongly solvated than hydrogen; presumably the solvation enthalpy is even less negative for tritium.

The authors thank the U.K.A.E.A. (Harwell and Culham) and S.R.C. for maintenance grants, (P.F.A.) and (G.P., A.E.T.), respectively.

REFERENCES

1. C. C. Addison, G. K. Creffield, P. Hubberstey and R. J. Pulham, J. Chem. Soc. (A), 1482, (1969).

2. G. Parry and R. J. Pulham, J. C. S. Dalton, in press.

3. J. C. Bailar, H. J. Emeleus, R. Nyholm and A. F. Trotman-Dickenson (ed.) Comprehensive Inorganic Chemistry, p. 97, vol. 1, Pergamon Press, London, 1973.

4. K. B. Wiberg, Chem. Rev. 55, 713, (1955).

5. P. Hubberstey, R. J. Pulham and Anne E. Thunder, J. Chem. Soc. Faraday I, in press.

6. P. F. Adams, M. G. Down, P. Hubberstey and R. J. Pulham, J. Less Common Metals. 42, 325, (1975).

7. C. E. Messer, E. B. Damon, P. C. Maybury, J. Mellor and R. A. Seales, J. Phys. Chem. 62, 220, (1958).

8. R. Thompson, J. Inorg. Nucl. Chem. 34, 2513, (1972).

TECHNIQUES FOR STUDYING HYDROGEN AND HELIUM ISOTOPES IN MATERIALS: ION BACKSCATTERING AND NUCLEAR MICROANALYSIS*

Robert A. Langley

Sandia Laboratories, Albuquerque, New Mexico 87115

ABSTRACT

The techniques of ion backscattering and nuclear microanalysis as tools for studying hydrogen and helium isotopes in solid materials are discussed and compared. The advantages, disadvantages and limitations of each of these techniques are explored. Experimental results obtained using the two techniques are analyzed to obtain information on concentration-versus-depth profiles for these light atoms in heavy atom substrates.

INTRODUCTION

The characterization of solids implanted or diffused with hydrogen and/or helium impurities is of concern to a variety of fields. Light atom impurities do not readily lend themselves to ion backscattering studies of concentration-versus-depth because of their low mass and atomic number. The difficulty of such measurements is aggravated by the fact that the elemental Rutherford cross section varies as the square of the impurity atomic number, and by the low energy of the backscattered ion which often results in superposition of the impurity and substrate spectra. In many cases nuclear reactions exist which overcome these problems and may be used to study various phenomena associated with light atom impurities. Many of the nuclear reactions used in nuclear microanalysis have been summarized and reviewed in previous articles.[1] Of particular interest are the properties of hydrogen isotopes (D and T)

*This work was supported by the United States Energy Research and Development Administration, ERDA.

and the helium isotopes (^{3}He and ^{4}He) in both metals and insulators for fusion technology and other studies.

In this paper the use of nuclear reactions to study D and ^{3}He in solid materials and the use of ion backscattering to study D, T, ^{3}He and ^{4}He will be discussed. These two techniques will be described in detail, and the advantages, disadvantages and limitations of each will be explained. Experiments which have been performed to date will also be reviewed.

NUCLEAR MICROANALYSIS

Nuclear reactions may be used to determine deuterium and ^{3}He concentration-versus-depth profiles in the near-surface region of solids. Pronko and Pronko[2] explored the use of D[^{3}He,p]^{4}He reaction for deuterium and ^{3}He profiling. The cross section for this reaction[3] is shown in Fig. 1. They detect the total reaction yield as the peak in the reaction cross section is swept through the depth of the sample by varying the incident beam energy. They suggest ~ 3000 Å as the ultimate resolution of this method for profiling ^{3}He, and ~ 600 Å as resolution in

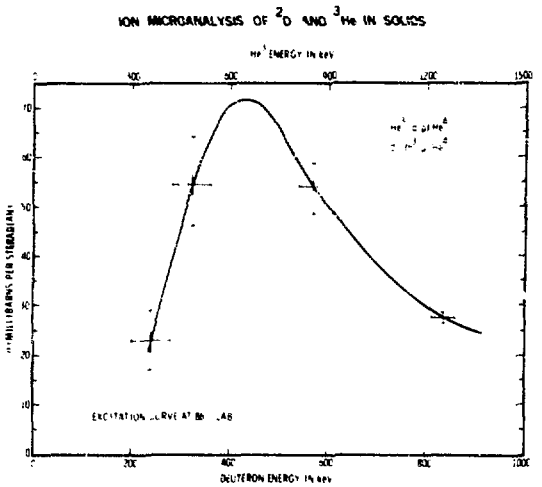

Fig. 1. Cross section vs energy for the reaction ^{3}He(d,p)^{4}He taken from Ref. 3 with representative error bars indicated.

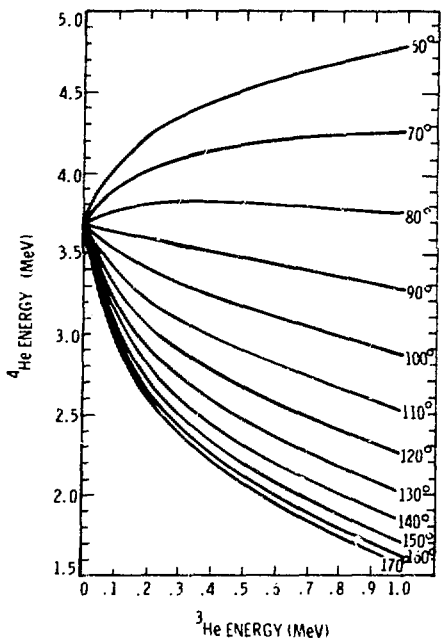

Fig. 2. Emitted ^{4}He energy vs incident ^{3}He energy at various laboratory emission angles for the reaction ^{3}He(d,p)^{4}He.

experimental geometry for a particular measurement one must consider angle of beam incidence and angle of observation relative to the target surface, incident ion energy, probing depth desired, and depth resolution desired. A tradeoff must be made between depth resolution and probing depth, i.e., increased depth resolution requires large energy loss/unit depth while increased probing depth requires small energy loss/unit depth. Better depth resolution is obtained at the forward scattering angles, but at these angles one must decrease the counting rate to avoid pulse pileup from Rutherford scattering of the incident beam into the detector. For backward detection geometries the depth resolution is decreased, but the data may be accumulated at a much higher rate. The angular acceptance of the detector also determines to a certain extent the energy resolution (and therefore the depth resolution of the system. For a silicon surface barrier detector of $\sim$ 10 keV resolution angular acceptance must be of the order of $\frac{1}{4}°$ at forward scattering angles, while in the backward directions it may increased considerably without loss of depth resolution.

In general, nuclear reaction cross sections are smaller than Rutherford scattering cross sections so that a considerable fluence of the probing beam may be implanted during the analysis, particularly if many spectra are taken at the same target spot. This may affect the results of the experiments, e.g., blistering and exfoliation.

This technique was applied to multilayer deuterided films to test its depth resolving capability. Samples consisted of a molybdenum substrate with an erbium deuteride film of thickness 0.411×10^{18} molecules/cm^2 ($\sim$ 1400 Å) overlaid with a chromium film of 1.49×10^{18} atoms/cm^2 ($\sim$ 1400 Å) overlaid with an additional erbium deuteride film of 0.312×10^{18} molecules/cm^2 ($\sim$ 1000 Å). Figure 3 shows a spectrum taken for this sample for normal ^{3}He incidence and an observation angle of 170°. The ^{3}He backscattering spectrum is shown at energies less than 800 keV and the layer thicknesses can be determined from this portion of the spectrum. The position of backscattered ^{3}He ions from surface Er is indicated by a vertical bar and the Cr and Mo edges are evident at lower energies. Above 1.7 MeV is shown the ^{4}He spectrum clearly indicating the double-peaked deuterium distribution arising from the two ErD_2 layers. The

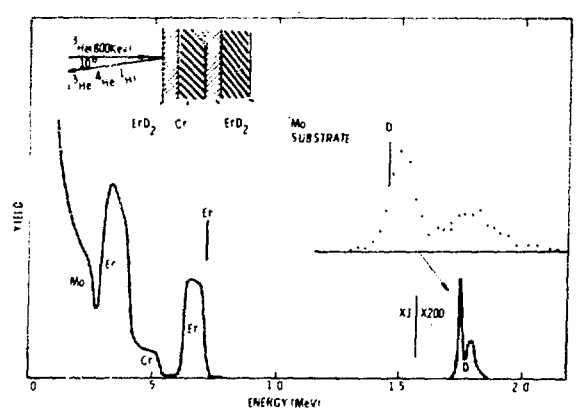

Fig. 3. Backscattering and nuclear reaction yields for 800 keV ^{3}He beam incident on multilayered ErD_2 target. Observation angle is 170°. The target is composed of a Mo substrate overlaid with 0.411×10^{18} ErD_2 molecules/cm^2, overlaid with 1.49×10^{18} Cr atoms/cm^2, overlaid with 0.312×10^{18} ErD_2 molecules/cm^2.

energy of the ^{4}He particles coming from the surface is indicated by a vertical bar on the inset spectrum. The ^{4}He particles coming from below the surface have higher energy due to the kinetics of the reaction (see Fig. 2). The smaller of the two peaks corresponds to ^{4}He coming from the deeper erbium deuteride layer.

A spectrum from the same sample utilizing a forward angle geometry is shown in Fig. 4. The angle of incidence to the surface was 20° and the ^{4}He emission angle with respect to the incident directions was 70°. The incident energy was 1.2 MeV and the backscattered ^{3}He spectrum is shown below this energy. Due to the scattering geometry the two erbium deuteride layers are not resolved in the ^{3}He part of the spectrum. The ^{4}He spectrum is shown around 4 MeV. Again a double peak corresponding to the deuterium in the two layers is resolved. In this case the energy of the ^{4}He decreases as the ^{3}He penetrates further into the sample so that lower energies correspond to deeper depths. The resolution obtained is far from minimum because of the lack of angular resolution ($\sim \frac{1}{2}°$) in the detection system..

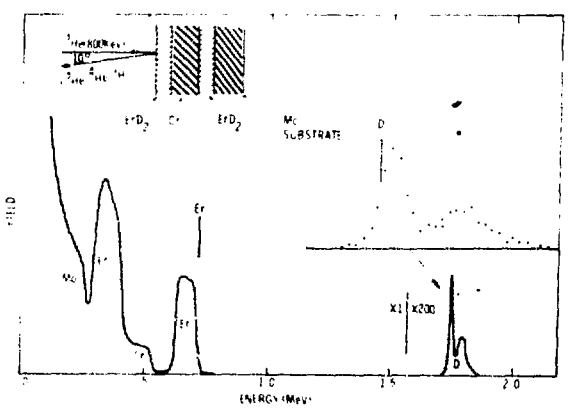

Fig. 4. Backscattering and nuclear reaction yields for 1.2 MeV ^{3}He beam incident on same target as in Fig. 3. Observation angle is 70°.

For films which are thick (> 1μm) the profile of deuterium concentration versus depth can be obtained by taking spectra at successively higher ^{3}He energies. The profiling region is that where the ^{3}He beam is slowed down to the vicinity of the maximum of the cross section. Probing depths and achievable depth resolutions in erbium are indicated in Table 1. This table gives calculated results for the depth at which the peak of the cross section ~ 600 keV is reached in erbium as a function of incident ^{3}He energy and the limitation on the depth resolution due to straggling of the beam.[4]

An analytical technique to reduce yield-versus-energy spectra to an impurity-concentration vs depth has been developed and applies to both elastic and inelastic reactions.[5] Using it, the depth distribution profiles are obtained directly from the observed data. This analytical technique will be discussed more fully later.

TABLE 1

^{3}He Initial Energy (MeV)	Mean Depth to reach 600 keV (Å)	Spread in Depth (Å)
1.6	26,000	1166
1.4	20,350	920
1.2	14,950	658
1.0	9,600	405
0.8	4,850	173

ION BACKSCATTERING

Recently the use of ion backscattering to observe deuterium and helium in thin films on thick substrates has been successfully accomplished.[5] Using the technique described in Ref. 5, the elastic scattering cross section for protons on deuterium at 170° (lab) was measured. The elastic scattering cross section was found to be approximately 140 times greater than the Rutherford cross section at 2 MeV and approximately 200 times greater at 3.6 MeV with enhancement increasing linearly with energy. In addition it was found that for protons incident on ^{4}He the elastic cross section is increased over the Rutherford cross section by a factor of approximately 400 at 2.6 MeV. Previously ion backscattering has been used to observe deuterium and helium in thin free-standing films.[7] The remainder of this section contains a discussion of the sensitivity of the experimental setup to proton backscattering from ^{1}H, ^{2}H, ^{3}He and ^{4}He; results of a measurement of the elastic scattering cross section for ^{2}H(p,p)^{2}H; and a demonstration of the technique on specially-prepared films.

In order to be able to optimize depth resolution and sensitivity, the target chamber must allow variation of certain parameters. These variables include the angle of incidence of the ion beam on the sample and the scattering angle. By increasing the angle of incidence with respect to the normal of the target surface, it is possible to increase both depth resolution and sensitivity but multiple scattering and straggling will limit the resolution for too small an angle.[6] Scattering angles between 150° and 175° are generally desirable. As the scattering cross section depends strongly on scattering angle in this region (generally increasing with increasing angle) precise measurement of the scattering angle is required for absolute measurement of the impurity concentration. Elastic scattering cross sections of interest have not been previously measured at the larger scattering angles needed for the sensitivity and depth resolution required for most experiments.

Figure 5 shows the elastic scattering cross section for protons on deuterium from 2.0 to 2.8 MeV at a center-of-mass scattering angle of 165°.[6] The cross section is rather large and decreases linearly with increasing energy. The enhancement (elastic cross section/Rutherford

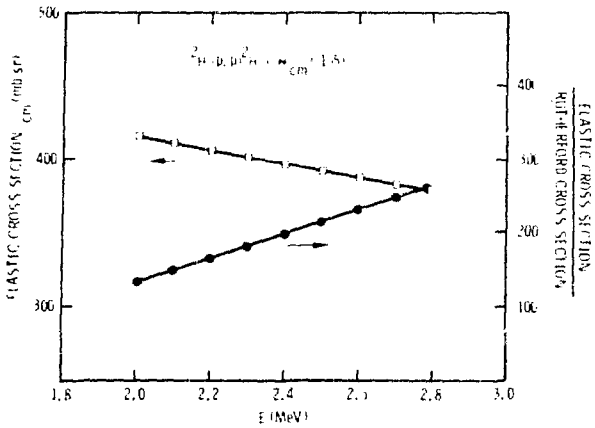

Fig. 5. Experimental elastic scattering cross section and cross section enhancement for D[p,p]D; θ_{cm} = 165°.

cross section) increases with increasing energy. Figure 6 shows the same information for protons elastically scattered from tritium at a center-of-mass scattering angle of 168.7°.[9] The energy range covered is .75 to 3.5 MeV. The elastic cross section decreases monotonically with increasing energy and again the enhancement increases almost linearly with increasing energy. The results for scattering of protons from ^{3}He at a center-of-mass scattering angle of 166° are shown in Fig. 7.[10] The elastic scattering cross section has a broad peak with the maximum at about 3.75 MeV. The enhancement monotonically increases with increasing energy. Figure 8 shows the results for protons on ^{4}He at a center-of-mass scattering angle of 168°.[11] The scattering cross section has a broad maximum with its center at about 2.4 MeV. The enhancement increases monotonically to 3.27 MeV and thereafter decreases slowly with increasing energy.

For comparison, sensitivity vs energy is shown in Fig. 9 for these four light atom impurities in an erbium host for a lab scattering angle of 160°. Sensitivity is defined here as the ratio of the backscattered

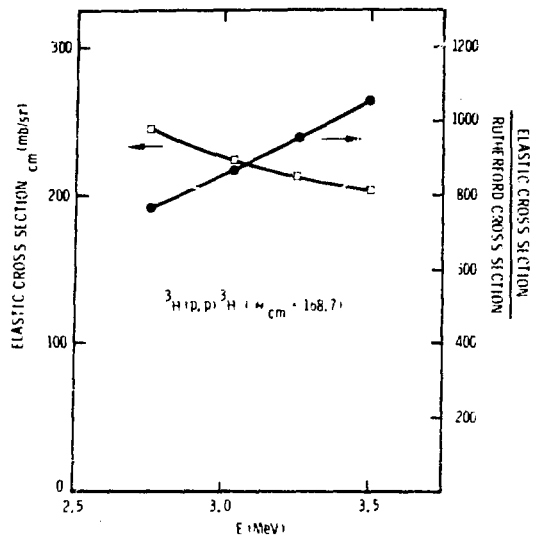

Fig. 6. Experimental elastic scattering cross section and cross section enhancement for T[p,p]T; θ_{cm} = 168.7°.

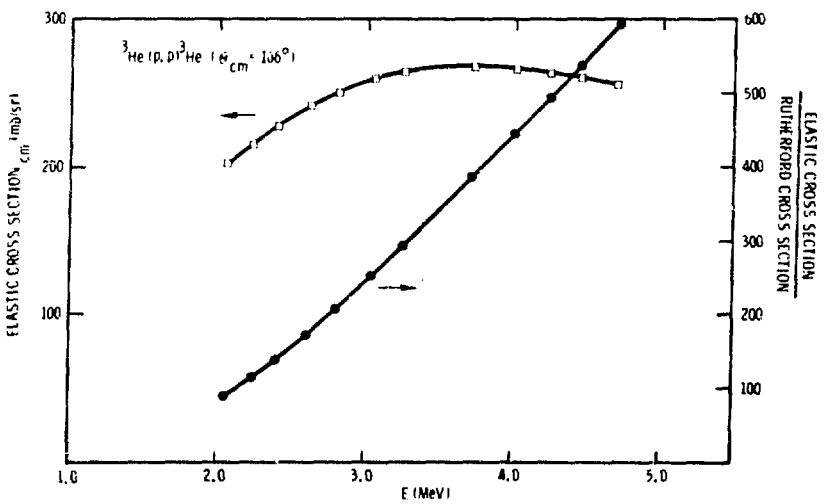

Fig. 7. Experimental elastic scattering cross section and cross section enhancement for ^{3}He[p,p]^{3}He; θ_{cm} = 166°.

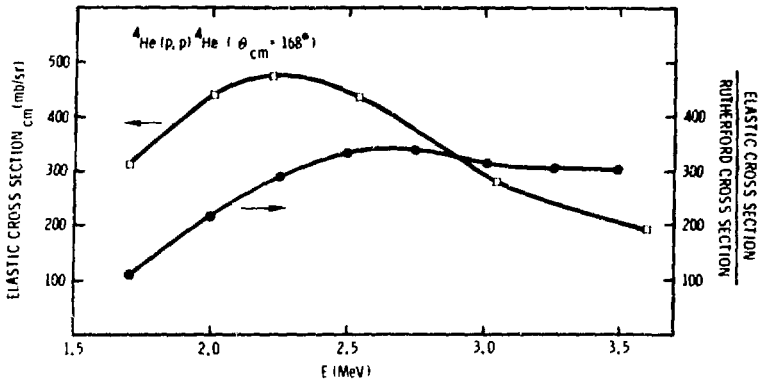

Fig. 8. Experimental elastic scattering cross section and cross section enhancement for ^{4}He[p,p]^{3}He; θ_{cm} = 168°.

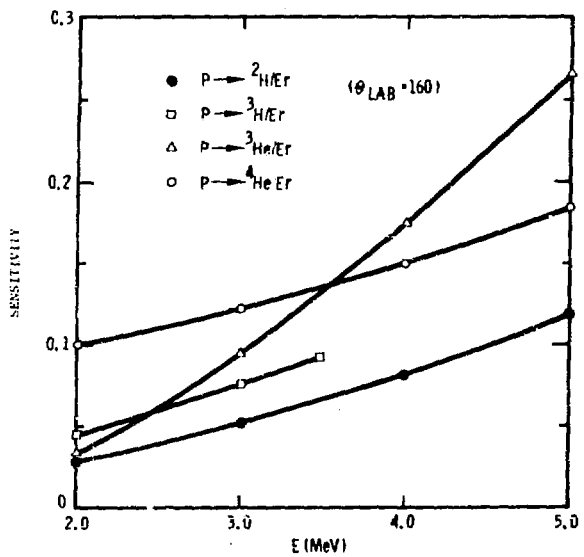

Fig. 9. Sensitivity for proton elastic backscattering from ^{2}H, ^{3}H, ^{3}He and ^{4}He at θ_{lab} = 160°. See text for definition of sensitivity.

proton yield from the low mass constituent to that from the heavier host material which would be observed in the region of the spectrum of proton backscattering from the low mass constituent in a target with atomic concentration ratio of 1:1 for the two species. This quantity is thus related to directly observable results in an ion backscattering experiment, and determines the sensitivity for detection of the low-mass constituents. Figure 9 shows that the sensitivity increases monotonically with increasing energy. The curves have essentially the same slope for deuterium, tritium and ^{4}He, but for ^{3}He the sensitivity increases much faster with increasing energy than the others. Depth resolution is increased as the incident particle energy is decreased since the stopping cross sections (which determine the depth resolution) increase with decreasing energy. Therefore a tradeoff must be made between sensitivity and depth resolution. One inherent problem with this technique is that the energy of protons backscattered from tritium and ^{3}He is essentially the same since their masses are nearly the same. Wherever there is tritium there is also ^{3}He due to the radioactive decay of the tritium. Sensitivity for the two appears to be about the same between 2-3 MeV, but the sensitivity for ^{3}He is increasing at a much more rapid rate than for the tritium at energies above 3 MeV. In general the sensitivity does not vary much for different substrates, but increases slightly with increasing scattering angle.

Backscattering has been used to measure the elastic scattering cross section for protons on deuterium.[6] Erbium deuteride films of thicknesses ~ 8000 Å were prepared by deposition of erbium on various substrates. After deposition films were in situ hydrated by exposing them to a deuterium atmosphere of 5 Torr To terminate the hydration procedure the chamber was pumped free of deuterium before the substrate temperature was returned to room temperature. This procedure precludes formation of erbium trideuteride. A typical backscattering spectrum is shown in Fig. 10. The elastic scattering cross section was determined by measuring the area under the deuterium peak and the area under the erbium peak, assuming that elastic scattering of protons from erbium is Rutherford, and independently measuring the loading ratio. Loading ratio is defined

as the atomic ratio of deuterium content to erbium content in the target, i.e., [D]/[Er].

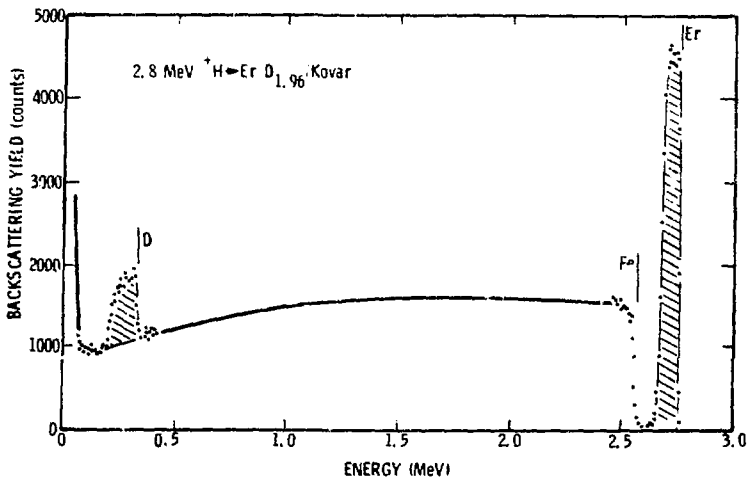

Fig. 10. Energy spectrum of 2.8 MeV protons backscattered from a vacuum-deposited Er film about 8000 Å thick. The Er film was deuterided to [D]/[Er] = 1.96. The energy edges for Er, Fe and D are indicated.

Rutherford scattering is considered valid for $\alpha \gg 1$, where $\alpha = 2Zz/137\ 8$.[12] For protons incident on erbium between 2.0 and 2.8 MeV $\alpha \simeq 14$ while for protons incident on deuterium in the same energy range $\alpha \simeq 0.4$, so that one can legitimately assume that the elastic scattering cross sections for protons from erbium is Rutherford, but not from deuterium. In determining the cross section it was necessary to account for the difference in the solid angles subtended in the center-of-mass system by the solid state detector for protons scattered from erbium and deuterium. The results for the elastic scattering cross section and the enhancement are shown in Fig. 5. The error associated with this measurement is ± 2% for the cross section and < 0.5% for the energy.

The technique was also demonstrated on specially-prepared multi-layered deuteride films. These are the same substrates which were described for use in the nuclear reaction measurements. The spectrum

for 2.8 MeV protons backscattered from this multilayered film is shown in Fig. 11. At energies around 2.6 MeV the two Er peaks are seen to be not completely resolved. The Mo substrate edge appears at 2.55 MeV with the Cr edge around 2.5 MeV. The well-separated deuterium peaks are seen near 0.3 MeV. The depth resolution for this particular spectrum was about 600 Å in the region of the deuterium peaks. If one cools the detector the resolution could be decreased to about 400 Å. It is noted from the spectrum that the depth resolution for D is improved over that for Er because of differences in the stopping cross section for protons after scattering from the two film components. This is because the stopping cross section is increasing with decreasing energy in this energy range and those protons backscattered from deuterium have energies much less than those backscattered from erbium.

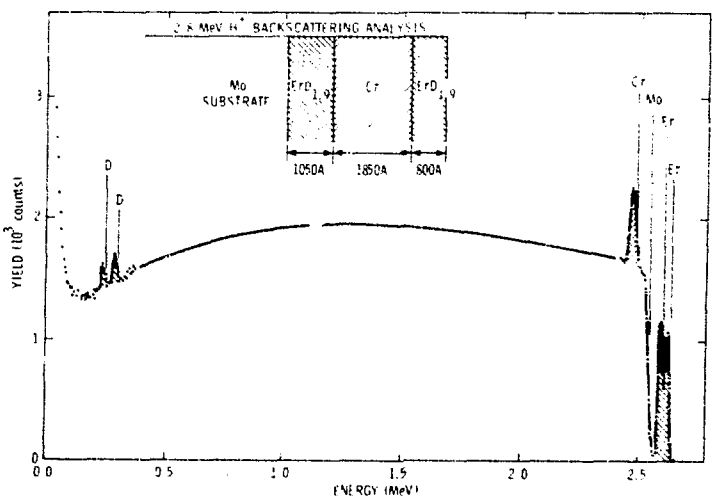

Fig. 11. Energy spectrum for 2.8 MeV protons on a multilayered deuterided film. The energy edges are identified.

An implantation of 2×10^{17} He atoms/cm^2 was made in an erbium dideuteride film on a kovar substrate at an energy of 50 keV. One can easily detect the implanted helium as is shown in the spectrum in Fig. 12. The mean projected range of the helium is 1500 Å. From spectra of this type the enhancement factor can be estimated.[6] However, since it is difficult to accurately measure the amount of implanted helium and its uniformity in the substrate, a precise value of the elastic scattering cross section enhancement over Rutherford cannot be obtained.

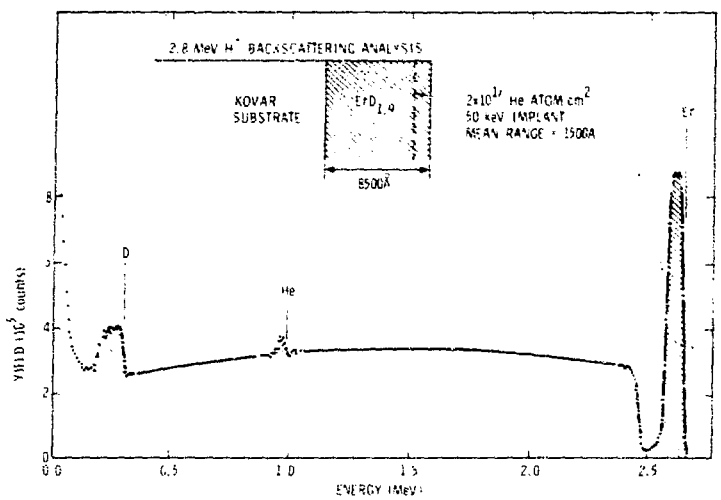

Fig. 12. Energy spectrum for 2.8 MeV protons on an ^{4}He implanted deuteride film.

ANALYSIS TECHNIQUE

The analytical technique used to reduce yield vs energy spectra to impurity concentration vs depth is described in detail elsewhere.[5] Previous techniques for data reduction have consisted of calculating an expected spectra from an assumed distribution and comparing that with the observed distribution,[13] or by a direct mathematical approach in which a reference spectrum and the spectrum to be analyzed are compared to give a concentration vs. depth.[14] This latter calculational method has only been implemented for elastic collisions and requires a reference spectrum. The present technique avoids these limitations.

The only experimental parameter which remains the same throughout a spectrum is the energy per channel. As the stopping cross sections for both the incoming and outgoing particles are functions of energy, the thickness layer associated with each energy channel will change accordingly and is defined as a depth channel. An iterative procedure was used to derive a general formula for the yield for scattering within the nth depth channel. A complete description and derivation of this formula is given in Ref. 5. Concentration vs depth of D atoms calculated by this technique are given in Fig. 13 for the spectra shown in Fig. 10. It should be pointed out that the analytical technique is not limited to elastic scattering, but may be used with nuclear microanalysis measurements involving inelastic scattering and nuclear reactions. The analysis does not account for straggling effects or multiple scattering effects.

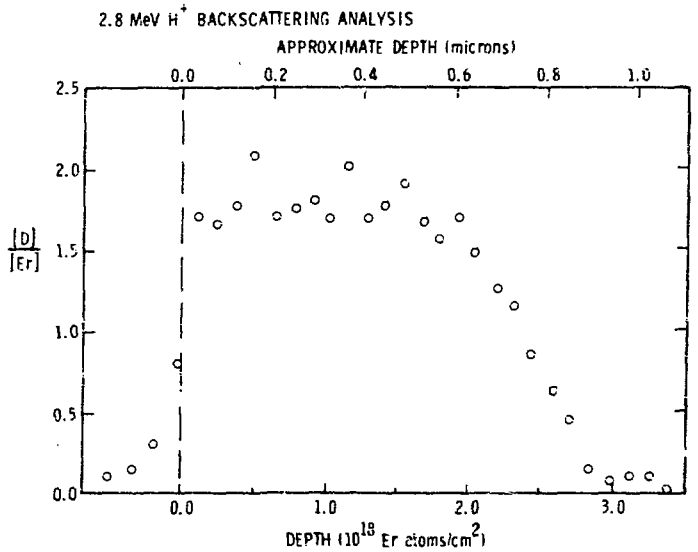

Fig. 13. D concentration vs depth for the spectrum of Fig. 11. These data are obtained by the calculational method explained in the text.

CONCLUSION

It has been demonstrated that deuterium profiles in thin film layers on thick targets can be measured using nuclear reactions and that deuterium and He profiles can be measured using elastic backscattering of protons. The two techniques have been compared and it was shown that the expected depth resolution for nuclear microanalysis is better than that for the backscattering technique. However, data collection may be made in a much shorter time using the backscattering technique.

ACKNOWLEDGMENT

I would like to thank Len Provo for the preparation of the erbium deuteride films used in the cross section measurements and the analytical measurements made on them, and to Dave Brice for a critical review of the paper.

REFERENCES

1. See, for example: G. Amsel, J. P. Nadai, E. D'Artemare, D. David, E. Girad and J. Moulin, Nucl. Instrum. Meth. 92, 481 (1971); E. A. Wolicki, "Material Analysis by Means of Nuclear Reactions," New Uses of Ion Accelerators (Plenum Press, NY, 1975), p. 159-228.

2. P. P. Pronko and J. G. Pronko, Phys. Rev. B9, 2670 (1974).

3. J. L. Yarnell, R. H. Lonberg, and W. R. Stratton, Phys. Rev. 90, 292 (1953).

4. R. A. Langley, S. T. Picraux and F. L. Vook, J. Nucl. Mater. 53, 257 (1974).

5. R. A. Langley, Sandia Laboratories Report SAND75-0331, 1975.

6. R. A. Langley, to be published in Proc. of International Conf. on Ion Beam Surface Layer Analysis, Karlsruhe, Germany, 1975.

7. Free-standing thin films were first used to observe implanted helium by proton backscattering by L. R. Mervine, R. C. Der, E. J. Portner, T. M. Kavanagh and J. M. Khan, Lawrence Livermore Laboratories Report #UCRL-73057 (1971), with further development by M. G. Blewer, Appl. Phys. Lett. 23, 593 (1973).

8. J. S. Williams, Nucl. Instr. Meth. 126, 205 (1975).

9. [illegible] Jaeger, [illegible] Brown, [illegible] Freier and W. [illegible] Stratton, Phys. Rev. [illegible], [illegible] (1951).

10. T. A. Tombrello, [illegible] M. Jones, [illegible] Phillips and J. L. Weil, Nucl. Phys. 39, 541 (1962).

11. G. Freier, E. Lampi, W. Sleator and J. H. Williams, Phys. Rev. 75, 1345 (1949).

12. R. D. Evans, The Atomic Nucleus (McGraw-Hill Book Company, Inc., New York, 1955), p. 671.

13. See for example A. Turos, L. Wielunski and A. Barcz, Nucl. Instrum. Meth. 111, 605 (1973).

14. J. K. Price, Sandia Laboratories Report SLA 73-0843 (1973).

HYDROGEN ISOTOPE PERMEATION IN ELASTOMERIC MATERIALS

R. H. Steinmeyer
J. D. Braun

Monsanto Research Corporation, Mound Laboratory

ABSTRACT

The permeabilities of elastomeric and polymeric materials to hydrogen isotopes were measured at room temperature. The technique for measuring permeation rates is based on the following constant-volume method: a fixed pressure of gas is applied to one side of the specimen to be studied and the permeability constant is determined from the observed rate of pressure increase in an initially evacuated volume on the other side of the specimen. Permeability constants for hydrogen, deuterium, and tritium were measured for Mylar, Teflon, Kapton, Saran, Buna-N, and latex rubber. Results were compared with literature values for hydrogen and deuterium where available and showed excellent agreement.

Application of existing tritium technology to fusion reactors requires careful evaluation of a variety of materials commonly used in containment systems with respect to tritium permeation and stability in a radiation environment. One class of materials of great importance in the fabrication and assembly of any tritium containment system is elastomers. There are many types required in assembling even simple systems: for example glovebox gauntlets of various types of rubber, gasket materials of a variety of elastomeric materials, sealing tapes of Teflon, plastic films for trash storage, and plastic tents required for maintenance. Figure 1 shows a typical inert-atmosphere glovebox system in a laboratory where the effects of tritium on mechanical properties of materials are measured. The extensive use of elastomers is evident in this photograph.

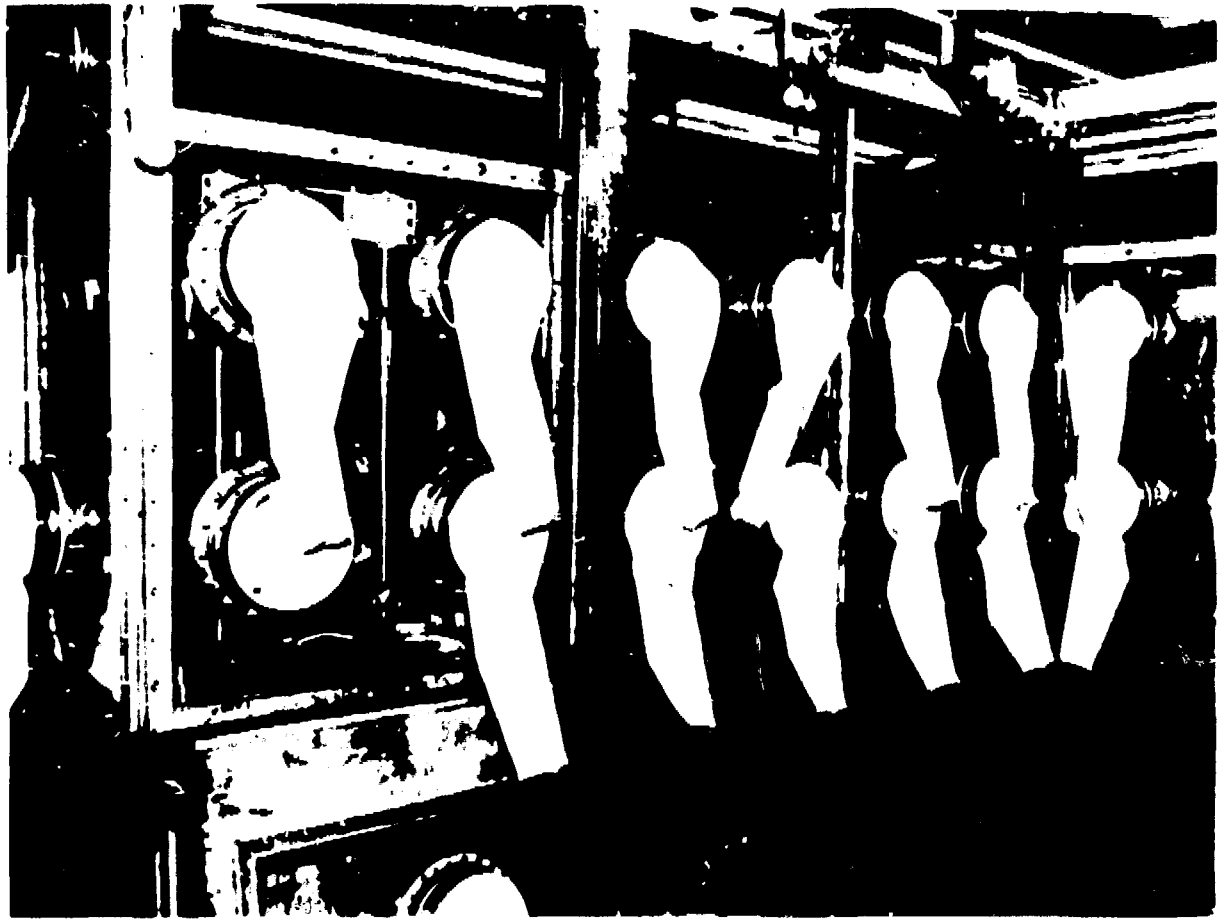

Fig. 1. Photograph of Typical Glovebox System Showing Extensive Use of Elastomeric Materials.

Information in the literature on the permeation of hydrogen isotopes through this class of materials is widely scattered and generally reported for hydrogen only. More information is available for deuterium; however, information on tritium is necessary both for design applications (choosing the proper material for each system application) and also for evaluation of effects of radiation or exchange reactions on the materials. For these reasons we have initiated a study of hydrogen isotope permeation in common elastomeric materials.

The initial experimental work was conducted with hydrogen and deuterium for design of the apparatus and evaluation of the experimental techniques. The majority of our current work is now devoted to the measurement of tritium permeation through these materials and evaluation of the effects of tritium on the properties of these materials. As designs for specific systems related to fusion technology are completed, additional materials will be studied to provide the necessary data for choosing materials of fabrication.

The process of permeation in elastomers generally is one of solution of the gas molecules on one surface of the material, followed by diffusion through the elastomer to the other side where the gas evaporates. The quantity of dissolved gas in the elastomer is proportional to the pressure, following Henry's law ($S = kp$), while Fick's law, $\frac{dc}{dt} = D\frac{d^2c}{dx^2}$, applied to the actual process of diffusion. On this assumption the quantity of permeating gas, q, is determined by $q = DhA[(p_1-p_2)/d]t$ where

D = diffusivity,
h = solubility,
A = area of the membrane,
d = thickness of the membrane,
p_1 and p_2 = pressures on both sides of the membrane, and
t = time.

If unit values are taken for the difference in p_1-p_2, area A, thickness d, and time t, then $Q = Dh$, where Q stands for the permeability.

The technique used for measuring permeation in this experimental work was based on the constant-volume method. In this method a fixed pressure of gas is applied to one side of the specimen to be studied, and the increase in pressure from the permeation of the gas into an initially evacuated chamber, separated from the fixed pressure side by the specimen, is measured. The permeability constant Q can then be determined from the observed rate of pressure increase and other parameters related to the permeability apparatus and the specimen according to the following relationship:

$$Q = \frac{(\Delta p)(V)(d)(273)}{(\Delta t)(p)(A)(T)}$$

where

Δp = pressure increase,
Δt = time interval of measurement,
p = fixed gas pressure applied to one side of specimen,
V = volume of initially evacuated chamber,
d = thickness of specimen,
A = exposed area of specimen, and
T = average temperature of the volume.

The apparatus used to determine Q is similar in principle to that used by several previous investigators such as van Amerongen[1] and consists of the following major components: (1) a permeation cell, (2) a manifold to supply gas and vacuum service, and (3) a pressure sensor to measure pressure change. The permeability cell (Figure 2) was a high-pressure membrane filter holder (Millipore Filter Corp.). The specimen to be studied, consisting of a thin disc cut to fit the cell, was mounted so that a seal was formed separating the apparatus into two chambers. The chamber volumes were calibrated by PVT determinations.

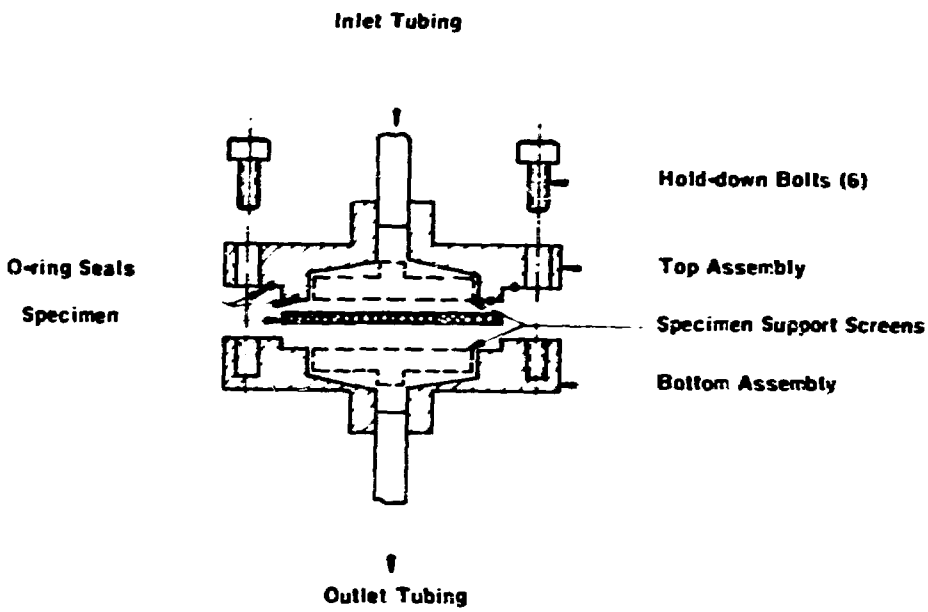

Fig. 2 Permeation Cell.

Figure 3 shows the complete permeability apparatus located within an inert-atmosphere glovebox line, and Figure 4 shows a schematic drawing of the apparatus. A permeation experiment was conducted by initially evacuating both sections of the apparatus, isolating the sections from each other and the pumping system, and introducing the hydrogen isotope into the largest volume which is the fixed pressure side (Volume A), usually at 1 atm. The elastomer specimen was supported in the cell on a screen to prevent rupture due to the pressure differential between the two volumes. The increase in pressure in the smaller volume (Volume B) was measured as a function of time.

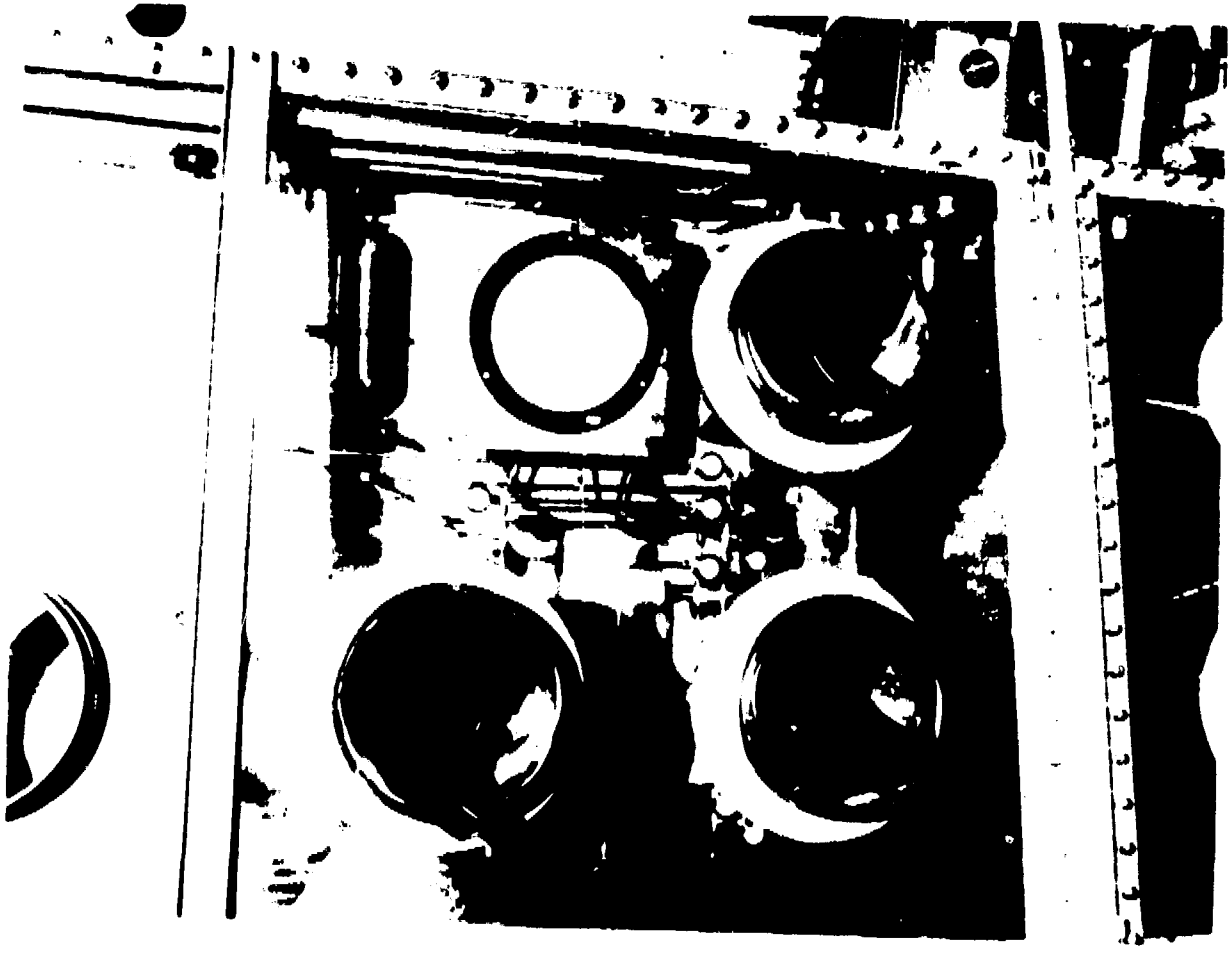

Fig. 1. Permeability Apparatus Located Within the Inert Atmosphere Glovebox Line.

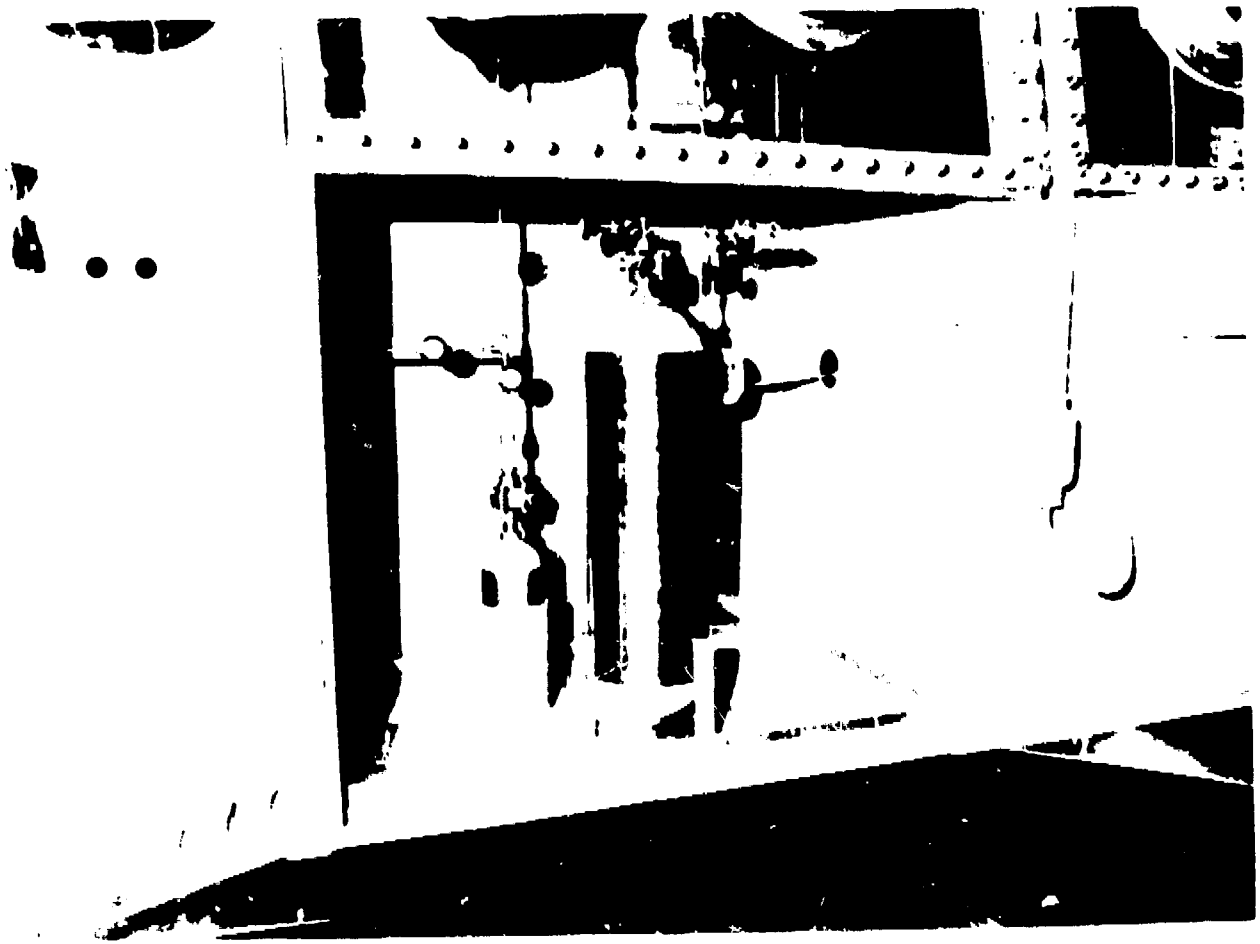

Fig. 2. Permeability Apparatus Located Within the Inert Atmosphere Glovebox Line.

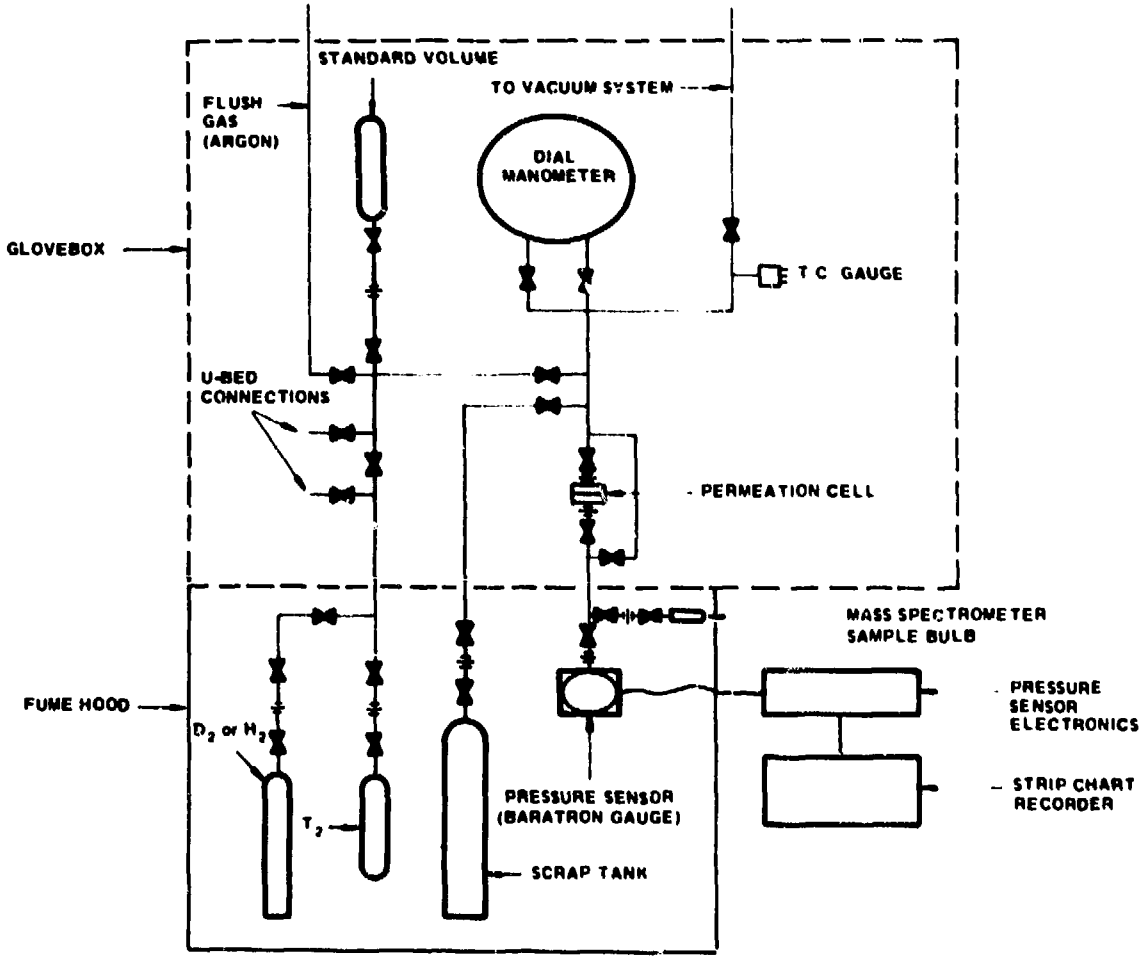

Fig. 4. Schematic Drawing of Permeation Apparatus.

A capacitance manometer (Baratron Instrument Corp.) was used to detect the pressure increase in the smaller volume (Volume B). The pressure was continuously plotted on a strip chart recorder providing a permanent record of pressure-time data and permitting immediate determination of steady-state permeation. The permeation apparatus was constructed so that the ratio between Volume A and Volume B was large enough to prevent a significant pressure drop in Volume A during the course of a permeation determination. Temperature during the experiments was ambient, averaging 24.8°C ± 1°C. The accuracies in determining the volumes of the permeation apparatus and the pressure in the smaller volume (Volume B) were ± .4 and ± 0.15% respectively. The specimen thickness was determined by checking several locations with a caliper micrometer. An average of these determinations was then computed. In general, the variation in measurements on a given specimen was 8-10% because of irregularities in the material as well as its resiliency. This measurement, being the least accurate, limited the overall accuracy of the experimental determinations.

The hydrogen isotope permeabilities of a number of readily available elastomeric and polymeric materials were measured and compared with values obtained from literature sources (where available). These experimental results and the literature comparisons are shown in Table 1. The agreement was good in most cases. The largest deviation occurred for very thin specimens where inaccuracies in thickness measurements or uncertainties as to the exact nature of the particular specimen was greatest. The permeation ratios of H/D/T as shown in the table do not follow the ratio of the square root of the mass as many isotope-effect results on other diffusion studies have. In the case of elastomers, the size of the molecules may have more significance in explaining the permeation ratios. In any case this points up the

Table 1. Permeability Constants of Water for Various Thermoplastic and Elastomeric Materials

Material	Thickness, cm	Test Temperature	Permeability Constant, g cm/cm² sec mm Hg Measured Value	Literature Value
Latex (natural rubber)	[illegible]	H	[illegible]	[illegible][b]
Latex	0.218	T	[illegible]	
	0.023	T	2.58×10^{-5}	
Buna-N (nitrite butadiene rubber)	0.025	D	1.6×10^{-5}	0.27×10^{-5}[c]
	0.032	T	4.4×10^{-5}	
Mylar (polyethylene teraphthalate)	0.005	H	3.5×10^{-5}	4.4×10^{-5}[d]
Mylar	0.005	D	4.1×10^{-5}	
Teflon (polytetrafluroethylene)	0.007	H	6.1×10^{-6}	
	0.007	D	0.98×10^{-7}	1.25×10^{-7}[e]
	0.007	T	1.01×10^{-7}	
Kapton (polyimide)	0.005	H	1.1×10^{-6}	
Kapton	0.005	D	1.1×10^{-6}	
	0.009	T	1.86×10^{-6}	
Saran (vinylidene chloride)	0.001	H	1.6×10^{-6}	1.1×10^{-6}[d]
Saran	0.001	D	2.1×10^{-6}	

[a] All measurements were made at room temperature (approx. 25°C)
[b] Reference 1
[c] Reference 2
[d] Reference 1
[e] Reference 4

need for direct experimental measurement of the permeation of tritium through materials rather than predictions based on theoretical assumptions.

REFERENCES

1. G. J. van Amerongen, J. Appl. Phys., 17, 972-85 (1946).

2. S. B. Tuwiner, Diffusion and Membrane Technology, Reinhold Publishing Corp., New York, N. Y., 1962.

3. T. W. Sarge, Anal. Chem., 19:6, 396-400 (1947).

4. R. G. Derrick and M. R. Loutha , Jr., J. Chem. Eng. Data, 19:1, 48-51 (1974).

[illegible] OF TRITIUM BY NEUTRON TIME-OF-FLIGHT

[illegible] Davis and J. D. Anderson

[illegible]rence Livermore Laboratory*

H. W. Lefevre

University of Oregon[illegible]

ABSTRACT

We have developed a method to measure the depth profile of tritium implanted or absorbed in materials. [illegible] to be analyzed is bombarded with a pulsed proton beam and the energy of neutrons produced by the [illegible] reaction is measured by the time-of-flight technique. From the neutron energy the depth in the [illegible] of the T atoms may be inferred. A sensitivity [illegible] T or greater is possible. The technique is non-destructive and may be used with thick or radioactive host materials. Samples up to 20 μm in thickness [illegible] profiled with resolution limited by straggling of the proton beam for depths greater than 1 μm. Deuterium depth profiling has been demonstrated using the D(d,n) reaction. The technique has been used to observe the behavior of an implanation spike of T produced by a 1.0 MeV H^+ beam stopping at a depth of 3 μm in 11 μm thick layers of Ti and TiH. The presence of H in the Ti lattice is observed to inhibit the diffusion of T through the lattice. Effects of the total hydrogen concentration (H + T) being forced above stochiometry at the implanation site are suggested by the shapes of the implanation spikes.

*Work performed under the auspices of the U. S. Energy Research and Development Administration under Contract Number W-7405-Eng-48.

†Work supported by the National Science Foundation.
Lawrence Livermore Laboratory Consultant.

The processes of tritium diffusion and hydrogen isotope induced embrittlement pose severe radiological and materials problems for fusion reactor designers. A technique which was developed to study the depth profiles of [illegible] for 14 MeV neutron generators has applicability as a diagnostic tool for the study of these processes. While the initial measurements have been made on tritium and deuterium implanted in titanium and copper, the technique may be used with any solid sample.

To assay the tritium content of a sample, it is bombarded with a pulsed proton beam of fixed energy. The energy spectrum of neutrons produced by the T(p,n) reaction on tritium atoms in the sample is measured by time-of-flight (TOF) spectroscopy. From the reaction cross section and kinematics the number of tritium atoms present in the sample may be calculated as a function of depth below the surface of the sample. To assay for deuterium content, a pulsed deuteron beam is used and the neutron spectrum from the D(d,n) reaction is measured.

In the initial measurements, the behavior of tritium implanted in empty and hydrogen filled layers of titanium (H:Ti 1.7-1.8:1) and in copper was observed. Relaxation of the implantation spikes in titanium shows the effects of the presence of hydrogen in the previously filled samples. The profiles of tritium retained in copper are consistent with the low solubility of hydrogen in copper, and suggest the presence of a surface barrier retarding tritium release or trapping of tritium on the surface.

Sensitivity of 0.1 at. % was obtained in these measurements. This can be readily improved to 1 ppm. For the proton energy used, resolution below 1 μm is limited by straggling and is better than that which can be obtained with light ion backscatter methods. Because the technique is non-destructive and allows profiles to be made rapidly, it allows the observation of the time history of tritium diffusion in materials.

SAMPLE PREPARATION

The titanium and titanium hydride host materials were prepared by the Isotopes Division of Oak Ridge National Laboratory. Titanium layers of nominal thickness 4.7 mg/cm^2 (11 μm) were vapor deposited on 1 mm thick copper backings. Half of the samples thus prepared were then loaded to near stoichiometry (2:1 hydrogen to titanium ratio) by heating in a hydrogen atmosphere. A loading ratio of 1.7 - 1.8:1 for these samples is inferred from the tritium concentration measured in similarly prepared samples containing tritium.

Tritium and deuterium implanations were performed with a 400 keV beam from the Lawrence Livermore Laboratory ICT accelerator. To control sample heating, the beam current was limited to 10 μA and the samples were cooled with an air jet during implanation. Total quantities of tritium or deuterium implanted were calculated from the total charge deposited on each sample. Implanation doses were 4 x 10^{16}, 4 x 10^{17}, and 8 x 10^{17} ions on a 30 mm^2 beam spot. Since range straggling for these ions is ∿ 0.2 μm, the highest doses should have produced tritium or deuterium concentrations exceeding the stoichiometric concentration (particularly for the TiH samples) at the end of the ion range. We were particularly interested in observing differences in the implanation profiles between the hydrogen loaded samples and in the pure titanium samples.

NEUTRON SPECTROMETRY

Neutron spectra from proton and deuteron bombardment of the samples were measured one month and seven months after implanation. Samples were stored at room temperature between measurements. The University of Oregon 5 MeV Van de Graaff accelerator and time-of-flight spectrometer were used for the measurements. The proton (or deuteron) beam from that accelerator is pulsed by sweeping the beam past an aperture in the high voltage terminal, and is bunched to produce a burst width of ∿ 1.2 nsec FWHM at the target. The neutron detector for these measurements was a NE218 liquid scintillator*

11.4 cm dia x 2.5 cm thick mounted on an RCA 4522 photomultiplier tube*. The detector was 10.3 m from the target at 0° with respect to the direction of the incident beam. Detector bias was set to accept pulses larger than those from 410 keV recoil protons in the scintillator.

Time intervals were measured with a time-to-amplitude converter followed by an analog to digital converter. Time-of-flight spectra were stored with an on-line PDP-7 computer. For each target, data were collected until a preset amount of charge - typically 400 μC - had been delivered to the target. As time averaged beam current was ∿ 2 μA during the spectrum measurements, measurement time was typically 3.5 minutes for each sample. Proton beam energy for the profiling measurements was 2.3 MeV. Typical spectra have been shown in previous publications.[1,2]

DEPTH RESOLUTION

Processes which cause uncertainty in or broaden the energy spread of the incident ion beam or of the outgoing neutrons limit the depth resolution obtained. There are three contributions to the overall resolution: the energy spread of the ion beam from the accelerator, the increase in energy spread of this beam with depth due to straggling, and the energy resolution of the neutron spectrometer.

These energy uncertainties were evaluated and were converted to depth resolution using the values of dE/dx for protons in titanium tabulated by Janni.[3] The individual contributions to depth resolution, and the overall depth resolution obtained by quadratic combination are shown in Fig. 1. One sees from Fig. 1 that for the present proton energy (2.3 MeV) the resolution is dominated by straggling at depths greater than 1 μm. At such depths, resolution of this technique exceeds that which can be obtained by light ion backscattering as the straggling of the backscattered ion contributes additional energy spread, hence depth uncertainty. Figure 2 shows depth resolution for deuterium profiling in titanium using the D(d,n) reaction with the same spectrometer.

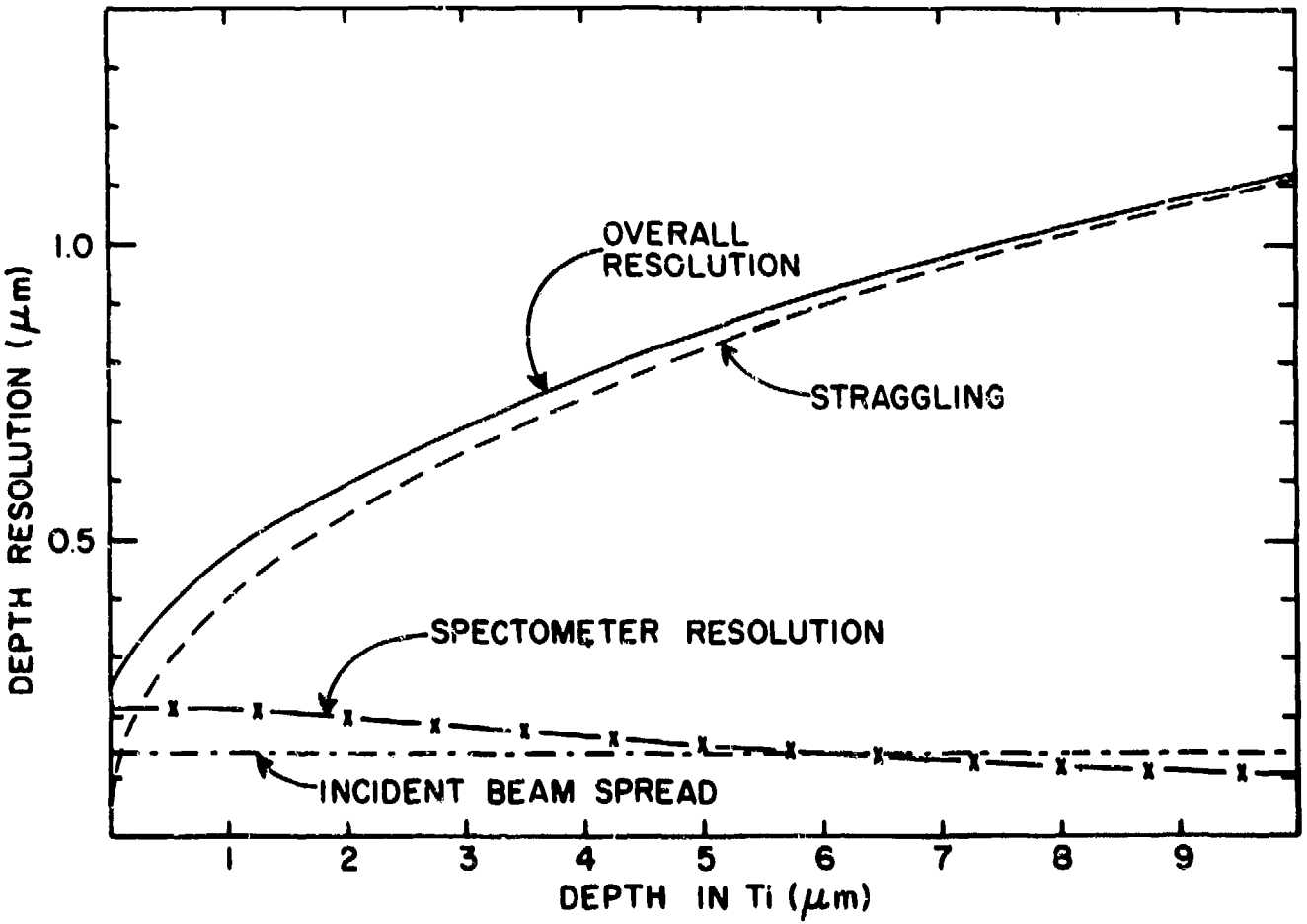

Fig. 1: Resolution vs depth curve for tritium in titanium. The calculations are for an incident proton energy of 2.3 MeV, flight path of 10 m, and spectrometer time resolution of 1.5 ns.

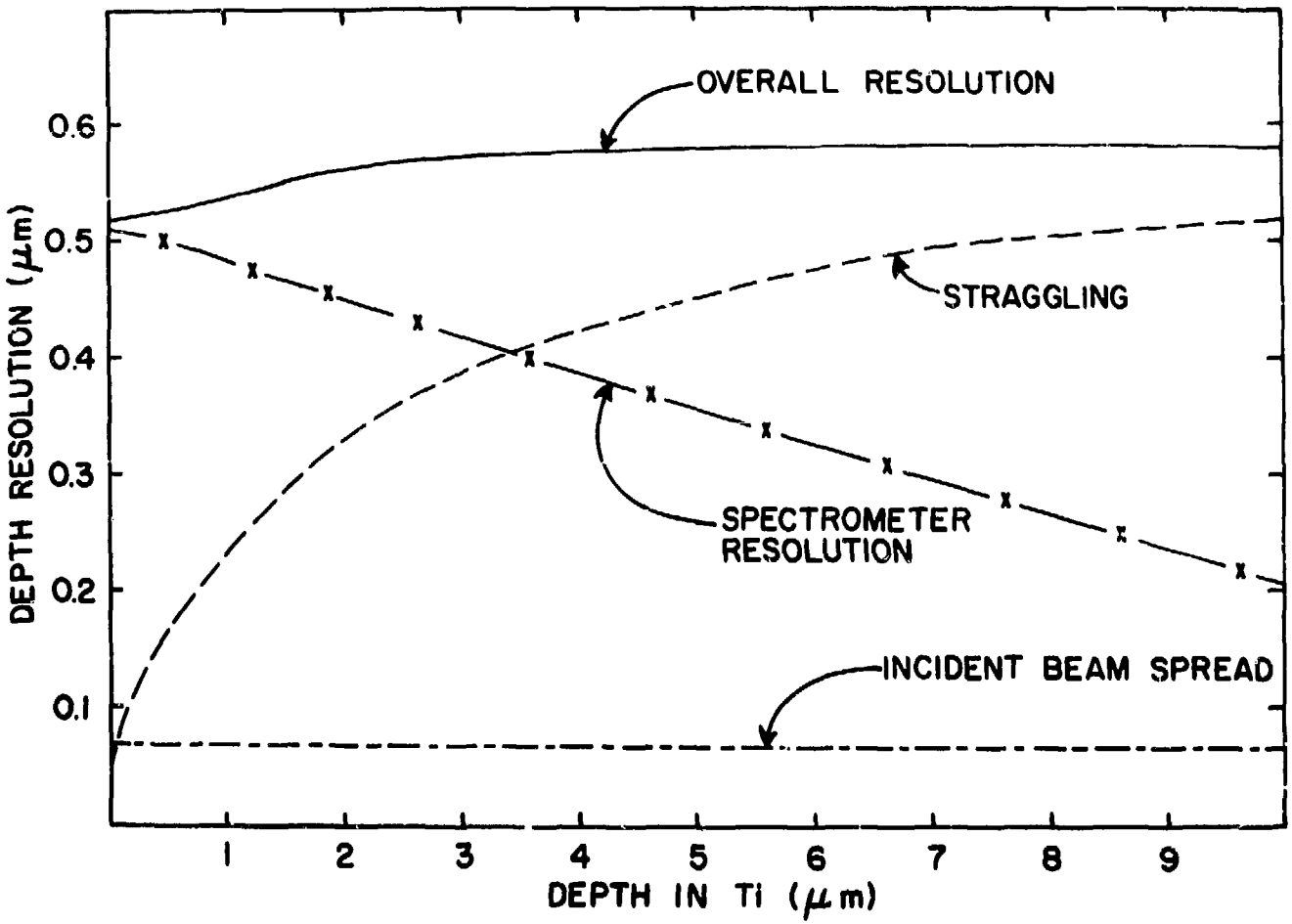

Fig. 2: Resolution vs depth curve for deuterium in titanium. Spectrometer parameters are the same as Fig. 1. Incident deuteron energy is 1.5 MeV.

ANALYSIS - DATA TRANSFORMATION

The neutron energy spectrum from a thick target may be expressed in absolute form as:

$$S(E_n) = \frac{N_n(E_n,\theta)}{N_p} = \frac{\sigma(\theta)}{\epsilon} = \frac{dE_p}{dE_n} \quad \frac{\text{neutrons}}{\text{proton MeV sr}} \tag{1}$$

where $\sigma(\theta)$ is the differential reaction cross section for protons of energy E_p, and ϵ is the compound stopping cross section per reactive atom in the target.[2] All quantities except ϵ are characteristic of the nuclear reaction while ϵ is characteristic of the atomic composition of the target.

The apparent stopping cross section per tritium atom is the compound stopping cross section given by:

$$\epsilon = \frac{n_T\epsilon_T + n_H\epsilon_H}{n_T} \tag{2}$$

where n_T and n_H are number densities of tritium and host atoms respectively, and ϵ_T and ϵ_H are the corresponding atomic stopping cross sections. The stopping cross sections are known to several percent for most elements. If the host substance consists of several different types of atoms one should replace $n_H\epsilon_H$ by a summation over all constituents of the host.

In order to obtain the tritium content, the ratio of the neutron spectrum from the sample to that calculated for a pure tritium target is determined. From Eqs. (1) and (2) then one obtains:

$$\frac{S_u(E_n)}{S_T(E_n)} = \frac{n_T\epsilon_T}{n_T\epsilon_T + n_H\epsilon_H} \tag{3}$$

The atomic percentage of tritium is then:

$$100 \times \frac{n_T(x)}{n_T(x) + n_H(x)} = 100\left[1 + \left(\frac{S_T(E_n)}{S_u(E_n)} - 1\right)\frac{\epsilon_T}{\epsilon_H}\right]^{-1} \tag{4}$$

This expression does not depend explicitly on nuclear reaction parameters since they cancel in the ratio given by Eq. (3). In order to evaluate Eq. (4), $S_T(E_n)$ must be calculated from Eq. (1), and $S_u(E_n)$ must be obtained from the experimental spectrum by correcting it for detector efficiency and other experimental parameters.

When Eq. (4) is evaluated at a neutron energy E_n, the concentration is determined at a specific depth x in the sample. This depth is:

$$x = -\int \frac{1}{n_L \varepsilon_L + n_H \varepsilon_H} \frac{dE_p}{dE_n} \, dE_n \qquad (5)$$

We do not evaluate Eqs. (4) and (5) directly but approximate them numerically. A depth increment is arbitrarily chosen and the corresponding neutron flight time interval is calculated assuming pure host material. The average tritium concentration is determined for this interval. This first order tritium content is then added to the host material to calculate revised flight time intervals. The procedure is iterated until self-consistency is achieved. We start at the front surface of the target and step through it by the chosen depth increment. The number density of host atoms is held constant for the calculations presented here. As titanium expands when hydrided, this latter assumption introduces a 7-10% uncertainty in the depth scale. A more sophisticated approach such as keeping the number density of atoms constant or maintaining constant total atomic volume would reduce this uncertainty. In this experiment, the maximum possible error from this source is less than other errors and has thus been neglected.

RESULTS

The profile of tritium absorbed in a 0.35 μm thick titanium layer on copper is shown in Fig. 3. This thin target was used for calibration purposes to check resolution. When the calculated resolution is combined with the target thickness, the apparent thickness should be 0.45 μm. This result is in good agreement with the measured width of 0.48 μm determined from Fig. 3.

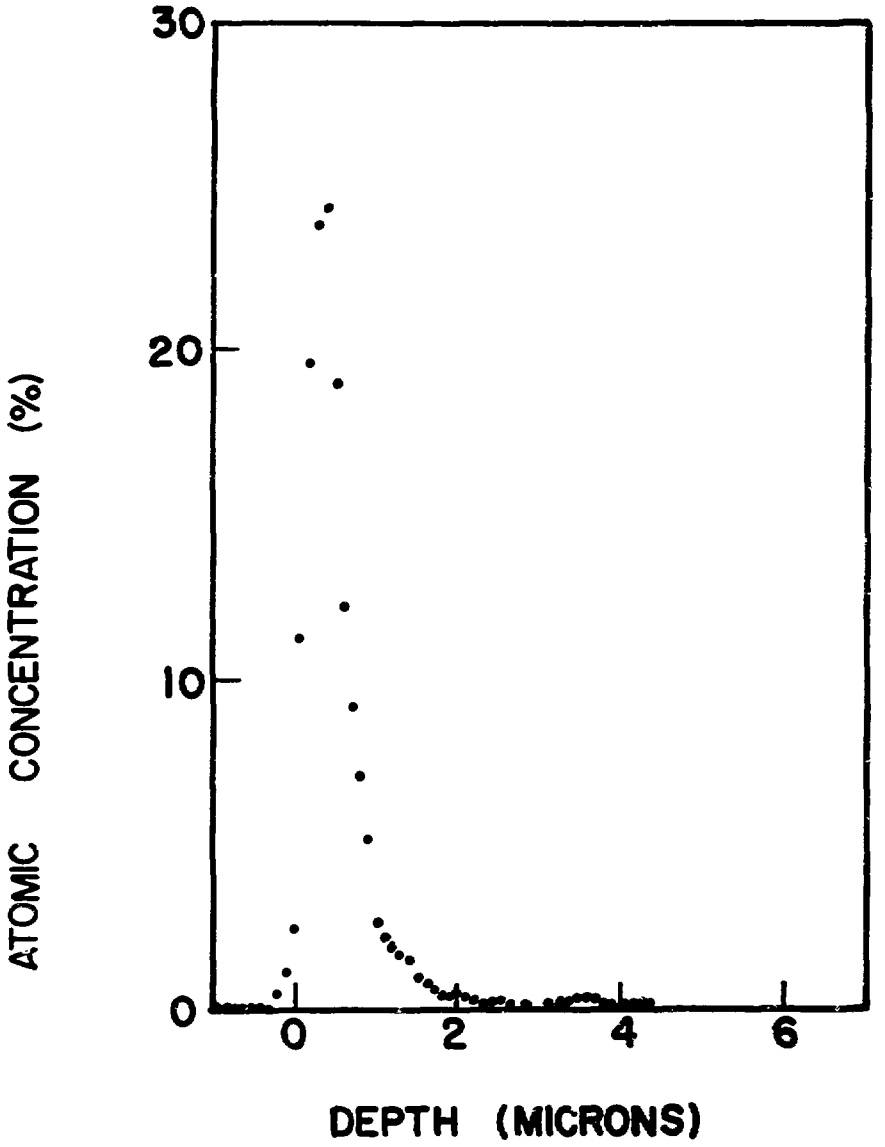

Fig. 3: Depth profile of tritium in 0.35 μm thick Ti target on a 1 mm Cu backing.

Depth profiles resulting from implanation doses of 4×10^{16} tritons in titanium and titanium hydride are shown in Fig. 4. This dose corresponds to a loading of 9 at. % (in empty titanium) if all the tritium stays at the implanation site. Depth profiles from implanation doses of 4×10^{17} tritons (50 at. %) and 8×10^{17} tritons (67 at. %) in both titanium and titanium hydride are shown in Figs. 5 and 6. Several interesting trends are apparent depending upon dose and whether or not the titanium is filled with hydrogen. First, in no case is the implantion peak centered about the nominal 3.7 μm range of the tritons. Rather, the peak of the distribution is about 2.7 μm below the front surface. This displacement may result from radiation enhanced diffusion and trapping or simple beam heating effects during tritium implanation. At the lower doses (9 at. % and 50 at. %) the tritium has diffused well beyond the implanation peak in the titanium samples, producing secondary peaks at a depth of about 9 μm. For the same doses in the titanium hydride there has been much less diffusion to deeper in the target. Virtually all diffusion of tritium appears to have occurred during or shortly after implanation as no significant changes in the profiles occurred during the six month interval between the two sets of measurements.

At the largest dose (67 at. % in empty titanium) the results are somewhat different. Surprisingly, there is less diffusion beyond the ion range in the empty titanium sample than at lower dose. However, the implanation spike in the empty sample is higher and narrower than that in the hydrogen filled sample. Also, in the hydrogen filled sample, there is now significant displacement of tritium to greater depths in the sample. Both these effects suggest that diffusion is enhanced as the lattice nears the stoichiometric hydrogen content. This is consistent with the FWHM of the implanation peak being greater at 67 at. % dose than at 50 at. % dose in both empty (1.4 μm vs. 1 μm) and hydrogen filled (2.4 μm vs. 1.4 μm) samples. Results obtained by profiling deuterium implanted in similar substrates were the same.

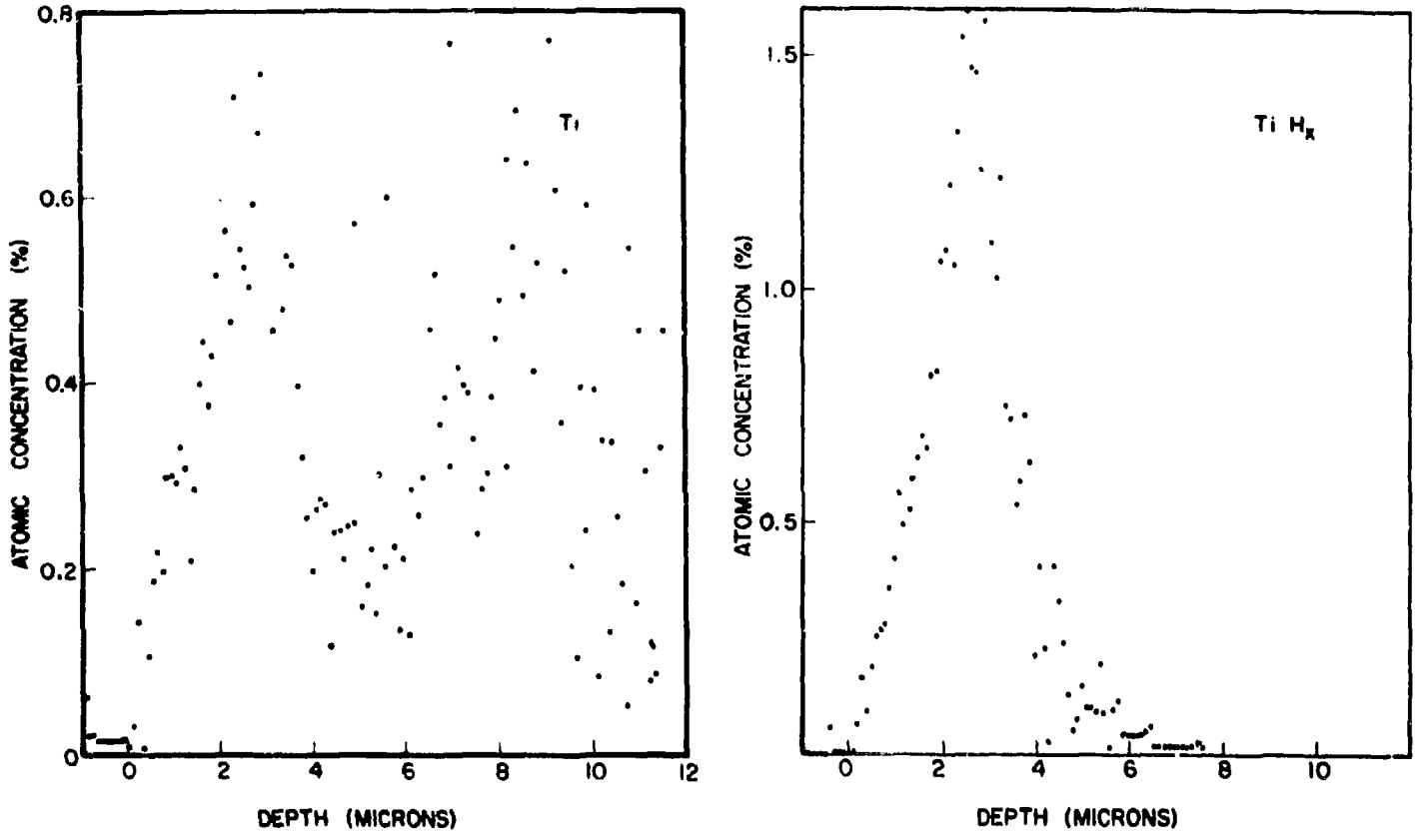

Fig. 4: Depth profiles of 9 at. % tritium doses (at end of tritium range) in titanium and titanium hydride. Samples 11 μm thick.

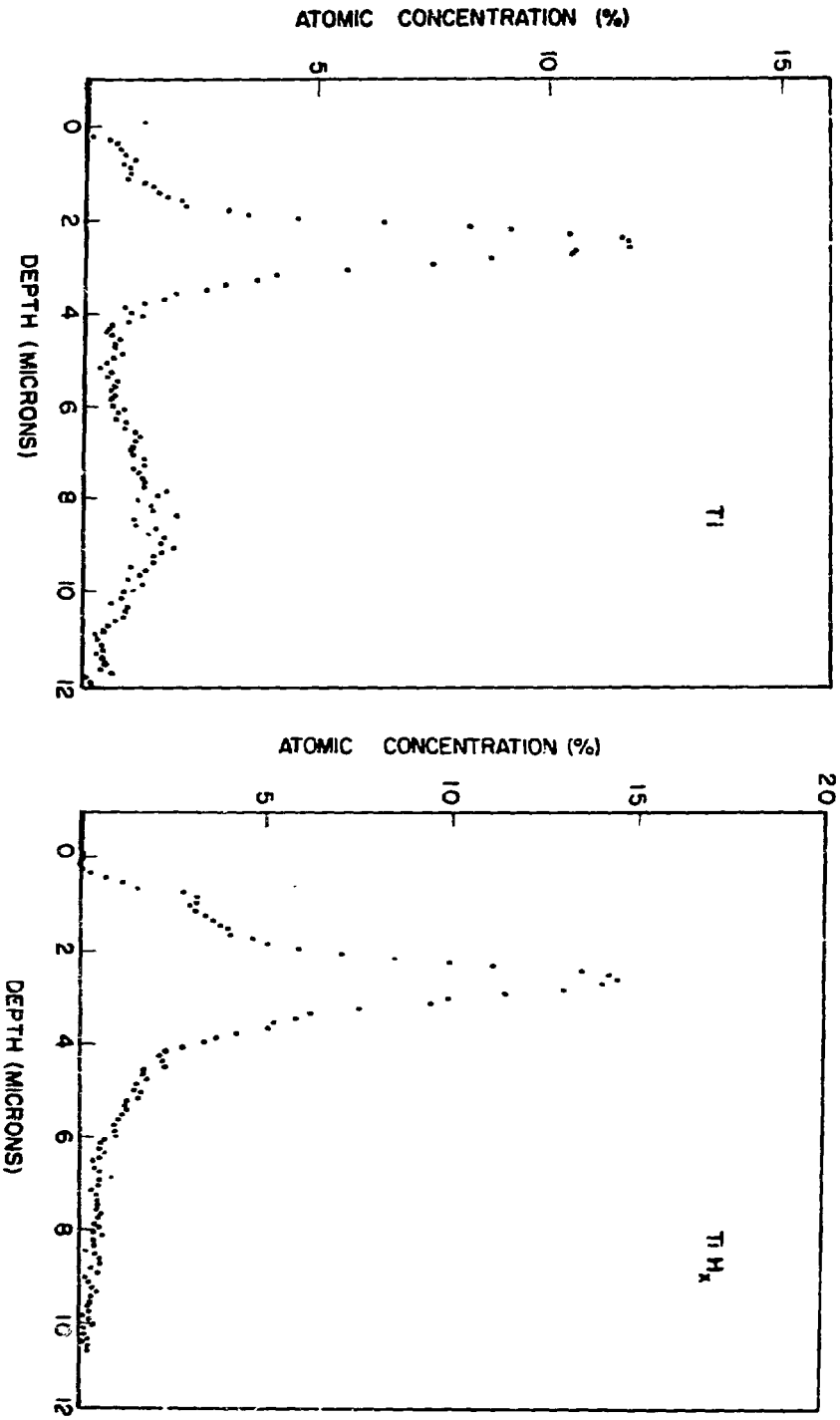

Fig. 5: Depth profiles of 50 at. % tritium doses in titanium and titanium hydride.

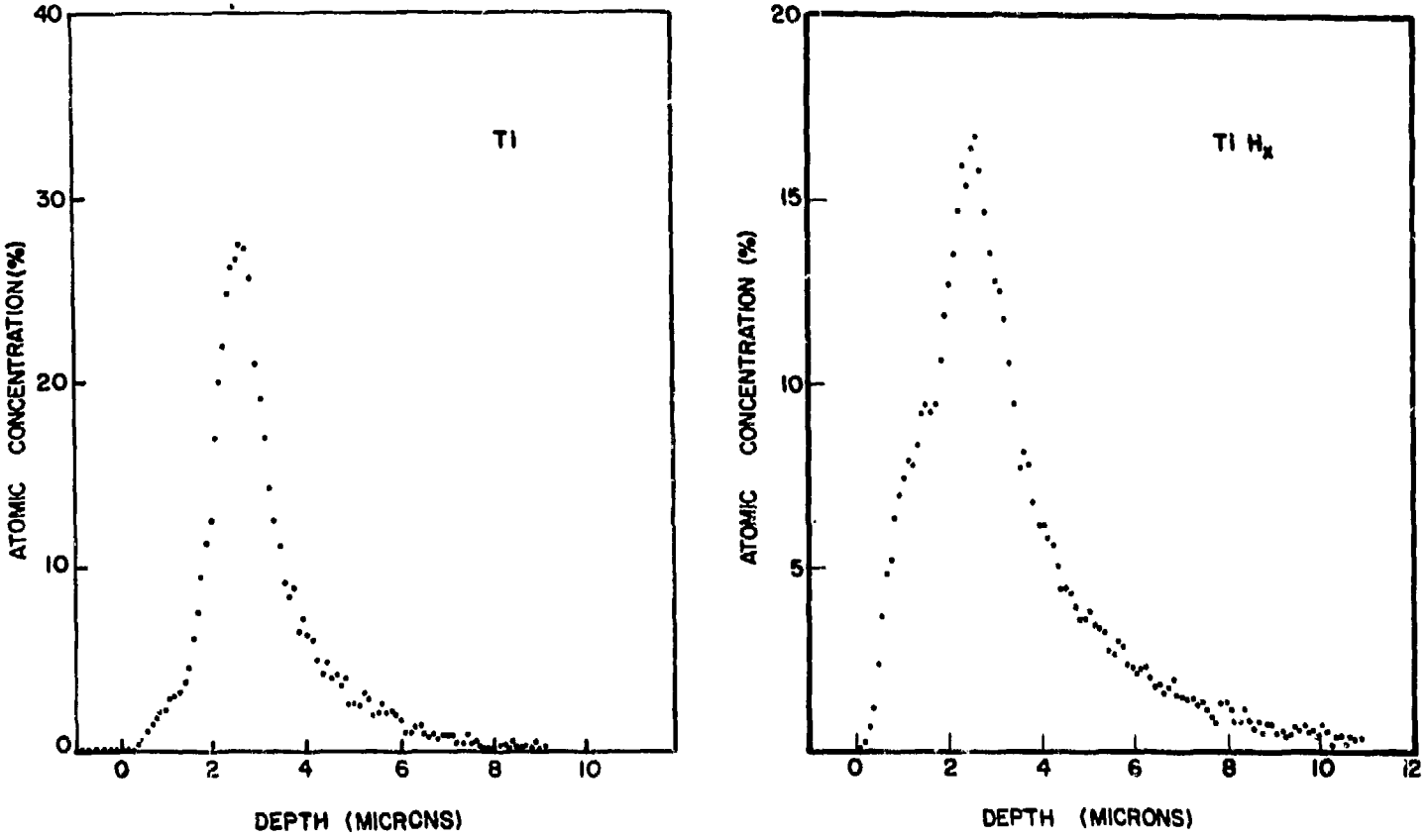

Fig. 6: Depth profiles of 67 at. % tritium doses in titanium and titanium hydride.

Finally, the absolute tritium content determined by this technique is qualitatively correct, i.e., the amount of tritium calculated by integrating these depth profiles and multiplying by the area of the beam spot is within 10% of that calculated by integrating the beam current. As no special effort was made to ensure uniformity of the tritium beam across the spot during implanation, this agreement is quite satisfactory.

For comparison, the depth profile resulting from implanation of 4×10^{17} ions in copper is shown in Fig. 7. This profile should be compared with those of Fig. 5. Only $\sim$ 20% of the tritium remains in the sample. A clear surface peak is obvious, suggesting a barrier retarding tritium release or some surface trapping.

CONCLUSIONS

The results obtained to date demonstrate that the time-of-flight profiling method is a powerful technique for the study of tritium and deuterium diffusion in solid hosts. The somewhat confusing results of the present observation of tritium diffusion in empty and hydrogen filled titanium suggest that an experiment with better controls is required, however. We plan to load tritium in samples held at liquid nitrogen temperature and then observe the behavior of the implanation spikes as the sample temperature is increased. Such an experiment would decouple beam-induced and temperature-induced transport processes.

The sensitivity and resolution of this profiling technique can be further improved. Examination of Fig. 4 shows that a sensitivity of 0.1 at. % was obtained in the present experiments with only a proton charge of 0.4 mC - a 3.5 minute run at 2 μA average beam current. If the time resolution of the spectrometer were reduced to below 1 ns and the neutron flight path shortened until spectrometer resolution was $\sim$ 70% of the beam straggling limit, then a sensitivity of 10^{-4} at. % or 1 ppm could be obtained with the same resolution but would require an hour long run. The effects of the amount of hydrogen injected into the sample by the proton beam might not be negligible, however.

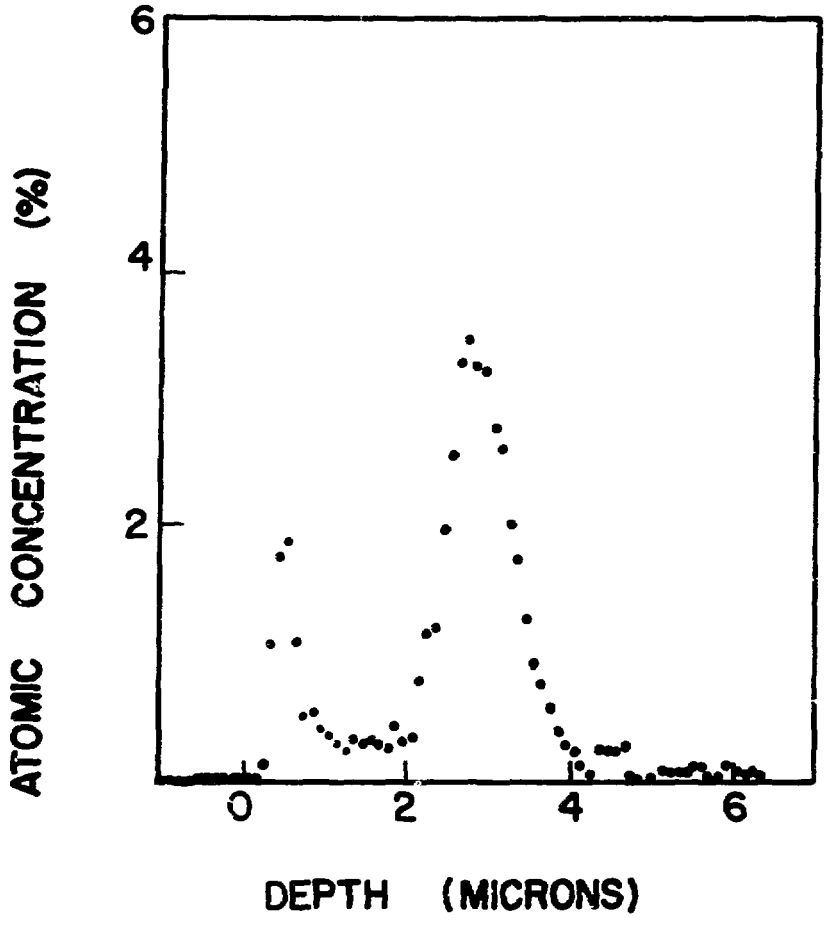

Fig. 7: Depth profile of tritium in Cu. The dose was the same as that given the samples in Fig. 5.

Improvements in resolution depend upon selecting operating parameters to optimize resolution at the depth region of interest and reducing spectrometer resolving time. In particular, to assay near the front surface of a material a much lower proton energy is preferred. This reduces the neutron energy, increases the time-of-flight, and reduces the limitation imposed by spectrometer resolution.

ACKNOWLEDGEMENTS

The advice and help of L. P. Mego, D. R. Rawles, R. M. Penpraze, and J. L. Garibaldi in producing the tritium beam from the ICT for the implanation runs is appreciated. Assistance of J. D. MacDonald and E. W. Ross during the depth profiling runs was also very helpful.

REFERENCES

1. J. C. Davis and J. D. Anderson, J. Vac. Sci. Technol. 12, 358 (1975).
2. J. C. Overley and H. W. Lefevre, Symposium on Radiation Effects on Solid Surfaces, Chicago, Illinois, August 25-29, 1975.
3. J. F. Janni, Air Force Weapons Laboratory Technical Report No. AFWL-TR-65-150 (1966, unpublished).

*Reference to a company or product name, here or elsewhere in this report, does not imply approval or recommendation of the product by the University of California or the U. S. Energy Research and Development Administration to the exclusion of others that may be suitable.

CHARACTERISTICS OF SORB-AC NON-EVAPORABLE GETTER CARTRIDGES AND THEIR POTENTIAL USE IN FUSION REACTORS

A. Barosi
T.A. Giorgi
L. Rosai

S.A.E.S. Getters S.p.A. Via Gallarate 215, Milan - Italy

ABSTRACT

The possible use of non-evaporable getter pumps and SORB-AC cartridges in the problems related to the storage and cycling of the hydrogen isotopes, deuterium and tritium, as well as those connected with nuclear fusion reactor experiments is reported. The structural characteristics of traditional and non-magnetic getter pumps and cartridges are described. Their use and characteristics in the high and ultra-high vacuum range are reviewed. The characterization is extended to the pressure range 10^{-2} - 10^{-4} torr for hydrogen and its isotopes so as to cover the application fields of present interest. Typical applications are illustrated as examples of the ability of these pumps to store, purify and recycle hydrogen and its isotopes. The operating conditions of the pumps in these different applications are linked to the reversible sorption capacity of hydrogen which depends on the hydrogen equilibrium pressure in the gas phase and the temperature of the getter material. The influence of gaseous impurities, for example CO, on the gettering characteristics for hydrogen are also considered.

INTRODUCTION

The use of hydrogen and its isotopes is a characteristic of all experimental devices which aim at controlled nuclear fusion as a source of power. In most previous experiments, and in some being planned at present, mainly hydrogen and to a lesser extent deuterium have been used since they have enabled the simulation of the necessary experimental operating conditions without the use of the more expensive radioactive tritium. However, in the near future the use of tritium will undoubtly become more common since, as the new generation of machines devoted to these studies tends towards the break-even point, the use of tritium-deuterium mixtures becomes ever more necessary. The safe handling and recovery of tritium is therefore of paramount importance since it cannot be discharged into the ambient but must be recovered and recycled.

The problems of tritium handling are also present in numerous other industrial applications such as, for example, the production of high energy neutrons by deuterium and tritium impact on metallic targets (1, 2).

Another very important problem encountered in magnetic confinement plasma machines is that of reducing the presence of impurities to a minimum. Such impurities can increase the energy loss by radiation, decrease the fuel density and increase the diffusion rates of the plasma. Permissible impurity levels of the order of 10^{-2} are reported for light ions (O_2 for example) while for heavy ions the permissible level is of the order of 10^{-3} (3, 4).

Up till now the methods of pumping these experimental machines have been based on the use of sputter-ion pumps, sublimation pumps, mercury or oil diffusion pumps, and more recently, turbomolecular pumps. To produce high localized pumping speeds use has also been made of titanium or other getter films deposited on large panels which in some cases have been cooled to liquid nitrogen temperatures. The use of liquid helium cryopumps has also been reported.

Present storage and recycling techniques for tritium and deuterium make use of materials such as uranium, yttrium and erbium [5, 6, 7]. These materials, at suitable operating temperatures, form solid solutions and/or hydrides characterized by low equilibrium pressures. Increasing the equilibrium pressure by raising the temperature the "trapped" deuterium and tritium are released.

The above techniques may, however, present some drawbacks involving technical, practical, economic and safety considerations. Among these drawbacks is the irreversible accumulation of radioactive material in the widely dispersed large areas of titanium films used for pumping. With tritium storage there are difficulties in attaining high sorption rates without incurring risks linked with the pyrophoric nature of the storage medium.

A new versatile technique for pumping, purifying and storing hydrogen and its isotopes in the large controlled nuclear fusion machines is now presented. This technique is based on the use of SORB-AC type non-evaporable getter cartridges which could overcome most of the problems now encountered.

DESCRIPTION OF SORB-AC CARTRIDGES

SORB-AC type non-evaporable getter cartridges have been industrially available for a number of years. They have found uses in traditional vacuum applications and in the getter field [8, 9, 10, 11]. The special properties of these devices make them particularly suitable for substituting or integrating presently used methods of pumping, purifying and storing hydrogen and its isotopes in the above mentioned applications [12].

In figure 1 is shown a typical SORB-AC cartridge pump with a summary of its fundamental characteristics. These pumps are based on the use of a non - evaporable getter material which is a binary alloy

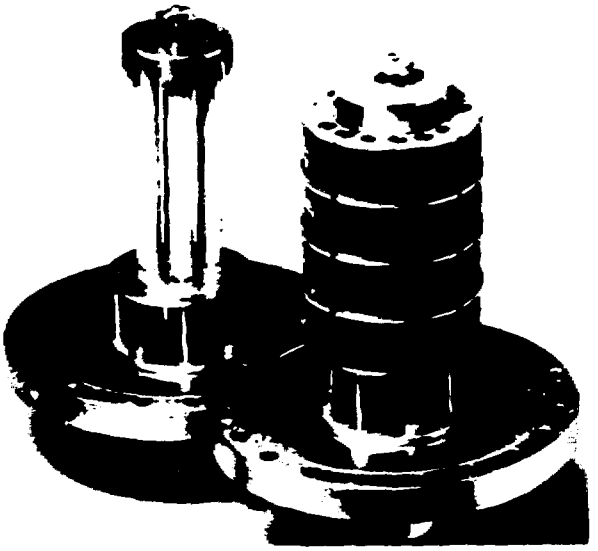

CARTRIDGE HEIGHT		12.7 cm
DIAMETER		9.6 cm
WEIGHT		1.6 kg
FLANGE DIAMETER		8 in.
MAXIMUM POWER TO REACH	200°C	60 W
	400°C	300 W
	600°C	1000 W
	750°C	1800 W

Fig. 1. Typical C500 SORB-AC cartridge pump and a summary of its fundamental characteristics.

84% zirconium and 16% aluminium (13). The Zr-Al alloy* in powder form is coated on a continuous metal strip, which is then precut and pleated in concertina fashion to form hollow cylinders which are used to make up the cartridges. The base material on which the non-evaporable getter alloy is coated may be pure iron or an amagnetic 45% Ni-Cu alloy. These cartridges, as shown in figure 1, are mounted on suitable flanges which also carry a special radiation type heating element immersed in the cartridge body. The heater's function is to activate the cartridge by raising its temperature to 700 - 750°C under vacuum for about 10 - 15 minutes. This treatment removes superficial oxide and nitride layers from the surface by diffusing them into the bulk. This layer protects the bulk of the getter material during air exposure, its removal makes the cartridge active. The radiation heater is also used to maintain the cartridge at preselected working temperatures.

The pump cartridge elements, shown in figure 1, may be mounted nude inside the vacuum chamber which is be pumped or they may be mounted in a suitable housing attached to the vacuum chamber itself.

The main advantages which may derive from the use of SORB-AC cartridges in machines designed for studying nuclear fusion processes may be summarized as follows:

1. Absence of large getter film deposition surfaces which have to be cooled by liquid nitrogen or hydrogen.
2. Possibility of concentrating in small volumes, instead of on large surfaces, high specific speeds and capacities for hydrogen and its isotopes.
3. Possibility of siting close to the plasma area with no danger of gas release due to plasma interaction with getter material.

---

* Commercially available from SAES Getters S.p.A., Milan, Italy under the tradename St101

4. Possibility of pumping hydrogen and its isotopes even at room temperature thus presenting notable fail safe features.
5. Possibility of regeneration by heating thus making it possible to transfer the previously pumped species (hydrogen and its isotopes) from one part of the system to another or even away from the system.
6. Possibility of physically defining a point where all radioactive material is located.
7. Wide pressure range of practical use, from 10^{-10} torr to a few torr.

SORB-AC CARTRIDGE CHARACTERISTICS IN THE UHV AND HV PRESSURE RANGE

In the range of pressures between 10^{-10} and 10^{-6} torr, the pumping speed for all active gases is independent of the pressure at which pumping occurs. This property, for hydrogen, is illustrated in figure 2. In the same figure the pumping speed for hydrogen of a sputter-ion pump is also given (14).

The pumping characteristics for SORB-AC cartridges in the high vacuum range are shown in figures 3 and 4 for carbon monoxide and hydrogen respectively. The method of presentation of these results is the one usually employed in the getter field (15). The pumping speed (litres per second) is reported as a function of the quantity of gas previously sorbed (torr litres) at a constant pumping pressure. The curves depict the behaviour of the speed in relationship with the amount of getter material used up.

The sorption process which controls the pumping of hydrogen is different from that which controls the pumping of other gases such as nitrogen, oxygen, carbon monoxide and carbon dioxide. In this latter case stable chemical compounds (nitrides, oxides, carbides) are formed, whereas for hydrogen a solid solution is obtained. The concentration of hydrogen in solution depends on the operational

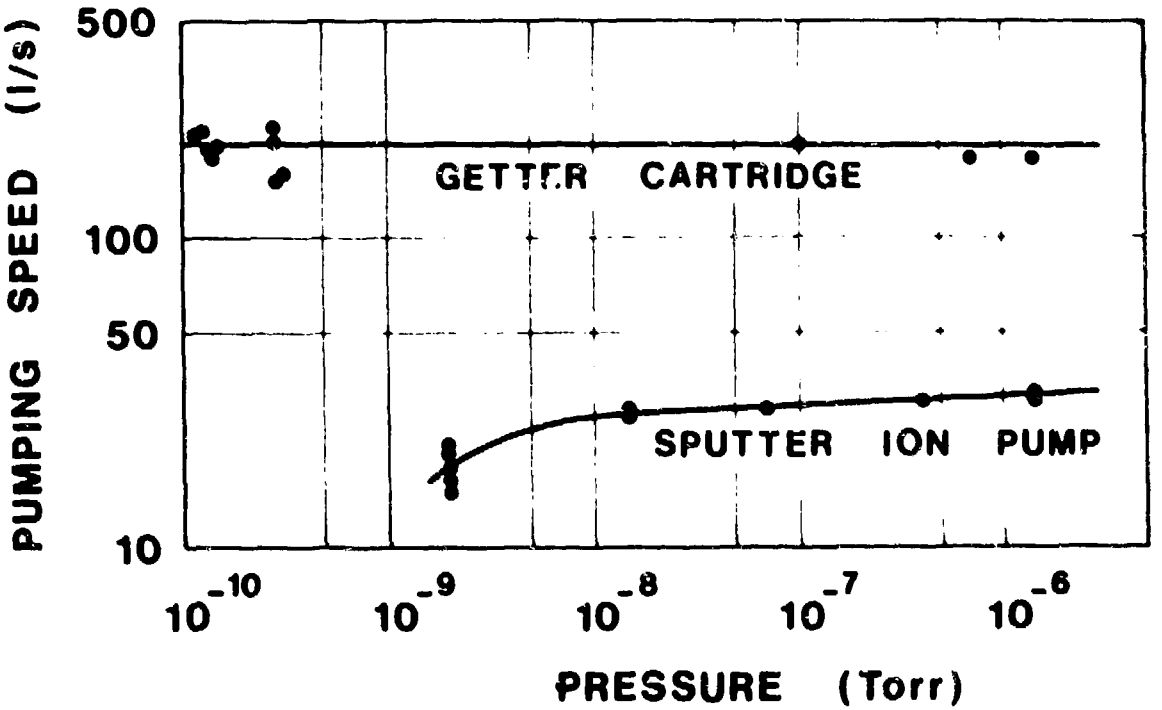

Fig. 2. H_2 pumping speed in the pressure range 10^{-10} - 10^{-6} torr of a SORB-AC getter pump and a sputter-ion pump.

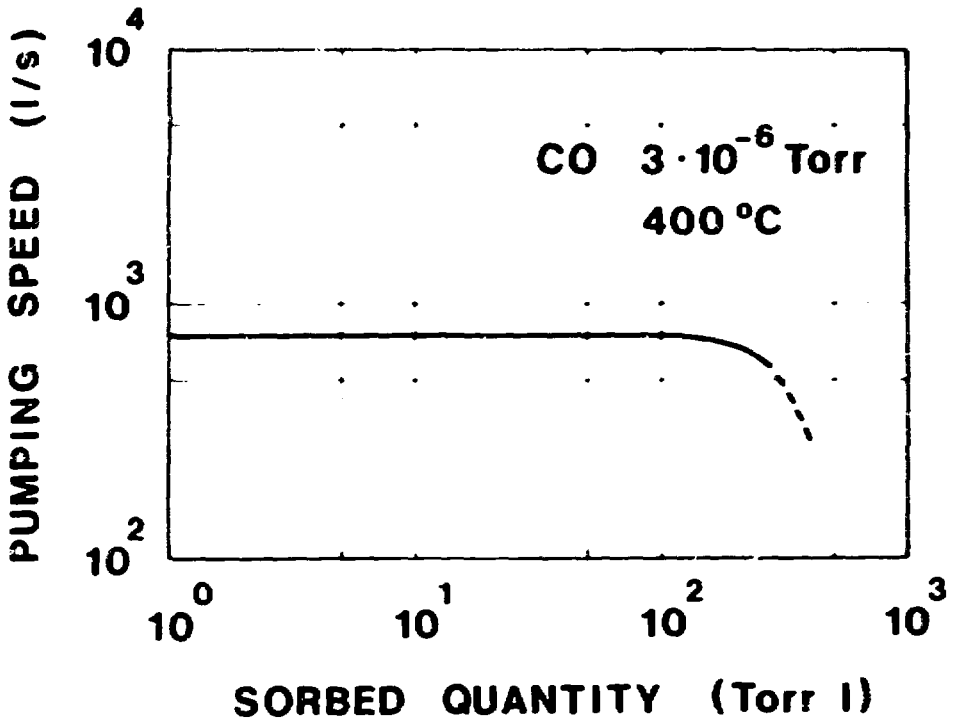

Fig. 3. Pumping characteristics of 400°C of a C500 cartridge for CO at 3.10^{-6} torr.

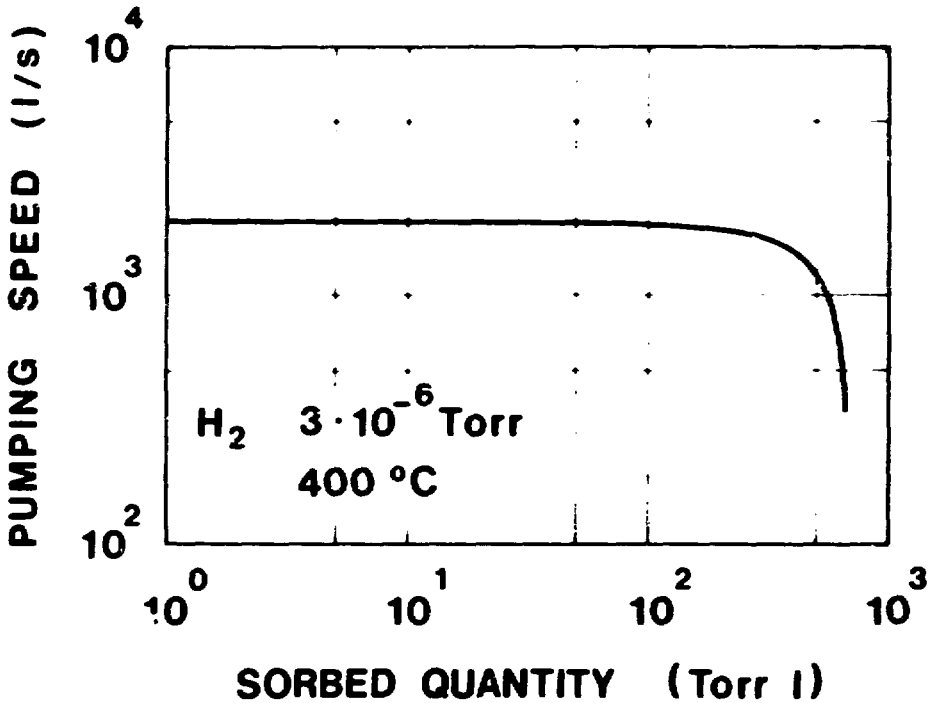

Fig. 4. Pumping characteristics at 400°C of a C500 cartridge for H_2 at 3.10^{-6} torr.

temperature of the material and on the partial pressure of hydrogen in the gas phase.

The relationship governing the hydrogen equilibrium pressure, concentration and temperature for the Zr-Al alloy used (16) is

$$\text{Log } P = 4.4 + \log q^2 - \frac{7000}{T}$$

where

P = the pressure in torr

q = the concentration in torr litre/g of getter material

T = the absolute temperature in degrees Kelvin.

SORB-AC CARTRIDGE CHARACTERISTICS AT HIGHER PRESSURES

The behaviour of the SORB-AC cartridges at pressures higher than those previously reported are also of particular interest in experiments studying the feasibility of controlled nuclear fusion and in the recycling of hydrogen isotopes. This behaviour has been studied for hydrogen on a C500 cartridge. The designation C500 is given to the type of cartridge used in SORB-AC getter pumps which have a nominal pumping speed of 500 litre per sec for carbon monoxide. The pumping speed for the nude cartridge can be considerably higher than the pump rating and also depends upon the gas being pumped.

The results obtained for hydrogen over the pressure range 10^{-6} to 10^{-1} torr are reported in figure 5. It will be noted that the pumping speed remains constant up to a pressure of 5×10^{-3} torr. It falls to 40% of the plateau value at pressures of the order of 2×10^{-2} torr. The dependance of the pumping characteristics for hydrogen, at 10^{-4} torr, and at different temperatures are illustrated in figure 6. The pumping speed values at the different temperatures and the equilibrium capacity value at 400°C are summarized in Table 1. The capacity values reported at 200°C and 25°C are not, as will be

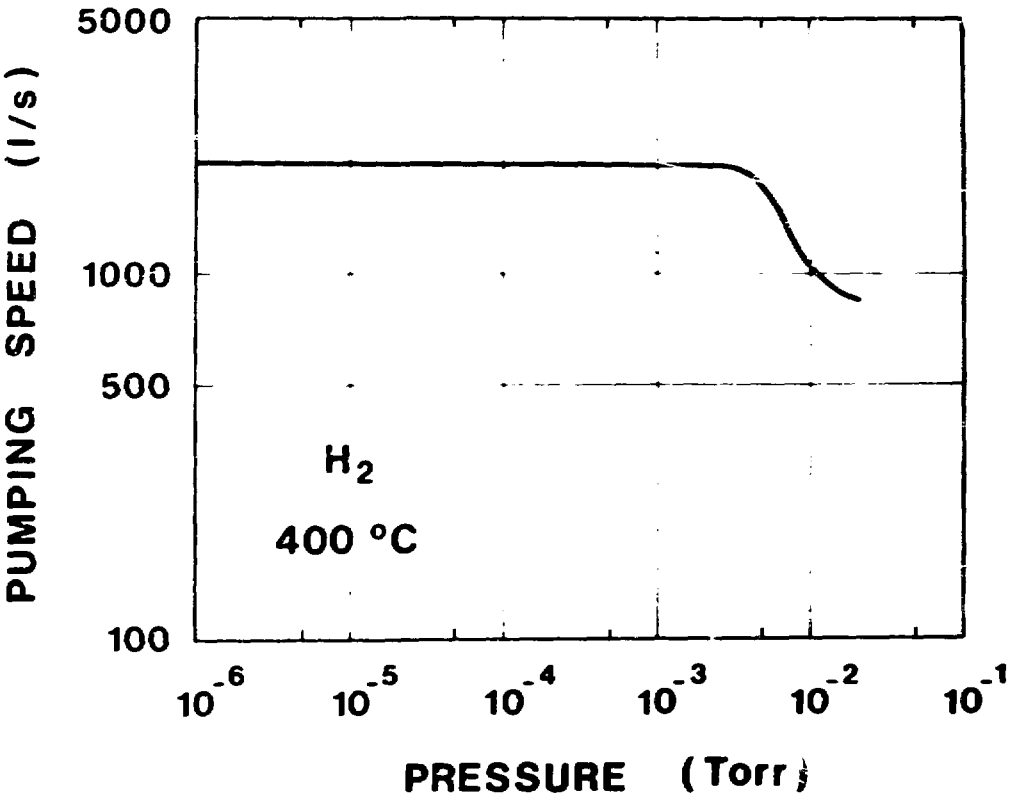

Fig. 5. H_2 pumping speed in the pressure range 10^{-6} - 10^{-2} torr of a C500 cartridge at 400°C.

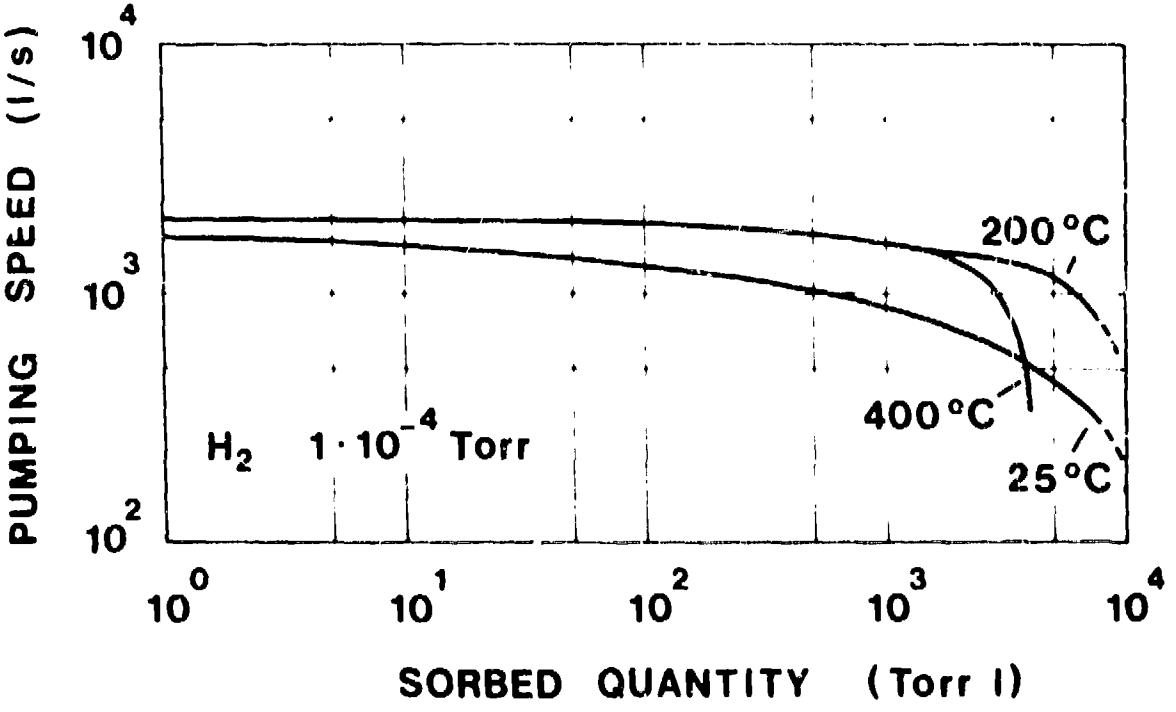

Fig. 6. Pumping characteristics of a C500 cartridge for H_2 at 1.10^{-4} torr at 25°C, 200°C and 400°C.

Table 1. Pumping characteristics for H_2 of a C500 cartridge.

PUMPING CARACTERISTICS FOR H_2 OF A GP 500 SORB-AC PUMP			
TEMPERATURE	25 °C	200 °C	400 °C
PUMPING SPEED (l/s)	1500	2000	2000
CAPACITY (Torr l)	8000	8000	4000

described later, those corresponding to equilibrium values but those which must not be exceeded if embrittlement problems are to be avoided.

The experimentally determined relationship between equilibrium pressure, temperature and hydrogen concentration given in equation 1, has been applied to describe the situation for a C500 cartridge. These results are shown in figure 7. The ranges of temperature and pressure reported are those of practical interest in the present context. The theoretical limiting hydrogen concentration is about 20000 litre torr in the case considered. However, as shown in this figure and reported in Table 1 we suggest a maximum concentration of only 8000 litre torr. This practical limit is set to enable safe hydrogen cycling. If this limit is exceeded danger of embrittlement of the alloy coating, with resulting particle loss, becomes serious.

Regeneration of a cartridge, saturated with hydrogen, may be obtained by raising its temperature and by removing the evolved hydrogen by means of a suitable vacuum line. An example of such a regeneration cycle for a C500 cartridge may be illustrated with reference to figure 8. In this case, as previously reported, the cartridge when working at 400°C and at a pressure of 10^{-4} torr is saturated at about 4000 litre torr of hydrogen (point A). To regenerate the cartridge its temperature is raised to 700°C thus raising the system pressure to about 10^{-1} torr (point B). If, while the cartridge is maintained at this temperature, the hydrogen evolved is removed by another pumping system, it is possible to reduce the hydrogen concentration in the cartridge by moving along the 700°C isotherm down to a concentration level which is only 10% of the initial value (point C). At this point by removing the vacuum line and reducing the temperature to 400°C again the equilibrium hydrogen pressure becomes of the order of 10^{-6} torr (point D). At this point the cartridge may be considered as being restored to its original condition.

In principle it is possible to cycle the cartridges over wider limits than those illustrated in figure 8. However, it must be borne in mind that lower temperatures (below about 300°C) and higher

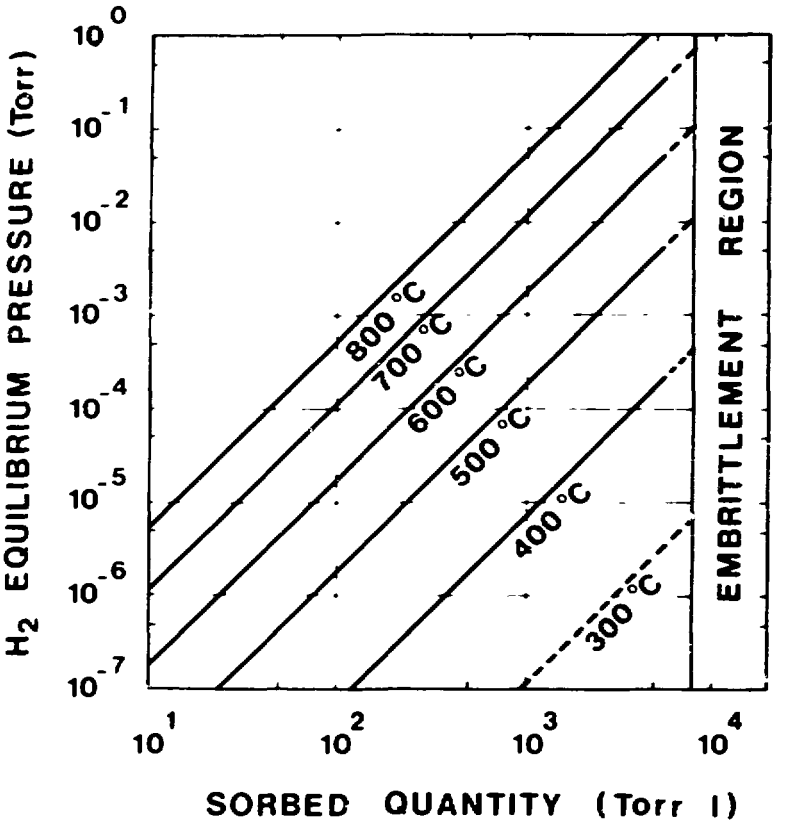

Fig. 7. H_2 equilibrium pressure on a C500 cartridge as a function of the quantity of H_2 sorbed at various temperatures.

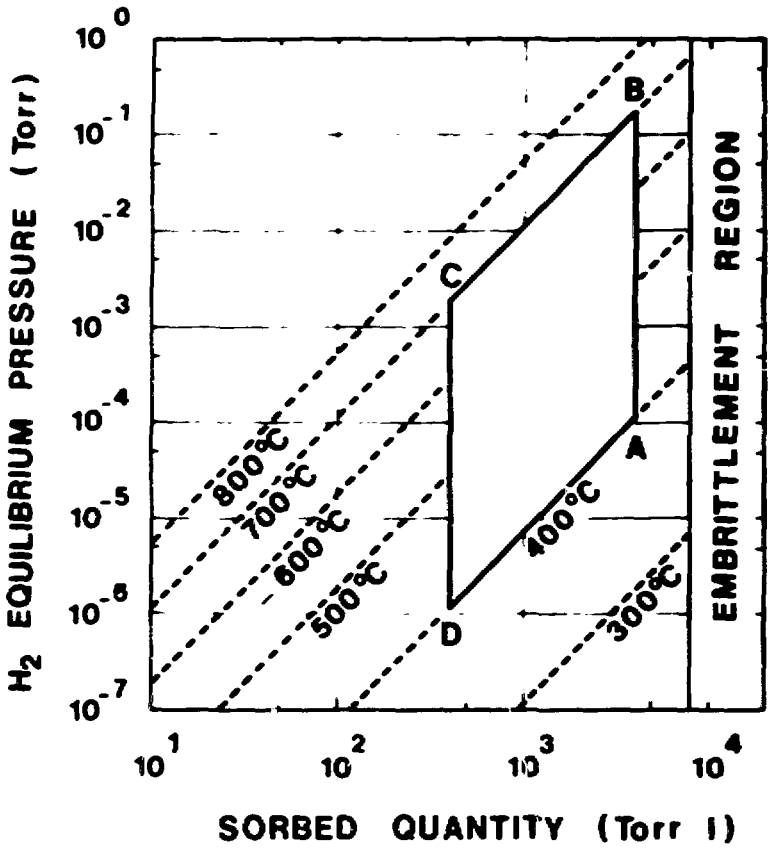

Fig. 8. H_2 regeneration cycle of a C500 cartridge.

concentrations slow down the diffusion processes appreciably thus making it impractical to reach equilibrium conditions within reasonable times.

ISOTOPE EFFECTS

All the experimental data presented has been with reference to hydrogen. However, from a theoretical point of view of the data can also be used for the hydrogen isotopes.

If it is assumed that the sticking probabilities are the same for the various isotopes, then the isotope effect on the pumping speed can be calculated from the mass effect on the number of molecules striking unit area; i.e.

$$\left(\frac{M_{D_2}}{M_{H_2}}\right)^{1/2} = 1.41 \quad \text{and}$$

$$\left(\frac{M_{T_2}}{M_{H_2}}\right)^{1/2} = 1.73$$

The pumping speed ($L^3 T^{-1} L^{-2}$) can be transformed to instantaneous mass throughput ($MT^{-1} L^{-2}$) when the speed is assumed to remain constant during the sorption time.

In Table 2 the appropiate correction factors which have been evaluated (D_2 and T_2) and experimentally observed (D_2) are reported (17). The parameters are referred to the arbitrarily given value of 100 for hydrogen.

Table 2. Isotope effect factors to obtain the pumping characteristics for D_2 and T_2 from those of H_2.

ISOTOPE EFFECT (%)	H_2	D_2		T_2
		CALC.	OBSER.	CALC.
PUMPING SPEED (units $L^3 T^{-1} L^{-2}$)	100	71	56	58
MASS THROUGHPUT (units $M T^{-1} L^{-2}$)	100	141	112	173

INFLUENCE OF IMPURITIES

All the experimental data reported up to now has been obtained using spectroscopically pure hydrogen. In order to have some indication as to the possible influence of impurities present in actual experimental conditions a study has been undertaken using contaminated hydrogen. Preliminary tests have been carried out using hydrogen contaminated with about 1% of nitrogen or carbon monoxide or oxygen. From this work it has been possible to determine that nitrogen has practically no adverse effects while oxygenated gases have appreciable adverse effects. As an example of this negative influence the pumping speed of a C500 cartridge at a temperature of 300°C is shown in figure 9 as a function of the hydrogen quantity sorbed when using both pure hydrogen and hydrogen with 1% of carbon monoxide as an impurity. The negative influence is more pronounced as the quantity of hydrogen pumped increases. Nevertheless useful practical results are still possible.

It has also been determined that at a fixed impurity level the poisoning influence of the impurities increases as the temperature decreases. It is therefore suggested that with high impurity levels the cartridge should be operated at temperatures greater than 200 - 250°C. This will increase the rate of diffusion of the poisoning species away from the surface of the non-evaporable getter material. In the case of low impurity levels (10^{-3} or lower) it may be assumed that hydrogen will be pumped effectively, even at room temperature, as long as the cartridge temperature is periodically raised to 300 - 400°C to diffuse away accumulated surface impurities.

EXAMPLES OF VARIOUS APPLICATIONS

The number of possible applications of the SORB-AC non-evaporable getter cartridges in fields linked with hydrogen and its isotopes are numerous. Therefore, a few examples are given to illustrate the

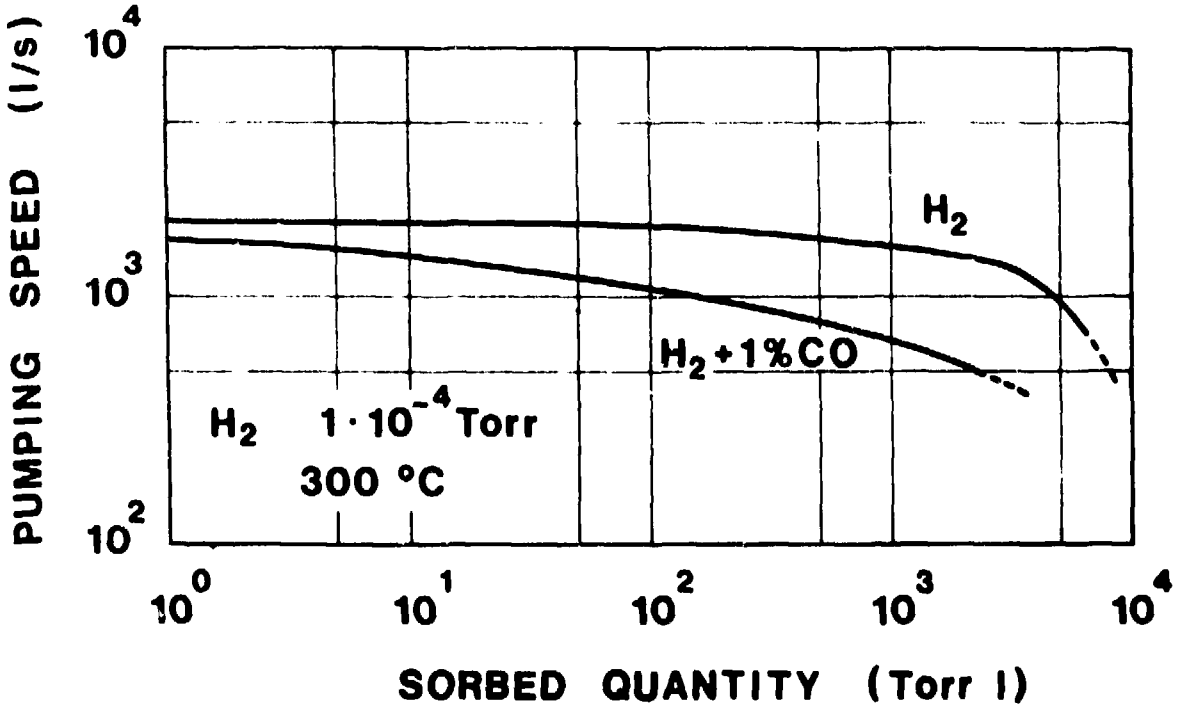

Fig. 9. Pumping characteristics at 300°C of a C500 cartridge for pure H_2 and H_2 + 1% CO at 1.10^{-4} torr.

versatility of these devices.

a) Hydrogen recovery and recycling. In this application the cartridges are part of a closed system and act as fore-pumps for traditional pumps which cannot discharge their gas load to the atmosphere. The cartridges can be mounted in valved canisters. Once saturated they may be used as in situ hydrogen sources or they may be transported to areas where their gas load may be recovered.
b) Hydrogen pumping in TOKOMAK divertor sections. The outer unstable fringes of the plasma are magnetically removed from the plasma core and are then directed onto suitable collectors. The beam reflected from the collectors must be trapped with high efficiency in order to avoid its return into the plasma area causing perturbations.
c) Intermediate storage of hydrogen previously pumped at high speed during the dynamic conditions of plasma discharge. With this technique it is possible to maintain the plasma free from impurities since it is continuously regenerated by the introduction of pure hydrogen.
d) Purification of hydrogen in static conditions just before plasma discharge. This is achieved by maintaining the cartridge at a suitably high temperature so that the hydrogen pressure is in equilibrium with the solid solution but the other impurities are removed with high efficiency.
   In this application the cartridges can be immersed in the plasma machine and removed just prior to the discharge.
e) Pumping and purification of hydrogen in neutral beam injectors in which differential high speed pumping is necessary thus minimizing gas flow from the injector into the torus in addition to pumping gas from the torus after each shot.

REFERENCES

1. R. Steinberg and D. L. Alger, A New Pumping System for a 150-Kilovolt Neutron Generator to Reduce the Present Tritium Hazard, BRH/DEP 73-2, (1972).

2. H. Fabian, Euratom Report EUR/C/1815, 204 (1964).

3. R. Behrisch and B. B. Kadomtsev, Impurities in Plasmas and their Implication with Respect to Fusion Reactors, IAEA CN-33.

4. M. Yoshikawa et al., Research on a Tokamak with an Axisymmetric Divertor and Impurity Problems in Tokamak Devices, IAEA CN-33.

5. M. H. Cooper, USA Patent 3,848,067.

6. E. J. Fernandez and D. M. Holloway, J. Vac. Sci. Technol. 11, 612 (1974).

7. J. Pivarč, Radiochem. Radioanal. Lett., 18, 1 (1974).

8. R. A. Tuck, Vacuum, 22, 409 (1972).

9. C. Pisani and P. della Porta, Suppl. Nuovo Cimento, Serie 1, 5, 261 (1967).

10. J. Vaumoron et al., J. Vac. Sci. Technol., 9, 982 (1972).

11. P. della Porta et al., J. Vac. Sci. Technol., 7, 300 (1970).

12. H. Hägelsperger et al. Vacuum System of the W VII B Stellarator, EUR 5182 e, 99 (1974).

13. A. Barosi, Residual Gases in Electron Tubes, p. 221, Academic Press, London, 1972.

14. P. della Porta and C. Pisani, Le Vide, 132, 331 (1967).

15. P. della Porta and F. Ricca, Seventh Trans. Nat. Vac. Symp., p. 352, Pergamon Press, Oxford, 1961.

16. A. Barosi and E. Rabusin, Japan J. Appl. Phys., Suppl. 2, Pt 1, 49 (1974).

17. M. Nagasaka and T. Yamashina, Japan J. Appl. Phys., Suppl. 2, Pt 1, 61 (1974).

A SECONDARY CONTAINMENT SYSTEM FOR A HIGH TRITIUM RESEARCH CRYOSTAT

R. T. Tsugawa, D. Fearon, P. C. Souers,
R. G. Hickman, and P. E. Roberts*

Lawrence Livermore Laboratory, University of California
Livermore, California 94550

ABSTRACT

A 4.2- to 300-K liquid helium cryostat has been constructed for cryogenic samples of D-T containing up to 4×10^{14} dis/s (10,000 Ci) of tritium radioactivity. The cryostat is enclosed in a secondary box, which acts as the ultimate container in case of a tritium release. Dry argon is flushed through the box, and the box atmosphere is monitored for tritium, oxygen, and water vapor. A rupture disk and abort tank protect the box atmosphere in case the sample cell breaks. If tritium breaks into the box, a powdered uranium getter trap reduces the 4×10^{14} dis/s (10,000 Ci) to 4×10^{9} dis/s (0.1 Ci) in 24 h. A backup palladium-zeolite getter system goes into operation if an overabundance of oxygen contaminates the uranium getter.

INTRODUCTION

There is considerable interest in controlled hydrogen fusion by lasers, electron beams, or magnetic confinement. The fusion fuel igniting at the lowest temperature is the three-component heavy hydrogen mixture, D_2-DT-T_2, commonly referred to as D-T. Because D-T can be used in liquid or solid form, the physical properties at cryogenic temperatures become of extreme interest.

*This work was performed under the auspices of the U.S. Energy Research & Development Administration.

In companion articles we reported on the phase diagram and other physical properties expected for D-T.[1,2] To measure some of these properties, we constructed a liquid helium research cryostat designed to hold up to 4×10^{14} dis/s (10,000 Ci) tritium, which is equivalent to only 7.5×10^{-6} m^3 of liquid D-T. Most of our design and construction effort went into the tritium containment system. This system is built in accordance with modern "zero release" standards, which have been adopted for protection of personnel and the environment. The method used is secondary containment, in which the entire experimental apparatus is housed in a gastight box. Although chances of a rupture in the cryostat are slight, any leaked tritium is again contained by the box.

THE D-T CRYOSTAT SYSTEM

The cryostat system is composed of the cryostat itself, liquid helium transfer lines, D-T gas pressure bottles and input lines, a rupture disk and abort tank, a quadrupole mass spectrometer, a helium leak detector, and two pumps.

The cryostat is a commercial, liquid helium unit (Air Products*) modified for tritium use by replacing all elastomer O-rings by metal (tritium radiation degrades elastomers). It is a small unit (1.5 W at 4.2 K, 8 W at 20 K), requiring no liquid nitrogen and containing only 2×10^{-6} m^3 liquid helium at any time. This liquid can evaporate into a large exhaust volume that passes out of the box. Therefore, no helium enters the box atmosphere; the entire path of the helium is gastight. The cryostat is insulated by a 1.3×10^{-6} Pa (10^{-8} Torr) vacuum, provided by a 0.175 m^3/s oil diffusion pump (with mechanical roughing pump). During assembly, leaks may be monitored by a helium leak detector (Varian), sensitive to 1.3×10^{-10} Pa (10^{-12} Torr) air, on the vacuum line.

---

*Reference to a company or product name does not imply approval or recommendation of the product by the University of California or the U.S. Energy Research & Development Administration to the exclusion of others that may be suitable.

The 2×10^{-6} m^3 liquid helium reservoir is inside a cold block, wrapped with heater wire to yield continuous temperatures from 4.2 to 300 K. The sample cell is attached to the cold block by a C-shaped copper connector. Varnish (General Electric 7031) is used for good thermal contact. A germanium temperature sensor, calibrated with liquid helium and the vapor pressure of D_2,[1] is glued to the sample cell. A stainless steel tube (3.18-mm o.d., 2.67-mm i.d.) runs the length of the cryostat to the sample cell and is pinned to the cold block to reduce thermal loss. This tube carries the D-T gas from an input pressure bottle and also removes the D-T to a small uranium getter trap outside the containment box. The D-T vapor may be analyzed by a quadrupole mass spectrometer (Uthe Technology International), sensitive to 1.3×10^{-12} Pa (10^{-14} Torr) N_2. The cryostat has been tested by the successful freezing of D_2.

The sample cell can contain up to 3×10^{-6} m^3 liquid or solid D-T. This amount, combined with that in the lines and pressure bottle, totals 4×10^{14} dis/s (10,000 Ci). Also, the thermal capacity of the cryostat is small to avoid large amounts of cryogenic liquid that might vaporize. Nevertheless, the possibility of a sudden breakage of even this small sample cell must be recognized. This is especially critical in optical experiments with glass sample tubes and viewports.

If the sample cell breaks, the tritium is contained in the cryostat vacuum jacket, because the vacuum pump to this space is closed off before loading the D-T. However, the pressure buildup in the vacuum space of the cryostat could reach 1 MPa (150 psi). To prevent the blowing out of optical windows or gaskets (and the tritium entering the box), a protective disk ruptures at 3.5×10^4 Pa (5 psi) over atmospheric pressure, and the gas passes into a 0.04-m^3 abort tank. Hence, the secondary tritium containment system is not required in this case.

THE TRITIUM CONTAINMENT SYSTEM

The main component of the tritium containment system (shown schematically in Fig. 1) is the argon flush box, inside of which are the cryostat and the tritium recovery equipment. A dry argon atmosphere

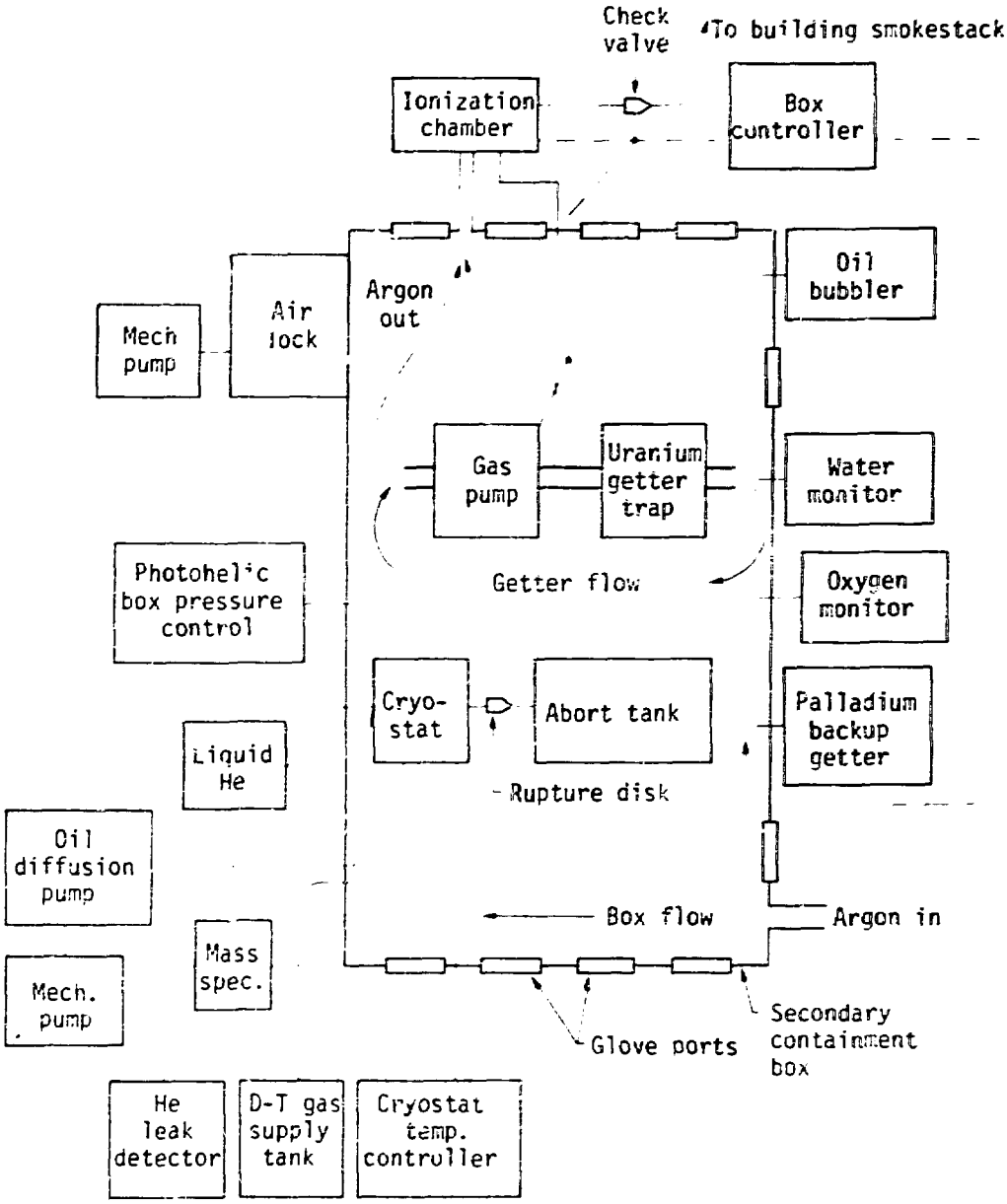

Fig. 1. Schematic of Tritium Cryostat Containment.

is maintained in the box to avoid conversion of tritium to the more dangerous tritiated water and to avoid contamination of the tritium recovery system. A large assortment of monitors and control valves are interfaced with the box. The completed containment system, including the enclosed cryostat, is shown in Fig. 2.

The box (Vacuum Atmosphere) is made of aluminum with Pyrex windows clamped into rubber gaskets and has an internal volume of 2 m^3. The cryostat is attached by O-ring seals to the box roof. There are 10 ports for rubber gloves along the sides, and air and water vapor slowly permeate through these gloves while in use. To purge these contaminants, a steady flow of dry argon (H_2O, O_2, and N_2, less than 1 ppm) is passed through the box at a 1.5×10^{-4} m^3/min rate. The argon passes through a one-way check valve and exhausts into the building smokestack. If a rubber glove is punctured, all operations must cease until the glove is replaced and the atmosphere reestablished. (It requires one week of argon purge at a high flow rate to achieve the equilibrium low-contaminant atmosphere.) When not in use, the glove ports are covered with aluminum plates seated against flat rubber gaskets. The space between the plates and the rubber gloves is pumped to 1.3 Pa (10^{-2} Torr) with the second 0.25-m^3/s mechanical pump. Articles may be brought into the box through an air lock connected to this mechanical pump. Dry argon is admitted to bring the air lock to atmospheric pressure.

The box argon atmosphere is controlled to 101 ± 0.4 kPa (1 atm ± 0.3%) by a photoelectric rubber diaphragm switch (Dwyer Instruments), which electrically opens the mechanical pump valve if the box pressure is too high or opens the argon inlet valve if it is too low. As a backup system, in the event of photoelectric control failure, the box is connected to the outside world via an oil bubbler. If the box pressure is too high, the excess gas will be forced out through the oil and into the stack. If the box pressure is too low, stack air will be sucked into the box, preserving the integrity of the atmosphere but saving the box from collapse.

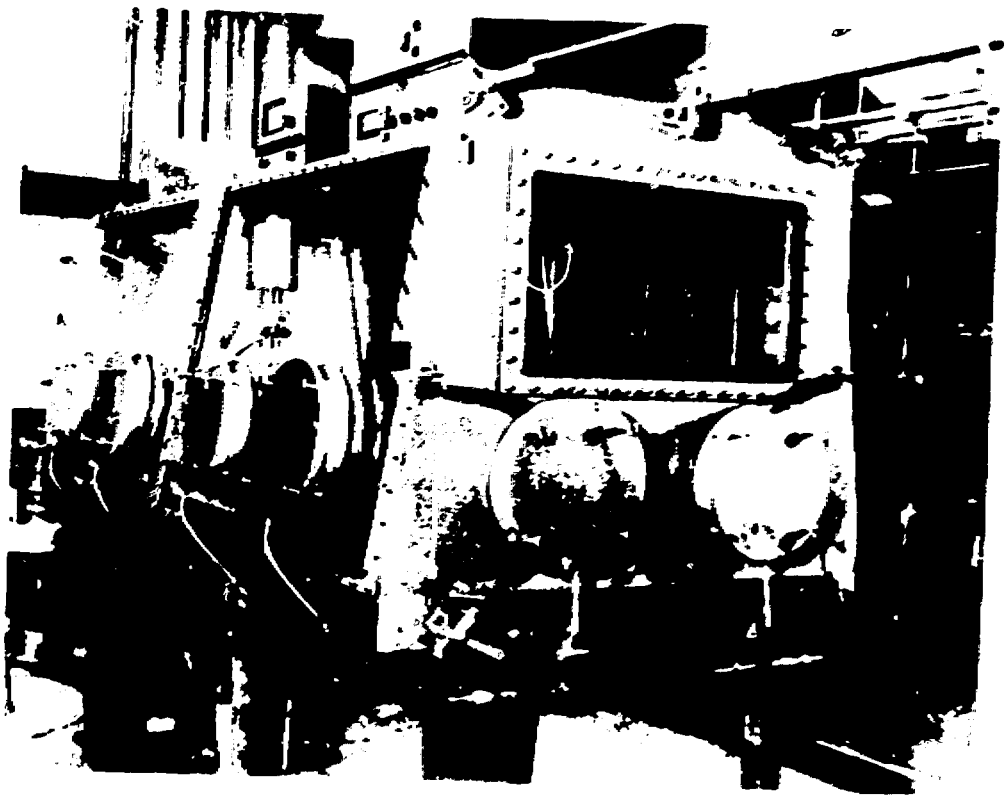

Fig. 2. Containment System for Cryostat.

The tritium concentration in the system is monitored by an ionization chamber in the argon outlet pipe. The ionization chamber is an all-metal unit, bakeable to 450°C, designed especially for low-level tritium work.[3] Its lowest sensitivity is about 7.4×10^7 dis/m^3·s (2 μCi/ℓ). The control system may be set to operate at activity levels as low as 4×10^{10} dis/s (1 Ci) in the entire box (1.9×10^{10} dis/s or 500 μCi/ℓ in the ionization chamber). If the box radioactivity rises above this value, the control system closes the argon inlet and argon exhaust, opens the uranium getter, and starts the getter circulating pump. As a final precaution, the laboratory containing the cryostat system is continuously monitored by a building system alarm set to trigger at only 1.9×10^6 dis/m^3·s (50 μCi/m^3).

Water vapor and oxygen must be kept low for several reasons. First, tritium may exchange with hydrogen in water to form tritiated water, which is readily absorbed into the human body and, therefore, is about a thousand times as dangerous as tritium gas. Second, both water and oxygen will react with the uranium getter trap to form UO_2, which cannot be removed by heating. This takes potential tritium-absorbing capacity from the getter. Last, the uranium powder of the getter is pyrophoric in the presence of large quantities of oxygen. For these reasons, the water vapor in the box is monitored to 1 ppm by ac impedance changes across an Al_2O_3 disk (Panametrics). The oxygen is monitored to 1 ppm (proprietary method, Teledyne). The systems give alarms at concentrations of 5 (water) and 10 (oxygen) ppm.

If the box fills with tritium because of a cell rupture, the radioactivity will be removed by the uranium getter trap. This getter, shown schematically in Fig. 3, is the most advanced design to date.[4,5] A metal bellows pump of 0.142-m^3/min capacity circulates the box atmosphere through the getter. The getter assembly is basically two concentric cylinders. The inner cylinder holds six trays of "activated" uranium, activated by reacting uranium chips to hydride and then thermally decomposing the compound. The result is a uranium powder of micrometer size and large surface area. The uranium powder is prevented from

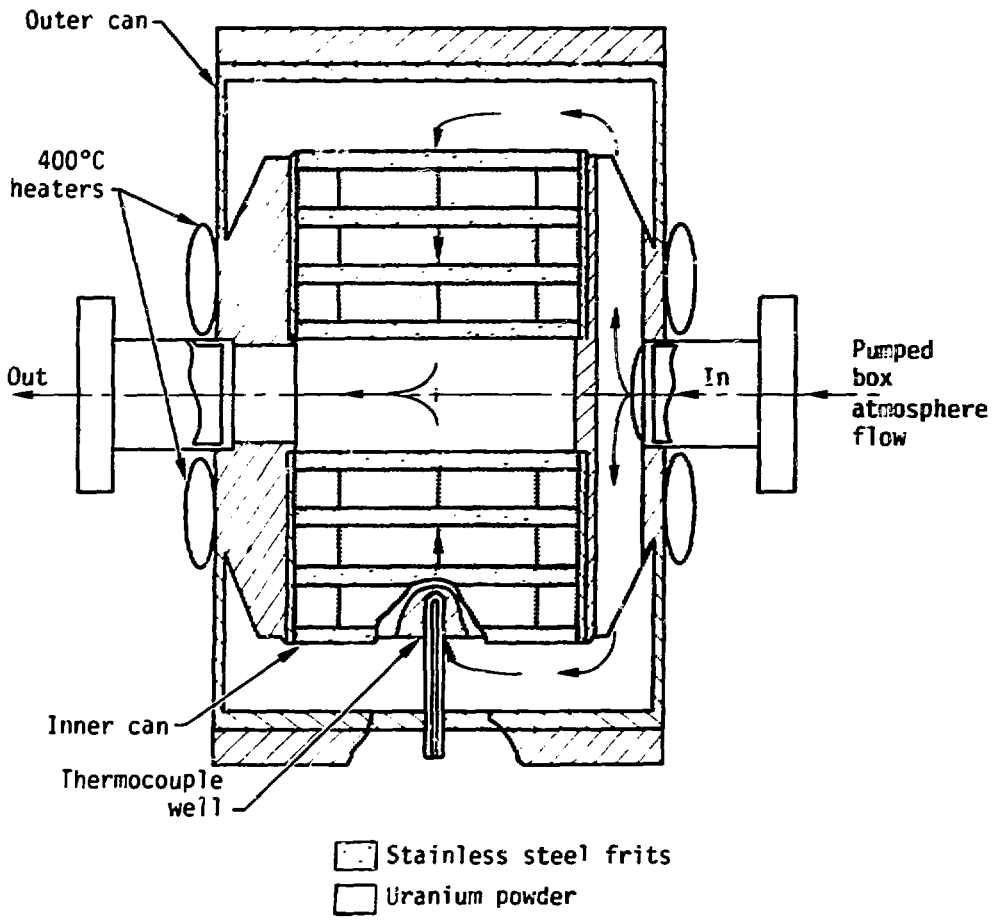

Fig. 3. Schematic of Powdered Uranium Getter Trap.

spilling out by 5-μm stainless steel frits through which the box atmosphere is passed. The outer cylindrical can serves to further enclose the uranium and also permits maintenance of an expected 3.5×10^4 Pa (5 psi) pressure differential across the uranium beds. The uranium reacts with hydrogen at room temperature. Four band heaters surround the outer cylinder and can heat the uranium hydride to 400°C. At this point, the hydride decomposes, and the tritium may be collected in a separate vessel.

The getter contains 1.5 kg of uranium, and only 1.75% of its capacity will be needed to hold 4×10^{14} dis/s (10,000 Ci) of tritium.

The gettering times for 4×10^{14} dis/s (10,000 Ci) tritium are estimated to be: after 4 h, 4×10^{12} dis/s (100 Ci); after 8 h, 4×10^{10} dis/s; (1 Ci), and after 24 h, 4×10^9 dis/s (0.1 Ci). The getter can, therefore, remove 99.999% of the total tritium in an accident of maximum size.

Finally, provision is made for a backup system for the uranium getter trap. Should the D-T gas from an accident be mixed with excess oxygen from a leak, a portable palladium-zeolite molecular sieve may be attached to the box. The palladium causes the tritium and oxygen to form water that is retained on the zeolite in a form not easily recoverable.

REFERENCES

1. C. K. Briggs, R. G. Hickman, R. T. Tsugawa, and P. C. Souers, "Estimates of Some Cryogenic DT Properties," presented at the International Conference on Radiation Effects and Tritium Technology for Fusion Reactors, Gatlinburg, TN, October 1-3, 1975.

2. P. C. Souers, R. G. Hickman, and R. T. Tsugawa, "Estimated D_2-DT-T_2 Phase Diagram in the Three-Phase Region," presented at the International Conference on Radiation Effects and Tritium Technology for Fusion Reactors, Gatlinburg, TN, October 1-3, 1975.

3. C. Colmenares, Bakeable Ionization Chamber for Low-Level Tritium Counting, Lawrence Livermore Laboratory, Rept. UCRL 74680 (1973).

4. C. L. Folkers and M. F. Singleton, Collection of Deuterium on a Uranium Getter during Dynamic Flow Conditions, Lawrence Livermore Laboratory, Rept. UCRL 76754 (to be published).

5. C. Colmenares, A. Ladd, B. Monahan, and C. L. Folkers, Lawrence Livermore Laboratory, private communication (1975).

KC/lc

ANALYSES AND HYDROGEN-ISOTOPE-TRANSPORT CALCULATIONS OF CURRENT AND FUTURE DESIGNS OF THE LLL ROTATING-TARGET NEUTRON SOURCE*

S. A. Steward, R. Nickerson, and R. Booth

Lawrence Livermore Laboratory

ABSTRACT

Analyses of the present titanium-tritide RTNS targets are presented. These results include the hydrogen-isotope content of new and used targets, metallography, scanning electron microscopy, and hydrogen-isotope-diffusion calculations using a heat-flow finite-difference computer code. These latter calculations indicate that a combination of long target life and high neutron output is optimized when the rate of hydrogen isotope evolution from the target balances the deposition rate from the beam. Auger spectra show that carbon and oxygen species are present in the bulk and on the surface.

INTRODUCTION

Description and Function of the Neutron Source

The Rotating-Target Neutron Source (RTNS) has been described in detail previously.[1-4] The current target design is shown in Fig. 1. The target itself is a 9" concave water-cooled Amzirc** dish coated with titanium tritide. A 15-mA deuteron beam accelerated to 400 keV impinges on this target, which rotates at 1100 rpm and produces a 14-MeV neutron-source strength greater than $3 \cdot 10^{12} s^{-1}$ for approximately 100 hr of intermittent operation.

*Work performed under the auspices of the U.S. Energy Research & Development Administration, under contract No. W-7405-Eng-48.

**Reference to a company or product name does not imply approval or recommendation of the product by the University of California or the U.S. Energy Research & Development Administration to the exclusion of others that may be suitable.

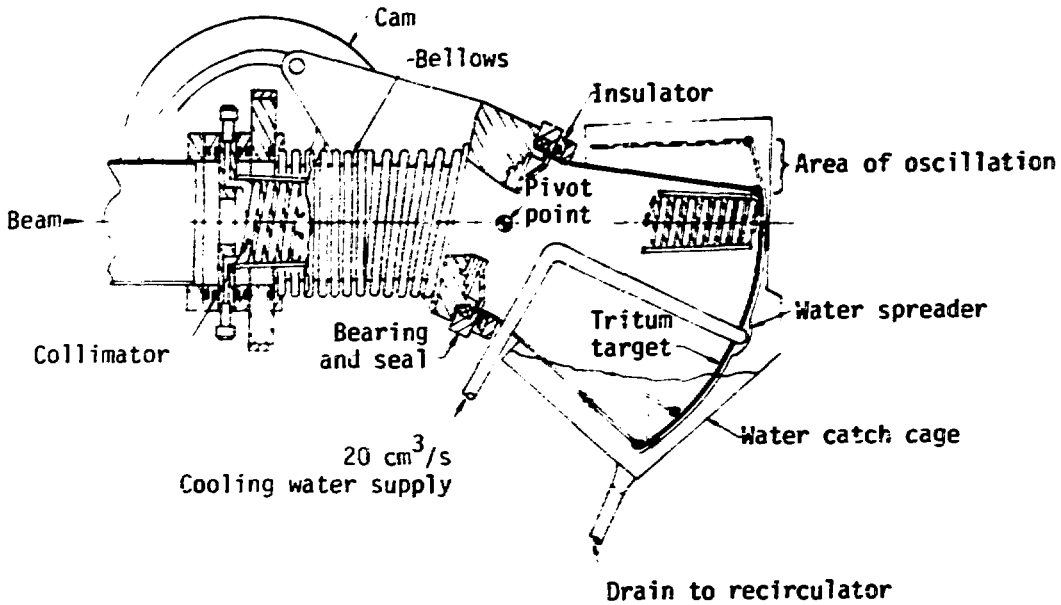

Fig. 1 Sketch of the rotating-target neutron source (RTNS) target section.

A high-intensity 14-MeV-neutron source is desirable especially for materials research in fusion-reactor technology and also in biomedical applications. Currently, fluences of approximately 10^{17} cm^{-2} have been achieved in 60 hr of experimental time on the LLL-RTNS.

Purpose for Studying Target Performance

It has been projected that neutron fluences of 10^{21} cm^{-2} may be needed to adequately predict some radiation effects that would arise in an operating CTR reactor. The realization of such experimental conditions is still many years away; however, the LLL RTNS is the most intense source of 14-MeV neutrons currently available. Therefore, it will be the premier instrument for radiation-effect studies in the near future. A program to upgrade the RTNS design for the proposed new facility has been undertaken, so that a ten-fold increase in the neutron-source

strength may be obtained, thus yielding greater possible fluences. This effort is in three areas:

- Ion source, accelerator, and beam transport.
- Mechanical design of the rotating target.
- Target materials and fabrication.

The latter category is the one to which this paper is devoted.

EVALUATION OF PRESENT TARGETS

The present titanium tritide targets, produced at Oak Ridge National Laboratory, lose half their neutron output in 30 - 100 hr of normal operation. The initial neutron output at the same operating conditions varies greatly between targets. Although considerable research with neutron generators employing metal tritides has been previously reported, most of it has dealt with units whose neutron output and useful operating life were considerably smaller than that demanded from the LLL RTNS. Also, their environments in use were much more controlled than is now possible with the Livermore instrument.

A program is being undertaken at the Laboratory to determine what parameters affect target life and neutron output. At present, three used targets have been analyzed, in addition to three small coupons that were especially prepared at Oak Ridge that were never bombarded with deuterons. Using these data, which are reported here as background information, we are initiating a program in which considerable data for each target will be collected in the next year. Besides a coupon for later analysis at LLL, production data will be provided for targets received from Oak Ridge. This will include substrate bakeout times and temperatures, vacuum conditions, and tritium absorption pressures and times. RTNS operational data for each target, such as target position, speed, beam current, and tritium release, will also be logged for comparison with the physical, chemical, and metallographic measurements that were obtained on each used target and the aforementioned coupons. The techniques outlined will tell us the condition of the new and used targets and how the RTNS operation has altered them.

Metallography

Small samples are punched from the coupons and targets without contact between the punch and the surface to be studied. A laboratory diamond saw is being investigated as an alternative cutting instrument. These samples are vertically encased in epoxy and then polished making it possible to study the target cross-sections under an optical microscope. These examinations provide information concerning tritide adhesion, sputtering, cracking, and substrate crystallization.

Chemical Analysis

Several punched discs are heated in vacuo in a mass spectrometer to determine the quantities of each hydrogen isotope species present; i.e., H_2, HD, D_2, HT, DT, and T_2. These degassed samples are then dissolved in acid and the total amount of titanium in each disc is determined by atomic absorption spectroscopy. From these two measurements the initial and final gas-to-metal ratios may be calculated.

Surface Analyses

Scanning Electron Microscopy (SEM) is employed to determine the surface characteristics of the targets before and after their use on the RTNS. In addition, the energy-dispersive accessory was utilized to determine whether there were any metallic impurities in upper layers of the bulk material.

Our Laboratory's Auger Electron Spectroscopy (AES) capability allows the study of light elements, except hydrogen, that may be present on the surface. Also, an Electron Spectroscopy for Chemical Analysis (ESCA) spectrometer exists and may be employed to study elemental valence states at the surface. Neither AES nor ESCA can currently be used with tritiated samples, however, because of the need to avoid radioactive contamination.

CURRENT STUDIES OF NEW TARGET MATERIALS

In cooperation with the General Electric Neutron Devices (GEND) Department, we have initiated a program to evaluate other binary metal tritides; e.g., scandium, erbium, and yttrium. Small, internally cooled targets coated with these tritides will be placed on the RTNS in a pulsed mode and compared for neutron strength and projected life. Gas-to-metal ratios, Auger, and SEM studies for each target are carried out at GEND. Similar measurements will be made after the RTNS irradiations.

Also, hydrogen absorption measurements of certain titanium alloys are being undertaken to determine their suitability as target materials.

FUTURE STUDIES OF NEW TARGET MATERIALS

Consideration will also be given to multilayered or composite films after sufficient information has been gathered from studies of the present titanium tritide targets and other candidate tritides. Such target concepts are not new. A patent describing a target consisting of a very stable tritide; e.g., erbium or scandium, on top of a less stable one; e.g., titanium, was published in 1973.[5] This target in principle would transfer tritium from the less stable tritide reservoir into the upper tritide reaction zone on heating, thus replenishing the depleted tritium.

Researchers at the NASA Lewis Research Center recently described a multilayered target, shown in Fig. 2, that consists of a copper substrate and layers of palladium, titanium, titanium oxide or nitride.[6] Such a design would flood the titanium layer with the unreacted deuterons and then drain the excess into the palladium and voids. The oxide or nitride barriers will supposedly prevent hydrogen isotope diffusion into or from the titanium tritide target layer. However, it has been shown that titanium oxide may not serve as an effective diffusion barrier.[7]

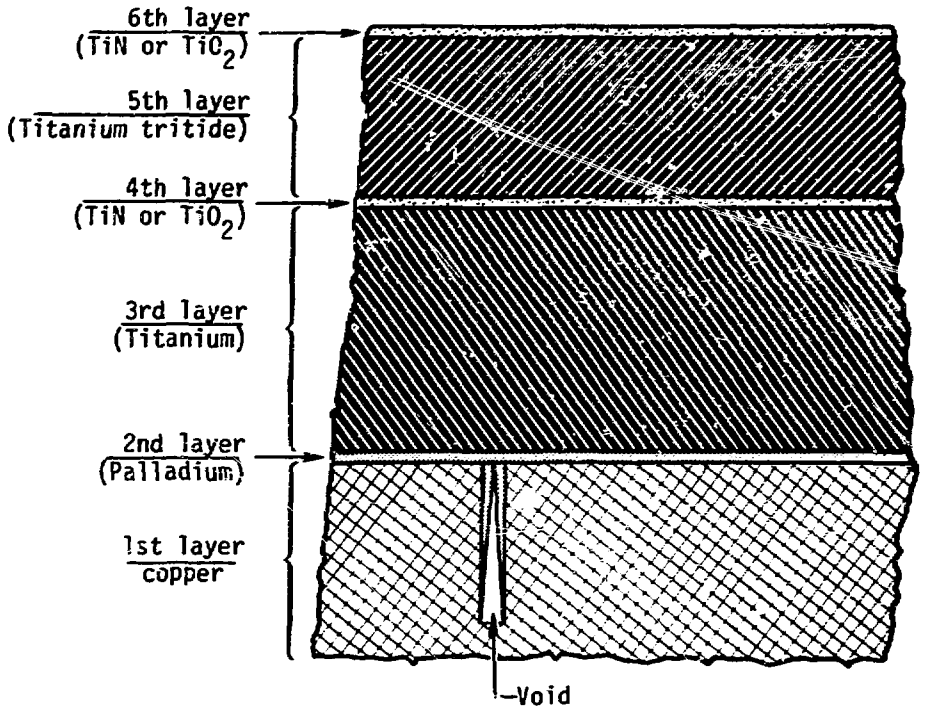

Fig. 2 NASA design of a multilayered tritide target.

PRELIMINARY EXPERIMENTAL RESULTS

Metallography

A photograph of a typical target after approximately 100 hr use is shown in Fig. 3. The concentric rings are caused by the deuteron beam. A fresh target has similar features and color, but without rings.

The metallographic cross section in Fig. 4 a) is typical of a fresh target. The tritide layer follows the substrate contour quite well, and the adhesion seems good. There was a cracking problem with one specimen, but this may have been a result of damage during sample preparation. In another case, poor adhesion to the substrate was observed.

Figure 4 b) is a similar cross section for a used target. The surface has been noticeably flattened by deuteron bombardment. Fragments produced by this bombardment are also apparent. Approximately 25% of the titanium tritide was removed by the beam during the life of the target, Figs. 4 a) and b).

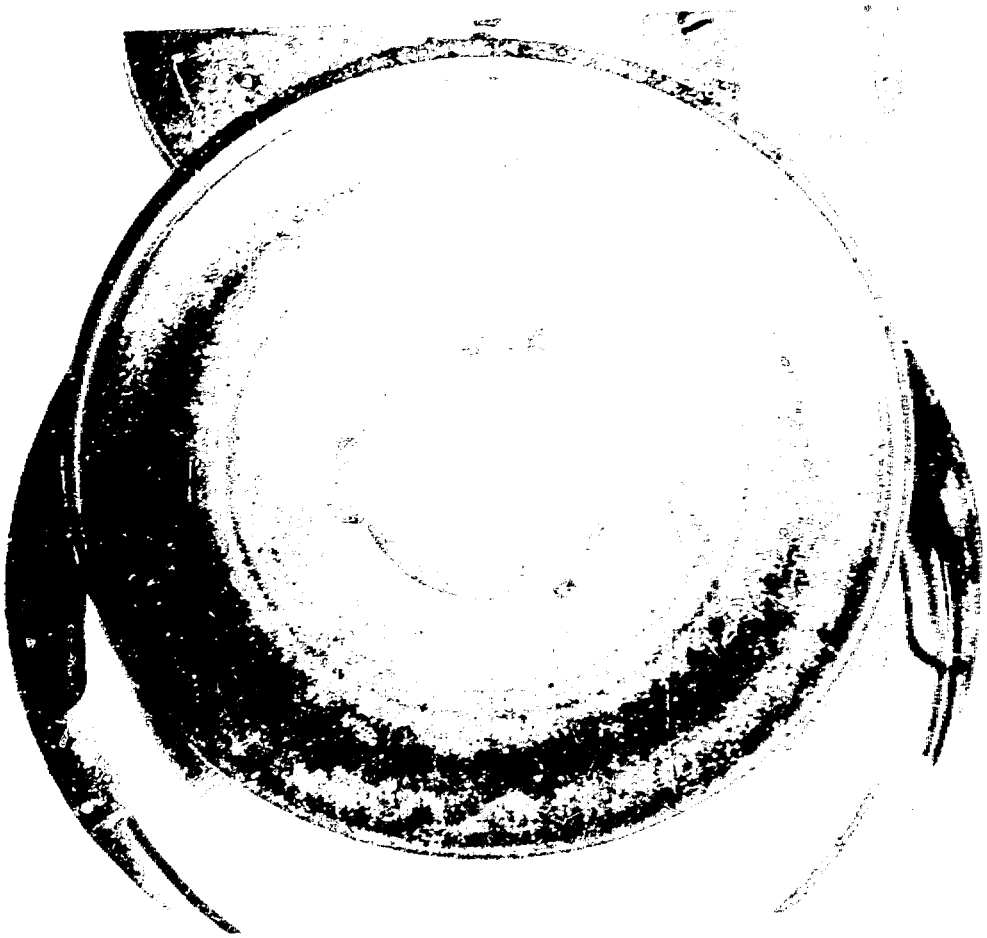

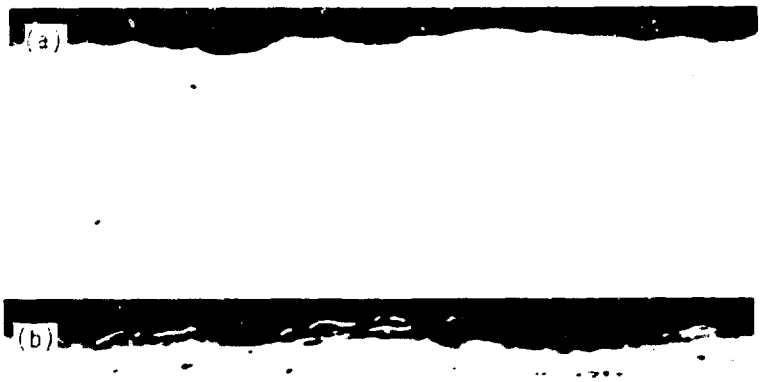

Fig. 4 Metallographic cross sections, X 500: a) new target, b) used target showing sputtering caused by deuteron beam.

Electron Microscopy

A SEM view of a new target surface is shown in Fig. 5a). This target was one of several special targets mentioned earlier. Although these are not actually coupons made simultaneously with RTNS targets, the similarity in processing should make them representative of new targets. The surface is reasonably flat, except for a number of linear ridges, which are probably reproductions of the substrate surface.

The surface of a bombarded target is shown in Fig. 5 b). Note the considerable difference in comparison with the new surface. The sputtering of the deuteron beam has produced a crater effect, and tritide particles can also be seen. These may be the same as seen in the previously described cross sections. It was formerly thought that the inner perimeter of the target was not bombarded by the beam, but in every case studied thus far, some sputtering is evident, although not to the same extent as is encountered further towards the outside edge.

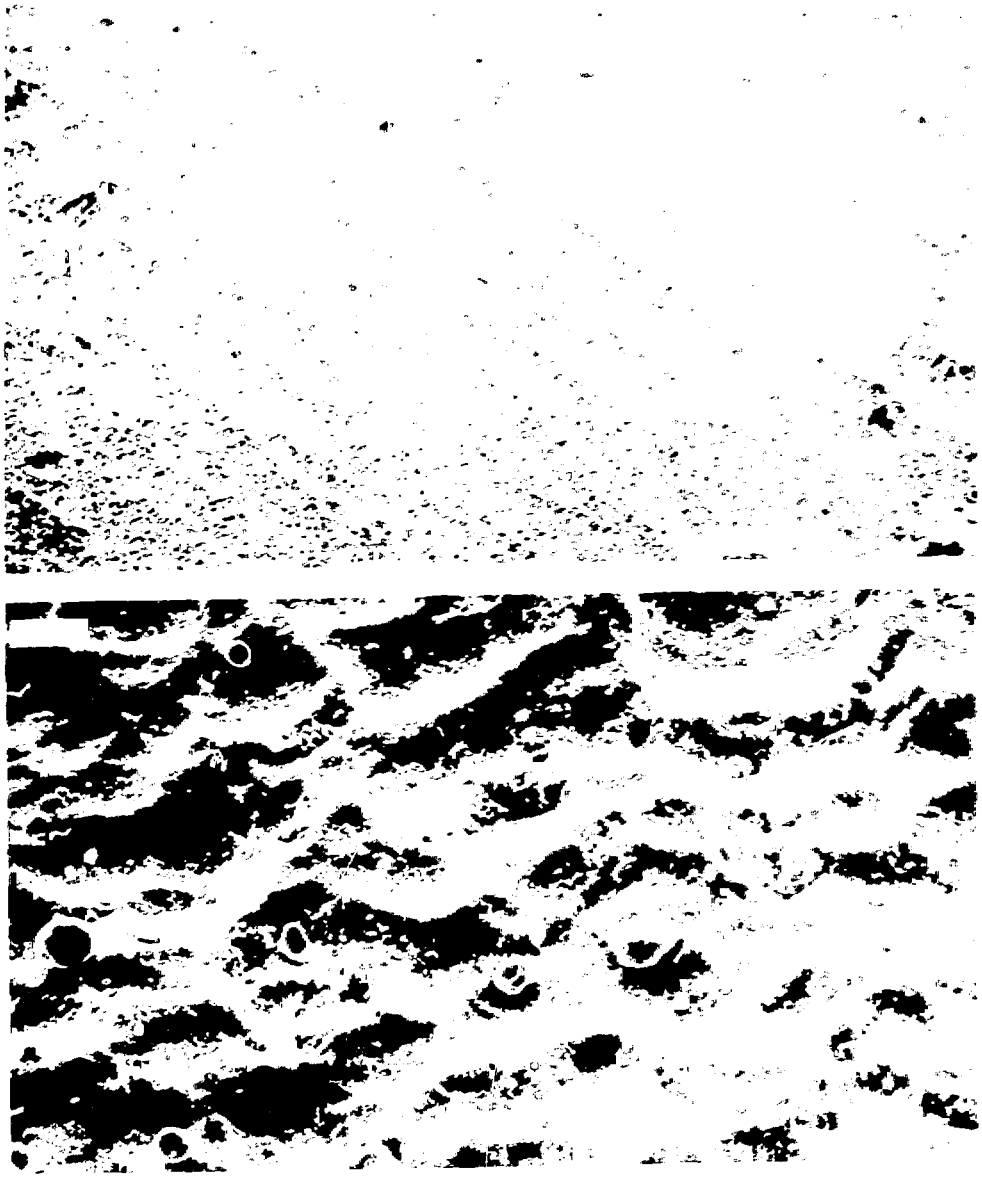

Fig. 5 Scanning electron microscope views: a) [illegible], b) used target, illustrating surface sputtering.

The energy-dispersive capability of the SEM was used to determine the metallic composition of the near-surface region. No metal other than titanium was detected.

Surface Analysis

An Auger spectrum was taken on a small hydrided Oak Ridge target. Since the available Auger spectrometer was not in a tritium-handling area, no tritided specimens could be examined. The surface information obtained from the small targets should give us an indication of the actual target surface prior to deuteron bombardment.

A reproduction of the Auger spectrum* of the target as received is seen in Fig. 6 a). The sample initially had a deep blue color, which stimulated the interest in studying its surface. Slight traces of sulphur and chlorine were found, in addition to some copper. As expected, numerous titanium peaks exist, although the carbon and oxygen peaks predominate. The chemical composition of these chemisorbed species cannot be deduced from Auger spectra.

The sample was subsequently ion bombarded in argon at 10 mPa ($8 \cdot 10^{-5}$ Torr) for one hour. The sputtering removed about 60 nm of material, changing the blue color back to the characteristic hydride gray. On exposure to air the blue color returned within 1 min., indicating that oxygen chemisorption was the probable cause. Such occurrences have not been noticed on the larger RTNS targets, however. Possibly the blue color is that of titanium sesquioxide, or interference produced by some other oxide layer. An ESCA study may resolve this uncertainty.

Figure 6 b) is the Auger spectrum of the specimen after argon sputtering. The spectrum of the sputtered sample was taken with a beam current three times greater than with the initial run. This will normally produce a signal approximately three times greater with the same surface concentration. Normalizing to the titanium signal, the carbon peak decreases by a factor of four and the oxygen peaks by three. The sulfur, chlorine, and copper peaks have disappeared. Two other

---

*These spectra were kindly provided by C. Colmenares of this Laboratory.

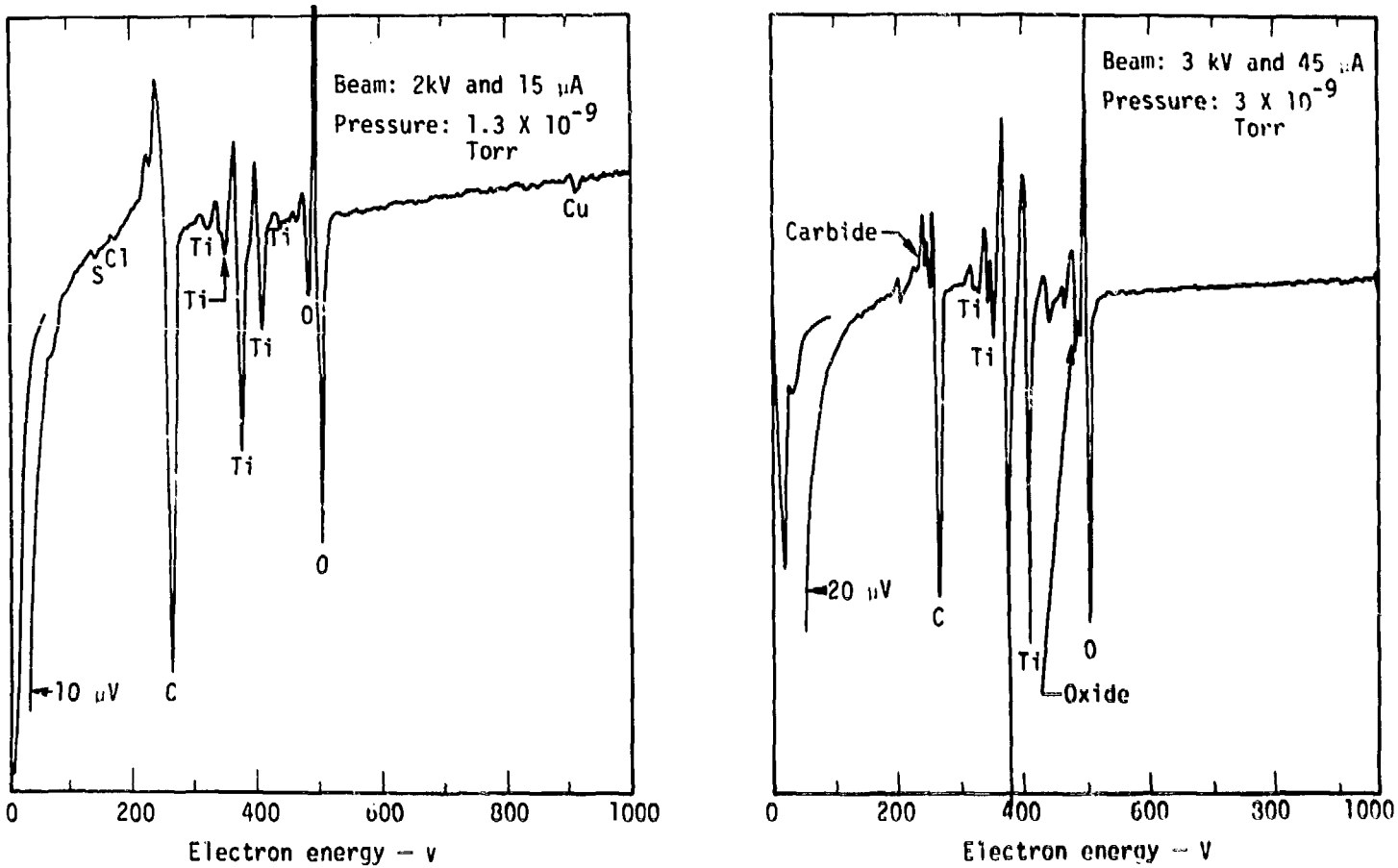

Fig. 6 Auger spectra: a) new target, showing various impurities on the surface, b) same target after argon bombardment, showing bulk carbide and oxide impurities.

signals previously interpreted as characteristic of carbide[8] and oxide[9] anions have appeared, however. These carbide and oxide peaks may be due to diffusion of adsorbed atoms during hydriding or to entrapment of residual gas and pump oil during titanium evaporation.

Hydrogen Isotopic Content in Targets

The computed gas-to-metal ratios and errors for each target studied are listed in Table 1. Although the number of targets we have examined is still small, certain consistent findings may be stated with regard to deuterium and tritium content.

1. If the small targets we have examined are representative of a new 9-in. one, the tritium loading is high. The tritium-to-titanium ratios are 1.8-2.0.

2. There is a 10-20% loss of tritium by thermal degassing, in addition to the losses due to beam sputtering.

Table 1. Experimental hydrogen-isotope-to-metal ratios for new and used targets.

Target No.	T/Ti New	T/Ti Bombardment		D/Ti Bombardment	
		Light	Heavy	Light	Heavy
1	1.78 ± 0.16				
2	1.81 ± 0.08				
3	2.02 ± 0.02				
4		1.17 ± 0.12	1.04 ± 0.11	0.107 ± 0.010	0.244 ± 0.02
5		1.74 ± 0.11	1.35 ± 0.08	0.128 ± 0.003	0.223 ± 0.12
6		1.84 ± 0.01	1.55 ± 0.03	0.012 ± 0.003	0.221 ± 0.011

3. The deuteron beam strikes the inner portion of the target, releasing some tritium. This confirms the evidence for sputtering seen in the SEM photographs.

4. A significant quantity of deuterium is implanted in the target. The amount depends upon the length of the bombardment.

In the future, when operational data have been gathered for each target studied, it may be possible to determine the relative influence of gettering action, diffusion and ion implantation on the hydrogen-isotope content of various regions on the target.

HYDROGEN-ISOTOPE-TRANSPORT CALCULATIONS[10]

The similarities between the mathematics of thermal conductivity and diffusion are well known. A finite-difference code, TRUMP, can be used to solve the familiar differential equation:

$$\rho C_{sp} \frac{\partial T}{\partial t} = k \frac{\partial^2 T}{\partial x^2} \qquad (1)$$

where T = absolute temperature
t = time
ρ = density
C_{sp} = specific heat
k = thermal conductivity
x = distance.

This code can handle other aspects of heat transfer; e.g., heat-generation sources, heat losses through surfaces and layers of different materials. By comparing Eq. (1) with Fick's second law for diffusion

$$\frac{\partial C}{\partial T} = D \frac{\partial^2 C}{\partial x^2} \qquad (2)$$

where D = diffusion coefficient
C = concentration

it can be seen that TRUMP may be applied to mass transport problems, in general, and the layered rotating target in particular.

Initially, two extreme cases of target operation were studied. The results of those calculations are given in Table 2.

For the high-power-density case, the high heating causes the gas release rate to dominate over deposition. Actual operation at such levels would cause rapid tritium loss and unacceptably short target life.

For operation at lower power density the deuterium deposition rate is greater than the temperature-dependent tritium loss. The target life is thus determined by the rate at which deuterium replaces tritium as the hydrogen-isotope content of the titanium approaches stoichiometry.

In order to determine the optimum operating conditions of targets planned for the new RTNS, TRUMP calculations were performed for a 28 cm diameter target rotating at 576 rad/s (5500 rpm). Initially heat flow calculations were employed to obtain time-temperature data at various beam sizes and power. These results are plotted in Fig. 7. Using these results, mass deposition and loss rates were determined and are shown in Fig. 8. It is obvious that the mass flow of deuterium and tritium out of

Table 2. Parameters of two extreme cases of RTNS operation.

	Case I	Case II
Linear target velocity ($cm \cdot s^{1}$)	115	51
Power (kW)	6	6
Beam density at FWHM ($kW \cdot cm^{-2}$)	21	85
Max. surface temp (K)	582	1223
D deposition (ng/cycle)	0.502	2.38
D + T release (ng/cycle)	0.138	320
Ratio of deposition-to-release (r_i/r_o)	3.64	0.0074

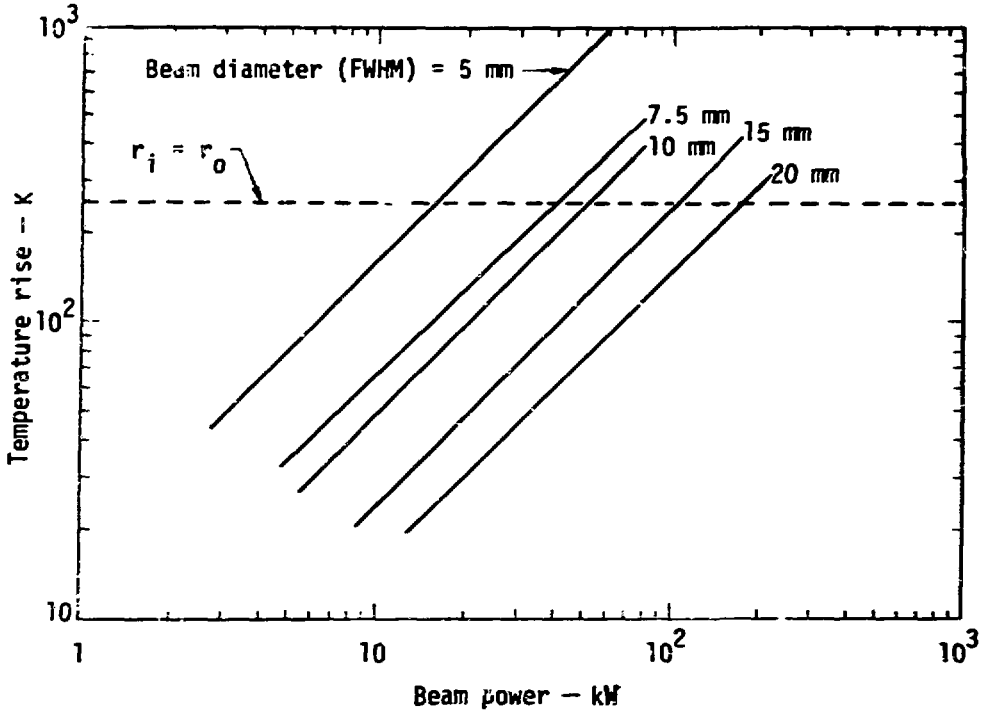

Fig. 7 Power-temperature results from heat-flow calculations.

the target is much more sensitive to beam power than is the deposition rate of deuterium into the target.

In Table 3, beam powers are given for the selected beam profiles at mass-flow ratios of 0.5, 1, and 2. A separate study indicated that for a 20-cm-diam target rotating at 576 rad/s (5500 rpm) and being bombarded at 0.05 ng/cycle, the tritium content would drop by 50% (the target half life); (a) in 35 hr with $2r_i = r_o$, (b) in 85 hr with $r_i = r_o$ and (c) in 242 hr when $r_i = 2\ r_o$. This information, coupled with the data in Table 3, shows that increasing the input power by ∿ 12% raises the front surface temperature enough to decrease the target half life by a factor of about 2.5. This results in an integrated neutron output loss of approximately 55% of the output at $r_i = r_o$. Decreasing the input power by ∿ 12% lowers the front face temperature and triples the target half life for an integrated neutron output gain of 164%. This increase in total neutron output occurs at the expense of neutron source strength, however.

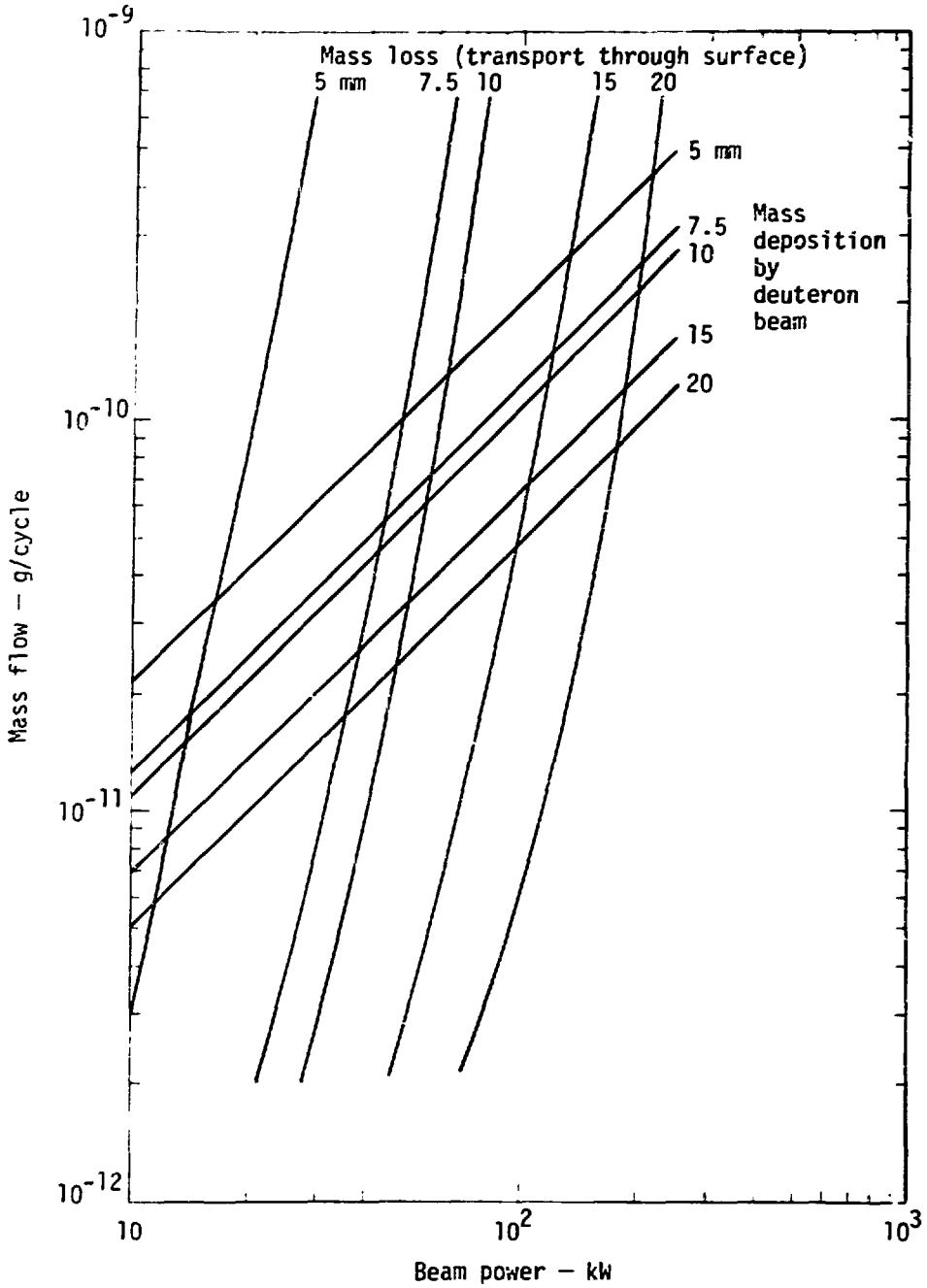

Fig. 8 Hydrogen-isotope deposition and loss rates.

Table 3. Beam powers at selected beam profiles and gas exchange rates.

Beam Profile FWHM (mm)	Beam Power (KW)		
	$r_i = r_o$	$2r_i = r_o$	$r_i = 2r_o$
5	16	18	14
7.5	42	48	37
10	56	62	49
15	101	112	89
20	166	180	146

In conclusion, adjusting the operating parameters to balance the input of deuterons from the beam against the combined losses of deuterium and tritium from sputtering and thermal degassing ($r_i = r_o$) gives an optimum combination of neutron source strength and target life. A large deviation from this condition imposes severe penalties in either lifetime or intensity.

SUMMARY

The theoretical and experimental studies presented in this report show several important features of targets as they relate to the LLL RTNS operation. These are:

- Deuteron-beam bombardment causes significant sputtering of the titanium tritide layer.
- Thermal heating from the beam degasses tritium from the remaining tritide.
- Carbon and oxygen species occur in the bulk and on the surface of the tritide layer.
- Theoretical calculations indicate that operation of the RTNS so that the deuteron bombardment rate equals the deuterium and tritium outgassing rate ($r_i = r_o$) permits both long target life and high neutron strength.

1. F. Booth, IEEE Trans. Nucl. Sci. NS-14, 943 (1967).

2. F. Booth and H. H. Barschall, Nucl. Instr. Methods 99, 1 (1972).

3. W. S. Lyon, Bibliography, H. H. Barschall, F. Booth, and C. Wong, Characteristics of the Rotating-Target Neutron Source and its Use in Radiation-Effects Studies, Lawrence Livermore Laboratory, Rept. UCRL-76557 (1975).

4. F. Booth, H. H. Barschall, and F. Colberg, IEEE Trans. Nucl. Sci. NS-20, 472 (1973).

5. H. Coplan, U.S. Patent No. 3,746,399, October 16, 1973.

6. Authors unknown. Long-Life Neutron-Generator Target Using Deuterium Pass-Through Structure, NASA Lewis Research Center, Rept. B74-10063 (1974).

7. C. W. Schoenfelder and J. F. Swisher, J. Vac. Sci. Technol. 10, 962 (1973).

8. S. P. [illegible] and J. C. Riviere, Surface Sci. 25, 609 (1971).

9. C. Colvenaros, Lawrence Livermore Laboratory, private communication (August 1975).

10. The results presented in this section were abstracted from: R. A. Nickerson, Hydrogen-Isotope Flow in the Rotating-Target Neutron Source, Lawrence Livermore Laboratory, Rept. UCRL-51737 (1975).

CHROMATOGRAPHIC MEASUREMENT OF ISOTOPIC HYDROGEN IMPURITIES IN PURIFIED TRITIUM

D. K. Warner
C. Kinard
D. R. Bohl

Monsanto Research Corporation, Mound Laboratory

ABSTRACT

A cryogenic gas chromatograph is described that was constructed for dedicated analysis of permanent gas and hydrogen isotopic impurities in tritium and deuterium-tritium mixtures. The operating characteristics of this instrument and some results are presented in order to introduce gas chromatography as an analytical technique for potential application to CTR technology situations that require accurate measurement of parts per million and higher levels of isotopic and permanent gas impurities in tritium, deuterium, or mixtures of the isotopes.

INTRODUCTION

The use of gas chromatography for qualitatively separating hydrogen isotopes has been previously demonstrated by several investigators,[1,2,3] and a brief description of its use as a quantitative method has also been published.[4] Chromatography has proven over the past two decades to be a sensitive, accurate, and low-cost analytical tool, but even with its demonstrated capability of separating hydrogen isotopes it has not been fully developed and exploited as a means of assay for these isotopes, and mass spectrometry remains the principal method for hydrogen isotopic analysis. As a technical objective, this paper will describe a cryogenic gas chromatograph (G.C.) that we have developed and used for over two years at Mound Laboratory for the determination of low-level hydrogen isotopic and permanent gas

[illegible] and in mixtures [illegible], we wish to [illegible] chromatographic [illegible] that require accurate [illegible], for example, the [illegible], gas storage or [illegible] in the assay of injection or exhaust [illegible].

EXPERIMENTAL

[illegible] the gas chromatograph is shown in [illegible] several basic design features which are [illegible] instruments, and some of these [illegible] for the containment and recovery [illegible] which pass through the instrument; other [illegible], mainly to maintain the simplicity of [illegible]. For example, (1) variable temperature [illegible] or detector, (2) the [illegible], (3) the columns are relatively [illegible], and (4) flow control changes are not easily [illegible]. These features serve to simplify the hardware required [illegible] of the unit.

Referring to Figure 1, notice that the instrument has [illegible] valves, each of which services one column, and that both columns are functional rather than one being merely a reference column. Also, the flow is split at the detector to reduce the flow rate through the low-volume thermistor detector channels; the effect of this reduced flow is to increase the sensitivity of the detector. A significant design feature of the G.C. is the backflow regulator/vacuum pump combination that isolates the instrument from flow restrictions that are characteristic of the effluent removal system that is required for the safe disposal of the exhaust [illegible] the chromatograph.

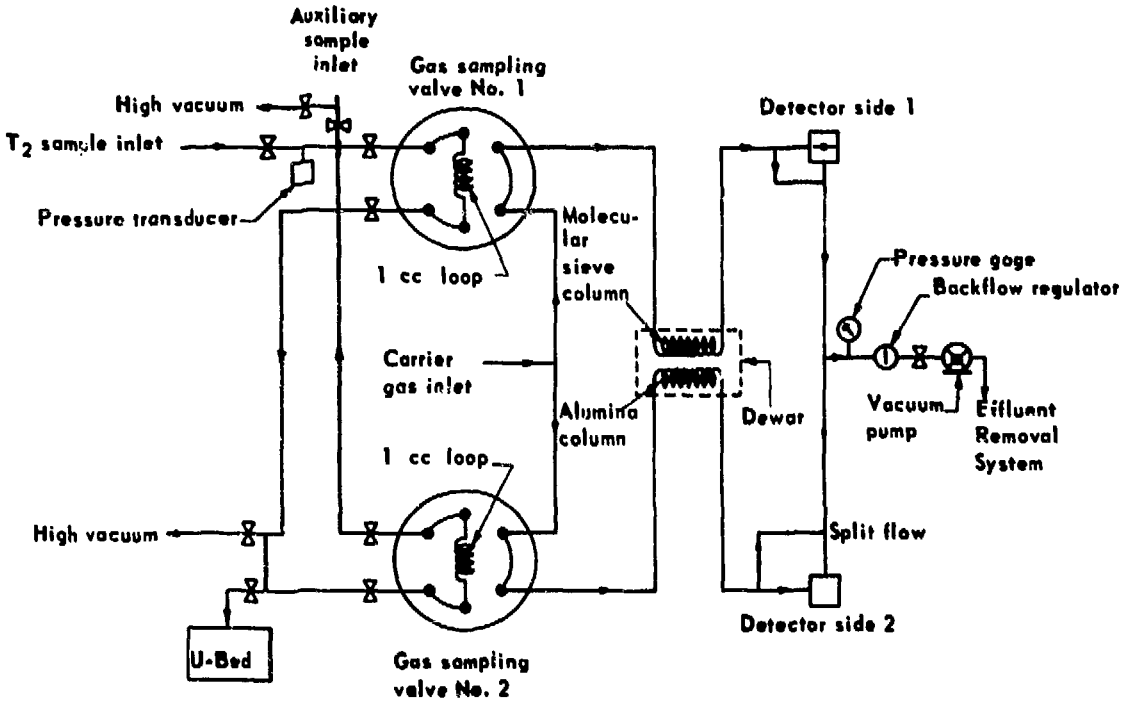

Fig. 1. Gas Chromatography Flow Diagram.

A photograph of the basic instrument is shown in Figure 2, and this portion is located inside a glovebox for secondary containment of the tritium being determined. Not shown in the photograph are the two columns which are coiled together and placed inside a 7 cm i.d. vacuum dewar; the coils are located in a controlled ventilation area below the glovebox to isolate them from the thermistor detector. This isolation is necessary since the coils are chilled in liquid nitrogen for the isotopic analysis and the local temperature variations would affect the detector stability if their proximity was close; also affected would be the sample pressure in the gas sampling volume which is measured by a 0-800 mm Grabenstein transducer. Minor daily temperature variations of the sample volume and detector are accounted for in the calculation of results. The detector in this unit is a Carle microthermistor thermal conductivity device in which the output voltage is integrated by a Hewlett Packard 5500 integrator.

Some of the experimental requirements for the operation of the chromatograph are shown in Table 1. It is apparent from this table that the isotopic and permanent gas separations are necessarily two individual experiments. Neon is used as the carrier gas for the isotopic separation in order to increase the sensitivity of the detector, and the more commonly used helium-4 is the carrier gas for the permanent gas separation. The column parameters d, e, and f in Table 1 are identical in order to maintain a roughly equivalent flow rate through both sides of the detector.

Virtually all of the tubing used in the instrument is stainless steel with the exception of the columns which are copper. The control valves are Nupro BW and H series bellows valves, and all fittings are either mechanical (Cajon VCR or Swagelok) or welded. Brazing is not acceptable because large

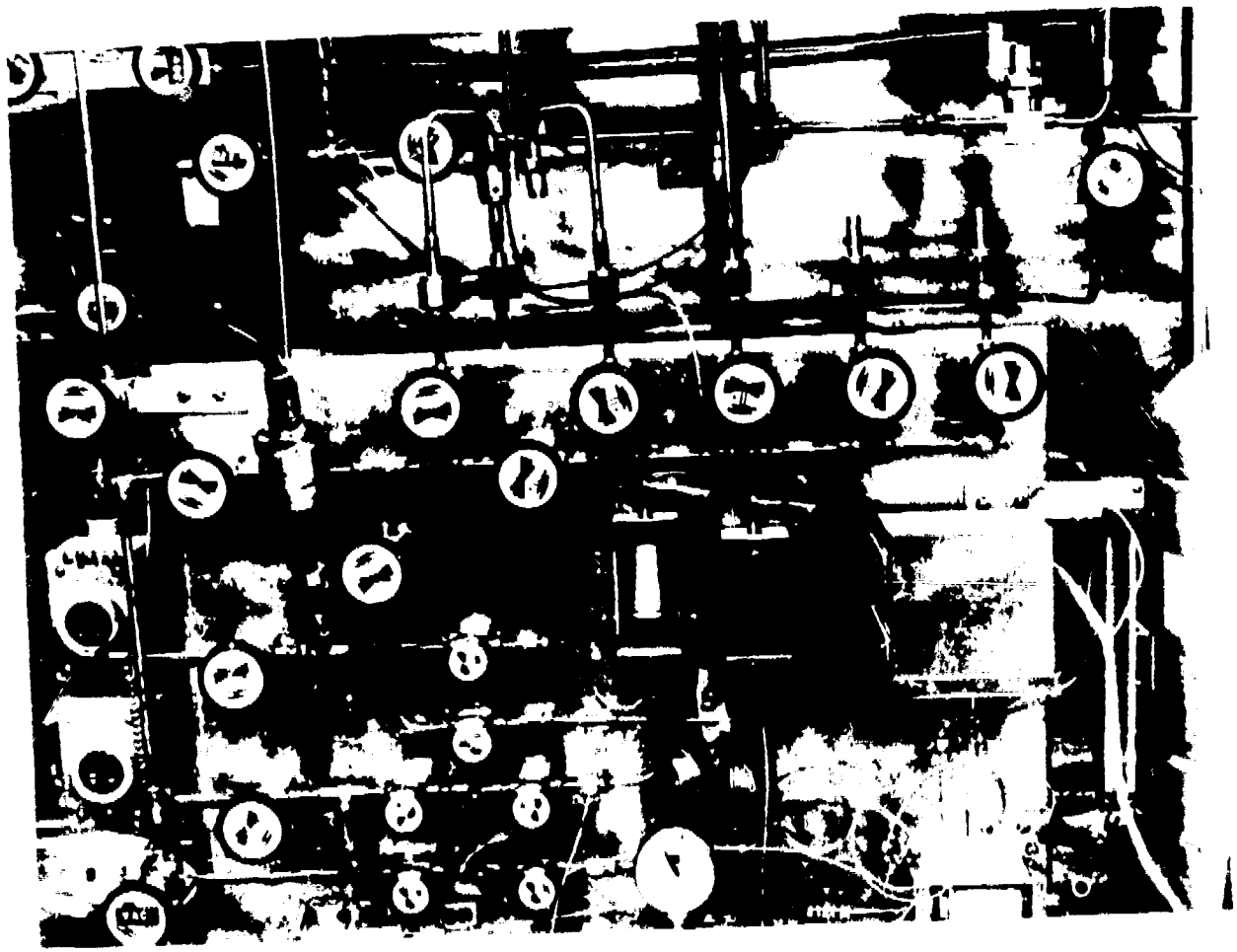

Fig. 2. Photograph of the Gas Chromatograph.

Table 1. Chromatographic Materials and Operating Conditions

	Permanent Gas Separation	Isotope Separation
a) Carrier Gas	^{4}He	Ne
b) Flow Rate (Est.)	50-60 cm^3/min	40-45 cm^3/min
c) Column Temperature	23°C	-196°C
d) Column Length	3.5 meters	3.5 meters
e) Column Diameter	2 mm i.d.	2 mm i.d.
f) Column Packing	80/100 Molecular Sieves 5A	80/100 Alumina

amounts of moisture and impurities are retained in and around the solder joint, and these impurities are a major source of protium that can lead to undesirable exchange with the isotopes contained in the brazed lines.

RESULTS AND DISCUSSION

Three examples will be given of isotopic analyses performed by the chromatograph. Figure 3 is a reproduction of an actual chromatogram of the isotopic impurities in a "purified" tritium sample (isotopic purity = 99.5%). The vertical peak height scale is logarithmic in order to maintain all peaks on the recorder scale, and thus the peak areas do not correspond directly to relative composition. Very little helium-3 is retained by the alumina packing and it elutes quickly, whereas the HT and DT impurities and the tritium are eluted in the order of their molecular weights. No deuterium nor hydrogen is observed in highly purified tritium because the isotopic exchange equilibria, (1) and (2),

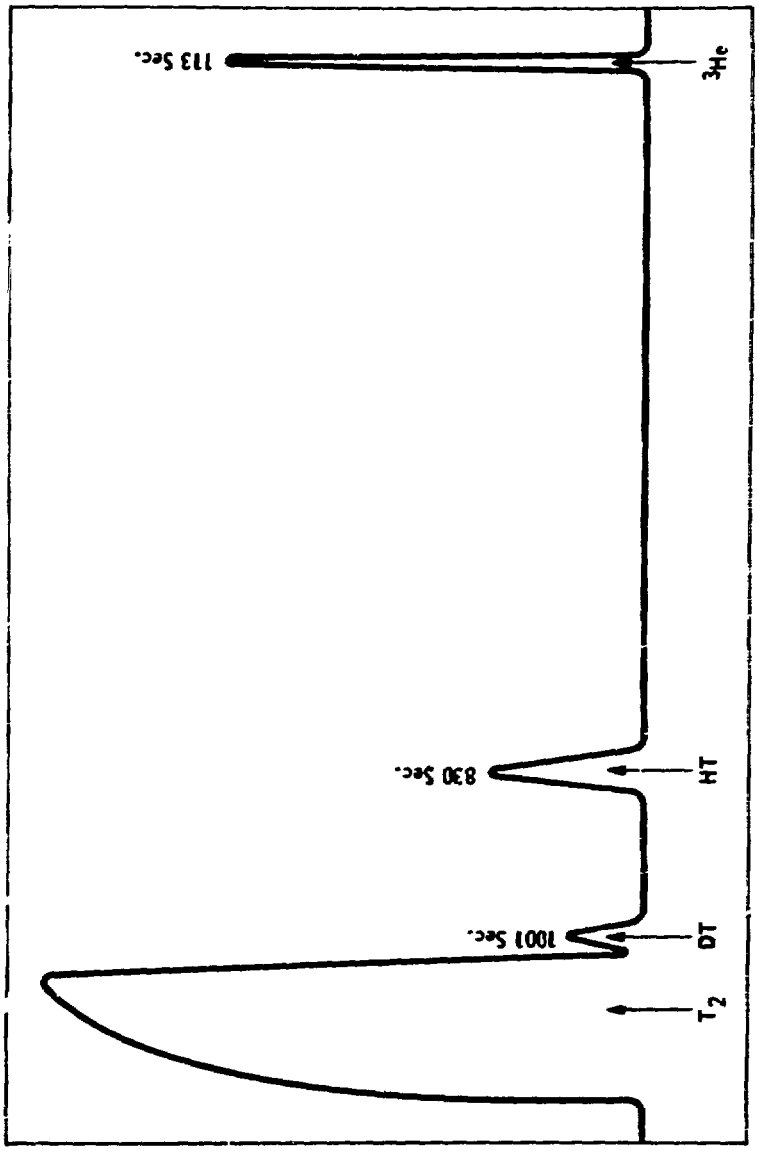

Fig. 3. Chromatogram of ^3He, HT, and DT in T_2.

(1) $H_2 + T_2 = 2HT$ $K_{eq} = 2.6$ at 300°C

(2) $D_2 + T_2 = 2DT$ $K_{eq} = 3.8$ at 300°C

favor the formation of the mixed isotopes HT and DT and the concentrations of hydrogen and deuterium are below their limits of detectability. The unsymmetric peak shape of tritium provides evidence that the distribution coefficients of the isotopes are nonlinear with respect to concentration, and indeed retention times do decrease when sample volumes are increased.

A second example of isotopic impurities is the determination of HD and HT in a standard gas mixture of deuterium and tritium plus the exchange product DT. The HD and HT are present due to exchange of protium in vessel walls and process lines, and the presence and growth of protium into D-T gases is a problem unless equipment and container surfaces are treated by various "conditioning" techniques. In Figure 4 the HD and HT impurities are seen to be well separated from the massive principal component peaks, deuterium, DT, and tritium. The vertical scale in Figure 4 is again logarithmic, and the impurity peaks represent 550 ppm and 400 ppm of HD and HT, respectively. That the adsorption isotherms are nonlinear is again demonstrated by the shapes of the principal mixture components. A typical analysis takes about 20 min to complete.

The third example illustrates not only the use of the G.C. technique for low-level determinations of HD and HT, but also the protium ingrowth problem mentioned previously. Figure 5 shows a series of HD + HT measurements in standard gas (1% DT in neon) stored in a SS-304 container. The range of the concentration sums, 100 to 500 ppm, shows the low levels attainable with the thermal conductivity detector, and the steady increase of the impurities over time graphically illustrates the exchange problem associated with storing even low concentrations of isotopic gases.

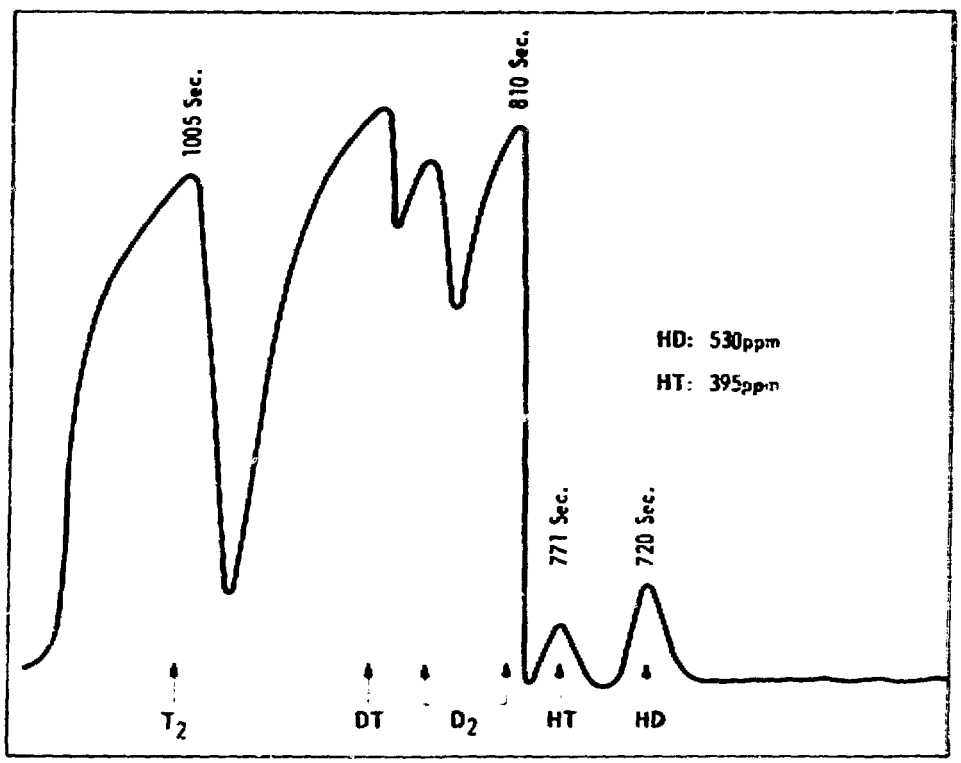

Fig. 4. Chromatogram of D and HT in a D-T Mix.

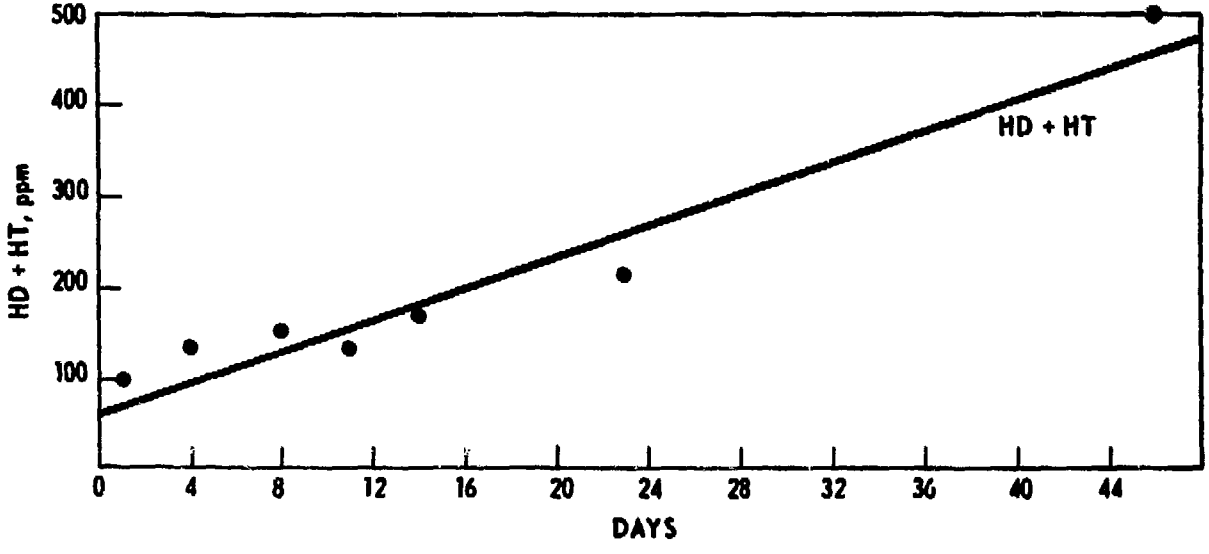

Fig. 5. Growth of HD and HT in a 1% DT in Neon Standard.

The accuracy of this instrumental technique is difficult to assess in its most useful range, i.e., 50 to 2000 ppm, principally because of the difficulties in attempting to prepare accurate, stable isotopic standards in this low range. However, comparative studies of gas chromatography and mass spectrometry results for common samples have been performed, and satisfactory agreement over a wide range of compositions has been obtained as shown in one experiment (Table 2). The good agreement of two different analytical techniques is powerful evidence of the basic accuracy of each method. All comparative data have shown G.C. results to fall within the 2σ precision limits of the respective mass spectrometry results.

Table 2. Comparison of Results of N_2 and HD Determination in D_2 by Two Instrumental Methods

	Mass Spectrometry	Gas Chromatography
HD	0.728%	0.715%
N_2	565 ppm	474 ppm
Number of Measurements	15 duplicate	1 triplicate

The precision, or relative standard deviation, of the G.C. methods was studied by a propagation of error calculation technique and by analysis of variance experiments. These statistical methods showed the precision to be concentration dependent: at 100 ppm the relative standard deviation is approximately 10%, and the error falls to about 3% at the 1000 ppm level and 2% at the 2000 ppm component concentration. Between-day variability is larger than within-day variability as a contributor to precision error.

In conclusion, gas chromatography has proven to be valuable as a means for determining low-level isotopic and permanent gas impurities in tritium and deuterium gases and mixtures. The analytical concepts and instrumentation are not complicated or unduly expensive, and the technique is amenable to automation or operation by a technician. Also suitable system design and sampling variations would allow total composition determinations if desired. This reliable analytical method should be seriously considered by CTR researchers as a viable tool for the assay of tritium and isotopic mixtures containing tritium.

REFERENCES

1. H. A. Smith and P. P. Hunt, J. Phys. Chem., 64, 383-84 (1960).

2. G. F. Shipman, Anal. Chem., 34, 877-78 (1962).

3. E. H. Carter and H. A. Smith, J. Phys. Chem., 67, 1512-16 (1963).

4. C. Genty and R. Schott, Anal. Chem., 42, 7-11 (1970).

HYDROGEN ISOTOPE SEPARATION SYSTEM FOR THE TOKAMAK EXPERIMENTAL POWER REACTOR

W. R. Wilkes

Monsanto Research Corporation, Mound Laboratory

ABSTRACT

An isotopic separation system for processing the fuel in the Tokamak Experimental Power Reactor is described. Two cryogenic distillation columns are used in sequence to recover 80% of the hydrogen from a fuel mixture originally containing equal parts of deuterium and tritium with a 1% hydrogen impurity. The hydrogen thus removed contains less than 1/2% tritium, which may be recovered in a separate system designed for that purpose. It is assumed that separation of the deuterium and the tritium is not required. A total tritium inventory of approximately 38,000 Ci (3.8 g) is projected.

Conceptual designs for a Tokamak Experimental Power Reactor (TEPR) are currently being developed at Argonne, Oak Ridge, and General Atomics. As these designs progress, we are able to obtain a better idea of the required tritium handling systems for TEPR. As a result of this improved knowledge, for example, it is now possible to describe a possible hydrogen isotope separation system for TEPR which is considerably smaller and has less inventory of tritium than did an earlier design.[1]

In the earlier design, the nature of the separation system was dictated by a desire to separate a 50-50 D-T mixture containing 1% hydrogen into deuterium and tritium streams of at least 90% purity, while simultaneously reducing the hydrogen concentration to a level of 0.1% or less. The purified streams were then used as feed material for neutral beam

injectors which require isotopically "pure" material to operate efficiently. The resulting system consisted of three distillation columns operating near 25 K with a combined tritium inventory of approximately 65 g (6×10^5 Ci).

The current system is based upon a very different set of criteria. Again, the feed material to the isotope separation system is a 50-50 D-T mixture with a 1% hydrogen impurity, whereas the quantity of material to be processed, 3,000 g/day, is 67% more than the earlier value. This time, however, it is assumed that deuterium and tritium may be fed into the plasma as a mixture, probably in the form of cold gas. For this reason, then, no attempt is made to separate deuterium and tritium; it is merely necessary to reduce the hydrogen concentration of the D-T mixture to a value which will not significantly degrade the plasma, and to strip most of the tritium from the hydrogen thus recovered. A value of 0.25% is chosen here for the hydrogen concentration of the purified D-T mixture, and 1% tritium is allowed in the extracted hydrogen.[2]

Because of the high temperature in the plasma, the D-T mixture, once nonhydrogen impurities have been removed, will consist of the six molecular forms of hydrogen in a high temperature equilibrium distribution. The high temperature equilibrium molecular concentrations, X_{H_2}, X_{HD}, X_{HT}, etc., are given by equations of the type

$$X_{H_2} = h^2$$
$$X_{HT} = 2ht,$$

where h, d, and t are the atomic fractions of hydrogen, deuterium, and tritium respectively.[3] With the assumed atomic concentrations, the molecular concentrations are H_2, 0.01%; HD, 0.99%; HT, 0.99%; D_2, 24.5%; DT, 49.0%; and T_2, 24.5%. In a cryogenic distillation system it is assumed that the molecular concentrations do not change significantly in the length of time (minutes) required to process the mixture. This is a

conservative assumption; if it is incorrect, the approach to lower temperature concentration values will improve the separation process.

In principle, one could design a distillation column to remove all the H_2 and HD, and half the HT from the fuel mixture. This would immediately reduce the atomic concentration of the hydrogen in the fuel to 0.25%. However, because of the presence of HT, two more columns and a molecular equilibrium stage would be required to recover the tritium from this waste.[2] A variation on this is to remove all the H_2, HD, and HT in the first column, and then pass this mixture through an equilibrator to get new molecular concentrations. This new mixture is approximately half hydrogen and one quarter each deuterium and tritium. As a result, the equilibrated mixture would contain about 25% each of H_2, HD, and HT, with the remainder being D_2, DT, and T_2. By separating the H_2 and HD from this mixture in a second column, 75% of the hydrogen is recovered, along with (in principle) an arbitrarily small amount of tritium.

In either case, however, the need to make a sharp split between adjacent components of the original mixture requires the use of a column with many separation stages and a high reflux ratio. Both factors lead directly to a large inventory of tritium. A study of the initial column for one of the above systems, for example, reveals that it is as large as the corresponding column described in Reference 1. This difficulty can be avoided if one is willing to waste some deuterium - or at least defer its recovery to a later part of the system. By withdrawing about half the D_2 from the first column along with the lighter components, one obtains a mixture that is mostly deuterium; hydrogen and tritium are on the order of 10% each. As a result of the large deuterium component, most of the hydrogen will combine with the deuterium as HD and most of the tritium will form DT, thereby simplifying the H - T

separation in a second column. By using a six component, multistage computer simulation[4] of a distillation column, I have determined the characteristics of a cryogenic distillation system which will perform the required separation.

The first column in the system operates with an overhead withdrawal rate of 15% of the feed rate. The reflux ratio is 16, and a total of 30 stages are used. With a feed rate of 3000 g/day, a reboiler heat input of 22.5 W is required to achieve the desired reflux.

The overhead from this column contains 95.4% of the hydrogen from the feed. Because of the large quantity of D_2 recovered, however, the hydrogen is only about 6% of the mixture. The deuterium comprises 84% and the tritium 10% of the total. After the equilibrium molecular concentrations have been achieved for this mixture, 90% of the hydrogen is either in the form of H_2 or HD, and only 10% is in HT. This mixture is then separated in a second column, which operates with an overhead recovery of 10.5% of the feed rate. The column also consists of 30 stages and requires a reboiler power of 5.3 W. The overhead product is 51.7% H, 47.8% D, and only 0.425% T. The bottom product from both columns is combined and returned to the fuel cycle. The hydrogen concentration in the return stream is reduced to 0.2%. The characteristics of the process streams are summarized in Table 1.

Both columns operate at 1000 torr pressure, with the result that the temperature ranges from about 23 K at the condenser to about 25 K at the reboiler. The pressure is not critical; however, higher pressures involve a greater risk of tritium loss, and although slightly subatmospheric pressures may be safer, pressures below about 500 torr are precluded by the possibility of freezing the T_2.

Table 1. Percentage Molecular and Atomic Concentrations

	H_2	HD	HT	D_2	DT	T_2	H	D	T	Flow Rate (m moles/ sec)
Fuel "Ash"	0.01	0.99	0.99	24.5	49.0	24.5	1	49.5	49.5	6.9
Col. 1 Overhead	0.067	6.56	6.03	73.1	14.0	0.26	6.4	83.3	10.3	1.04
Col. 2 Feed	0.405	10.6	1.31	69.5	17.2	1.06	6.4	83.3	10.3	1.04
Waste	3.85	94.9	0.855	0.388	0.002	10^{-5}	51.7	47.8	0.425	0.11
Purified Fuel	10^{-6}	0.10	0.27	24.3	50.3	25.0	0.18	49.5	50.3	6.8

The inventory required to operate the two columns may be estimated readily. A column cross section of 0.2 cm^2 is required to support the vapor flow of 1 W of reboiler power in a packed column, and a liquid holdup of about 18%[5] of the packed volume has been observed. Each stage of separation requires on the order of 1.6-cm column length,[5] so that the volume of the first column is 206 cm^3 and that of the second is 50 cm^3. From a stage-by-stage concentration map provided by the simulation code, the average tritium concentrations in the two columns were found to be 37% and 5.4%, respectively. With an additional 10% added to account for the reboiler volumes, the total tritium inventory is less than 40,000 Ci. Several characteristics of the two columns are summarized in Table 2. A schematic of the distillation is shown in Figure 1.

The effectiveness of carrying a large D_2 component along in the first column overhead may be seen in the small column size and in the flexibility of the system. The tritium inventory of this system is 20 times less than for the one described earlier[1], and the flexibility is shown by the fact that changing the first column overhead fraction by 50%, from 0.15 to 0.10, had little effect on the overall results.

Table 2. Column Parameters

Column No.	Reflux Ratio	Boiler Power (W)	Diameter (cm)	Length (cm)	T Inventory (Ci)
1	16	22.5	2.4	48	3.6×10^4
2	50	5.3	1.4	48	2.5×10^3

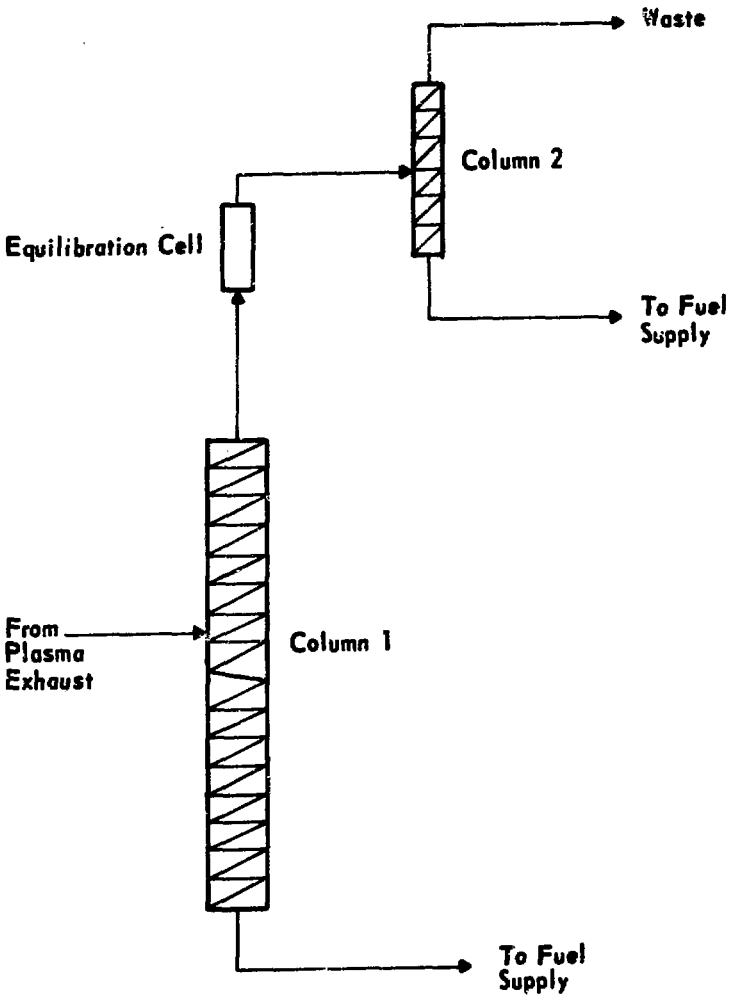

Fig. 1. Distillation Schematic.

Deuterium is removed from the fuel at a rate equal to the hydrogen removal (4.7 moles/day), and about 2300 Ci/day of tritium are lost as well. These are not disposed of, but rather are sent to a different isotope separation system which is designed to recover small amounts (~1%) of tritium from hydrogen. This system will be treated in a later report.

REFERENCES

1. W. R. Wilkes, "Hydrogen Isotope Distillation in a Fusion Reactor System," Trans. Am. Nucl. Soc., 19, 20 (1974).

2. V. A. Maroni, Argonne National Laboratory, private communication (1975).

3. W. R. Wilkes, "Separation of Hydrogen Isotopes for Tritium Waste Removal," Proceedings of the Symposium on Tritium Technology Related to Fusion Reactor Systems - October 1 and 2, 1974, ERDA-50 (1975), pp. 113-119.

4. Tritium Effluent Control Project Progress Report: October-December 1973, MLM-2129(UD), Mound Laboratory (March 1974), pp. 8-9.

5. T. M. Flynn, K. D. Timmerhaus, D. H. Weitzel, and J. W. Draper, Adv. Cryo. Eng., 3. 58 (1960).

EXPERIMENTAL MEASUREMENTS OF THE PERMEATION OF HYDROGEN ISOTOPES IN LITHIUM FILLED NIOBIUM CELLS

D H J Goodall G M McCracken and G E Austin

Euratom-UKAEA Association for Fusion Research
Culham Laboratory, Abingdon, Oxon, OX14 3DB, UK

ABSTRACT

Lithium filled niobium cells have been heated in vacua at temperatures in the range 300 to 900°C. By measuring the flow of deuterium into the cell it has been possible to make estimates of the rate of permeation of deuterium in the niobium wall. After initial fast diffusion into the capsule the rate of permeation becomes very much slower than that determined by diffusion in the bulk niobium indicating that a second, slower, rate process is involved. Measurements of the rate of deuterium permeation out of the cell have been made for a number of different cell geometries and a range of temperatures. The results indicate that the slow rate process, which is dominant at low concentrations, is the desorption step from the metal to the gas phase.

INTRODUCTION

The use of liquid lithium as the breeding material for fusion reactor blankets has the advantage of a high breeding ratio and the possibility of using the lithium simultaneously as both breeding material and as the coolant. Its disadvantages are the possibility of chemical incompatibility with some structural materials and the possible difficulties of extracting tritium from the liquid metal. A number of previous studies have been made of the lithium-hydrogen system with a view to estimating the conditions required for tritium extraction[1,2,3,4,5]. The results from various laboratories for the partial pressure of deuterium vapour above lithium-deuterium solutions are in good agreement with each other and now extend down to atomic concentration of less than 1 p.p.m.[4]. In addition it has been shown by Ihle using a Knudsen cell technique that there are significant fractions of other species in particular LiD and Li_2D which are of particular importance at low concentrations. The present experimental studies have concentrated on the dynamics of the interaction in particular the permeation rates of deuterium into and out of the lithium filled niobium cell. The measurements have been made at lower deuterium concentrations than previous investigations.

EXPERIMENTAL

The apparatus has been described in detail in a previous paper[2] and is essentially unaltered. A niobium cell is heated in an evacuated silica tube by an r.f. generator. The partial pressure of the constituents of

the vacuum system are monitored with a mass spectrometer. The niobium cells have been made both by pressing from Nb sheet and by machining from solid bar. In each case a cap is pressed on and electron beam welded in position after filling with lithium. A significant number of capsules have failed during experiments while being heated in the temperature range 700-900°C. In every case the failure was at or near the weld and resulted in release of lithium into the vacuum system. Cell life has varied from a few hours to over 1000 hours and the life appears to depend on weld quality. The weld failure of niobium in lithium has been reported elsewhere[6]. We have not investigated this effect in detail but we feel that it may be a significant problem which should receive attention.

PERMEATION INTO THE CELL

Measurements of the permeation into the cell were made by introducing a known pressure of deuterium into the vacuum system and observing the change of pressure with time as the deuterium diffused through the niobium into the cell. The concentration of deuterium in the lithium was initially negligible. In this case since the thickness d of the capsule is small compared with the total surface area A it is reasonable to assume plane parallel geometry and it can thus simply be shown that the pressure P should vary with time - according to

$$p^{\frac{1}{2}} = p_o^{\frac{1}{2}} - \frac{R'At}{2dV} \qquad (1)$$

where p_o is the initial pressure, R' the permeation rate and V the system volume. Typical results are shown in Fig. 1 and from the initial slope the permeation rate R' can be obtained. Measurements have been made from 900°C to 300°C and the variation of the permeation constant with temperature is shown in Fig. 2. Previous results for the permeation of hydrogen through niobium have been reviewed by Stickney[7]. The few measurements which have been made show a discontinuity between the two sets of results, the results due to Steigerwald[8] having a much higher

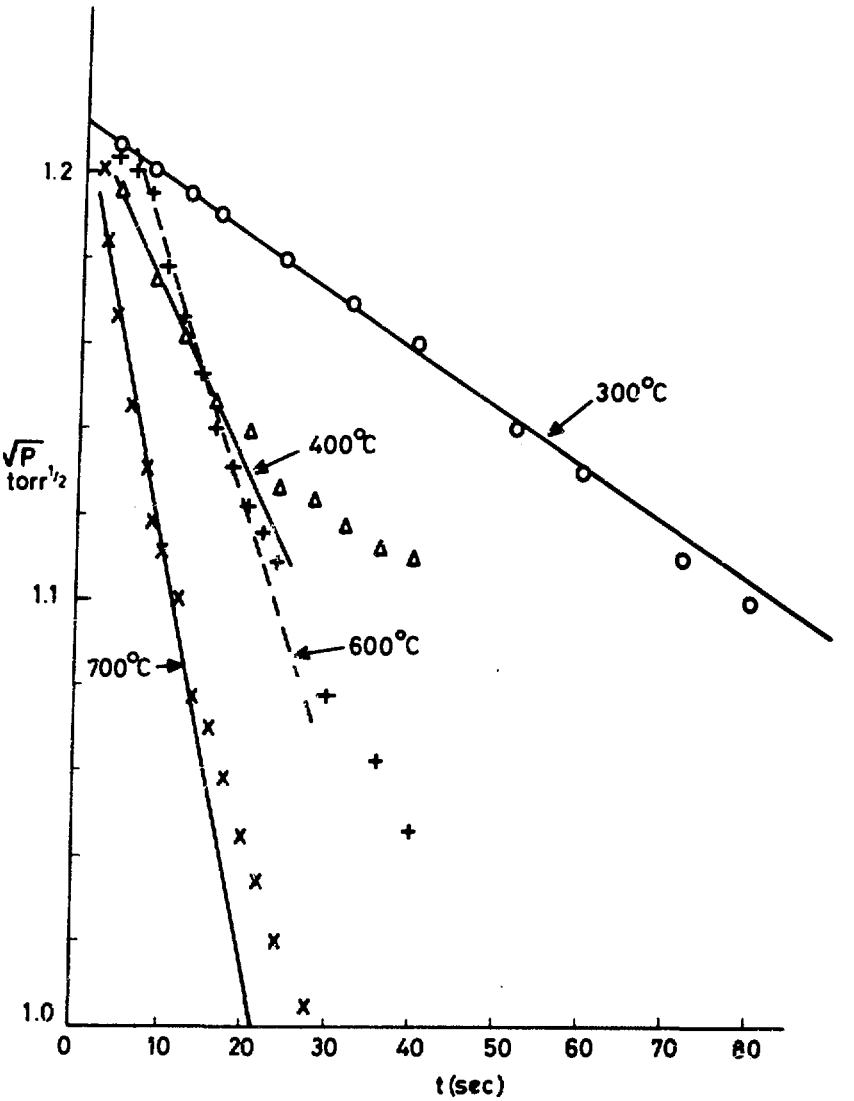

Fig. 1. The change in the external deuterium pressure as the gas permeates into a cylindrical, lithium filled niobium cell. Cell wall thickness 0.91mm.

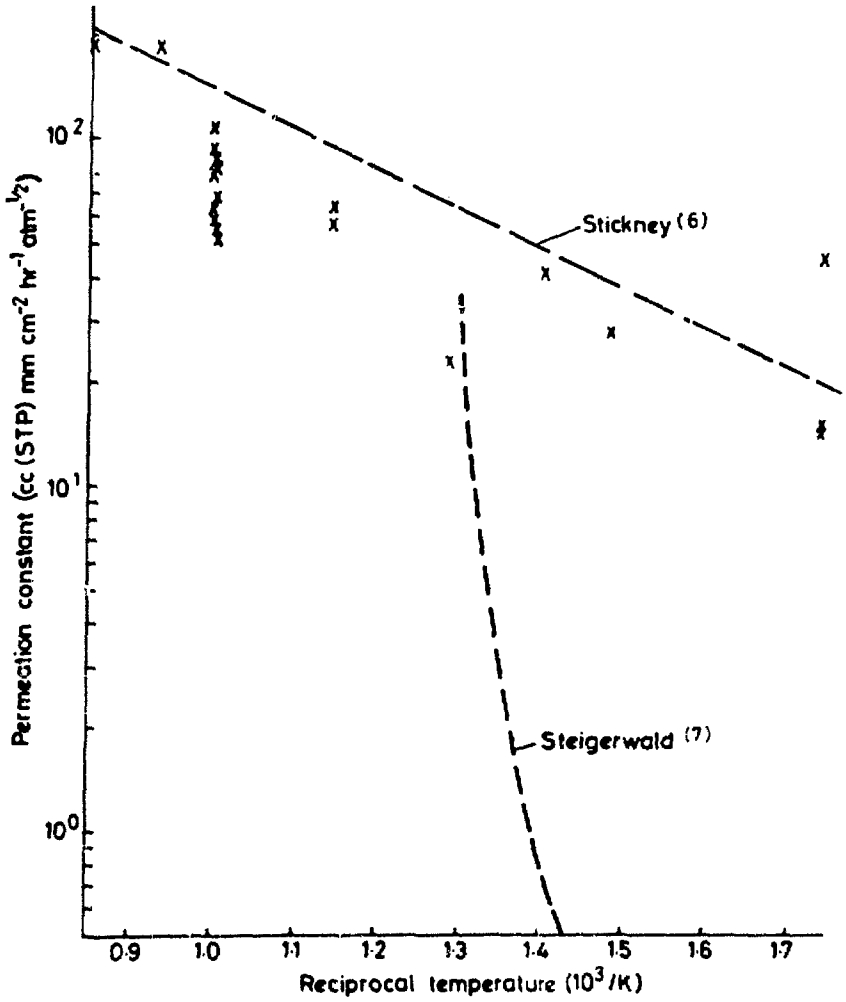

Fig. 2. Comparison of measured permeation constants for deuterium in niobium with other reported results.

activation energy than those made at high temperature. Our results for deuterium agree within a factor of 2 over the whole temperature range with the evaluation due to Stickney for hydrogen, and confirm his suggestion that Steigerwald's measurements were affected by surface impurities. The difference may be partially accounted for by the expected lower permeation rate of deuterium relative to hydrogen but can in fact be accounted for by the estimated experimental error. The permeation rate was found to vary inversely with the thickness of the sample as expected. These measurements relating to gas permeation into the sample are carried out at relatively high pressure in the range $1.0\text{-}10^{-1}$ torr. Levin and Stickney's measurements of diffusion of hydrogen through a thin niobium membrane,[9] had results which were different in different pressure ranges. At pressures of less than 10^{-2} torr the permeation rate was dependent on the square root of the pressure whereas at higher pressures the dependence was close to linear. This was attributed at least partially to the fact that the concentration of hydrogen in niobium exceeded that at which it forms an ideal dilute solution and therefore the $p^{\frac{1}{2}}$ relation would not be expected to apply. However, it was not possible to explain results completely as being due to this effect and it was thought probable that the results were also influenced by the presence of surface impurities.

PERMEATION OUT OF THE CELL

The measurements of deuterium into the cell can be simply analysed at short times, which correspond to high pressures. At longer times the pressure deviates from the relationship given in Eqn. 1. It was argued previously[2] that this was due to the finite concentration of deuterium built up in the lithium and that in turn this implies a relatively slow rate of diffusion into the bulk of the lithium. Measurements were therefore made of the rate of diffusion out of the cell starting from a known concentration. An analysis of this situation assuming spherical geometry has been given previously.[2] However, the experimental results did not agree very well with the form of the theoretical curves and it had to be assumed that the diffusion coefficient was concentration dependent.

Moreover the diffusion coefficients derived were very low compared ever with the self diffusion of liquid metals such as Na and K[10] (no data is available for lithium), and were therefore suspect.

To attempt to resolve the difficulty other measurements have been made on a range of capsules of various geometries and containing varying thicknesses of lithium. In each experiment a known amount of deuterium was introduced into the system and allowed to diffuse into the lithium. It has previously been shown that > 99% of the deuterium goes into the lithium. Sufficient time was allowed for the system to reach equilibrium (typically 1 hour) after which the partial pressure of the deuterium could be measured and checked against previous measurements for a given concentration. The system was then evacuated so that deuterium diffused out of the capsule for a given time. The concentration remaining in the capsule was then estimated by a further static measurement of the partial pressure of deuterium in equilibrium with the solution. The concentration was measured as a function of evacuation time. Results are shown in Fig. 3 for one cylindrical and two annular capsules. The annular capsules had a thickness of lithium of 1 mm and 2 mm. The cylindrical capsule had an outside diamater of 15 mm. All the results follow an empirical relation of the form

$$C(t) = At^{n} \exp(-Q/RT) \qquad (2)$$

where n is a constant close to -1. The temperature dependence is shown in Fig. 4. The value of Q is 35 ± 5 Kcal/mole for all the results obtained so far.

Experiments at much higher initial concentrations were also carried out with cylindrical and annular capsules which indicated a more complex behaviour, Fig. 5. Initially the slope n was about -1.5, but appears to decrease to a value nearer -1.0 at a concentration below 100 p.p.m., corresponding to pressures < 10^{-4} torr. The fact that the curves which were started at low concentration, (2000p.p.m., Fig. 3) have a slope

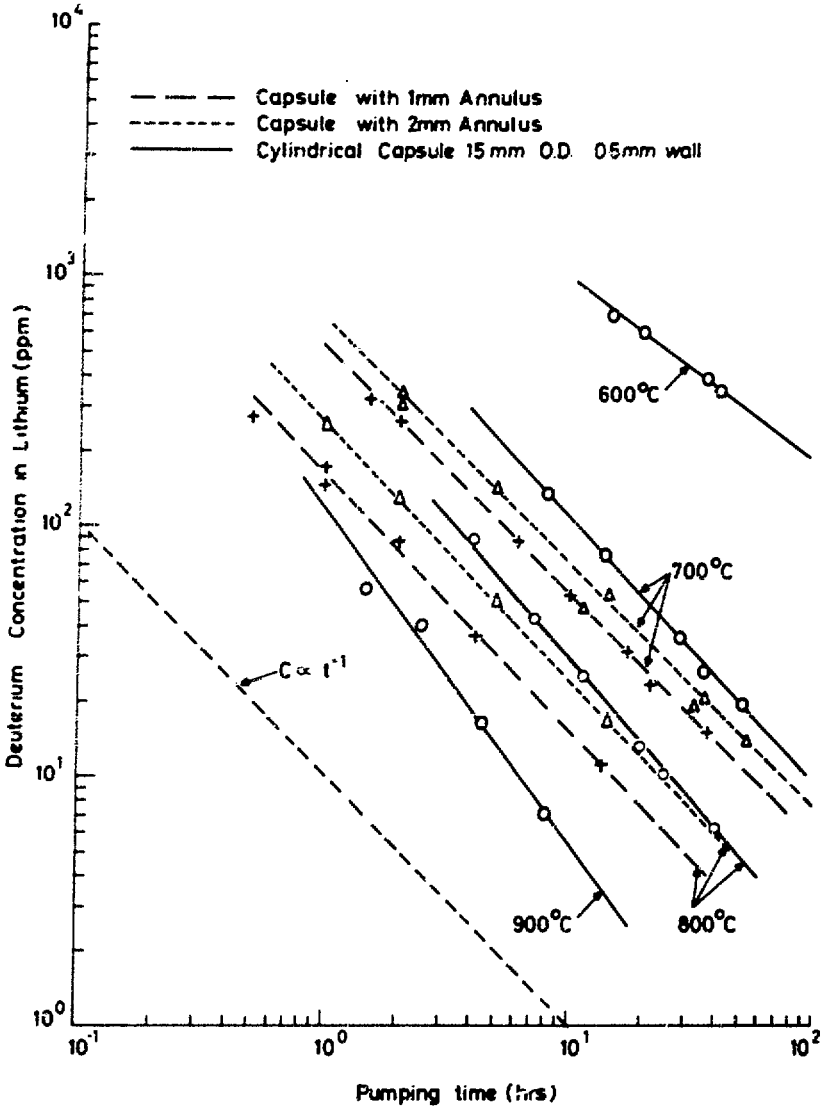

Fig. 3. A comparison of the change of deuterium concentration in the cell as a function of time of evacuation of the external surface, for 3 different capsules at various temperatures. Initial concentration 2000p.p.m.

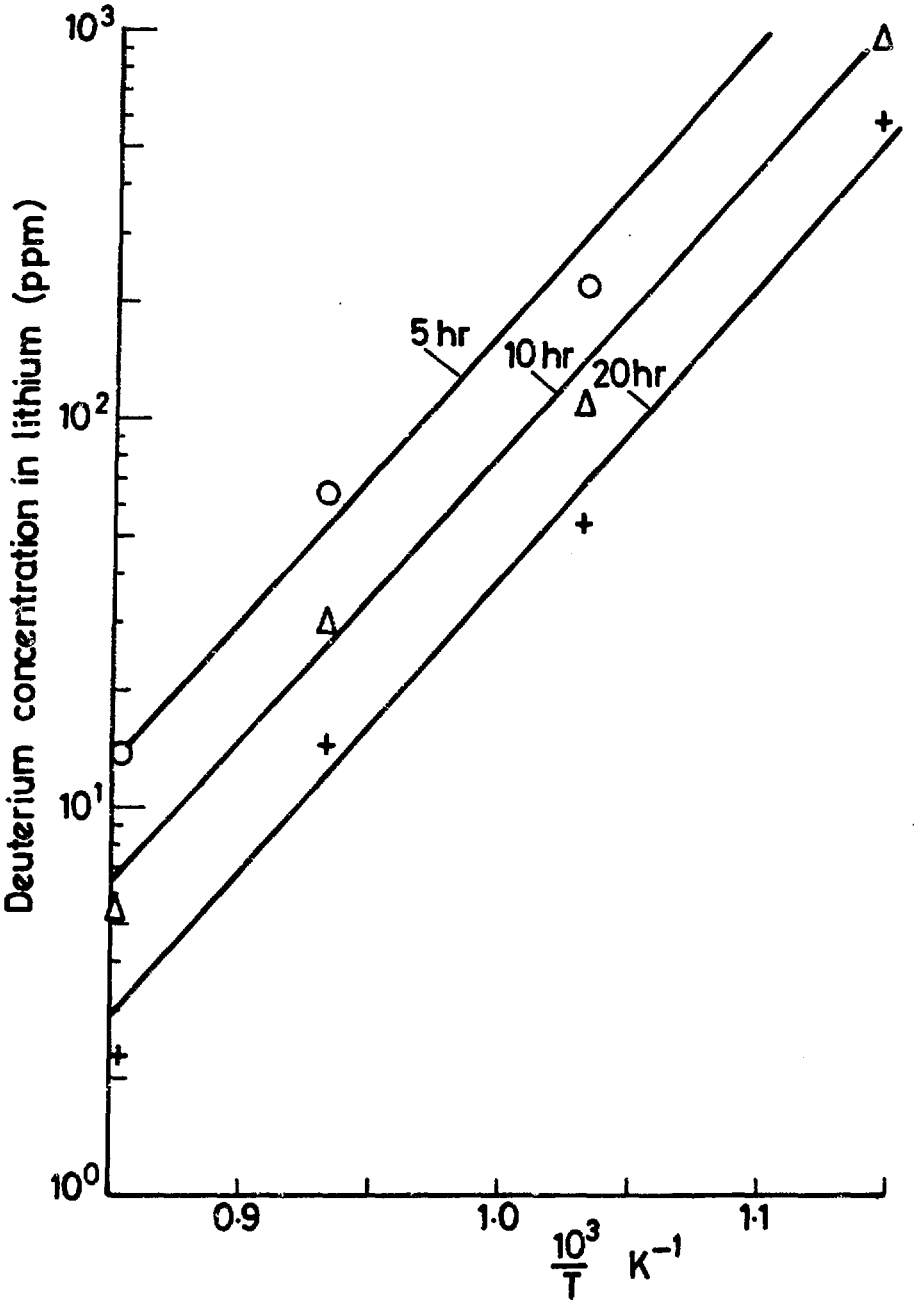

Fig. 4. Measured deuterium concentration in lithium as a function of ceil temperature for various times of evacuation of the external cell surface. Cylindrical cell 15mm dia 0.5mm wall.

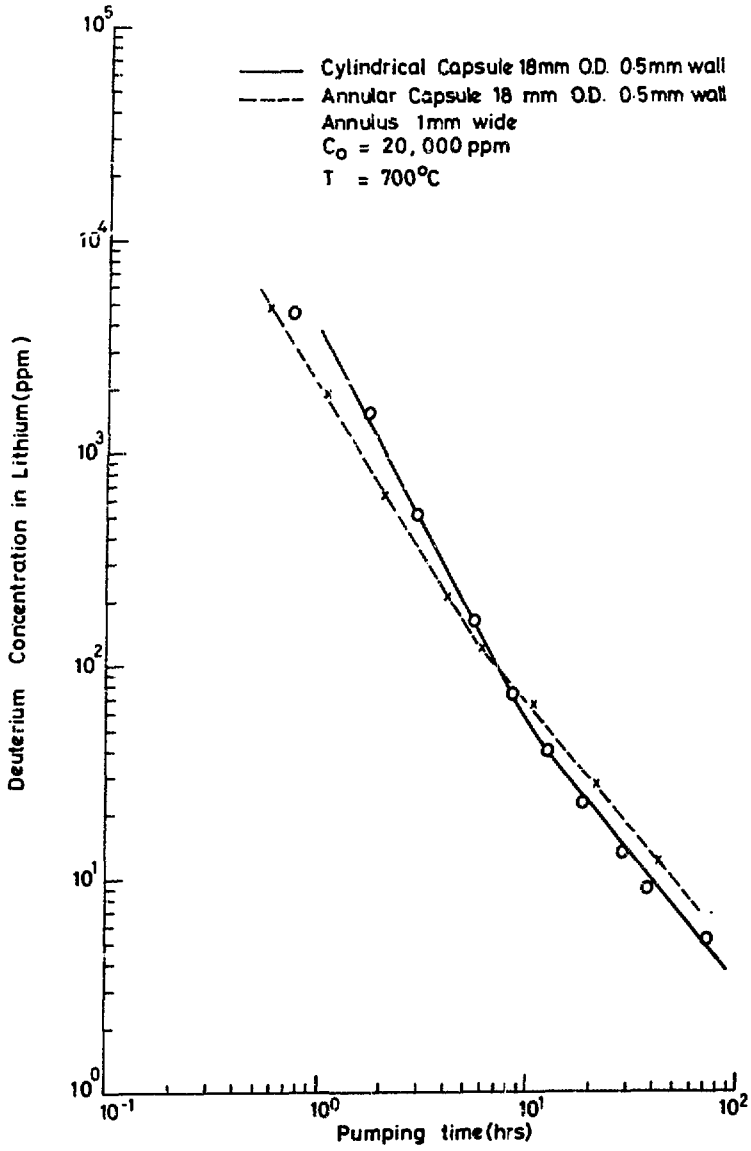

Fig. 5. A comparison of deuterium concentration in the cell as a function of time of evacuation of the external surface, for annular and cylindrical capsules. Initial concentration 20,000p.p.m. Capsule temperature 700°C.

of -1.0 at higher concentrations than those in Fig. 4 is probably due to the fact that the curve must bend over to approach the initial concentration of 2000p.p.m. at short times.

DISCUSSION

One feature is clearly evident, that the rate of change of concentration is almost independent of the thickness of the lithium, whereas if diffusion in the lithium were the rate determining step then it would be expected that the diffusion rate would be dependent on the square of thickness. Another feature becomes clear when these results are compared with the theoretical calculation based on a diffusion model of the dependence of concentration on time. Calculations for three geometries, spherical,[2] infinite cylinder and plane parallel plates,[10] are shown in Fig. 6. The form of the curves is strikingly different to that obtained experimentally. There is some doubt about the best geometrical approximation to the short cylinder used experimentally; it is expected to fall somewhere between the infinite cylinder and the sphere but is likely to be closer to the sphere. The annular cylinder is expected to be a good approximation to a plane parallel plate geometry. In any case the shape of the curves for all geometries is similar and markedly different to the experimental results. These two features - the independence of results on the thickness of the lithium cell and the qualitative difference in the shape of the experimental and theoretical curves are fairly conclusive evidence that our previous assumption[2] is incorrect, i.e. the slow rate of release is not determined by diffusion of deuterium in lithium. However the experimental results are consistent with those obtained earlier and it is evident that the rate of release of deuterium from the cell is very much slower than expected on the basis of extrapolating higher pressure data on the permeation rate of deuterium through niobium. The system is a very good small scale model of a cell of a fusion reactor breeding blanket. It is therefore important to understand what the rate determining step is and what the consequences are for the extraction of tritium from the

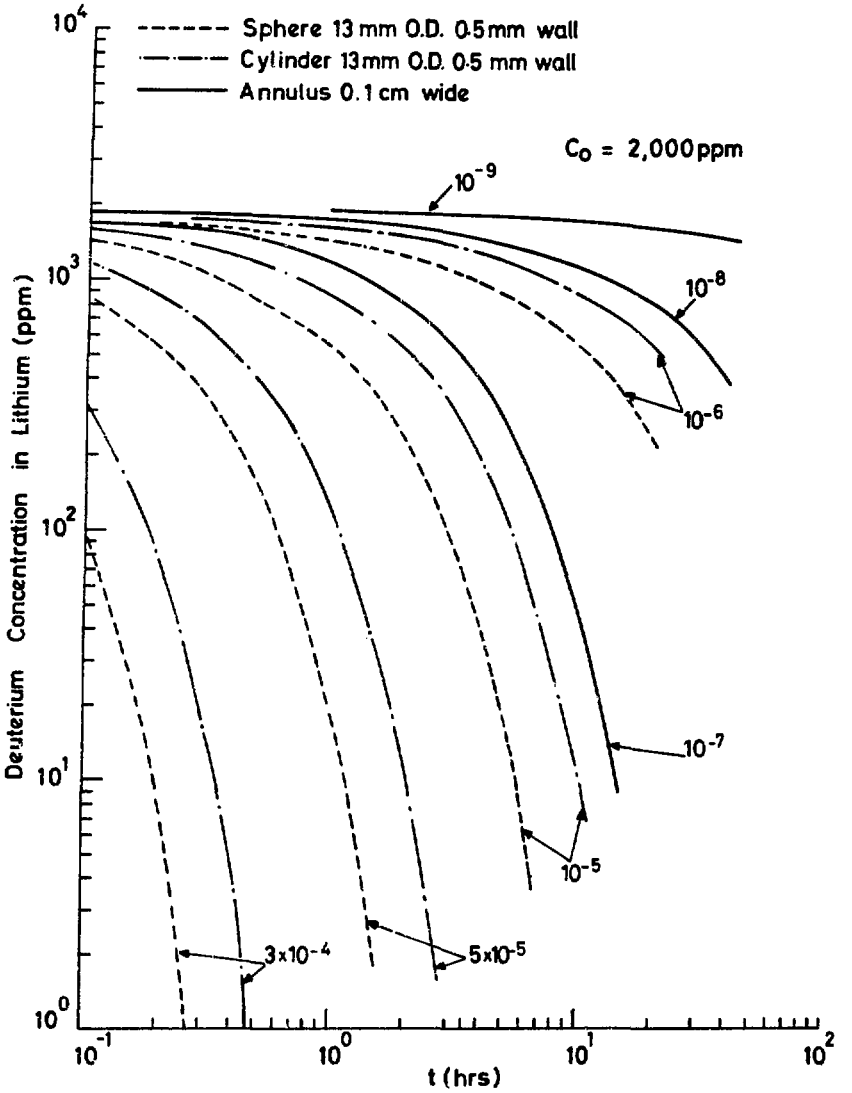

Fig. 6. Theoretical calculations of deuterium concentration in lithium assuming that diffusion in the lithium is the rate determining step. Spherical geometry (2), infinite cylinder (11) and infinite slab (11) geometry is assumed for various values of diffusion coefficient, stated in $cm^{-2}\ s^{-1}$.

reactor blanket.

The system has two bulk diffusion steps and two boundary steps in the sequence

$$\underset{\text{Bulk}}{2H(Li)} \xrightarrow{(a)} \underset{\text{Wall}}{2H(Li)} \xrightarrow{(b)} \underset{\text{Inner wall}}{2H(Nb)} \xrightarrow{(c)} \underset{\text{Outer wall}}{2H(Nb)} \xrightarrow{(d)} \underset{(gas)}{H_2}$$

We have dismissed the bulk diffusion through the niobium, step (c), on the grounds thay it is much too rapid and the bulk diffusion through the lithium, step (a), on the several grounds discussed above. That leaves as possibilities only the boundary step from H(Li) → H(Nb) at the inner wall (b), or 2H(Nb) → H_2(gas) at the outer wall (d). If the transfer from H(Li) → H(Nb) were the rate determining step then

$$\frac{dC_{Li}}{dt} \quad \alpha \quad C_{Li}$$

$$\text{i.e.} \qquad \text{Log } C \quad \alpha \quad t$$

which the data does not follow. However if the step from the 2H(Nb) → H_2(gas) were the rate determining step then the rate of change of concentration will be proportional to the square of the concentration

$$\text{i.e.} \qquad \frac{dC}{dt} = - kA \; C^2 \; \exp\left(- \frac{Q}{RT}\right)$$

$$\text{from which we obtain} \qquad C = \frac{C_o}{1 + C_o \; k \; A \; t \; \exp(-Q/RT)} \qquad (3)$$

where Q is the activation energy associated with the step, T is the absolute temperature, t is time, A is the surface area and k is an unknown rate constant.

Equation (3) has a form which is in good agreement with the data. The concentration starts from an initial value C_o at time t = o, and then becomes inversely proportional to time at long times. At long times

equation (3) reduces to the form obtained empirically, equation (2), and concentration is exponentially dependent on inverse temperature as shown in Fig. 4.

Since the rate of this boundary step is proportional to C^2 whereas all other steps depend on C, it is clear that as we go to higher concentrations the rate at the outer boundary step will increase more rapidly than the others and at some concentration it will no longer be the rate determining step. The results obtained by starting from higher concentrations seem to confirm this, with the region having a slope $n = -1$ only being the rate determining step at concentrations below 100p.p.m.

One difficulty remains with this interpretation: According to equation (3) the time required to reach a given concentration should be inversely proportional to the surface area A. The ratio of the total surface area of the annular to the cylindrical capsules is about a factor 4 while from Fig. 3 the ratio of times is less than a factor 2. On the other hand the two annular capsules whose surface areas differ by less than 1% have a ratio of about 1.5 in the time taken to reach a given concentration. No explanation for this surprising result has yet been found.

The question also arises as to what the rate determining step is at higher concentrations if it is no longer the $2H(Nb) \rightarrow H_2(gas)$ boundary step. It can readily be shown still to be too slow to be explained by bulk diffusion either in niobium or lithium. In the case of liquid lithium there are no results available for self diffusion. However assuming that self diffusion is the same as for sodium[10] then a diffusion coefficient of 3×10^{-4} cm^2 s^{-1} is obtained at 700°C. The calculated dependence of concentration on time for this diffusion coefficient, shown in Fig. 5, is obviously some orders of magnitude faster than the experimentally observed values shown in Fig.3. By a process of elimination one is tempted to conclude that the $H(Li) \rightarrow$

H(Nb) boundary step is responsible, but as yet we have no positive evidence in favour of this.

CONCLUSIONS

The results of the in-diffusion experiment have confirmed the assessment due to Stickney that hydrogen diffusion in niobium has a low activation energy and that there is no abrupt transition in activation energy.

In the experiments on out-diffusion a substantial body of data has been obtained on the permeation of deuterium out of lithium filled niobium cells over the rage of concentrations from 5 to 20,000p.p.m. The rates of permeation are much lower than expected on the basis of extrapolation of the permeation of deuterium in niobium at higher concentrations. Moreover, our previous hypothesis that the slow rate was due to diffusion in the lithium being the rate limiting step has now been disproved. The experimental results are in general consistent with the rate determining step at concentrations below 100p.p.m. being due to the desorption step from the niobium metal to the gas phase.

Assuming that the permeation of tritium in this system will be very similar to deuterium, the slow permeation rate at low concentrations is a factor which must be taken into account in the design of systems for the extraction of tritium from the lithium breeding blanket of a fusion reactor. A time of the order of 10 hours is required to reduce the concentration from 2,000p.p.m. to 20p.p.m. at 800°C, and a time of about 4 hours at 900°C. It is thus likely that temperatures of greater than 900°C will be required for the operation of the extraction system.

ACKNOWLEDGEMENT

The authors are grateful to G Long for some valuable discussion on the interpretation of the experimental results.

REFERENCES

1. G M McCracken and D H J Goodall, 7th Symp on Fusion Technology Grenoble. 1972 EUR 4938e pg 151.

2. G M McCracken D H J Goodall R T P Whipple and G Long, Nuclear Fusion Supplement pg 439-448, 1974.

3. E Veleckis E H van Deventer and M Blander, J of Physical Chemistry 1974.

4. H R Ihle and C H Wu, 8th Symposium on Fusion Technology Noordwijkerhout Netherlands 1974. EUR 5182 pg 787-799.

5. H R Ihle and C H Wu, 7th Symposium on Fusion Technology Grenoble 1972. EUR 4938e pg 89-97.

6. H Weichselgartner, 8th Symposium on Fusion Technology Noordwijkerhout Netherlands 1974. EUR 5182 pg 753-762.

7. R E Stickney, "The Chemistry of Fusion Technology" Plenum Press New York, Ed D M Green pg 241-319 1972.

8. E A Steigerwald, TRW Electromechanical Division Report E 5623. NASA CR-54004 Cleveland 1963.

9. R L Levin and R E Stickney, Proc of the 5th Symp on Engineering Problems in Fusion Research. Princeton IEEE 1973 pg 212-216.

10. C J Smithells, Metals Reference Book. 4th Edn. Butterworth London 1967 Vol II pg 644.

11. H A Carslaw and J C Jaeger, Conduction of Heat in Solids. 2nd Edition. Oxford University Press (1959.)

ON THE RECOVERY OF TRITIUM BY PERMEATION FROM LIQUID LITHIUM THROUGH NIOBIUM

H. Weichselgartner J. Perchermeier

Max-Planck-Institut für Plasmaphysik

Garching

ABSTRACT

Among the suggested tritium extraction processes those which deal with the permeation processes through niobium membranes are most attractive. In most cases they require large membrane areas and efficient removal of tritium on the downstream side of the membrane. To avoid these large membranes a fluidized bed assembly was set up and investigated under the aspect of T-removal. The permeating T will be bonded onto the solid phase of the fluidized bed and so the partial pressure will be reduced to a minimum. In the first stage, liquid lithium was doped with hydrogen at temperatures up to 700 C. The permeation area in this stage was formed by a niobium pot which was flushed with high-purity helium. The permeated hydrogen was measured with a highly sensitive gas-chromatograph with a He ionizations detector system. A resolution of about 10 ppb hydrogen could be attained by a special procedure. To eliminate the influence of a hydrogen background, mainly produced by the stainless steel vacuum vessel, deuterium was introduced into the liquid lithium for the second stage of the experiments. At the same time Nb-pot was replaced by a Nb-membrane in order to avoid weldings. In the investigated temperature range, the measured H and D permeation-rates allow the conclusion, that it will be advantage to keep the temperature of the molten Li relatively low. In this paper experimental data are presented and discussed.

INTRODUCTION

The tritium inventory in the blanket of a fusion reactor depends on several parameters. One of them is the effectiveness of the separation process. There are some factors which make it desirable to keep the tritium concentration in the lithium at a low level:

- so that the fusion reactor will show a net breeding gain
- so that the niobium structure will not become embrittled
- so that the tritium leakage to the atmosphere will not constitute a serious hazard.

Therefore, it seems necessary to separate the tritium continuously and entirely.

The requirement of a minimum tritium inventory is complicated by the tremendous capacity of lithium to retain tritium relative to most other materials.

After all, liquid lithium is a leading candidate for the breeding medium in DT reactor concepts, so that the problem of T-recovery from lithium deserves special attention.

Johnson[1] and Fraas[2,3] first suggested methods of T-recovery, and somewhat later Maroni[4] and Watson[5] showed that processes based on gas sparging, distillation, evaporation or mechanically pumped permeable diaphragms are not likely to reduce the tritium concentration in a lithium blanket below a level of about 10 ppm. Maroni is of the opinion that solid-hydrogen gettering has a chance, but that its usefulness has yet to be proved.

A FLUIDIZED-BED ASSEMBLY

Since 1972 we have been pursuing the idea of using a fluidized-bed assembly to separate and recover tritium from liquid lithium[6]. We believe that this method constitutes a real separation process which is coupled with neither special cooling processes nor special blanket arrangements or geometries[7].

This process consists of three steps: the first involves permeation, i.e. the conversion of the tritium into a new component of the fusion reactor which has to fulfill the following tasks:

1. it must assimilate the tritium by chemical reaction,
2. it has to prevent back-diffusion and undesired permeations,
3. it must be able to transfer the tritium into an external recovery system.

I think that these requirements might be realized in a fluidized-bed assembly.

The second part of the procedure consists of the absorption of permeated tritium by the solid phase of the bed. This is achieved by means of a chemical element or compound which is capable of absorbing relatively large amounts of tritium under the prevailing temperature conditions.

The third step is the transfer of the chemically bonded tritium from the fluidized bed to the T-separation unit outside the reactor. If, with an appropriate design of impermeable wall next to the shielding and thermal insulation, the tritium can be prevented from diffusion further, the system

will also meet the requirement of preventing undesired loss through permeation.

A scheme of the fluidized-bed arrangement in the reactor is shown in Fig. 1.

What materials must the components be made of in order to meet the requirements? On the basis of current material data and the analogy between hydrogen and tritium, the following can be stated: The tritium-permeation wall can be made of niobium, palladium or nickel.

The solid phase of the bed can be made of titanium (at 600°C, 100 g Ti is bonded to 23 litres of hydrogen or tritium to form hydride/tritide), metallic Ce, Zr, Th, and V, uranium compounds, UO_2 or metallic uranium

Titanium powder seems favourable because the Ti-hydride decomposes into its elements simply by being heated to above 900°C.

EXPERIMENTAL SET-UP - FIRST STAGE

I should now like to describe the experimental set-up which we built last year to investigate experimentally the permeation of hydrogen and deuterium from liquid lithium through a niobium diaphragm, and which should enable us to do the same with tritium somewhat later.

Figure 2 shows the basic layout of our first apparatus:

An isothermal oven operated with Na (max. operating temperature 800 - 900°C) contains a stainless-steel vessel which can hold about 100 g of lithium. This vessel is sealed

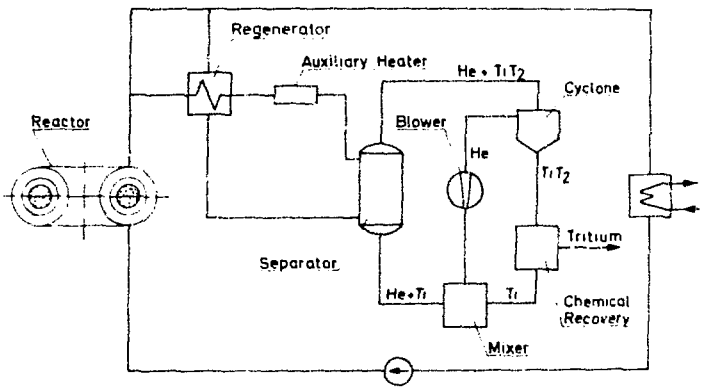

Bypass Tritium Removal System

Fig. 1 Scheme of the Fluidized-Bed Arrangement in the Reactor

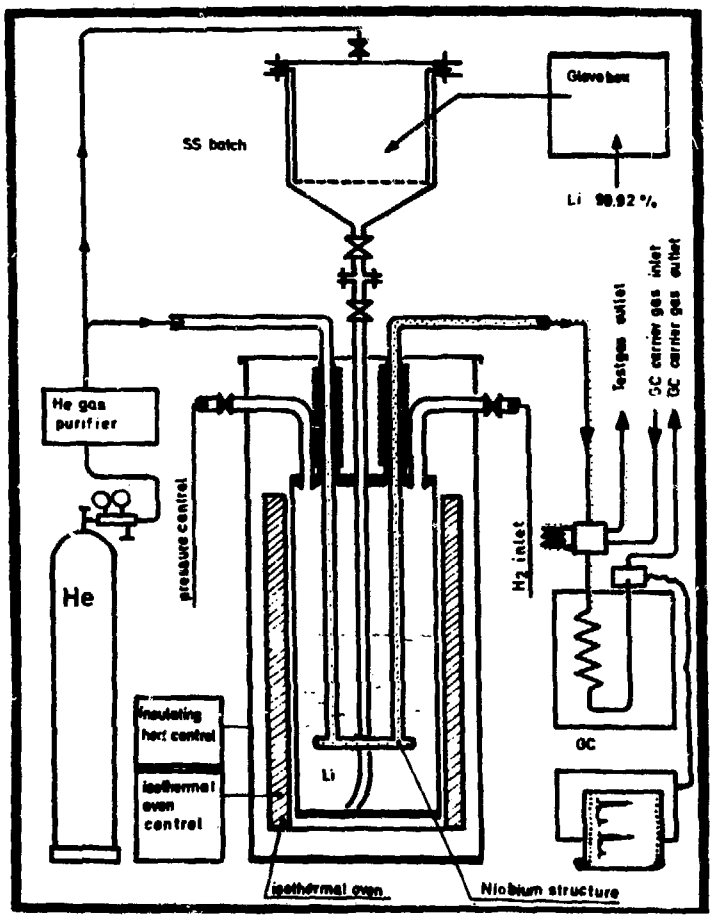

Fig. 2 Pilot Plant

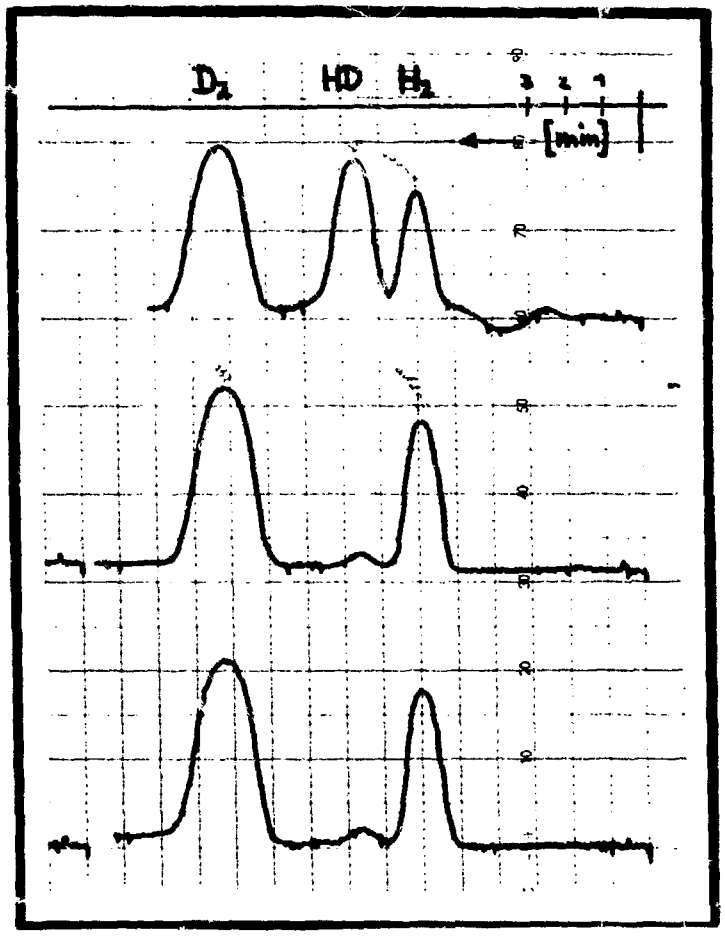

Fig. 3 Calibration Plots of H_2, HD and D_2

with a solid cover flange which has several lead-throughs:

- a tube reaching to the bottom of the vessel for filling in the liquefied lithium. This tube is connected by a small self-sealing flange and a stainless-steel Gachot bellows valve to a lithium supply vessel through which the pre-purified lithium can be filtered into the main vessel.

- an electrical level indicator

- and, finally, two Nb tubes (8 mm in dia., wall thickness 0.2 mm) which can be moved by means of spring bellows, and which are welded into a Nb vessel with a surface of approx. 35 cm^2. The spring bellows allows this Nb-vessel, which constitutes the actual permeation wall to be dipped in the liquid lithium to the required depth. The hydrogen permeating into the vessel through the wall (also 0.2 mm thick) can now be removed by a He-carrier gas flow which we set so that it served simultaneously as the carrier gas flow of the gas chromatograph with which we recorded the hydrogen.

The stainless-steel vessel with all its lead-throughs is placed in an insulating vacuum vessel which, in turn, is surrounded by a baking oven which is kept at 200°C to ensure that solid lithium is not deposited anywhere.

QUANTITATIVE DETERMINATION

For quantitative determination of the hydrogen and deuterium we use a gas chromatograph with a He ionization detector. The separation column (100 cm long) is packed with molecular sieve and is kept at liquid-nitrogen temperature. Normally this allows determination of a few 10 parts per

million hydrogen, besides other gases such as Ne, N_2, CO_2 and the like. By means of extremely fine purification of the carrier gas, exclusive use of diffusion-free valves and metal gaskets, and, in particular, effective back flushing of the dosing system and the ionization detector with purified helium it was possible to reduce the sensitivity to 2 parts per ppb billion and determine as little as 10 ppb in a reproducible manner. For calibration we used test gas cylinders in the region of 10 ppm and an electrolytic cell in the region of 10 ppb. Figure 3 shows typical calibration curves in which you can see the peaks due to deuterium, HD and hydrogen.

PURIFICATION AND FILLING OF LITHIUM INTO THE VESSEL

The available lithium was 99.92 % pure; it was in the form of wire immersed in paraffin oil.

For purification we used a glove-box operated with post-purified helium as protective gas. First we cleaned the Li wire in cyclohexane and evaporated the solvent. We then melted the Li in batches of 50 g and skimmed off the oxide and nitride crusts floating in the melt. The pre-cleaned lithium was poured into stainless-steel vessels through stainless-steel sieves. To fill the batch vessel, which was then flanged to the apparatus, we did the very same and used, in addition, a getter bath, which cleared the protective gas atmosphere of O_2 and N_2 residues. This gettering process was checked with a gas chromatograph. Not until the getter bath showed a bright reflecting surface over a long period and the air peaks of the gas chromatogram remained constant was the batch vessel filled. It was then immediately connected to the apparatus while being flushed with protective gas and the liquid lithium was filtered through the sintered stainless-steel batch with

an excess pressure of ~ 3 atm into the stainless-steel vessel. When the electrical level indicator acted the bellows valve was closed. The weight of Li was found to be 80 g.

The lithium then had to be doped with hydrogen or deuterium. We chose the solid compounds LiH and LiD and filled the apparatus for example with 28,56 mg LiD, which is equivalent to 200 ppm D_2.

This procedure was applied in the glove-box, too.

MEASURING RESULTS

The results obtained with this first apparatus were described in more detail in a previous publication[8]; just let me summarize these at this point:

1. As the apparatus contained hydrogen from the outset (as a result of welding and owing to SS-structure material) we had to start with a level of about 500 ppm H_2 (we intended to start with 100 ppm).

2. For all measurements the He carrier gas flow was kept at 60 ml He/min. (The apparent hydrogen production rate, i.e. the quantity of hydrogen which can be detected in ml per min in the He carrier gas flow, depends, of course, on the He flow rate. In Fig. 4 this relation is shown for a constant Li temperature of 700° C. In the top curve you see the results of the measuring series made in the first 24 hours after filling in the lithium; the bottom curve gives the relation after about 100 hours. The hydrogen inventory (Nb structure, lithium and stainless-steel spring bellows) dropped to about 400 ppm in this time.

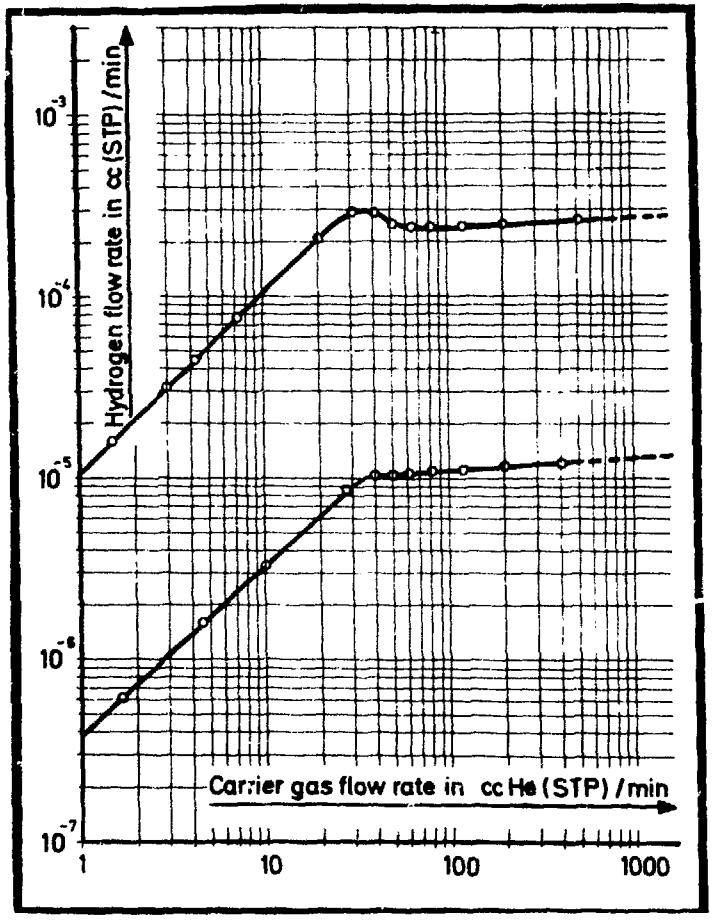

Fig. 4

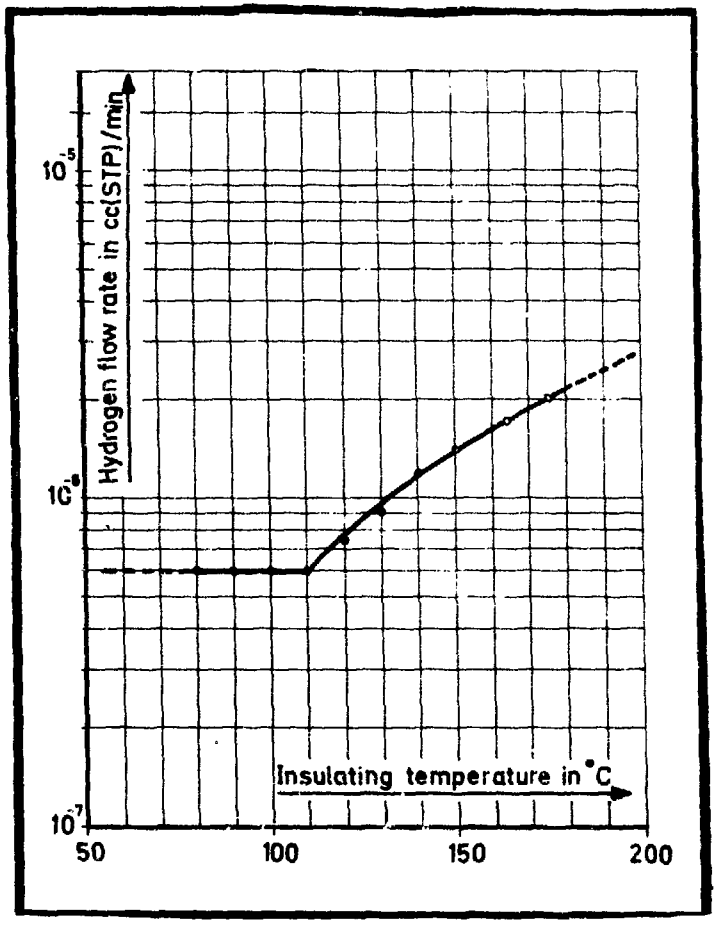

Fig. 5 Nb-Temperature Curve

Moreover, the two curves are rather identical in shape, the peak probably being due to diffusion effects of the hydrogen in the streaming helium.
Beyond a flow rate of 60 ml He/min the apparent H_2 rate no longer appreciably increases; we therefore chose this helium flow rate for all subsequent measurements).

3. Irrespective of the Li temperature, the measured hydrogen concentrations in He were practically constant.

4. If the Nb tubes passing through the gas volume above the Li melt are additionally heated, large quantities of hydrogen are found in the He.

We therefore concluded that it will be of advantage to keep the temperature of the Li melt relatively low and merely additionally heat the diaphragm above the melt (see Fig. 5).

It is unsatisfactory that this conclusion results in only one test series which was not repeatable at all:

After a total of 295 hours of operation, 160 of them at 700° C, the niobium structure was destroyed by corrosion, mainly at the welding seams. We were therefore unable to repeat this series of measurements.

EXPERIMENTAL SET-UP / SECOND STAGE

Therefore, we improved the experimental arrangement in the following respects:

1. To avoid the influence of the high hydrogen background of the SS-structure, we doped the lithium with D_2 instead of H_2. In a similar manner, we used the solid compound LiD

which we introduced to the Li-vessel after filling it with molten Li in the glove-box.

2. The Nb-pot was replaced with a Nb-membrane 0.2 mm thick. We thus have no welding seams which could corrode.

3. The next figure (6) shows the entire arrangement. There is no free space above the molten Li, and it is not possible to check our guess that a substantial amount of the permeated hydrogen could have escaped directly from the gas volume into the He through the Nb tubes. This obvious disadvantage is, however, outweighed by the advantages afforded by the clear layout of the Li melt, the Nd diaphragms and the transport gas volume. There are no longer any hidden corners nor should there be Li zones of different temperatures, and so I assume that the measuring results will be more readily reproducible.

4. A technical difficulty is created in sealing the Nb diaphragms with the base flange of the lithium vessel. Figure 7 shows the three Nb permeation devices we have used up till now:

   4.1 The Nb vessel with the welded Nb tubes from the first experiment
   4.2 The new Nb diaphragms with two soft-iron gaskets secured by the base flange, and
   4.3 A directly sealed Nb diaphragm.

According to Beskorovainy[9] technical soft-iron melted in vacuum should only show inter-crystalline corrosion phenomena after 500 hours at 600° C (as compared with 18/8 steel, which shows only limited stability treated with liquid Li after 6 days at 300° C). To come to the point, we had certain difficulties here, i.e. liquid Li was able to

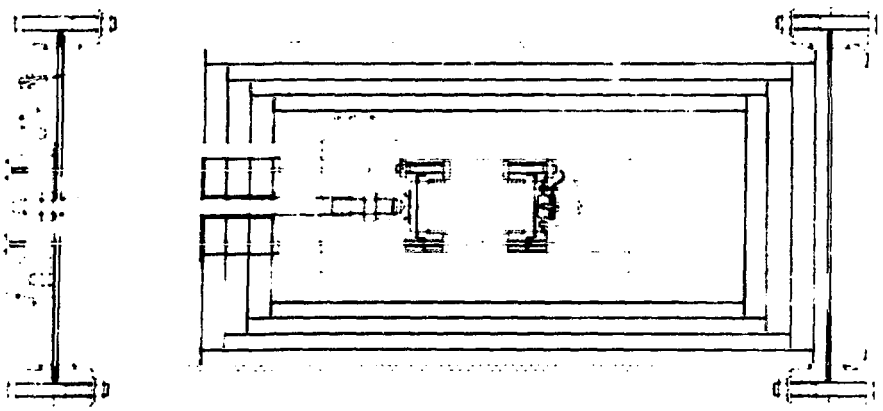

Fig. 6 Experimental Arrangement, Stage 2

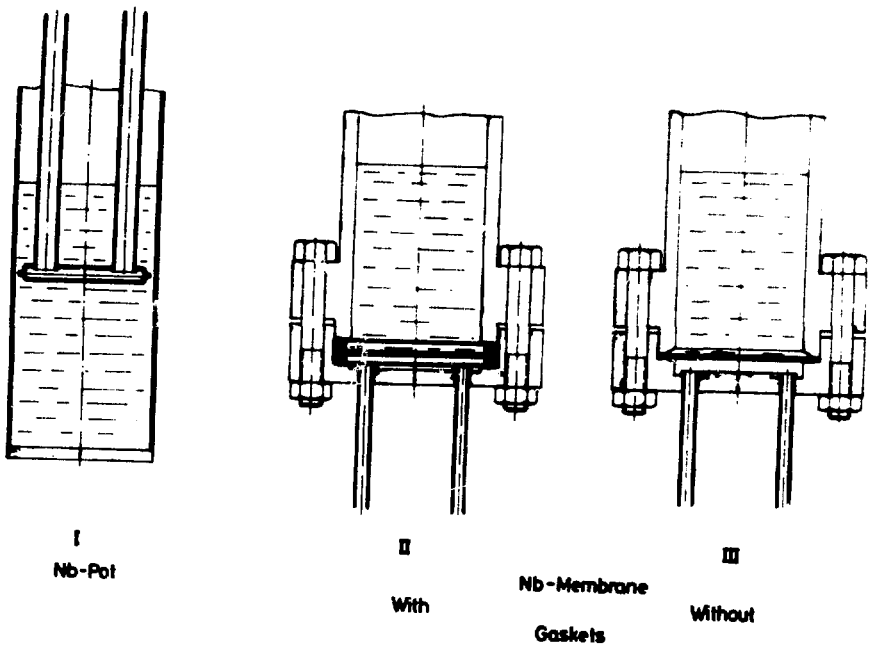

Fig. 7 Three Types of the Nb-Permeation Area

escape in the region of the base flange. Originally, we assumed that the soft-iron gaskets were corroded so that the Li could enter the gas volume, where it then blocked the He lines with the result that the test series had to be discontinued.

An exact investigation then revealed, however, that the 0.2 mm diaphragm had been clearly penetrated by Li without suffering mechanical damage.

The next figures (8.a - c) show results of metallographic investigations performed by H. Häglsperger[10]:

Fig. 8.a; Intercrystalline corrosion of soft-iron gasket caused by Li, starting at the edge after approx. 24 hours at 700° C. Structure in the core as yet unaffected (ferrite).

Fig. 8.b: Nb sheet prior to incorporation in the experimental apparatus. Grain boundary formation after etching for 5 min.

Fig. 8.c: Strong cracking of grain boundaries already after 10 s of etching by sensitization of the grain boundaries after Li action of approx. 24 hours at $\leq$ 700° C. Possibly also splitting of the grain boundaries by H_2O vapour pressure (total expositions-time 337 h at 500 - 700° C).

In 1973 D.L. Smith and K. Natesan[11] reported that niobium containing 200 ppm oxygen is rapidly penetrated by lithium above 600° C, whereas niobium containing $<$ 100 ppm oxygen is highly resistant to attack by lithium under similar conditions.

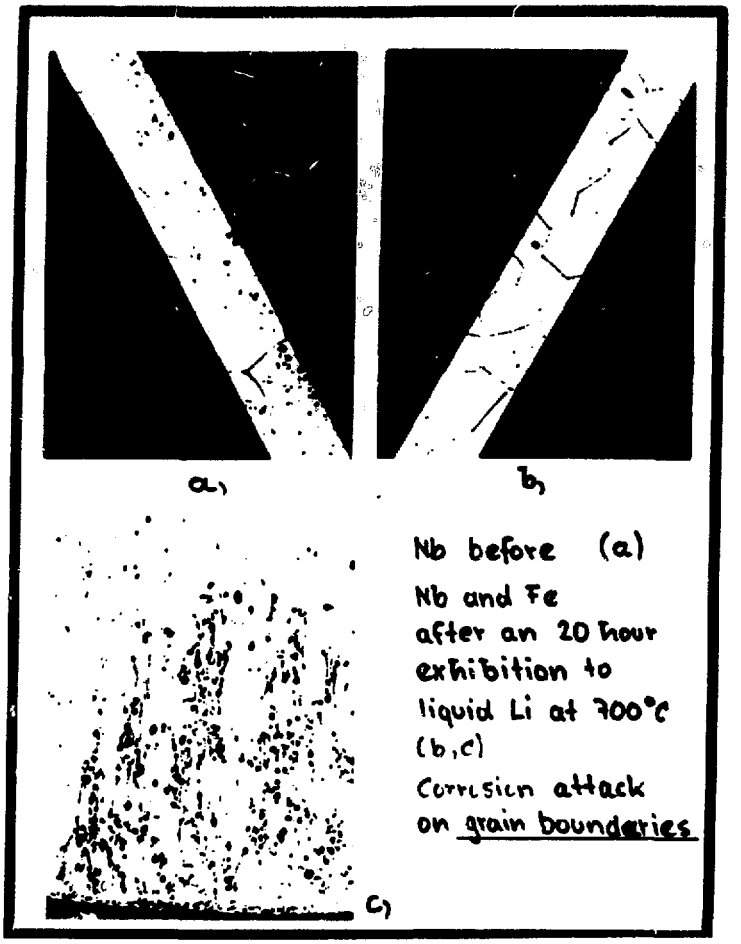

Fig. 8 Metallographic Analysis

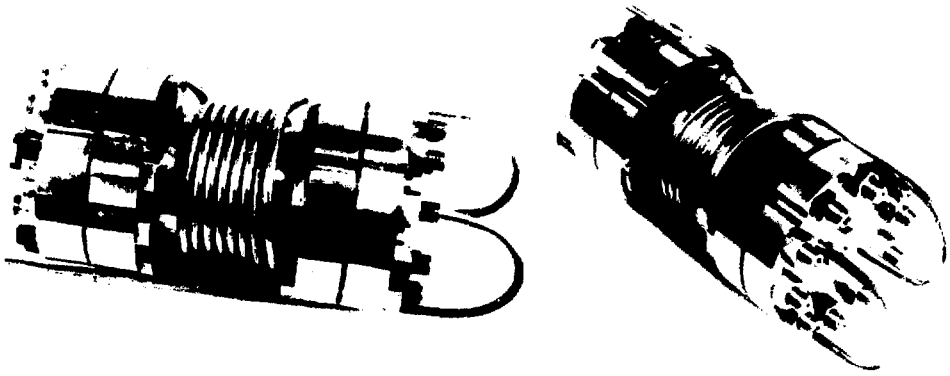

Fig. 9 The New Li-Vessel, made of Nimonic

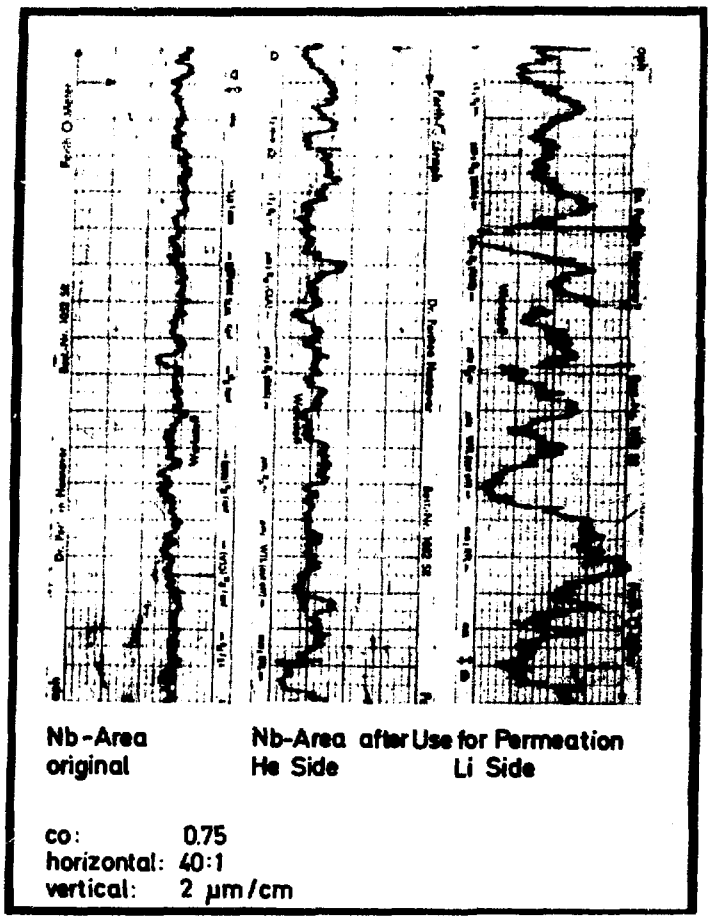

Fig. 10 Roughness on Niobium

In the version described last we therefore not only dispensed with the soft-iron seals but also used Nb sheet with not more than 100 ppm O_2. Since, furthermore, it cannot be ruled out that the yield point of SS 304 (4301) is exceeded at high temperatures, we have now made both the Li vessel and the two flanges and screws from Nimonic 75. This alloy, which contains mainly Ni, has a yield point of $\sigma_{0.2}$ = 36 kp/mm^2 at room temperature and even 6.3 kp/mm^2 at 900^o C (see Table 1).

DEUTERIUM PERMEATION IN THE TEMPERATURE RANGE 300 - 800^{o}C

In this last section some deuterium output curves are shown, which are registrated at dependency of rising temperature on the one hand, and various He-carrier gas flows on the other. These curves are based on more than 120 single measurements with the gas chromatograph.

The resulting gas chromatogram shows three peaks: the first after a retention time of 360 s corresponds to hydrogen, the second after 480 s to HD, and the third is due to D_2 after a retention time of 660 s. For quantitative determination we had to evaluate the second and the third peaks.

We measured during several heating and cooling cycles in temperature steps of about 20^o C. Most of the points were measured twice or three times to compensate spontaneous deviations due to electronic instabilities.

Figure 11 shows the permeation rate over the flow rate. As already mentioned, the quantity of deuterium measured increases with increasing flow rate of the carrier gas. Figure 12 shows the permeated deuterium depending on the applied temperature. This curve stems from the investigations with the first Nb diaphragm, containing about 200 ppm oxygen.

Table 1. Composition of Nimonic 75

Ni	70 - 75 %	C	0.08 - 0.15
Cr	18 - 21	Mn	max 1.0
Fe	max. 5.0	Si	max.1.0
Ti	0.2 - 0.6	Cu	max 0.5

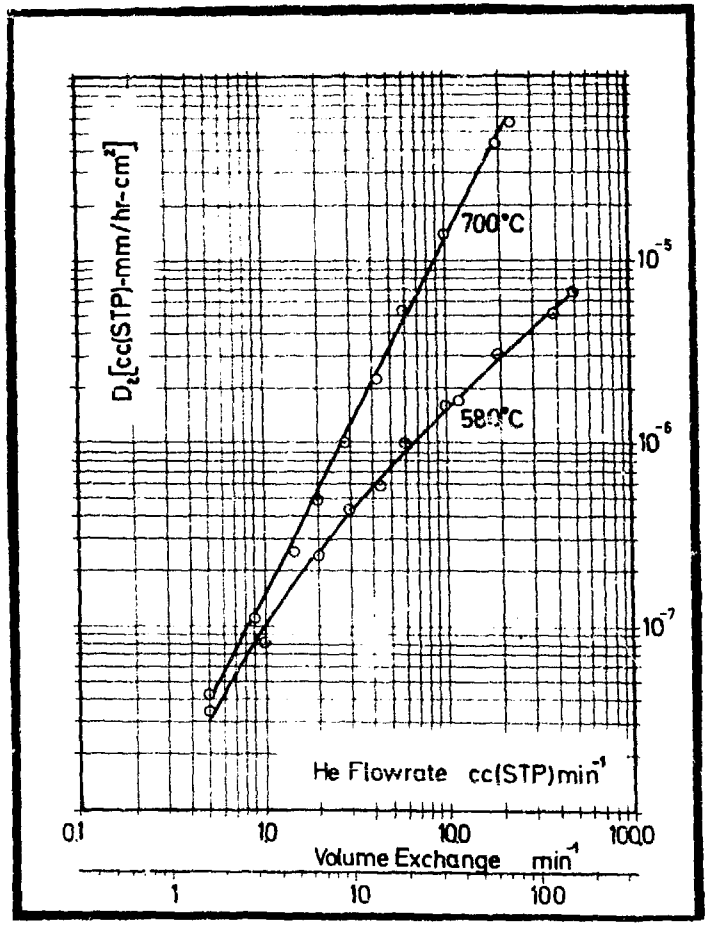

Fig. 11 Permeation Rate over Flow Rate

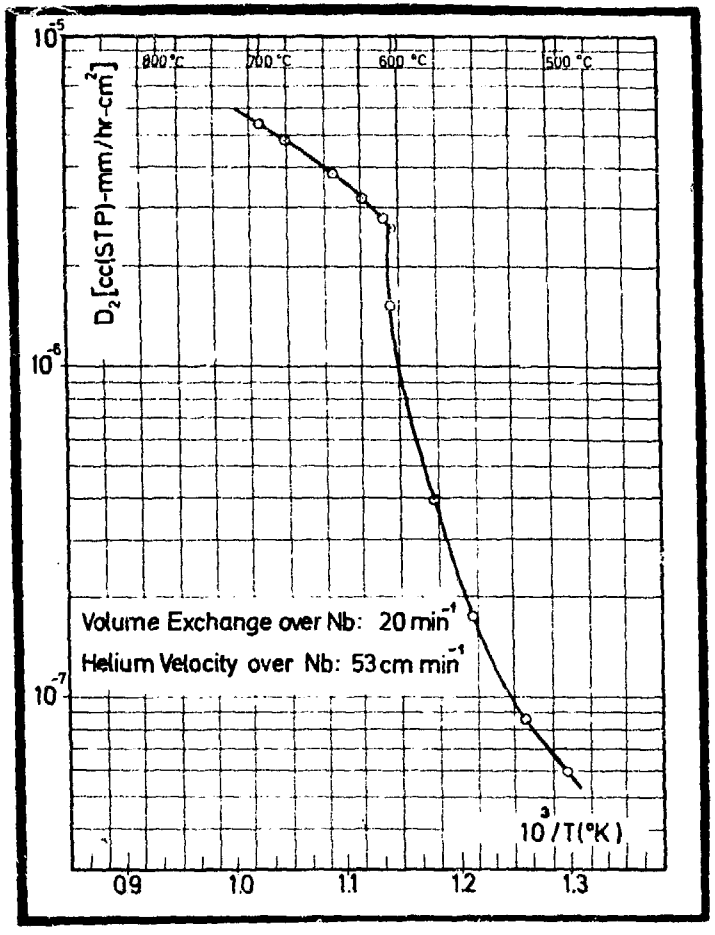

Fig. 12 Permeation Rate versus Temperature

At a temperature of about 600° C the curve becomes insteady and we record a breaking point. In his fundamental work, Webb[12] shows this in a family of curves, too, but without special comment. R.L. Levin and R.E. Stichney[13] measured the temperature dependence of the permeation rate of hydrogen through niobium, too. Figure 4 in their paper presents a family of curves showing all breaking points in a temperature region from about 400 to 620° C. The authors draw the conclusion that the permeation of H through Nb is strongly affected by surface impurities.

I think that our curve might be interpreted in terms of the oxygen content of the niobium used, especially because we did not record this breaking point in repeating these permeation measurements with a new Nb diaphragm containing only 100 ppm O_2.

The results of these measurements are shown in Fig. 13. The measuring points constituting this curve were recorded within 24 hours of one another. We may assume that during this time the D_2-concentration in the molten Li remained constant because the maximum D_2 transport rate through the Nb diaphragm was only 3×10^{-5} ml per hour. From a temperature of about 725° C we recorded a rapid decrease in measured D_2 coming through the Nb via transport He.

For the carrier gas flow of 60 ml Helium applied, this tremendous decrease is a fact we can only make some attempts at interpretation:

1. Although the measuring points form a point of inflection, we call it a breaking point, too, and assume that surface effects, contamination and so on are responsible. So we have the similar case as in the curve shown earlier; only the temperature dependence is different.

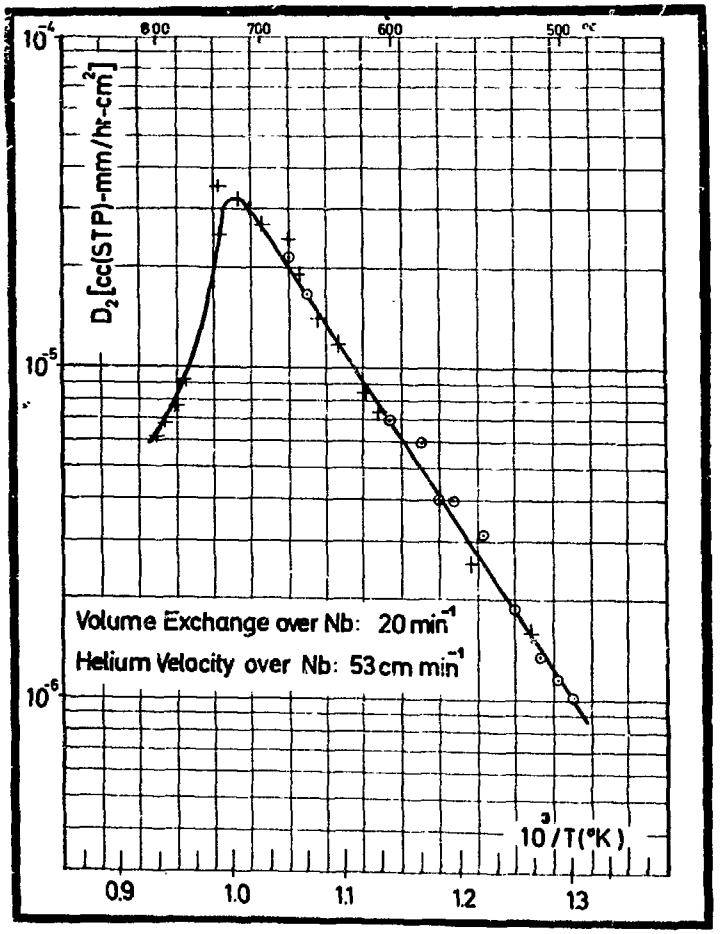

Fig. 13 Permeation Rate versus Temperature

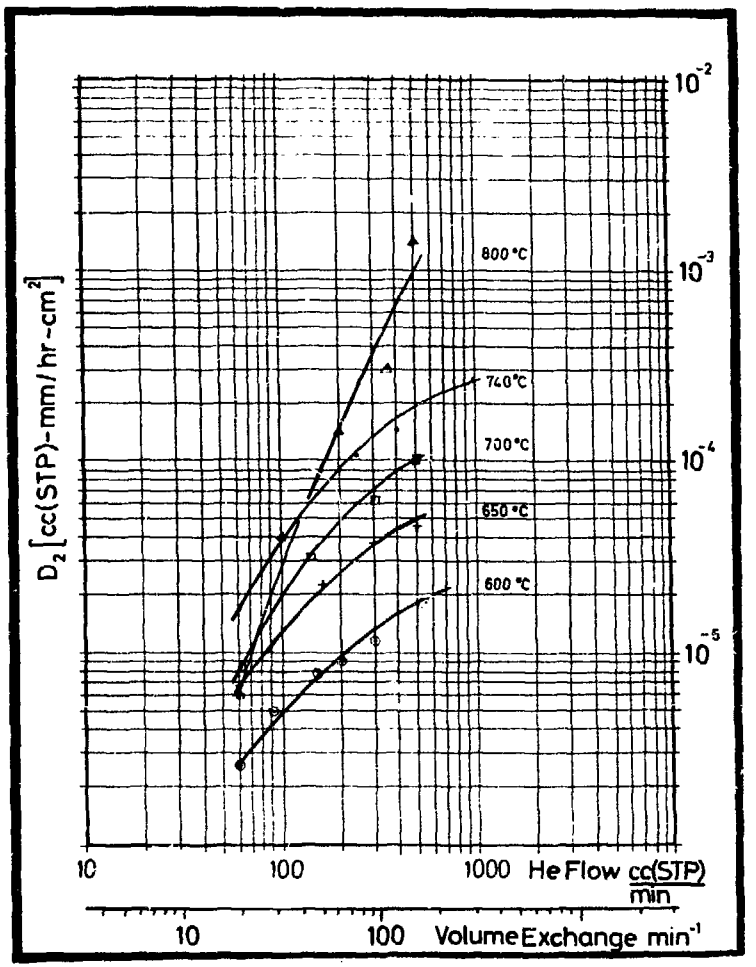

Fig. 14 Permeation Rate over Flow Rate

2. On the other hand, it seems to be clear that the major part of the D_2 might have disappeared through the walls of the Li-containing vessel owing to a high permeability of Ni for H_2 and D_2 at high temperatures. Since nimonic consists of > 70 % Ni, this attempt could be valid. As the surface of the nimonic-vessel is much greater than the surface of the Nb-diaphragm, the measured permeation rate was found to decrease.

3. As hydrogen absorption in Nb is an endothermic process, the solubility of hydrogen in Nb increases with decreasing temperature. This is valid at temperatures below $\sim 175^{\circ}$ C and H_2 pressures above $\sim 1 \times 10^{-1}$ Torr. Since the H-Nb system does not behave as an ideal dilute solution in the concentration ranges of the available data, it is difficult to make reliable extrapolations to lower concentrations. Stickney[14] made a comparison of experimental data, which do not overlap very well. So we cannot draw comparisons with investigations earlier made.

   But we can follow Völkl[15], who suggested that the permeation of H through Nb may be estimated from the equation $P = S_V D_S$. Where S_V is the solubility constant and D_S is the diffusion constant. According to the known equation

$$J_H = P_{H_2} \left(P_{1H_2}^{\frac{1}{2}} - P_{2H_2}^{\frac{1}{2}}\right)/L,$$

   the activation energy for permeation E_{PH_2} is negative, and therefore the predicted permeation rate <u>decreases</u> with increasing temperature.

4. Since we completed this series of measurements by a serie in which we kept the temperature constant at 600, 650, 700, 740 and 800° C and increased the He carrier gas

flow from 60 ml/min up to 1000 ml/min, we recorded, that the breaking point becomes softer. In Fig. 14 this family of curves is shown. When we transfer the points of measurements of the 800°-curve corresponding to higher carrier gas-fluxes, for instance 500 ml/min, the breaking point disappears and we get a steadily increasing output of D_2.

Therefore, we assume, that the breaking point is not due to effects in the Nb-diaphragm but due to solubility of D_2 in the nimonic structure.

CONCLUSION

My purpose has been to report an experiment making a contribution to the recovery of T from liquid Li. Particularly the usefulness of a fluidized-bed arrangement should be examined; in this respect only a first step has been taken since we worked with hydrogen and deuterium and since we were able to show that we can transport a sufficiently large amount of deuterium from liquid Li by a permeation process and can regulate this by three different possibilities:

1. with increasing carrier gas flow (limitations given here by arrangement geometries)
2. with increasing temperature (limitations given here by material technology; $\sim 620^{\circ}$ C, Nimonic $\sim 725^{\circ}$ C)
3. With process variations, which have not yet been undertaken
   - 3.1 vacuum extraction
   - 3.2 in applying getter material particles to the carrier gas in order to reduce the D_2 partial pressure at the downstream side and at the same time have a transport medium for the permeated H isotope.

Besides the experimental data,

a) we gained some experience in handling and purifying liquid lithium;
b) we found a practicable way of mounting a Nb-diaphragm without using gaskets;
c) we investigated some materials with respect to the attack of liquid Li and,
d) last but not least, we improved the sensitivity of a normally operating gas chromatograph, so that we can determine H and its isotopes in concentrations of about 10^{-9}.

The sum of these experiences and the experimental results will enable us to design and construct the next apparatus. Then we intend to introduce T in order to reach the smaller concentration range of 1 ppm because the sensitivity of our determination method will then not be sufficient.

REFERENCES

1. E.F. Johnson, Recovery of Tritium from Dilute Solutions of LiT in Lithium, Princeton Report 1959

2. A.P. Fraas, A Diffusion Process for Removing Tritium from the Blanket of a Thermonuclear Reactor, ORNL-TM-2358 (1968)

3. A.P. Fraas, Comparison of Two Tritium Removal Systems Designed to Minimize Contamination of Steam Systems in Full-Scale Thermonuclear Power Plants. ORNL-TM 2932 (1970)

4. V.A. Maroni et al., Some Preliminary Considerations of a Molten-Salt Extraction Process to Remove Tritium from Liquid Lithium Fusion Reactor Blankets, Nuclear Technology, Vol. 25, Jan. 1975, p. 83

5. J.W. Watson, An Evaluation of Methods for Recovery Tritium from the Blankets or Coolant Systems of Fusion Reactors, ORNL-TM-3794 (1972)

6. H. Weichselgartner, Tritium Separation and Recovery System Using a Fluidized Bed, 7th Symposium on Fusion Technology, Grenoble 1972

7. W. Dänner, Tritium Economy and Tritium Safety of Fusion Power Plants, IPP 4/112 (1974)

8. H. Weichselgartner, Contributions to the Diffusion of Tritium from Liquid Lithium Through Niobium, 8th Symposium on Fusion Technology, Jutphaas (Netherlands), June 17-21, 1974

9. N.M. Beskoravainy et al., Metallurg. u. Metallk. reiner Metalle (1963) (4) 130.

10. H. Häglsperger, Metallogr. Unters. von Fe und Nb-Proben in fl. Li, priv. comm. IPP/ZT 1975

11. D.L. Smith and V. Natesan, Influence of Non-Metallic Impurity Elements on the Compatibility of Liquid Lithium with Potential CTR Containment Materials, Nuclear Technology, Vol. 22, June 1974, p. 392

12. W. Webb, Permeation of Hydrogen Through Metals, NAA-SR-10462 Atomic International (1965)

13. R.L. Levin and R.E. Stickney, Permeation of Hydrogen Isotopes Through Fusion Reactor Materials

14. R.E. Stickney, In the Chemistry of Fusion Technology, D.M. Gruen, ed., Plenum Press, N.Y. 1972, p. 241

15. J. Völkl, Proc. of the 6th Symposium on Fusion Technology, March 22-25, 1970, Aachen, Germany

TRITIUM PERMEATION THROUGH STEAM GENERATOR MATERIALS*

J. T. Bell J. D. Redman
R. A. Strehlow F. J. Smith

Oak Ridge National Laboratory
Oak Ridge, Tennessee 37830

ABSTRACT

A model for tritium permeation through metals with oxide coatings is developed. The development includes considerations of permeation through clean non-oxidized metals, through metals with perfect oxide coatings, and through metals that have defective oxide coatings. The mathematical model includes a film quality factor which represents the quality of the film with respect to covering the surface of the metal. A set of curves of tritium flux vs tritium driving pressure calculated with this model shows how a film and the film quality factor will affect the pressure dependence of permeation through a coated metal.

INTRODUCTION

The production of tritium in nuclear power plants (fission and fusion) and the necessary containment of tritium in these facilities demands that we understand the mechanisms of tritium transport through construction materials. Tritium, as T_2 or as HT, easily permeates metals at high temperatures, and thus can escape from the primary containment into the secondary portions of a power plant. The tritium that escapes from the core and coolant areas can be trapped in a secondary containment medium. However, the tritium that escapes from the coolant through the steam generator material into the steam system must be considered lost to the

* Research sponsored by the U. S. Energy Research and Development Administration under contract with the Union Carbide Corporation.

environment since it is impractical to remove the tritium from the water. Therefore, the permeation of tritium through steam generator materials must be minimized.

Previous experimental studies[1-5] have shown that the oxide coating formed by the steam oxidation of certain metals and alloys markedly retards permeation of hydrogen isotopes through the oxide-coated metal or alloy. It is possible, therefore, that the oxide film formed in an actual steam generator system would provide the necessary retardation of tritium permeation.[6] Experimental work at high steam pressures is not yet in progress, but we are studying tritium permeation through steam generator materials at sub-atmosphere steam pressures. Concurrent with experiments,[5] we are developing a descriptive model for tritium permeation through oxide-coated alloys. The purpose of the present work has been to develop a model for hydrogen isotope permeation through metals that have one side coated with a material through which the transport of hydrogen is directly dependent on the pressure of hydrogen. Testing of the model with experimental data can only be accomplished in the future after a considerable bulk of data is available.

DEVELOPMENT OF THE MODEL

The steady-state permeation flux, J_M, of hydrogen through unoxidized metals is given as follows with consistent and commonly used units:

$$J_M = \frac{DK}{x}\left(P_2^{1/2} - P_1^{1/2}\right) \quad \text{cc(STP)}\cdot\text{cm}^{-2}\cdot\text{sec}^{-1}, \tag{1}$$

where D [$\text{cm}^2\cdot\text{sec}^{-1}$] is the diffusivity of hydrogen in the metal, K [cc (STP)$\cdot\text{cm}^{-3}\cdot\text{torr}^{-1/2}$] is the solubility constant for the metal, P_2 [torr] and P_1 [torr] are the upstream and downstream pressures, and x [cm] is the metal thickness. The application of Eq. (1) to hydrogen permeation at low driving pressures has been frequently questioned in the literature. However, Strehlow and Savage[4] showed that Eq. (1) adequately represented data for hydrogen permeation through nickel over a pressure range from $<10^{-3}$ to 750 torr. Both K and D are generally accepted as exponential

functions of temperature; thus, the general expression for permeation flux through an unoxidized metal is:

$$J_M = \frac{D_o K_o}{x} [\exp(-E/KT)] \; (P_2^{1/2} - P_1^{1/2}) \qquad (2)$$

where D_o and K_o are pre-exponential constants, E is the energy of activation for permeation (the sum of the enthalpy of solution for gas in the metal and the energy of activation for diffusion), K is the gas constant and T [°K] is the temperature. This equation differs from that of Richardson, Nicol, and Parnell[7] only in that a term containing $T^{1/2}$ is not present. This term was incorporated in that earlier work because of a kinetic theory argument which may not apply to permeation. [Equation (2) is presented here for general information and is not further considered in this work.]

In considering tritium permeation, the role of isotopic dilution with protium must be included in a functional description. This subject was addressed in an earlier paper,[5] in which it was shown that the primary consideration is the hydrogen isotope equilibria. Assuming equilibrium between tritium and protium according to the reaction:

$$1/2 \; H_2 + 1/2 \; T_2 = HT,$$

we have

$$K_p = \frac{P_{HT}}{(P_{H_2} P_{T_2})^{1/2}} , \qquad (3)$$

or

$$P_{T_2}^{1/2} = \frac{1}{K_p} \frac{P_{HT}}{P_{H_2}^{1/2}} , \qquad (4)$$

where K_p is the equilibrium constant for the reaction as written above. When an expression for permeation of tritium in the presence of protium through an unoxidized metal is desired, Eq. (4) may be used for P_2 and/or P_1 in Eq. (1) or Eq. (2).

The above equations are generally applied to the permeation of hydrogen isotopes through clean metals. The situation becomes more complex for permeation of hydrogen through an oxidized metal, and several additional factors need to be considered. These are:

(1) Oxides generally have lower permeabilities than metals;
(2) The oxide may exist on one or two surfaces of the metal;
(3) The oxide may be increasing in thickness by an oxidation or corrosion process, thereby decreasing the permeation rate;
(4) The oxide may have defects which permit non-uniform concentrations of hydrogen to exist in the metal with consequent channeling of hydrogen through the metal.

Corrosion is itself a complex function of the oxidation potential of the system and the detailed kinetics involve numerous diffusion processes. The role of the oxidation potential in permeation was discussed by Strehlow and Savage[4] who expressed the oxidation potential for the steam oxidation of a metal as the H_2O/H_2 ratio. Although the oxidation potential in the gas phase may be controlled by the H_2O/H_2 ratio, the rate of oxidation is not necessarily controlled by this ratio. In fact, many alloys contain metals that, in small quantities or as powders, are easily oxidized; however, in bulk form oxide films may be produced on these alloys by slow kinetics because of a low rate of diffusion of the metal atoms through the bulk metal and the oxide to the surface. Furthermore, the rates of diffusion of H_2 and H_2O through the oxide are different, and the oxidation potential at the metal-oxide interface will be different from that at the oxide surface. The present model will consider hydrogen permeation through metals with oxide coatings in simplified manner; future models will be more complicated.

In steam generators designed for nuclear power plants, the construction material is in contact with steam on one side and an environment of lower oxidation potential on the opposite side. Consequently, we will consider the case of hydrogen permeation through a metal with only one surface oxidized. We assumed that the hydrogen permeated from the oxide surface to the opposite and oxide-free metal surface as indicated in Fig. 1. It should be noted, however, that the development of the model does

ORNL-DWG 75-12229

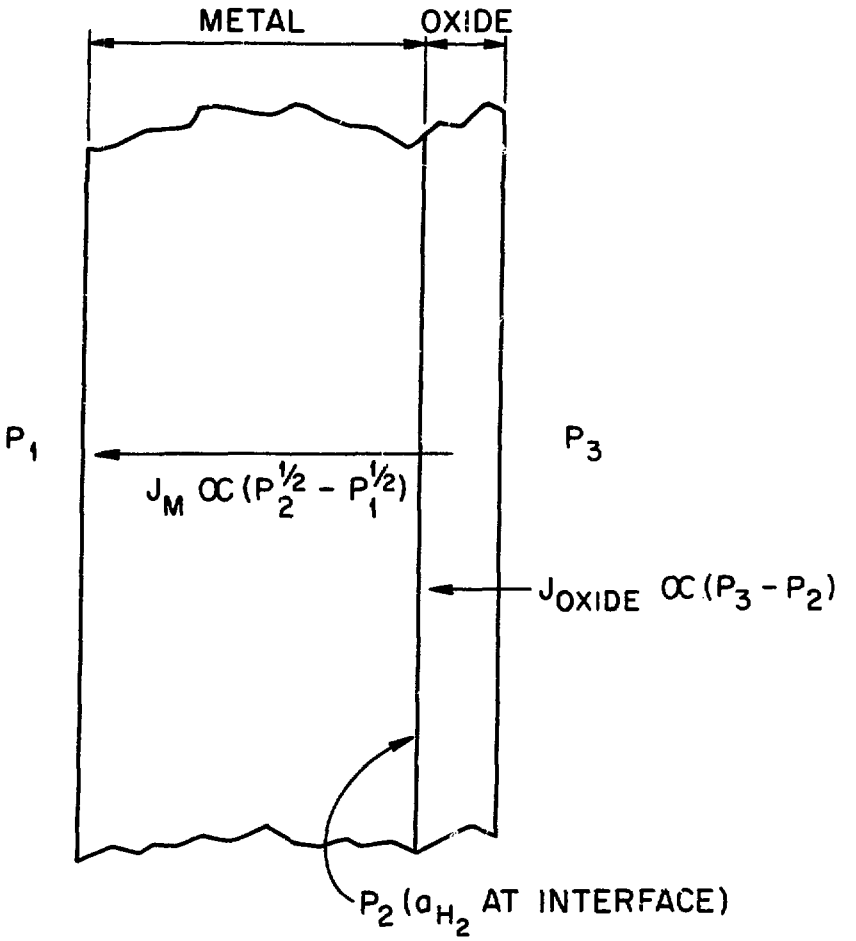

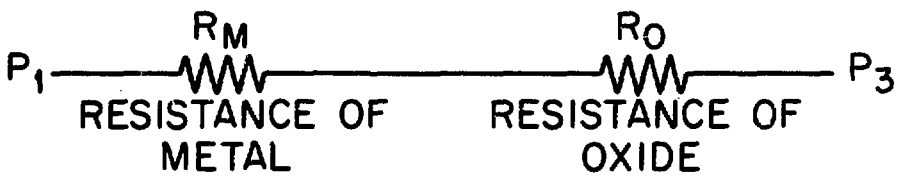

Fig. 1. Model for Permeation of Hydrogen Through Metals with Perfect Oxide Coatings. The flux through the sample depends on the total resistance of the sample, which may be considered as the resistance of the oxide in series with that of the metal.

not depend on the direction of flow; thus, the following arguments would apply to the flow in either direction. The permeation through a coated sample will depend on the characteristics of the two materials; but, at steady-state conditions the flux through the oxide will be equal to that through the metal, regardless of the direction of flow.

Hydrogen permeates through most oxides as molecular H_2, and the equation for the flux, J_o, through the oxide has been given[8] as

$$J = \frac{F}{Y(t)} (P_3 - P_2), \tag{5}$$

where F is a proportionality constant similar to a diffusion constant, P_3 and P_2 are the respective upstream and downstream H_2 pressures and Y(t) is a function describing the time dependent thickness of the oxide. (Note that the downstream pressure for the oxide is the upstream pressure for the metal.) The kinetics for the formation of an oxide film on a metal is often a parabolic function of time,[9] such that

$$Y(t) = mt^{1/2} \tag{6}$$

where m is a proportionality constant and t is time. For this case, the flux through the oxide may be rewritten as

$$J_o = \frac{K'}{t^{1/2}} [P_3 - P_2]. \tag{7}$$

[Other functions for Y(t) could be substituted into Eq. (5) without changing the course for the model.] For permeation through the oxide-coated metal, the flux through the oxide equals that for the metal, and Eqs. (1) and (7) may be combined to give

$$\frac{DK}{x} [P_2^{1/2} - P_1^{1/2}] = \frac{K'}{t^{1/2}} (P_3 - P_2), \tag{8}$$

where P_3 is the driving pressure at the oxide surface, P_2 is the pressure at the metal-oxide interface, and P_1 is the pressure at the metal surface (Fig. 1). Since Eq. (8) is quadratic with respect to $P_2^{1/2}$, a solution is

$$P_2^{1/2} = -\frac{DKt^{1/2}}{2xK'} + 1/2 \left[\left(\frac{DK}{K'x} \right)^2 \cdot t + 4 \left(P_3 + \frac{DK\, t^{1/2}\, P_1^{1/2}}{K'x} \right) \right]^{1/2}. \tag{9}$$

The product, DK, may be determined for the metal without the oxide coating, and a value for K' would be determined for the oxide in a separate experiment. The calculated value for P_2 would be used in Eq. (1) or (7) to calculate the permeation flux through the oxide-coated sample.

The above equations could be used to describe permeation through a sample of metal with a perfect oxide coating; i.e., one that has no cracks, holes, etc. However, the surface oxidation of most metals will produce oxide coatings with imperfections, and in power-plant steam generators there may be physical changes in the oxide, such that some of the hydrogen can diffuse through the metal essentially independent of the oxide. In this case, the total flux is the sum of that hydrogen which diffuses through the oxide and then through the metal and that hydrogen which passes through the imperfections and diffuses only through the metal. The differences in flux through a sample with a perfect oxide coating and a sample with a defective oxide coating can be visualized by comparing Fig. 1 and Fig. 2. These two figures also show the resistances of the samples to hydrogen permeation, indicating the similarity of hydrogen permeation and electrical conductivity. Using this analogy, one deduces that the total flux, J_t, for permeation through a sample with a defective coating is equal to the sum of the fluxes for the perfect portion of the sample, J_M' or J_o', and the flux for the defective portion of the sample, J_D; i.e.,

$$J_t = J_M' + J_D = J_o' + J_D. \tag{10}$$

Expressions for the flow of a gas from a metal through an oxide coating with cracks, holes, etc. have been given by Strehlow and Savage[9] in the general form,

$$J_D = \frac{DK}{f(d)} \left(P_3^{1/2} - P_1^{1/2}\right), \tag{11}$$

where f(d) is related to the size, geometry and spacing of the imperfections in the oxide. The direction of the flux has no effect on the form of Eq. (11). Regardless of the mathematical character of f(d), the

ORNL-DWG 75-12231

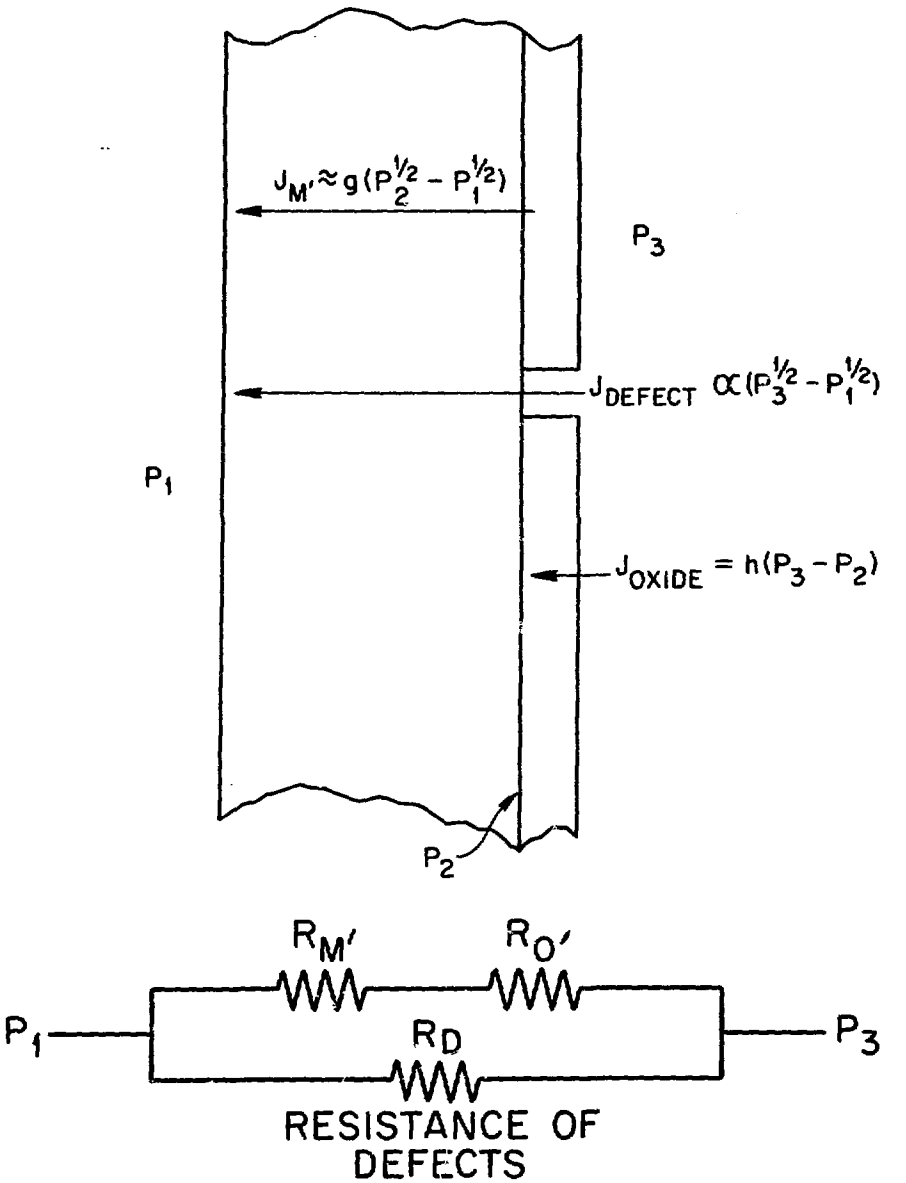

Fig. 2. Model for Permeation of Hydrogen Through Metals with Defective Oxide Coatings. The flux depends on the total resistance of the sample which is considered as the resistance of the defective portion parallel to that of the perfect portion of the sample. In the text, $g = DK/x$ and $h = K'/t^{1/2}$.

quality of the oxide film may be expressed as the flux that passes through the defective portions of the sample relative to the flux for the sample with no oxide film. Then f(d) in Eq. (11) may be replaced with a film quality factor, M^{-1}, and Eq. (11) becomes

$$J_D = M \frac{DK}{x} (P_3^{1/2} - P_1^{1/2}). \tag{12}$$

For a sample with large voids in the oxide film or with large areas of unoxidized metal, M is the fraction of the surface that is not oxidized or covered. For a film with pores of circular cross-section and with the sizes and spacings of the defects small compared to the metal thickness,

$$M = \frac{ax}{\ell^2} \tag{13}$$

where a is the average radius of the defects, and ℓ is the average half-distance between the defects.[10]

Likewise, the flux through the perfect oxide portion will be

$$J_M' = (1 - M) \frac{DK}{x} (P_2^{1/2} - P_1^{1/2}) \tag{14}$$

or

$$J_o' = (1 - M) \frac{K'}{t^{1/2}} (P_3 - P_2). \tag{15}$$

Then the sum of Eq. (12) with (14) and with (15) are respectively

$$J_t = (1 - M) \frac{DK}{x} (P_2^{1/2} - P_1^{1/2}) + M \frac{DK}{x} (P_3^{1/2} - P_1^{1/2}), \tag{16}$$

and

$$J_t = (1 - M) \frac{K'}{t^{1/2}} (P_3 - P_2) + M \frac{DK}{x} (P_3^{1/2} - P_1^{1/2}). \tag{17}$$

The relation between the total flux and the driving pressure, P_3, is obvious from Eq. (17). A good oxide film with $M \to 0$ will cause the total flux to be first-power dependent on P_3, and a poor oxide film ($M \to 1$) will not affect the conventional half-power dependence on the driving pressure.

It is difficult to visualize the changes in J_t for intermediate values of M. We have assumed values for $K'/t^{1/2}$ and for DK/x, and calculated J_t as functions of M and P_3 when $P_1 = 0$. Plots of flux vs P_3

are shown in Fig. 3 for five values of M. Values of M apparently need to be <0.3 (the surface more than 70% covered) for an oxide to significantly change the flux. The most common effect of surface oxidation will be to change the pressure relationship on flux from a square-root dependence to a relationship that includes a square-root dependence for high pressures, a first-power dependence at intermediate pressures, and a square-root dependence at low pressures. Furthermore, there will be some wide range of pressures where the flux will be dependent on the pressure to a power between 0.5 and 1.0.

This model for the permeation of hydrogen through steam generator materials will be extended and tested in the future. In order to make the model more applicable, a better definition of the kinetic term Y(t) [Eq. (6)] to accurately describe the effects of continuous oxidation is necessary. Further definition of the film quality factor to better describe the chemical and physical integrity of oxide coatings is also required. For now, the most significant conclusions are that the effects of oxide coatings to impede tritium permeation can be determined, and that the physical quality of the oxide coating will be very significant.

REFERENCES

1. R. W. Webb, Permeation of Hydrogen Through Metals, NAA-SR-10462, Atomics International (1965).

2. R. Gibson, P. M. S. Jones, and J. A. Evans, The Permeation and Diffusion of Hydrogen Isotopes Through Stainless Steels: Part 1, Niobium Stabilized 5110 Steel, AWRE-47/65, U. K. Atomic Energy Authority, Aldermaston (1965).

3. P. S. Flint, The Diffusion of Hydrogen Through Materials of Construction, KAPL-659, Knolls Atomic Power Laboratory (1951).

4. R. A. Strehlow and H. C. Savage, Nucl. Technol. 22, 127 (1974).

5. J. T. Bell, R. A. Strehlow, J. D. Redman, H. C. Savage, and F. J. Smith, Proc. 23rd Conf. Remote Systems Technology, 1975. In press.

6. J. S. Watson, An Evaluation of Methods for Recovering Tritium from the Blankets or Coolant Systems of Fusion Reactors, ORNL-TM-3974 (1972).

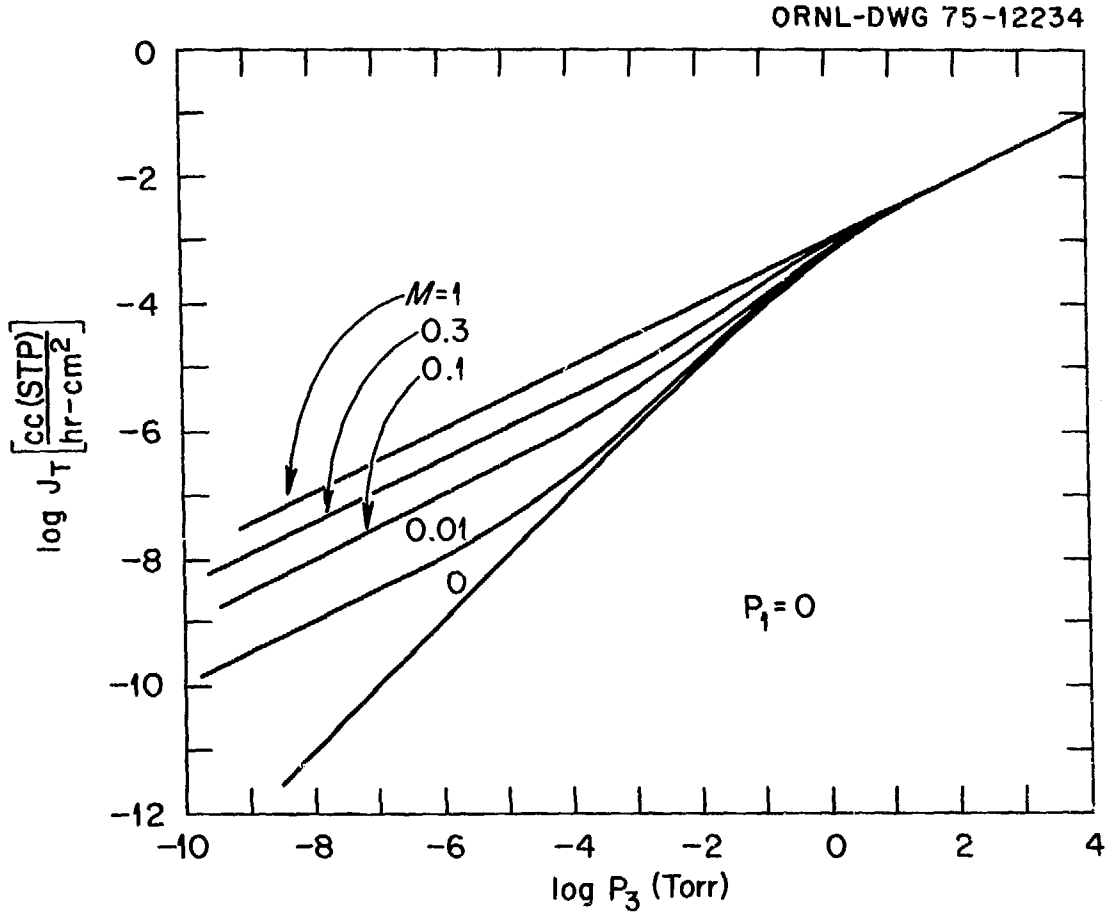

Fig. 3. Calculated Flux vs Driving Pressure Based on the Model for Hydrogen Permeation Through Metals with Defective Oxide Coatings [see Eq. (17) in text]. For these calculations, $DK\,x^{-1} = K't^{-1/2} = 10^{-3}$, and M was chosen to display the effects of this film quality factor on the flux.

7. O. Richardson, J. Nicol and T. Parnell, Phil. Mag. Ser. 6, 8, 1 (1904).

8. Saul Dushman, Scientific Foundations of Vacuum Technique, 2nd ed., ed. by J. M. Lafferty, pp. 574-581, John Wiley and Sons, Inc., New York.

9. O. Kubaschewski and B. E. Hopkins, Oxidation of Metals and Alloys, 2nd ed., pp. 82 et seq., London Butterworths, 1962.

10. R. A. Strehlow and H. C. Savage, J. Nucl. Materials 53, 323-327 (1974).

EXPERIMENTAL STUDIES OF TRITIUM BARRIER CONCEPTS FOR FUSION REACTORS*

V. A. Maroni, E. H. Van Deventer,
T. A. Renner, R. H. Pelto** and C. J. Wierdak†

Chemical Engineering Division
Argonne National Laboratory
Argonne, Illinois 60439

ABSTRACT

On going experimental studies at ANL aimed at the development of methods to reduce tritium migration in fusion reactor systems currently include (1) work on the development of multilayered metal composites and impurity-coated refractory metals as barriers to tritium permeation in elevated temperature (>300°C) structures and (2) investigations of the kinetics of tritium trapping reactions in inert gas purge streams under conditions that emulate fusion reactor environments. Significant results obtained thus far are (1) demonstration of >50-fold reductions in the hydrogen permeability of stainless steel structures by using stainless steel-clad composites containing an intermediate layer of a selected copper alloy and (2) verification that surface-oxide coatings lead to >100-fold reductions in the hydrogen permeability of vanadium, but that severe oxygen penetration and embrittlement of the vanadium occur at temperatures in the range from 300 to 800°C and under conditions of extremely low oxygen potential. Other considerations pertaining to the large-scale use of metal composites in fusion reactors are discussed, and progress in efforts to demonstrate the fabricability of metal composites is reviewed. Also presented are results of studies of the efficiencies of (1) CuO and CuO-MnO_2 beds in converting HT to HTO and (2) magnesium metal beds in converting HTO to HT.

* Work performed under the auspices of the U.S. Energy Research and Development Administration.

** Undergraduate research program participant from Michigan State University.

† Undergraduate research program, participant from Illinois Institute of Technology.

INTRODUCTION

An experimental program is in progress at ANL to evaluate various concepts for improving tritium containment and control in fusion reactor systems. The methods that have been or are currently being studied include (1) multilayered metal laminates containing at least one layer of material with a relatively low hydrogen permeability (2) hydrogen-impermeable impurity coatings on metal surfaces, and (3) inert gas purge streams with tritium trapping capabilities. The principal objective of this effort is to contribute to the development of a more advanced technology for preventing tritium migration (by leakage, permeation, etc.) in experimental fusion devices and fusion power reactors. The following sections contain capsule summaries of recent progress in each of the areas of study outlined above.

HYDROGEN PERMEATION CHARACTERISTICS AND MECHANICAL BEHAVIOR OF MULTILAYERED METAL LAMINATES

The objective of this portion of the ANL tritium barrier development work is to prepare and characterize multilayered laminates in which a material with a relatively low hydrogen permeability (*e.g.*, selected copper or beryllium alloys, aluminum) is sandwiched between layers of the kinds of structural metals currently considered to have application in fusion technology (*e.g.*, refractory metal alloys, stainless steels). These multilayered materials are expected to be useful in the construction of (1) steam generator tubing and other heat-transfer/energy conversion system components; (2) liners for the blanket-shield interface; and (3) ductwork and other hardware for the transport, processing, and storage of tritium. An added advantage of the use of composite or multiplex materials is that compatibility problems associated with the interfacing of blanket, primary coolant, and secondary working fluids can be ameliorated by selecting (for the exterior layers of the multiplex) metals that are compatible with the fluid being contacted. For example, a liquid lithium circuit could be interfaced with a high pressure helium loop as follows: lithium to Nb-1%Zr/barrier layer/304-SS to helium.

Experimental Procedure For Hydrogen Permeation Studies

The 316-SS(0.5mm)/Cu(1.0mm)/316-SS(0.5mm), 304-SS(0.25mm)/Nb(0.27mm), and 304-SS(0.25mm)/Cu(0.42mm)/Nb(0.19mm) bonded metal laminates were obtained on a special order from Texas Instruments Incorporated, Attleboro, Massachusetts. (The numbers in parentheses indicate the individual layer thicknesses.) Each laminate was in sheet form and was used essentially as received. The individual studies of 304- and 316-SS were carried out on sheet material that conformed to ASME Specification SA-240. The pure copper was the Electrolytic Tough Pitch Grade, 99.9+% Cu. The "aluminum bronze" (Cu-10 wt % Al - 4 wt % Fe) was obtained from Copper and Brass Sales, Inc. without specifications. The hydrogen gas, ultra-high purity grade (99.99+%), obtained from Air Products and Chemicals, Inc., was passed through a silver-palladium thimble at 300°C prior to use.

Circular membranes were assembled for the hydrogen permeation studies as shown in Fig. 1. The membrane seal-weld indicated in Fig. 1 was made in vacuo with an electron beam welder and was helium leak tested prior to use. Each membrane assembly was enclosed in a quartz jacket and placed in a clam-shell type Marshall furnace. A dry helium purge was maintained inside the jacket in order to avoid excessive oxidation of the seal-weld and to reduce the possibility of having any hydrogen permeate through the tubing on the downstream (low hydrogen pressure) side of the membrane.

The area of each membrane was determined by opening the membrane assembly (with a lathe) and taking an average value of several measurements of the diameter of the seal-weld, as measured with a moving-stage microscope. The thickness of each membrane was determined from a photomicrographic measurement made on a mounted sample of the as-received material. The areas and thicknesses of the membranes studied are listed in Table 1.

The hydrogen permeation apparatus consisted of (1) a pyrex vacuum system with a liquid nitrogen trapped mercury diffusion pump and mechanical forepump (ultimate vacuum $\leq 10^{-5}$ Torr), (2) an all-metal hydrogen pressure control (HPC) system, and (3) a Toepler pump to

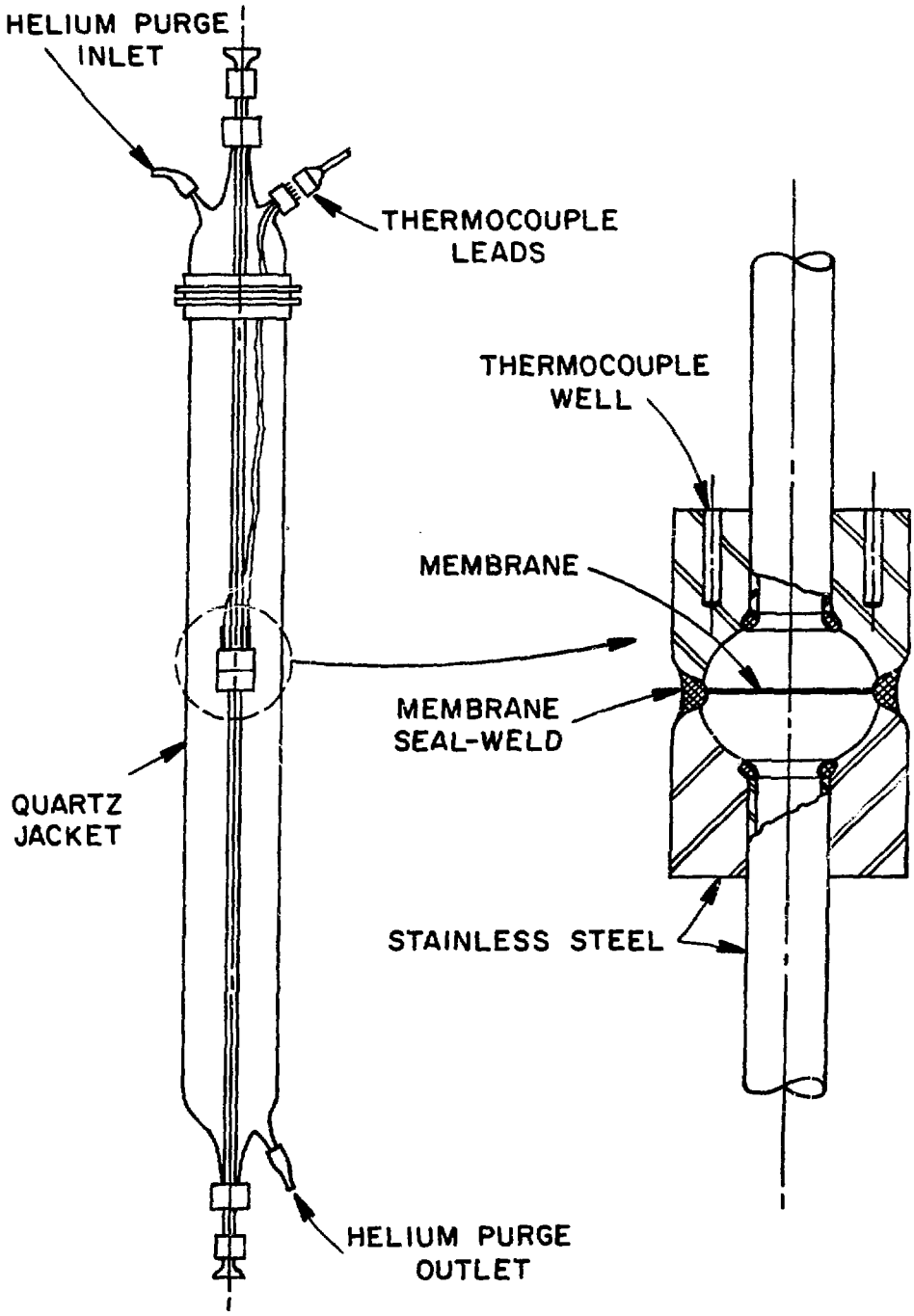

Fig. 1. Membrane Assembly Used for the Hydrogen Permeation Studies

Table 1. Areas and Thicknesses of the Metallic Membranes on Which Hydrogen Permeation Measurements Were Made

Membrane	Total Thickness (mm)	Area (cm^2)
316-SS/Cu/316-SS	1.85	6.40
304-SS/Nb	0.53	6.22
304-SS/Cu/Nb	0.86	6.16
304-SS	0.61	5.89
316-SS	1.52	5.04
Copper	0.86	5.93
Aluminum Bronze[a]	0.67	4.34

[a] Copper - 10 wt % Al - 4 wt % Fe

collect the permeating gas. Constant upstream pressures of purified hydrogen were maintained in the HPC system by using a capacitance manometer (MKS Baratron Model 170-M) as a null-meter which in turn operated a solenoid valve. Hydrogen, that had passed through the silver-palladium thimble, was admitted (by the solenoid valve) to a fine metering valve which in turn controlled the rate of entry of hydrogen into the upstream portion of the system. The hydrogen pressure on the downstream side of the membrane was maintained at $<10^{-1}$ Torr by the Toepler pump.

At each temperature and upstream hydrogen pressure for which a measurement was made, equilibrium (steady-state) flow was established by overnight pumping on the downstream side of the membrane. Rate studies were initiated by simultaneously starting a chronometer and redirecting the downstream hydrogen flow to the Toepler pump via a three-way stopcock. The gas collected by the Toepler pump was forced into a calibrated volume held at a measured, reasonably constant temperature. The amount of gas collected by the Toepler pump was determined at random time intervals (over roughly an

eight-hour period) by measuring the gas pressure in the calibrated volume. Pressure readings were taken by cathetometer measurements of the height of a mercury column connected to the Toepler pump. Plots of gas volume (STP) collected versus time yielded reasonably straight lines that extrapolated close to the origin. Periodic mass spectrometric and gas chromatographic analyses of the gas collected by the Toepler pump revealed that hydrogen constituted >99% of the gas volume in all cases. In most cases, the major impurity was methane (~100 volume ppm).

Hydrogen Permeabilities of Selected Metal Laminates

Hydrogen permeability data for the materials listed in Table 1 were reported in two earlier publications.[1,2] Preliminary analyses of these permeation data were made on the basis that the hydrogen flow through each material was controlled by bulk diffusion (as given by Fick's law) and that the solubility of hydrogen in each material was proportional to the square root of the hydrogen pressure. The resulting expression for the permeation rate, R, (as developed for example by Webb[3] and Stickney[4]) is given in equation 1

$$R = \Phi \cdot \Delta(P)^{0.5} \tag{1}$$

where

$$\Phi = \Phi^{\circ} \exp(-Q_p/RT). \tag{2}$$

In these expressions Φ is the intrinsic hydrogen permeability of the material, $\Delta(P)^{0.5}$ is the difference of the square roots of the upstream and downstream hydrogen pressures, and T is the Kelvin temperature. Values of Φ for a given temperature and pressure are determined from the measured hydrogen throughput rate, F, as follows:

$$\Phi = [F \cdot X]/[A \cdot \Delta(P)^{0.5}] \tag{3}$$

where X and A are respectively the thickness and area of the membrane.

Values of the preexponential term Φ° and the activation energy Q_p (in equation 2) obtained by least-squares-refinement of the Φ-T data sets collected for each material, are given in Table 2.

Table 2. Values of Φ° and Q_p Derived From Hydrogen Permeation Data for the Indicated Materials

Material	Φ°, cc(STP)·mm/cm^2·hr·atm$^{0.5}$	Q_p Calories/Mole
316-SS-/Cu/316-SS	3,162	23,566
304-SS/Nb	10,230	27,013
304-SS/Cu/Nb	9,736	21,332
304-SS	2,259	17,223
316-SS	1,149	15,605
Copper	11,920	21,451

The data from which the results in Table 2 were derived were collected over the range from 10 to 600 Torr (upstream hydrogen pressure) and 400 to 800°C. It is probably not advisable to use these results for computations at very low hydrogen pressures (<<1 Torr) where effects due to unreduced surface impurities may be expected to dominate the permeation process.[5] (Studies of the hydrogen permeabilities of the materials in Table 1 and of related materials at driving pressures considerably below 1 Torr are currently in progress in our laboratory.)

In recent months an attempt has been made to give further refinement to the permeation data presented in references 1 and 2. To determine more accurately the exact power dependence on pressure, sets of permeation data collected at constant temperature were plotted as a function of upstream hydrogen pressure in the log-log fashion recommended by Strehlow and Savage.[5] This plot (shown in Fig. 2) gives pressure dependencies that range from 0.44 to 0.61 for the materials listed in Table 1, indicating that the previous assumption

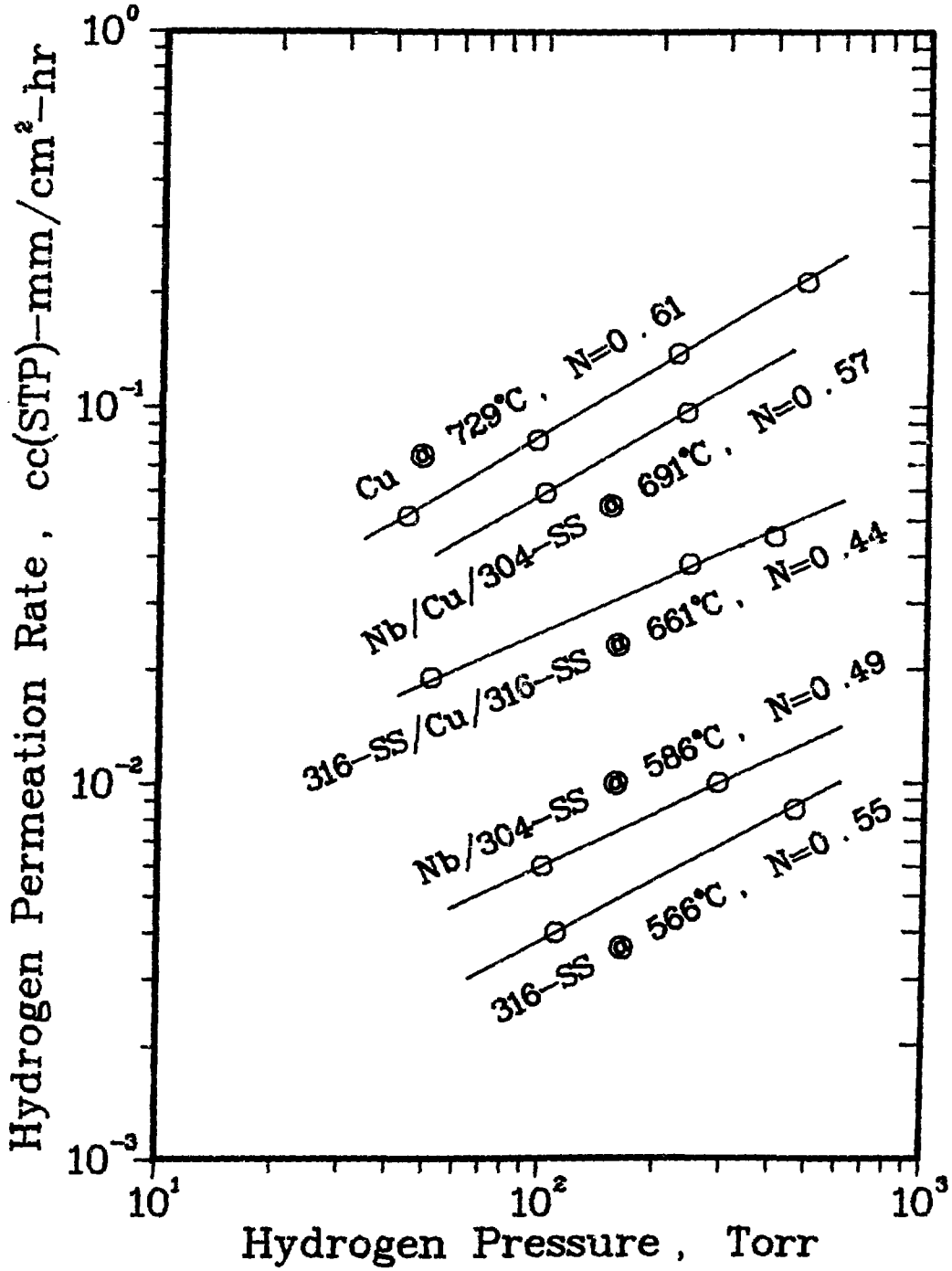

Fig. 2. Log-Log Plot of Hydrogen Permeation Rate versus Hydrogen Pressure for the Materials Listed in Table 1

of a half power dependence[1,2] represents a reasonably accurate portrayal of the permeation behavior. Although the deviations from an exact 0.5 power dependence could well be ascribed to experimental uncertainty in most cases, we have found that linear plots of permeation rate vs (hydrogen pressure)^N do extrapolate to the origin (see Fig. 3) if the correct value of N from Fig. 2 is used for each material but do not extrapolate to the origin if N = 0.5 is used.

An additional finding from our studies of multilayered metal laminates has been that the layers of a laminate act as a series of resistors to hydrogen flow such that the calculated permeability of the laminate (based on the permeabilities of the individual layers) is well within a factor of two of the measured permeability.[1,2] Alternative use of permeation expressions based on pressure to the 0.5 power or on pressure to the specific power determined from Fig. 2 has no significant effect on this finding. In other studies carried out by electron microprobe techniques we have demonstrated that large scale hydrogen throughput [in excess of 8cc(STP)/cm^2] has no measurable effect on the integrity of the metallurgical interfaces in the bonded metal laminates studied thus far.[6]

Development of Barrier Layer Materials for Multiplex Metal Structures

The preceding section contained a summary of the potential applicability of multiplex metal composites as barriers to tritium migration (by permeation) through fusion reactor construction materials that are subject to operation at elevated temperature (>300°C). In this section, we discuss the results of experimental studies to identify and characterize materials that would be suitable for use as the barrier layer in stainless steel-clad multiplexes. Initial studies have focused on copper and its alloys because (1) their relevant physical and mechanical properties (particularly thermal expansion coefficients) are well matched with those of stainless steels insofar as composite preparation and high temperature integrity are concerned, and (2) a substantial industrial technology base for the preparation of both metallurgically- and mechanically-bonded copper/stainless steel composites appears to exist.

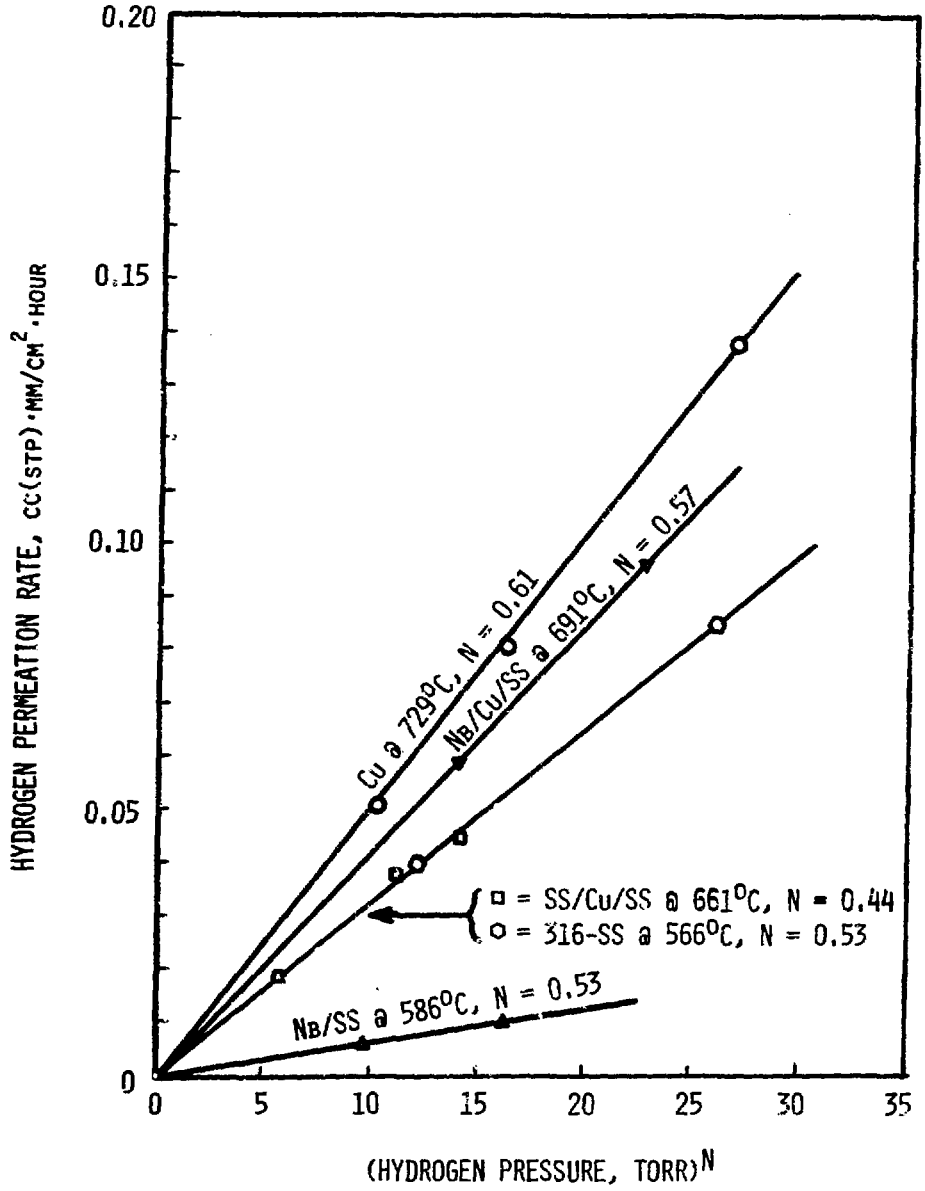

Fig. 3. Linear Plot of Hydrogen Permeation Rate versus Hydrogen Pressure to the N^{th} Power Using Values of N from Fig. 2

Hydrogen permeation data obtained for pure copper and the copper-aluminum-iron alloy (from reference[2]) are shown in Fig. 4 together with the least-squares refined permeation curves (solid lines) derived using equation 2. Also shown in Fig. 4 are the permeability curves for these same materials obtained by other investigators.[7-10] In the case of pure copper, the agreement with the results of Belyakov and Zvezdin[10] and Perkins and Begeal[7] is very good. The work of Smithells and Ransley[9] dates back to 1935, and the apparent discrepancy may be a reflection of the purity of the samples used in their studies. The curve representing the results of Ehrmann *et al.*,[8] was extrapolated from the temperature region of their data (170 to 240°C). Also, there was some uncertainty in the conversion of the permeability units used by Ehrmann *et al.*, to the units that we normally use. In the case of the copper-aluminum-iron alloy, there is a sizeable disparity between our data and the data of Belyakov and Zvezdin. We are of the opinion that the reduced permeability of this alloy (compared to the permeability of pure copper) is due to formation of an extremely stable bimetallic impurity coating on the alloy's surface. If this is indeed the case, and if the extent of formation of this coating is dependent on impurity potentials in the environment surrounding the alloy prior to or during permeation measurements, then the disparity between our work and that of Belyakov and Zvezdin may be attributable to differences in background impurity levels and/or prior sample history. However, it should also be noted that the permeation rates measured in our study of this alloy are near the background levels of our gas collection apparatus (Toepler pump), which may have biased our readings in the direction of being too high. In order to circumvent this problem in future work, we have constructed an all-metal hydrogen permeation apparatus capable of measuring permeation rates that are orders of magnitude lower than those measurable with the Toepler pump.

Because the hydrogen permeability of pure copper is only a factor of from 2 to 5 lower than that of most conventional stainless steels at elevated temperatures (>400°C), its potential value as a tritium-barrier

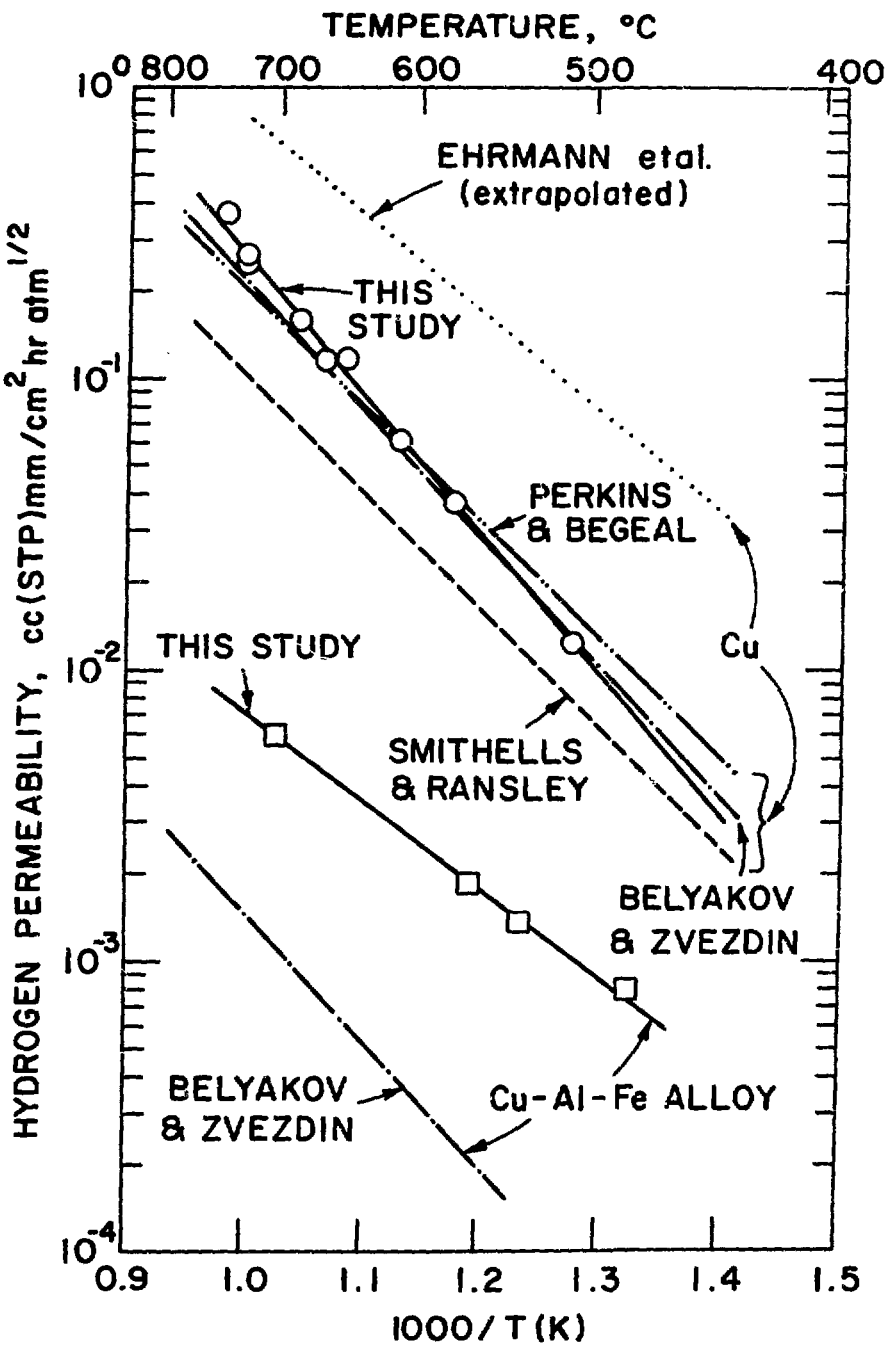

Fig. 4. Compilation of Hydrogen Permeation Data for Copper and the Copper-Aluminum-Iron Alloy

layer in stainless steel-clad composites is low. However, the copper-aluminum-iron alloy would be very attractive for use as a barrier layer, if its permeability can be kept at least as low as our results in Fig. 4 indicate. For example, at 600°C, the hydrogen permeability of a 304-SS/Cu-Al-Fe alloy/304-SS composite (with all three layers having the same thickness) would be ∿50 times lower than the permeability of an equally thick layer of 304-SS (based on our data for the copper-aluminum-iron alloy and for 304-SS).

Work is currently in progress to prepare a series of metallurgically-bonded 304-SS/Cu-Al-Fe alloy/304-SS composites in which the 304-SS and Cu-Al-Fe alloy are subjected to a variety of surface pretreatments prior to bonding. The hydrogen permeation characteristics of these composites will then be examined.

Fabrication Efforts on Multiplex Materials

During the past year, an effort has been undertaken to investigate the prospects for preparing multiplex metal laminates in seamless tube form and joining sections of these laminates by various welding procedures. The ANL Materials Science Division prepared a mechanically-bonded 304-SS/Cu/304-SS composite in seamless tube form by drawing concentric cylindrical billets of 304-SS and copper into intimate contact with one another. Sections of this composite tubing were then joined contiguously (layer to corresponding layer) to form a linear joint as shown in Fig. 5. The joint was fabricated by sequentially electron beam welding (with controlled penetration) all the seams formed by (1) the interior 304-SS layer, (2) the copper half-cylindrical inserts, and (3) the outer 304-SS half-cylindrical inserts. X-rays of the entire welded zone showed no evidence of weld imperfection. In actual operation, this linear joint could be given additional support by surrounding the weld region with a cylindrical 304-SS collar.

Tests of the integrity of the linear joint followed by sectioning to determine the weld penetration depths are planned. Future work will also include an attempt to contiguously T-weld two sections of composite seamless tubing.

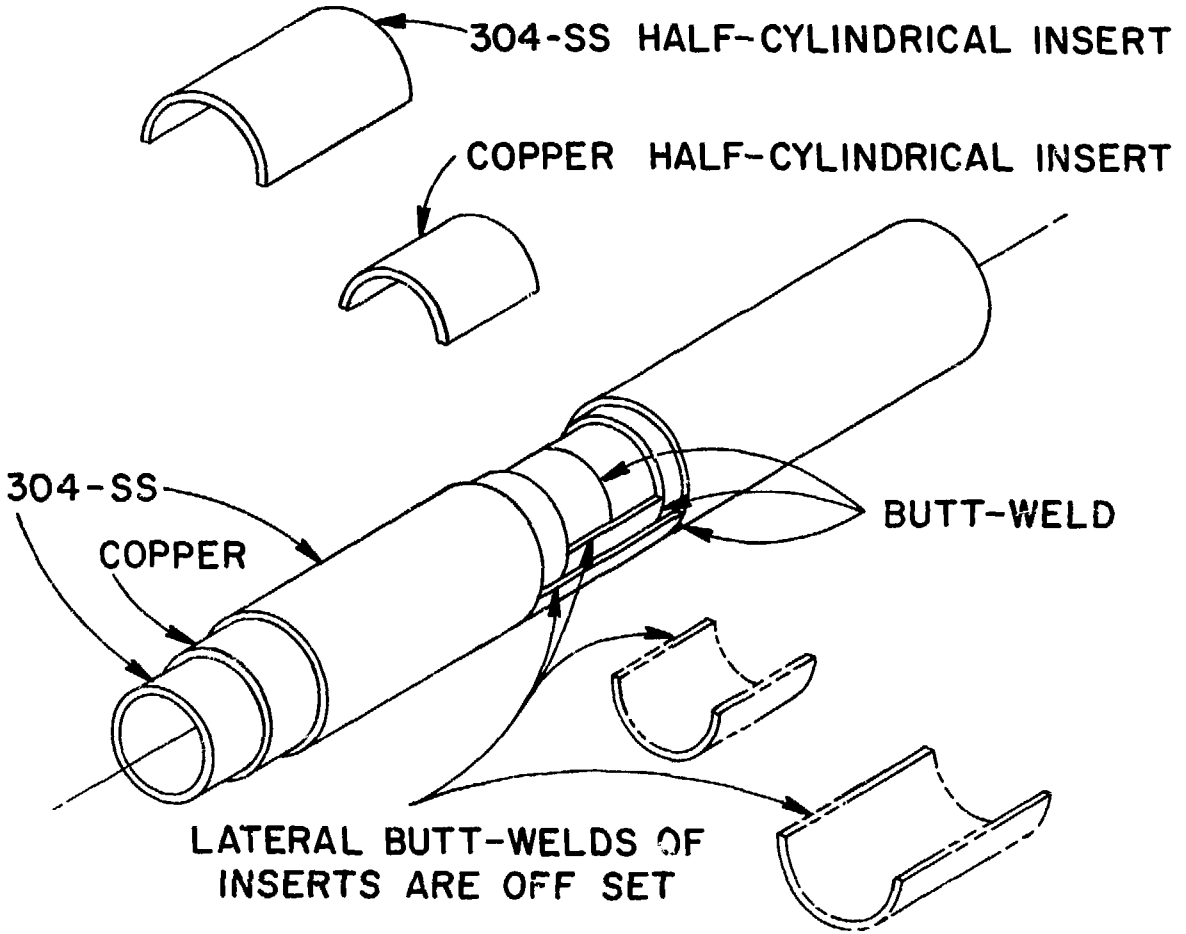

Fig. 5. Contiguous Butt-Weld of a 304-SS/Copper/304-SS Multilayered Seamless Tube

HYDROGEN PERMEATION CHARACTERISTICS OF VANADIUM

Prior studies conducted in our laboratory by Heinrich *et al.*[11] showed that relatively high hydrogen permeation rates could be achieved in the 450 to 550°C range and at 1 atm upstream hydrogen pressure for vanadium samples which had been hydrogen fired (activated) at 850°C just prior to permeation measurements. In order to maintain these high rates, Heinrich *et al.*, indicated that it was necessary to periodically re-fire (reactivate) the samples in hydrogen. The hydrogen permeation curve obtained from their data is shown as a dashed line in Fig. 6. More recently, we have completed a series of studies in which an attempt was made to determine the mechanisms involved in activating and deactivating the hydrogen permeability of vanadium. Results of permeation rate measurements and ion microprobe analyses for several vanadium membranes, examined during the course of these studies, are summarized below.

Hydrogen Permeation Studies

The experimental configuration and procedures used in the studies of vanadium were the same as those described in the preceeding experimental section for the measurements on composite materials. Because of problems associated with flooding of the gas collection equipment (Toepler pump) it was not possible to measure hydrogen throughputs corresponding to permeabilities greater than 10 cc(STP)·mm/cm^2·hr·atm$^{1/2}$; therefore, the high rates achieved by Heinrich *et al.*, for activated vanadium were not substantiated in our work. We did observe, however, that at temperatures above 850°C the hydrogen permeability of a newly mounted vanadium membrane was considerably greater than the upper limit collection rate of our apparatus. In one experimental run an 0.5-mm-thick membrane (MARZ Grade Vanadium) was activated according to the procedure of Heinrich *et al.*[11] and subjected to sixty days of hydrogen permeation at temperatures between 400 and 850°C, upstream hydrogen pressures between 5 and 200 Torr, and a downstream hydrogen pressure of $<10^{-1}$ Torr. The hydrogen permeability of this membrane was measured at periodic intervals and was found to drop monotonically

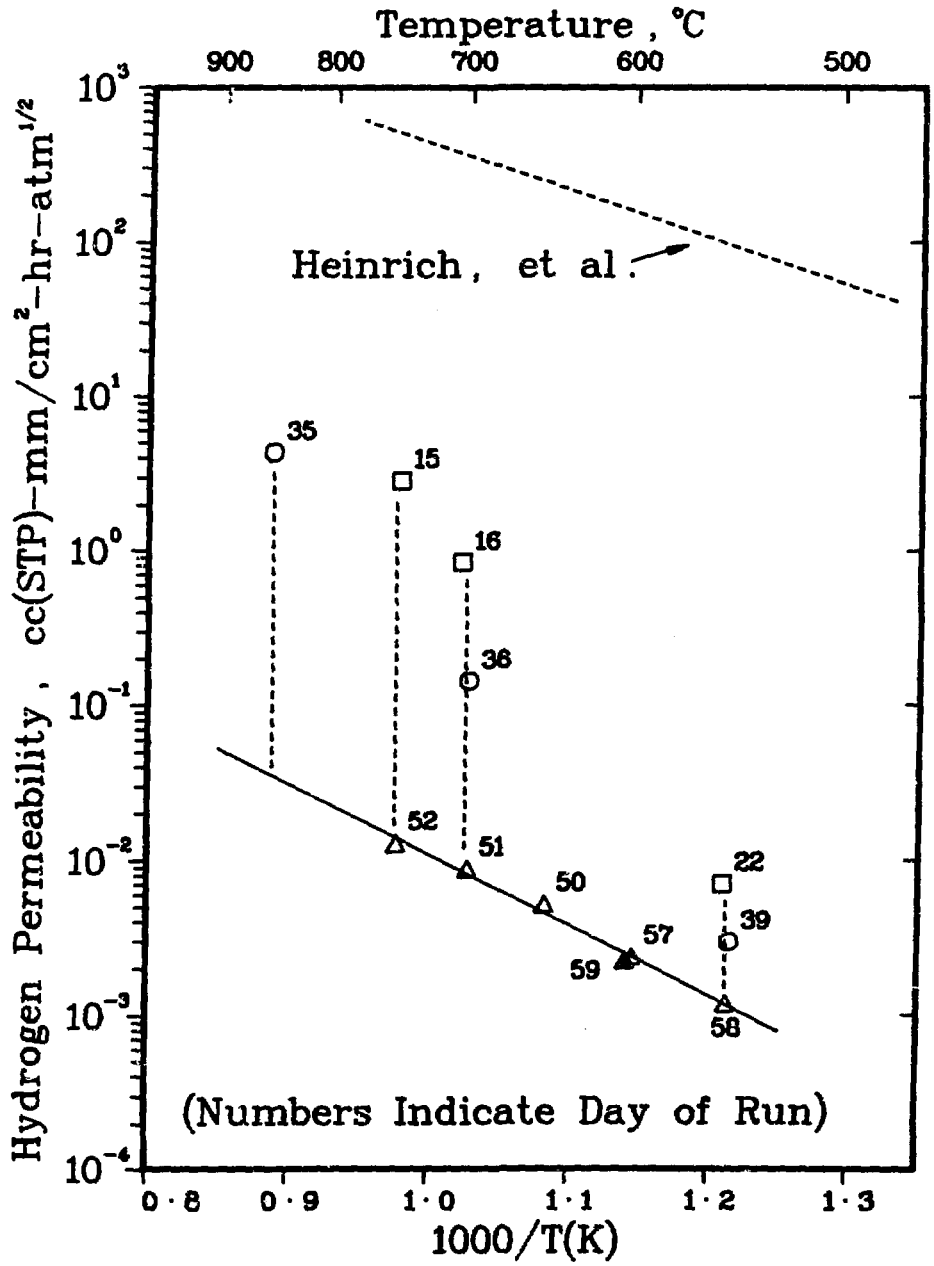

Fig. 6. Hydrogen Permeation Data for Vanadium from Heinrich *et al.*[11] and from the Sixty Day Run Described in the Text

with time. Because of this steady (day-to-day) drop in rate it was not possible to make an accurate determination of the pressure dependence; hence, for the sake of comparison with the data of Heinrich *et al.*, a half-power dependence was assumed.

Some of the results from this sixty day experiment are summarized in Fig. 6. During the first two weeks the rate of decrease of permeability was extremely rapid. Selected results from the third, sixth, and eighth weeks, shown in Fig. 6, give evidence of the continuing decrease in permeability and indicate a leveling off of the permeation rate in the latter stages of the run (after the fiftieth day). The overall decrease in permeability compared to the data of Heinrich *et al.* (assuming they are correct) is roughly five orders of magnitude.

Microprobe Studies

Previously published results obtained from ion microprobe mass analyzer (IMMA) scans of activated and deactivated vanadium samples[12] showed that the major impurity element on the surface of deactivated vanadium (which was not present in significant amounts on activated samples) was oxygen. More extensive IMMA studies than those reported previously have been carried out to obtain a better understanding of the behavior of oxygen on vanadium surfaces at elevated temperatures. The experimental methods used in these studies were the same as those reported in reference 12. Oxygen to vanadium (O/V) ratios as a function of depth into the sample are given in Fig. 7 for four different treatments. The relative oxygen level was determined by ratioing the $^{16}O^+$ and $^{51}V^+$ (0.24% natural abundance) mass peaks. These O/V ratio data were calibrated using IMMA data for the as-received MARZ grade material (indicated by diamonds in Fig. 7) and the analytically determined oxygen content of the as-received material (~150 wppm). (The uncertainty in the O/V ratios given in Fig. 7 is estimated to be around $\pm$ 50%.) With the exception of the data for the as-received vanadium, all other IMMA results in Fig. 7 were obtained on samples that were treated in our permeation apparatus for comparable time periods (~1500

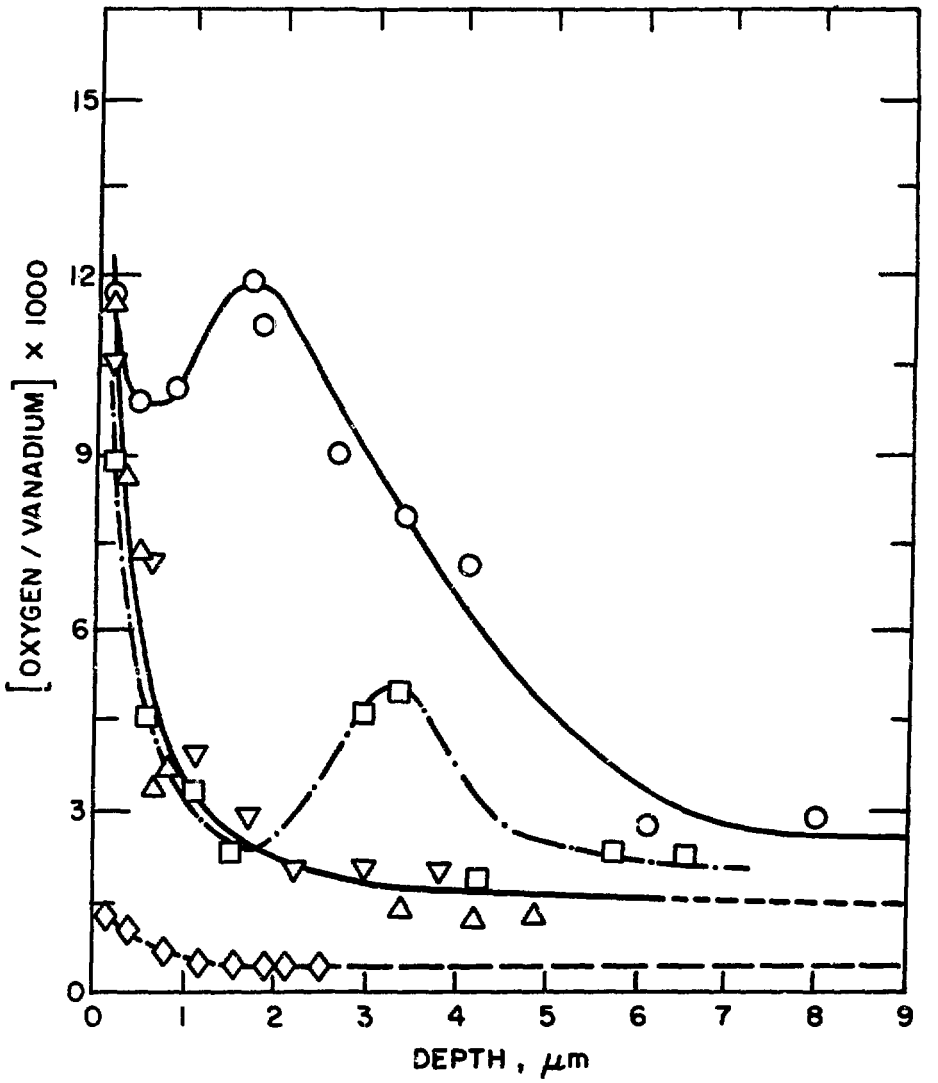

Fig. 7. Ion Microprobe Data for Oxygen to Vanadium Ratio versus Depth. ◊ = as-received vanadium (MARZ Grade), ○ = heavily oxidized sample (see text), △ and ▽ = downstream side of a 1500 hr sample (two separate scans of the same surface)

hours) at temperatures in the range from 350 to 850°C. Data collected for a sample that was inadvertently exposed to atmospheric oxygen levels at an elevated temperature (~500°C) for a short period of time are indicated by circles in Fig. 7. This sample is believed to be the one subjected to heaviest oxidation during its treatment, and the results in Fig. 7 appear to reflect this belief.

Efforts to characterize the source of the occasional humps in the O/V versus depth curves were not overly successful. The humps were not observed with any consistency for a given surface and the depth at which their maxima occurred varied from sample to sample and from location to location on a given sample. Since the results in Fig. 7 do indicate that the oxygen distribution profile within the vanadium used for these studies is, for the most part, relatively smooth, the humps are taken as evidence for the formation (to some extent) of oxide-rich clusters or occlusions. Attempts to correlate these humps with the presence of other impurity species detected by the IMMA scans were largely inconclusive.

Whereas the hydrogen permeability of activated vanadium (as measured by Heinrich *et al.*[11]) is comparable to that of palladium and the silver-palladium alloys commonly used as hydrogen filters,[13] the permeability of the impurity coated vanadium observed in our study actually falls well below the range of permeabilities exhibited by most conventional unoxidized stainless steels.[5,14,15] Although the data in Fig. 6 do reflect the achievement of a relatively steady permeation rate after fifty days of study, this rate (the solid line in Fig. 6) is undoubtedly fixed by the intrinsic oxygen potential in our apparatus. That being the case, any use of the data in Fig. 6 to predict the hydrogen permeability of vanadium should be made discriminately.

Conclusions from the Vanadium Studies

Based upon the results of this investigation and on a cursory examination of thermodynamic property data for the appropriate materials, several conclusions can be drawn regarding the ultimate utility of vanadium in fusion reactors. Results of the studies of oxygen concentration profiles (Fig. 7) show that even in a relatively clean environment,

build-up of oxygen at the vanadium surfaces and significant oxygen penetration into the bulk metal occur readily. In order to avoid severe oxygen penetration, the oxygen potential in fusion reactor coolant circuits employing liquid sodium, liquid potassium, or high pressure helium would probably have to be controlled at levels corresponding to O_2 partial pressures $<10^{-30}$ Torr.[16,17] Consequently, the interfacing of vanadium with liquid sodium or potassium and the containment of high pressure helium streams with vanadium at elevated temperatures will present considerable difficulty.[16,18] In addition, for vanadium-structured fusion reactor designs which employ helium as a coolant, the low oxygen potentials required to preserve the integrity of the vanadium, would compromise the beneficial effects on tritium containment and trapping that result from having ppm levels of O_2 present in the helium.[19]

In liquid lithium blanketed fusion reactors with vanadium support structures, oxygen potentials in the lithium will be much lower than those which would lead to oxidation of the vanadium.[20] (This is a consequence of the fact that the thermodynamic stability of lithium oxide is considerably greater than the stability of any of the oxides of vanadium.[20]) While oxygen penetration of vanadium is not expected to occur in liquid lithium systems, the low oxygen potential created by the lithium environment will preclude the formation of an oxide layer at the lithium-vanadium interface. This being the case, the hydrogen permeation characteristics of the vanadium support structure in contact with lithium could approach those of the activated material shown in Fig. 6, unless the opposing surface of the vanadium is sealed by an oxide layer. Maintenance of an oxide layer on one surface of vanadium without incurring destructive penetration of the bulk metal, will undoubtedly require a carefully controlled oxygen potential. Duplex tubing or other multi-metal configurations in which the interior vanadium surface (the surface between layers of the multiplex) is mildly oxidized, could provide a means of utilizing oxide layers on vanadium to reduce hydrogen, deuterium, or tritium permeation rates.[21]

TRITIUM TRAPPING KINETICS IN INERT GAS STREAMS

This effort is directed toward studies of the kinetics of chemical trapping reactions involving tritium in inert gas streams (*e.g.*, helium, argon, nitrogen). Specific gas stream environments that have practical applications in fusion devices and reactors include (1) high-pressure helium streams used as coolant circuits for power reactor blankets, (2) low-pressure inert gas streams used in conjunction with either double containment jackets for isolated reactor components or whole-room atmosphere purges, and (3) the mainstream fuel cycle for D-T fueled devices or reactors. With regard to the behavior of tritium in helium coolant circuits and in inert gas purge streams, significant advantage in terms of overall tritium containment can be gained by converting the tritium present in these streams to T_2O or THO and then sorbing, desiccating, or otherwise fixing the T_2O or HTO in a medium that is suitable for (1) tritium regeneration and reinsertion into the mainstream fuel cycle or (2) consolidation of low-level tritiated wastes in preparation for long-term burial.

The chemical trapping requirements imposed by the needs of the mainstream fuel purification and recycle system of a D-T fueled fusion reactor are substantially different from those of the gaseous coolant and purge circuits. During the course of passage through the plasma chamber, the D-T fuel mixture will invariably pick up low levels of nonmetallic impurities (*e.g.*, O, N, and C). Since only a small fraction (<5%) of the injected fuel actually undergoes fusion in a single burn cycle, it is absolutely essential (for power reactors) to continuously recycle the unburned D-T mixture. Because of the deleterious effects of impurities on plasma energy balance and stability, the impurities picked up during one burn cycle must be removed prior to reinjection of the recycled fuel mixture. It would be desirable to identify chemical trapping media that can effectively remove these nonmetallic impurities without simultaneously tying up a large quantity of tritium.

The objective of this effort is to evaluate the performance of materials that might be suitable for the two types of chemical trapping operations summarized above. As a beginning for these studies, a trapping

kinetics apparatus was assembled, and a series of tests were performed to evaluate (1) the efficiency of heated CuO/MnO_2 mixtures in converting HT to HTO, (2) the efficiency of heated magnesium beds in converting HTO to HT without simultaneously pumping the HT, and (3) the effectiveness of selected water sorbing media in trapping HTO from flowing inert gas purge streams. The results of these various tritium trapping studies will be used to gain insight concerning the optimum size, configuration, and flow parameters that should be applied to the design of equipment for fuel conditioning and purge stream processing circuits of near term experimental fusion devices and future fusion power reactors.

Experimental Procedure

The apparatus developed for these studies is shown in Fig. 8. The initial branch is designed to permit series testing of an oxidizer bed (*e.g.*, CuO/MnO_2) and a reducer bed (*e.g.*, magnesium metal with provision for by-passing of either or both beds. The second branch is designed to permit testing of various water sorbing or desiccating media and is also fitted with a by-pass. Tritium from the carrier gas cylinder ($\sim$1.7 μCi/cc of HT in argon) is introduced to the pulse chamber with both solenoid valve B and backup valve C closed. Pulses of the tritiated carrier gas are delivered to the trapping circuit by closing valve A, opening valve C and triggering solenoid valve B. (After triggering of a pulse, valve C is closed to guard against any low-level tritium leakage across the seat of solenoid valve B.) Solenoid valve B is controlled by an electronic pulser which opens the valve for a set length of time; hence, uniform-sized pulses of the tritiated carrier gas should be delivered with each triggering. (This uniformity of pulses was demonstrated experimentally.) Tritium counting is performed with a Johnston Laboratories Model 955B Tritium Monitor.

The apparatus in Fig. 8 is set up for either once-through flow studies using an inert sweep gas (valve D open, valve E closed, and valve F open) or recycled-flow studies (valve D closed, valve E open, and valve F closed). In this way, both instantaneous and long-term performance of various conversion beds and water trapping media can be investigated.

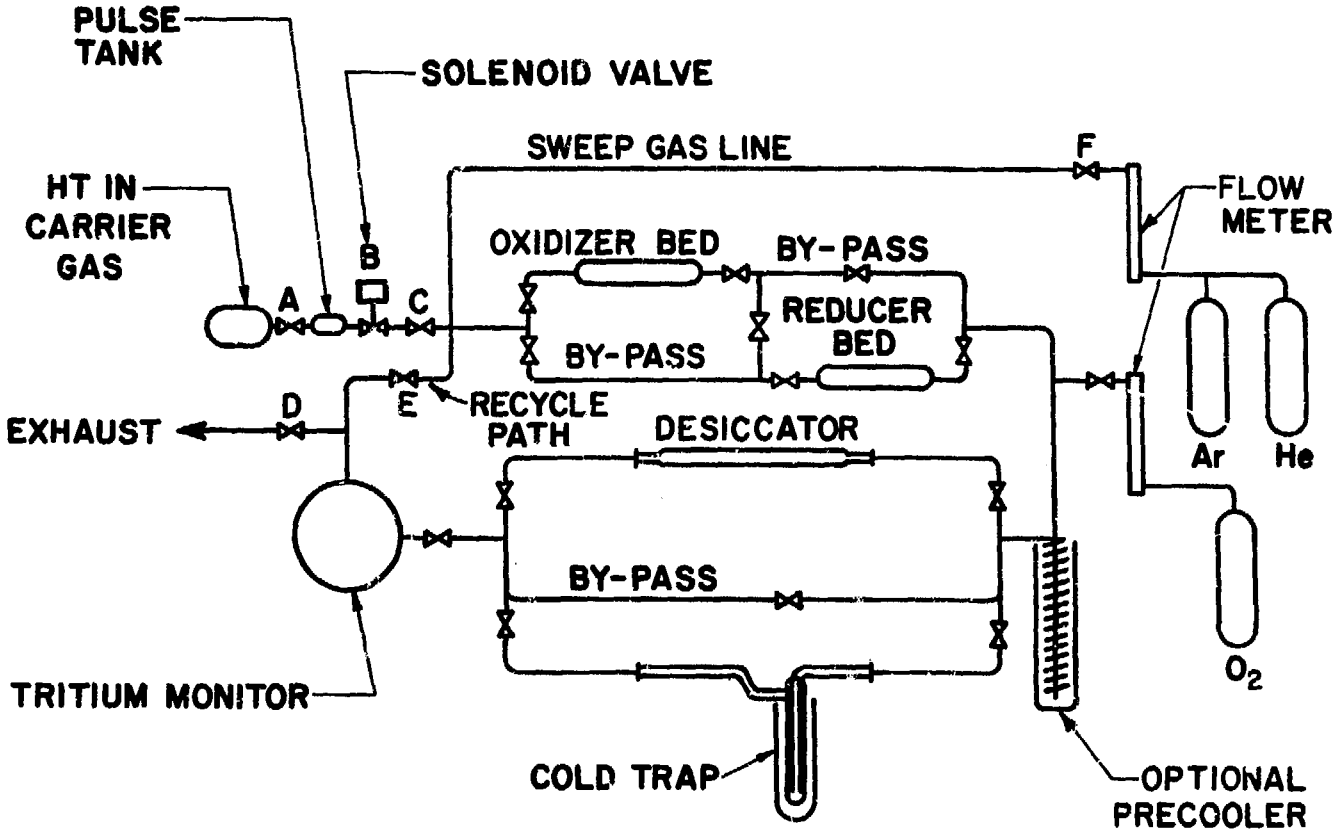

Fig. 8. Apparatus Used for the Tritium Trapping Kinetics Studies

Results of Once-Through Pulse-Flow Studies

In this series of experiments, the tritium pulses were swept once through selected conversion bed and trap configurations and exhausted. The objective of the experiments was to test the effectiveness of a particular bed and trap combination on tritium concentration in the sweep gas, when tritium is admitted to the system in bursts. Preliminary experiments showed that the tritium in the carrier gas is mostly in the form HT when it leaves the pulse chamber and that a liquid nitrogen cooled copper mesh trap effectively removes HTO from the sweep gas but does not remove HT. Results of several different types of pulse-flow studies are summarized below:

Effects of Flow Rate on Monitor Response

The effects of sweep gas flow rate and bed temperature on tritium monitor response to single pulses of the tritiated carrier gas were evaluated for a series of oxidizer bed/reducer bed/water stripper configurations. A set of data collected for the B/Mg/B, B/Mg/N_2 and B/B/N_2 configurations [B = by-pass, Mg = magnesium bed, N_2 = liquid nitrogen cold trap] is given in Fig. 9. The results in Fig. 9 show that the effect of flow rate on the integrated tritium signal is close to linear in the 2 to 8 LPM range for all three configurations. (The integrated tritium signal is obtained by measuring the area under the recorded tritium count rate *vs.* time curves using a planimeter). Similar results for configurations with CuO and CuO-MnO_2 oxidizer beds are currently being evaluated. Linearity of the tritium monitor response during pulse-flow operation is essential to the attainment of reasonably quantitative results from reaction kinetics studies.

Performance of CuO and CuO-MnO_2 Oxidizer Beds

In another series of studies, we investigated the effects of particle size and composition on the performance of CuO-MnO_2 mixtures used in oxidizer beds. The performance characteristics evaluated were (1) effectiveness in oxidizing HT to HTO, (2) magnitude and duration of tritium hold-up in the bed, and (3) pressure drop in the bed. All experiments were carried out (1) at a bed temperature of 600°C, (2) in the same bed

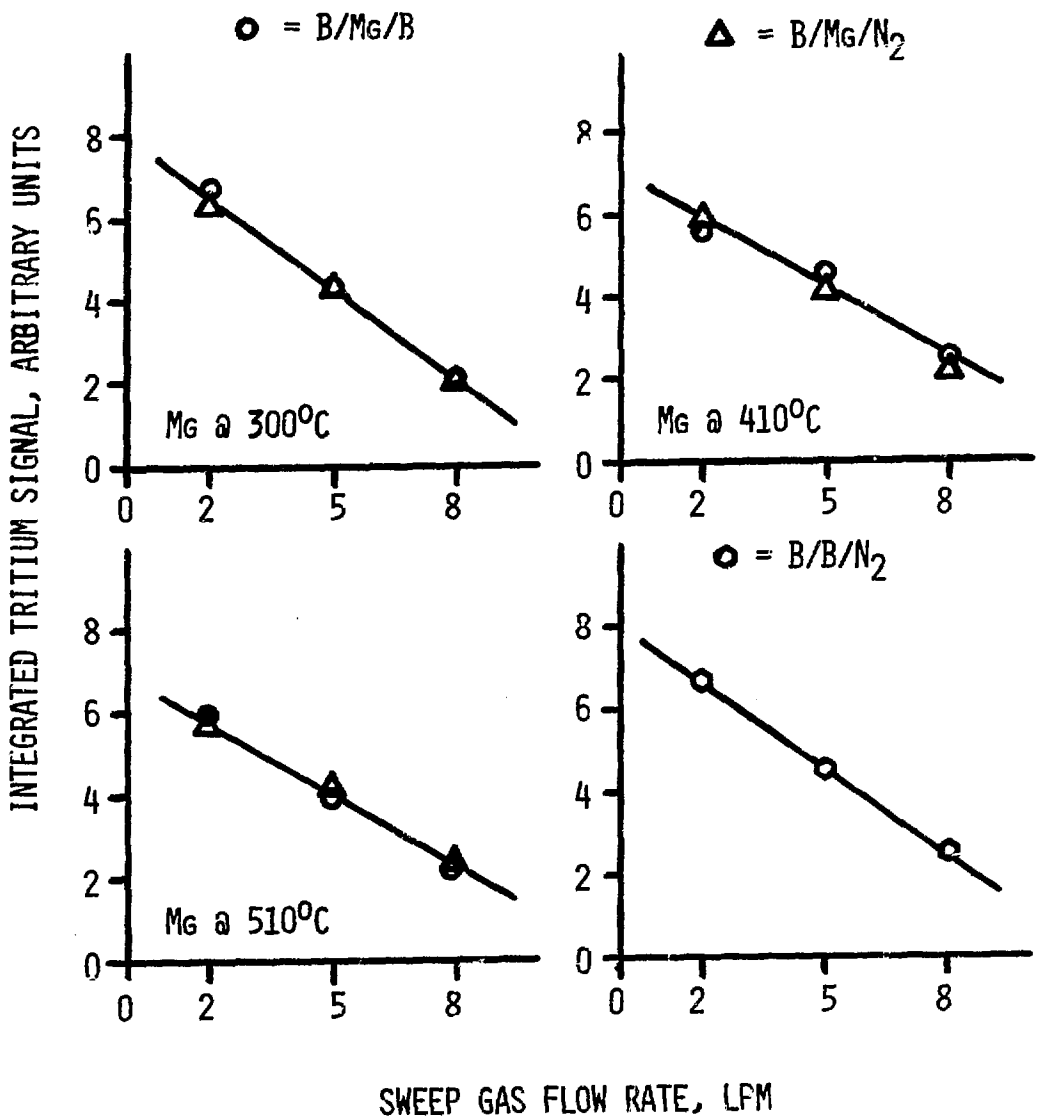

Fig. 9. Effect of Sweep Gas Flow Rate on Integrated Tritium Signal

container and apparatus configuration, and (3) at a sweep gas flow rate of 2 LPM. The objective of this study was to identify a bed composition and particle size range that gave high efficiency conversion of HT to HTO, low pressure drop in the bed, and minimum tritium hold-up. Results obtained for the compositions and particle sizes examined thus far are summarized in Table 3. Generally speaking, roughly equal volume mixtures of CuO and MnO_2 with particles in the size range -16 +42 mesh gave the best performance, although hold-up was a problem to some extent in all of the beds studied. Volume fractions $\geq$30% of -42 mesh material (either CuO or MnO_2) increased the pressure drop across the bed and led to greater tritium hold-up (probably because of the increased surface area). CuO by itself was found to be relatively ineffective in converting the low levels of HT in the sweep gas to HTO, regardless of particle size. HT to HTO conversion efficiency increased with increasing quantities of MnO_2; however, increasing the volume percent of MnO_2 above 50% tended to give increasingly larger tritium hold-up. Composition VII in Table 3 appears to be near optimum in terms of the objectives stated above.

Effects of H_2 Addition to Sweep Gas

This series of experiments was conducted to determine the effects of increased amounts of H_2 in sweep gas on CuO-MnO_2 oxidizer beds that showed relatively high tritium hold-up in the previous series of experiments. Comparative runs were made with either helium or helium-1% hydrogen as the sweep gas. Results of experiments with the CuO-MnO_2/B/B and CuO-MnO_2/B/N_2 configurations are shown in Fig. 10. The composition of the CuO-MnO_2 bed used for Test V in Table 3 was selected for this study because of its relatively high tritium hold-up characteristics. Curves A and A' in Fig. 10 show that the tritium hold-up is greatly reduced by swamping the HT in the sweep gas with H_2. In a second experiment, a pulse of the HT carrier gas was added to a helium swept stream and, after sufficient equilibration time, the sweep gas was changed to He-1% H_2. The results of this experiment (curve B in Fig. 10) show that the original pulse is cleared from the bed by the H_2-containing sweep gas. Curves C and C' in Fig. 10 are a repeat of the sequence represented

Table 3. Summary of Studies of the Effect of Composition and Particle Size on the Performance of $CuO-MnO_2$ Oxidizer Beds at 600°C and a Sweep Gas Flow Rate of 2 LPM

Test	Composition (Volume %)	Particle Size Range (Mesh)	Relative Performance: HT to HTO Conversion Efficiency	Relative Performance: Relative Pressure Drop	Relative Performance: Relative Tritium Hold-up
I	100% CuO	-42	low	large	moderate
II	100% CuO	-32 +42	low	low	low
III	90% CuO 10% MnO_2	-32 +42 -42	moderate	moderate	moderate
IV	70% CuO 30% MnO_2	-32 + 42 -42	high	moderate	moderate
V	60% CuO 40% MnO_2	-32 +42 -42	intermediate†	moderate	high
VI	60% CuO 40% MnO_2	-32 +42 -16 +32	high	low	low
VII	50% CuO 50% MnO_2	-32 +42 -16 +32	high*	low*	low*

† Not possible to determine because of high tritium hold-up.

* Slight improvement over Test IV.

by curves A and A' except that the $CuO-MnO_2/B/N_2$ configuration is used. These results demonstrate that the HT to HTO conversion efficiency of the $CuO-MnO_2$ bed is not grossly affected by the large excess of H_2. In the near future, an attempt will be made to determine the lower limits for H_2 levels in the sweep gas that can effectively reduce tritium hold-up in $CuO-MnO_2$ beds. Incentives for this extension of the H_2-swamping studies are (1) the fact that 1% H_2 levels lead to rapid depletion of the active material in the oxidizer bed, (2) the need to minimize insofar as possible the magnitude of isotopic dilution of tritium from the standpoint of subsequent tritium enrichment and recycle, and (3) a recent observation that the efficiency of magnesium metal reducer beds is adversely affected by the large excess of H_2 in the sweep gas.

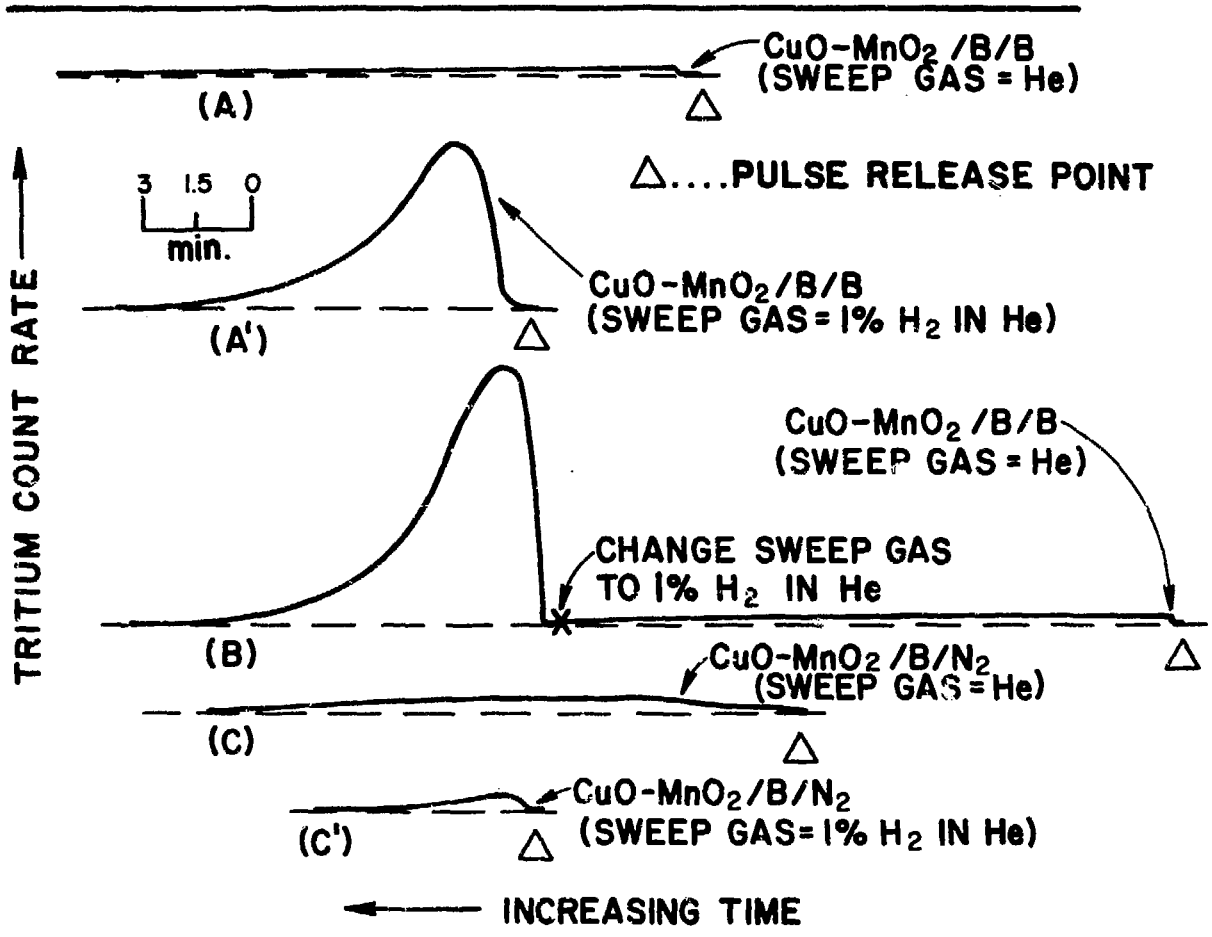

Fig. 10. Effects of H_2 in the Sweep Gas on the Performance of $CuO-MnO_2$ Oxidizer Beds

Results of Recycle-Flow Studies

In this type of experiment the apparatus in Fig. 8 is filled to ambient pressure with the sweep gas, set in the recycle configuration with all beds and traps by-passed, and a pulse of tritium is introduced. (Continuous circulation is provided by the circulation pump in the tritium monitor.) Thereafter, the desired sequence of beds and traps are valved into and out of the circuit. A typical series of experiments is shown in Fig. 11 where a comparison is made of the performance of a magnesium metal reducer bed at 300 and 550°C. In the all by-pass configuration (B/B/B) the tritium monitor signal rapidly reaches a steady level. Insertion of the magnesium bed (B/Mg/B) has relatively little effect, although we have often observed a slight increase in signal which may be due to residual tritium from a prior pulse. Insertion of the nitrogen trap (B/Mg/N_2) always leads to a slight drop in signal because the relatively large internal volume of the trap (compared to the piping) causes a dilution of the tritium in the sweep gas. The plateau in this latter configuration proves that most of the tritium is in the oxidized form. Insertion of the CuO-MnO_2 oxidizer bed (composition for Test VII in Table 3) leads to two distinctly different effects. In curve A where the magnesium bed is at 300°C, the tritium is rapidly removed from the circuit as HTO indicating that the magnesium bed is not back-reducing the HTO coming out of the oxidizer bed. In curve B where the magnesium bed is at 550°C, it does effectively back-reduce the HTO. (The initial drop in the signal in Curve B, when the CuO-MnO_2/Mg/N_2 configuration is introduced, is believed to be due to hold-up of some tritium by the oxidizer bed.) The response to the final configuration in curve B (CuO-MnO_2/B/N_2) gives evidence that the oxidizer bed was operating effectively prior to removal of the magnesium bed.

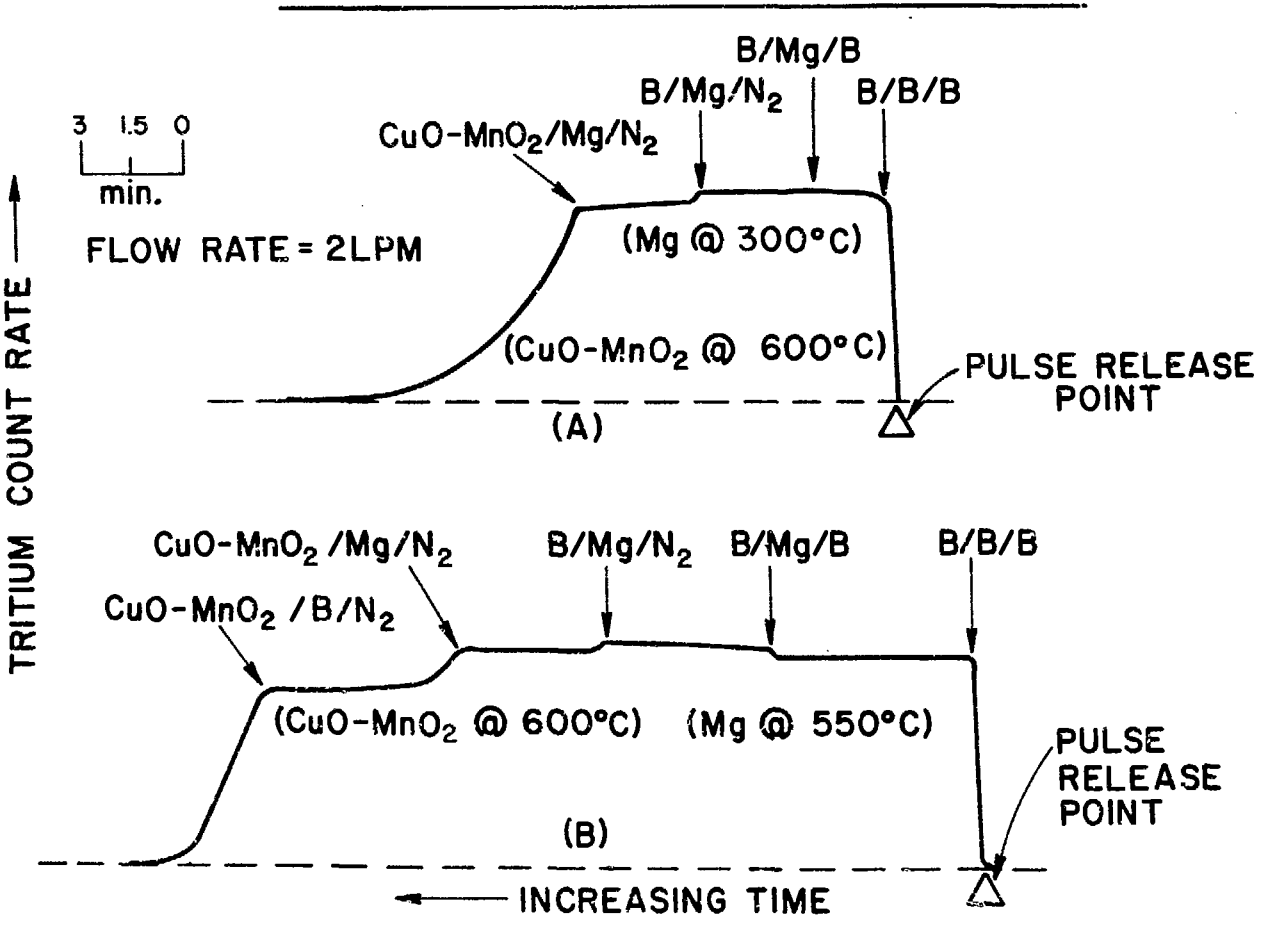

Fig. 11. Recycle Flow Studies of the Performance of Magnesium Metal Reducer Beds

REFERENCES

1. V. A. Maroni, E. Veleckis, and E. H. Van Deventer, "A Review of ANL Research on Lithium-Hydrogen Chemistry and Tritium-Containment Technology," in the Proceedings of the Symposium on Tritium Technology Related to Fusion Reactor Systems, October 1-2, 1974, Mound Laboratory, Miamisburg, Ohio: USERDA Report ERDA-50, p. 120, (June 1975).

2. V. A. Maroni *et al.* Liquid Metals Chemistry and Tritium Control Technology Annual Report: July 1974-June 1975, USERDA Report ANL-75-50 (September 1975).

3. R. W. Webb, Permeation of Hydrogen Through Metals, USAEC Report NAA-SR-10462 (July 1965).

4. R. E. Stickney, "Hydrogen Isotopes in Fusion Reactors," in The Chemistry of Fusion Technology, D. M. Gruen, (ed.), Plenum Press, p. 241, New York (1972).

5. R. A. Strehlow and H. C. Savage, Nucl. Technol. 22, 127 (1974).

6. See Reference 2, p. 31.

7. W. G. Perkins and D. R. Begeal, Permeation and Diffusion of Hydrogen in Ceramvar, Copper, and Ceramvar-Copper Laminates, USAEC Report SC-DC-614493 (Sandia Laboratories, March, 1972).

8. F. M. Ehrmann, P. S. Gajardo, and S. C. Droguett, J. Phys. Chem. 77, 2146 (1973).

9. C. J. Smithells and C. E. Ransley, Proc. Roy. Soc. 150A, 172 (1935).

10. Yu. I. Belyakov and Yu. I. Zvezdin, Uch. Zap. Lenigrad Gos. Univ. Ser. Fiz. Nauk. No. 345, 44 (1968).

11. R. R. Heinrich, C. E. Johnson, and C. E. Crouthamel, J. Electroch. Soc. 112, 1071 (1965).

12. V. A. Maroni, J. Nucl. Mater. 53, 293 (1974).

13. G. L. Holleck, J. Phys. Chem. 74, 503 (1970).

14. See Reference 3, p. 8.

15. W. A. Swansiger, R. G. Musket, L. J. Weirick, and W. Bauer, J. Nucl. Mater. 53, 307 (1974).

16. The relationship between oxygen potential and extent of oxidation for vanadium is comparable to that for niobium as given by L. A. Charlot and R. E. Westerman, Helium Coolant Compatibility with Candidate Fusion Reactor Structural Materials, USAEC Report BNWL-1842 (July 1974).

17. D. L. Smith, J. Less-Common Metals 31, 345 (1973).

18. J. H. DeVan, "Compatibility," published in Fusion Reactor First Wall Materials, USAEC Report WASH-1206 (1972) p. 25.

19. V. A. Maroni, "Analysis of Tritium Distribution and Leakage Characteristics for Two Fusion Reactor Reference Designs," Proc. Fifth Symposium on Engineering Problems of Fusion Research, Princeton University, 6-9 November 1973, IEEE Publication No. 73CH0843-3-NPS (1974) p. 206.

20. D. L. Smith and K. Natesan, Nucl. Technol. 22, 392 (1974).

21. T. S. Elleman, North Carolina State University (personal communication).

PERMEATION OF HYDROGEN AT LOW PRESSURES THROUGH STAINLESS STEEL AND IMPLICATIONS FOR TRITIUM CONTROL IN FUSION REACTOR SYSTEMS

Robert C. Axtmann, Ernest F. Johnson and Christopher W. Kuehler

Department of Chemical Engineering
Princeton University, NJ

ABSTRACT

New experimental data on the permeation of hydrogen through stainless steel indicate that at driving pressures below 10^{-2} torr, the permeation rate is linearly dependent on the driving pressure. A possible consequence is that the permeation rates of hydrogenic species in fusion reactor systems might be much lower than those reported in contemporary conceptual design studies which assume that the rates are dependent on the square root of the driving pressure. The important implications of these low permeation rates are: (1) tritium losses to the environment may be more dependent on ordinary leaks from equipment than on permeation to the steam cycle; (2) recovery of tritium from breeding blankets via permeation windows may be impracticable; and (3) recovery of tritium from breeding blankets not dependent on permeation windows may be simplified by the possibility of operating at much higher average tritium concentrations in the blanket and cooling systems.

INTRODUCTION

The permeation of hydrogen gas through metals has been studied for many years, principally because of the deleterious effects on mechanical properties of the metal. New interest in the area has been stimulated by problems in fusion devices where tritium migration and holdup are important phenomena for both operational and environmental reasons.

These recent problems occur in temperature and pressure regimes that are not well-explored. The first wall aside, it is likely that much of the structural hardware in fusion reactors will be fabricated from stainless steels or other iron alloys. So far as we are aware, no reproducible hydrogen permeation experiments on any stainless steel have heretofore been reported for driving pressures less than about 0.1 torr.

The classical expression for describing the permeation of diatomic, homonuclear molecules through a metal membrane is Richardson's Equation,[1] *viz*,

$$J = \frac{P}{d} (P_1^{1/2} - P_2^{1/2}) \tag{1}$$

where

$$P = P_o \exp[-\frac{1}{2} E_p/RT] \tag{2}$$

and

J = the permeation rate,
P = the permeability,
P_o = a constant,
E_p = the activation energy for diffusion,
R = the gas constant,
T = the absolute temperature,
d = the thickness of the metal,
P_1, P_2 = the pressures at upstream and downstream surfaces, respectively.

Experimental verifications of Equation (1) are sparse in the case of iron or iron alloys. Chang and Bennett[2], for example, found the exponent of P_1 to vary (with pressure) between 1/2 and 1; Phillips and Dodge[3] found only a weak dependence on d; Randall and Salmon reported that a lengthy period of "activation" was necessary before tritium permeation through 347 stainless steel rose to a reproducible value[4]; and Flint's measured hydrogen permeation rates through 347 stainless decreased markedly over a period of 300 hours at a temperature of 600°C.[5]

All of these anomalies suggest that at least in some circumstances, diffusion through the metal is not the rate-limiting step in the overall permeation process.

EXPERIMENTAL

Apparatus

Physical Description

In order to observe hydrogen permeation under conditions at which diffusion may not be rate limiting, the ultra-high vacuum apparatus depicted schematically in Figure 1 was constructed. Fabricated from 305 stainless steel to minimize surface contamination, the system is all metal.

The high pressure chamber (I) can be evacuated by a sputter-ion pump rated at 11 liter-sec^{-1}. The upstream pressure, P_1, is measured with a nude ionization gauge that has been calibrated for H_2. The low pressure chamber (II) is pumped by a triode sputter-ion pump rated at 270 liter-sec^{-1} for H_2 and a titanium sublimation pump. The speed of the latter is estimated, very conservatively, to be at least 10,000 liter-sec^{-1}. A second nude ionization gauge permits total pressure measurements, P_2, on the downstream side of the membrane.

The permeation membrane assembly is shown in Figure 2. The membrane was machined from an ingot of warm-rolled, 304 stainless steel to 5 mil thickness and a diameter of two inches. This piece was welded to lengths of stainless steel tubing which were, in turn, welded to water-cooled vacuum flanges. Two baffles in front of the membrane insured thermal

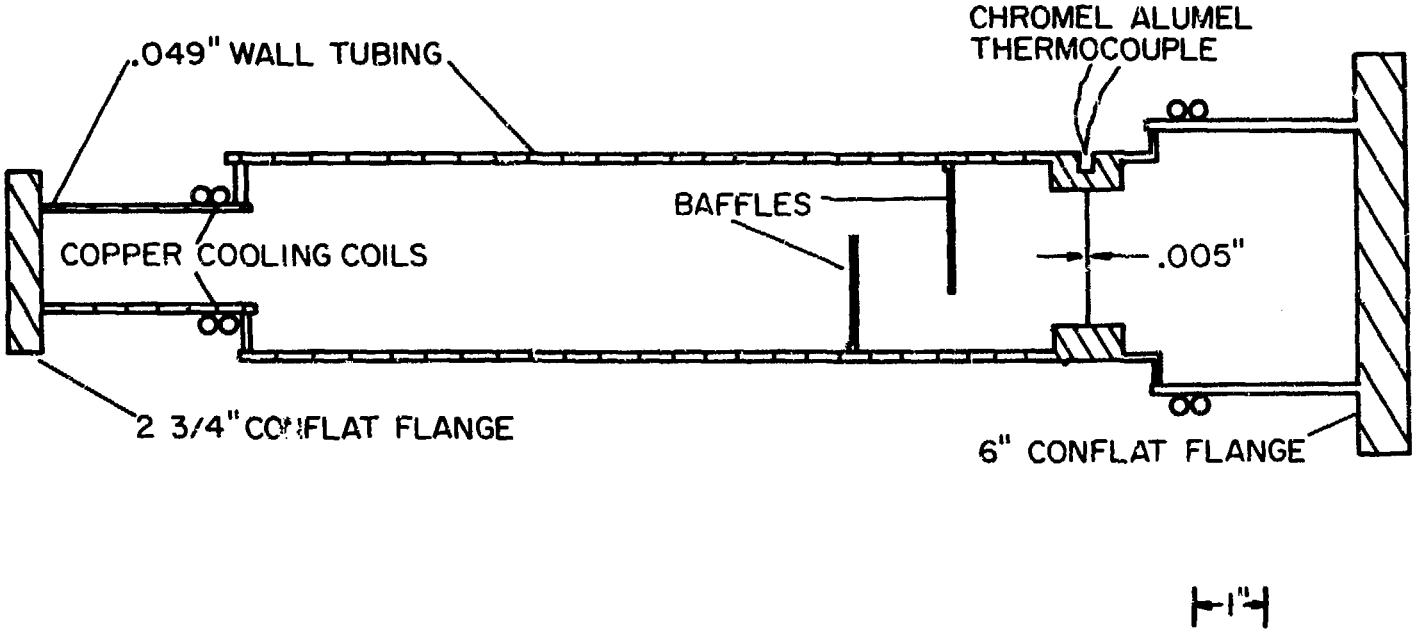

IV-364

Fig. 1. Schematic of Permeation Apparatus

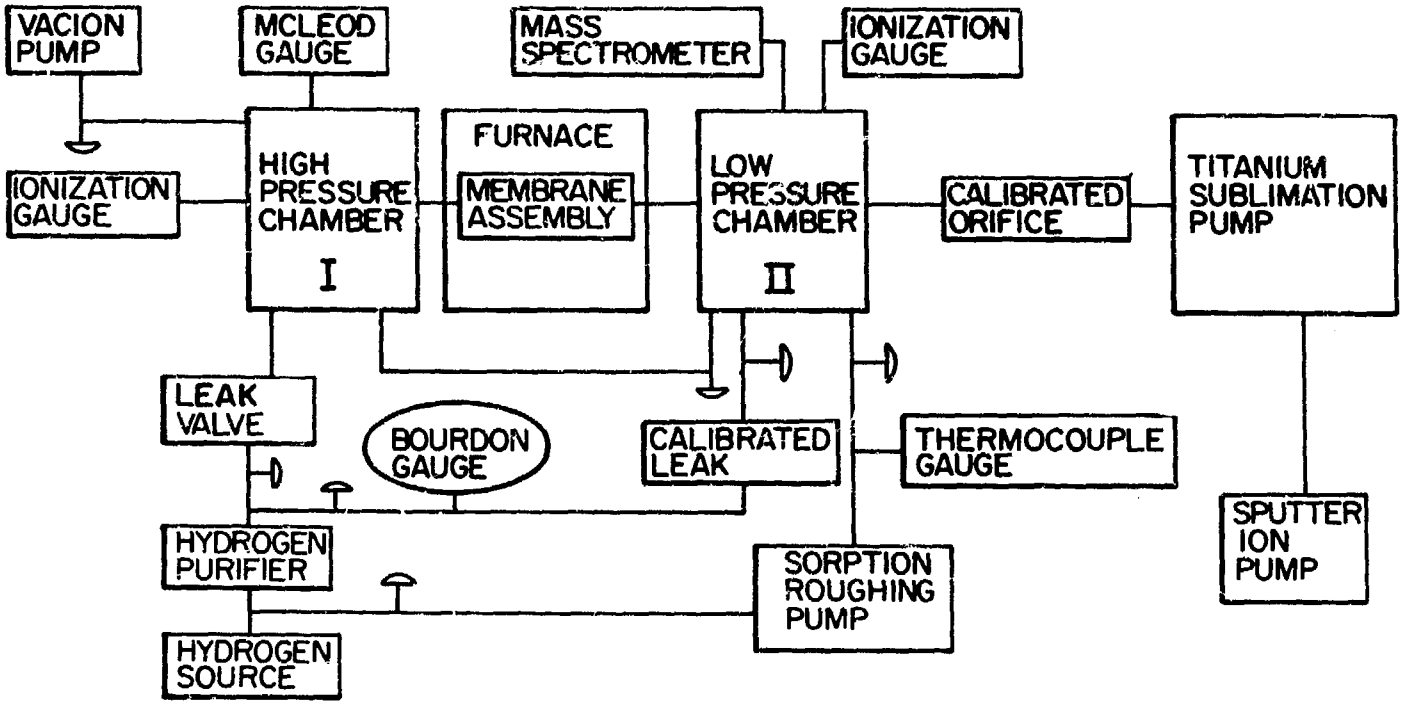

Fig. 2. Permeation Membrane Assembly

equilibrium between the gas and the membrane surface. Before incorporation into the apparatus, the freshly machined membrane surface was degreased with acetone.

The temperature of the membrane is maintained by an external ensemble of insulated heating elements. A thermowell, drilled close to the membrane's edge (cf. Fig. 2), allows temperature measurements with a chromel-alumel thermocouple.

Baking at 200°C overnight brought the base pressure in chamber II into the 10^{-10} torr range while chamber I reached 1×10^{-9} torr. To maintain these vacua under no gas load requires activating the sublimator for two minutes, once a day.

Method

To measure permeation rates, a conductance-limited orifice method is utilized. In this technique, gas entering chamber II is pumped out through a calibrated orifice by the high-speed pumping system. The flow rate, Q, into the chamber is

$$Q = \frac{UP_2}{1 + U/S} \tag{3}$$

where

U = the conductance of the orifice,

P_2 = the pressure in chamber II,

S = the pumping speed at the orifice.

The conductance of a circular orifice[6] is given by

$$U = 62.5\ Am^{-1/2} \tag{4}$$

where

A = the area (cm^2),

m = the molecular weight of the gas,

For hydrogen and our orifice (1.69 cm diameter), $U = 100$ liter-sec^{-1}. Since the pumping speed is >10,000 liter-sec^{-1}, then from Equation (1) $Q \simeq UP_2$, i.e., the flow is definitely conductance-limited.

Since it is possible that significant partial pressures of gases other than hydrogen may be present, an ionization current proportional to P_2 is measured with a quadrupole mass spectrometer. The proportionality between spectrometer ionization current at mass two and flow-rate into chamber II was determined by admitting, in a separate experiment, pure hydrogen to the chamber via a calibrated leak (cf. Fig. 1).

Hydrogen

Two sources of purified gas were used. Initially, research grade hydrogen from Air Products Corp. was admitted directly into the evacuated gas inlet system via a standard regulator valve. Later, Matheson UHP hydrogen was passed through a Matheson purification train (Models 64-1000 and 450) before entering the inlet system. Analyses of each gas, obtained from the vendors, are given in Table I. The purified Matheson gas that entered the permeation apparatus is expected to be of higher purity than is indicated in the table.

The two samples of hydrogen gave identical results.

Procedure

Prior to this experiment, the membrane assembly was held at ~700°C for one week. Pressures of 10^{-8} torr on the high pressure side and 10^{-9} torr on the low pressure side could be maintained under these conditions. To insure that the membrane was free of leaks, 10^{-3} torr of helium was admitted to chamber I with the mass spectrometer in chamber II set to mass four. No increase in signal was observed.

P_1 was controlled by adjusting both the variable leak valve through which hydrogen was admitted and by varying the conductance of a 1 1/2" valve attached to the 11 liter-sec^{-1} pump. In a typical run at a given temperature, hydrogen was admitted to chamber I at the minimum value of P_1 desired, by opening the variable leak. The mass spectrometer current rose and approached a steady-state with a period that ranged from one to ten minutes, depending on the temperature. The difference between the currents, with and without permeation, was taken to be proportional to the permeation rate. Subsequent, higher values for P_1, up to the maximum

Table I. Hydrogen Analysis (ppm)

	Air Products Research Grade (Actual)	Matheson Ultra High Purity (Typical)
Acetylene	<0.05	
Argon	<5	
Carbon Dioxide	<0.5	<1.0
Carbon Monoxide	<1.0	<1.0
Helium		50
Hydrocarbons	<0.2	8
Methane	<0.5	
Nitrogen	<5	<1.0
Nitrous Oxide	<0.1	
Oxygen	<0.5	<1.0
Water	.82	5

allowable in the 11 liter-sec^{-1} ion pump, were obtained by opening the leak further, closing off the pump more, or both. P_1 was then lowered through the same sequence of values and the mass spectrometer readings were confirmed.

RESULTS

Figure 3 displays the results of hydrogen permeation measurements through 304 stainless steel between 637°C and 709°C and driving pressures from 2.0×10^{-4} to 1.6×10^{-2} torr. The experimental sequence involved: three runs at temperatures which included the highest and the lowest; a one week interval during which the sample was held at room temperature under ultrahigh vacuum; and two runs at intermediate temperatures. When the data at single values of P_1 from the five temperature runs were plotted *versus* reciprocal temperature, smooth curves resulted. This circumstance argues that no significant changes occured on the membrane surfaces during the course of the experiment. Moreover, data from a run in which the pressure was raised at a given temperature agreed well with those obtained when the pressure was lowered (cf. *Procedure* secti .n above).

Least squares fits were made of the five, single-temperature runs displayed in Fig. 3 to the empirical equation

$$J = b(P_1)^n \qquad (5)$$

where

J = the permeation rate.

All gave values of $0.980 < n < 1.017$.

Budgetary constraints precluded *in situ* studies of the surface characteristic of the stainless steel sample. Elsewhere[7] we have marshalled evidence to support the thesis that, whatever the surface contaminants (primarily O,S,P), their concentrations are those characteristic of 304 stainless steel in ultra-high vacuum at the temperature of our experiments and that the surfaces equilibrate rapidly. We did not observe either the "activation" period observed by Randall and Salmon[4] nor the "aging" reported by Flint[5] on 347 stainless steel. Both of the latter permeation

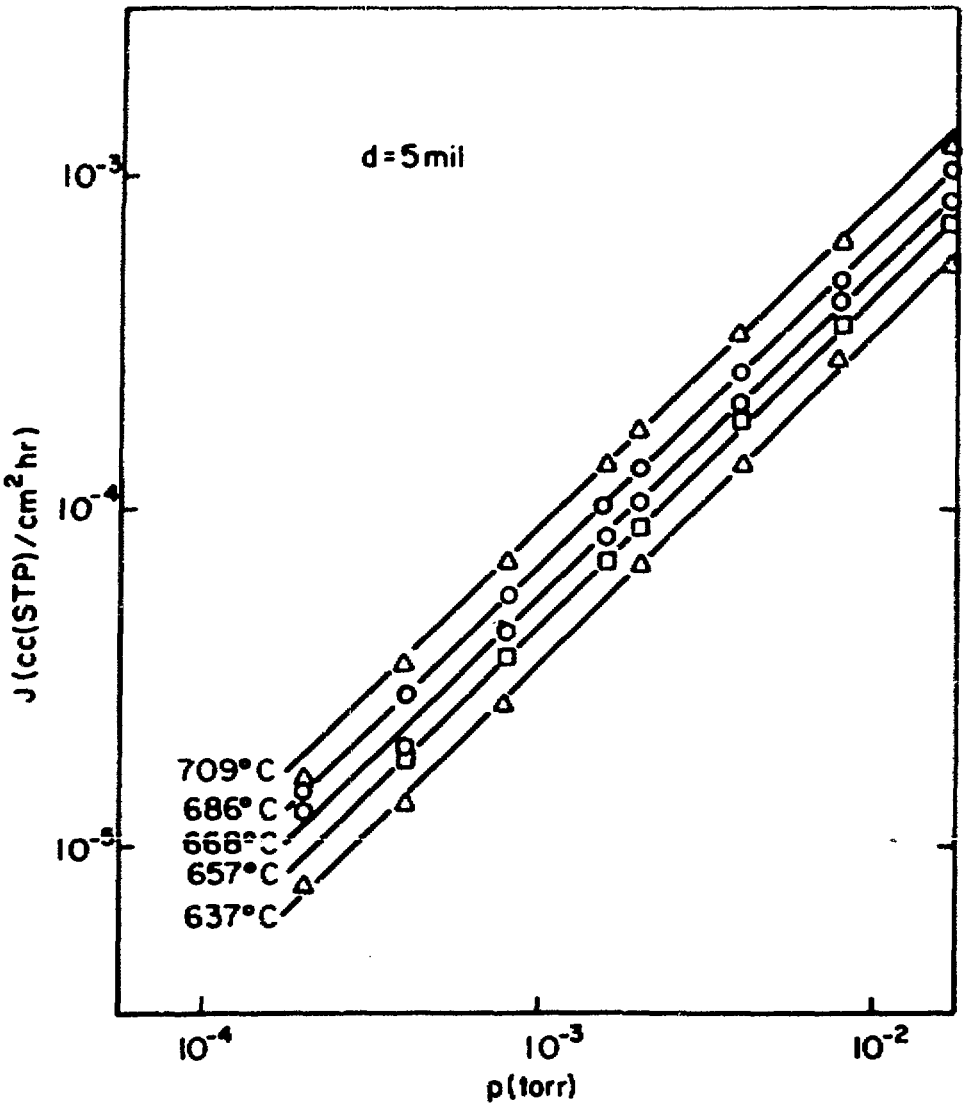

Fig. 3. Permeation Rate versus Pressure for a Membrane of 304 Stainless Steel.

studies were performed at driving pressures in the torr range or above.

A more detailed account of the experimental design and procedures is available[7]; a theoretical interpretation of the results will be offered elsewhere[8].

DISCUSSION

Although the results of any single, new experiment must be regarded with caution, it is instructive to examine the possible implications for fusion reactor systems of the observed linear dependency of permeation rates on driving pressures.

It is clear that a linear dependency would mean that the actual permeation rates at very low driving pressures will be much lower than would be estimated from a dependency on the square-root of the driving pressures. Since certain important features of conceptual designs for fusion reactors are governed by estimates of tritium permeation rates, any major changes in these estimates would require major alterations to the conceptual designs.

Tritium Loss to the Environment

For most recent conceptual designs of fusion power reactor systems, including those from Oak Ridge[9], Princeton[10], and Wisconsin[11], a controlling parameter has been the allowable loss to the environment. In these designs the tritium concentrations in the coolant streams flowing to the principal steam generators have been set at levels that would limit the permeation of tritium into the steam to rates approximating the present maximum allowable, tritium release rate to the environment. This design restriction is based on the assumptions that tritium entering the steam cycle would not be recoverable and ultimately would reach the environment and that all other tritium releases would be tightly controlled by secondary containment systems.

Actually, the maximum allowable tritium loss to the environment is only one of three constraints on tritium concentration levels in fusion power machines. The others are the maximum allowable, overall tritium inventory and the maximum tolerable concentration of hydrogenic species

in the machine structures fixed by the tendency for hydrogen to embrittle metals at concentrations above a few hundred parts per billion. The former depends primarily on the cost of tritium, which for first generation power machines would be very high, and the latter depends on the solubility of hydrogen in the particular metals and its effect on metallurgical properties, exacerbated in the case of tritium by the decay to helium.

In the Princeton Reference Design (PRD) the maximum tritium pressure in the coolant helium flowing through the steam generators was set at 10^{-15} atm to limit the permeation loss to the steam to approximately 10^{-4} gm-day^{-1}. For the same system the embrittlement constraint would permit a concentration corresponding to approximately 10^{-7} atm tritium pressure in the helium[19] and the inventory constraint corresponds to about 10^{-5} atm. Thus the permeation constraint is the most stringent of the three applicable constraints by many orders of magnitude. However, if we assume the linear law for estimating the likely permeation rates and then compute the allowable tritium pressure for the same tritium loss rate to the environment, we find that embrittlement becomes nearly coequal in controlling importance. From Equation (1) the driving force for permeation, for a tritium driving pressure of 10^{-15} atm, is $10^{-15/2}$ or 0.32×10^{-7} atm$^{1/2}$. Ceteris parabis, the tritium pressure giving the same numerical value for the driving force under a linear law assumption would be 0.32×10^{-7} atm, only slightly less than the safe pressure from the standpoint of wall embrittlement.

Smith has carried out this kind of calculation for the PRD in somewhat more conservative fashion by making use of data relevant for each form of the permeation rate equations[12]. He also assumed, for both cases, that the metal wall was stainless steel without any cladding to hinder permeation. For the Richardson's law case, the total transfer of tritium from the coolant helium to the steam cycle is given by

$$J = (A/x)\ B\ (p)^{1/2}\ \exp(-E_p/RT) \qquad (6)$$

where

a = metal surface area normal to the flux,

x = metal wall thickness,

B = overall coefficient for permeation,

p = tritium pressure in the coolant helium,

E_p = activation energy for diffusion,

R = gas constant,

T = absolute temperature.

In this equation the effective pressure of molecular tritium in the steam side of the heat exchangers is taken to be zero. Using data from Maroni[13] for all variables except J and p and assuming uniform temperatures throughout a given heat exchanger and equal to the highest temperature in that exchanger, Smith estimated that the average tritium pressure in the coolant helium system should be held to a maximum of 2.3×10^{-17} atm to insure that the total permeation rate would not exceed 10^{-4} gm-day^{-1} (ca, one curie-day^{-1}).

Under the same assumption of negligible downstream tritium pressure, the linear law expression for the tritium transport from the coolant helium to the steam system is given by

$$J = AK(p) \exp(-E_a/RT) \qquad (7)$$

where

K = surface coefficient for permeation

E_a = activation energy for this permeation process

and the other symbols have the same significance as before.

Smith used values for K and E_a from the experimental data of the present study[7] and summed $A \exp(-E_a/RT)$ over all the heat exchangers in the same manner as for the Richardson's law case. This procedure gave the result that an average pressure of tritium in the coolant helium of 2.3×10^{-12} atm would be required for a permeation loss to the steam system of 10^{-4} g/day.

The calculations for both cases were based on data for protium rather than tritium since the isotopic effect at the relatively high temperatures in the heat exchangers is likely to be small[14] -- probably not greater than the factor of $(1/3)^{1/2}$ predicted from diffusion theory, which is insignificant for this comparison.

Although there are considerable uncertainties in the reliability of these values of tritium pressures, it is apparent that the permeation rates at very low driving pressures might be substantially lower than would be anticipated from an application of the Richardson's law rate expression. This conclusion is supported by the study of Briggs[15] who analyzed the observed distribution of tritium in structures in the molten salt reactor experiment at Oak Ridge. The tritium concentrations there corresponded to permeation rates three orders of magnitude lower than would be predicted by Equation (1), even though the principal permeation pathways involved surfaces cleaned by the fluxing action of the molten salt on the confining metals.

We conclude that the control of permeation losses of tritium to the steam cycle is unlikely to be as critical an item for fusion power plants as has been visualized heretofore. Rather, the principal causes of tritium escape to the environment will be leakages through wall cracks, pump seals, and the like; and releases during maintenance shutdowns. A helpful feature here is that the stream pressures under normal operating conditions will tend to mitigate the transport losses to the environment. Thus cracks in the walls of the steam generators will result in the leakage of steam into the coolant stream rather than the reverse. Similarly, cracks in the cooling tube walls in the reactor blanket would result in leakage from the coolant into the breeder medium.

Implications for Tritium Recovery

First generation fusion power machines based on the D - T reaction must be self-sufficient in tritium, and, since the ultimate breeding ratios are likely to be small (because of the many constraints imposed on typical breeder blankets), high yield and efficient recovery of the bred tritium will be mandatory. If the permeation losses through structures are much lower than earlier estimates have indicated, it will be possible to operate fusion plants at much higher average tritium concentrations. An immediate consequence is that the recovery of tritium from the breeder blanket should be correspondingly simpler since the driving potential for any recovery system will be greater and the amount of breeder material

that must be processed and the size of processing equipment will be correspondingly less for a given tritium production rate.

However, for recovery schemes based on the permeation of tritium through membranes at low tritium pressures, the deleterious effects of the linear law will tend to offset any advantage arising from possible increases in the tritium pressure. For example, if the tritium pressure were increased from 10^{-10} atm to 10^{-8} atm, the driving potential for permeation would similarly increase for the linear law. From Richardson's law at the original pressure the driving potential would be 10^{-5} $atm^{1/2}$, whereas for the linear law at the new pressure it would be 10^{-8} atm, i.e., the permeation rate would actually be three orders of magnitude lower than the rate estimated by Richardson's law at the original pressure.

Watson has estimated the costs of metal permeation windows for the Oak Ridge conceptual design to range from $100,000 to $500,000 for tritium pressures in lithium of 10^{-9} to 10^{-11} atm respectively.[16] These costs should be multiplied by about 10 to include ancillary equipment and installation under nuclear standards of construction. If the resulting costs must be scaled up further by a factor of 1,000 to correct for the effect of the linear permeation law, the final investment requirement makes permeation an impracticable option.

We conclude that permeation processes for tritium recovery might be, at best, only marginally feasible if tritium pressures in excess of 10^{-5} atm are intolerable.

For systems like the PRD where the tritium pressures in the coolant helium do not influence the ease of recovery of tritium from the breeder salt, the tritium concentrations in the coolant can be allowed to rise two or three orders of magnitude, and the scale of the mole sieve driers for removing tritiated water from the helium and the related pumping requirements would be correspondingly reduced. These items were relatively modest in the original design[17], hence the economic advantage would not be great.

For systems in which the breeding medium is a solid alloy or salt (including metal oxides), with bred tritium diffusing from the solid into the coolant or into an evacuated region, as in the Brookhaven conceptual design[18], the effect of the linear law would be to permit higher tritium pressures in the coolant or evacuated region and correspondingly easier recovery of the tritium. It is not clear, however, that the transfer of bred tritium from the solid breeder to the evacuated region will occur at rates any faster than for permeation windows. The slow rate dictated by the linear law surface effect for stainless steels at low hydrogen pressures might reasonably be expected to obtain for aluminum alloys and solid compounds.

SUMMARY

The principal conclusions that emerge from this study are:

1. Permeation losses of tritium from coolant fluids into the steam system of fusion reactors are unlikely to contribute significantly to the release of tritium to the environment. Rather, the releases are more likely to arise from leaks through cracks in structures and at seals, from unavoidable releases during maintenance shutdowns, and from accidental releases.
2. An immediate consequence of the reduced permeation losses is that it may prove practicable to maintain tritium concentrations at higher average levels in the breeder blanket and in the coolant streams. Furthermore, there may be no need to seek claddings to provide permeation barriers on heat exchanger surfaces as has been suggested for most conceptual designs. Higher tritium concentrations in the breeder system should make the recovery of tritium easier and less expensive for recovery systems not dependent on permeation windows. However, permeation windows may not be practicable for tritium recovery unless much higher tritium concentrations are permissible.
3. The uncertainties involved in extrapolating available data on tritium permeation rates and tritium solubilities in metals to the very low concentrations that must obtain in fusion reactor systems are great. A very high priority must be given, therefore, to experimental programs aimed at eliminating the uncertainties.

ACKNOWLEDGMENTS

This work benefitted from useful conversations with Dr. Harolyn K. Perkins and Messrs. Charles M. Smith and Andrew Zarchy of Princeton University. Financial support derived from the U.S. Energy Research and Development Agency under Contracts AT(11-1)-3028 and AT(11-1)-3073; and from the Electric Power Research Institute under Contract RP 113.

REFERENCES

1. O. W. Richardson, Phil. Mag. 7, 266 (1904).

2. P. L. Chang and W. D. G. Bennett, J. Trans. Steel Inst. 170, 205 (1952).

3. J. A. Phillips and B. G. Dodge, A.I.Ch.E. J., 14, 392 (1968).

4. D. Randall and O. N. Salmon, Diffusion Studies I. The Permeability of Type 347 Stainless Steel to Hydrogen and Tritium, KAPL-904 (March 17, 1953).

5. P. S. Flint, The Diffusion of Hydrogen through Materials of Construction, KAPL-65 (Dec. 14, 1951).

6. G. W. Green, The Design and Construction of Small Vacuum Systems, Chapman and Hall Ltd., London, 1968.

7. C. W. Kuehler, Ph.D. Thesis, Princeton University (Dec. 1974).

8. C. W. Kuehler, Paper submitted to the Sixth Symposium on Engineering Problems of Fusion Research, San Diego, Nov. 18-21, 1975.

9. A. P. Fraas, Conceptual Design of the Blanket and Shield Region of a Full Scale Toroidal Fusion Reactor, ORNL-TM-3096, (1972).

10. R. G. Mills (ed.), A Fusion Power Plant, MATT-1050 (August 1974). (available through NTIS, United States Department of Commerce, Springfield, Va. 22151).

11. B. Badger, et al, Wisconsin Tokamak Reactor Design, Report No. UWFDM-68, Nuclear Engineering Department, University of Wisconsin, Madison, Vol I (1973).

12. C. M. Smith, A Re-evaluation of Tritium Permeation in Fusion Reactors, Junior Independent Work Report, Princeton University, Princeton, N.J. (May 1975).

13. V. A. Maroni, Chap. 15 of Ref. 10.

14. R. E. Stickney, Chapter on Hydrogen Isotopes in Fusion Reactors in The Chemistry of Fusion Technology, D. M. Gruen (ed.), Plenum Press, New York, 1972).

15. R. B. Briggs, Reactor Technology 14 (4), 335 (1971-2).

16. J. G. Watson, An Evaluation of Methods for Recovering Tritium from the Blankets or Coolant Systems of Fusion Reactors, ORNL-TM-3794 (1972).

17. E. F. Johnson, Chap. 14 in Ref. 10.

18. J. R. Powell, et al, Studies of Fusion Reactor Blankets with Minimum Radioactive Inventory and with Tritium Breeding in Solid Lithium Compounds: A Preliminary Report, BNL 18236 (June 1973).

19. V. A. Maroni, private communication, July 1973.

TRITIUM HOLDUP DUE TO COATINGS ON THE FIRST WALL OF FUSION REACTORS

Harolyn K. Perkins

W.R. Bottoms and T.A. Pandolfi

School of Engineering and Applied Science
Princeton University

ABSTRACT

Coatings on vacuum vessels are expected to affect the re-emission of tritium implanted by energetic bombardment from the plasma. Based on experiments with the ST tokamak and the ATC tokamak, the first plasma devices to use tritium will probably have deliberate or accidental metallic films on their interior vacuum walls. This paper presents the result of energy dispersive X-ray analysis and ion scattering spectometry on samples taken from the ST tokamak vacuum vessel; the stainless steel vessel has acquired a molybdenum-tungsten coating attributed to the evaporation of the limiter and to gettering experiments. Scanning electron micrographs reveal a cauliflower-like appearance suggesting nodular growth. Metallic coatings such as these with low hydrogen diffusion coefficients would present a barrier to the re-emission of tritium implanted in the bulk material, beneath the thin coating. Tritium holdup will depend on the mobility of hydrogen within the coating and substrate as well as the frequency and duration of plasma shots. These considerations are expected to be more important for first generation tritium machines, which could have short confinement times and a high flux of tritium bombarding the wall.

INTRODUCTION

The first part of this paper presents evidence that the late ST tokamak had a tungsten-molybdenum coating over part of its stainless steel vacuum vessel whereas the second part will speculate about how such coatings could affect tritium holdup in future tokamaks. ST-tokamakers are not at all surprised that near the plasma-confining limiter the wall became coated with tungsten and molybdenum. Figures 1 and 2 show pictures of limiters removed from the ST machine after overheating via a plasma phenomenon called run-away electrons. Plasma conditions improved so much after a run-away-electron-induced evaporation, that molybdenum rods were inserted in the plasma to deliberately coat the wall providing a "getter" pump for impurities [1]. In ST's dying days, its walls were coated with aluminum. Recent experiments on ATC have involved coating interior walls with titanium [2].

We consider it quite possible that the walls of future tokamaks may acquire coatings during their use. If machine plans include the use of tritium, it is important to recognize that the holdup and re-emission of tritium implanted in the vacuum wall during a D-T discharge will depend on the chemical composition of the wall surface.

ANALYSIS OF THE ST VACUUM VESSEL

This section contains data obtained by energy-dispersive X-ray analysis on samples taken from the ST vacuum vessel, which indicate major fractions of molybdenum and tungsten in the first 10^{-4} cm thick region near the surface. (The incident 30 keV electron beam used in these studies excited X-rays to a depth of about 10^{-4} cm.) Following a discussion on the variation in surface composition at different locations in the tokamak machine, depth profiles of these surfaces are presented. Ion scattering spectra or Auger electron spectra

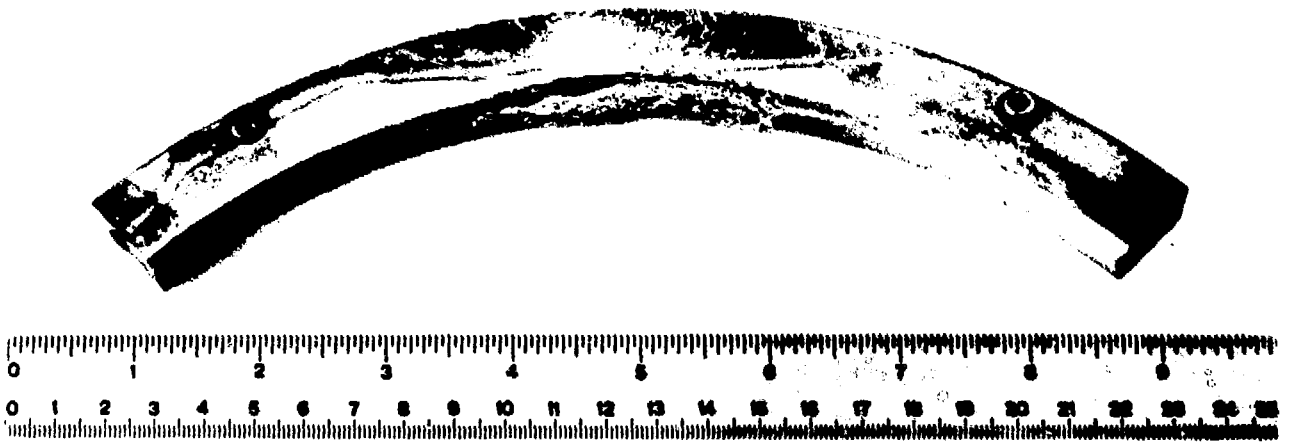

Fig. 1. One quarter section of the W limiter removed from ST tokamak. Note melted part.

Fig. 2. A portion of the Mo limiter after removal from the ST tokamak. Note melted portion.

which sample only the first few atomic layers of the surface, were taken sequentially while the surface was being eroded by sputtering.

Figure 3 shows the plan view of the ST tokamak which was dismantled last year after three years of operation. Its toroidal vacuum vessel had a 109 cm major radius, a 15.8 cm minor radius, and was constructed from 305 stainless steel. The sections that we analyzed, shown in Figure 4, came from the inside and outside of the torus near B; the limiters shown in Figures 1 and 2 were located at A, which was 49 cm away from B, measured on the outside of the torus.

The scales beneath the two strips in Figure 4 are used to designate sample origin and the letter I or E to designate whether it was on the inside or the outside of the toroidal vacuum vessel. Reference to Figure 4 shows that samples at I10, I36, E8, and E18 had been taken prior to the photograph. The left hand ends, I2 and E1, were located about 20 cm and 30 cm respectively from the limiter location A in the ST vacuum vessel. Distance from the limiter increases with increasing scale number.

Scanning elctron micrographs of the plasma-facing surface show a complex of overlapping spherical shapes (Figures 5 and 6). The cauliflower-like appearance of the surface resembles coatings that can result from radio frequency diode sputtering [3]. Samples taken from the outside of the torus, E locations, seemed to have a more complicated, nodular appearance than those from the inside of the torus. The surface cracks on sample 35 (E21) were not found on samples taken from E17 and E22.

Weighted surface compositions of samples from a number of locations, as determined by energy dispersive X-ray analysis, are given in Table 1. These compositions were calculated by dividing the peak height for the $MoL\alpha_{1,2}$, $WM\alpha,\beta$,

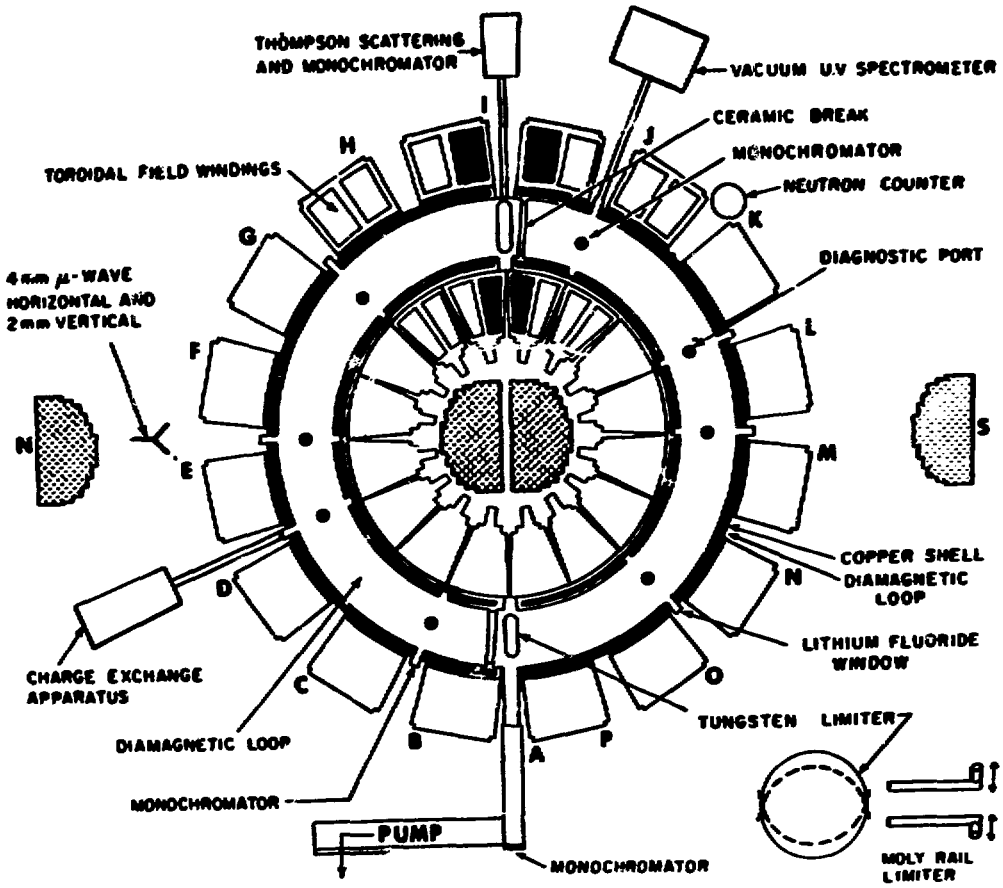

Fig. 3. Plan view of ST tokamak.

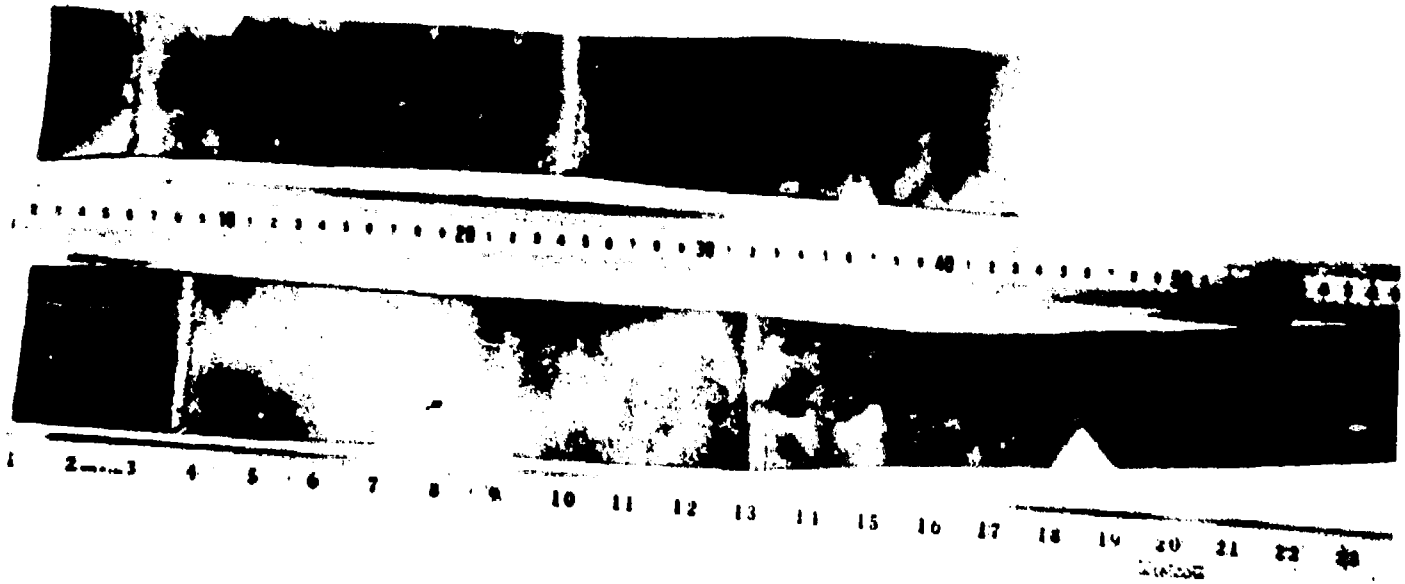

Fig. 4. Sections of the ST tokamak vacuum vessel. The upper section designated I was from the inside of the toroidal vessel. The lower section, designated E, was from the outside of the toroidal vessel. The number on the scale beneath each strip is used to designate its location.

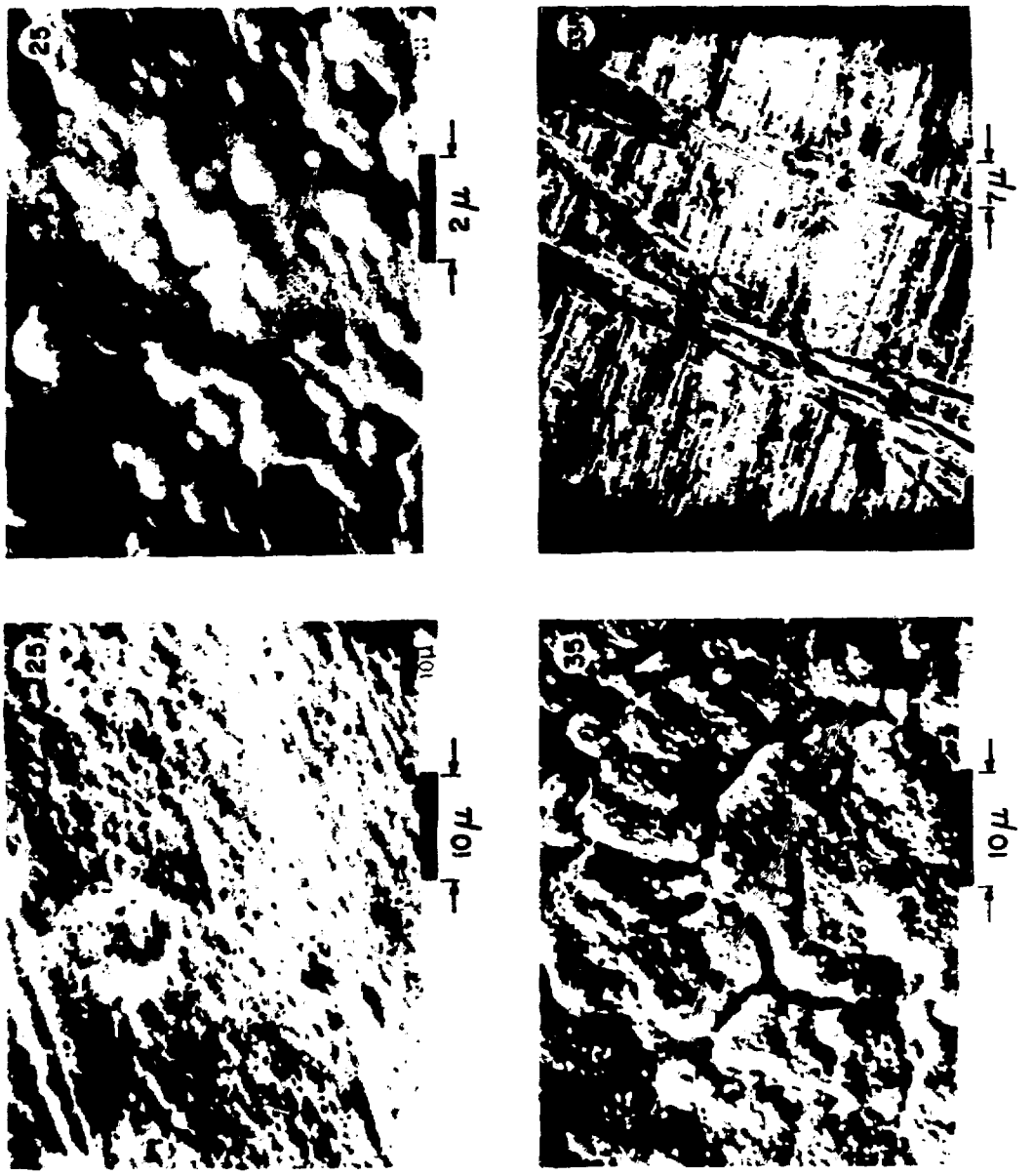

Fig. 5. Scanning electron micrographs of samples taken from the lower strip shown in Figure 4. Sample 25 came from E2, Sample 35 from E21, and 33R was the non-vacuum side of a sample from E21.

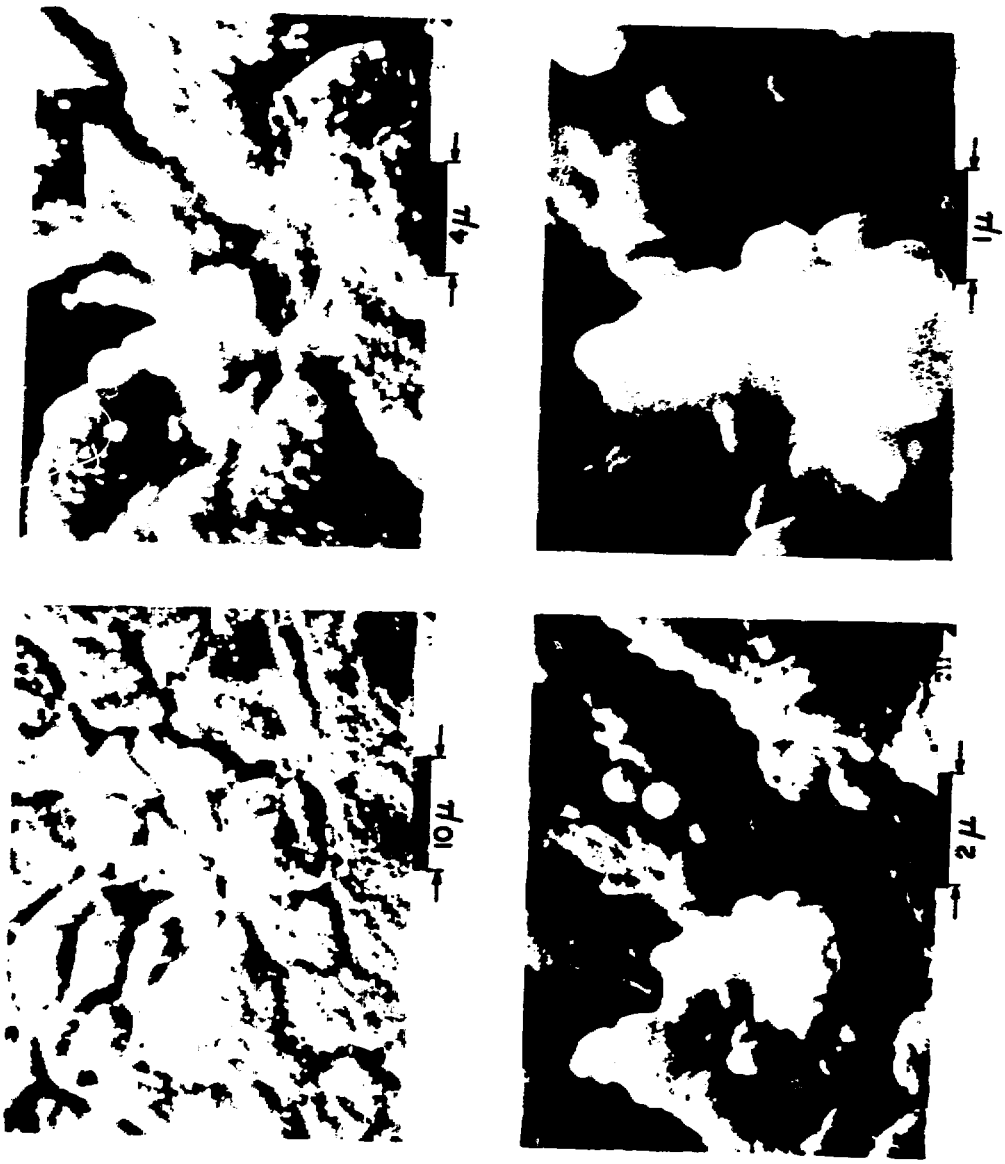

Fig. 6. Scanning electron micrographs of a sample from the ST vacuum vessel located at E21.

Table 1. Weighted Composition of the First 10^{-4} cm of the ST Tokamak Vacuum Wall [a]

Location [b]	%Mo	%W	%SS
E1 - E8	44 ± 1	31 ± 2	25 ± 2
E21	36 ± 2	20 ± 2	49 ± 3
I1 - I9	17 ± 4	13 ± 2	70 ± 6
I44	24 [c]	16 [c]	59 [c]

[a] These compositions should be taken only as relative numbers since no corrections were made for variation in composition with depth which is important in energy dispersive X-ray analysis. Also, it was not possible to correct the composition for those elements not readily detected by this technique, e.g., oxygen and carbon.

[b] See text and Figure 4 for notation.

[c] Only one spectrum taken.

and $FeK\alpha_{1,2}$ lines in the sample spectrum by the height found in pure Mo, W, or 305 stainless steel. The spectra for the pure Mo, W, and 305 stainless steel were obtained within a thirty minute period with the same instrument settings and same sensitivity. These normalized peak heights are assumed to be proportional to the atomic fraction of Mo, W, or SS in the sample. Percent compositions are calculated by assuming Mo, W, or SS are the only substances present in the surface. Probably the two major contributors to errors in Table I are composition changes with depth and ignored elements such as oxygen and carbon. Typical spectra obtained are shown in Figure 7.

By examining Table 1 one sees that the outside of the torus has a thicker coating of Mo and W than the inside. The thickness decreases as one moves farther away from the limiter.

Figure 8 shows a depth profile of a sample from E2 using ion scattering spectroscopy which samples only the first few Å of the surface. This confirms our earlier supposition that the wall had a Mo and W coating. For this sample no iron is seen in the first 400Å and significant amounts of iron start to appear only after the removal of 1500Å.

A depth profile to 800Å of a sample from E21 using Auger electron spectroscopy was used to calculate the compositions listed in Table 2. Again the intensity is compared to intensity from the pure metal or MgO for O. Oxygen was a major impurity in the ST tokamak discharge which is consistent with its presence through the first 800Å. The surface was exposed to atmospheric oxygen for a year prior to these measurements and a machine shop environment for a number of days. The exposure of these samples to machine shop environments insures the presence of carbon on the outer surfaces and the sputtering process used for depth profiling of the chemical composition can push the carbon into the substrate. The distribution of carbon through the first 800Å is therefore con-

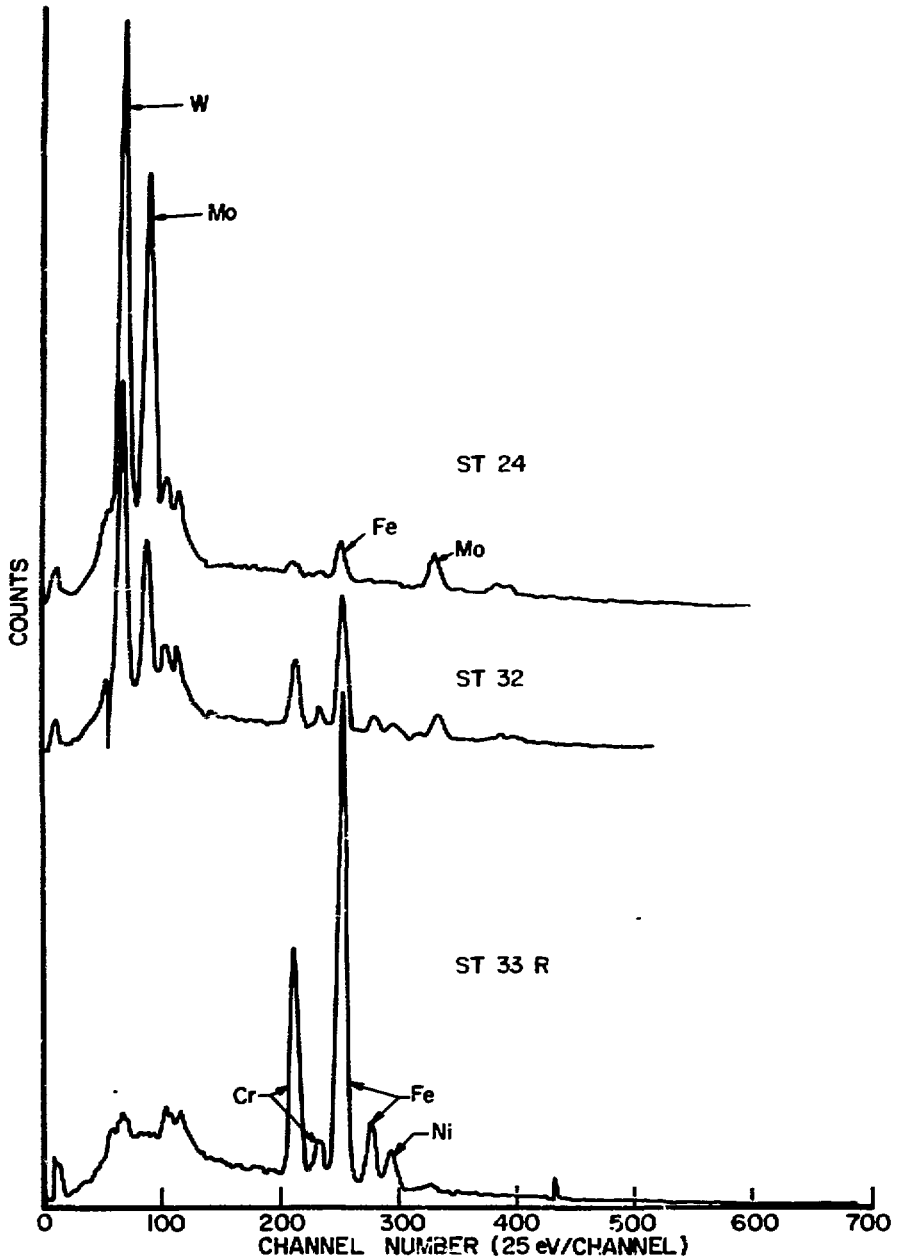

Fig. 7. Typical X-ray energy dispersive spectra from a ST tokamak interior surface. Sample ST 24 was located at E2, sample ST 32 was located at E21, and sample ST 33R was the reverse side of a sample located at E21.

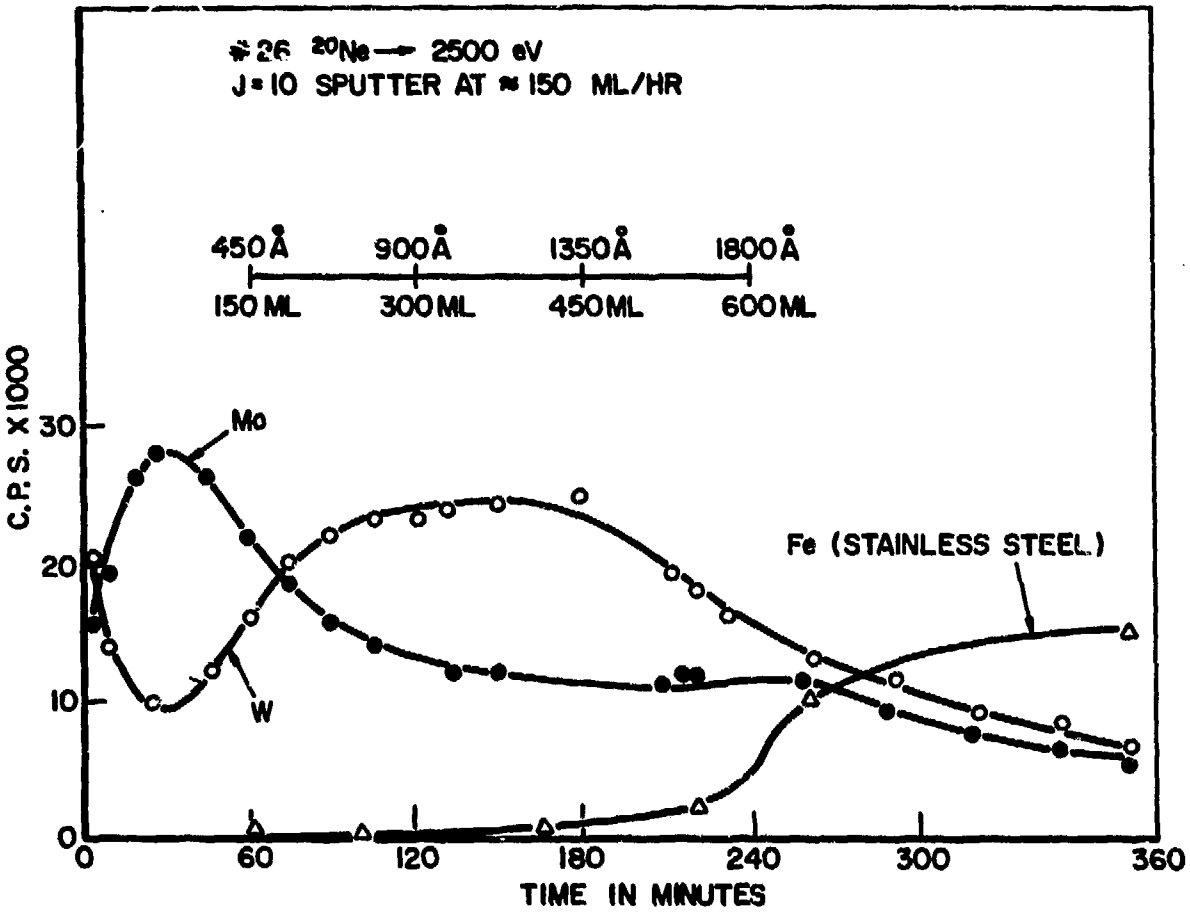

Fig. 8. Depth profile of a sample from the ST tokamak located at E2 using ion scattering spectroscopy. This technique as used here is insensitive to carbon and oxygen.

sidered to be artifactual. Additional experiments will be required to determine carbon distribution.

In summary the section of the ST vacuum vessel studied showed W and Mo present in varying amounts. Depth profiles performed on samples taken from the outside of the torus showed the metals in the near surface regions to be primarily W and Mo. Presumably these coatings were formed by evaporation of W and Mo exposed to the plasma, most notably the limiters. The electron micrographs show that the surface of this coating is a complicated overlapping of spherical shapes.

Table 2. Composition Using Auger Electron Spectroscopy of a Sample from E21

Depth from Surface	%Mo	%W	%Fe	%Sn	%O	%C[a]
10Å	4	33	8	4	4	47
800Å	11	55	8	3	3	20

[a] The sputtering process employed in our experiments can cause surface carbon to move deeper into the metal surface region. See text.

THE EFFECT OF COATINGS ON TRITIUM TRANSPORT AND HOLDUP IN THE FIRST WALL

The bombardment of the plasma containing vacuum wall by energetic tritium neutrals and ions results in a certain fraction being implanted beneath the metal surface. Both the average implantation depth and the fraction of implanted ions increase with increasing energy [4,5]. McCracken and Erents [6] have performed a series of studies on deuterium re-emission from metals bombarded with energetic (7-36keV)D^+ ions. Their initial papers proposed a diffusion model for the re-emission of D from metals, such as Ni, Mo, W and SS which react endothermically with D. Later studies have shown the importance of traps, either produced during or prior to irradiation, on the re-emission process. Other phenomenon such as blistering and gas sputtering can also occur.

This section uses a simplified diffusion model for re-emission to illustrate that coatings can change the quantity of implanted tritium which eventually returns to the plasma. The model follows.

A uniform coating of metal M_1 with a thickness ℓ has been deposited on the vacuum wall of metal M_2 with a thickness d. Tritium is either a) implanted in the coating at a distance $-X_1$ or b) in the wall at a distance X_2 (Figure 9). The diffusion constant D, solubility S, and permeability P for each metal are constant. The following boundary conditions on the concentration of tritium $C_1(x,t)$ and $C_2(x,t)$ exist.

$$
\begin{aligned}
&C_1(x,0) = 0 \qquad && x < 0 \\
&C_2(x,0) = 0 \qquad && x > 0 \\
&C_1(-\ell,t) = 0 \\
&C_2(d,t) = 0 \\
&\frac{C_1(x,t)}{S_1} = \frac{C_2(x,t)}{S_2} \qquad && \text{as } x \to 0
\end{aligned}
\tag{1}
$$

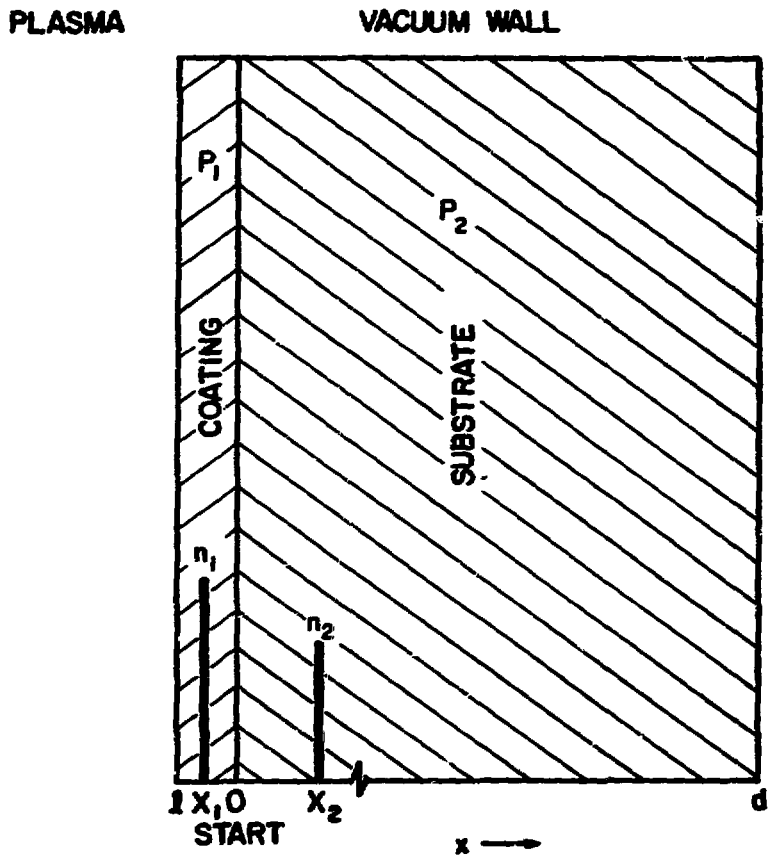

Fig. 9. Schematic of surface coating on vacuum wall. X_1 and/or X_2 designate positions that N_1 and/or N_2 tritons are implanted. The numbers X_1, X_2, ℓ, and d as used in the text are positive and negative signs are explicitly written. P_1 and P_2 are the permeability constants for tritium in the coating and vacuum wall respectively.

and a) $C_1(-X_1,0) = N_1\delta(x+X_1)$

or b) $C_2(X_2,0) = N_2\delta(x-X_2)$.

At $t = \infty$ all the implanted tritium N_1 or N_2 will have diffused out of the wall. The quantities of interest are the fraction of the tritium implanted at X_i ($i = 1$ or 2) that returns to the plasma $F(-\ell, X_i)$ and the fraction that leaves the wall at d $F(d,X_i)$. Their ratio varies inversely as the ratio of the permeation impedance $I(x,X_i)$ of each path

$$\frac{F(d,X_1)}{F(-\ell,X_1)} = \frac{I(-\ell,X_1)}{I(d,X_1)} \tag{2}$$

For calculational purposes use is made of the analogy between Ohms law and the permeation equation [7]. The impedances to the plasma and outside surfaces for implantation in the coating depend on distance divided by the corresponding permeability P_i

$$\begin{aligned} I(-\ell,X_1) &= (\ell - X_1)P_1^{-1} \\ I(d,X_1) &= X_1P_1^{-1} + dP_2^{-1} \ . \end{aligned} \tag{3}$$

The fraction exiting at d is

$$F(d,X_1) = \frac{(\ell - X_1)P_1^{-1}}{\ell P_1^{-1} + dP_2^{-1}} \tag{4}$$

For implantation in the vacuum wall at X_2 this fraction is

$$F(d,X_2) = \frac{\ell P_1^{-1} + X_2P_2^{-1}}{\ell P_1^{-1} + dP_2^{-1}} \ . \tag{5}$$

The linearity of F with X_i means that one can sum (4) or (5) over a distribution of ranges to obtain $F(d,X_i)$. Now the implications of (4) and (5) will be examined.

Tritium permeability varies over many orders of magnitude for materials such as stainless steel, W, and Mo (Table 3). The TFTR under design at Princeton Plasma Physics Laboratory will have a 0.80 cm thick wall (presumably stainless steel) that faces the plasma.* The characteristic time for diffusion through this wall at room temperature is

$$T = \frac{d^2}{D} = 6 \times 10^{11} \text{sec} = 10^4 \text{ years.}$$

Machine plans call for the use of tritium for about 4 years (after 18 morths of experiments using only deuterium and hydrogen); therefore, essentially none of the implanted tritium will escape the vessel during its lifetime.† The quantities $F(d,X_i)$ in this case are the fractions of implanted tritium that will remain in the wall.

Without a coating ($\ell = 0$) equation (5) shows that

$$F(d,X_2) = \frac{X_2}{d} \quad .$$

With a coating of tungsten

$$F(d,-X_1) = \frac{(\ell - X_1)(6\times10^{20})}{\ell(6\times10^{20})+d(10^{11})}$$

$$F(d,X_2) = \frac{\ell(6\times10^{20})+X_2(10^{11})}{\ell(6\times10^{20})+d(10^{11})}$$

---

* The bellows section which is 0.1 cm thick is shielded from the plasma by an extension of the 0.80 cm wall.

† The maximum bakeout temperature is 250°C but it probably will not be baked out after tritium has been used; at 250°C T = 1 year.

Table 3. Tritium Solubility, Diffusivity, and Permeability

304 Stainless Steel[a]	T = 300°K
$S = 1.6 \times 10^{-3} \exp(-\frac{4300}{RT})$	1.2×10^{-6}
$D = 1.8 \times 10^{-2} \exp(-\frac{14000}{RT})$	1.3×10^{-12}
$P = 1.6 \times 10^{2} \exp(-\frac{18300}{RT})$	9.1×10^{-12}
Tungsten[b]	
$S = 8.2 \times 10^{-3} \exp(-\frac{24000}{RT})$	3.5×10^{-20}
$D = 2.4 \times 10^{-3} \exp(-\frac{9000}{RT})$	7.3×10^{-10}
$P = 1.1 \times 10^{2} \exp(-\frac{31500}{RT})$	1.7×10^{-21}
Molybdenum[b]	
$S = 1.1 \times 10^{-3} \exp(-\frac{6800}{RT})$	1.3×10^{-8}
$D = 1.1 \times 10^{-2} \exp(-\frac{14700}{RT})$	2.5×10^{-13}
$P = 5.4 \times 10^{1} \exp(-\frac{21500}{RT})$	1.5×10^{-14}

Units $S(atm^{-1/2})$, $D(cm^2 sec^{-1})$, $P(cc(STP)cm^{-1}h^{-1}atm^{-1/2})$

a. Data for S from [8], D from [9], and P from [10].

b. Data from [11].

Using the projected ranges in Table 4 one finds that a 10^{-5} cm coating of W would result in 3% and 50% of the implanted tritium remaining in the wall for an incident particle energy of 0.5 keV and 10 keV respectively. This compares to 3×10^{-5}% to 1×10^{-3}% for uncoated stainless steel.

Table 4. Projected Range for Tritium Based on Shiøtt's Approximation[a]

Energy (keV)	Range x 10^8 cm		
	Fe	Mo	W
0.5	30	30	30
1.0	50	50	50
10.0	900	700	500

[a] Ref. [4]

A 200Å layer of W would result in all the tritium implanted at a depth greater than 200Å remaining in the wall. The larger permeability constant for Mo means that the effects from Mo coatings would be several orders of magnitude less.

No discussion has been made about the energy distribution and flux to the first wall. Even if our simplified model were correct, these quantities will determine whether a coating causes appreciable holdup in the wall.

The model proposed above can make only semi-quantitative statements about tritium holdup and transport in steel reactor walls that have been coated during use. The effects of chemical contamination at the vacuum vessel surface and at internal surfaces will undoubtedly be

important. The roughness of the internal surface of the coating and degree of coverage are important as well as radiation damage. In the case of high fluxes in materials with low hydrogen solubility, such as tungsten, blistering may occur. This discussion is designed only to identify the nature of the problem and point out areas which must be investigated before predictions of the magnitude of tritium holdup are possible. The model suggests that tritium holdup could be minimized by having a coating with a very high permeability for tritium, such as vanadium.

ACKNOWLEDGEMENTS

This manuscript benefitted from discusions with Prof. R.C. Axtmann, Dr. S. Cohen, Mr. V. Corso, Dr. E. Meservey, and Prof. B. Royce at Princeton University. Special thanks are deserved by Dr. D. Malm and Dr. H. Schreiber at Bell Laboratory, Murray Hill, for doing the depth profiles reported; and to Dr. W. Christie at Oak Ridge National Laboratory. Mr. P. Roitman helped with the X-ray and SEM studies.

This work was supported by U.S. Energy Research and Development Contract AT(11-1)-3028.

REFERENCES

1. E. B. Messervey and V. L. Corso, Princeton Plasma Physics Laboratory, Private Communication.

2. P. E. Stott, C. C. Daughney, and R. A. Ellis, Jr., Control of recycling and impurities in the ATC tokamak by means of gettered surfaces, MATT-1111, Plasma Physics Laboratory, Princeton University, Princeton, New Jersey, March 1975.

3. T. Spalvins and W. A. Brainard, Nodular growth in thick-sputtered metallic coatings. J. Vac. Sci. Technol. 11, 1186 (1974).

4. H. E. Shiøtt, Rad. Effects 6, 107 (1970).

5. G. M. McCracken, Rep. Prog. Phys. 38, 241 (1975); Japan. J. of Appl. Physics, Suppl 2, Part 1, 269 (1974).

6. E. Erents and G. M. McCracken, Rad. Effects 3, 123 (1970); Applications of Ion Beams to Metals, S. T. Picraux et al., eds, Plenum Publishing Corp., New York 1974. p. 585.

7. R. A. Strehlow and H. C. Savage, J. of Nucl. Mater. 53 299 (1974).

8. E. E. Fletcher and A. R. Elsea, Hydrogen movement in steel - entry, diffusion, and elimination. DMIC Report 217, June 30, 1965. Data on pg. 8 was used.

9. J. H. Austin and T. S. Elleman, J. Nucl. Mater. 43, 119 (1972).

10. W. A. Swansiger, R. G. Musket, L. J. Weirick, and W. Bauer, J. Nucl. Mater. 53, 307 (1974).

11. Dieter M. Gruen ed., The Chemistry of Fusion Technology, Plenum Press, New York, 1972. p. 305.

PERMEATION OF TRITIUM AND DEUTERIUM THROUGH 21-6-9 STAINLESS STEEL*

W. A. Swansiger

Sandia Laboratories, Livermore, CA

ABSTRACT

Tritium and deuterium permeabilities were measured for annealed 21Cr-6Ni-9Mn stainless steel at hydrogen isotope pressures of 1.3 to 13.3 kPa (10 to 100 torr) and sample temperatures of 95 to 430°C. The effects of two surface treatments were compared. The tritium permeability of a sample which had been sputter-cleaned then sputter-coated with 200 Å of palladium is given by:

$$\phi = 9.9\times10^{-3} \exp(-15760\ \text{cal}\cdot\text{mol}^{-1}/RT)\ \text{cc(STP)}T_2\cdot\text{cm}^{-1}\cdot\text{sec}^{-1}\cdot\text{atm}^{-1/2}$$

The tritium permeability of a sample which had been passivated using a common nitric acid - Nitradd treatment is given by:

$$\phi = 4.5 \exp(-24500\ \text{cal}\cdot\text{mol}^{-1}/RT)\ \text{cc(STP)}T_2\cdot\text{cm}^{-1}\cdot\text{sec}^{-1}\cdot\text{atm}^{-1/2}$$

This treatment, which is often used to clean stainless steel prior to welding, creates a thin, stable oxide film. Deuterium permeabilities were determined for two samples which had received the same treatments as the tritium permeation samples. The activation energies for permeation were the same (within experimental error) as for the corresponding tritium samples.

---

*This work is supported by the U. S. Energy Research and Development Administration.

INTRODUCTION

In a fusion reactor, the principal tritium flow path to the environment is through the liquid metal heat exchangers to the steam system where tritium would be released to the environment as part of the blowdown of the steam-water system.

Stainless steels are prime candidate materials for steam system construction because of their relatively low cost, ease of fabrication, and resistance to corrosion. Calculations have shown that meeting the tritium release limits now in effect for light water reactors may require some means to reduce the permeability of the steels used in the steam system.[1,2] Since the introduction of a permeation barrier could affect cost of fabrication and probably operational lifetime, it is important for the reactor designer to have accurate values of tritium permeabilities for stainless steels with and without permeation barriers so that barriers can be compared with each other and with other alternatives. This paper reports deuterium and tritium permeabilities for 21-6-9 stainless steel with two different surface treatments.

EXPERIMENTAL TECHNIQUES

Circular permeation specimens (approximately 0.092-mm thick, 18.3-mm diameter) were machined from a sheet of annealed 21-6-9* stainless steel. The foils were chemically cleaned using a solution of 20% Nitradd,** 30% nitric acid in demineralized water. Auger analyses performed before and after this treatment showed that the oxygen signal decreased and the chromium signal increased as a result of the cleaning. The surface of bright stainless steel is typically covered by a thin oxide layer less than 150 Å thick.[3] Since the effects of oxide films on permeation are

---

*Nominal composition (in wt%): Cr = 20.2, Ni = 6.3, Mn = 9.0, Si = 0.5, balance Fe.

**Turco Products, Wilmington, CA

variable,[2,4] an effort was made to minimize surface effects on certain of the samples. To this end, several of the foils were sputter-cleaned, then 200 Å of palladium was sputter-deposited on both faces of the samples. The palladium coating serves to protect the sputter-cleaned sample from oxidation, which would occur on unprotected stainless steel surfaces even at room temperature. Since palladium itself is relatively unreactive and since it is so highly permeable to hydrogen isotopes compared to stainless steel, this technique should allow the measurement of true bulk permeabilities. Variations of this technique have been used by others with good results.[5,6]

Each permeation specimen was placed between two 1-mm thick copper gaskets, which in turn were sealed between two Varian mini-conflat fittings. The assembly was bolted into the permeation apparatus and enclosed in a 76-mm diameter copper heat sink. Thermocouples to monitor sample temperature were placed in contact with the edge of the specimen via holes drilled through the heat sinks and Varian fittings. The heat sink was surrounded by a heating blanket. Sample temperature was held constant to within ±0.3°C.

Deuterium and tritium permeation measurements were carried out in separate all-metal ion-pumped vacuum systems. The time-lag (TL) permeation method was used in the tritium system whereas a modified time lag (MTL) method was used for the deuterium measurements. In both cases, a constant hydrogen isotope pressure is maintained on the upstream side of the sample. In the TL method, the permeating gas collects on the downstream side of the sample in a closed volume. From the rate of buildup of this gas, the diffusivity and permeability can be computed. In the MTL method, the downstream volume is continuously pumped at a constant rate. This modification yields the time derivative of the time-lag data.

In the deuterium system a quadrupole mass spectrometer was used to detect the permeating gas. Since the permeating deuterium can exchange with other hydrogen-containing species, masses 3, 19, and 20 were scanned in addition to mass 4. Permeation rates were determined by comparison with calibrated orifice leaks. Before admission to the upstream side of the system, deuterium was purified by permeation through a heated

Pd-25 percent Ag tube. Deuterium pressure was held constant within ±0.013 kPa over the range 1.3 to 13.3 kPa (10 to 100 torr) by a servo-controlled leak valve receiving feedback from a capacitance manometer.

The upstream side of the tritium system is similar to that of the deuterium system, but it simultaneously feeds up to six permeation samples, each with its own temperature controller and tritium detector. Each of the tritium samples is close-coupled downstream to a specially designed ionization chamber having no elastomeric components.[7] The ionization chambers were filled with 700 torr of ultra-high purity helium-4 and were charged to +1000 V DC. The current generated by tritium decay in the chambers was measured by vibrating-reed electrometers. The chambers were calibrated using standards containing known quantities of tritium. All tritium measurements were made with an upstream tritium pressure of 1.3 kPa (10 torr).

RESULTS AND DISCUSSION

Figure 1 is an Arrhenius plot showing tritium permeability as a function of temperature for two samples of 21-6-9 stainless steel which received different surface treatments. The permeability of sample C401, which received the chemical cleaning described earlier, can be represented by $\phi = 4.47 \, ^{+.74}_{-.53} \exp(-24500 \pm 800 \text{ cal}\cdot\text{mol}^{-1}/RT)\text{cc(STP)}T_2\cdot\text{cm}^{-1}\cdot\text{sec}^{-1}\cdot\text{atm}^{-1/2}$. The limits represent precision, not accuracy. The permeability of sample C202, which had been sputter-cleaned then sputter-coated with 200 Å of palladium, is (in the same units): $\phi = (9.913 \pm .0005) \times 10^{-3} \exp(-15755 \pm 9/RT)$. The chemical cleaning resulted in a greatly reduced tritium permeation rate in the temperature range of the measurements. Extrapolation of the data to room temperature indicate tritium permeation through the chemically cleaned sample would be lower by a factor of 5700 than through the palladium coated sample.

An indication of whether true bulk properties are being measured is how well the time-dependent hydrogen flux compares with the theoretical curve obtained by solution of Fick's second law

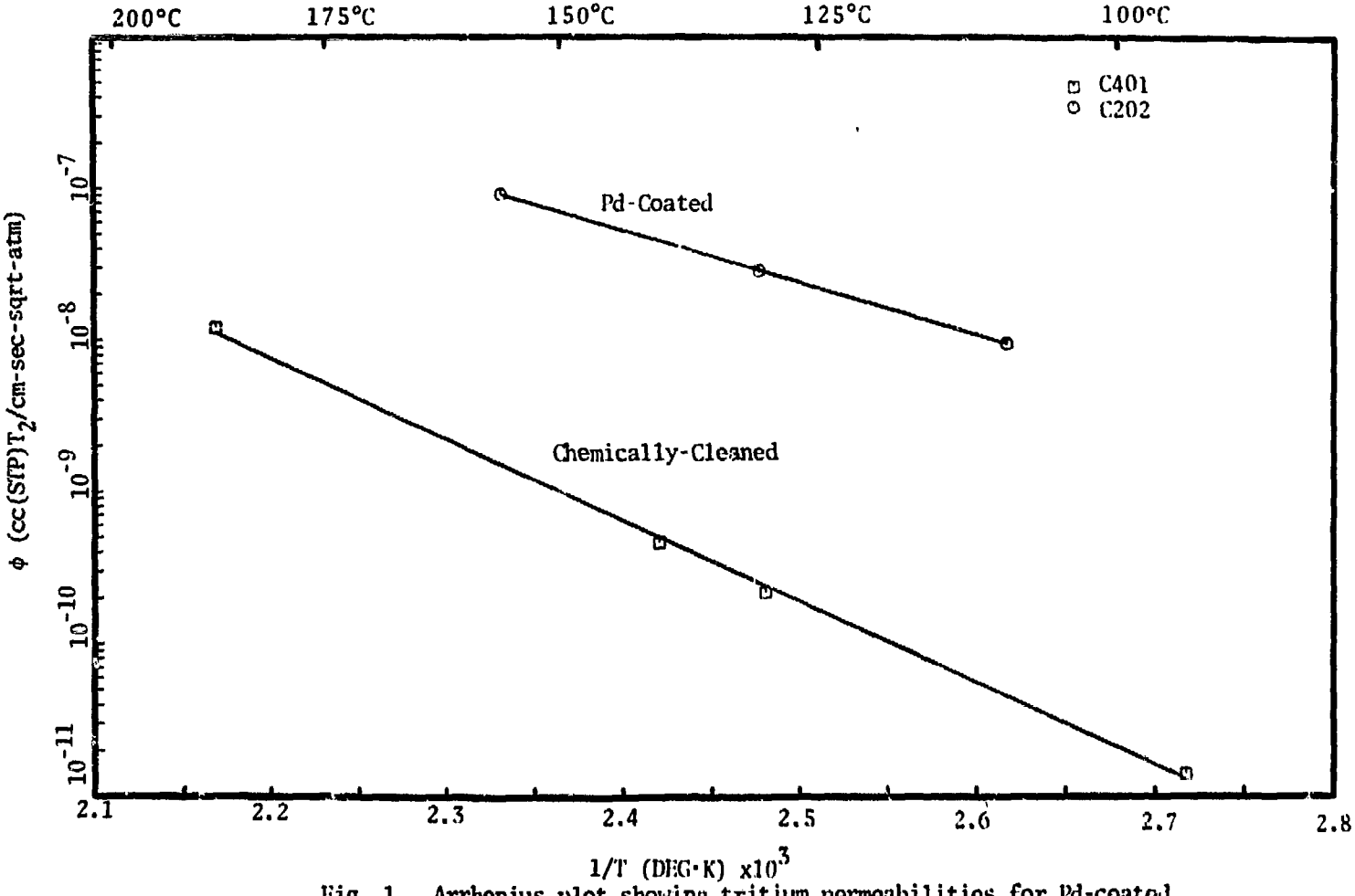

Fig. 1. Arrhenius plot showing tritium permeabilities for Pd-coated and chemically-cleaned samples.

TM-405

$$\frac{\partial C}{\partial t} = D \frac{\partial^2 C}{\partial x^2}$$

with the experimentally defined boundary conditions. The diffusion coefficient is represented by D, concentration by C, time by t, and distance parallel to the direction of hydrogen flux by x. The dashed line in Fig. 2 is the thoretical curve (2 parameter fit, diffusivity and permeability being varied) generated by a least squares fit to over 1400 experimental points for sample C202 at 156°C (Pd-coated, T_2 permeation). The fit appears to be very good and is not significantly improved by a model introducing two more adjustable parameters. This 4-parameter model corresponds to simultaneous diffusion along two parallel paths (e.g., nonuniform surface film or bulk and grain boundary diffusion). Figure 3 shows a 2-parameter fit for sample C401 (chemically-cleaned, T_2 permeation). The fit is very poor and is greatly improved by use of the 4-parameter model as shown in Fig. 4. Work is in progress to develop and verify models for such non-ideal cases as represented by the chemically-cleaned samples.

Figure 5 is an Arrhenius plot showing deuterium permeability as a function of temperature for two samples of 21-6-9 stainless steel which received surface treatments identical to those received by samples C202 and C401 referred to earlier. Sample A102 was sputter-cleaned and palladium coated in the same apparatus and at the same time as sample C202. Sample A101 was likewise cleaned at the same time and in the same way as sample C401. The deuterium measurements were made at upstream pressures of 1.3 to 13.3 kPa (10 to 100 torr). The deuterium permeabilities can be represented by:

$$\text{A101 } \phi = 2.0 \begin{smallmatrix}+45.2\\-1.99\end{smallmatrix} \exp(-27600 \pm 6200 \text{ cal}\cdot\text{mol}^{-1}/RT)\text{cc(STP)}D_2\cdot\text{cm}^{-1}\cdot\text{sec}^{-1}\cdot\text{atm}^{-1/2}$$

$$\text{A102 } \phi = (3.97 \begin{smallmatrix}+1.03\\-0.81\end{smallmatrix}) \times 10^{-2} \exp(-16280 \pm 740/RT)\text{(same units)}$$

Permeation rate was found to vary linearily with the square root of D_2 pressure for the palladium coated sample but not for the chemically cleaned sample. This is an indication that permeation through sample A101 was not bulk-diffusion controlled and would account in part for the scatter

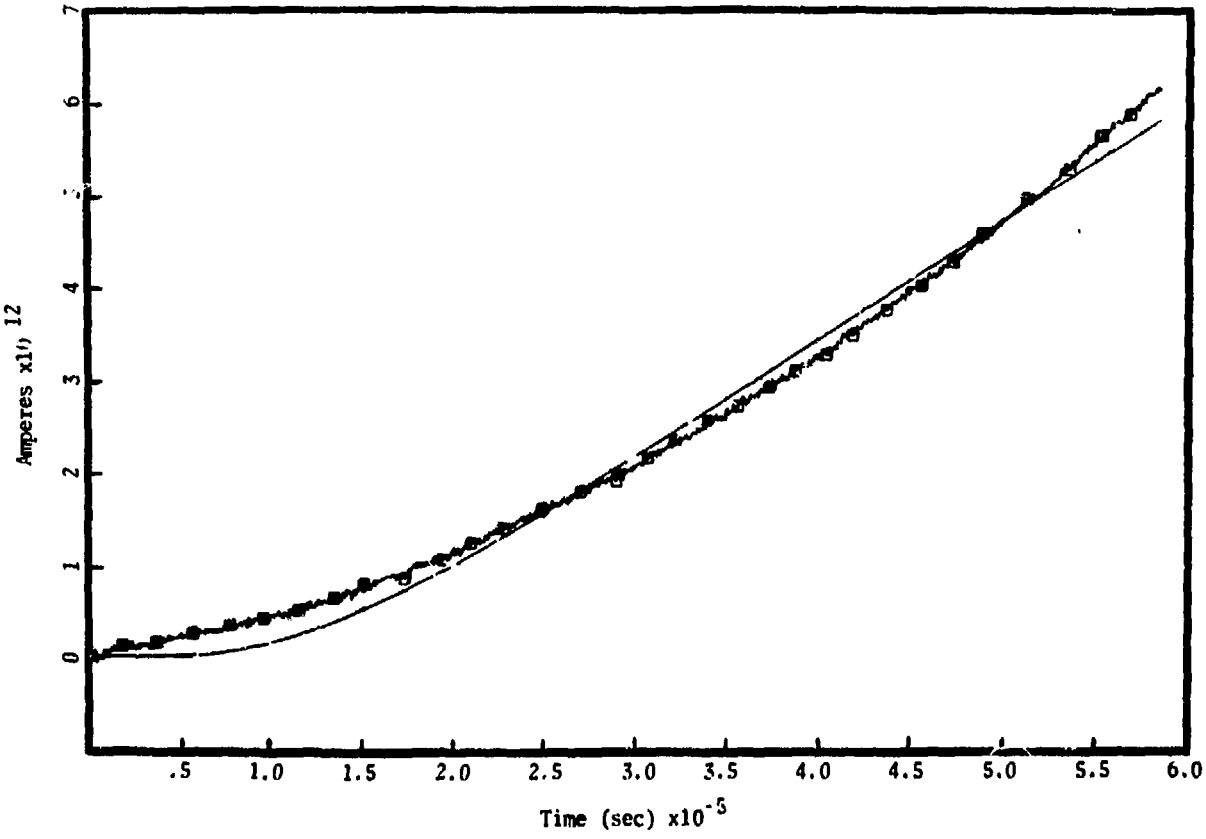

Fig. 2. Ionization chamber current (proportional to total quantity of tritium permeated) as a function of time for Pd-coated 21-6-9 stainless steel at 156°C, 10-torr tritium pressure. The dashed line representing the best 2-parameter fit (diffusivity and permeability) is virtually coincident with the solid line connecting the data points.

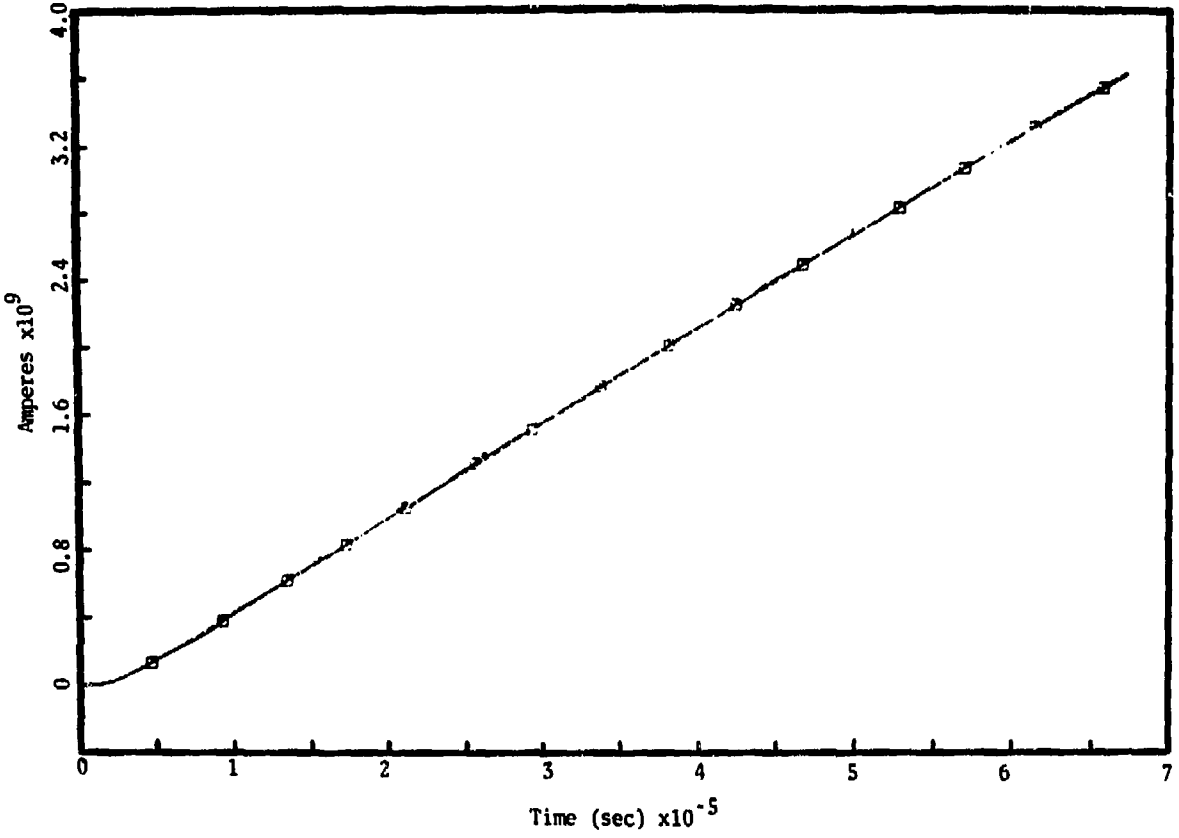

Fig. 3. Ionization chamber current as a function of time for chemically-cleaned 21-6-9 stainless steel at 130°C, 10-torr tritium pressure. Smooth curve is best 2-parameter fit by the least squares method.

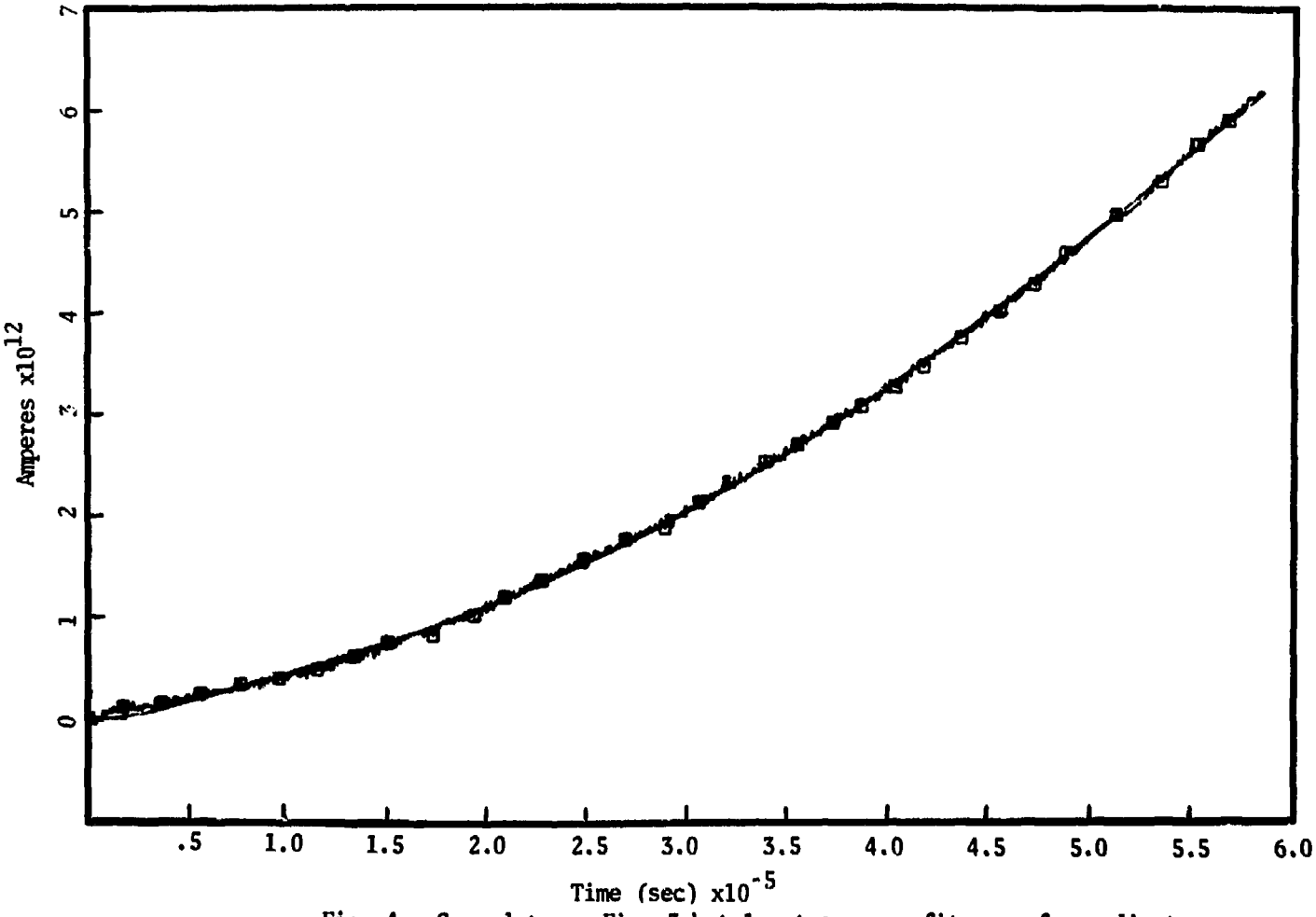

Fig. 4. Same data as Fig. 3 but least-squares fit uses four adjustable parameters.

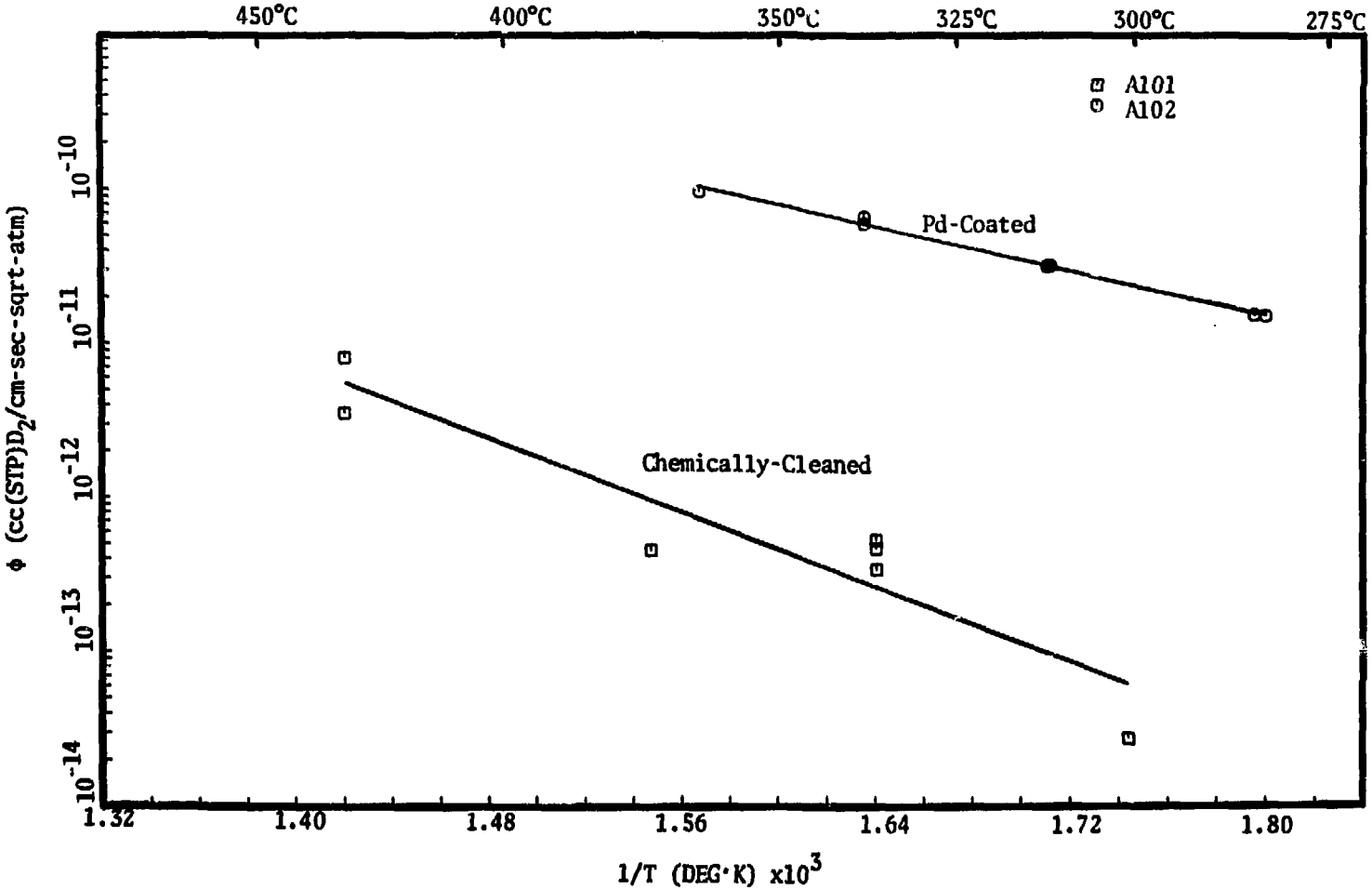

Fig. 5. Arrhenius plot showing deuterium permeabilities for Pd-coated and chemically-cleaned samples.

in the data. Least squares fits of the type shown in Figs. 2 through 4 were applied to the deuterium data. They confirmed that permeation through the chemically-cleaned sample was not bulk-diffusion controlled because the 2-parameter fits were invariably poor.

It is apparent from the Arrhenius plots that the permeability of A101 (chemically cleaned sample in the deuterium system) when extrapolated to the temperature range of C401 (chemically cleaned sample in the tritium system) is lower than would be expected. The most likely reason for this is sample-to-sample variability in the surfaces produced by the chemical-cleaning process. As a demonstration of this variability, data were obtained at two temperatures for a third chemically cleaned sample in the tritium system. Though the activation energy for permeation was about the same as for samples A101 and C401 (about 25 kcal/mol), the permeation rate was 7 times lower than that of C401 at 100°C. This is small compared to the factor of 300 difference at 100°C between sample C401 (chemically cleaned) and sample C202 (Pd-coated) but is still much larger than experimental error.

CONCLUSIONS

Tritium and deuterium permeation measurements on annealed 21-6-9 stainless steel have shown that a simple chemical cleaning treatment can reduce the tritium permeation rate by a factor of 300 at 100°C over that of Pd-coated 21-6-9. Extrapolation of the data to room temperature predicts a permeability reduction of 5700. Although the surface layer created by the passivation treatment appears to be stable in hydrogen at temperatures >400°C, the high activation energy for permeation of the passivated steel makes the permeability of the Pd-coated and passivated steels about equal at the temperatures the steam system of a fusion reactor is likely to operate.

ACKNOWLEDGEMENTS

The author gratefully acknowledges D. R. Folk for assistance in making the permeation measurements and for building most of the apparatus, F. Danielli for making possible the transition from strip chart recorder to computer-controlled data acquisition, T. H. Jefferson for numerical analysis, A. J. West for the Auger analyses, and J. P. Darginis for the palladium deposition.

REFERENCES

1. A. P. Fraas, Comparison of Two Tritium Removal Systems Designed to Minimize Contamination of Steam Systems in Full-Scale Thermonuclear Power Plants, Oak Ridge National Laboratory, ORNL-2832, May 1970.

2. H. C. Savage and R. A. Strehlow, Trans. Am. Nucl. Soc. 17, 152 (1973).

3. R. G. Musket and W. Bauer, J. Appl. Phys. 43 (1972) 4786.

4. W. A. Swansiger, R. G. Musket, L. J. Weirick, and W. Bauer, J. Nucl. Matls. 53, 307 (1974).

5. W. J. Kass and W. J. Andrzejewski, Internal Report SC-DR-720136, Sandia Laboratories (April 1972).

6. G. L. Holleck, J. Phys. Chem. 74, 1967 (1970).

7. C. A. Colmenares, Nucl. Insts. & Methods 114, 269 (1974).

THE PERMEATION OF TRITIUM THROUGH ALUMINIUM IN THE TEMPERATURE RANGE OF 25 TO 250 °C

H. Ihle, U. Kurz and G. Stöcklin

Institut für Chemie der Kernforschungsanlage Jülich GmbH
Institut 1: Nuklearchemie
D-5170 Jülich, FRG

ABSTRACT

Permeation of tritium through aluminium is expected to be very low at ambient temperatures due to the high endothermic heat of solution of hydrogen in this metal.

In order to obtain experimental data for its use as tritium-barrier, the permeation of T_2 at about 0.2 atm pressure through a 1 mm wall of an Al-capsule with an area of 100 cm^2 was measured in the temperature range of 25 to 250 °C. Gas flow counting was used for detection.

In the temperature range from 150 to 250 °C the permeation rate appears to be controlled by bulk diffusion, since the measured heat of permeation, Q = 29,400 kcal/mol, agrees well with the heat of permeation of H_2 through Al calculated from known diffusion and solubility data, obtained from measurements close to the melting point of Al.

Between 25 and ≈ 150 °C the observed permeation of tritium through Al was higher than expected from calculations, possibly due to grain boundary diffusion; however, it is still many orders of magnitude lower than that through most common metals.

INTRODUCTION

Permeation of hydrogen through most materials of construction, e.g. for large vacuum chambers or gas handling equipment filled with tritium, is high enough to cause significant

leakage of tritium to the surroundings even at ambient temperature. Since parameters influencing the total release of tritium like physical size, pressure, and temperature are usually fixed by considerations other than minimization of tritium-leakage, appropriate choice of wall materials of low hydrogen-permeability can reduce the tritium release substantially.

A survey on hydrogen permeation rates through some metals as a function of temperature is given in Fig. 1. The information in this figure was obtaind from various compilations[1,2] and should serve for illustration only.

It is seen that experimental data are generally limited to permeation fluxes $\gtrsim 10^{-5} - 10^{-6}$ cc(STP)mm/cm^2·h·atm$^{1/2}$. The widely differing slopes in the log Φ vs. $10^3/T$ curves are chiefly due to the large differences in the heats of solution of hydrogen in various metals; the activation energy of diffusion for hydrogen in metals is rather similar for all metals and therefore has little influence on the large differences in permeability expected in the extrapolated region at low temperatures.

Of the more common metals, aluminium should have a particularly low permeability because of the high endothermic heat of solution of hydrogen in this metal. To obtain experimental data with respect to a possible use of aluminium as tritium-barrier at relatively low temperatures, we carried out tritium permeation experiments under conditions which allow the measurement of very small fluxes of tritium.

EXPERIMENTAL

The apparatus used is shown in Fig. 2. The source for the permeation experiments is a cylindrical, electron beam-welded capsule of 100 cm^3 volume, about 100 cm^2 surface area and 1 mm wall-thickness; the disks at both ends are 6 mm thick. The

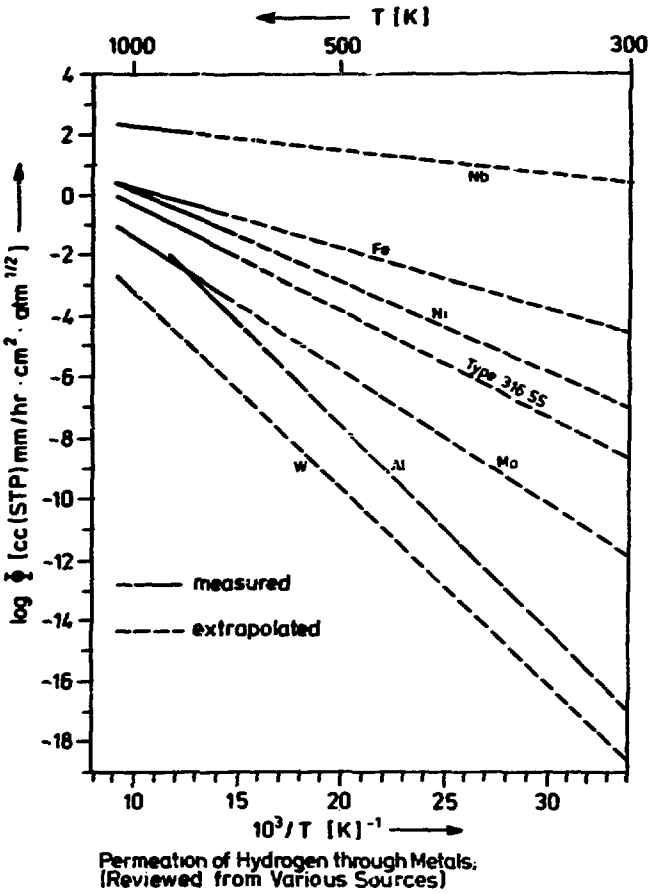

Permeation of Hydrogen through Metals.
(Reviewed from Various Sources)

Fig. 1 Permeation of hydrogen through metals as a function of temperature

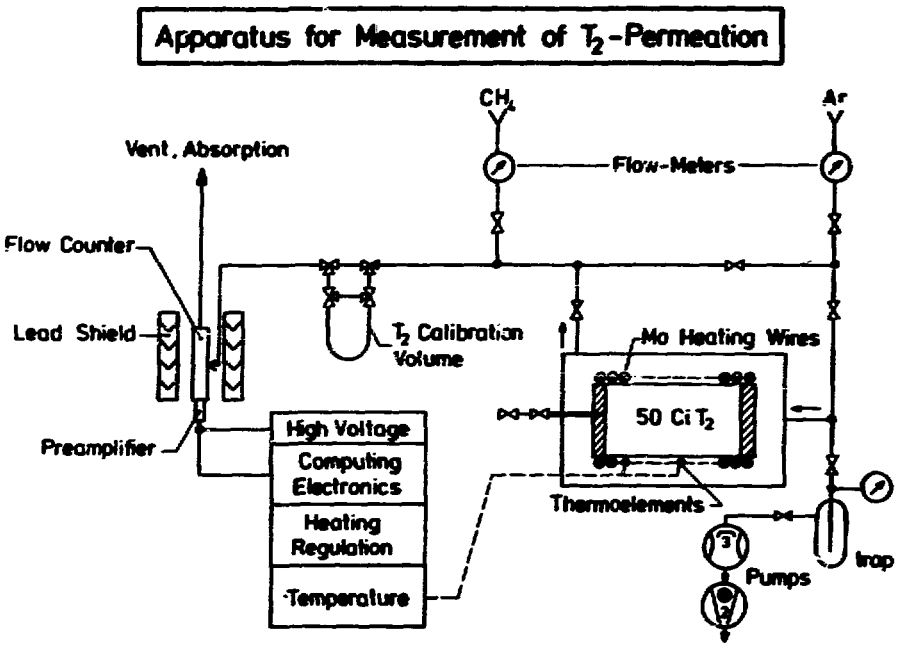

Fig. 2 Apparatus for measurement of tritium permeation (for details cf. Experimental part)

capsule contains 50 Ci of tritium, corresponding to a pressure of about 0.2 atm at 25 ^{o}C, and is heated by a Mo wire heater. The temperature was measured with several Pt-wires directly welded onto the aluminium surface, whereby small temperature gradients could be detected. A stream of argon entering the space between the capsule and an outer containment, which also consists of aluminium, mixes with the permeated tritium and is lead to a gas proportional flow counter after admixture of about 10 % methane.

In steady state, the permeation rate through the aluminium wall is directly proportional to the product of the argon flow and the concentration of tritium in the gas, which is measured radiometrically. The smallest measured permeation rate was $1.3 \cdot 10^{-13}$ cc(STP)·mm/cm^2·h·atm$^{1/2}$ corresponding to a flux of $\sim 10^3$ T_2 molecules/cm^{2}sec at 1 atm pressure within the capsule. For the measurement of very small fluxes [$\Phi \lesssim 10^{-12}$ cc(STP)·mm/cm^2·h·atm$^{1/2}$], the gas flow was interrupted and the tritium accumulated in the space surronding the capsule for about one hour. We estimate that, by extension of the accumulation time by a factor of 10 and the use of low level tritium-counting, the limit of detection could be lowered to about 10 to 20 T_2-molecules/cm^{2}sec.

For the dependence of the permeation rate on the pressure of tritium inside the capsule due to changing temperature, the square root law was assumed to be valid, which was experimentally verified in early work on the permeation of hydrogen through aluminium at a temperature close to the melting point[3] in the range of pressure used in our experiments.

RESULTS AND DISCUSSION

The measured permeability of tritium through aluminium is shown in Fig. 3. The values cover a range of 10^6 in a region of low fluxes, where no direct measurement was possible up till now. Our results are directly compared which those obtained by Cochran[4], who also used aluminium with an untreated surface for his measurements of the permeation of hydrogen between 400 and 600 °C. His results and our own values for the tritium permeation between 150 and 250 °C agree reasonably well with the permeability calculated from solubility and diffusivity data for hydrogen in aluminium based on the experimental results of Eichenauer and Pebler[5].

It is therefore concluded that in the range from 150 to 250 °C, lattice diffusion is the rate determing step in the permeation process. The temperature dependence of the permeability of aluminium to tritium in this range can be expressed by the following equation:

$$\Phi = (1.5 \pm 1.0)\,10^5 \cdot \exp\left(-\frac{29{,}400 \pm 340}{RT}\right) \text{cc(STP)} \cdot \text{mm/cm}^2 \cdot \text{h} \cdot \text{atm}^{1/2}$$

Below 150 °C the measured permeation is higher than expected from values obtained at higher temperature, which may be due to grain boundary diffusion.

The results on tritium permeation were directly compared with those obtained at higher temperatures with hydrogen because the isotope effects on solubility and diffusivity in aluminium are not known.

Surface phenomena, to which the low permeability of aluminium was attributed in some earlier work[6], do not appear to have any significant influence on the results of this work, which was carried out with untreated aluminium metal. It would be interesting to obtain results on the influence of atomic tritium by the method described, e.g. from a discharge in the

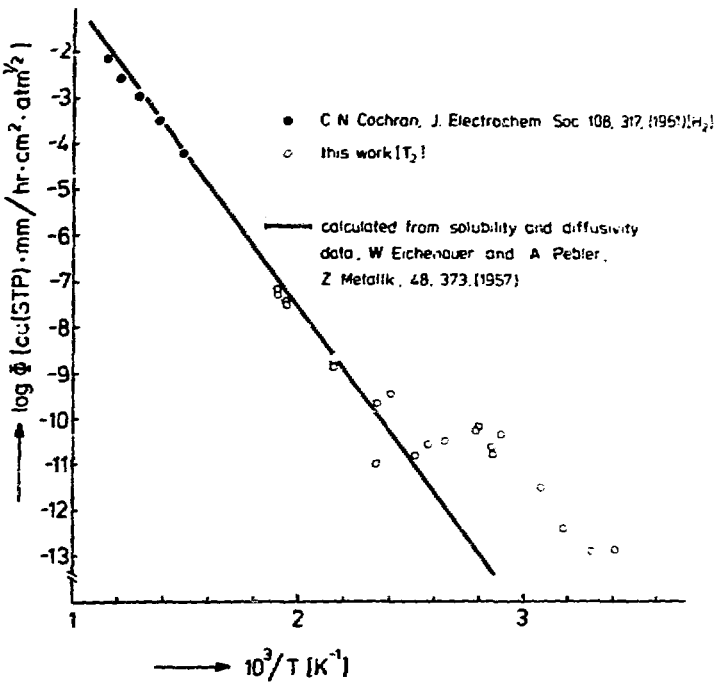

Fig. 3 Experimental results on the permeation of tritium through aluminium

capsule as obtained at higher temperatures and discussed in ref.[4]. The permeation rates should be much higher, but the effects of surface films and their catalytic activity on the recombination of atomic hydrogen, or its reaction with adsorbed impurities or other components of the system, will depend on temperature and other parameters which are not known.

CONCLUSION

In the temperature range covered in this study, the permeation rate of tritium through aluminium is very low and appears to be controlled by lattice diffusion with some contribution from grain boundary diffusion. The radiometric method applied is simple, and owing to its high dynamic range and sensitivity seems to be well suited for further investigation of diffusion barriers for tritium.

Our results suggest the use of aluminium for tritium handling devices which are operated at relatively low temperature, and its use as a cladding layer at the outer surface of vacuum tanks of plasma experiments with tritium.

REFERENCES

1. R. W. Webb, Permeation of Hydrogen through Metals, NAA-SR-10462 (1965).

2. S. Dushman, Scientific Foundations of Vacuum Technique, Wiley, New York, 1962.

3. C. J. Smithells and C. E. Ransley, Proc. Roy. Soc. London A, 152, 706 (1936).

4. C. N. Cochran, J. Electrochem. Soc. 108, 317 (1961).

5. W. Eichenauer and A. Pebler, Z. Metallk. 48, 373 (1957).

6. P. S. Flint, The Diffusion of Hydrogen through Materials of Construction, KAPL-659 (1951).

TRITIUM DIFFUSION IN CERAMIC CTR MATERIALS*

J. D. Fowler R. A. Causey

D. Chandra** T. S. Elleman

K. Verghese

North Carolina State University
Raleigh, North Carolina 27607

ABSTRACT

Gas release experiments have been used to measure diffusional release of recoil-injected tritons from the following materials: Al_2O_3 (single crystal, sintered and MgO-doped), BeO (single crystal and sintered), alpha-SiC (single crystal, hot pressed, and Al-doped), beta-SiC (single crystal), Y_2O_3, Yttralox,*** and SCB glass. Diffusion coefficients were obtained over five orders of magnitude at temperatures between 320°C and 1400°C. In most cases, fractional release curves are indicative of classical diffusion, and Arrhenius plots for a given material can be described by a constant activation energy. Characteristic activation energies varied from 30 to 70 kcal/mole. Isothermal diffusion coefficients increased by several orders of magnitude with the addition of small amounts of heterovalent impurities. Diffusion in the 0.1 weight percent MgO-doped alumina was five orders of magnitude larger than the single crystal alumina, and similar enhanced diffusion was observed for Al-doped SiC over undoped SiC.

*Work supported under ERDA Contract AT-(40-1)-4721

**Present address: Brookhaven National Laboratory
Upton, New York

***General Electric Company

INTRODUCTION

Ceramic materials offer many advantages over metals for potential use as first wall materials in controlled thermonuclear reactors (CTR's). These advantages are the ability to withstand higher temperatures than the metal systems, decreased plasma contamination that results from wall erosion and cheap availability of material resources. Some of the current designs of CTR's [1,2] propose to use ceramic materials in various parts of the blanket regions as first wall materials and as insulator coatings on metal components. The materials under consideration include silicon carbide, silicon nitride, beryllium oxide, silica, alumina, and yttria.

Tritium permeation rate through ceramic layers in CTR blankets is an important design consideration because of possible problems with environmental release of tritium and with possible buildup of large tritium inventory in the blanket components. Tritium diffusion data necessary for these design calculations is currently lacking. Except for SiO_2, TiO_2 and BeO, few direct measurements of tritium diffusion coefficients in ceramics have been reported in the literature.

In this paper, tritium diffusion coefficients for several ceramic materials of interest for CTR systems are reported. These materials are single crystals of Al_2O_3, BeO and SiC, sintered BeO and Al_2O_3, polycrystalline Y_2O_3, Lucalox, Yttralox, hot-pressed SiC, SCB glass and pyrolytic carbon. The tritium concentrations and measurement temperatures are believed to be in the range of application for CTR designs. The experimental results for pyrolytic carbon are to be considered preliminary.

EXPERIMENTAL METHODS

Tritium diffusion coefficients for the different materials were determined by release rate measurements of recoil injected tritium from samples. Tritium injections were carried out by irradiation in the North Carolina State University Pulstar reactor of samples surrounded by a thick blanket (~16 mg/cm^2) of ^6Li enriched Li_2CO_3. The $^6Li(n,\alpha)^3H$ reaction results in a linear tritium concentration profile in the sample with the concentration going to zero at the maximum recoil range in the sample

(between 20 and 35 μm in the ceramic materials considered in the paper). Most of the samples were irradiated in a neutron flux of 1×10^{11} n/cm^2-sec for 30 minutes, resulting in a tritium recoil into the surface of 1×10^{14} atoms/cm^2. The maximum tritium concentration ranged from 0.03 to 0.09 ppm (wt.) for the different materials.

A gas release system (See Figure 1) was used for all release rate measurements. Helium was purified by use of a titanium O_2 getter and cold trap and then mixed with hydrogen. The hydrogen addition was found necessary to prevent anomalous and irreproducible release measurements. These are believed to be due to tritium absorption on the mullite sample tube. This helium-hydrogen mixture was then swept over the isothermally heated sample and through an ion chamber. The current produced by the tritium in the ion chamber was measured by an electrometer and converted to digital output by an analog to frequency converter. In some measurements, the ion chamber was replaced by a proportional counter with a 90% argon-10% methane sweep gas. Data taken with both systems were in agreement.

As an aid in understanding diffusion results, it is generally desirable to measure concentration profiles. For most ceramic materials, however, sectioning techniques are quite difficult. Pyrolytic carbon is one exception. Pyrolytic carbon coated microspheres were etched, 5 μm at a time, using chromium trioxide and sulfuric acid[3], and aliquots of tritiated water were distilled from the polish solution and liquid scintillation counted. Release measurements and profiles were also made for pyrolytic carbon samples that were exposed to tritium gas. Gas tagging was accomplished by sealing the samples in evacuated ampoules containing irradiated $LiAlO_2$ powder, and heating the ampoules to drive the tritium from the powder and into the carbon.

RESULTS

Method of Data Analysis

Experimental data were gathered from printouts of the electrometer output at specific time intervals (usually 100 sec.). These counts were proportional to the average tritium release during that interval. After the subtraction of background readings, graphs were plotted of cumulative

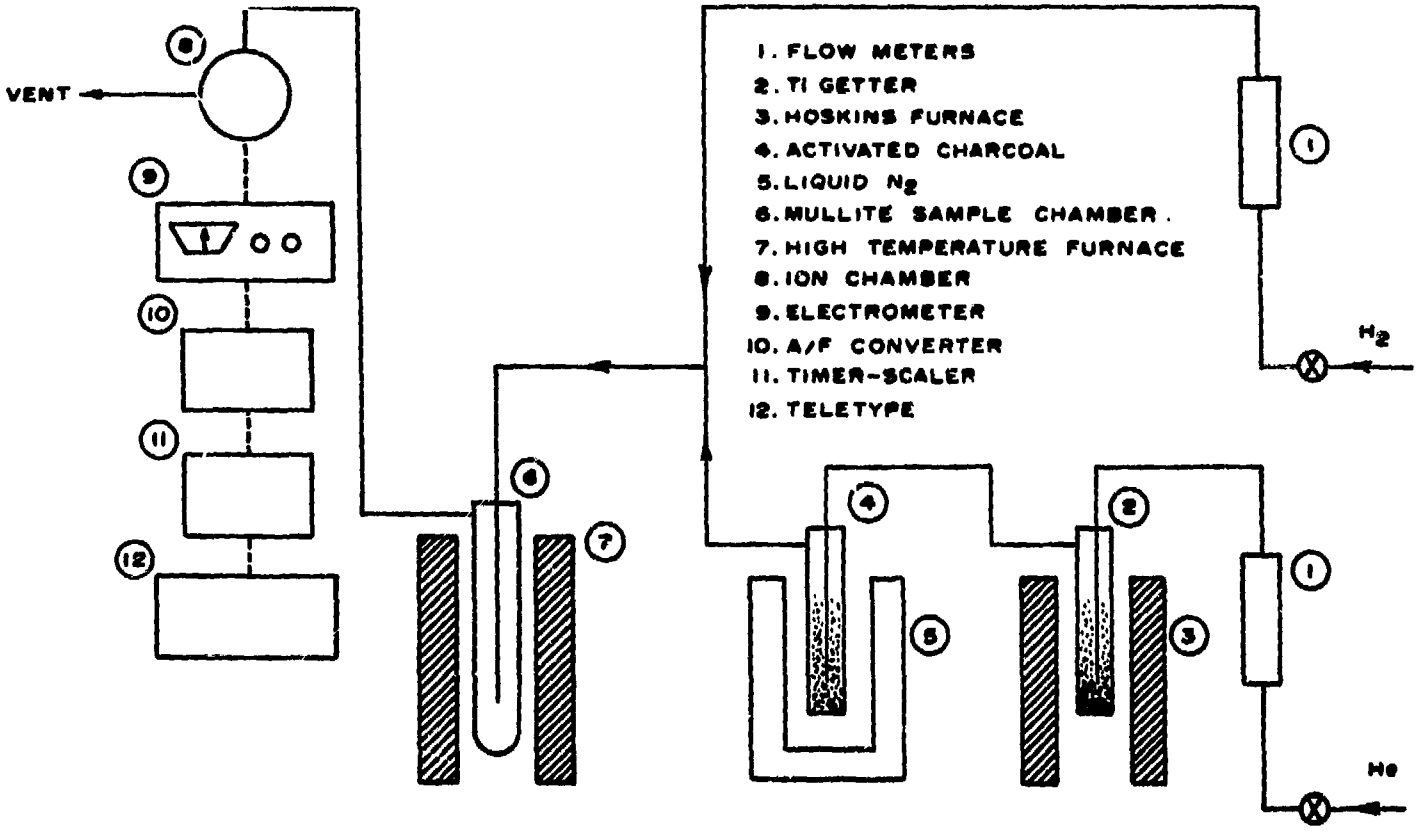

Fig. 1. Gas-release system used for tritium diffusion measurements.

fractional release vs. $(\text{time})^{1/2}$. For one-dimensional diffusion from a plane surface and small fractional releases (<.20), the diffusion coefficient can be determined from the slope of the graph by the relation

$$\text{Slope} = \frac{f}{\sqrt{t}} = \frac{4}{R}\left(\frac{D}{\pi}\right)^{\frac{1}{2}} \qquad (1)$$

where R is the recoil range of tritium in the material.[4] Recoil ranges were calculated by the Bragg-Kleeman rule[5] using the measured 21 micron recoil range in niobium as a reference.

Except for some of the Lucalox results (see below), data analyzed by this method gave unambiguous diffusion coefficients. Arrhenius plots (ln D vs. 1/T) were straight lines over the measured range of diffusion coefficients. Least squares best-fit values of D_o (cm^2/sec) and activation energy Q (kcal/mole) for the expression $D = D_o \exp(-Q/RT)$ were determined from the data and are presented in Table 1.

Alpha-alumina and Lucalox

Single crystal samples of α-alumina were purchased from Union Carbide. The samples were 1.0 cm x 0.5 cm x 0.1 cm with one of the large faces polished at an orientation of approximately ten degrees with respect to the basal plane. Release curves taken over the temperature range studied (Table 1) were in agreement with standard classical diffusion solutions. The diffusion coefficients determined from the release curves are presented in an Arrhenius plot in Figure 2.

Sintered polycrystalline samples of α-alumina with low impurity levels (≤ 50 ppm MgO) and grain sizes of one to six microns were fabricated locally and used in tritium release measurements. The resulting data were analyzed as if the samples had one-dimensional slab geometry. These results are also presented in Figure 2 and Table 1 and are seen to be somewhat higher with a lower activation energy than the single crystal data. If the extreme case of grain boundaries as instantaneously rapid diffusion paths is considered and a model based on four micron diameter spherical particles is applied,[6] the diffusion coefficients listed would be reduced by a multiplicative factor of

TABLE I. Measured tritium diffusion coefficients - least squares best-fit values for $D = D_0 \exp(-Q/RT)$. D_0^+ is upper limit on D_0, D_0^- is lower limit on D_0, and $\sigma(Q)$ is the standard deviation of the activation energy.

Material (S. C. = single crystal)	Number of points	D_0 (cm^2/sec)	D_0^+ (cm^2/sec)	D_0^- (cm^2/sec)	Q (kcal/mole)	σ (Q) (kcal/mole)	Temperature range (°C)
Al_2O_3 S.C.	9	3.26	9.86	1.08	57.2	2.4	600-1000
Al_2O_3 sintered	7	7.35×10^{-2}	0.247	2.19×10^{-2}	43.8	2.5	600-900
BeO S. C.	14	1.11×10^{-2}	8.91×10^{-2}	1.39×10^{-3}	52.5	4.7	650-1200
BeO sintered	11	7.00×10^{-2}	0.445	1.10×10^{-2}	48.5	3.6	500-950
Lucalox	15	39.8	357	4.43	41.8	3.2	360-570
α - SiC S. C.	12	1.09×10^{-2}	2.92×10^{-2}	4.05×10^{-3}	54.9	2.5	700-1300
β - SiC S. C.	10	28.0	172	4.55	65.0	4.1	750-1000
Al-doped α - SiC S. C.	8	4.04×10^{-4}	3.80×10^{-3}	4.29×10^{-5}	34.0	4.2	450-950
Al-doped hot-pressed α - SiC	11	0.904	6.68	0.147	48.2	3.5	500-800
SCB glass	10	2.95×10^{-4}	6.34×10^{-4}	1.37×10^{-4}	30.2	1.2	350-800
Y_2O_3 hot-pressed	8	0.431	7.13	2.6×10^{-2}	39.1	4.3	420-620
Yttralox	6	3.87	32.2	0.464	39.5	3.1	350-600

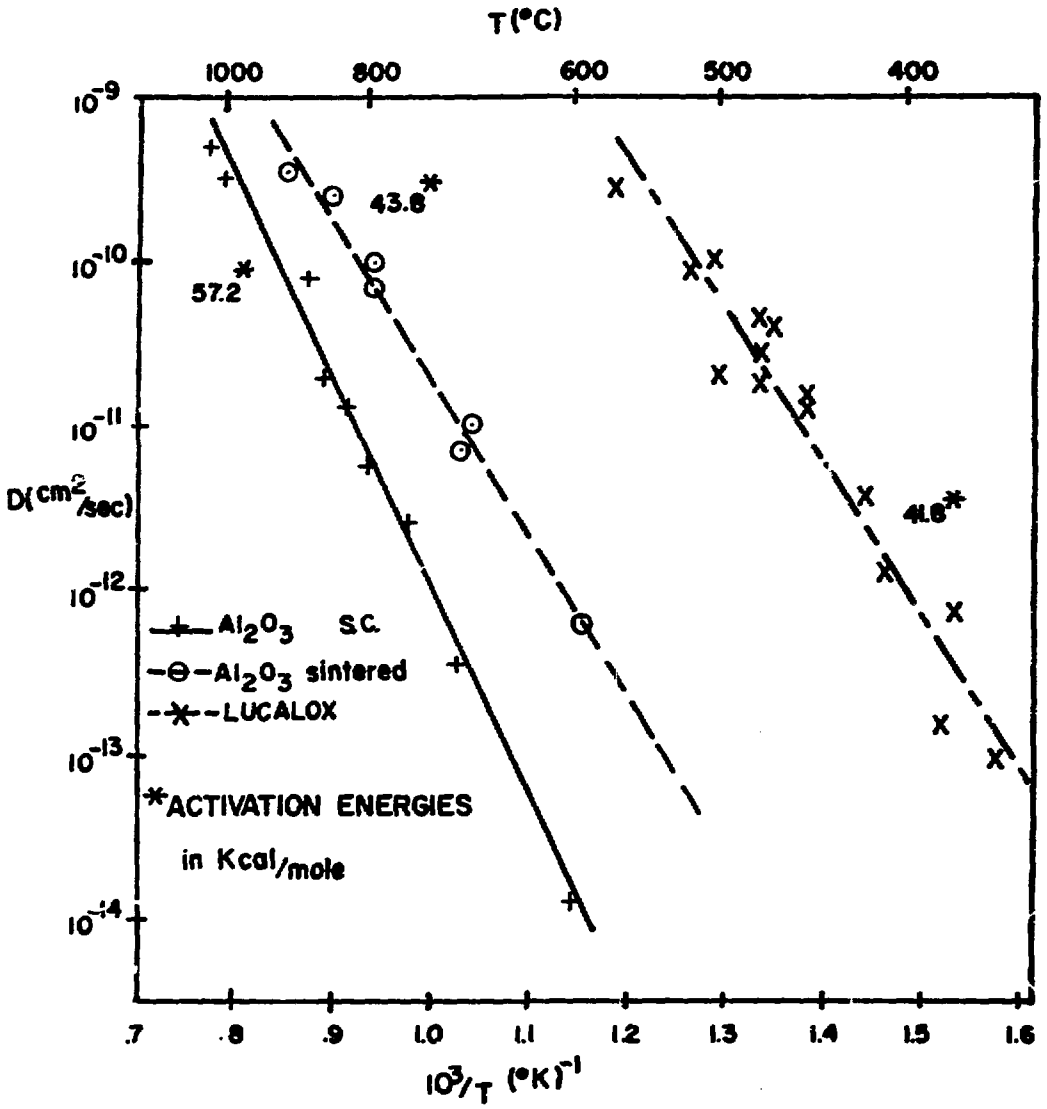

Fig. 2. Arrhenius plot for tritium diffusion in single crystal and sintered alumina and Lucalox.

4.03×10^{-3}. This correction would place them about two orders of magnitude below the single crystal data.

As-fired samples of Lucalox were obtained from the General Electric Company. Analysis of the composition by electron microprobe (Table 2) reveals a small amount of MgO impurity, with some silica appearing near grain boundaries. The nominal grain size was about 30 microns, which is 1.5 times the tritium recoil range, with free grain surfaces appearing slightly rounded and smooth under the scanning electron microscope.

Anomalous diffusion was observed in all five Lucalox samples run at temperatures below 450°C. In these samples, fractional release was linear with $(t)^{1/2}$ for the first 1000 to 2000 seconds, after which the slope sharply increased to another linear relationship. This change in slope occurred at total fractional releases of one to four percent. Diffusion distances corresponding to the change in slope and calculated from the formula $X = 2(Dt)^{1/2}$, ranged from 0.1 to 0.7 micron. Diffusion coefficients obtained from the initial slopes were smaller and had a much higher activation energy (~63kcal/mole) than D's obtained from the second (t>1000 to 2000 sec) slope. The latter values for D agree well with the extended Arrhenius expression obtained at higher temperatures, which is presented in Figure 2 and Table 1. The data for Lucalox show much larger diffusion coefficients than were observed in single crystal or sintered alumina.

In order to investigate the possibility of concentration effects on tritium diffusion, one sample of Lucalox was irradiated to only three percent of the usual tritium concentration. The resulting diffusion coefficient fell within the measurement standard deviation of the other Lucalox samples, indicating that no major tritium concentration effect exists at this level.

Beryllium Oxide

Single crystal samples of beryllium oxide were provided by [illegible] Laboratories. Two of the samples had been sliced and etched in molten salt to remove cutting marks, and two were as-grown crystals about 5 mm in diameter. One of the sliced samples was analyzed by the

TABLE II. Characterization of materials.

Material	Composition or Impurities
Lucalox[a, c]	Al_2O_3, 99.8%; MgO, 0.2%. Si, 0.5% near grain boundaries.
BeO[b] sintered	Mg, 0.2%; Si, 0.32%.
BeO S. C.[a,d]	no measurable impurities.
Al-doped α - SiC S.C.[a,e]	Al, 0.6%.
Al-doped α- SiC hot-pressed[b,f]	Al, 1%.
α - SiC[a,e]	small amount of oxygen.
β - SiC[a]	no measurable impurities.
Yttralox[b,c]	Y_2O_3, 89%; ThO_2, 10%; Nd_2O_3, 1%.
SCB glass[b,d]	SiO_2, 46.1%; BaO, 31.3%; Al_2O_3, 8.3%; TiO_2, 12.5%; Cr_2O_3, 1.0%; Eu_2O_3, 0.8%.

[a]by electron microprobe

[b]by supplier

[c]supplied by General Electric Company.

[d]supplied by Rockwell International.

[e]supplied by Carborundum.

[f]supplied by The Norton Company.

electron microprobe and no measurable impurities were found. The limit of detectability ranges from 0.01 to 0.05 percent, depending on impurity species, so this technique is suitable only for major impurity levels. Diffusion results for single crystal and sintered BeO are listed in Table 1 and are shown in Figure 3.

Sintered samples of beryllium oxide were obtained from the Brush-Wellman Company. Grain size was listed as 5 to 15 microns. Major impurities as listed by the manufacturer are presented in Table 2 and electron microprobe analysis gave similar impurity levels. Data for these samples have been corrected for a specific surface area of 0.11 m^2/g, determined by BET surface area measurement. Inspection of Figure 3 and Table 1 reveals that the sintered specimens had higher diffusion coefficients than the single crystals.

As with sintered alumina samples, the question of enhancement of diffusion by rapid movement of tritium along grain boundaries arises. Several of the sintered BeO samples were quenched in liquid nitrogen after irradiation but prior to diffusion measurements. The diffusion coefficients taken from these samples were about an order of magnitude higher than those obtained from unquenched samples. This was attributed to enhanced diffusion along cracked grain boundaries and the data were discarded. One fresh sample was annealed prior to irradiation in a helium atmosphere at 1500°C for 12 hours. The diffusion result for this sample was identical to results from unannealed samples, indicating that prior annealing has a negligible effect on the results.

Yttria and Yttralox

Samples of hot-pressed yttria fabricated from powder of 99.99 percent purity were obtained from the Ceradyne Company. The quoted grain size was 30 microns, which is somewhat larger than the recoil range of tritium in yttria.

Yttralox, a material which is about 90 percent yttria, was obtained from the General Electric Company. Composition, as listed by the supplier, is shown in Table 2. The samples were optically clear, with specularly reflecting surfaces. Tritium diffusion results, which are presented in

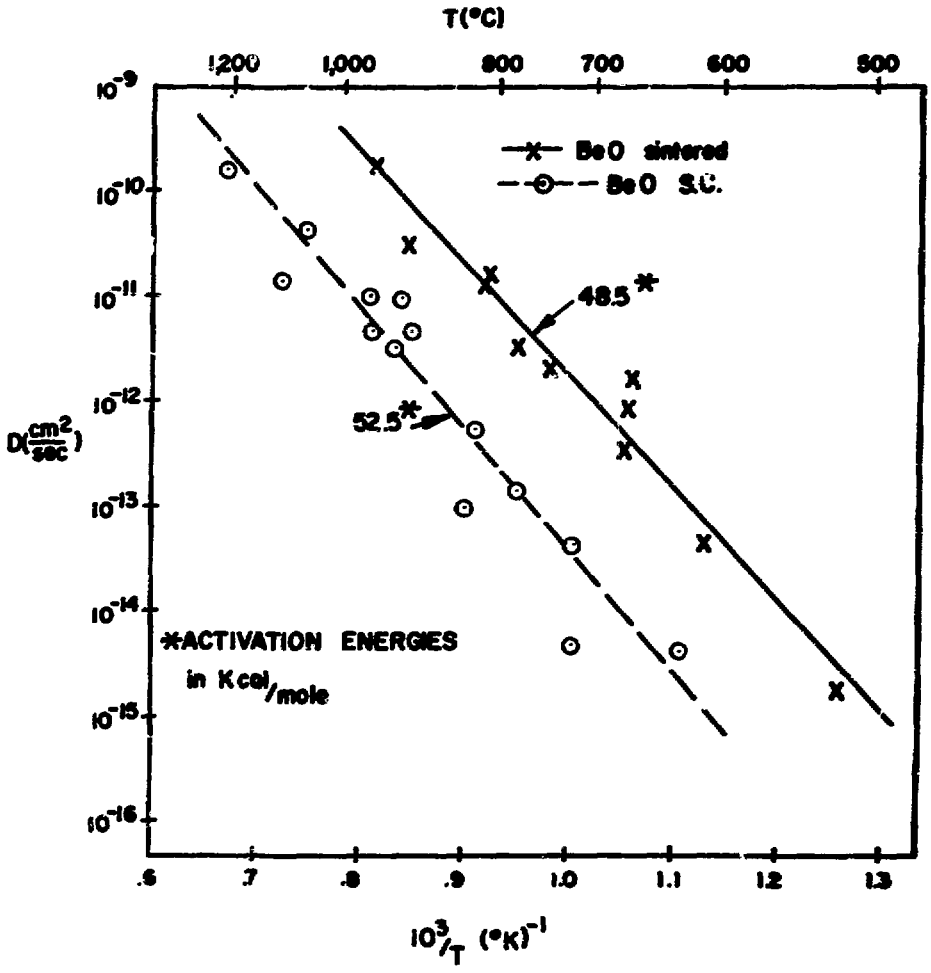

Fig. 3. Arrhenius plot for tritium diffusion in single crystal and sintered beryllia.

Figure 4 and Table 1, show a close similarity between yttria and Yttralox.

SCB Glass

Samples of SCB glass approximately 85 microns thick coated on Hastelloy X substrates were supplied by Atomics International. This glass was developed as a hydrogen permeation barrier for the SNAP reactor program. The composition is listed in Table 2, and the tritium release results are presented in Figure 4 and Table 1. After anneals for several hours above 820°C, the sample color changed from light green to black. This color change is apparently due to reduction of the TiO_2 constituent by the hydrogen component of the sweep gas.[7]

Silicon Carbide

Several samples of silicon carbide were obtained for this study, as follows: (a) Single crystals of α-silicon carbide with flat surfaces approximately 0.5cm^2 in area were obtained from Carborundum. These samples were believed to be very pure, with the major impurity being aluminum at about 50 ppm. (b) A large piece of as-grown α-silicon carbide with numerous single crystal pieces grown on the surface was supplied from Carborundum. The single crystals, which had smooth surfaces of the order of 0.5cm^2, were removed from the large piece by fracturing. The stated purity was 99.0 percent, but electron microprobe analysis yielded an oxygen impurity of several percent. Because of the inefficiency of the electron microprobe for detecting low atomic weight elements, the exact amount of oxygen is not known. (c) A large piece of as-grown α-silicon carbide similar to the one just described but black instead of green was also obtained from Carborundum. This was nominally listed as being 98.6 percent pure. The electron microprobe analysis of a sample of this material showed 0.6 percent aluminum impurity. This material is subsequently referred to as aluminum-doped single crystal silicon carbide. (d) Samples of hot-pressed α-silicon carbide with 1.0 percent nominal aluminum impurity were obtained from the Norton Company. These samples will be referred to as aluminum-doped hot-pressed silicon carbide. (e) Two different sets of small single crystals of β-silicon carbide were obtained locally. No history is avail-

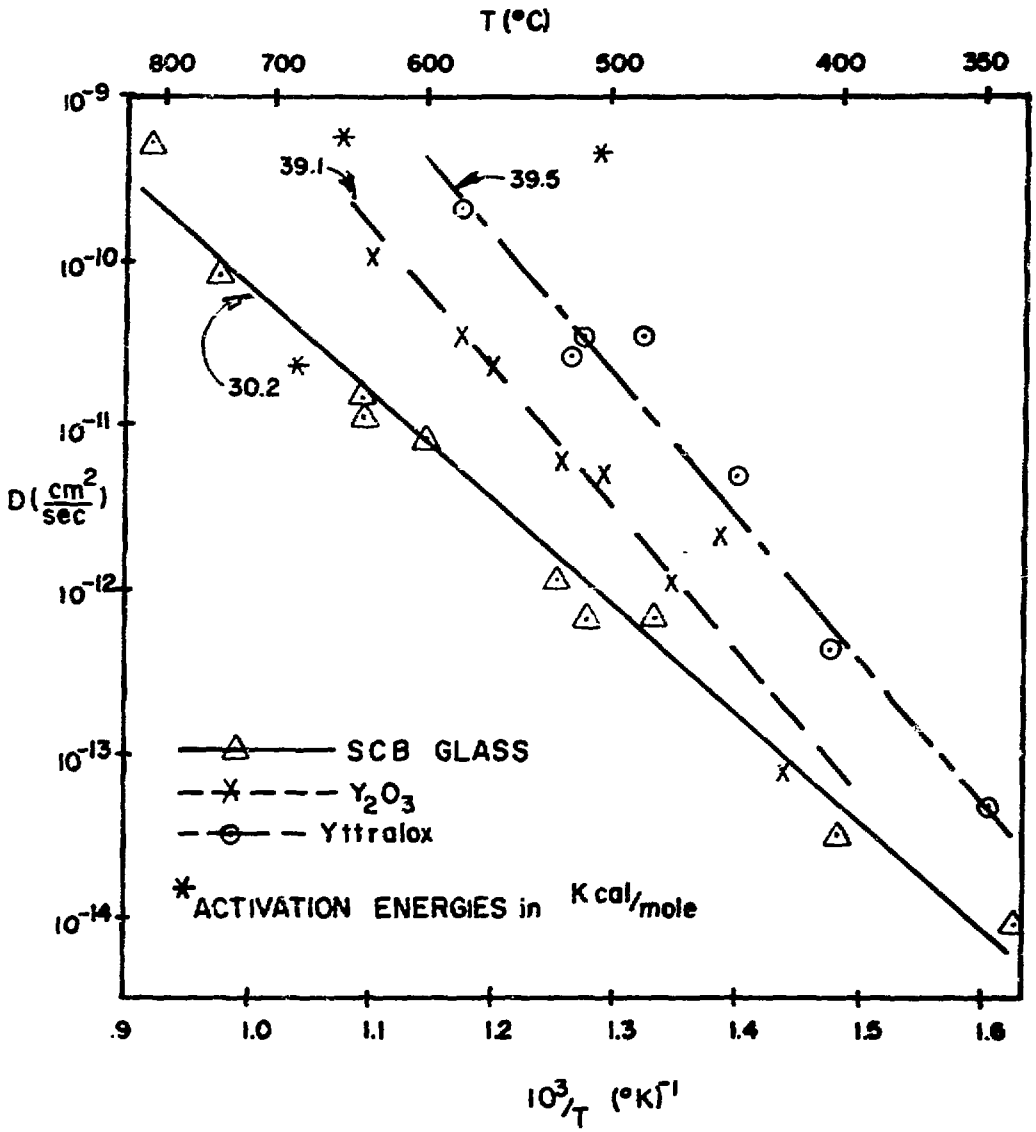

Fig. 4. Arrhenius plot for tritium diffusion in SCB glass, yttria, and Yttralox.

able for these samples. Electron microprobe analysis of these samples showed no measurable impurities. It is estimated that the level of detectability of impurities is 0.01 to 0.05 percent.

The results for the silicon carbides are presented in Figure 5 and in Table 1. Surprisingly, types (a) and (b) (see above) gave identical diffusion coefficients and are listed together as "S. C. α-silicon carbide." Similarly, results for both lots of β-silicon carbide were identical, and these are listed together. Over the temperature range measured, the results for both of the Al-doped materials were in fairly close agreement, but they are listed separately since least-squares values of D_o and activation energy differed somewhat for these two materials.

Pyrolytic Carbon

Initial research for pyrolytic carbon was concentrated on release rate measurements for recoil injected pyrolytic carbon microspheres. These samples, supplied by General Atomic Corporation, consisted of a 150 μm LTI pyrolytic carbon coating on a 550μm diameter ZrO_2 substrate. The coatings are similar to those used on coated fuel particles for HTGR reactors. It was noticed that the tritium release rate was dependent on the partial pressure of hydrogen in the sweep gas, the release rate increasing as the hydrogen partial pressure increased. Figure 6 shows two separate Arrhenius relationships for pyrolytic carbon, one for experimental runs in pure helium, the other in a 10% hydrogen-90% helium atmosphere.

Chemical sectioning was used to determine tritium profiles for samples before and after annealing (See Figure 7). Profiles for samples before annealing showed agreement between calculated and observed tritium recoil ranges. The tritium profiles for recoil injected samples annealed for different times and temperatures in the absence of hydrogen closely resembled results expected from classical diffusion. Those annealed in the presence of hydrogen at lower temperatures showed the outer region to be depleted of tritium with the inner portion virtually undisturbed. Profiles were also measured for samples that were impregnated with tritium by exposure to $^3H_2$ gas at different temperatures (see Figure 8). These

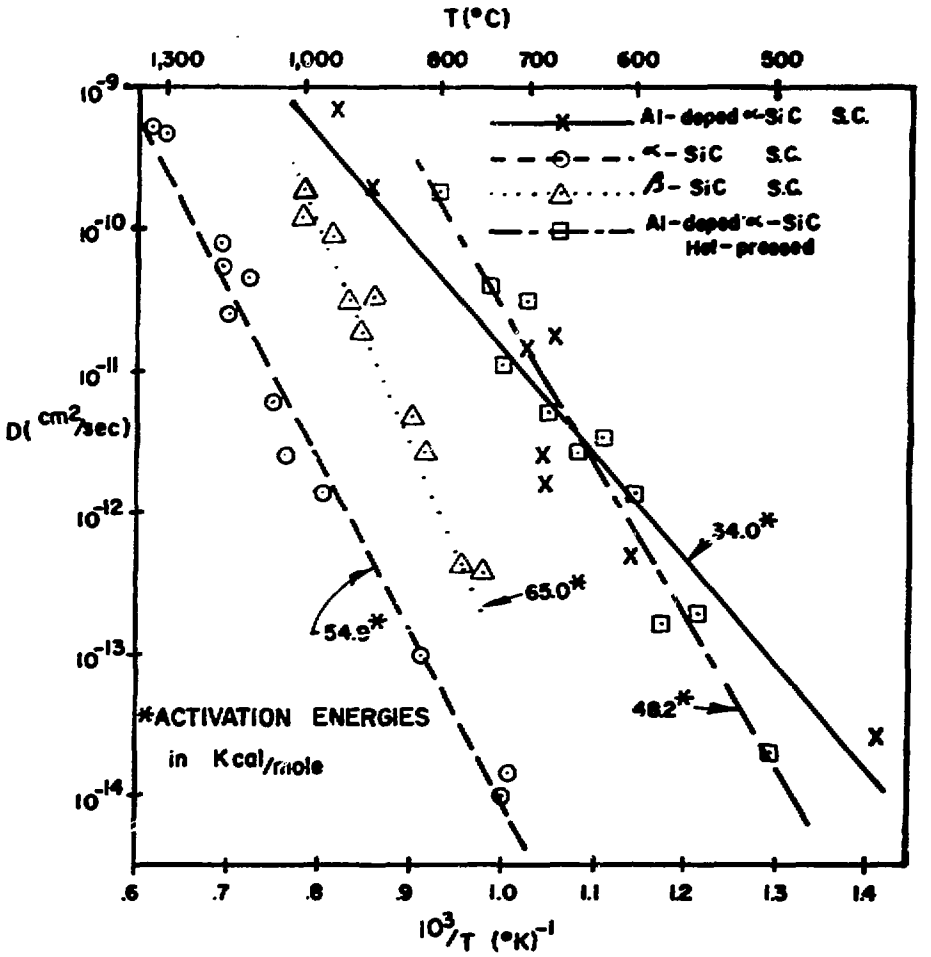

Fig. 5. Arrhenius plot for tritium diffusion in α- and β-silicon carbide single crystals, aluminum-doped single crystal α-silicon carbide, and aluminum-doped hot-pressed α-silicon carbide.

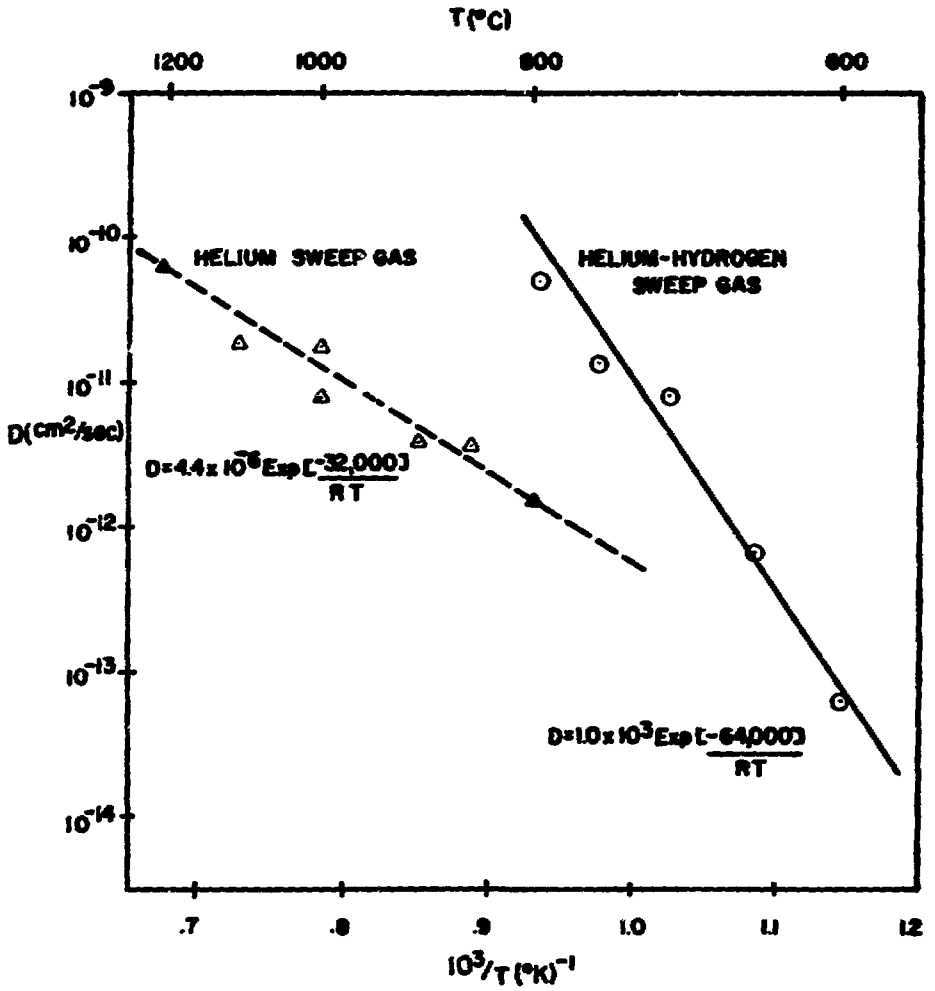

Fig. 6. Arrhenius plots for tritium diffusion in LTI pyrolytic carbon.

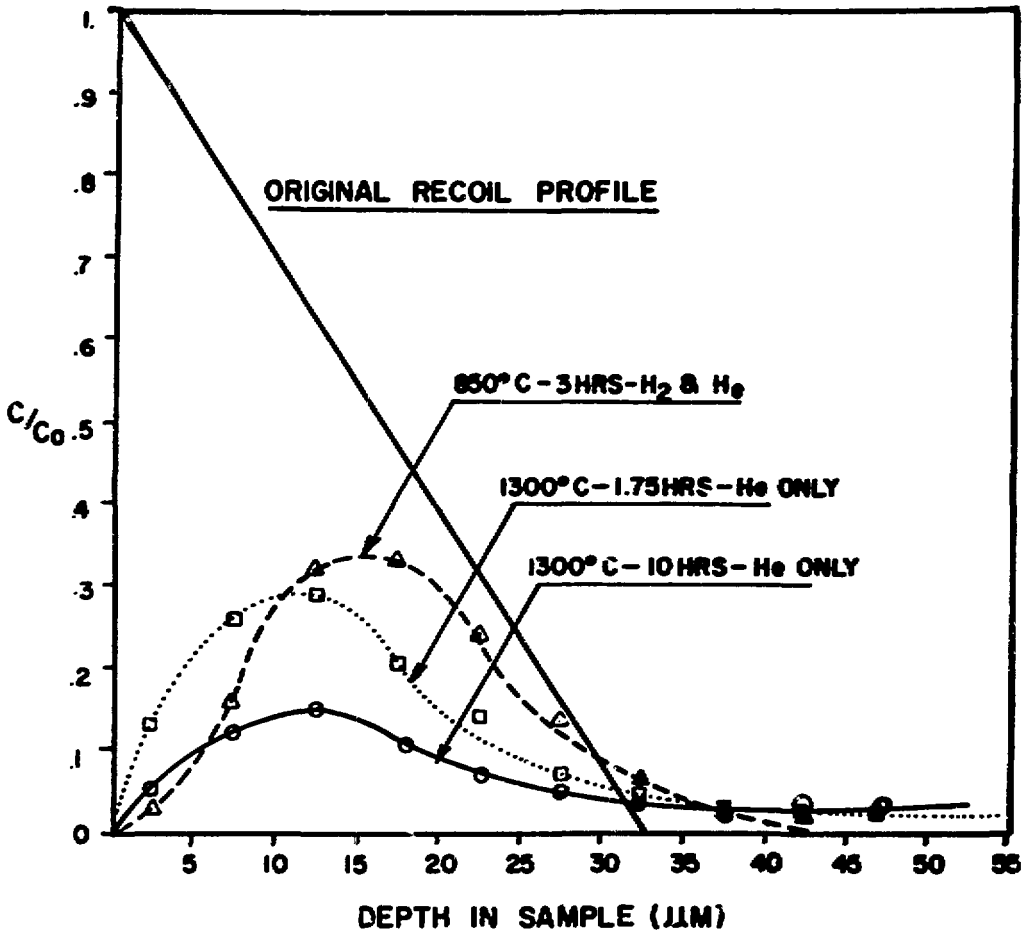

Fig. 7. Tritium profiles in recoil injected pyrolytic carbon after annealing.

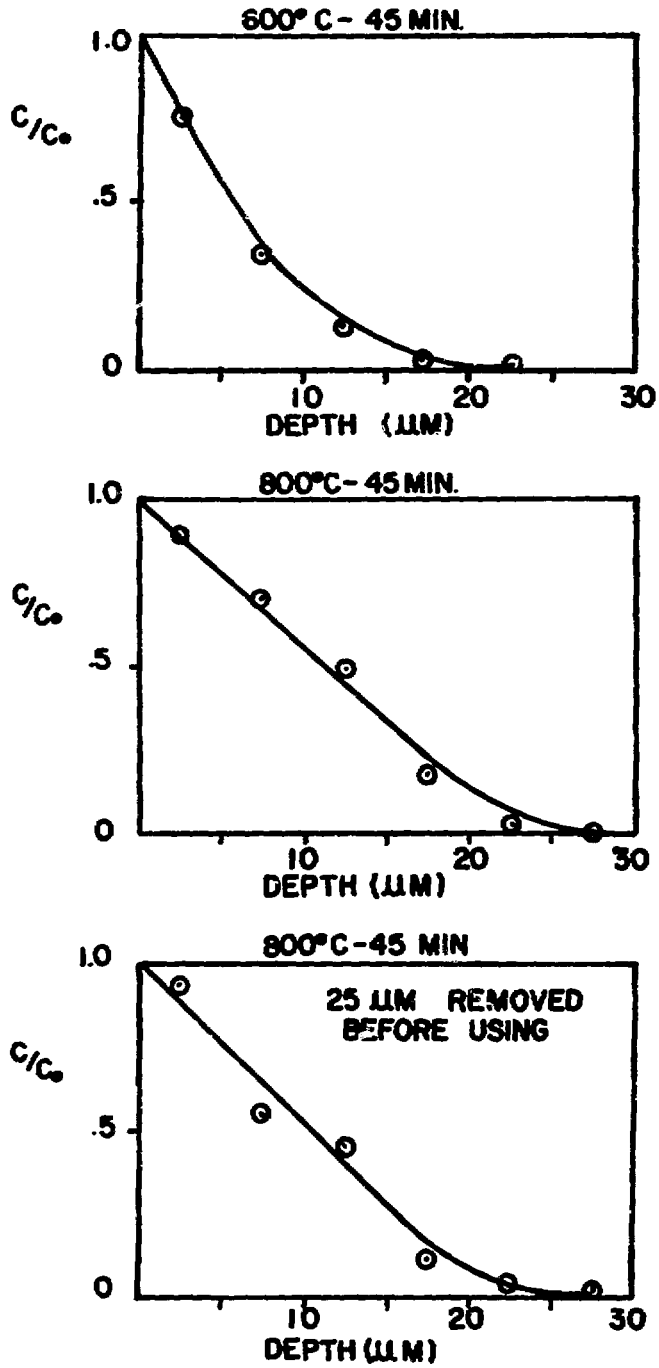

Fig. 8. Tritium profiles for pyrolytic carbon after gas tagging at different temperatures.

profiles showed that tritium diffused rapidly inward at all temperatures above 600°C to approximately 25 μm with only very slow penetration to greater depth. The same experiment performed after the first 25 μm were removed from the particles gave similar results.

DISCUSSION

Diffusion coefficients measured in this study are smaller and activation energies much larger than those usually observed for metals at similar temperatures. Other measurements made on ceramics have given similar results.[9,10]

BeO

Scott and Wassell[9] measured activation energies of 49 to 60 kcal/mole in single crystal and powdered samples of beryllia. Our results agree substantially with their findings for single crystals but are about three orders of magnitude larger than their results for powders. In their experiment tritium was produced by fast-neutron transmutation of ^{9}Be, which involved irradiation fluences nearly 10^{6} greater than in our work.

A possible explanation of the discrepancy which they found between powders and single crystals is that in powders with radii of several hundred lattice constants, tritium would likely diffuse out atomically, whereas in bulk materials tritium atoms might combine to form molecules before reaching the surface. A simple random walk calculation based on the concentrations in our samples indicates that tritium atoms are likely to come within first neighbor distances of other tritium atoms before reaching the surface. Since molecular tritium would be influenced to a much smaller extent by lattice electrostatic forces and chemical bonding than the atomic form, the jump frequency might be increased, resulting in a higher diffusion coefficient for the molecular species.

Scott and Wassell also found that during postirradiation anneal some of the tritium left the samples as water vapor, contrary to our findings. For some of our measurements with beryllia, single crystal alumina, and alumina powder, a liquid nitrogen cold trap was inserted between the sample heating tube and the detector, but essentially no tritium was found to be trapped in the cold trap.

A BET surface area measurement was made on the sintered beryllia used in our experiments, but the diffusion coefficients in sintered samples were more than an order of magnitude higher than in single crystals even after this correction was applied. This might be due to rapid diffusion in the sintered samples or to an impurity effect (see below) since the sintered samples contained greater amounts of impurities than the single crystal specimens.

If fast diffusion does occur along grain boundaries, a more accurate description of release would be given by the uniform sphere model discussed above. Using a sphere diameter of ten microns, which is the average grain size in the sintered samples, the diffusion coefficients for the sintered data listed in Figure 3 and Table 1 would be reduced by a multiplicative factor of 6×10^{-2}. This correction would place the sintered and single crystal data in almost complete agreement.

Al_2O_3

Results for single crystal alumina fall about a factor of ten below the results of Roberts and Roberts[10] when extended to the temperature range 1400 - 1630°C. Considering the large temperature extrapolation and the fact that their sample purities were in the 99.5 to 99.9 percent range, this agreement appears satisfactory. A comparison between the results for Al_2O_3 and Lucalox is presented in a later section.

SCB Glass

Activation energies for hydrogen isotope diffusion measured in glasses usually range from eight to thirteen kcal/mole, depending on composition.[11] The more highly doped glasses usually have higher activation energies. These measurements often are taken from permeation studies and likely involve molecular diffusion. Matzke,[12] on the other hand, obtained much higher activation energies of 42 to 52 kcal/mole for ion-injected tritium using 40 keV ions to a dose of 4×10^{14} ions/cm^2. These unusually large activation energies were attributed to the existence of radiation damage during ion bombardment and the possibility of ionic or atomic diffusion following ion bombardment.

SCB glass was developed originally as a hydrogen barrier for SNAP ZrH reactors. A permeation activation energy for hydrogen has been measured as 30 kcal/mole[7] which agrees with our tritium diffusion activation energy. It has been found that hydrogen solubility is not a strong function of temperature in glasses,[11] and therefore permeation and diffusion activation energies should be similar.

The high activation energy for this glass therefore does not appear to reflect trapping effects which resulted from the energetic introduction of the tritium atoms.

Pyrolytic Carbon

One possible explanation for the anomalous results for pyrolytic carbon is that the microspheres have pores throughout the coatings with a maximum pore length connecting with the surface of approximately 25μm. Research performed at General Atomic Corporation[13] on microscopic studies of pyrolytic carbon appears to confirm this explanation. The existence of these pores is supported by the data showing that $^3H_2$ gas diffuses the same distance inward regardless of the temperature. The rapid release of tritium from the outer region of the recoil injected samples in the hydrogen-helium atmosphere is also consistent with this hypothesis as hydrogen from the sweep gas may rapidly diffuse into the pores and release tritium from the pore surfaces by isotope exchange. From the high temperatures necessary (above 700°C) to obtain measureable tritium release from the recoil injected samples in pure helium, it would appear that tritium atoms become chemisorbed on the pore surfaces. High temperatures were also necessary to release tritium in pure helium from samples that were gas tagged by tritium gas.

It should be pointed out that the Arrhenius relationships in Figure 6 are based on classical diffusion models but may not represent true diffusion coefficients for tritium in pyrolytic carbon. However, it is a convenient way at present to compare tritium release rates under the different experimental conditions.

Impurity Effects

One striking result of the present investigation has been the apparent sensitivity of tritium diffusion coefficients to small amounts of heterovalent impurities (alumina vs. Lucalox, silicon carbide vs. Al-doped silicon carbide). A similar effect has been observed for defect diffusion in alumina,[14,15] boron diffusion in silicon carbide,[16] hydrogen diffusion in rutile,[17] cation self-diffusion in beryllia,[18] and nickel in defective spinels.[19] Several theoretical papers have been published on the effects of impurities and charge-compensating defects on diffusion properties.[20,21,22]

That tritium diffusion exhibits such an effect is an indication that tritium motion is associated at least partly with a lattice defect mechanism in materials.

It should be emphasized that the enhanced diffusion observed in Lucalox and doped silicon carbide cannot be due to rapid diffusion along grain boundaries since the grain size in Lucalox is 1.5 times the tritium recoil range, and some of the silicon carbide samples were large single crystals.

The tritium itself represents an impurity in the lattice which could give rise to an impurity effect. However, in the concentrations used in this study, tritium was not the major impurity in any of the materials. Diffusion coefficients for Lucalox were not affected by lowering tritium concentrations a factor of 30, so no H_2 concentration effect on diffusion appears to exist over this concentration range. Further evidence of no concentration effect is given by long-time diffusion anneals which gave a good fit to the expected behavior for concentration-independent diffusion coefficients.[4]

Chemical Bonding

A possible explanation for the high activation energies in ceramic oxides might be the formation of hydroxyl groups by the recoiled tritium atoms. This has been observed in IR absorption spectra of proton and deuteron-bombarded alumina.[23] We have obtained IR absorption spectra of

several alumina and beryllia samples with recoiled tritium (10^{14} ions/cm^2) and some samples which had been annealed for several hours in the sweep gas (90 percent helium-10 percent hydrogen). No hydroxyl formation has yet been observed. However, detectability thresholds have not yet been established, and the measurements will be continued at higher recoil densities and annealing pressures.

The possibility of hydrogen reaction effects in silicon carbide cannot be neglected, as evidenced by the face that hydrogen etches silicon carbide appreciably at temperatures near the highest used in this study.[24]

CONCLUSIONS

1. Except for PYC and Lucalox, tritium release curves agree with classical diffusion solutions Diffusion measurements in pyrolytic carbon appear to be complicated by sorption processes on the carbon.

2. Results are in fair to good agreement with those of other workers in those few cases where comparison is possible.

3. Tritium diffusion coefficients are considerably lower than in metals at equivalent temperatures. Ceramic materials, therefore, appear to be promising candidates for tritium barriers in CTR blankets.

4. Tritium diffusion activation energies, which are higher than the values typically observed for metals, lie in the range 30-65 kcal/mole.

5. The addition of small amounts of heterovalent impurities appears to significantly increase measured diffusion coefficients.

6. Diffusion release of tritium from single crystals is smaller than release from sintered or hot-pressed materials, implying some enhanced mobility along grain boundaries.

7. Tritium was not detected as water vapor in the release stream, implying release as hydrogen gas and not the oxide.

8. At 700°C, diffusion coefficients for the materials used in this study span a range of 6 orders of magnitude.

ACKNOWLEDGMENTS

The authors express appreciation to the following people who furnished materials for this project: S. B. Austerman, Rockwell International (single crystal beryllia); J. H. Walter, Atomics International (SCB glass); C. Greskovich, General Electric (Lucalox and Yttralox); R. Alliegro, Norton Company (Hot Pressed Silicon Carbide); and J. L. Kaae, General Atomic Corporation (Pyrolytic Carbon).

REFERENCES

1. R. A. Krakowski et. al. ERDA Report No. LA-5336 (1974).
2. General Atomics Corp., Personal Communication.
3. J. Engelhard, Report No. JUL-752-RG (1971).
4. G. DiCola and H. Matzke, Nucl. Instr. and Meth. 57, 341 (1967).
5. R. Evans, The Atomic Nucleus, p. 652, McGraw-Hill, New York, 1955.
6. T. Lagerwall and K. E. Zimen, EURAEC Rept. No. 772 (1964).
7. Personal communication with J. Walter, Atomics International.
8. Y. Adda and J. Philbert, La Diffusion dans les Solides, vol. 2, pp. 1143-1203, Presses Universitaires de France, Paris, 1966.
9. K. T. Scott and L. L. Wassell, Proc. Brit. Ceram. Soc.7, 375 (1967).
10. E. W. Roberts and J. P. Roberts, Bull. Soc. Fr. Ceram. 77, 3 (1967).
11. R. Doremus, Glass Science, Chap. 8, John Wiley, New York, 1973.
12. Hj. Matzke, Z. Naturforschg. 22a, 965 (1967).
13. J. L. Kaae, Carbon 13, 55 (1975).
14. T. P. Jones, R. L. Coble and C. J. Mogab, J. Am. Ceram.Soc. 52, 331 (1969).
15. K. Kitazawa and R. L. Coble, J. Am. Ceram. Soc. 57, 250 (1974).
16. E. N. Mokhov, S. K. Koprov, and Y. A. Vodakov, Sov. Phys.-S.C. 13, 3120 (1972).
17. O. W. Johnson, S. H. Paek, and J. W. DeFord, J. Appl. Phys. 46, 1026 (1975).
18. S. B. Austerman, J. Nucl. Mat. 14, 248 (1964).
19. G. Yamaguchi, M. Nalsano, and M. Tosaki, Bull. Chem. Soc. Japan 42, 2801 (1969).
20. J. W. DeFord and O. W. Johnson, J. Appl. Phys. 46, 1013 (1975).
21. M. D. Feit, J. L. Mitchell, and D. Lazarus, Phys. Rev. B8, 1715(1973).

22. J. L. Mitchell and D. Lazarus, Phys. Rev. B 12, 734 (1975).

23. D. M. Gruen, R. B. Wright, R. L. McBeth, and I. Sheft, J. Chem. Phys. 62, 1192 (1975).

24. M. Kumagawa, H. Kuwabara, and S. Yamada, Japan J. Appl. Phys. 8, 421 (1969).

AUTHOR INDEX